Brigham Young University
BYU ScholarsArchive

Theses and Dissertations

2020-04-28

Thin Film Deposition on Powder Substrates using ALD and its Characterization using XPS, TEM, and SE

Dhruv Shah
Brigham Young University

Follow this and additional works at: https://scholarsarchive.byu.edu/etd

Part of the Physical Sciences and Mathematics Commons

BYU ScholarsArchive Citation
Shah, Dhruv, "Thin Film Deposition on Powder Substrates using ALD and its Characterization using XPS, TEM, and SE" (2020). *Theses and Dissertations*. 8990.
https://scholarsarchive.byu.edu/etd/8990

This Dissertation is brought to you for free and open access by BYU ScholarsArchive. It has been accepted for inclusion in Theses and Dissertations by an authorized administrator of BYU ScholarsArchive. For more information, please contact ellen_amatangelo@byu.edu.

المنارة للاستشارات

www.manaraa.com

Thin Film Deposition on Powder Substrates Using ALD

and Its Characterization Using XPS, TEM and SE

Dhruv Shah

A dissertation submitted to the faculty of
Brigham Young University
in partial fulfillment of the requirements for the degree of

Doctor of Philosophy

Matthew R. Linford, Chair
David V. Dearden
Jaron C. Hansen
Barry M. Lunt

Department of Chemistry and Biochemistry

Brigham Young University

Copyright © 2020 Dhruv Shah

All Rights Reserved

المنارة للاستشارات

www.manaraa.com

ABSTRACT

Thin Film Deposition on Powder Substrates Using ALD
and Its Characterization Using XPS, TEM and SE

Dhruv Shah
Department of Chemistry and Biochemistry, BYU
Doctor of Philosophy

The major part of my dissertation consists of thin films deposited using atomic layer deposition on flat and powder substrates. It details the various optimization experiments for process parameters like dose time, purge time, temperature, and pressure on silicon shards and powder substrates. Spectroscopic ellipsometry (SE) was used to characterize these films over a wide wavelength range (191-1688 nm). An optical model with a BEMA (Bruggeman effective medium approximation) layer was used to fit the ellipsometric data to investigate the optical properties of the alumina surface. The optimized process parameters on the flat surfaces were used for coating powder substrates. I propose a set of experiments to optimize the conditions for coating of powders and high aspect ratio structures by atomic layer deposition (ALD). The coated powders were analyzed by surface analytical techniques like X-ray photoelectron spectroscopy, spectroscopic ellipsometry, transmission electron microscopy, energy X-ray dispersive spectroscopy (EDAX), and BET.

The first chapter introduces the technique of atomic layer deposition, and details its advantages and limitations over conventional thin film deposition techniques like chemical vapor deposition and physical vapor deposition. The second chapter details the initial deposition experiments performed on flat surfaces and characterization of thin films using surface analytical tools. I conducted multi-sample analysis on eleven different thin films for calculation of optical constants of alumina. The third chapter introduces thin film deposition experiments performed on powder substrates, several challenges associated with achieving conformal thin films and characterization. The fourth chapter details the experiments to achieve unilateral ALD achieved on one side of the substrates. The fifth chapter details various unconventional materials including liquid water, Coca-Cola, a coffee bean, nitrogen gas, human tooth, and printed office paper, which were analyzed by near ambient pressure XPS (NAP-XPS).

This dissertation contains appendices of other tutorial articles I wrote on obtaining optical constants liquid samples using spectroscopic ellipsometry, and good experimental techniques for maintenance of vacuum equipment.

Keywords: ALD, Alumina, powder coating, XPS, ESCA, TMA, spectroscopic ellipsometry, optical model, MSA, Sellmeier, GPC, TEM, SEM, BET

المنارة للاستشارات
www.manaraa.com

ACKNOWLEDGEMENTS

I started as a graduate student at BYU in the fall 2016 semester, and it would not have turned into a successful one without the contribution of numerous people around me. I would like to convey my greatest gratitude to my advisor Dr. Matthew R. Linford for his constant support, enthusiasm and guidance. He is a great motivator, mentor, realist and because of him, that I had the opportunity to collaborate with great scientists around the world. I would also like to thank my committee members: Drs. Jaron C. Hansen, David V. Dearden, and Barry M. Lunt for their valuable suggestions throughout my graduate studies. I would like to thank Dr. David J. Michaelis for being a part of the committee.

The major part of this work was performed in association with applications engineers at Kurt J. Lesker (PA, USA). While many people at Lesker have provided their valuable insights to this project, I am indebted to Dr. G. Bruce Rayner and Noel O'Toole. I would also like to especially thank Duane Bingaman for providing financial assistance and travel assistantship during my Ph.D. tenure at BYU. I also had the opportunity to work with some excellent surface analysts, notably, James N. Hilfiker (J.A. Woollam Company, NE, USA), and Paul Dietrich of SPECS GmbH (Berlin, Germany). I wrote numerous publications with them, and I appreciate their timely feedback while writing them. I would especially like to thank James, as he helped us in numerous projects and publications.

At BYU, I met many helpful and generous people. I would like to thank the administrative staff of the Department of Chemistry and Biochemistry for their financial support. A special thanks for the Roland K. Robbins scholarship for the year 2019-2020 as it helped me focus on finishing work and writing dissertation. I would like to give my special thanks to Janet Fonoimoana for being very helpful during the first two years of my stay here at BYU. I would also

المنارة للاستشارات
www.manaraa.com

like to acknowledge the help of Anna Kennington, Amy Cetz, and Sue Mortensen. I would also like to help Mike standing and Paul Minson for help during SEM and TEM analysis and data collection.

It has been an enlarging experience to share the lab with wonderful group of people from various parts of the world. I would like to acknowledge my friends and lab mates; Dhananjay I. Patel (DJ), Tahereh G. Avval, and George Major. Furthermore, special thanks go to Dr. Brian Johnson, Dr. Tuhin Roychowdhury, Dr. Varun Jain, and Dr. Cody V. Cushman for mentoring me during my first years of graduate school. I would like to thank fellow graduate students Parag Gajjar, Mukul Sonker, Basu Aryal, and Nitish Bhardwaj. Two people, Anubhav Diwan and Pankaj Aggarwal deserve special mention, as they were instrumental during the process of me joining BYU. It would have been difficult to deal with stress and burdens of graduate life without their fun talks and incessant enthusiasm.

A special thanks to Dylan Jacobsen, Jacob Erickson, James O'Tani, and Collin Jacobsen who have worked with me for various projects. They entered the labs as undergraduate students, became friends and have helped me a lot during the completion of my work at BYU. I wish them all good luck in their future careers.

One of the most difficult part of this wonderful journey has been to live away from my family. I would like to pay indebt acknowledgment to my parents, Mrs. Promila Shah and Mr. B. H. Shah, and my younger brother, Paras Shah, for their constant love and support during all these years. I always save the best for last, and this journey could not have been complete without the love and support of my wife, Dr. Priya Vadi Shah. She has provided me the strength and worked with me for the last two months in completing this dissertation. It would have been difficult

المنارة للاستشارات
www.manaraa.com

to finish here at BYU, and plan for the move to the next job without her love and support. A special shout-out to the Vancouver contingent, they have been supportive throughout the years.

I would like to god for all the gifts and blessing it has bestowed upon me during graduate school. I hope that my small contribution to the field of surface science would benefit the community. I would like to dedicate my dissertation to my family. It has been a long but fulfilling journey and I will continue to work in the field. I dedicate my dissertation to my family members who have helped me throughout the process.

المنارة للاستشارات
www.manaraa.com

TABLE OF CONTENTS

Title i
ABSTRACT ii
ACKNOWLEDGEMENTS iii
TABLE OF CONTENTS vi
LIST OF ABBREVIATIONS xiii
LIST OF FIGURES xv
LIST OF TABLES xxv
CHAPTER 1: Introduction to atomic layer deposition (ALD), X-ray photoelectron spectroscopy (XPS), and surface analysis 1
1.1 Atomic layer deposition (ALD) 3
1.1.1 Principles of atomic layer deposition 3
1.1.2 Deposition of oxide films using ALD 5
1.1.3 Deposition of other miscellaneous films using ALD 6
1.2 Particle coating by ALD 8
1.2.1 Challenges in powder coating 8
1.2.2 Reactors for coating powder substrates 11
1.2.3 Applications of ALD-coated particles 14
1.3 Area-selective atomic layer deposition (AS-ALD) 17
1.3.1 Literature examples of AS-ALD 17
1.3.2 Challenges of area-selective atomic layer deposition 19
1.3.3 Unilateral deposition 20
1.3.4 Potential applications of unilateral deposition 21
1.4 Surface characterization 22
1.4.1 X-ray photoelectron spectroscopy (XPS)[125, 126] 23
1.4.2 Spectroscopic ellipsometry (SE)[136, 137] 26

المنارة للاستشارات
www.manaraa.com

1.4.3 Near-ambient pressure X-ray photoelectron spectroscopy (NAP-XPS)[133] 29

1.5 Conclusions 30

1.6 Figures 33

1.7 References 43

CHAPTER 2: Deposition of thin alumina (Al_2O_3) films on flat surfaces and characterization by spectroscopic ellipsometry (SE) and X-ray photoelectron spectroscopy (XPS) 52

2.1 Statement of Attribution 52

2.2 Abstract...52

2.3 Introduction 53

2.4 Experimental 58

2.4.1 Samples and deposition system 58

2.4.2 ALD process...58

2.4.3 Optimization of ALD parameters 59

2.4.4 Sample characterization 60

2.5 Results and Discussion 61

2.5.1 Initial ALD runs 61

2.5.2 Film characterization by XPS...66

2.5.3 Optical modeling of ALD alumina films 67

2.6 Specimen Description..72

2.7 Specimen Component Layers (see Figure 2.4) 73

2.8 Instrument Configuration...74

2.9 Data Analysis 75

2.10 Conclusions 77

2.11 Oscillator or effective medium approximation equations.....................................78

2.11.1. Free parameters in the Cauchy model...79

2.11.2. Fixed parameters in the Cauchy model..79

المنارة للاستشارات
www.manaraa.com

2.11.3. Free parameters in the Sellmeier model 80

2.11.4. Fixed parameters in the Sellmeier model 80

2.12 Figures 85

2.13 References 93

CHAPTER 3: A New Holder/Container with a Porous Cover for Atomic Layer Deposition on Particles, with Detailed Characterization of the Resulting Materials 97

3.1 Statement of Attribution 97

3.2 Abstract 97

3.3 Introduction 98

3.4 Experimental 101

3.4.1. Substrates 101

3.4.2. Sample Cleaning 101

3.4.3 ALD Deposition 102

3.4.5 Brunauer–Emmett–Teller (BET) Studies 105

3.4.6 Spectroscopic Ellipsometry (SE) 105

3.4.7 Transmission Electron Microscopy (TEM) and Scanning Electron Microscopy (SEM) 105

3.4.8 Particle Holder and Cover 106

3.5 Results and Discussion 106

3.5.1. Development and Optimization of the Porous Cover for the Particle Holder 106

3.5.2. ALD of Alumina on Powders using the Holder 109

3.5.3 Zinc oxide deposition on zirconia particles 111

3.6 Equilibration 113

3.7. Conclusions 116

3.8. Figures 117

3.8 References 140

المنارة للاستشارات
www.manaraa.com

CHAPTER 4: Substrate Protection and Deprotection with Salt Films to Prevent Surface Contamination and Enable Selective Atomic Layer Deposition 144
4.1 Statement of Attribution 144
4.2 Abstract 144
4.3 Introduction 145
4.4. Experimental 147
4.4.1. Substrates 147
4.4.2. Sample cleaning 147
4.4.3. Thermal deposition 148
4.4.4. Atomic layer deposition[37, 38] 148
4.4.5. Spectroscopic ellipsometry (SE)[39, 40] 149
4.4.6. X-ray photoelectron spectroscopy (XPS)[35] 149
4.4.7. Removal of sodium chloride 149
4.5. Results and Discussion 150
4.5.1. Sodium chloride deposition for surface protection 150
4.5.2 Substrate protection with evaporated NaCl 151
4.5.3. ALD on salt-protected substrates and deprotection of these surfaces 153
4.5.4. Effect of salt thickness on deprotection 154
4.5.5. ALD of zinc oxide on NaCl-protected fused silica 154
4.6 Conclusions 155
4.7 Figures 156
4.8 References 165
CHAPTER 5: Analysis of Non-conventional samples by Near-Ambient Pressure XPS (NAP-XPS) and examples of XPS Peak Fitting in Material Characterization 168
5.1 Introduction 168
Section 5.1.1 Liquid water, by near-ambient pressure XPS 170

المنارة للاستشارات
www.manaraa.com

Section 5.1.2 Coca-cola, by near-ambient pressure XPS 176

Section 5.1.3 Coffee bean, by near-ambient pressure XPS 184

Section 5.1.4 Nitrogen gas (N_2), by near-ambient pressure XPS 190

Section 5.1.5 Zirconia particles, by near-ambient pressure XPS....................195

Section 5.1.6 Human tooth, by near-ambient pressure XPS....................201

Section 5.1.7 Printed and unprinted office paper, by near-ambient pressure XPS 212

5.2 Figures 228

5.3 References....................287

CHAPTER 6: Conclusions and Future Work....................293

6.1 Key Findings from Each Chapter....................293

6.2 Future Work 295

Appendix 1: Good Surface Characterization Starts with Good Sample Preparation - Poor Equipment Maintenance Leads to Poor Sample Quality 296

A1.1 Statement of Attribution 296

A1.2 Introduction 296

Suggestion #1. Do some research/reading on the material you will be making 297

Suggestion #2. Use high quality reagents, at least at first, and understand the chemistry of your reagents....................297

Suggestion #3. Maintain the base pressure in your deposition chamber....................298

Suggestion #4. Maintain the O-rings in your deposition system 299

Suggestion #5. Monitor the performance of vacuum systems with pump down and rate-of-rise curves 300

Suggestion #6. Carefully transport samples to their place of analysis....................301

A1.3 Conclusion....................302

A1.4 Figures....................303

A1.5 References 304

المنارة للاستشارات
www.manaraa.com

Appendix 2: Material characterization using X-ray photoelectron spectroscopy (XPS) and tutorial on principles of XPS 306
A2.1 Statement of Attribution 306
A2.2 Abstract 306
A2.3 Introduction 307
A2.3.1 X-ray Photoelectron Spectroscopy 307
A2.4 Experimental 310
A2.4.1 XPS data collection 311
A2.5 Results and Discussion 311
A2.6 Conclusions 320
A2.7 Acknowledgments 320
A2.8 Figures 321
A2.9 References 325
Appendix 3: Polyethylene glycol: Optical constants from 191 to 1688 nm (0.735–6.491 eV) by spectroscopic ellipsometry 328
A3.1 Statement of Attribution 328
A3.2 Abstract 328
A3.3 Technical Information 329
A3.4 Introduction 329
A3.5 Specimen Description 332
A3.6 Specimen Component Layers 334
A3.7 Instrument Configuration 335
A3.8 Data Analysis 336
A3.9 Oscillator or effective medium approximation equations 337
A3.10 Figures 340
A3.11 References 346

المنارة للاستشارات
www.manaraa.com

Appendix 4: A Tutorial on Spectroscopic Ellipsometry (SE), 2. The Cauchy Model................348
A4.1 Statement of Attribution 348
A4.2 Introduction 348
A4.3 Instrumentation...349
A4.4 Principles of Ellipsometry..350
A4.5 Data Analysis in Spectroscopic Ellipsometry 351
A4.6 Figures...355
A4.7 References 363
Appendix 5: A Tutorial on Spectroscopic Ellipsometry (SE), 4. Using the 'Angle Offset' when fitting Ellipsometric Data 364
A5.1 Statement of Attribution 364
A5.2 Introduction 364
A5.3 Conclusions 367
A5.4 Figures...368
A5.5 References 372

المنارة للاستشارات
www.manaraa.com

LIST OF ABBREVIATIONS

AFM	Atomic force microscopy
ALD	Atomic layer deposition
ALE	Atomic layer epitaxy
AS-ALD	Area selective atomic layer deposition
BEMA	Bruggeman effective medium approximation
BET	Brunauer-Emmett-Teller
C-L	Cody-Lorentz
CVD	Chemical vapor deposition
DEZ	Diethylzinc
DMZ	Dimethylzinc
EDX	Energy-dispersive X-ray spectroscopy
FBR	Fluidized bed reactor
GC	Gas chromatography
GPC	Growth per cycle
GLP	Gaussian-lorentzian product function
GLS	Gaussian-lorentzian sum function
LC	Liquid chromatography
MSA	Multiple sample analysis
MSE	Mean squared error
NAP-XPS	Near-ambient X-ray photoelectron spectroscopy
PA-ALD	Plasma-assisted atomic layer deposition

المنارة للاستشارات
www.manaraa.com

PEG	Polyethylene glycol
PMMA	Poly meth methyl acrylate
PVD	Physical vapor deposition
SE	Spectroscopic ellipsometry
SEM	Scanning electron microscopy
SAM	Self-assembled monolayers
T-ALD	Thermal Atomic layer deposition
T-L	Tauc-Lorentz
ToF-SIMS	Time-of-flight secondary ion mass spectrometry
TEM	Transmission electron microscopy
TMADF	Tetrakis(dimethylamido)hafnium(IV)
WCA	Water contact angle
XPS	X-ray photoelectron spectroscopy
XRD	X-ray diffraction

المنارة للاستشارات
www.manaraa.com

LIST OF FIGURES

Figure 1.1. Schematic description of the stepwise ALD deposition of alumina and zinc oxide using trimethylaluminum (TMA) and water, and diethylzinc (DEZ) and water, respectively.[15] 33

Figure 1.2. Schematic showing the effect of deposition temperature on growth per cycle on alumina deposition using ALD. (Image adapted from George, S. *Chem. Rev.* **2010**, *1*, 111-131.) 34

Figure 1.3. Schematic showing the nucleation behavior that be exploited for achieving AS-ALD. The image shows the possible selectivity window which can be used for achieving AS-ALD. (Image adapted from Mackus et al. Chem. Mater. 2019, 31, 2-12.)..........35

Figure 1.4. Schematic showing an overview of various approaches for AS-ALD. (a1) Approach for selective precursor adsorption where functionalized area is the desired region for deposition (a2) Conventional approach for co-reactant adsorption (b) Surface is pre-functionalized before the deposition occurs to achieve AS-ALD. (Image adapted from Mackus et al. *Chem. Mater.* **2019**, *31*, 2-12.) 36

Figure 1.5. Schematic showing selective thermal deposition and non-selective ALD deposition. These two deposition techniques were used in conjunction to achieve unilateral area-selective deposition on one side of silicon substrate. 37

Figure 1.6. Schematic showing unilateral deposition on a silicon substrate using protection/deprotection strategy. The first step, thermal deposition selectively deposits NaCl on one side of the substrate. The next step, ALD deposits ALD on both the sides of the substrate. The final step, water treatment removes NaCl and any alumina (or a similar metal oxide) adsorbed on top of the NaCl layer. 38

Figure 1.7. Schematic representation of a) the photoelectron emission and Auger emission, b) XPS spectra collected from the substrate, c) the basic instrumentation of the XPS. (Image reproduced from Paul van der heide, X-ray Photoelectron Spectroscopy: An introduction to Principles and Practices). 39

Figure 1.9. Image of the J. A. Woollam spectrometer M-2000DI used in the Linford lab showing its major parts. 41

Figure 1.10. Schematic of environmental charge compensation used in near-ambient pressure X-ray photoelectron spectroscopy. (Figure used with permission from Dr. Paul M. Dietrich and SPECS, Germany)..........42

المنارة للاستشارات
www.manaraa.com

Figure 2.1. (a) Film thickness vs. cycle number for ALD of alumina from TMA and water at 332 ºC. The intercept of the fit line was zero, its slope was 0.082 nm/cycle, and its R-squared value was 0.99993. (b) GPC values (Å/Cycle) versus cycle number for the same alumina ALD depositions as in (a) demonstrating the near constant nature of these values, especially at higher numbers of cycles..85

Figure 2.2. XPS survey spectra from 0 – 1100 eV of alumina films deposited by ALD onto silicon shards after 5, 10, 20, 50, and 100 cycles. Some of the data in this figure was previously published in a paper entitled "Tutorial on interpreting x-ray photoelectron spectroscopy survey spectra: Questions and answers on spectra from the atomic layer deposition of Al_2O_3 on silicon".[1] This information is reused here with permission from AIP Publishing...86

Figure 2.3. XPS survey spectra plotted from 0 – 210 eV of alumina films deposited by ALD onto silicon shards after 5, 10, 20, 50, and 100 cycles. Some of the data in this figure was previously published in a paper entitled "Tutorial on interpreting x-ray photoelectron spectroscopy survey spectra: Questions and answers on spectra from the atomic layer deposition of Al_2O_3 on silicon".[1] This information is reused here with permission from AIP Publishing......................................87

Figure 2.4. Representation of the materials/layers used to model the ALD alumina films on silicon created in this study. The optical functions for the substrate and the native oxide layer above it were obtained from the instrument software: Si_JAW and NTVE_JAW, respectively. Note that the SiO_2 film thickness in all the modeling was fixed at 1.6 nm, where the actual silica thicknesses measured prior to ALD varied between 1.57 nm and 1.62 nm..88

Figure 2.5. Experimental results (ψ and Δ) modeled using Cauchy's equation for an Al_2O_3 film prepared via 100 ALD cycles. 89

Figure 2.6. Experimental results (ψ and Δ) modeled using Sellmeier's equation for an Al_2O_3 film prepared via 100 ALD cycles. 90

Figure 2.7. Real part (ε_1) of the complex dielectric function of alumina obtained from Cauchy and Sellmeier models as a function of photon energy..91

Figure 2.8. Comparison of optical functions determined for ALD alumina thin films obtained from the Cauchy and Sellmeier models in this study to literature results. The two single points are literature results at 633 nm. The other two results are represented as dashed lines because the authors of these studies specified a range of wavelengths, but not a particular wavelength. 92

Figure 3.1. Engineering design of the particle holder obtained from Kurt J. Lesker................117

المنارة للاستشارات
www.manaraa.com

Figure 3.2. Left. Holder covered with a frit with a silicon witness shard on top of it. Right. Holder without cover with a witness shard in it. 118

Figure 3.3. Representation of the chemistry in the deposition of alumina from trimethylaluminum (TMA) and water (top), and zinc oxide from diethylzinc (DEZ) and water (bottom). 119

Figure 3.4. SEM images of the frits and mesh used as porous covers for the particle holder developed in this work. (a) First porous frit studied. (b) Second porous frit studied. (c) '635' mesh. 120

Figure 3.5. (a) Film thicknesses, t, for 5 - 500 cycles of ALD alumina on witness shards placed inside and outside the second frit (see **Figure 3.5b**). The linear fits (t = mx + b) to this data are $t_{outside}$ = 0.100x + 0.037 with R^2 = 0.99948 (top line), and t_{inside} = 0.087x - 0.033 with R^2 = 0.99928 (bottom line). We do *not* claim that all of the digits in these numbers are significant. (**b)** Refractive indices obtained by SE from multi-sample analyses (MSA) of the data in **Figure 3.5a**, where each MSA used all the data in the corresponding data set. 121

Figure 3.6. (a) Thicknesses of alumina films created via 100 ALD cycles as measured on silicon shards placed inside and outside the particle holder, where the holder was covered with 2 – 7 '635' meshes. (b) Refractive indices obtained by SE from MSAs of the alumina films deposited inside and outside the holder covered with 2 – 4 '635' meshes. That is, each MSA here used the SE data from 3 samples. 122

Figure 3.7. Entire XPS survey spectra for zirconia particles coated with 100 ALD cycles. 123

Figure 3.8. Abbreviated XPS survey spectra for alumina deposited on zirconia particles via 0, 25, 50, 75, and 100 ALD cycles. The Zr signals decrease as the number of ALD cycles increases. The negative slopes of the baselines from 240 – 270 eV in counts/eV are given between the dashed lines. The thicknesses of the alumina films measured by SE on silicon witness shards inside (t_{in}) and outside (t_{out}) the particle holder are also listed for each sample. 124

Figure 3.9. Same SE data as in Figure 6 in the main paper, except error bars are provided for the data points. The values of these data points and the error bars were obtained from the averages and standard deviations, respectively, of three measurements on each sample. 125

Figure 3.10. XPS survey spectra of alumina-coated zirconia particles, where 50 – 500 mg of particles were coated with 100 ALD cycles of TMA and water. 126

Figure 3.12. (a) and (b) TEM images of zirconia particles coated with 100 ALD cycles of alumina showing (a) a thickness measurement of the alumina film, and (b) the path of a line spectrum (35

المنارة للاستشارات

www.manaraa.com

data points with a dwell time of 3 s). (c) EDS spectra of Al, Zr, and O from the line spectrum in (b). 128

Figure 3.13. a) TEM images of the coated zirconia particles showing uniformity of thin alumina films surrounding the particles. These images show the thin film of alumina over the zirconia particles, which is possible because of the Z-contrast between zirconia (substrate) and alumina oxide (coating). Note that alumina is lighter than zirconia in these images...............................129

Figure 3.14. Thickness and GPC data for zinc oxide data for different ALD cycles. ALD cycles were increased from 5 to 250 sequentially, such that film thickness ranged from 1 nm to 35 nm. 130

Figure 3.15. XPS results of zinc oxide deposition on flat surfaces using different number of ALD cycles. Dose time for DEZ and water was 21.0 ms and 15.5 ms, purge times for both precursors was 15 seconds. Deposition temperature was 200 ºC and equilibration time was 10 minutes. ..131

Figure 3.16. XPS results (210- 0 eV) of zinc oxide deposition on flat surfaces using different number of ALD cycles. Dose time for DEZ and water was 21.0 ms and 15.5 ms, purge times for both precursors was 15 seconds. Deposition temperature was 200 ºC and equilibration time was 10 minutes..132

Figure 3.17. Entire XPS survey spectra for coated zirconia particles after 100 ALD cycles.....133

Figure 3.18. XPS survey spectra from 0 – 625 eV of ZrO_2 particles coated with ZnO by ALD as a function of the number of ALD cycles. The thicknesses of the zinc oxide films measured by SE on silicon witness shards inside (t_{in}) and outside (t_{out}) the particle holder are also listed for each run. 134

Figure 3.19. TEM image of zinc oxide coated particle showing the line spectra......................135

Figure 3.20. EDS spectrum (bottom) for the data point indicted as an orange dot in the image (top) of a zirconia particle coated by ALD with 100 cycles of DEZ and water to form ZnO. Copper peaks are present due to the copper grid on which the particles were mounted. Minor oxygen and nitrogen peaks are present due to small amounts of air in the chamber....................................136

Figure 3.21. EDS spectrum (bottom) for the data point indicted as an orange dot in the image (top) of a zirconia particle coated by ALD with 100 cycles of DEZ and water to form ZnO. Copper peaks are present due to the copper grid on which the particles were mounted. Minor oxygen and nitrogen peaks are present due to small amounts of air in the chamber....................................137

المنارة للاستشارات
www.manaraa.com

Figure 3.22. EDS spectrum (bottom) for the data point indicted as an orange dot in the image (top) of a zirconia particle coated by ALD with 100 cycles of DEZ and water to form ZnO. Copper peaks are present due to the copper grid on which the particles were mounted. Minor oxygen and nitrogen peaks are present due to small amounts of air in the chamber....................................138

Figure 3.23. Film thickness and GPC for a 100-cycle ALD run using different recipes. The chamber was heated at 150 °C as an oven, such that the temperature was essentially the same at all places inside the chamber. The substrate was allowed to equilibrate at 150 °C for 30 min prior to deposition...139

Figure 4.1. Protection of a substrate with a thin salt film, conventional ALD on the unprotected side of the substrate, and removal of the salt film, which removes unwanted ALD deposition on the backside of the substrate. 156

Figure 4.2. Schematic illustrating non-directional deposition of alumina in the ALD. The side, which shows non-uniform deposition of alumina, was in contact with loading tool. The exposed side of fused silica shows uniform alumina deposition..157

Figure 4.3. XPS spectra from 0 – 350 eV of (a) a ca. 100 nm film of NaCl evaporated onto a fused silica slide, and (b) an uncoated fused silica slide. 158

Figure 4.4. XPS spectra from 0 – 350 eV. (Top) NaCl – coated fused silica after ALD deposition of Al_2O_3 via 100 cycles of TMA and water. (Bottom) - Fused silica after the same ALD deposition. Note that the uncoated surface was facing up during the deposition.......................................159

Figure 4.5. XPS spectra from 0 – 325 eV obtained from a fused silica substrate after three stepwise processes (i) protection with NaCl on one side, (ii) ALD of Al_2O_3, and (iii) sonication/rinsing with water. 160

Figure 4.6. XPS spectra from 0 – 325 eV of two different thicknesses of NaCl coated on fused silica slides. (Top) NaCl (50 nm) on the surface of the fused silica slide, note that film thickness completely mask over the silanol groups eliminating any probability of silanol groups reacting with ALD precursors. (Bottom) NaCl (10 nm) film thickness showing the Na and Cl peaks along with Si peaks. This suggests lack of complete coverage of the surface by NaCl film. The small peak in the 50 nm NaCl coating is a loss peak associated with Cl 2*p*. 161

Figure 4.7. XPS spectra from 0 – 210 eV of the salt-protected sides of three different fused silica substrates previously coated on one side with 10 (top), 50 (middle), and 100 (bottom) nm of NaCl after ALD of Al_2O_3 and sonication/rinsing with water. Note the small peaks corresponding to Al

المنارة للاستشارات
www.manaraa.com

2*s* and Al 2*p* at 118.0 eV and 74.0 eV, which suggest small amount of alumina was deposited on quart slide. 162

Figure 4.8. XPS spectra from 0 – 1100 eV of a fused silica substrate after (i) one side was coated with NaCl, (ii) ALD of ZnO, and (iii) deprotection of the substrate by sonication/rinsing with water. Zn is only present on the side of the surface that was not protected with NaCl. 163

Figure 4.9. XPS spectra from 0 – 200 eV of a fused silica substrate after (i) one side was coated with NaCl, (ii) ALD of ZnO, and (iii) deprotection of the substrate by sonication/rinsing with water. Zn is only present on the side of the surface that was not protected with NaCl. 164

Figure 5.1.1.1. NAP-XPS survey spectrum of liquid water. 228

Figure 5.1.1.2. NAP-XPS O 1*s* spectrum stack of liquid water collected at different nozzle length. 229

Figure 5.1.1.3. NAP-XPS O 1*s* spectrum stack of liquid water collected at different nozzle length. 230

Figure 5.1.1.4. NAP-XPS O 1*s* spectrum of liquid water. 231

Figure 5.1.1.5. NAP-XPS O *KLL* spectrum of liquid water. 232

Figure 5.1.2.1. NAP-XPS Survey spectrum of Coca-Cola. 233

Figure 5.1.2.2. NAP-XPS C 1*s* spectrum of Coca-Cola. 234

Figure 5.1.2.3. Stack of NAP-XPS C 1*s* spectrum of Coca-Cola. 235

Figure 5.1.2.4. Uniqueness plot of the C 1*s* fit (varying C-3) of Coca-Cola. 236

Figure 5.1.2.5. NAP-XPS O 1*s* spectrum of Coca-Cola. 237

Figure 5.1.3.1. NAP-XPS Survey spectrum of Coffee bean. 238

Figure 5.1.3.2. Expanded NAP-XPS Survey spectrum of Coffee bean. 239

Figure 5.1.3.3. NAP-XPS C 1*s* spectrum of Coffee bean. 240

Figure 5.1.3.4. NAP-XPS O 1*s* spectrum of Coffee bean. 241

Figure 5.1.4.1. NAP-XPS Survey spectrum of Nitrogen (N_2) gas. 242

Figure 5.1.4.2. NAP-XPS N 1*s* spectrum of Nitrogen (N_2) gas. 243

Figure 5.1.4.3. NAP-XPS N *KLL* spectrum of Nitrogen (N_2) gas. 244

Figure 5.1.5.1. NAP-XPS Survey spectrum of Zirconia (ZrO_2) particles. 245

Figure 5.1.5.2. Expanded NAP-XPS Survey spectrum of Zirconia (ZrO_2) particles. 246

Figure 5.1.5.3. NAP-XPS 3*d* spectrum of Zirconia (ZrO_2) particles. 247

Figure 5.1.5.4. NAP-XPS Zr 3*p* spectrum of Zirconia (ZrO_2) particles. 248

المنارة للاستشارات

www.manaraa.com

Figure 5.1.5.5. NAP-XPS O 1*s* spectrum of Zirconia (ZrO_2) particles....................................249
Figure 5.1.6.1. NAP-XPS survey spectrum of Top Part of a Molar human tooth....................250
Figure 5.1.6.2. NAP-XPS survey spectrum of Middle Part of a Molar human tooth...............251
Figure 5.1.6.3. NAP-XPS survey spectrum of Root Part of a Molar human tooth....................252
Figure 5.1.6.1.1. NAP-XPS C 1*s* spectrum of Top Part of a Molar human tooth. 253
Figure 5.1.6.2.1. NAP-XPS C 1*s* spectrum of Middle Part of a Molar human tooth. 254
Figure 5.1.6.3.1. NAP-XPS C 1*s* spectrum of Root Part of a Molar human tooth...................255
Figure 5.1.6.1.2. NAP-XPS O 1*s* spectrum of Top Part of a Molar human tooth. 256
Figure 5.1.6.2.2. NAP-XPS O 1*s* spectrum of Middle Part of a Molar human tooth...............257
Figure 5.1.6.3.2. NAP-XPS O 1*s* spectrum of Root Part of a Molar human tooth...................258
Figure 5.1.6.1.3. NAP-XPS Ca 2*p* spectrum of Top Part of a Molar human tooth. 259
Figure 5.1.6.2.3. NAP-XPS Ca 2*p* spectrum of Middle Part of a Molar human tooth. 260
Figure 5.1.6.3.3. NAP-XPS Ca 2*p* spectrum of Root Part of a Molar human tooth.................261
Figure 5.1.6.1.4. NAP-XPS P 2*p* spectrum of Top Part of a Molar human tooth. 262
Figure 5.1.6.2.4. NAP-XPS P 2*p* spectrum of Middle Part of a Molar human tooth. 263
Figure 5.1.6.3.4. NAP-XPS P 2*p* spectrum of Root Part of a Molar human tooth...................264
Figure 5.1.6.4. Different parts of human tooth analyzed by NAP-XPS in this study...............265
Figure 5.1.6.5. Uniqueness plot of the C 1s fit for top part of the Adult tooth. 266
Figure 5.1.7.1. NAP-XPS survey spectrum of white unprinted paper....................................267
Figure 5.1.7.2. NAP-XPS survey spectrum of blue printed-paper. 268
Figure 5.1.7.3. NAP-XPS survey spectrum of dark blue printed-paper...................................269
Figure 5.1.7.4. NAP-XPS survey spectrum of yellow post-it note..270
Figure 5.1.7.1.1. NAP-XPS C 1*s* spectrum of white unprinted paper. 271
Figure 5.1.7.2.1. NAP-XPS C 1*s* spectrum of blue printed paper..272
Figure 5.1.7.3.1. NAP-XPS C 1*s* spectrum of dark blue printed paper. 273
Figure 5.1.7.4.1. NAP-XPS C 1*s* spectrum of yellow post-it note. 274
Figure 5.1.7.1.2a NAP-XPS O 1*s* spectrum of white unprinted paper. 275
Figure 5.1.7.2.2a NAP-XPS O 1*s* spectrum of blue printed paper..276
Figure 5.1.7.3.2a NAP-XPS O 1*s* spectrum of dark blue printed paper. 277
Figure 5.1.7.4.2a NAP-XPS O 1*s* spectrum of yellow post it note. 278
Figure 5.1.7.1.2b NAP-XPS O 1*s* spectrum of white unprinted paper (alternate fit)...............279

المنارة للاستشارات
www.manaraa.com

Figure 5.1.7.2.2b NAP-XPS O 1*s* spectrum of blue printed paper (alternate fit)......................280
Figure 5.1.7.3.2b NAP-XPS O 1*s* spectrum of dark blue paper (alternate fit)..........................281
Figure 5.1.7.4.2b NAP-XPS O 1*s* spectrum of yellow post-it note (alternate fit).....................282
Figure 5.1.7.5 White paper notepad containing the SPECS logo analyzed by NAP-XPS.........283
Figure 5.1.7.6 Uniqueness plot of the C 1*s* fit for the white unprinted paper. 284
Figure 5.1.7.7 Uniqueness plot of the O 1s fit performed with four fit components for white, unprinted paper. 285
Figure 5.1.7.8 Percentages of the total fitted area of each of the synthetic peaks in the four-component O 1s fits performed in this study..286
Figure A1.1. Pump down curve (pressure vs. time) obtained for the turbo-pumped PVD 75 sputter system in our lab at BYU (curve generated April 2017).[20] 303
Figure A2.1 (Color online). XPS survey spectra shown from 0 – 1100 eV of ALD alumina films on silicon substrates. (a) The bare silicon substrate, and the silicon surface after (b) 10, (c) 50, and (d) 100 TMA/water ALD cycles. The lower case Roman numerals are used to indicate peaks in the spectra..321
Figure A2.2. (Color online). XPS survey spectra shown from 0 – 210 eV of ALD alumina films on silicon substrates. (a) The bare silicon substrate, and the silicon surface after (b) 10, (c) 50, and (d) 100 TMA/water ALD cycles. The lower case Roman numerals are used to indicate peaks/features in the spectra. 322
Figure A2.3. (Color online). XPS survey spectra from 0 – 1100 eV of two ALD alumina films prepared on silicon substrates with 10 TMA/water cycles. One surface had been treated in a dirty plasma chamber and had thus become ‘Contaminated’. The lower case Roman numerals are used to indicate peaks/features in the spectra...323
Figure A2.4. (Color online). XPS survey spectra from 0 – 210 eV of two ALD alumina films prepared on silicon substrates with 10 TMA/water cycles. One surface had been treated in a dirty plasma chamber and had thus become ‘Contaminated’. The lower-case Roman numerals are used to indicate peaks/features in the spectra...324
Figure A3.1. Transmission intensities for PEG calculated using cuvettes with three different path lengths (2 mm, 5 mm, and 10 mm). 340
Figure A3.2. Extinction coefficient of PEG measured from three different dual-cuvette ratios where the range of results was used to show error-bars at each wavelength. In general, the error

المنارة للاستشارات
www.manaraa.com

bars are about the same size as the symbols in this plot. However, they are rather large at the largest and shortest wavelengths considered here. 341

Figure A3.3. Extinction coefficient, k(λ), for PEG. 342

Figure A3.4. Experimental results (ψ and Δ) for PEG300 modeled using a Sellmeier function and a BEMA surface interface layer. 343

Figure A3.5. Optical constants (n and ϵ_1) obtained for PEG. 344

Figure A3.6. Pictures of two fused silica cuvettes used in this study. 345

Figure A4.1. Optical constants of three dielectrics: SiO_2, Al_2O_3, and ZrO_2, modeled using the Cauchy model. 355

Figure A4.2. Ψ and Δ values (colored lines) and an initial attempt to fit them (grey lines) from a film of PECVD SiO_2 on silicon. The data were collected at three different angles (65°, 70°, and 75°), and over a moderately wide wavelength range (210.7 - 997.5 nm). (Top) All the Ψ and Δ data. (Bottom) The Ψ data collected at 75° (purple line) and an initial attempt to fit it (grey line). 356

Figure A4.3. Ellipsometric (Ψ) data from a film of YbF_3 on Ge. The decrease in oscillations (interference fringes) at shorter wavelengths suggests this film is absorbing light here. 357

Figure A4.4. Experimental values of Ψ (colored lines) and an initial attempt at fitting them (dotted lines), which consisted of manually increasing the thickness of the SiO_2 film in the model in Figure 4 until the experimental data and theoretical curves matched reasonably well. The thickness of the SiO_2 film in the model here was 530.0 nm. 358

Figure A4.5. Experimental values of Ψ (colored lines) and an attempt at fitting them (dotted lines) using the model in Figure 4. This modeling was performed with the instrument software, where the thickness of the SiO_2 layer was allowed to vary and the starting point for this fit was the conditions outlined in the caption to Figure 5. The thickness predicted by this modeling was 528.36 nm with a mean squared error (MSE) of 86.787. 359

Figure A4.6. Experimental values of Ψ (colored lines) and an attempt at fitting them (dotted lines) based on a two-parameter (A and B) Cauchy model. The SiO2 film thickness predicted by this modeling was 506.14 nm with a mean squared error (MSE) of 33.300. 360

Figure A4.7. Experimental values of Ψ (colored lines) and an attempt at fitting them (dotted lines) based on a three-parameter (A, B, and C) Cauchy model. The SiO_2 film thickness predicted by this modeling was 506.11 nm with a mean squared error (MSE) of 19.749. 361

المنارة للاستشارات
www.manaraa.com

Figure A4.8. Optical constants predicted by the three-parameter Cauchy model for the SiO_2 film on Si considered in this article. 362
Figure A5.1. Simplified model of an ellipsometer..........368
Figure A5.2. Analysis of a 'native oxide' film on a silicon shard using the 'NTVE_JAW' model. Note that the angle offset was fixed at 0.00°. The thickness of the film was 1.38 nm and the MSE for the fit was 7.78. 369
Figure A5.3. Determination of the in situ angle of incidence. We are fitting a data point just before the alumina deposition starts by ALD (near t = 4 min). Here, the angle and native oxide layer are fit parameters, and the Si substrate temperature is fixed at the nominal value of 300 °C. 370
Figure A5.4. Analysis of an ALD alumina film using the FS-1 software. The Angle is *fixed* at the value determined from the model in **Figure A5.3**. The substrate "Pseudo" optical constants are determined from the data acquired immediately before the deposition is started (near t = 4 min). The alumina film thickness and Cauchy parameters for the index of refraction are selected as fitting parameters..........371

المنارة للاستشارات
www.manaraa.com

LIST OF TABLES

Table 2.1. Summaries of literature reports of ALD of alumina. The papers in this table are listed by lead author, and each entry also summarizes the precursors, deposition temperature, substrate, substrate pretreatment, final thickness of the alumina layer, and GPC. 54

Table 2.2. Film thickness and GPC for different number of ALD cycles using 15.5 ms as water dose time and 21.0 ms dose time for TMA. Purge time for water and TMA was 15000 ms........62

Table 2.3. Film thickness and GPC for various runs while varying the dose time of TMA keeping all the variable constant including the number of cycles and temperature of deposition. (The thickness and GPC were uncharacteristically less when the dose time for water was 11.0 msec. The experiment was repeated three times and gave similar results)...63

Table 2.4. Film thickness and GPC for various runs while varying the dose time of water keeping all the other variables constant including the number of cycles and temperature of deposition. ..64

Table 2.5. Film thickness and GPC for various runs while varying the purge time of TMA keeping all the other variables constant...64

Table 2.6. Film thickness and GPC for various runs while varying the purge time of water keeping all the other variables constant...65

Table 2.7 Film thickness and GPC for various runs selected for XPS determinations. 66

Table 2.8. Summaries of Literature reports on the deposition of thin films of alumina and their optical properties...67

Table 2.9. Fit parameters for the Cauchy model...80

Table 2.10. Spectral features for the Cauchy model 82

Table 2.11. Fit parameters for the Sellmeier model..83

Table 2.12. Spectral features for the Sellmeier model 84

Table 3.1. Descriptions of the deposition and analytical equipment employed in this work. 100

Table 3.2. Process parameters for ALD on planar and powder substrates. 103

Table 3.3. Film thickness and GPC values for different numbers of ALD cycles for witness shards placed inside and outside the second frit (see Figure 4). 103

Table 3.4. Representative process parameters for a Static dosing recipe for coating thin zinc oxide films on powder substrates. Note: the dose and purge times are 5 times the typical dose and purge times was 4 times the purge times used for deposition on silicon surfaces. 112

Table 3.5. Thickness and GPC data for zinc oxide data for different ALD cycles...................112

www.manaraa.com

Table 3.6. A standard recipe for depositing zinc oxide showing the process parameters. They were used for the initial depositing experiments on silicon shards to obtain a wide range of zinc oxide films. 114
Table 3.7. Representative process parameters for powder deposition experiments for a variable residence mode (VRM) recipe. The precursors used for this deposition were TMA and water, with pressure ranging from 1.2 torr to 1.8 torr. RCN represents the number of ALD cycles in a recipe. 115
Table 3.8. Film thickness and GPC for 100 cycle ALD run using different recipes. The chamber was heated at 150 ^{0}C as an oven, such that the temperature was essentially the same at all places inside the chamber. 115
Table 4.1. Experimental data for NaCl-coated and uncoated silicon shards after exposure to the laboratory environment and ALD of alumina. 152
Table 5.1.1.1. Spectral features of interest 172
Table 5.1.2.1. Spectral features of interest 179
Table 5.1.3.1. Spectral features of interest 186
Table 5.1.4.1. Spectral features of interest 192
Table 5.1.5.1. Spectral features of interest 197
Table 5.1.6.1. Spectral features of interest 204
Table 5.1.7.1. Spectral features of interest 217
Table A3.1. Fit parameters for PEG300 (Sellmeier with BEMA roughness layer)...................339

المنارة للاستشارات
www.manaraa.com

CHAPTER 1: Introduction to atomic layer deposition (ALD), X-ray photoelectron spectroscopy (XPS), and surface analysis

The field of vacuum deposition includes numerous processes like atomic layer deposition (ALD), physical vapor deposition (PVD), chemical vapor deposition (CVD), pulsed laser deposition, spin coating, and e-beam deposition.[1, 2] Thin film deposition is followed by surface characterization, which includes techniques by which the structure and properties of a thin film present on a substrate are analyzed. Over the past few decades, significant advances have taken place in the equipment used for surface and material characterization, including improvements in speed, resolution, automation, data collection, and processing. Usually, surface analysis requires multiple techniques, each of which provides valuable information about the deposited material.[3]

The Linford group at BYU works in three main areas: vacuum deposition, surface characterization, and data analysis. This focus has allowed me to understand the process of atomic layer deposition and optimize thin film deposition on powder substrates. The group members deposit materials on a wide variety of substrates with intended applications in separation science,[4] catalysis,[5] protective coatings,[6] and pharmaceutical dosage forms.[7, 8] Some of the analytical tools that are regularly used in the Linford group include X-ray photoelectron spectroscopy (XPS), time-of-flight secondary ion mass spectrometry (ToF-SIMS), spectroscopic ellipsometry (SE), water contact angle goniometry, atomic force microscopy (AFM), scanning electron microscopy (SEM), and transmission electron microscopy (TEM).

المنارة للاستشارات
www.manaraa.com

I had the opportunity to work on four projects in which I have developed and characterized thin films on several substrates for various applications. These projects include the following:

(i) Preparation of thin ALD films on flat silicon shards for collecting the optical constants of alumina,

(ii) Deposition, optimization and characterization of ALD alumina and zinc oxide on powder substrates,

(iii) Collection of optical constants of liquid samples by spectroscopic ellipsometry (SE), and

(iv) Characterization of unconventional materials by near ambient pressure X-ray photoelectron spectroscopy (NAP-XPS).

These four projects comprise the major part of my dissertation.

My major contributions have been in ALD. They involved thin film deposition on planar and particulate substrates, and subsequently, their surface characterization. The common aspects of these projects were thin film deposition by ALD, and their multi-instrument characterization using XPS, SE, and TEM. I will discuss key principles of atomic layer deposition, X-ray photoelectron spectroscopy, and spectroscopic ellipsometry, as they were the key tools used for thin film characterization. This will be followed by a discussion of near-ambient pressure XPS (NAP-XPS), and its use in analyzing non-conventional samples like solids, liquids, gases, and biological tissues. I will present the key differences and advantages of NAP-XPS over conventional XPS. It will be followed by a discussion of environmental charge compensation and its importance in NAP-XPS.

www.manaraa.com

1.1 Atomic layer deposition (ALD)

1.1.1 Principles of atomic layer deposition

ALD was initially developed as 'atomic layer epitaxy (ALE)' by Suntola and co-workers for electroluminescent zinc sulfide (ZnS) displays in the 1970's.[9] Early work in ALD was in the field of semiconductor materials for displays. However, because most of the materials deposited using ALD are amorphous, 'atomic layer deposition' was preferred instead of ALE. The development of ALD was slow in the initial years due to its slow rate of deposition compared to the other methods of vacuum deposition. However, the continuous reduction in the sizes of semiconductor device features and microelectronics has generated new interest in the field. ALD has been applied in coating thin films on powder substrates and high-aspect ratio structures. More than 1500 literature reports of ALD on different substrates (powder, high-aspect ratio, and planar substrates) have been published to date.[6] These publications represent the recognition of ALD as a valuable vacuum deposition technique. The materials deposited using ALD include most of the metals present in the periodic table along with metal oxides, nitrides, sulfides, and others.[5, 10]

There are two main variants of ALD: thermal and plasma-assisted. Plasma-assisted ALD (Pl-ALD) offers a wider choice of material substrates, reaction temperatures, processing conditions, and precursors. Pl-ALD involves exposing the surface to species generated by a plasma.[11] Thermal ALD (T-ALD) involves employing the reactant gas, which is a highly reactive molecular species, at elevated thermal conditions. In general, most Pl-ALD processes take place at lower temperatures compared to T-ALD processes.

ALD works by exposing the substrate to gaseous precursors at relatively low working pressures (ca. 1 torr), followed by removal of the excess precursor.[12, 13] The gaseous

المنارة للاستشارات
www.manaraa.com

precursors have high vapor pressures, which facilitates saturation of the surface sites. ALD has become a technique of choice for thin-film deposition in the semiconductor industry.[12] Since both precursors enter the reactor separately and do not interact with each other, problems such as parasitic CVD and overexposure of the substrate are eliminated.[14] Thus, ALD proceeds by saturation of surface sites with the precursor, followed by removal of the excess reagent before the entry of the second precursor.[15] The highly favored reactions between the surface and the precursor molecules are the driving force in ALD deposition. Once the surface sites are saturated, excess reagent is removed by a constant flow of inert gas like high purity nitrogen (99.999 %). This is to ensure that deposition proceeds through the ALD route. This overall process is repeated until the desired film thickness is achieved on the substrate.[16] Since the precursor molecules do not interact or react with each other, the deposition process enjoys high reproducibility with few side products or reactants.

ALD processes depend on self-saturating half-reactions between a substrate and a reactant that deposit a film on a substrate.[17] The use of high vapor pressure gaseous precursors ensures that precursors fill all the surface sites on a substrate irrespective of geometry and do not require line-of-sight to the substrate. This feature is responsible for conformal deposition on high-aspect ratio structures and powder substrates. The degree of specific control over film thickness and uniformity makes ALD an ideal process for nanofabrication for applications in the semiconductor industry. The semiconductor industry has been moving towards miniaturization of transistors, creating numerous challenges in achieving conformal coatings on devices.[18] Intel was the first major semiconductor company to introduce ALD in its production line in 2007.[17] Since then, the use of ALD for thin films deposition has increased exponentially.

المنارة للاستشارات
www.manaraa.com

Even though ALD has numerous advantages over commercial vapor deposition processes and is used in numerous industrial applications, it has several limitations. ALD is an inherently slow process as it involves repeated exposures of gaseous precursors to a substrate, which increases the total time needed for thin film deposition. Another limitation of ALD as a process is the frequent use of reactive, and in some cases, pyrophoric reagents like trimethylaluminum and diethylzinc.

1.1.2 Deposition of oxide films using ALD

T-ALD has been widely used to deposit metal oxides and metal sulfides. However, it is not usually the preferred technique for depositing metals and metal nitrides. Metal nitrides can be deposited using Pl-ALD, as nitrides need a highly reactive nitrogen species. In general, metal deposition through ALD is an inefficient process. Thus, sputtering and physical vapor deposition are the preferred methods for metal deposition.

ALD is most commonly used for deposition of metal oxides like aluminum oxide, zinc oxide, hafnium oxide, and titanium dioxide.[16, 17, 19, 20] Alumina is one of the most common material deposited using ALD. In numerous cases, it will be the first material deposited in an ALD system. This was the principal reason for using alumina as the standard/model material in my studies. In particular, I used trimethylaluminum and water as the precursors for deposition of thin alumina films (see **Figure 1.1**). I used diethylzinc and water to deposit zinc oxide thin films on flat and powder substrates. For these studies, water can be substituted with ozone. Both water and ozone act as oxidizers and achieve a similar effect in a deposition, even though they differ chemically. In fact, ozone is usually a better precursor than water, as it is easier to remove. The disadvantage of ozone is the need for additional equipment in the form of an ozone generator.

المنارة للاستشارات
www.manaraa.com

In general, for water and TMA precursors, higher temperatures lead to more uniform and reproducible ALD processes.[17] The reason for this is that it is easier to remove water at higher temperatures. There are quite a few studies reporting the deposition of alumina from TMA and water. Other precursors that have been used for the ALD deposition of alumina include aluminum trichloride ($AlCl_3$), and aluminum ethoxide $Al(OC_2H_5)_3$.[21] For example, Broas *et al.*[22] reported alumina deposition on silicon shards at 300 ºC and 450 ºC from TMA and aluminum trichloride. However, aluminum trichloride has been replaced with other aluminum precursors like TMA and aluminum ethoxide due to production of hydrochloride acid as byproduct. In each case, the oxidizer used was either water, ozone, or an alcohol.[23]

Zinc oxide is a metal oxide that is also deposited via ALD. Zinc oxide is a wide-band gap material, which is transparent to visible light and has tunable conductivity. These properties, along with its wide availability, makes it one of the most widely used materials in the semiconductor industry. Deposition of zinc oxide films by ALD has gained favor during the last decade.[24] Various precursors used for the deposition of zinc oxide include diethylzinc,[25] dimethylzinc,[26] and zinc acetate,[27] and zinc oxide deposition has been demonstrated on glass,[28] soda lime glass,[27] silicon,[28] and sapphire substrates.[29] Other metal oxides similarly deposited by ALD include titanium oxide,[30] silicon oxide,[31] germanium oxide,[32] and copper oxide.[33] The large number of literature references that describe the deposition and characterization of aluminum oxide and zinc oxide was a significant motivation for their use in this work.

1.1.3 Deposition of other miscellaneous films using ALD

As noted, ALD has been used to deposit a variety of materials including metal oxides,[21, 34] metal nitrides,[35] metal sulfides,[36] metals,[10] and others.[37] While metal nitrides are one of the more challenging classes of materials that are deposited using atomic layer deposition,[38]

المنارة للاستشارات
www.manaraa.com

silicon nitride *is* regularly deposited by ALD. Silicon nitride has applications in high-k dielectrics and in ultra-large scale integration technology.[39] Thermal and plasma-assisted ALD have been used to deposit silicon nitride. Thermal ALD of silicon nitride relies on the energy provided by the increased temperature in the reactor, while plasma ALD takes advantage of the high-energy plasma species so that the deposition can take place at lower temperature.[40, 41]

Interest in the deposition of sulfide films has increased due to their applications in storage batteries, and photonics.[36] Metal sulfides are also promising materials as a low-cost alternative to silicon for the semiconductor industry.[42] The initial precursors of sulfur for the ALD processes included elemental sulfur, however, hydrogen sulfide (H_2S) is the preferred precursor for most deposition processes.[9] H_2S is a preferred precursor for sulfur due to its high volatility and reactivity. However, it has the limitations of being toxic, flammable, and corrosive.[43] Hence, if hydrogen sulfide has to be used as an ALD precursor, several adjustments have to be made to the instrument.

Thin metal film deposition by atomic layer deposition has some limited applications in the microelectronics and the semiconductor industry.[44] Its limitations include a lack of availability of suitable metal precursors, difficult in reducing the metal cations to their metallic state, and low reactivity of certain metals precursors.[45-47] Moreover, some metals require extreme temperatures for deposition. ALD deposition of metals is chemically different from other deposition processes, as the metal species have to be chemically reduced. Hence, metal deposition often utilizes molecular hydrogen (H_2) as the reducing species. Copper films represent the most widely studied metal films deposited by ALD.[48] Park and co-workers reported ALD of copper films using a Cu(II)ethylketomiminate precursor, which is a liquid at room temperature and has a

المنارة للاستشارات
www.manaraa.com

relatively high vapor pressure.[49] Other copper precursors, which have been used in the literature, include fluorinated diketonates, alkoxides, and copper metalorganics.[47]

Various literature reports confirm the importance of ALD as a vacuum deposition technique. I will cover this topic in some detail.

1.2 Particle coating by ALD

Coated particles have numerous industrial applications. These applications coupled with the advantages of vacuum deposition by ALD have resulted in renewed attention towards development of ALD processes for particle coating. Until now, liquid deposition processes have played a major role in the development of new coated particles. These methods were used because of their high growth per cycle and ease of deposition. However, they suffer from numerous limitations including low diffusion rates, poor mixing, extremely low deposition rates and non-uniform coating of powder substrates.[6, 50, 51] The complete potential of coated nano-materials can only be fully harnessed via reproducible processes. The reproducible and predictable nature of the ALD process makes it an ideal choice for coating thin films on powder substrates.[52]

1.2.1 Challenges in powder coating

While ALD has several advantages over vacuum deposition techniques like CVD and PVD, its use for particle coating has been limited and requires further development (see **Figure 1.2**).[6] The chief reasons for its lack of use include drastic increase in surface area for powder substrates compared to planar substrates and difficulty in achieving conformal thin films on particulate materials.[53] Low deposition rates and the need for agitation add to the difficulty of

المنارة للاستشارات
www.manaraa.com

achieving conformal thin films on powder substrates. Hence, initial studies for coating thin films on particle substrates required external agitation in the form of fluidized bed reactors.

The biggest problem associated with achieving conformal thin films on particles is agglomeration and aggregation. These limitations make it difficult to achieve conformal thin films on powder substrates.[54] Disintegration of agglomerates to smaller fragments has been achieved to deposit conformal coatings, especially while dealing with larger quantities of materials. Note that even though 'aggregation' and 'agglomeration' are used interchangeably in the literature, there are subtle differences between them. Particle aggregation is defined as the formation of a cluster of particles. Particle agglomeration refers to formation of assemblages and generally takes place in liquids. There are contrasting reports in the literature about the difference between the use of 'aggregation' and 'agglomeration'. [55, 56]

The other disadvantage associated with coating particles is their propensity to move and/or escape from the chamber. If the particle moves and escapes, it can clog the tubing and potentially damage other parts of the equipment. Furthermore, one may lose essential starting material that may be expensive. Hence, ALD processes for depositing thin film on particles requires a specially designed cover. This cover should have the following characteristics: a) it should be inert and should not affect the deposition process, b) the cover should be porous to allow the entry of precursor molecules so that they can react with the substrate, c) the pores present on the cover should not be big enough to allow the particles to escape, and d) the cover should allow the byproducts of the reaction and excess, unreacted precursor molecules to leave.[6]

The chief reasons for the lack of development of reproducible ALD processes on particles have included difficulty in uniformly coating the particle substrate.[21,53] Planar surfaces have small surface areas and do not require large dose times for the precursor. It is more difficult

المنارة للاستشارات
www.manaraa.com

to achieve conformal films on powder substrates and high-aspect ratio structures due to their drastic increase in surface area. For example, I found that a 100 mg sample of ca. 5 µm zirconia particles has a surface area of 4.4 m^2 by Brunauer-Emmett-Teller (BET) surface area measurements, which is 4400 times higher than a 1 x 1 cm silicon shard used for many initial ALD experiments in our laboratory.[57, 58]

The drastic increase in the surface area of particles has to be compensated to achieve conformal thin films on the particle surfaces. The first option to compensate for this drastic increase in surface area would be to increase the dose and purge times of the precursors. However, dose time alone cannot compensate for the significant increase in surface area. Several other parameters had to be optimized, which included substrate and precursor reactivity. For example, it is important to optimize substrate residence time, the chamber temperature, and pressure inside the chamber. These optimization experiments are useful in obtaining baseline dose times, purge times, and other deposition parameters for other high-aspect ratio structures or particulate materials.

The exposure time of any gaseous precursor with a solid substrate is expressed in terms of Langmuirs.[59] This is a way of quantifying the amount of gaseous substrate adsorbed on the reactant surface. The exposure time is calculated by multiplying the pressure of the gaseous precursor in Torr with the exposure time in seconds,[60] as follows

$$\text{One Langmuir} = 10^{-6} \text{ Torr Second} \quad (1.1)$$

Hence, two ways to increase the exposure time are to increase the residence time of the precursor or to increase the pressure in the chamber. Thus, while experimenting with different recipes and parameters for coating thin film on particles, substrate reactivity, reagent residence time, and

المنارة للاستشارات
www.manaraa.com

pressure inside the chamber should be varied. A series of optimized parameters ultimately leads to a 'static dosing recipe', which is suitable for high surface area powders and substrates. Note that a 'recipe' is a collection of ALD parameters and conditions that are uses for deposition of thin films on substrates.

There are several literature reports detailing ways to deal with the various challenges associated with coating thin films on powder substrates. Most of these changes involve achieving constant agitation while depositing the thin films. The various types of reactors that have been used for coating particles include: fluidized bed reactors,[61] rotary reactors,[62] and centrifugal accelerated fluidized reactors.[63]

1.2.2 Reactors for coating powder substrates

1.2.2.1 Fluidized bed reactors (FBR) for coating particles

Longrie and co-workers have reviewed various literature reports describing the coating of thin films on powder substrates using fluidized bed reactors.[64] Constant agitation of particles using a fluidized bed reactor has helped in reducing agglomeration and achieving conformal thin films. This helps reduce particle agglomeration and leads to conformal coating on the particle surface. A concern associated with using external force to reduce particle agglomeration is that it can affect particle size and damage the surfaces of the particles.[18 65] Hence, there has to be a balance between constant agitation and depositing conformal thin films on particle surfaces. FBR facilitates high rates of heat and mass transfer from the precursor molecules to the powder substrates. When a larger quantity of a powder substrate has to be coated by ALD, constant agitation in the form of a FBR becomes necessary.

المنارة للاستشارات
www.manaraa.com

The limitation of using an FBR for ALD is the need for additional equipment and the cost associated with it.[6] The other challenge with using the FBR is that gas flow during the deposition process severely dilutes the precursor concentration leading to long residence times and inefficient deposition rates. There have been several examples of FBRs used for depositing conformal thin films on powder substrates.[66-68] However, most of them suffer from limitations including low deposition rate, impractical dosing times, and the need for additional equipment.

In addition to acoustic- and vibration assisted fluidization in FBRs, supplementary techniques like gas pulsation and secondary jet flow are used to achieve constant agitation of powders for depositing thin films on powder substrates.[69, 70] Other methods including application of magnetic and electric fields, which help improve the fluidization of the particles.[70] In each of these approaches, there have been no significant effects on particle size during the depositions. However, there have been contrasting reports about the effect of agitation on particle size. Hence, removal of external agitation would be beneficial for coating thin films on powder substrates.

1.2.2.2 Rotary reactors for coating particles

Due to the several limitations of FBRs, McCormick and co-workers first developed a rotary-based reactor for coating conformal thin films on nanoparticles.[6] [62] Rotary reactors are able to deposit thin films on larger quantities of substrates compared to fluidized bed reactors. Rotary reactors have been used previously for depositing thin films using CVD.[71] In a typical rotary reactor, a porous metal cylinder is placed inside the vacuum chamber, which acts as a powder holder and rotates on a longitudinal axis. The particles present inside the particle holder experience several forces like viscous drag, gravitational, centrifugal, centripetal, and mechanical forces. This makes it difficult to analyze the coated particles after the deposition process, making

المنارة للاستشارات
www.manaraa.com

the process less suitable for long-term use. McCormick and co-workers developed several novel methods to achieve higher static exposure times inside the chamber to make the process reproducible.[72]

Rotary reactors do not require special attention and can be used to coat different sized particles.[73] The limitation of rotary reactors is the long exposure times and lack of reproducibility. Moreover, the use of rotary reactors is cost-efficient when the quantity of particles to be coated is larger than 10 g (the process is impractical for smaller quantities of starting materials).[74] The high surface area of powders makes it difficult to remove water and can lead to parasitic CVD in ALD depositions, limiting its practical use.[75] These limitations have forced researchers to explore other options.

1.2.2.3 Centrifugally accelerated fluidized reactors

The chief reason for the use of a centrifugal force in a fluidized reactor is to reduce agglomerates and powder aggregates. A typical setup consists of three different concentric cylinders, which have micrometer sized pores in them. The pores allow constant exchange of particles between the different parts of the instrument and uniform distribution of precursors for reaction with the substrate molecule. The gaseous precursor present inside the chamber exerts a viscous drag on the particles, which can affect particle shape and size.

The fluidization behavior of various particles like silica, titania, and alumina was studied by Quevedo *et al.,*[76] and Watano *et al*.[77] using a centrifugal assisted fluidized reactor. There are several other literature reports of centrifugal assisted reactors that have been used for coating thin films on powder substrates.[78] The chief limitation of centrifugal-assisted reactors is the lack of applicability and cost-effectiveness for industrial applications. Another challenge seen while

المنارة للاستشارات
www.manaraa.com

using centrifugal assisted reactors is clogging of the pores present between the cylinders. This creates a requirement for constant cleaning of the cylinder.

1.2.2.4 Summary

There have been several types of reactors used for coating thin films on powder substrates. Most of these reactors suffer from certain limitations including but not limited to lack of practicality, expense, requirement of large quantities of substrate for the process to be cost-effective, and the need for additional equipment. All these limitations have led researchers to explore different options to achieve conformal thin films on powder substrates. These limitations motivated us to design a methodology, which eliminates the need of external agitation and any additional equipment. Our solution works effectively for small quantities of particles.

1.2.3 Applications of ALD-coated particles

ALD coated particles find applications in several areas such as pharmaceutical dosage forms, catalysis, and batteries. Most of these applications are due to the protective nature of coatings deposited by ALD. I now discuss the various applications of coated particles.

1.2.3.1 Pharmaceutical dosage forms

Most active pharmaceutical agents are small organic molecules that are affected by the acidic pH present in the stomach.[79] Additionally, most dosage forms require improved flow properties and better surface characteristics, which have been difficult to achieve via conventional methods.[80] A recent study by McCormick and co-workers detail deposition of thin films of alumina (Al_2O_3), silica (SiO_2), and titania (TiO_2) on acetaminophen particles using a rotary reactor.[62, 72]

المنارة للاستشارات
www.manaraa.com

Acetaminophen, also known as paracetmol or APAP, is a common phenol-based pain reliever that is one of the most widely used active pharmaceutical ingredients (API). Acetaminophen is known to be cytotoxic and hepatotoxic at higher doses, and it exhibits numerous polymorphic structures.[81] Hence, several studies have tried to reduce its toxicity and improve its flow properties. In general, most studies involving thin film deposition on pharmaceutical powders lead to less cohesive powders, improved processability, and longer half-lives.[6, 62, 72]

A similar study of alumina coatings on budesonide exhibited precise control over the deposition parameters and film thickness. However, results were less ideal when lactose was used as the substrate.[80] The coated lactose and budesonide particles exhibited lower rates of dissolution and better half-lives, which were desirable features for pharmaceutical dosage forms. Porous polystyrene-divinylbenzene (PS-DVB) particles were coated with alumina and titania at low-temperatures in a fluidized bed reactor.[82] These reports suggest that ALD can be used for coating and depositing thin films on pharmaceutical powders. However, the chief concern of using ALD in pharmaceutical technology is thermal incompatibility of the pharmaceutical ingredients with the ALD processes. Also, several key parameters need to be optimized for the development of novel functional materials using ALD on pharmaceutical powders.[83]

1.2.3.2 Catalysis

Catalysts are widely used in industrial processes to improve yields of chemical reactions and reduce reaction times.[84] Catalysts offer numerous advantages for industrial applications, especially if they can be recovered easily.[85] Since the activity of heterogenous catalysts is generally dependent on the surface area of particles, surfaces of metal oxides have been

المنارة للاستشارات
www.manaraa.com

coated with ALD to address sintering problems and protect their catalytic activity.[86] In a recent study, titania nanoparticles were coated with alumina and the results showed a significant decrease in degradation.[87] While ALD has successfully coated powder substrates, there have also been reports of loss of catalytic activity and increased aggregation.[88]

1.2.3.3 Applications in the field of Energy and Batteries

There is huge potential for coating nanoparticles in the manufacture of lithium-ion battery systems. Yan and co-workers performed a detailed study on the performance and stability of ALD-coated thin films.[89] The prime applications of these ALD coatings are to tune the designs of active battery components by modifying active sites.[90, 91]

1.2.3.4 Miscellaneous Applications

A recent study by Valdesueiro and co-workers showed the deposition of alumina thin films on standard polyester-based particles, which yielded a glassy surface. The alumina thickness was varied between 1 – 30 nm, which softened the coated particles above the glass transition temperature and improved flow. ALD thin films had no effect on mechanical strength, particle size, or particle aggregation. In another study, micrometer-sized diamond nanoparticles were coated with ultra-thin films to increase their life cycles by preventing surface oxidation and graphitization.[92] Polycrystalline diamond compacts (PDC) are the major components used in fabricating drill bits. Improving their lifetime while maintaining their bulk properties is a prime requirement for their industrial application. Alumina was an ideal candidate for coating polycrystalline diamond compacts due to impermeability to oxygen and inertness to oxygen.

المنارة للاستشارات
www.manaraa.com

The applications of coated particles suggest that coated particles have a viable future. These applications, along with various literature reports, was the motivation behind our development of a non-agitated system for depositing thin films on powder substrates.

1.3 Area-selective atomic layer deposition (AS-ALD)

Area-selective ALD involves achieving ALD deposition selectively on a substrate, part of the substrate, or on one side of the substrate.[93] AS-ALD limits deposition to specific areas by exploiting differences in local surface chemistry or interactions between the substrate and precursor (see **Figure 1.3**). The semiconductor industry is facing numerous challenges due to device downscaling, decrease in node size, and demand for increased processing output.[94, 95] AS-ALD offers a solution to these challenges via bottom-up nanofabrication compared to a top-down approch.[96] It has the advantage of depositing the material at desired places and creating novel nanomaterials for use in several fields such as the semiconductor industry,[93] catalysis,[97] in nanoparticles,[98] and for development of novel patterns.[99]

1.3.1 Literature examples of AS-ALD

ALD processes rely on the surface chemistry between the precursor and the substrate for thin film deposition. Nucleation delay is seen in numerous AS-ALD processes. It represents the time between the initial exposure of the precursor to the substrate and when growth initiates on the surface. AS-ALD could be achieved in those cases when a longer nucleation delay is observed for one material.[100] AS-ALD has attracted attention in the semiconductor industry as a means of self-aligned fabrication. Early AS-ALD processes focused on device patterning for

المنارة للاستشارات
www.manaraa.com

nanoelectronics.[101, 102] There are other examples of area-selective deposition, which use etching to create differences in the surface chemistry. This approach offers a potential solution to the constant downscaling of device and node sizes in semiconductor devices.[99] The challenge going forward for the semiconductor industry will be to fabricate smaller features and to achieve alignment of novel device stacks.[94]

A way to achieve selective ALD would be to functionalize the surface where growth is needed. This is often referred to as selective precursor adsorption.[93, 103] The substrate temperature greatly influences this approach. The limitation here is that deposited films are thinner, mostly a few nanometers thick, which can limit the practicality of this approach.[104] Another common strategy for achieving AS-ALD is to exploit the chemical differences between hydroxyl-terminated and hydrogen-terminated regions on a substrate.[105]

Longo and co-workers investigated the selective deposition of various metal oxides using $TiCl_4$, TMA, and TDMAHf, on hydroxyl terminated substrates at 150 ºC. They used XPS to check the selectivity of deposition on a hydrogen-terminated substrate and found no deposition after 25 cycles. In contrast, there was little difference between the two surfaces when hafnium oxide (HfO_2) was deposited.[106] Hence, they were partially successful in their attempts to selectively deposit thin oxide films. This lack of reproducibility represents the biggest challenge in the use of AS-ALD in the semiconductor industry.

Another common strategy for achieving selective deposition would be selective co-reactant adsorption.[93, 107] This strategy focuses on deposition of metals by exploiting the surface activity of nanoparticles.[108] Area-selective metal deposition occurs by using oxygen as the co-reactant. Metals have the ability to catalyze the dissociative chemisorption of oxygen leaving

المنارة للاستشارات
www.manaraa.com

oxygen radicals on the surface, which catalyze selective deposition. Reactive oxygen radicals can lead to combustion of the precursor molecules leading to area-selective deposition. Several studies have been performed for area-selective deposition of metals like Pt, Ru, and Pd.[109-111]

The most extensively used approach for area-selective deposition is the use of self-assembled monolayers (SAM) to deactivate ALD growth on a certain part of a substrate.[112, 113] The use of SAMs employs the binding of a head group of a molecule to a surface for its functionalization. Once SAM monomers are selectively adsorbed on the surface, and selectivity relies on the directed adsorption of the precursor and co-reactant. A commonly used strategy involves the use of a CF_3 head group, which prevents the surface interaction of the precursor due to steric hindrance.[114] There are several examples of the use of self-assembled monolayers for achieving area-selective ALD deposition in the literature.[115-117]

Literature reports demonstrate the significance of AS-ALD for industrial applications. These studies serve as a motivation for selective deposition on one side of fused silica slides (unilateral deposition). Some of the challenges associated with achieving area-selective deposition on substrates are described in the next section.

1.3.2 Challenges of area-selective atomic layer deposition

There are two main challenges associated with area-selective ALD. The most common is mushroom growth, which refers to lateral broadening on a substrate while depositing in an isotropic manner.[118] This leads to deposition of a thin film in an undesired region or the non-growth region. This can lead to non-uniformity of the thin film or loss of starting material. The second major challenge while trying to achieve selective ALD is the lack of selectivity in the non-growth region.[94] In practice, there are several defects and impurities in the non-growth area that

المنارة للاستشارات
www.manaraa.com

are difficult to achieve or eliminate after the overall deposition process is completed. Another concern would be that the non-growth area could be affected while interacting with the precursor and co-reactant. This limitation will play a role when the non-growth region has to be functionalized.

The other challenges with AS-ALD are the need for expensive reagents that increase the overall cost of the process. Most nanopatterning techniques rely on etching, lithography, selective deposition, or a combination of these processes. These processes can be complicated and may require aggressive reagents, which limits their practicality.[119] Due to the various challenges and limitations of the current area-selective ALD processes, we wanted to establish a protocol for unilateral (one-sided) deposition. This involved simple reagents and conventional, inexpensive deposition techniques and raw materials. Our strategy relied on simple directional thermal deposition of salt films, which created a barrier layer against ALD deposition.

1.3.3 Unilateral deposition

Unilateral deposition represents a unique case of area selective deposition. This approach consists of selective deposition of thin ALD films on one side of a substrate by protecting and deprotecting a surface, which is analogous to a commonly used synthetic strategy for small molecule organic synthesis. We selectively protected one side of a substrate against ALD deposition by depositing a thin salt (NaCl) film (see **Figure 1.4**). Sodium chloride is an extremely common and inexpensive material. Evaporation, i.e., sublimation of NaCl, is advantageous here because it is a line-of-sight technique – it will only coat one side of the substrate. After coating with a salt layer, ALD was performed on the substrate, with the salt-coated side placed against the sample holder. ALD deposition is not a line-of-sight technique, hence, it will, at least to some

المنارة للاستشارات
www.manaraa.com

degree, deposit on both sides of the substrate. After ALD, the surface was rinsed with water, which removes the salt coating and any unwanted material adsorbed on top of it. Thus, this method consists of coating/masking one side of a substrate with a thin, e.g., ca. 100 nm, evaporated film of a salt, e.g., NaCl. An additional advantage of NaCl is that it is stable under most ALD deposition conditions, i.e., high deposition temperatures.

I chose thermal evaporation of sodium chloride because it is inexpensive, non-toxic, and the equipment needed for its deposition is readily available to us. The ease of removal of NaCl was another factor that influenced this decision. We confirmed NaCl depositions and the removal of the salt films by X-ray photoelectron spectroscopy (XPS) and/or spectroscopic ellipsometry (SE). Thus, we present a simple approach to deposit and remove barrier layer, which allows selective ALD deposition on only one side of a substrate.[120] Other applications of this strategy could be long term protection of substrate surfaces, e.g., glass slides to be used for pathology.

1.3.4 Potential applications of unilateral deposition

A situation where unilateral ALD deposition might be used would be the preparation of samples for measuring transmission intensities of thin films deposited on substrates (see **Figure 1.4**) That is, in standard ALD, we will obtain some deposition on the back side of fused silica slides in contact with the loading tool, primarily due to incomplete blockage of the gaseous precursors. Hence, for transmission measurements, the polarized light will interact with a high-quality ALD film on the front of the substrate and also with a low quality, partial film on the back of it. Partial coating of the back side of substrates in ALD is inevitable, even if the surfaces are very flat. That is, even exquisitely flat surfaces have some curvature to them and will actually

المنارة للاستشارات
www.manaraa.com

only make contact with each other at a few points. I confirmed non-uniform deposition on the backside of substrate using spectroscopic ellipsometry.

The ideal sample for transmission studies would be a thin film of metal oxide only on one side of a fused silica slide such that it interacts with air while the other side of the fused silica is uncoated. In this case, the light will interact with the following interfaces: air- fused silica, fused silica-alumina, and alumina-air. To achieve this, we need selective, preferential, uniform deposition on one side of the substrate. This capability will add to the advantages of conventional ALD that include uniformity, excellent conformality, and atomic level thickness.

The thin salt film, we used prevented the interaction of gaseous precursors with the substrate. Thin salt films of sodium chloride or a similar water-soluble salt act as a protective layer preventing interactions between the precursor and the substrate. Hence, the principal strategy was to use a directional, line-of-sight deposition with non-directional ALD. This can be equated to a protection/deprotection strategy commonly used in the organic synthesis of small molecules.[121]

I used several forms of surface analysis in my work, which include X-ray photoelectron spectroscopy (XPS), spectroscopic ellipsometry (SE), transmission electron microscopy (TEM), scanning electron microscopy (SEM), and water contact angle goniometry. Two specific analytical tools (XPS and SE) will be discussed in detail in the next section.

1.4 Surface characterization

Surface characterization plays an essential role in the development of novel thin films. It involves analyzing and detecting the structure, properties, and elemental compositions of

المنارة للاستشارات
www.manaraa.com

thin films and substrates. I was heavily involved with spectroscopic ellipsometry (SE) on planar substrates and liquid samples,[122, 123] and X-ray photoelectron spectroscopy (XPS)[124] of thin films on planar and powder substrates. I also used transmission electron microscope (TEM) for analysis of thin films on particle substrates and scanning electron microscopy (SEM) for determining particle sizes. The details and principles of these important surface analytical tools are discussed below.

1.4.1 X-ray photoelectron spectroscopy (XPS)[125, 126]

XPS, which was once commonly referred to as electron spectroscopy for chemical analysis (ESCA), is the most widely used technique for chemically analyzing surfaces.[127] XPS is often the first surface analytical tool used on thin films. XPS is used to determine both qualitative and quantitative elemental compositions of thin films. The importance of XPS is evident from the fact that it gets more than 10,000 mentions in the literature annually.[125] The use and importance of XPS as a surface analytical tool continues to grow every year. XPS can provide a great deal of important information about the composition, empirical formulas, and chemical and electronic states of the elements present at a surface.

XPS is based on the photoelectric effect, i.e., when X-rays irradiate a surface they eject core electrons (see **Figure 1.5**) .[127] A useful mathematical description of the photoelectric effect is as follows:

$$E_{photon} = E_{binding} + E_{kinetic} + \Phi, \quad (1.2)$$

where E_{photon} is the energy of the incident X-ray, $E_{binding}$ is the binding energy of the photoelectron, $E_{kinetic}$ is the kinetic energy of the photoelectron once it is ejected from the atom and Φ is the work function of the spectrometer. Because Φ is generally small compared to the other terms in Equation

المنارة للاستشارات
www.manaraa.com

1.2, it is often approximated as $E_{photon} \approx E_{binding} + E_{kinetic}$. The spectrometer work function is a constant for the instrument that is determined from reference materials. XPS is based on an indirect measurement, i.e., it determines the kinetic energies of ejected photoelectrons but plots/refers to their binding energies.[128]

The maximum depth that XPS can probe is ca. three mean free paths of the photoelectron in the material, which is generally 5 – 15 nm for most materials. X-rays penetrate deeply into most surfaces, i.e., about a micron. However, the ejected secondary electrons created by these X-rays can only travel a relatively short distance before losing energy, i.e., three mean free paths. This makes XPS very surface sensitive.[129]

A typical XPS instrument consists of an electron source (often a tungsten filament), a metal anode, a monochromator that allows only a specific wavelength of X-rays to pass, a flood gun for charge compensation of insulating samples, and a detector (most commonly a concentric hemispherical analyzer). These components are kept at very low pressure to ensure their cleanliness and to allow transport of photoelectrons from the sample to the detector. That is, the extremely low pressures in conventional XPS instruments ensures that ejected electrons travel freely. The two most common types of metal anodes for stand-alone XPS spectrometers are Al and Mg, which produce Al Kα and Mg Kα X-rays with energies of 1486.6 eV and 1253.4 eV, respectively. A synchrotron source can be used for XPS. However, synchrotrons are limited in availability. The XPS analytical chamber comprises two chief parts: a) a prep chamber where the pressure is ca. 10^{-3} – 10^{-7} torr, which can be exposed to the atmosphere, and b) a main chamber where the pressure is ca. 10^{-8} – 10^{-11} torr. The prep chamber and the main chamber are separated by a barrier (usually a gate valve), which allows for easy sample transfer.

المنارة للاستشارات
www.manaraa.com

When a beam of X-rays strikes a sample, core-level electrons from elements near the surface of the material are ejected. The analyzer measures the kinetic energies of these photoelectrons, which are converted to their corresponding binding energies using the above-mentioned equation. These peaks help identify and quantify the elements present on the surface of a material (only hydrogen and helium cannot be detected by XPS).[130] A typical XPS spectrum is plotted as the number of counts obtained as a function of binding energy. The reason for plotting binding energy is that it is unaffected by a change in the X-ray source. That is, the binding energies of photoelectron signals will remain unaffected while Auger signals will shift if an X-ray source with a different energy is used.

When X-rays irradiate surfaces, they eject electrons leaving them positively charged. If the resulting positive charge on the surface is not compensated, i.e., replaced, it will become progressively more difficult for an electron present on the surface to be ejected. Some of the problems seen with sample charging, i.e., a lack of charge compensation, are peaks shifting to higher apparent binding energies for most samples, and in the worst cases, gross distortion and even complete disappearance of the peaks from an XPS spectrum. Hence, it becomes imperative that charge compensation be applied for most insulating samples. Some examples of insulating samples include many coated and uncoated particles, biological samples, and other insulators like glasses and plastics. The various ways in which charge compensation can be applied include with a flood gun, a grounded nickel mesh close to the sample, indium foil with particles pressed into it, or a combination of these ways.

When a grounded nickel mesh is placed above an insulating sample, X-rays irradiate the mesh and eject photoelectrons. These photoelectrons interact with the surface to be analyzed and help in its charge compensation. In addition, biological samples like a human tooth,

المنارة للاستشارات
www.manaraa.com

a fish bone, etc. often show charging to varying degrees at different positions, a phenomenon referred to as differential charging. Charging and differential charging are commonly seen in XPS.[131, 132] An innovation in XPS is where the sample is analyzed at comparatively higher pressure, ca. 2500 Pa, which is called near-ambient pressure XPS (NAP-XPS). NAP-XPS deals with charging in a different way. I will describe this in the next section.[124, 126, 128, 133-135]

The labeling convention in XPS is important to understand. First, the symbol for the element is written, which is followed by three quantum numbers: a number, a letter, and another number, which is a fraction that identifies the orbital resulting from photoemission, for example, S $2p_{1/2}$. These numbers and letter correspond to the principal quantum number, n, the angular momentum quantum number, l, and the value of the j quantum number. For example, a gold surface will show two intense peaks, the Au $4f_{7/2}$ and Au $4f_{5/2}$ signals, that correspond to electrons ejected from the Au 4f level.[126]

XPS was usually the first surface analytical tool I used for analyzing and characterizing thin films on flat and powder substrates. I will present XPS data in Chapter 2, Chapter 3, and Chapter 4.

1.4.2 Spectroscopic ellipsometry (SE)[136, 137]

Spectroscopic ellipsometry (SE) is one of the most important tools for characterizing surfaces and materials. In SE, the data collection is fast, convenient, and takes place at room temperature and pressure. SE can measure thin film thicknesses, and optical functions of substrates, films, and interfaces. SE is sensitive to the presence of interfaces between layers and film roughness.

المنارة للاستشارات
www.manaraa.com

A typical ellipsometer consists of a light source, a polarization generator, the sample stage, another polarizer, and a detector (see **Figure 1.6**). Most ellipsometers also have at least one compensator (quarter-wave plate). The light source generates unpolarized light that passes through a polarizer. The light source installed in the M-2000DI Woollam ellipsometer in the Linford lab emits between 191 - 1688 nm. The polarizer only allows light of a preferred electric field orientation to pass, i.e., it converts unpolarized light to polarized light, e.g.,, the light that strikes the sample may be linearly polarized. The polarizer axis is oriented between the *p*- (in the plane of incidence) and *s*- (perpendicular to the plane of incidence) planes (see **Figure 1.7**). The reflected light from the sample surface is generally elliptically polarized, and it travels through a continuously rotating polarizer before it is detected. The change in light from linearly to elliptically polarized provides the technique its name, ellipsometry.[122, 123]

The analyzer allows only a certain amount of light to pass, which depends on the polarizer orientation relative to the electric field coming from the sample. The change in polarization between the input and output signals provides information about the sample, such as film thickness, surface roughness, optical functions, and film anisotropies. The ellipsometer collects information from the sample in the form of psi (ψ) and delta (Δ) and uses this information to get material characteristics from the sample. Ellipsometric analysis is based on the Fresnel equations for polarized light interacting with multi-layered planar substrates and ellipsometric measurements are often expressed as follows:

$$\frac{r_p}{r_s} = \tan\psi e^{i\Delta} \tag{1.2}$$

where r_p and r_s are the complex Fresnel reflection coefficients of the sample for p- and s- polarized light. The ellipsometric parameter ψ provides information about the ratio of the two amplitudes,

المنارة للاستشارات
www.manaraa.com

and Δ is the phase shift between the two components. The sample is usually probed at or near the Brewster angle as this is where the sample will display the maximal change in the ellipsometric parameters.[138]

A theoretical model is constructed after collecting the ellipsometric data. This is the part of the analysis that can take a significant amount of time. Various parameters in a model are varied to improve the match between the experimental data and model calculations. However, the number of unknown parameters should not exceed the amount of information contained in the experimental data to avoid fit-parameter correlation. Calculated model values are compared to the experimental data through regression analysis. The mean squared error (MSE) is employed to get the best match between the model and the experimental data. MSE is a measure of the closeness of the data between the theoretical and experimental values. The MSE values for the fits in my work were calculated using:

$$MSE = \sqrt{\frac{1}{3n-m}\sum_{i=1}^{n}\left[\left(\frac{N_{Ei}-N_{Gi}}{0.001}\right)^2+\left(\frac{C_{Ei}-C_{Gi}}{0.001}\right)^2+\left(\frac{S_{Ei}-S_{Gi}}{0.001}\right)^2\right]}$$

where n is the number of wavelengths, i.e., (ψ, Δ) pairs, m is the number of variable parameters in the model and σ represents a standard deviation. Terms superscripted with an E denote experimentally measured values at a given data point i, and terms superscripted with a G indicate the data generated by the model at the data point i.

I used spectroscopic ellipsometry for analyzing liquid samples like polyethylene glycol, solid thin film alumina, and zinc oxide layers. I will present the data for these studies in chapter 2 and Appendix 3 of this dissertation.

المنارة للاستشارات
www.manaraa.com

1.4.3 Near-ambient pressure X-ray photoelectron spectroscopy (NAP-XPS)[133]

Near-ambient pressure X-ray photoelectron spectroscopy (NAP-XPS) was developed to analyze non-conventional materials that are not vacuum compatible.[133] Some of the advantages of NAP-XPS include reduced sample preparation (often none is needed) and very short pump down times during sample introduction. For example, unlike conventional XPS, both sample loading and analysis in NAP-XPS can often be achieved in a few minutes.[139] Various examples of materials that can be analyzed by near-ambient pressure X-ray photoelectron spectroscopy include liquids, gases, human tissues, biological cells, and samples that outgas significantly.

Differential pumping is employed to keep the different regions of the NAP-XPS instrument at different pressures (from relatively high to ultra-high vacuum). That is, the analysis chamber of the instrument is maintained at comparatively higher pressure (up to 2500 Pa or even higher in some cases) with an inert gas like nitrogen, argon, or helium entering this chamber, while other parts of the instrument like the detector are under high vacuum. This means that an NAP-XPS instrument has multiple vacuum pumps, which increases the overall cost of the instrument. For example, eight vacuum pumps are used in the SPECS EnviroESCA, and the number can be higher in other instruments. The sheer size of the instrument (3 meters by 2 meters) creates another issue.[140] The cost of the instruments is also high.

A unique attribute of NAP-XPS is its intrinsic ability to neutralize charge when a sample is irradiated with X-rays. This is referred to as environmental charge compensation and it eliminates the need for additional charge compensation (see **Figure 1.8**).[141] When X-rays collide with the gas molecules around a sample, both electrons and cations are generated, which compensates for the build up of positive charge. The pressure and the type of gas molecules present

www.manaraa.com

inside the analytical chamber dictates the degree of charge compensation. Thus, insulating samples can be analyzed by NAP-XPS without any external charge compensation. In conventional XPS, an external flood gun is employed for charge compensation, which has the potential for sample damage.

These following materials have been analyzed by the first, standalone near-ambient pressure XPS instrument: human tooth,[142] printed and unprinted office paper,[143] coffee bean,[144] Coca-Cola,[145] liquid water,[146] nitrogen gas,[147] and zirconium oxide.[148] I analyzed the data for these materials, which was published in Surface Science Spectra. These samples demonstrate the ability of NAP-XPS to analyze non-conventional samples.

1.5 Conclusions

Atomic layer deposition is used to deposit thin films on substrates including silicon, fused silica slides, glass slides, high-aspect ratio structures, and powder substrates. ALD consists of sequential exposures of two different high vapor pressure reactive precursors to a substrate separated by a purging step that removes any excess and unreacted precursor from the chamber. An efficient purging step ensures that reaction of the precursor with the substrate proceeds in an ALD-like manner, i.e., the two precursors do not react with each other and only with the substrate. ALD is now one of the most commonly used vacuum deposition techniques owing to its precise control over thickness and uniformity. Hence, the use and popularity of ALD have increased in the last two decades due to miniaturization of semiconductor and microelectronic devices.

Chapter two describes optimization experiments on planar surfaces and collection of optical constants of alumina from thin films deposited on silicon substrates. I performed here a

المنارة للاستشارات
www.manaraa.com

multi-sample analysis on eleven different thin films for calculation of the optical constants of alumina. The various parameters that were optimized for thin film deposition include the dose time and purge times for both precursors. The goal of these experiments was to achieve optimal film thickness, conformal films, and predictable growth per cycle (GPC) for thin film deposition. I characterized these films using spectroscopic ellipsometry, X-ray photoelectron spectroscopy, and water contact angle goniometry. These experiments were used to provide optimal deposition conditions for powder substrates.

Chapter three describes thin film depositions on powder substrates. Powder substrates have several issues that pertain to obtaining conformal thin films due to their significant increase in surface area and particle aggregation. Hence, while optimizing thin film deposition experiments on powder substrates, a simple increase in dose time was not sufficient. Hence, I had to develop a different way of increasing the reactivity between the precursors and the substrate. The absence of any agitation during the deposition process provides advantages for the ALD instruments. I designed a cover for powder substrates on a loading tool, which prevents escape of the powder substrates from the reactor chamber. The cover also allowed entry of the precursor molecules so that they will react with the substrate, and allows for the escape of byproducts from the reaction chamber. The goal for these powder deposition experiments was to achieve conformal thin film deposition on powder substrates in a non-agitated system.

Chapter four describes unilateral selective deposition of salt films on fused silica substrates for selective area-selective deposition. I protected fused silica slides with directional, thermally deposited sodium chloride films, which was followed by non-directional atomic layer deposition on them. Sodium chloride will act as a protective layer and inhibit the deposition of alumina or a similar material by ALD. The salt films were removed by water treatment. This

المنارة للاستشارات
www.manaraa.com

removes any alumina deposited on top of the sodium chloride films. This process can be used to prepare samples for optical transmission studies with selective ALD on one side of a fused silica slide.

Chapter five of this dissertation includes near-ambient pressure XPS analysis of non-conventional materials like liquid water, nitrogen gas, a human tooth, printed office paper, and zirconium oxide particles. These materials demonstrate the wide range of samples that can be analyzed with NAP-XPS. I will also discuss the advantages of near-ambient pressure XPS over conventional XPS and environmental charge compensation.

www.manaraa.com

1.6 Figures

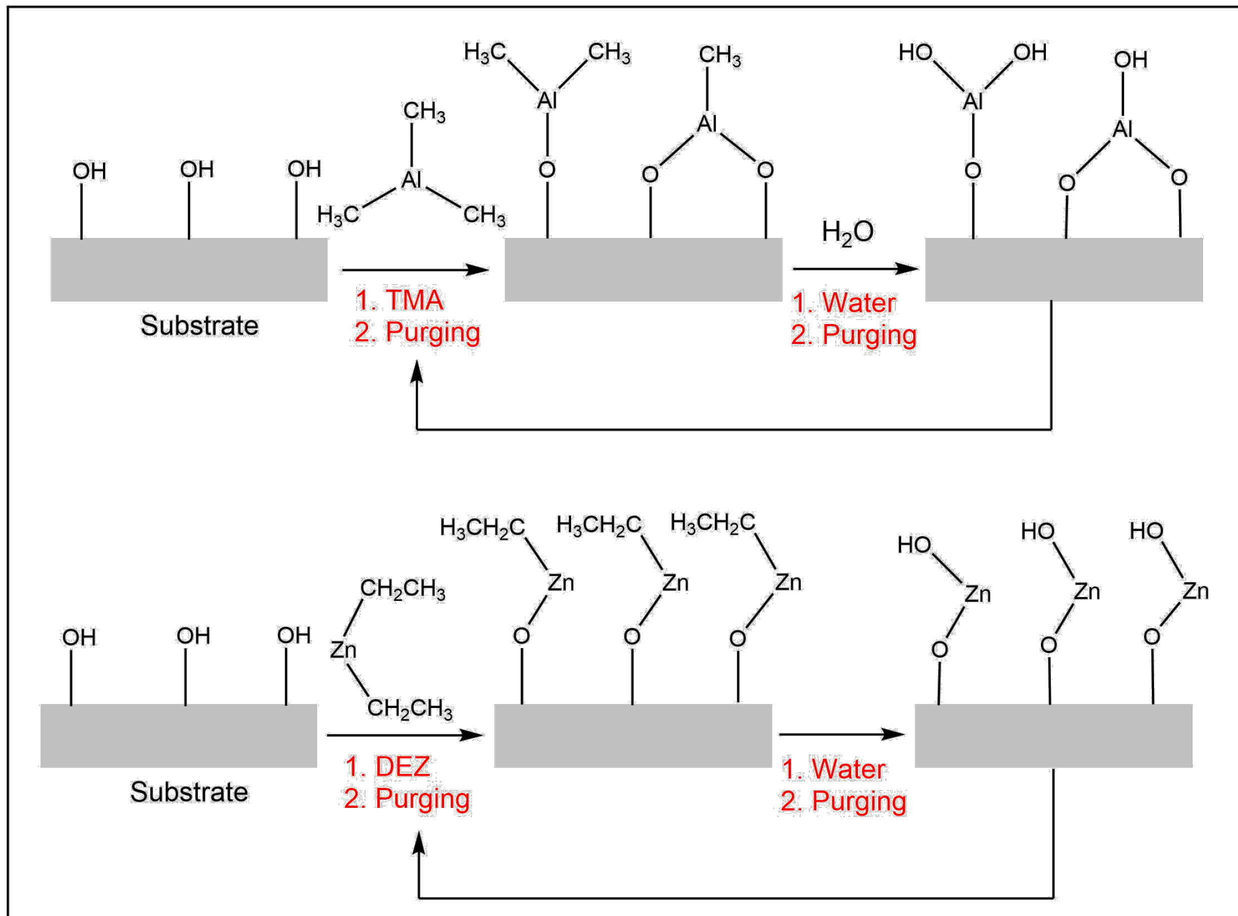

Figure 1.1. Schematic description of the stepwise ALD deposition of alumina and zinc oxide using trimethylaluminum (TMA) and water, and diethylzinc (DEZ) and water, respectively.[15]

www.manaraa.com

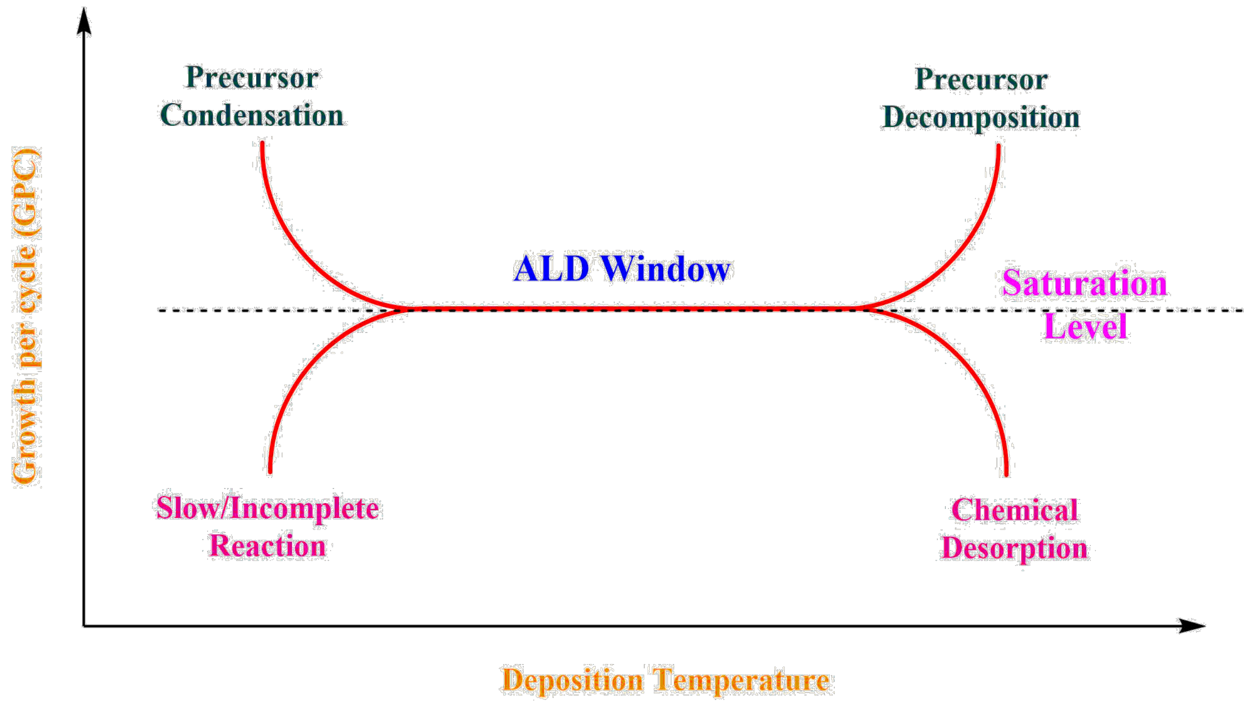

Figure 1.2. Schematic showing the effect of deposition temperature on growth per cycle on alumina deposition using ALD. (Image adapted from George, S. *Chem. Rev.* **2010**, *1*, 111-131.)

المنارة للاستشارات
www.manaraa.com

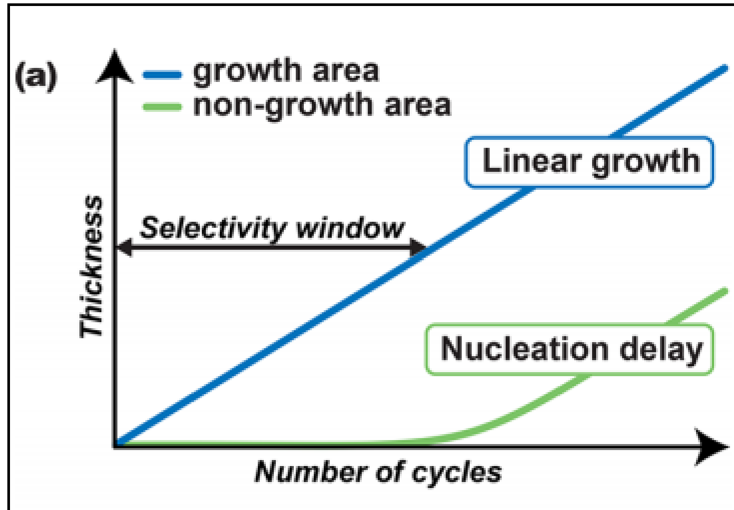

Figure 1.3. Schematic showing the nucleation behavior that be exploited for achieving AS-ALD. The image shows the possible selectivity window which can be used for achieving AS-ALD. (Image adapted from Mackus et al. Chem. Mater. 2019, 31, 2-12.)

المنارة للاستشارات
www.manaraa.com

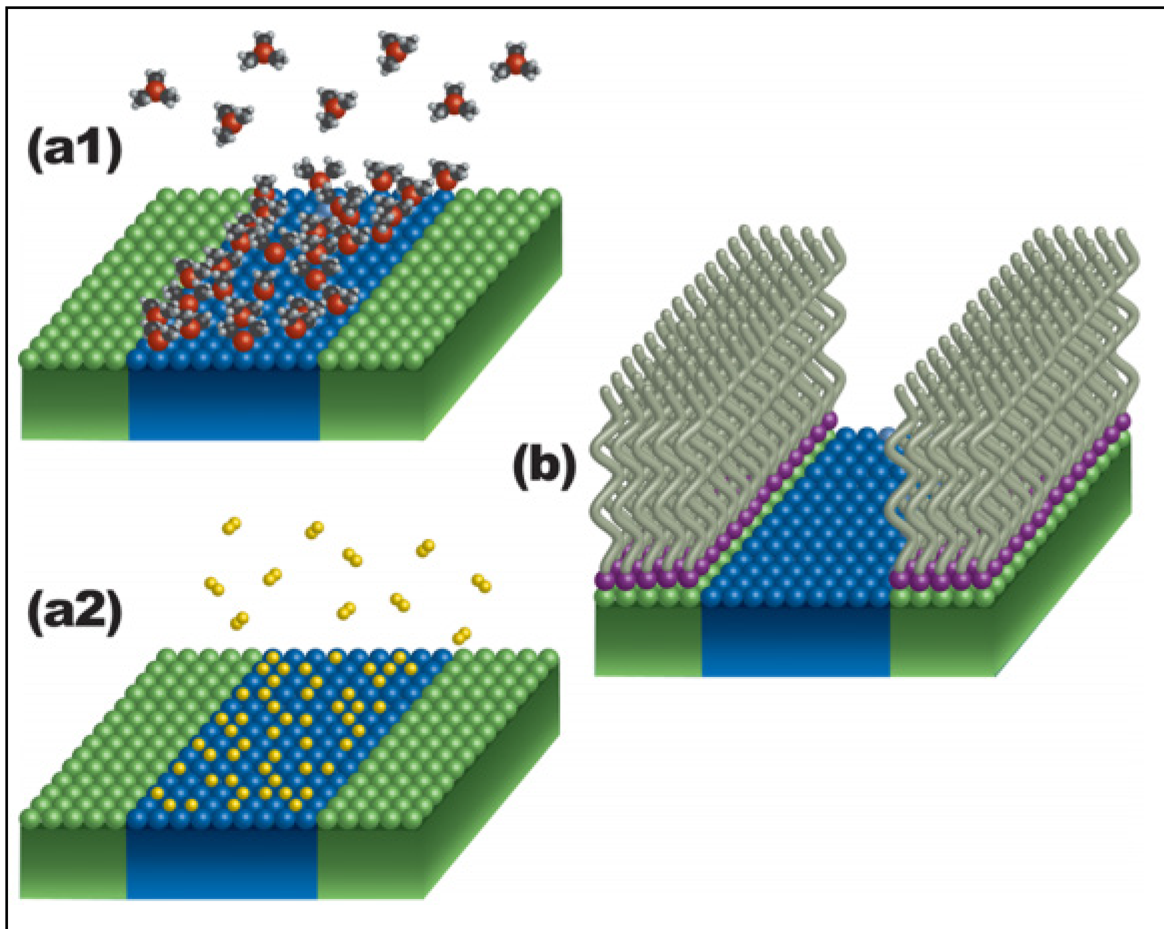

Figure 1.4. Schematic showing an overview of various approaches for AS-ALD. (a1) Approach for selective precursor adsorption where functionalized area is the desired region for deposition (a2) Conventional approach for co-reactant adsorption (b) Surface is pre-functionalized before the deposition occurs to achieve AS-ALD. (Image adapted from Mackus et al. *Chem. Mater.* **2019**, *31*, 2-12.)

المنارة للاستشارات
www.manaraa.com

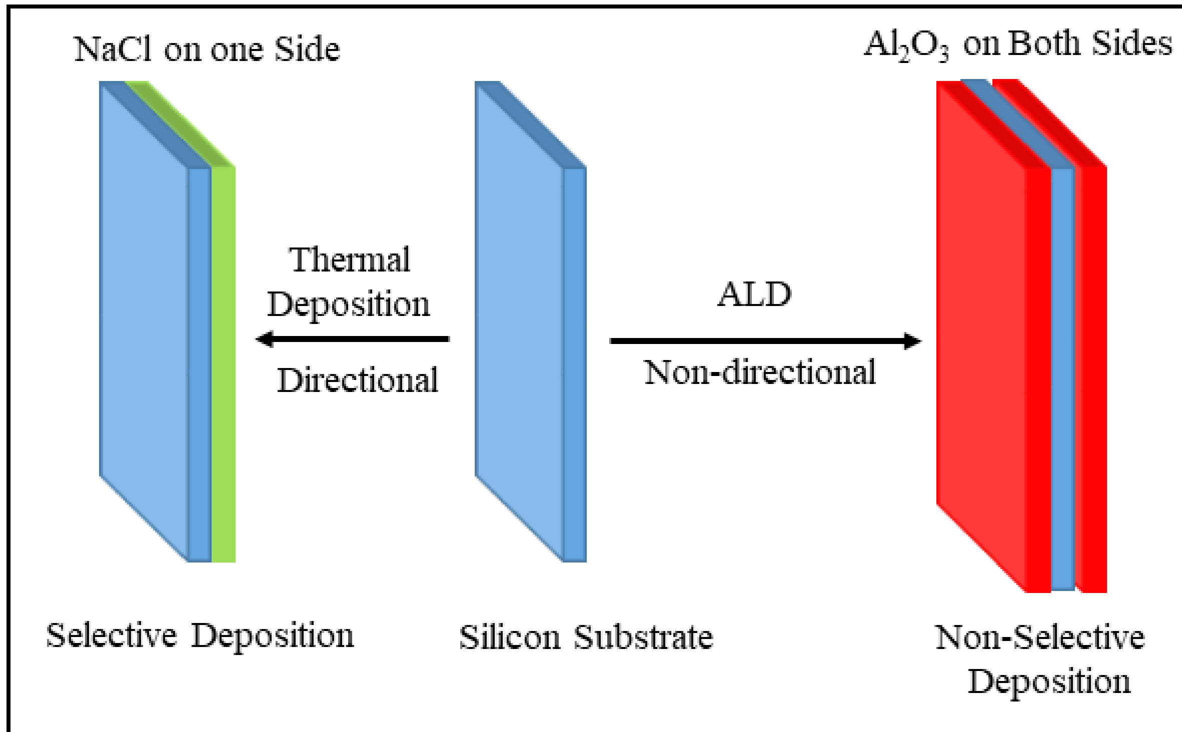

Figure 1.5. Schematic showing selective thermal deposition and non-selective ALD deposition. These two deposition techniques were used in conjunction to achieve unilateral area-selective deposition on one side of silicon substrate.

المنارة للاستشارات
www.manaraa.com

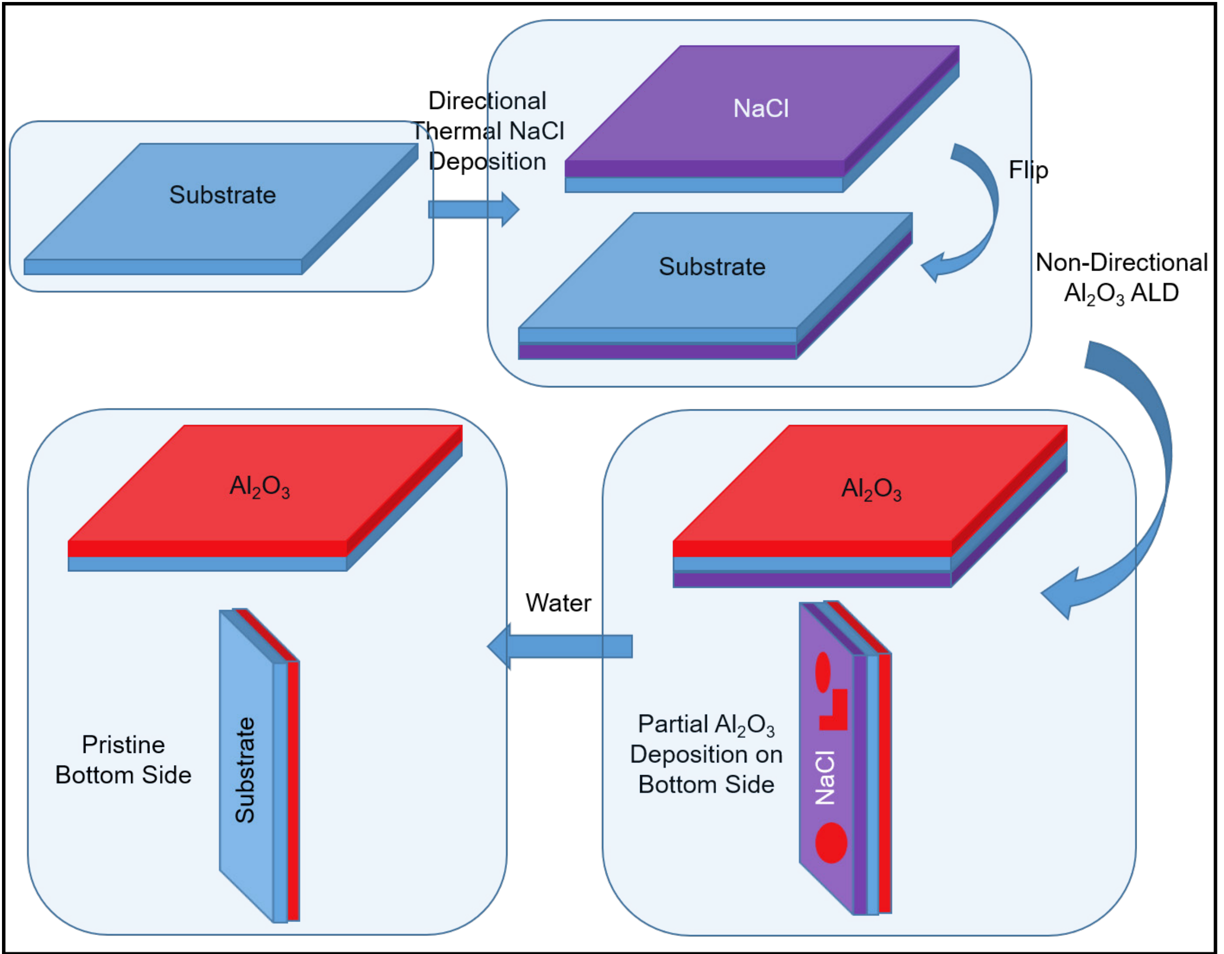

Figure 1.6. Schematic showing unilateral deposition on a silicon substrate using protection/deprotection strategy. The first step, thermal deposition selectively deposits NaCl on one side of the substrate. The next step, ALD deposits ALD on both the sides of the substrate. The final step, water treatment removes NaCl and any alumina (or a similar metal oxide) adsorbed on top of the NaCl layer.

المنارة للاستشارات
www.manaraa.com

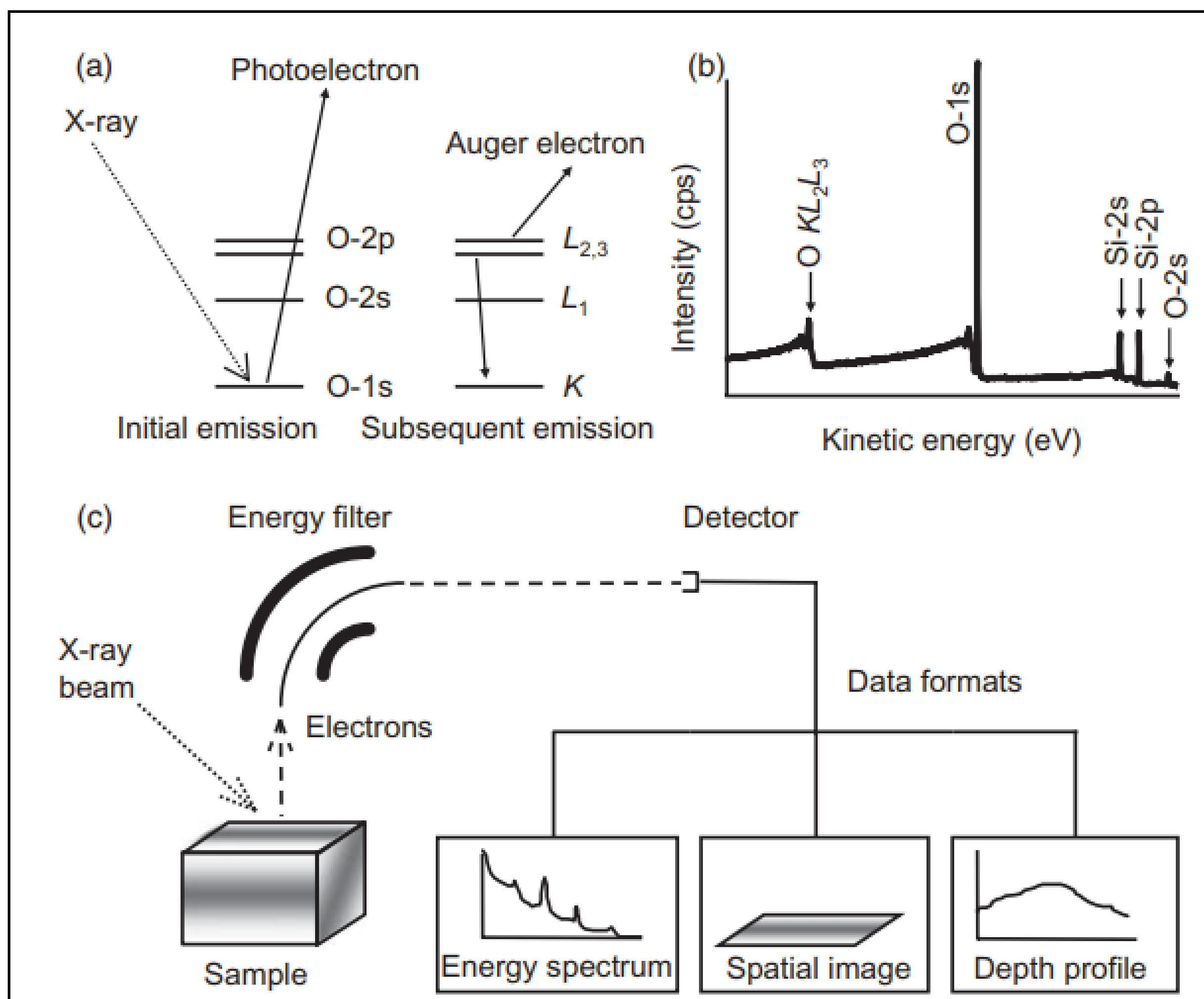

Figure 1.7. Schematic representation of a) the photoelectron emission and Auger emission, b) XPS spectra collected from the substrate, c) the basic instrumentation of the XPS. (Image reproduced from Paul van der heide, X-ray Photoelectron Spectroscopy: An introduction to Principles and Practices).

المنارة للاستشارات
www.manaraa.com

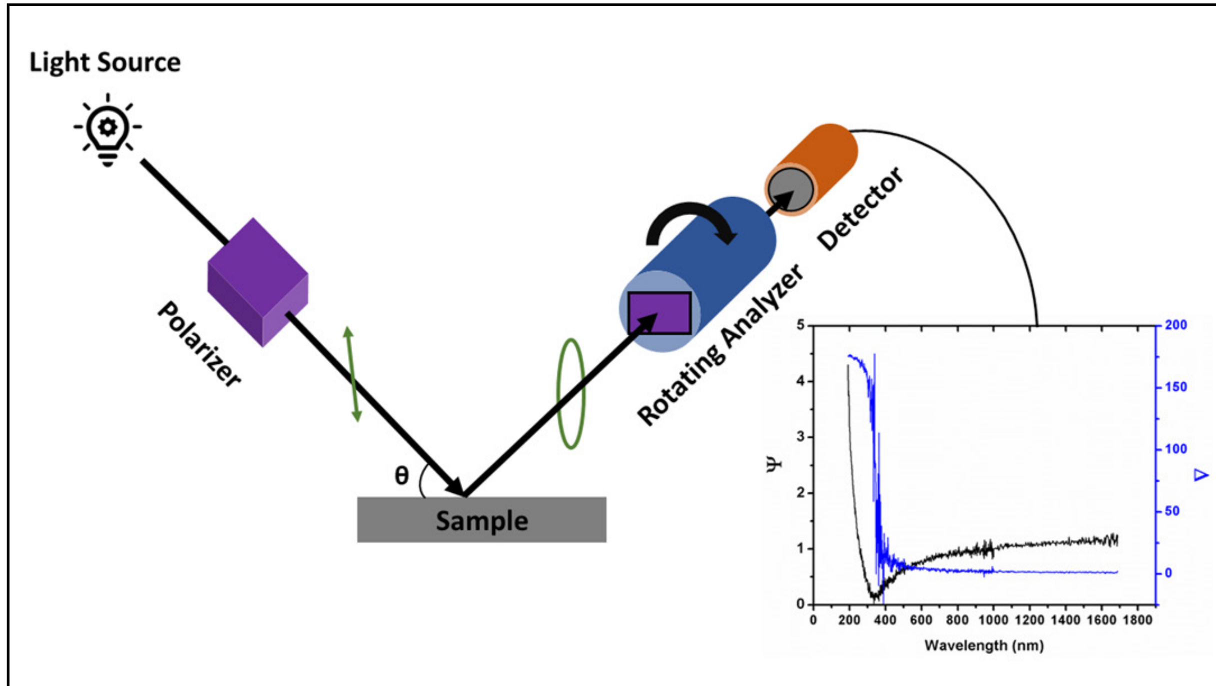

Figure 1.8. Simplified model of an ellipsometer. Reprinted with permission from reference [2]. Copyright (2016) Momentum Press.

.

المنارة للاستشارات
www.manaraa.com

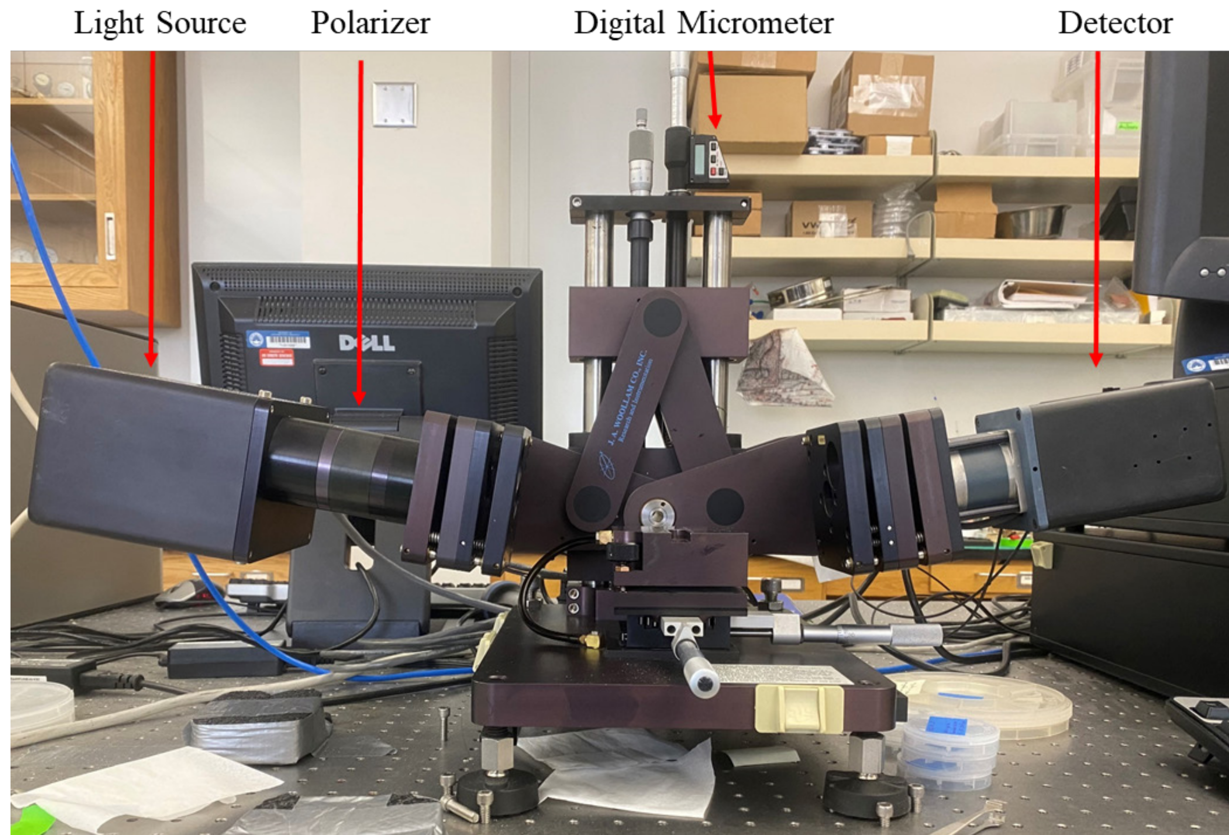

Figure 1.9. Image of the J. A. Woollam spectrometer M-2000DI used in the Linford lab showing its major parts.

المنارة للاستشارات
www.manaraa.com

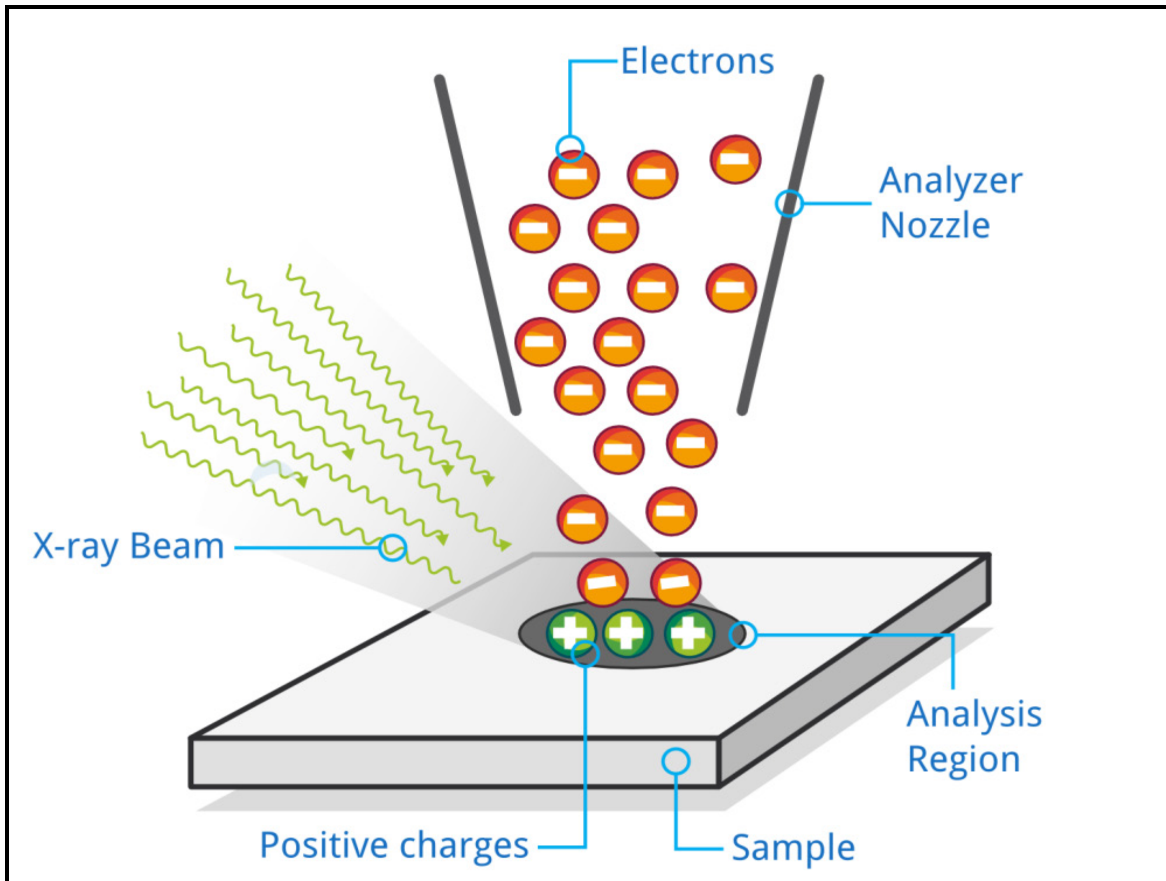

Figure 1.10. Schematic of environmental charge compensation used in near-ambient pressure X-ray photoelectron spectroscopy. (Figure used with permission from Dr. Paul M. Dietrich and SPECS, Germany).

المنارة للاستشارات
www.manaraa.com

1.7 References

1. Burakowski, T.; Wierzchon, T., *Surface Engineering of Metals: Principles, Equipment, Technologies*. CRC Press: 1998.
2. Oshida, Y., *Surface Engineering and Technology for Biomedical Implants*. Momentum Press: New York, 2014; p 320.
3. Jensen, D. S.; Kanyal, S. S.; Madaan, N.; Hancock, J. M.; Dadson, A. E.; Vail, M. A.; Vanfleet, R.; Shutthanandan, V.; Zhu, Z.; Engelhard, M. H.; Linford, M. R., Multi-instrument characterization of the surfaces and materials in microfabricated, carbon nanotube-templated thin layer chromatography plates. An analogy to 'The Blind Men and the Elephant'. *Surface and Interface Analysis* **2013,** *45* (8), 1273-1282.
4. Saini, G.; Wiest, L. A.; Herbert, D.; Biggs, K. N.; Dadson, A.; Vail, M. A.; Linford, M. R., C18, C8, and perfluoro reversed phases on diamond for solid-phase extraction. *J. Chromatogr. A* **2009,** *1216* (16), 3587-3593.
5. Hämäläinen, J.; Ritala, M.; Leskelä, M., Atomic Layer Deposition of Noble Metals and Their Oxides. *Chem. Mater.* **2014,** *26* (1), 786-801.
6. Adhikari, S.; Selvaraj, S.; Kim, D.-H., Progress in Powder Coating Technology Using Atomic Layer Deposition. *Adv. Mater. Interfaces* **2018,** *5* (16).
7. Perrotta, A.; Werzer, O.; Coclite, A. M., Strategies for Drug Encapsulation and Controlled Delivery Based on Vapor-Phase Deposited Thin Films. *Adv. Eng. Mater.* **2018,** *20* (3), 1700639.
8. Beiner, M.; Rengarajan; Pankaj, S.; Enke, D.; Steinhart, M., Manipulating the Crystalline State of Pharmaceuticals by Nanoconfinement. *Nano Letters* **2007,** *7* (5), 1381-1385.
9. Suntola, T.; Hyvarinen, J., Atomic Layer Epitaxy. *Annu. Rev. Mater. Sci.* **1985,** *15* (1), 177-195.
10. Chen, L.; Connell, J. G.; Nie, A.; Huang, Z.; Zavadil, K. R.; Klavetter, K. C.; Yuan, Y.; Sharifi-Asl, S.; Shahbazian-Yassar, R.; Libera, J. A.; Mane, A. U.; Elam, J. W., Lithium metal protected by atomic layer deposition metal oxide for high performance anodes. *J. Mater. Chem. A* **2017,** *5* (24), 12297-12309.
11. Profijit, H. B.; Potts, S. E.; van de Sanden; M.;, M. C.; Kessels, W. M. M., Plasma-assisted Atomic Layer Deposition: Basics, Oppurtunities, and CHallenges. *J. Vac. Sci. Technol. A* **2011,** *29*, 1-26.
12. Zaera, F., The Surface Chemistry of Atomic Layer Depositions of Solid Thin Films. *J. Phys. Chem. Lett.* **2012,** *3* (10), 1301-9.
13. Puurunen, R. L., Surface chemistry of atomic layer deposition: A case study for the trimethylaluminum/water process. *J. Appl. Phys.* **2005,** *97* (12), 121301-121311.
14. Van Bui, H.; Grillo, F.; van Ommen, J. R., Atomic and molecular layer deposition: off the beaten track. *Chem. Commun.* **2017,** *53* (1), 45-71.
15. Johnson, R. W.; Hultqvist, A.; Bent, S. F., A brief review of atomic layer deposition: From fundamentals to applications. *Mater. Today* **2014,** *17*, 236-246.
16. Pakkala, A.; Putkonen, M., Atomic Layer Deposition. In *Handbook of Deposition Technologies for Films and Coatings (Third Edition)*, Martin, P. M., Ed. William Andrew Publishing: Boston, 2010; pp 364-391.
17. George, S. M., Atomic layer deposition: An overview. *Chem. Rev.* **2010,** *110*, 111-131.
18. Hwang, C. S. K., S. K.; Lee, S. W., Mass-production memories (DRAM and Flash). In *Atomic layer deposition for semiconductors*, Hwang, C. S., Ed. Springer: New York, 2012.

المنارة للاستشارات
www.manaraa.com

19. Kumar, P.; Wiedmann, M. K.; Winter, C. H.; Avrutsky, I., Optical properties of Al_2O_3 thin films grown by atomic layer deposition. *Appl. Opt.* **2009,** *48*, 5407-5412.
20. Houska, J.; Blazek, J.; Rezek, J.; Proksova, S., Overview of optical properties of Al_2O_3 films prepared by various techniques. *Thin Solid Films* **2012,** *520* (16), 5405-5408.
21. Sophia, J.; Attolini, G.; Bosi, M., *Review on Atomic Layer Deposition and Applications of Oxide Thin Films*. 2013; Vol. 38.
22. Broas, M.; Kanninen, O.; Vuorinen, V.; Tilli, M.; Paulasto-Kröckel, M., Chemically stable atomic-layer-deposited Al_2O_3 films for processability. *ACS Omega* **2017,** *2* (7), 3390-3398.
23. Elliott, S. D.; Scarel, G.; Wiemer, C.; Fanciulli, M.; Pavia, G., Ozone-Based Atomic Layer Deposition of Alumina from TMA: Growth, Morphology, and Reaction Mechanism. *Chem. Mater.* **2006,** *18* (16), 3764-3773.
24. Tynell, T.; Karppinen, M., Atomic layer deposition of ZnO: a review. *Semicond. Sci. Tech.* **2014,** *29* (4), 043001.
25. Elam, J. W.; Sechrist, Z. A.; George, S. M., ZnO/Al_2O_3 nanolaminates fabricated by atomic layer deposition: growth and surface roughness measurements. *Thin Solid Films* **2002,** *414* (1), 43-55.
26. Lujala, V.; Skarp, J.; Tammenmaa, M.; Suntola, T., Atomic layer epitaxy growth of doped zinc oxide thin films from organometals. *Appl. Surf. Sci.* **1994,** *82-83*, 34-40.
27. Tammenmaa, M.; Koskinen, T.; Hiltunen, L.; Niinistö, L.; Leskelä, M., Zinc chalcogenide thin films grown by the atomic layer epitaxy technique using zinc acetate as source material. *Thin Solid Films* **1985,** *124* (2), 125-128.
28. Guziewicz, E.; Kowalik, I. A.; Godlewski, M.; Kopalko, K.; Osinniy, V.; Wójcik, A.; Yatsunenko, S.; Łusakowska, E.; Paszkowicz, W.; Guziewicz, M., Extremely low temperature growth of ZnO by atomic layer deposition. *J. Appl. Phys.* **2008,** *103* (3), 033515.
29. Lin, Y.-T.; Chung, P.-H.; Lai, H.-W.; Su, H.-L.; Lyu, D.-Y.; Yen, K.-Y.; Lin, T.-Y.; Kung, C.-Y.; Gong, J.-R., Self-limiting growth of ZnO films on (0001) sapphire substrates by atomic layer deposition at low temperatures using diethyl-zinc and nitrous oxide. *Appl. Surf. Sci.* **2009,** *256* (3), 819-822.
30. Niemelä, J.-P.; Marin, G.; Karppinen, M., Titanium dioxide thin films by atomic layer deposition: a review. *Semiconductor Science and Technology* **2017,** *32* (9), 093005.
31. Lee, W.-J.; Han, C.-H.; Park, J.-K.; Lee, Y.-S.; Rha, S.-K., Atomic Layer Deposition and Properties of Silicon Oxide Thin Films Using Alternating Exposures to $SiH_2Cl_2$and O_3. *Jap. J. Appl. Phys.* **2010,** *49* (7), 071504.
32. Chua, D.; Kim, S. B.; Sinsermsuksakul, P.; Gordon, R., Atomic layer deposition of energy band tunable tin germanium oxide electron transport layer for the SnS-based solar cells with 400 mV open-circuit voltage. *Appl. Phys. Lett.* **2019,** *114* (21), 213901.
33. Iivonen, T.; Hämäläinen, J.; Marchand, B.; Mizohata, K.; Mattinen, M.; Popov, G.; Kim, J.; Fischer, R. A.; Leskelä, M., Low-temperature atomic layer deposition of copper(II) oxide thin films. *J. Vac. Sci. Technol. A* **2015,** *34* (1), 01A109.
34. Leskelä, M. R., M., Atomic layer deposition (ALD): From precursors to thin film structures. *Thin Solid Films* **2002,** *409*, 138-146.
35. Kim, H., Atomic layer deposition of metal and nitride thin films: Current research efforts and applications for semiconductor device processing. *J. Vac. Sci. Technol. B* **2003,** *21* (6), 2231-2261.
36. Dasgupta, N. P.; Meng, X.; Elam, J. W.; Martinson, A. B. F., Atomic Layer Deposition of Metal Sulfide Materials. *Acc. Chem. Res.* **2015,** *48* (2), 341-348.

المنارة للاستشارات
www.manaraa.com

37. Lim, B. S.; Rahtu, A.; Gordon, R. G., Atomic layer deposition of transition metals. *Nat. Mater.* **2003,** *2* (11), 749-54.
38. Meng, X.; Byun, Y.-C.; Kim, H. S.; Lee, J. S.; Lucero, A. T.; Cheng, L.; Kim, J., Atomic Layer Deposition of Silicon Nitride Thin Films: A Review of Recent Progress, Challenges, and Outlooks. *Materials* **2016,** *9* (12), 1007.
39. Meng, X.; Byun, Y.-C.; Kim, H. S.; Lee, J. S.; Lucero, A. T.; Cheng, L.; Kim, J., Atomic Layer Deposition of Silicon Nitride Thin Films: A Review of Recent Progress, Challenges, and Outlooks. *Materials* **2016,** *9* (12), 1007.
40. Profijt, H. B.; Potts, S. E.; van de Sanden, M. C. M.; Kessels, W. M. M., Plasma-Assisted Atomic Layer Deposition: Basics, Opportunities, and Challenges. *J. Vac. Sci. Technol. A* **2011,** *29* (5), 050801.
41. Kim, H.; Oh, I.-K., Review of plasma-enhanced atomic layer deposition: Technical enabler of nanoscale device fabrication. *Jap. J. Appl. Phys.* **2014,** *53* (3S2), 03DA01.
42. Meng, X.; Yang, X. Q.; Sun, X., Emerging applications of atomic layer deposition for lithium-ion battery studies. *Adv. Mater.* **2012,** *24* (27), 3589-615.
43. Dasgupta, N. P.; Mack, J. F.; Langston, M. C.; Bousetta, A.; Prinz, F. B., Design of an atomic layer deposition reactor for hydrogen sulfide compatibility. *Rev. Sci. Instrum.* **2010,** *81* (4), 044102.
44. Hagen, D. J.; Pemble, M. E.; Karppinen, M., Atomic layer deposition of metals: Precursors and film growth. *Appl. Phys. Rev.* **2019,** *6* (4), 041309.
45. Mårtensson, P.; Carlsson, J.-O., Atomic Layer Epitaxy of Copper on Tantalum. *Chem. Vap. Deposition* **1997,** *3* (1), 45-50.
46. Ritala, M., Atomic Layer Epitaxy Growth of TiN Thin Films from TiI_4 and NH_3. *J. Electrochem. Soc.* **1998,** *145* (8), 2914.
47. Kanarik, K. J.; Lill, T.; Hudson, E. A.; Sriraman, S.; Tan, S.; Marks, J.; Vahedi, V.; Gottscho, R. A., Overview of atomic layer etching in the semiconductor industry. *J. Vac. Sci. Technol. A* **2015,** *33* (2), 020802.
48. Lee, S.; Kim, J. Y.; Lee, T.-W.; Kim, W.-K.; Kim, B.-S.; Park, J. H.; Bae, J.-S.; Cho, Y. C.; Kim, J.; Oh, M.-W.; Hwang, C. S.; Jeong, S.-Y., Fabrication of high-quality single-crystal Cu thin films using radio-frequency sputtering. *Sci. Rep.* **2014,** *4* (1), 6230.
49. Park, K.-M.; Kim, J.-K.; Han, B.; Lee, W.-J.; Kim, J.; Shin, H.-K., Influence of the deposition temperature on the properties of copper thin films prepared by alternating injection of Cu(ethylketoiminate)2 and H2 on a ruthenium substrate. *Microelectron. Eng.* **2012,** *89*, 27-30.
50. King, D. M.; Spencer, J. A.; Liang, X.; Hakim, L. F.; Weimer, A. W., Atomic layer deposition on particles using a fluidized bed reactor with in situ mass spectrometry. *Surf. Coat. Technol.* **2007,** *201* (22), 9163-9171.
51. Detavernier, C.; Dendooven, J.; Pulinthanathu Sree, S.; Ludwig, K. F.; Martens, J. A., Tailoring nanoporous materials by atomic layer deposition. *Chem. Soc. Rev.* **2011,** *40* (11), 5242-5253.
52. Leskelä, M.; Ritala, M., Atomic Layer Deposition Chemistry: Recent Developments and Future Challenges. *Angew. Chem. Int. Ed.* **2003,** *42* (45), 5548-5554.
53. Ritala, M.; Kemell, M.; Lautala, M.; Niskanen, A.; Leskelä, M.; Lindfors, S., Rapid Coating of Through-Porous Substrates by Atomic Layer Deposition. *Chem. Vap. Deposition* **2006,** *12* (11), 655-658.
54. Seville, J. P. K.; Willett, C. D.; Knight, P. C., Interparticle forces in fluidisation: a review. *Powder Technol.* **2000,** *113* (3), 261-268.

المنارة للاستشارات
www.manaraa.com

55. Nichols, G.; Byard, S.; Bloxham, M. J.; Botterill, J.; Dawson, N. J.; Dennis, A.; Diart, V.; North, N. C.; Sherwood, J. D., A review of the terms agglomerate and aggregate with a recommendation for nomenclature used in powder and particle characterization. *J. Pharm. Sci.* **2002,** *91* (10), 2103-2109.
56. Sokolov, S. V.; Tschulik, K.; Batchelor-McAuley, C.; Jurkschat, K.; Compton, R. G., Reversible or Not? Distinguishing Agglomeration and Aggregation at the Nanoscale. *Anal. Chem.* **2015,** *87* (19), 10033-10039.
57. Gelb, L. D.; Gubbins, K. E., Characterization of Porous Glasses: Simulation Models, Adsorption Isotherms, and the Brunauer−Emmett−Teller Analysis Method. *Langmuir* **1998,** *14* (8), 2097-2111.
58. Naderi, M., Surface Area: Brunauer–Emmett–Teller (BET). In *Progress in Filtration and Separation*, Tarleton, S., Ed. Academic Press: Oxford, 2015; pp 585-608.
59. Gordon, R. G.; Hausmann, D.; Kim, E.; Shepard, J., A Kinetic Model for Step Coverage by Atomic Layer Deposition in Narrow Holes or Trenches. *Chem. Vap. Deposition* **2003,** *9* (2), 73-78.
60. Arts, K.; Vandalon, V.; Puurunen, R. L.; Utriainen, M.; Gao, F.; Kessels, W. M. M.; Knoops, H. C. M., Sticking probabilities of H_2O and $Al(CH_3)_3$ during atomic layer deposition of Al_2O_3 extracted from their impact on film conformality. *J. Vac. Sci. Technol. A* **2019,** *37* (3), 030908.
61. King, D. M.; Spencer, J. A.; Liang, X.; Hakim, L. F.; Weimer, A. W., Atomic layer deposition on particles using a fluidized bed reactor with in situ mass spectrometry. *Surf. Coat. Tech.* **2007,** *201* (22), 9163-9171.
62. McCormick, J. A.; Cloutier, B. L.; Weimer, A. W.; George, S. M., Rotary reactor for atomic layer deposition on large quantities of nanoparticles. *J. Vac. Sci. Technol. A* **2007,** *25* (1), 67-74.
63. Quevedo, J. A.; Flesch, J.; Pfeffer, R.; Dave, R., Evaluation of assisting methods on fluidization of hydrophilic nanoagglomerates by monitoring moisture in the gas phase. *Chem. Eng. Sci.* **2007,** *62* (9), 2608-2622.
64. Longrie, D.; Deduytsche, D.; Detavernier, C., Reactor concepts for atomic layer deposition on agitated particles: A review. *J. Vac. Sci. Technol. A* **2013,** *32* (1), 010802.
65. Liu, H.; Zhang, L.; Chen, T.; Wang, S.; Han, Z.; Wu, S., Experimental study on the fluidization behaviors of the superfine particles. *Chem. Eng. J.* **2015,** *262*, 579-587.
66. Hakim, L. F.; Blackson, J.; George, S. M.; Weimer, A. W., Nanocoating Individual Silica Nanoparticles by Atomic Layer Deposition in a Fluidized Bed Reactor. *Chem. Vap. Deposition* **2005,** *11* (10), 420-425.
67. Tamadondar, M. R.; Zarghami, R.; Tahmasebpoor, M.; Mostoufi, N., Characterization of the bubbling fluidization of nanoparticles. *Particuology* **2014,** *16*, 75-83.
68. Wank, J. R.; George, S. M.; Weimer, A. W., Nanocoating individual cohesive boron nitride particles in a fluidized bed by ALD. *Powder Technol.* **2004,** *142* (1), 59-69.
69. Espin, M. J.; Valverde, J. M.; Quintanilla, M. A. S.; Castellanos, A., Electromechanics of fluidized beds of nanoparticles. *Phys. Rev. E* **2009,** *79* (1), 011304.
70. Valverde, J. M.; Quintanilla, M. A. S.; Espin, M. J.; Castellanos, A., Nanofluidization electrostatics. *Phys. Rev. E* **2008,** *77* (3), 031301.
71. Ferguson, J. D.; Weimer, A. W.; George, S. M., Atomic layer deposition of ultrathin and conformal Al_2O_3 films on BN particles. *Thin Solid Films* **2000,** *371* (1), 95-104.

المنارة للاستشارات
www.manaraa.com

72. McCormick, J. A.; Rice, K. P.; Paul, D. F.; Weimer, A. W.; George, S. M., Analysis of Al_2O_3 Atomic Layer Deposition on ZrO_2 Nanoparticles in a Rotary Reactor. *Chem. Vap. Deposition* **2007,** *13* (9), 491-498.
73. Longrie, D.; Deduytsche, D.; Haemers, J.; Driesen, K.; Detavernier, C., A rotary reactor for thermal and plasma-enhanced atomic layer deposition on powders and small objects. *Surf. Coat. Tech.* **2012,** *213*, 183-191.
74. Wilson, C. A.; McCormick, J. A.; Cavanagh, A. S.; Goldstein, D. N.; Weimer, A. W.; George, S. M., Tungsten atomic layer deposition on polymers. *Thin Solid Films* **2008,** *516* (18), 6175-6185.
75. Jung, Y. S.; Cavanagh, A. S.; Riley, L. A.; Kang, S.-H.; Dillon, A. C.; Groner, M. D.; George, S. M.; Lee, S.-H., Ultrathin Direct Atomic Layer Deposition on Composite Electrodes for Highly Durable and Safe Li-Ion Batteries. *Adv. Mater.* **2010,** *22* (19), 2172-2176.
76. Yu, Q.; Dave, R. N.; Zhu, C.; Quevedo, J. A.; Pfeffer, R., Enhanced fluidization of nanoparticles in an oscillating magnetic field. *AIChE Journal* **2005,** *51* (7), 1971-1979.
77. Nakamura, H.; Watano, S., Fundamental particle fluidization behavior and handling of nano-particles in a rotating fluidized bed. *Powder Technol.* **2008,** *183* (3), 324-332.
78. Duan, C.-L.; Liu, X.; Shan, B.; Chen, R., Fluidized bed coupled rotary reactor for nanoparticles coating via atomic layer deposition. *Rev. Sci. Instrum.* **2015,** *86* (7), 075101.
79. Kääriäinen, T. O.; Kemell, M.; Vehkamäki, M.; Kääriäinen, M.-L.; Correia, A.; Santos, H. A.; Bimbo, L. M.; Hirvonen, J.; Hoppu, P.; George, S. M.; Cameron, D. C.; Ritala, M.; Leskelä, M., Surface modification of acetaminophen particles by atomic layer deposition. *Int. J. Pharm.* **2017,** *525* (1), 160-174.
80. Ghoroi, C.; Han, X.; To, D.; Jallo, L.; Gurumurthy, L.; Davé, R. N., Dispersion of fine and ultrafine powders through surface modification and rapid expansion. *Chem. Eng. Sci.* **2013,** *85*, 11-24.
81. Ghanem, C. I.; Pérez, M. J.; Manautou, J. E.; Mottino, A. D., Acetaminophen from liver to brain: New insights into drug pharmacological action and toxicity. *Pharmacological Res.* **2016,** *109*, 119-131.
82. Liang, X.; Lynn, A. D.; King, D. M.; Bryant, S. J.; Weimer, A. W., Biocompatible Interface Films Deposited within Porous Polymers by Atomic Layer Deposition (ALD). *ACS Appl. Mater. Interfaces* **2009,** *1* (9), 1988-1995.
83. Zhang, D.; Quayle, M. J.; Petersson, G.; van Ommen, J. R.; Folestad, S., Atomic scale surface engineering of micro- to nano-sized pharmaceutical particles for drug delivery applications. *Nanoscale* **2017,** *9* (32), 11410-11417.
84. Lindström, B.; Pettersson, L. J., A Brief History of Catalysis. *CATTECH* **2003,** *7* (4), 130-138.
85. Schmidt, F., The Importance of Catalysis in the Chemical and Non-Chemical Industries. In *Basic Principles in Applied Catalysis*, Baerns, M., Ed. Springer Berlin Heidelberg: Berlin, Heidelberg, 2004; pp 3-16.
86. Ma, Z.; Brown, S.; Howe, J. Y.; Overbury, S. H.; Dai, S., Surface Modification of Au/TiO_2 Catalysts by SiO_2 via Atomic Layer Deposition. *J. Phys. Chem. C* **2008,** *112* (25), 9448-9457.
87. Azizpour, H.; Talebi, M.; Tichelaar, F. D.; Sotudeh-Gharebagh, R.; Guo, J.; van Ommen, J. R.; Mostoufi, N., Effective coating of titania nanoparticles with alumina via atomic layer deposition. *Appl. Surf. Sci.* **2017,** *426*, 480-496.

المنارة للاستشارات
www.manaraa.com

88. Guo, J.; Van Bui, H.; Valdesueiro, D.; Yuan, S.; Liang, B.; Van Ommen, R. J., Suppressing the Photocatalytic Activity of TiO_2 Nanoparticles by Extremely Thin Al_2O_3 Films Grown by Gas-Phase Deposition at Ambient Conditions. *Nanomaterials* **2018,** *8* (2).
89. Yan, B.; Li, X.; Bai, Z.; Song, X.; Xiong, D.; Zhao, M.; Li, D.; Lu, S., A review of atomic layer deposition providing high performance lithium sulfur batteries. *J. Power Sources* **2017,** *338*, 34-48.
90. Ritala, M.; Leskelä, M., Atomic layer epitaxy - a valuable tool for nanotechnology? *Nanotechnology* **1999,** *10* (1), 19-24.
91. Wang, X.; Yushin, G., Chemical vapor deposition and atomic layer deposition for advanced lithium ion batteries and supercapacitors. *Energy Environ. Sci.* **2015,** *8* (7), 1889-1904.
92. Liang, X.; Zhan, G.-D.; King, D. M.; McCormick, J. A.; Zhang, J.; George, S. M.; Weimer, A. W., Alumina atomic layer deposition nanocoatings on primary diamond particles using a fluidized bed reactor. *Diam. Relat. Mater.* **2008,** *17* (2), 185-189.
93. Mackus, A. J. M.; Merkx, M. J. M.; Kessels, W. M. M., From the Bottom-Up: Toward Area-Selective Atomic Layer Deposition with High Selectivity. *Chem. Mater.* **2019,** *31* (1), 2-12.
94. Clark, R.; Tapily, K.; Yu, K. H.; Hakamata, T.; Consiglio, S.; O'Meara, D.; Wajda, C.; Smith, J.; Leusink, G., Perspective: New process technologies required for future devices and scaling. *APL Mater.* **2018,** *6* (5), 058203.
95. Fang, M.; Ho, J. C., Area-Selective Atomic Layer Deposition: Conformal Coating, Subnanometer Thickness Control, and Smart Positioning. *ACS Nano* **2015,** *9* (9), 8651-8654.
96. Tour, J., Top-Down versus Bottom-Up Fabrication of Graphene-Based Electronics. *Chem. Mater.* **2013,** *26*, 163–171.
97. Cao, K.; Cai, J.; Liu, X.; Chen, R., Catalysts design and synthesis via selective atomic layer deposition. *J. Vac. Sci. Technol. A* **2017,** *36* (1), 010801.
98. Singh, J. A.; Thissen, N. F. W.; Kim, W.-H.; Johnson, H.; Kessels, W. M. M.; Bol, A. A.; Bent, S. F.; Mackus, A. J. M., Area-Selective Atomic Layer Deposition of Metal Oxides on Noble Metals through Catalytic Oxygen Activation. *Chem. Mater.* **2018,** *30* (3), 663-670.
99. Biyikli, N.; Haider, A.; Deminskyi, P.; Yilmaz, M. In *Self-aligned nanoscale processing solutions via selective atomic layer deposition of oxide, nitride, and metallic films*, SPIE Nanoscience + Engineering, SPIE: 2017.
100. Mackus, A. J. M.; Bol, A. A.; Kessels, W. M. M., The use of atomic layer deposition in advanced nanopatterning. *Nanoscale* **2014,** *6* (19), 10941-10960.
101. Suresh, V.; Huang, M. S.; Srinivasan, M. P.; Guan, C.; Fan, H. J.; Krishnamoorthy, S., Robust, High-Density Zinc Oxide Nanoarrays by Nanoimprint Lithography-Assisted Area-Selective Atomic Layer Deposition. *J. Phys. Chem. C* **2012,** *116* (44), 23729-23734.
102. Park, M. H.; Jang, Y. J.; Sung-Suh, H. M.; Sung, M. M., Selective atomic layer deposition of titanium oxide on patterned self-assembled monolayers formed by microcontact printing. *Langmuir* **2004,** *20* (6), 2257-2260.
103. Kwon, J.; Saly, M.; Kanjolia, R. K.; Chabal, Y. J., Surface Reactions of μ2-η2-(tBu-acetylene)dicobalthexacarbonyl with Oxidized and H-terminated Si(111) Surfaces. *Chem. Mater.* **2011,** *23* (8), 2068-2074.
104. McDonnell, S.; Longo, R. C.; Seitz, O.; Ballard, J. B.; Mordi, G.; Dick, D.; Owen, J. H. G.; Randall, J. N.; Kim, J.; Chabal, Y. J.; Cho, K.; Wallace, R. M., Controlling the Atomic Layer Deposition of Titanium Dioxide on Silicon: Dependence on Surface Termination. *J. Phys. Chem. C* **2013,** *117* (39), 20250-20259.

المنارة للاستشارات
www.manaraa.com

105. Longo, R. C.; Owen, J. H. G.; McDonnell, S.; Dick, D.; Ballard, J. B.; Randall, J. N.; Wallace, R. M.; Chabal, Y. J.; Cho, K., Toward Atomic-Scale Patterned Atomic Layer Deposition: Reactions of Al_2O_3 Precursors on a Si(001) Surface with Mixed Functionalizations. *J. Phys. Chem. C* **2016,** *120* (5), 2628-2641.
106. Longo, R. C.; McDonnell, S.; Dick, D.; Wallace, R. M.; Chabal, Y. J.; Owen, J. H. G.; Ballard, J. B.; Randall, J. N.; Cho, K., Selectivity of metal oxide atomic layer deposition on hydrogen terminated and oxidized Si(001)-(2×1) surface. *J. Vac. Sci. Technol. B* **2014,** *32* (3), 03D112.
107. Weber, M. J.; Mackus, A. J. M.; Verheijen, M. A.; van der Marel, C.; Kessels, W. M. M., Supported Core/Shell Bimetallic Nanoparticles Synthesis by Atomic Layer Deposition. *Chem. Mater.* **2012,** *24* (15), 2973-2977.
108. Lei, Y.; Liu, B.; Lu, J.; Lobo-Lapidus, R. J.; Wu, T.; Feng, H.; Xia, X.; Mane, A. U.; Libera, J. A.; Greeley, J. P.; Miller, J. T.; Elam, J. W., Synthesis of Pt–Pd Core–Shell Nanostructures by Atomic Layer Deposition: Application in Propane Oxidative Dehydrogenation to Propylene. *Chem. Mater.* **2012,** *24* (18), 3525-3533.
109. Mackus, A. J. M.; Mulders, J. J. L.; van de Sanden, M. C. M.; Kessels, W. M. M., Local deposition of high-purity Pt nanostructures by combining electron beam induced deposition and atomic layer deposition. *J. Appl. Phys.* **2010,** *107* (11), 116102.
110. Färm, E.; Lindroos, S.; Ritala, M.; Leskelä, M., Microcontact Printed RuOx Film as an Activation Layer for Selective-Area Atomic Layer Deposition of Ruthenium. *Chem. Mater.* **2012,** *24* (2), 275-278.
111. Mackus, A. J. M.; Verheijen, M. A.; Leick, N.; Bol, A. A.; Kessels, W. M. M., Influence of Oxygen Exposure on the Nucleation of Platinum Atomic Layer Deposition: Consequences for Film Growth, Nanopatterning, and Nanoparticle Synthesis. *Chem. Mater.* **2013,** *25* (9), 1905-1911.
112. Lee, J. P.; Sung, M. M., A New Patterning Method Using Photocatalytic Lithography and Selective Atomic Layer Deposition. *J. Am. Chem. Soc.* **2004,** *126* (1), 28-29.
113. Liu, J.; Mao, Y.; Lan, E.; Banatao, D. R.; Forse, G. J.; Lu, J.; Blom, H.-O.; Yeates, T. O.; Dunn, B.; Chang, J. P., Generation of Oxide Nanopatterns by Combining Self-Assembly of S-Layer Proteins and Area-Selective Atomic Layer Deposition. *J. Am. Chem. Soc.* **2008,** *130* (50), 16908-16913.
114. Lee, H.-B.-R.; Bent, S. F., Nanopatterning by Area-Selective Atomic Layer Deposition. *Atomic Layer Deposition of Nanostructured Materials* **2012**, 193-225.
115. Wink, T.; J. van Zuilen, S.; Bult, A.; P. van Bennekom, W., Self-assembled Monolayers for Biosensors. *Analyst* **1997,** *122* (4), 43R-50R.
116. Bobb-Semple, D.; Nardi, K. L.; Draeger, N.; Hausmann, D. M.; Bent, S. F., Area-Selective Atomic Layer Deposition Assisted by Self-Assembled Monolayers: A Comparison of Cu, Co, W, and Ru. *Chem. Mater.* **2019,** *31* (5), 1635-1645.
117. Wang, C.; Pan, X.; Sun, C.; Urisu, T., Area-selective deposition of self-assembled monolayers on SiO_2/Si(100) patterns. *Appl. Phys. Lett.* **2006,** *89* (23), 233105.
118. Ras, R. H. A.; Sahramo, E.; Malm, J.; Raula, J.; Karppinen, M., Blocking the Lateral Film Growth at the Nanoscale in Area-Selective Atomic Layer Deposition. *J. Am. Chem. Soc.* **2008,** *130* (34), 11252-11253.
119. Thoms, S.; Macintyre, D. S.; Docherty, K. E.; Weaver, J. M. R., Alignment verification for electron beam lithography. *Microelectron. Eng.* **2014,** *123*, 9-12.

المنارة للاستشارات
www.manaraa.com

120. Shah, D.; Patel, D. I.; Roychowdhury, T.; Johnson, B.; Linford, M. R., Substrate Protection and Deprotection with Salt Films to Enable Area-Selective – Atomic Layer Deposition on only One Side of a Substrate. *Chem. Mater.* **2020,** *Submitted.*
121. Schelhaas, M.; Waldmann, H., Protecting Group Strategies in Organic Synthesis. *Angew. Chem. Int. Ed.* **1996,** *35* (18), 2056-2083.
122. Roychowdhury, T.; Shah, D.; Hilfiker, J. N.; Linford, M. R., Polymethyl methacrylate: Optical properties from 191 to 1688 nm (0.735–6.491 eV) by spectroscopic ellipsometry. *Surf. Sci. Spectra* **2020,** *27* (1), 016002.
123. Shah, D.; Roychowdhury, T.; Hilfiker, J. N.; Linford, M. R., Polyethylene glycol: Optical constants from 191 to 1688 nm (0.735–6.491 eV) by spectroscopic ellipsometry. *Surf. Sci. Spectra* **2020,** *27* (1), 016001.
124. N. H. Turner, Surface analysis: X-ray photoelectron spectroscopy and Auger electron spectroscopy. *Anal. Chem.* **1988,** *60* (12), 377-387.
125. J. E. Castle, Module to guide the expert use of x-ray photoelectron spectroscopy by corrosion scientists. *J. Vac. Sci. Technol., A* **2007,** *25* (1), 1-27.
126. Shah, D.; Patel, D. I.; Roychowdhury, T.; Rayner, G. B.; O'Toole, N.; Baer, D. R.; Linford, M. R., Tutorial on interpreting x-ray photoelectron spectroscopy survey spectra: Questions and answers on spectra from the atomic layer deposition of Al2O3 on silicon. *J. Vac. Sci. Technol. B* **2018,** *36* (6), 062902.
127. P. van der Heide, *X-ray Photoelectron Spectroscppy: An introduction to principles and practices*. John Wiley & Sons: 2011.
128. D. Briggs; Grant, J. T., *Surface analysis by Auger and X-ray Photoelectron spectroscopy*. IM Publications: Chicester, UK, 2003; Vol. 1.
129. Lv, B.; Qian, T.; Ding, H., Angle-resolved photoemission spectroscopy and its application to topological materials. *Nat. Rev. Phys.* **2019,** *1* (10), 609-626.
130. Shah, D.; Patel, D. I.; Roychowdhury, T.; Jacobsen, D.; Erickson, J.; Linford, M. R., Optical function of atomic layer deposited alumina (0.5–41.0 nm) from 191 to 1688 nm by spectroscopic ellipsometry with brief literature review. *Surf. Sci. Spectra* **2019,** *26* (2), 026001.
131. Suzer, S., Differential Charging in X-ray Photoelectron Spectroscopy: A Nuisance or a Useful Tool? *Anal. Chem.* **2003,** *75* (24), 7026-7029.
132. Bergman, S. L.; Sahasrabudhe, G. S.; Ji, H.; Cava, R. J.; Bernasek, S. L., Useful X-ray Photoelectron Spectroscopy-Based Chemical Tool: Differential Charging Studies of Complex Composite Materials. *Chem. Mater.* **2017,** *29* (10), 4162-4166.
133. Patel, D. I.; Roychowdhury, T.; Jain, V.; Shah, D.; Avval, T. G.; Chatterjee, S.; Bahr, S.; Dietrich, P.; Meyer, M.; Thißen, A.; Linford, M. R., Introduction to near-ambient pressure X-ray photoelectron spectroscopy characterization of various materials. *Surf. Sci. Spectra* **2019,** *26* (1), 016801.
134. Bhupinder Singh; Ronald Hesse; Linford, M. R., Good Practices for XPS (and other Types of) peak Fitting. *Vac. Tech. Coat.* **2015,** *15* (12), 25-31.
135. Bhupinder Singh; Linford, M. R., An Introduction to the Equivalent Width and the Autocorrelation Width. Their Possible Application in XPS Narrow Scan Analysis. *Vac. Tech. Coat.* **2015,** *15* (10), 22-25.
136. Woollam, J.; Johs, B.; Herzinger, C.; Hilfiker, J.; Synowicki, R.; Bungay, C. In *Overview of variable-angle spectroscopic ellipsometry (VASE): I. Basic theory and typical applications*, SPIE's International Symposium on Optical Science, Engineering, and Instrumentation, SPIE: 1999.

المنارة للاستشارات
www.manaraa.com

137. Johs, B.; Woollam, J.; Herzinger, C.; Hilfiker, J.; Synowicki, R.; Bungay, C., *Overview of variable-angle spectroscopic ellipsometry (VASE): II. Advanced applications*. SPIE: 1999; Vol. 10294.
138. Woollam, J. A.; Snyder, P. G., Fundamentals and applications of variable angle spectroscopic ellipsometry. *Materi. Sci. Eng.: B* **1990,** *5* (2), 279-283.
139. Dietrich, P. M.; Bahr, S.; Yamamoto, T.; Meyer, M.; Thissen, A., Chemical surface analysis on materials and devices under functional conditions – Environmental photoelectron spectroscopy as non-destructive tool for routine characterization. *J. Electron Spectros. Relat. Phenomena* **2019,** *231*, 118-126.
140. Cushman, C.; Dahlquist, C.; Dietrich, P.; Bahr, S.; Thissen, A.; Schaff, O.; Banerjee, J.; Smith, N.; Linford, M., Trends in Advanced XPS Instrumentation. 5. Near-Ambient Pressure XPS. *Vac.Tech. Coat.* **2017**.
141. Kjærvik, M.; Schwibbert, K.; Dietrich, P.; Thissen, A.; Unger, W. E. S., Surface characterisation of Escherichia coli under various conditions by near-ambient pressure XPS. *Surf. Interface Anal.* **2018,** *50* (11), 996-1000.
142. Shah, D.; Roychowdhury, T.; Bahr, S.; Dietrich, P.; Meyer, M.; Thißen, A.; Linford, M. R., Human tooth, by near-ambient pressure x-ray photoelectron spectroscopy. *Surf. Sci. Spectra* **2019,** *26* (1), 014016.
143. Shah, D.; Bahr, S.; Dietrich, P.; Meyer, M.; Thißen, A.; Linford, M. R., Printed and unprinted office paper, by near-ambient pressure XPS. *Surf. Sci. Spectra* **2019,** *26* (2), 024009.
144. Shah, D.; Bahr, S.; Dietrich, P.; Meyer, M.; Thißen, A.; Linford, M. R., Coffee bean, by near-ambient pressure XPS. *Surf. Sci. Spectra* **2019,** *26* (2), 024006.
145. Shah, D.; Cushman, C. V.; Bahr, S.; Dietrich, P.; Meyer, M.; Thißen, A.; Linford, M. R., Coca-Cola, by near-ambient pressure XPS. *Surf. Sci. Spectra* **2019,** *26* (2), 024005.
146. Shah, D.; Patel, D. I.; Bahr, S.; Dietrich, P.; Meyer, M.; Thißen, A.; Linford, M. R., Liquid water, by near-ambient pressure XPS. *Surf. Sci. Spectra* **2019,** *26* (2), 024003.
147. Shah, D.; Bahr, S.; Dietrich, P.; Meyer, M.; Thißen, A.; Linford, M. R., Nitrogen gas (N_2), by near-ambient pressure XPS. *Surf. Sci. Spectra* **2019,** *26* (1), 014023.
148. Shah, D.; Bahr, S.; Dietrich, P.; Meyer, M.; Thißen, A.; Linford, M. R., Zirconium oxide particles, by near-ambient pressure XPS. *Surf. Sci. Spectra* **2019,** *26* (2), 024001.

المنارة للاستشارات
www.manaraa.com

CHAPTER 2: Deposition of thin alumina (Al_2O_3) films on flat surfaces and characterization by spectroscopic ellipsometry (SE) and X-ray photoelectron spectroscopy (XPS)

2.1 Statement of Attribution

This article was originally submitted as **Shah, D.**; Patel, D. I.; Roychowdhury, T.; Jacobsen, D.; Erickson, J.; Linford, M. R. Optical Function of Atomic Layer Deposited Alumina (0.5-41.0 nm) from 191 – 1688 nm by Spectroscopic Ellipsometry *Surf. Sci. Spectra,* **2019**, 26(2), 026001-01 to 026001-12.

Some of the data was also published in a separate publication entitled, **Shah, D.**; Patel, D. I.; Roychowdhury, T.; Rayner, G. B.; O' Toole, N.; Baer, D. R. Linford, M. R. A Tutorial on Interpreting X-ray Photoelectron Spectroscopy (XPS) Survey Spectra: Questions on Spectra from the Atomic Layer Deposition (ALD) of Al_2O_3 on Silicon, *J. Vac. Sci. Technol. B*, **2018**, 36(6), 062902-1 to 062902-10.[1] Here, the texts and figures are reproduced with the permission from AIP publishing.

2.2 Abstract

Atomic layer deposition (ALD) is widely used in the semiconductor industry to provide atomic level control over film thicknesses and layer conformality. Herein, we report the thermal (332 ºC) ALD of thin amorphous films (0.5 – 41 nm) of alumina from water and trimethylaluminum (TMA) precursors. Our alumina deposition was optimized by varying the dose and purge times for both precursors with an eye towards obtaining uniform film thicknesses and constant growth per cycle (GPC). Films were characterized by X-ray photoelectron spectroscopy

www.manaraa.com

(XPS), which confirmed increasing deposition of alumina with cycle number, and by spectroscopic ellipsometry (SE) (from 191 - 1688 nm). The subsequent work up of the SE data was based on a multi-sample analysis. It considered Cauchy and Sellmeier functions and accounted for surface roughness. This modeling yielded an optical function for ALD alumina over the measured wavelength range. We recommend the optical function determined from the Sellmeier model.

2.3 Introduction

Atomic layer deposition (ALD) is an increasingly important thin film deposition technique that is based on sequential, self-limiting half reactions of precursors with a substrate and/or a growing film.[2] ALD was originally developed by Suntola and co-workers[3] who referred to it as 'atomic layer epitaxy (ALE)'.[4] It appears that ALD has its roots in experiments done in the 1960s and early 70s in the former Soviet Union.[5-7] Much of ALD's current growth and significance is driven by the needs of the semiconductor industry, where ALD is used in the preparation of high-k transistors, high-aspect ratio devices, and diffusion barriers for metal interconnects.[8] ALD has found important applications in other areas of science and technology, including in catalysis and analytical chemistry.[8-11] The various categories of materials that can be deposited by ALD include metal oxides, metal nitrides, metal sulfides, and even metals themselves.[9]

One of the most reliable and widely studied ALD reactions is the deposition of alumina from trimethylaluminum (TMA) and water.[12, 13] No doubt, part of the success of this reaction is due to the extreme reactivity of TMA. This reaction, or variants of it, have been studied at different temperatures, under a variety of conditions, and on different substrates. **Table 2.1** summarizes some of these previous reports of the ALD of alumina. Most of this work has involved TMA and water as precursors, although other aluminum precursors and oxidants/sources of

المنارة للاستشارات
www.manaraa.com

oxygen, e.g., ozone, have also been considered. Deposition temperatures have ranged from 110 – 450 ºC. In addition, different substrates, including powders, different pre-treatments for these substrates, a wide range of final film thicknesses, and different deposition rates have been reported. In general, with water and TMA precursors, higher temperatures lead to more uniform films and growth per cycle (GPC) values. This was an important reason for our choosing a higher deposition temperature in this study (332 ºC), even though a lower temperature can lead to higher film thicknesses and GPC. Note that 332 ºC is below the degradation temperature of TMA (370 ºC).[14] The GPC of ALD alumina at 300 ºC is reported at 0.8 - 1.0 Å/cycle.[5, 15]

Table 2.1. Summaries of literature reports of ALD of alumina. The papers in this table are listed by lead author, and each entry also summarizes the precursors, deposition temperature, substrate, substrate pretreatment, final thickness of the alumina layer, and GPC. Various cleaning solutions for silicon are described. SC-1 refers to a mixture of deionized water, ammonia, and hydrogen peroxide (H_2O:NH_3:H_2O_2 :: 5:1:1), and SC-2 refers to a mixture of deionized water, ammonium hydroxide, and hydrogen peroxide (H_2O:NH_4OH:H_2O_2 :: 5:1:1).[16] The RCA clean involves cleaning with SC-1, followed by SC-2, and finally rinsing and drying.[17, 18] There is an optional step (immersion in 1:50 solution of HF) between the SC-1 and SC-2 cleaning steps that is meant to remove the oxide layer from silicon. Piranha solution is a strong oxidizing solution composed of sulfuric acid (H_2SO_4) and hydrogen peroxide (H_2O_2), which is used to clean organic residues from substrates.[19] *Warning: these cleaning solutions are, in general, extremely dangerous and should be handled with great care and appropriate safety equipment.*

Author	**Precursors**	**Temperature**	**Substrate**	**Substrate Pretreatment**	**Thickness and GPC**

المنارة للاستشارات
www.manaraa.com

Rammula *et al.*[20]	TMA, and water or ozone	200 ºC	Graphene	1-3 seed alumina layers by e-beam evaporation	12-16 nm
Brazeau *et al.*[21]	Aluminum amidinates and guanidinates, water (Al precursors were prepared from TMA)	125-300 ºC, most commonly 175 ºC	Silicon	Sonication in acetone, a rinse with deionized water, followed by a dip in 10 % HF	28-56 nm, GPC: 1.75 - 2.75 Å/cycle
Prokes *et al.*[22]	TMA, water	200 ºC	Ga_2O_3, ZnO, Si nanowires	None	5 nm, GPC: 1.2 Å/cycle
Manandhar *et al.*[23]	TMA, water	150 ºC	Nano and micro powders of TiO_2	Heating at 150 ± 10 ºC inside an ALD drum rotating at 140 rpm	10-16 nm, GPC: 1.7 - 2.0 Å/cycle
Ylivaara *et al.*[16]	TMA, water	110-300 ºC	Silicon wafers	SC-1, dil. HF, SC-2	GPC: 0.73-1.2 Å/cycle

المنارة للاستشارات
www.manaraa.com

Kukli *et al.*[24]	TMA, Water	300 ºC	Modified steel substrates	None	
Aguilar-Gama *et al.*[25]	TMA, Water	150 ºC or 175 ºC	Silicon wafers and Corning® glass slides	Glass slides were cleaned with soap and acetone/water. Si wafers were etched with dil. HF.	800 nm, GPC: 1.4 Å/cycle at 150 ºC and 1.5 Å/cycle at 175 ºC
Sneh *et al.*[15]	TMA, Water	300 ºC	Silicon wafers	None	GPC: 0.84 Å/cycle
Batra *et al.*[26]	TMA, Water	300 ºC	Silicon wafers	Si wafers were cleaned with piranha solution and 5% HF	7 nm
Groner *et al.*[27]	TMA, Water	125 ºC	Silicon wafers	5% HF, water (HPLC Grade), piranha solution	10 nm
Gharachorlou *et al.*[28]	TMA, oxygen	200 ºC	Cu (111) surfaces	Oxygen at 400 ºC	GPC: 3-4 Å/cycle

المنارة للاستشارات
www.manaraa.com

Broas *et al.*[14]	TMA, and water or ozone	300 ºC	Silicon wafers	Washing with acetone, isopropanol, and DI water, and then immersion in SC-1	103 nm, GPC: 1.0 Å/cycle
Broas *et al.*[14]	$AlCl_3$, H_2O, or TMA, H2O, or TMA, O_3	300 ºC for TMA, 450 ºC for $AlCl_3$	Silicon wafers	Washing with acetone, isopropanol, and DI water, and then immersion in SC-1	89 nm, GPC: 0.7 Å/cycle

We report the thermal ALD of alumina at 332 ºC from TMA and water precursors. This specific temperature was chosen because it is recommended in the 'standard recipe' from the manufacturer of our equipment. The dose and purge times of the precursors were optimized to obtain uniform film thicknesses and constant GPC. The resulting ALD depositions of 5 to 500 cycles, where each cycle consists of an introduction of TMA, a purge, an introduction of water, and a final purge, yielded alumina films with thicknesses that varied monotonically from 0.5 to 41 nm. These alumina films (eleven of them) were analyzed by spectroscopic ellipsometry via a multi-sample analysis (MSA), i.e., a single model was used to describe all the data and all the data were fit together. MSAs are important in SE for reducing/breaking fit parameter correlation.[29] In particular, our SE model accounted for the silicon substrate, the native oxide layer on it, the alumina film, and possible roughness on the alumina film.

www.manaraa.com

Both Cauchy and Sellmeier functions were considered. Two models that consider absorption were also evaluated. The resulting fits returned reasonable results: a single, consistent optical function for this important material was determined from 191 – 1688 nm with a low mean squared error (MSE) value. The films were also analyzed by XPS, which confirmed the deposition of an alumina overlayer that steadily attenuated the silicon signal from the substrate. Other surface spectra from alumina have previously appeared in Surface Science Spectra, including the characterization of this material by XPS[30, 31] and time-of-flight secondary ion mass spectrometry.[32]

2.4 Experimental

2.4.1 Samples and deposition system

ALD of alumina from TMA and water precursors was performed with a Kurt J. Lesker ALD-150LX™ system on small silicon shards (1 cm x 1 cm) cut from wafers purchased from University Wafer (South Boston, MA). Prior to deposition the substrates were plasma cleaned with an air plasma (Harrick plasma cleaner, Model No. PDC-32G, Ithaca, New York) or with piranha solution. The cleaning step leads to removal of surface contaminants and it does not affect the surface chemistry. That is, identical alumina film thicknesses were obtained after 100 ALD cycles on piranha- and plasma-treated silicon. The precursors were kept at room temperature, and the reactor was heated to 332 ºC prior to initiation of deposition. While the ALD heater is set to 332 ºC, the actual temperature of the substrate (six-inch wafer) may be lower. The precursors were automatically introduced into the reactor from cylinders with the help of a constant flow of an inert gas like nitrogen (99.999 % pure).

2.4.2 ALD process

المنارة للاستشارات
www.manaraa.com

All appropriate variables and process parameters, including temperature, were kept constant during a given deposition. The temperature of the deposition chamber was 332 ± 0.1 ºC during the deposition process. The ALD reactor was pre-heated to 332 ºC prior to initiation of deposition and kept at this temperature during a deposition. For the initial runs, we used the dose times (21.0 ms for TMA and 15.5 ms for water) that were recommended for our ALD system. The purge times used for the initial runs were 15000 ms for both water and TMA. The dwell time is the time provided for the silicon shard to equilibrate from room temperature to the deposition temperature.[27] Unless otherwise indicated, the dwell time was 10 min. For the initial runs, the standard recipe in the instrument software (eklipse^{TM}) was used without modification, which included dose and purge times. In general, optimization of both dose and purge times for both precursors is an important step in achieving optimum film thickness and growth per cycle.[13] The uniformity of these depositions was determined by averaging the thicknesses obtained at three different spots on a sample.

2.4.3 Optimization of ALD parameters

The advantages of using shorter dose times in a deposition include: (i) use of less reagent (less expense and less frequent need to refill reagent reservoirs), (ii) shorter process times (shorter dose and subsequent purge times), and (iii) less use of toxic and/or pyrophoric reagents. We optimized the dose and purge times for TMA and water, beginning with the dose times. All of the experiments described in this section were performed in random order, the number of ALD cycles in these experiments was 50, and the depositions were at 332 ºC. The dose time for TMA in the standard recipe (21.0 ms) was increased from 15.0 ms to 30.0 ms in 1 ms increments.

Most of these ALD runs with TMA gave similar results in terms of film thickness and GPC (see Supporting Information). Accordingly, we kept the TMA dose time at 21.0 ms. A

المنارة للاستشارات
www.manaraa.com

similar optimization was done for the water dose time, increasing it from 10.0 to 20.0 ms, while keeping all other parameters constant. These changes in dose time did not substantially alter the film thickness or GPC (see Supporting Information), so the water dose time was also kept at the value in the standard recipe (15.5 ms). The next two parameters to be optimized were the purge times for TMA and water. The purging process removes excess unreacted precursor from the reactor, preventing side reactions, e.g., parasitic chemical vapor deposition. Here the purge times were increased from 5000 ms to 25000 ms in multiples of 5000 ms. A purge time of 15000 ms (the recommended value) gave the best results (see Supporting Information), so this value was used.

The purge time for water was similarly optimized (see Supporting Information) and found to be consistent with the recommended value of 15000 ms. Of course, there is a tension between using the lowest possible dose and purge times in a process and having a reasonable margin for error for the process parameters so that they are insensitive to minor/random variations in the deposition conditions and/or system.

2.4.4 Sample characterization

Samples were characterized by spectroscopic ellipsometry from 191 to 1688 nm with a J. A. Woollam M-2000 ellipsometer. This ellipsometer can collect data at different angles and is equipped with a CCD array detector, a rotating compensator, and a near IR extension (out to 1688 nm). Ellipsometric data were evaluated using the instrument software (CompleteEase®), and unless otherwise stated the entire wavelength range (191 – 1688 nm) was used for modeling/calculating film thickness, roughness, and the optical function of the material. Film thickness was probed at multiple spots and an average value was calculated. Ellipsometric data were collected at 75°, which is around the Brewster angle/principal angle of silicon – the measurement will be most sensitive here.

المنارة للاستشارات
www.manaraa.com

X-ray photoelectron spectroscopy (XPS)[33] was performed with a Surface Science SSX-100 X-ray photoelectron spectrometer (serviced by Service Physics, Bend, OR) with a monochromatic Al K_α source, a hemispherical analyzer, and a take-off angle of 35°. Survey scans were recorded with a spot size of 800 µm x 800 µm and a resolution of 4 (nominal pass energy of 150 eV). Peaks were referenced to the C 1*s* hydrocarbon signal taken at 284.6 eV. No electron flood gun (charge compensation) was employed for these measurements. XPS of bare silicon wafers and electron beam deposited alumina on silicon have previously been reported in the literature.[30, 34]

2.5 Results and Discussion

2.5.1 Initial ALD runs

An ALD cycle in this work consists of exposing a substrate to gas phase TMA, a purge step (pumping) to remove excess TMA, exposure of this surface to gas phase water, and finally another purge to remove excess water. The purge step is necessary to remove any excess precursor (TMA or water) and any side products. Our first experiments consisted of performing 5 - 500 ALD cycles on silicon shards using the standard recipe recommended by the manufacturer of our equipment. These depositions were done in random order to eliminate instrument or user bias. In this manner, we obtained a diverse range of alumina thicknesses.

The use of the standard instrument conditions yielded a GPC that became more constant (0.82 - 0.83 Å/cycle) as the number of ALD cycles increased, and that was in good agreement with previous reports in the literature.[14,15] These results provided us with a comparison to use in the optimization of our depositions. A plot of alumina film thickness, as measured by SE,

المنارة للاستشارات
www.manaraa.com

vs. number of cycles resulted in data that were well fit by a straight line with zero intercept (see **Figure 2.1**). Ultimately, as described below, these samples were analyzed using a multi-sample analysis (MSA)[35] to obtain the optical function(s) for ALD alumina over a wide range of wavelengths (191-1688 nm). These optical functions should be valid over the range of film thicknesses considered in this analysis (0.5 - 41 nm), and perhaps somewhat outside of this range as well.[36] We performed several control experiments to evaluate the roles of TMA and water. As expected, absence of either or both precursors did not produce any alumina deposition.

Table 2.2. Film thickness and GPC for different number of ALD cycles using 15.5 ms as water dose time and 21.0 ms dose time for TMA. Purge time for water and TMA was 15000 ms.

Number of Cycles	**Thickness (nm)**	**GPC (Å/cycle)**
5	0.44	0.98
10	0.94	0.94
20	1.58	0.79
40	3.44	0.86
50	4.25	0.85
80	6.38	0.80
100	8.38	0.84
200	16.22	0.82

المنارة للاستشارات
www.manaraa.com

300	24.75	0.83
400	33.14	0.83
500	41.08	0.82

Table 2.3. Film thickness and GPC for various runs while varying the dose time of TMA keeping all the variable constant including the number of cycles and temperature of deposition. (The thickness and GPC were uncharacteristically less when the dose time for water was 11.0 msec. The experiment was repeated three times and gave similar results)

	Thickness on test shards kept inside the particles holder (nm)									
Dose time (ms)	**21**	**22**	**23**	**24**	**25**	**26**	**27**	**28**	**29**	**30**
Thickness -I	4.15	4.07	4.07	4.14	4.08	3.93	4.06	4.09	4.08	4.12
Thickness -II	4.10	4.06	4.06	4.14	4.07	3.94	4.07	4.11	4.08	4.13
Avg Thickness	4.13	4.06	4.06	4.14	4.08	3.94	4.06	4.10	4.08	4.12

المنارة للاستشارات
www.manaraa.com

GPC	0.83	0.81	0.81	0.83	0.82	0.78	0.81	0.81	0.81	0.82

Table 2.4. Film thickness and GPC for various runs while varying the dose time of water keeping all the other variables constant including the number of cycles and temperature of deposition.

	Thickness on test shards kept inside the particles holder (nm)											
Dose time (msec)	**10**	**11**	**12**	**13**	**14**	**15**	**15.5**	**16.0**	**17.0**	**18.0**	**19.0**	**20.0**
Thickness-I	4.07	1.05	3.44	3.96	4.10	4.08	4.21	4.27	4.18	4.10	4.14	4.20
Thickness-II	4.08	1.12	3.43	3.99	4.11	4.10	4.22	4.26	4.15	4.10	4.09	4.20
Avg Thickness	4.08	1.09	3.44	3.98	4.10	4.09	4.21	4.26	4.16	4.10	4.11	4.20
GPC (A/Cycle)	0.82	0.21	0.68	0.80	0.82	0.82	0.84	0.85	0.83	0.82	0.82	0.84

Table 2.5. Film thickness and GPC for various runs while varying the purge time of TMA keeping all the other variables constant.

المنارة للاستشارات
www.manaraa.com

	Thickness on test shards kept inside the particles holder (nm)				
Purge Time (ms)	**5000**	**10000**	**15000**	**20000**	**25000**
Thickness-I	3.82	3.57	4.21	3.80	3.87
Thickness-II	3.89	6.59	4.23	3.83	3.86
Thickness-III	3.84	3.61	4.24	3.80	3.83
Avg Thickness	3.85	3.59	4.22	3.81	3.85
GPC (Å/Cycle)	0.77	0.72	0.84	0.76	0.77

Table 2.6. Film thickness and GPC for various runs while varying the purge time of water keeping all the other variables constant.

	Thickness on silicon shards				
Purge Time (msec)	**5000**	**10000**	**15000**	**20000**	**25000**
Thickness-I	3.65	3.06	4.21	3.57	3.49
Thickness-II	3.71	3.03	4.23	3.56	3.51
Thickness-III	3.71	3.06	4.24	3.55	3.47
Avg Thickness	3.69	3.06	4.22	3.55	3.49

المنارة للاستشارات
www.manaraa.com

GPC (Å/Cycle)	0.738	0.61	0.84	0.71	0.70

Table 2.7 Film thickness and GPC for various runs selected for XPS determinations.

Number of cycles	**Thickness (nm)**	**GPC (Å/Cycle)**
5	0.49	0.98
10	0.94	0.94
20	1.58	0.79
50	4.25	0.85
100	8.38	0.84

2.5.2 Film characterization by XPS

X-ray photoelectron spectroscopy[35, 36] was performed to confirm the elemental/chemical compositions of the alumina films prepared in this study. XPS is highly surface sensitive, probing the upper 5 - 10 nm of a material.[37] For this analysis, we selected five films of varying alumina thicknesses (0.4 - 8.5 nm) prepared from 5, 10, 20, 50, and 100 TMA/water ALD cycles.[1]

The resulting XPS spectra (see **Figures 2.2** and **2.3**) showed the expected elements and signals from the films, including the O Auger signal, and the O 1*s*, C 1*s* (adventitious hydrocarbon contamination), Si 2*s*, Si 2*p*, Al 2*s*, Al 2*p*, and O 2*s* photoemission peaks. Silicon appeared in two oxidation states (see Figure 3): Si 2*p* at 103.5/99.5 eV and Si 2*s* at 152.7/150 eV,

المنارة للاستشارات
www.manaraa.com

where the higher and lower values of these binding energies refer to signals from the native oxide (1.5 - 1.7 nm thick) and the reduced, bulk substrate, respectively.[34] Aluminum appeared in a single oxidation state that corresponded to aluminum oxide; the Al 2*p* and 2*s* signals appeared at 74.4 eV and 119.3 eV, respectively.[30] As expected, the silicon signals progressively decreased in size as the number of ALD cycles increased (the substrate is being covered), while the signals from aluminum increased.[37]

2.5.3 Optical modeling of ALD alumina films

The Literature contains multiple reports of the optical characterization of alumina thin films (see **Table 2.8**). These films have been deposited in many ways, including by ALD, electron beam evaporation, oblique angle deposition/electron beam evaporation, filtered cathodic vacuum arc deposition, plasma immersion ion implantation and deposition (PIII&D), and anodization from dilute, aqueous sulfuric acid.

The optical functions of these films have been determined over different wavelength ranges including 400 - 1000 nm, 400 – 1800 nm, 240 - 1700 nm, 200 - 800 nm, and 400 - 800 nm. The resulting optical constants were modeled by Sellmeier's formula, Cauchy's equation, and O'Leary's approach. For our study, a multi-sample analysis (MSA) by SE was performed on various thin films (0.5 – 41.0 nm) of ALD alumina over a relatively wide wavelength range (191 - 1688 nm). In general, an MSA breaks fit parameter correlation and allows more complex models to be considered.[29] Since alumina is widely used in multiple industries, the optical function we derive for it should be useful.

Table 2.8. Summaries of Literature reports on the deposition of thin films of alumina and their optical properties.

المنارة للاستشارات
www.manaraa.com

Reference	Notes on deposition	Optical properties
Eriksson *et al.*[38]	Electron beam evaporation onto silicon and glass substrates 300 – 3600 nm films	Spectral absorbance from 2.5 – 50 µm with strong absorbance at 15 - 20 µm Alumina was non-absorbing from 350 – 2100 nm
Kumar *et al.*[39]	ALD at 300 ºC onto silicon and soda lime glass substrates Dose time for TMA was 100 ms, followed by a 3000 ms N_2 purge Water dose time was 100 ms followed by a 3000 ms N_2 purge.	Optical properties probed by reflection ellipsometry Data fit from 400 – 1800 nm with a Sellmeier model Refractive index values ranged from 1.63 - 1.67 for alumina films deposited on silicon and from 1.66 - 1.70 for films on soda lime glass
Huang *et al.*[40]	Films deposited on Kapton polymer by plasma immersion ion implantation and deposition (PIII&D)	Transmittance and absorbance for alumina were reported from 400 - 1000 nm Optical constants were not provided
Soserov *et al.*[41]	Alumina was formed by anodization of an aluminum thin film obtained by DC magnetron sputtering	A two-layer model was used to describe the films The optical constants of the lower layer were modeled from 400-1600 nm using the Sellmeier equation

المنارة للاستشارات
www.manaraa.com

	Anodization was done under a constant voltage (20 or 30 V) in an aqueous sulfuric acid solution (2 or 4 wt. %)	The index of refraction of the lower film varied from 1.74 – 1.78
Jung *et al.*[42, 43]	Substoichiometric films were deposited by reactive sputtering of Al in O_2 on 'quartz glass'	Optical properties were determined from 240 - 1700 nm using spectroscopic ellipsometry Data were fitted using a Sellmeier model The index of refraction varied from 1.61 – 1.78 for three different Al_2O_3 films
Zhao *et al.*[44]	Alumina films were deposited on quartz (presumably fused silica) and Si(100) using an off-plane filtered cathodic vacuum arc (FCVA) system at 400 ºC	Optical properties were reported from 200 - 850 nm The refractive index (n) ranged from 1.72 - 1.95 The extinction coefficient, k, was non-zero everywhere From 200 - 250 nm, k ranged from ca. 0.002 to 0.0005, respectively n was 1.72 at 550 nm. Data were modeled using the approach suggested by O'Leary *et al.*[45]

المنارة للاستشارات
www.manaraa.com

He *et al.*[46]	Films deposited on glass and silicon substrates by electron beam evaporation using oblique angle deposition (OAD)	Optical properties reported from 400 - 800 nm and modelled using Cauchy's formula The refractive index decreased with an increase in the angle of deposition (from 0º to 80º)
Koushki *et al.*[47]	Films prepared by dispersing aluminum oxide nanoparticles (average size 40 nm) in water and depositing them on glass substrates	Optical properties were studied by reflectance and transmittance from 300 – 800 nm Average value of the refractive index was 1.65
Patil *et al.*[48]	Thin films ranging in thickness from 50 - 200 nm were prepared by electron beam evaporation of aluminum oxide	Refractive index of alumina films prepared through different methods was calculated using Abele's method Refractive index of an electron beam deposited film was 1.59 - 1.60
Boidin *et al.*[49]	Thin amorphous films were deposited by pulsed laser deposition Film thickness ranged from 8.5 to 106 nm with RMS roughness values between 0.35 and 1.5 nm	Optical constants reported from 300 – 2300 nm Optical data was modeled using Cauchy's model with an Urbach absorption tail

المنارة للاستشارات
www.manaraa.com

Groner *et al.*[27]	Thin alumina films were deposited by ALD at temperatures from 33 ºC – 177 ºC using 300 cycles Thickness and refractive index were calculated using spectroscopic ellipsometry from 406 to 806 nm	Refractive indices and density of alumina increased with increase in temperature. Refractive indices varied by less than 1% in the spectral range (406 – 806 nm) Growth rate of alumina films increased as we go from 33 ºC to 100 ºC, staying constant from 100 ºC to 150 ºC and decreasing as we increased the temp to 177 ºC

www.manaraa.com

2.6 Specimen Description

Specimen Number:	Description
Sample Description:	A series of alumina thin films were deposited on native oxide-terminated silicon wafers by atomic layer deposition (ALD)
History & Significance	Alumina is an extremely important material with a wide range of applications
Analyzed Region:	Reflection ellipsometry data were collected with our ellipsometer from 191-1688 nm
Specimen Temperature During Analysis:	300 K
Maximum Chamber Pressure During Analysis, Pa:	Ambient
Sample Conditions During Measurement:	Measurements were made in the air
Ex Situ Preparation and Mounting:	No sample preparation was done prior to recording the ellipsometric data

المنارة للاستشارات
www.manaraa.com

2.7 Specimen Component Layers (see **Figure 2.4**)

- **Layer 2**

Chemical Name:	**Alumina**
Layer Composition:	Al_2O_3
Structural Formula:	Amorphous Al_2O_3
CAS Registry No:	1344-28-1
Layer Manufacturer/Supplier:	Alumina thin films were deposited by atomic layer deposition (ALD) using trimethylaluminum and water precursors.
As-received Condition:	N/A
Host Material Characteristics:	Solid, homogeneous, insulator, inorganic compound, thin film
Layer Form:	Solid on solid surface
Features Observed:	Transparent over the entire wavelength range

المنارة للاستشارات
www.manaraa.com

2.8 Instrument Configuration

Instrument Manufacturer:	**J. A. Woollam Company**
Manufacturer Model No:	M-2000DI
Instrument Configuration:	Variable angle spectroscopic ellipsometer equipped with a CCD array detector, a rotating analyzer, and a near IR extension to allow data collection out to 1688 nm
Spectral Range:	191 - 1688 nm
Measurement Angle(s) of Incidence:	75°
Acquired Data Type:	Ψ, Δ

المنارة للاستشارات
www.manaraa.com

2.9 Data Analysis

Modeling of optical data often benefits from the use of parameterized models like Cauchy's or Sellmeier's equation, where both the Cauchy and Sellmeier equations have been routinely used to model transparent dielectrics. However, the Sellmeier equation is generally preferred over wider wavelength ranges because it more accurately models the natural dip in the index of refraction at longer wavelengths and is Kramers-Kronig consistent.[49] Our approach consisted of a multi-sample analysis with data derived from eleven ALD alumina layers with different thicknesses, where the model was initially simplified to have three layers (silicon substrate, native oxide, and alumina layer), and the alumina was modeled with a Cauchy or Sellmeier function. Addition of a roughness layer to these models did not significantly change the mean square error (MSE) values in this modeling. Thus, roughness layers were not employed in this study.

The Cauchy model in the MSA yielded an MSE value of 0.461, with an index of refraction of 1.67 at 550 nm for alumina.[44, 49] However, there have been multiple reports that show absorbance of alumina in the UV-vis.[40, 44] Accordingly, an Urbach tail was introduced into the Cauchy model. Interestingly, this absorbing feature did not affect the MSE. Accordingly, the Urbach tail was excluded from further modeling/consideration. As noted, introduction of roughness (in the Cauchy model and also in the Cauchy model with an Urbach tail) similarly had minimal effect on the MSE. Indeed, the roughness layers in these models gave negative thicknesses in some cases. Hence, roughness was omitted (see **Figure 2.5**). A Cody-Lorentz model was also considered in this work. However, it did not give improved results over the models shown herein.

We next experimented with a Sellmeier model of our alumina films in our multi-sample analysis. For a three-layer model (no roughness), this model gave a low MSE of 0.394 and

المنارة للاستشارات
www.manaraa.com

an optical function that was similar to that obtained through the Cauchy model. Again, addition of a roughness layer had minimal effect on the MSE (less than 5 %) and optical function. Moreover, the thickness of the roughness layer was negative in numerous cases, which is unphysical. Hence, we eliminated the roughness layer from the Sellmeier model.

The Cauchy and Sellmeier models that were used in this study gave similar results. We compare these optical functions to the result of Kim *et al.*,[50] who used ALD to deposit thin alumina on Si(100) substrates under conditions similar to the ones we used (deposition temperature of 300 °C). They reported an index of refraction that increased as a function of deposition temperature (up to 1.65 at 300 °C), which we might compare to our refractive index of 1.66 at 633 nm for a deposition temperature of 332 °C, which was obtained via a Sellmeier model. (Unfortunately, Kim *et al.* did not specify the wavelength for their value. However, alumina has relatively low dispersion so some comparison can be made.)

Uniqueness plots were generated for both the Cauchy and Sellmeier approaches.[51] In both cases, 'U'-shaped plots were obtained, which suggests that the fit parameters in these fits are not correlated. Because ultrathin film thicknesses are relatively insensitive to the optical functions used to model them,[52] either of the two optical functions for alumina determined in this study should be appropriate for modeling 0.5 – 41 nm alumina ALD films deposited under conditions similar to those reported herein. However, we recommend using the results from the Sellmeier function for modeling ultra-thin ALD films of alumina.

The optical constants obtained from both the models differ substantially in the UV-vis region (see **Figure 2.8**), even after good agreement between the experimental and model calculated data for both the fits (see **Figures 2.5** and **2.6**). This may seem peculiar, however, similar differences in alumina optical constants have been reported in the literature by Kumar et

المنارة للاستشارات
www.manaraa.com

al.,[39] Kim et al.,[53] and Groner et al.[27] Kumar and co-workers[39] deposited alumina on silicon substrates at 300 °C, optical properties were investigated in the 400-1800 nm wavelength range and refractive index of these films was 1.64 at 633 nm. Kim et al.,[53] deposited alumina at 370 °C using ALD on Si(100) substrates, refractive index of these films was between 1.62 and 1.64 at 633 nm. Groner and co-workers[27] deposited alumina using ALD at low temperatures ranging from 33 °C to 177 °C.

These films were analyzed using spectroscopic ellipsometry between 406 to 806 nm. The refractive index of these alumina films increases from 1.51 to 1.60 as the temperature rises from 33 °C to 177 °C. These literature references confirm that there is variation in the reported optical constants of alumina deposited using ALD.[48] Hence, the substantial difference in the optical constants of alumina thin films resulting from the two models (Cauchy and Sellmeier) are acceptable and in accordance with the literature.

2.10 Conclusions

Alumina thin films were reproducibly deposited by ALD at 332 °C. They were characterized by XPS, which showed the expected elements and trends. A literature review of the ALD deposition of Al_2O_3 was given. Eleven alumina films of different thicknesses were modeled in a multi-sample analysis by SE. An accompanying literature review of the optical properties of alumina thin films was presented. Various approaches for determining the optical function of ALD alumina were considered, and best results were obtained with simple Cauchy and Sellmeier models without roughness layers or absorption. In both cases, MSE results were less than 0.5. These results are similar to values previously reported in the literature. We recommend the results from the

المنارة للاستشارات
www.manaraa.com

Sellmeier modeling because of its lower MSE value, more physical shape, and Kramers-Kronig consistency.

2.11 Oscillator or effective medium approximation equations

This theory has previously been published in Surface Science Spectra in a more detailed fashion.[54-56]

The Cauchy dispersion model can be expressed as:

$$(1)\quad n(\lambda) = A + \frac{B}{\lambda^2} + \frac{B}{\lambda^4}$$

where A, B, and C control the shape of n(λ).

A pole-pole (Sellmeier) model[56] can be described by:

$$(2)\quad n^2 = \varepsilon_\infty + \frac{A_{UV}\lambda^2}{\lambda^2 - \lambda_{UV}^2} + \frac{A_{IR}\lambda^2}{\lambda^2 - \lambda_{IR}^2},$$

where n is the refractive index, A_UV is the UV amplitude, A_IR is the IR amplitude, λ_UV is the position of the UV pole, λ_{IR} is the position of the IR pole, and λ is the wavelength for which the refractive index is being calculated. ε_∞ is the low-frequency offset, which should be fixed at an appropriate value—we used the default value for this parameter provided in our software, i.e., unity. The values for λ_{UV} and λ_{IR} are provided in terms of energy instead of wavelength. ε_∞, A_{UV}, and A_{IR} are unitless. In the analysis, no IR pole was used, i.e., A_{IR} was zero.[54, 56]

A Bruggeman effective medium approximation (BEMA) layer, which represented the roughness on a film, has the following form:[57]

المنارة للاستشارات
www.manaraa.com

$$(3) \quad f_a \frac{\varepsilon_a - \varepsilon}{\varepsilon_a + 2\varepsilon} + f_b \frac{\varepsilon_b - \varepsilon}{\varepsilon_b + 2\varepsilon} = 0$$

where f_a is the volume fraction of material a, f_b is the fraction of material b, ε_a is the dielectric constant of material a, ε_b is the dielectric constant of material b, and ε is the dielectric constant of the composite material.[54, 55]

The MSE was calculated using the following equation:

$$(4) \quad MSE = \sqrt{\frac{1}{3n-m}\sum_{i=1}^{n}\left[\left(\frac{N_{Ei}-N_{Gi}}{0.001}\right)^2 + \left(\frac{C_{Ei}-C_{Gi}}{0.001}\right)^2 + \left(\frac{S_{Ei}-S_{Gi}}{0.001}\right)^2\right]},$$

Where i refers to a given data point, $N = \cos(2\Psi)$, $C = \sin(2\Psi)\cos(\Delta)$, $S = \sin(2\Psi)\sin(\Delta)$, n is the number of wavelengths, m is the number of fit parameters in the model, and E and G denote experimental and generated, respectively.

2.11.1. Free parameters in the Cauchy model

The 'A' and 'C parameter are free parameters in the Cauchy model (see **Table 2.9**).

2.11.2. Fixed parameters in the Cauchy model

In this modeling, the value of the 'B' parameter was $-1.59e^{-05} \pm 1.32e^{-4}$. Because 'B' is extremely small and the error on 'B' is larger than the value of 'B' itself, 'B' was set to zero in the fitting. The thickness of the SiO_2 (native oxide) layer was fixed at 1.60 nm (see **Table 2.10**).

المنارة للاستشارات
www.manaraa.com

2.11.3. Free parameters in the Sellmeier model

The Sellmeier model has five free parameters: UV amplitude, UV energy, IR amplitude, E_{inf} and the thickness of the alumina films. These are summarized in **Table 2.11**.

2.11.4. Fixed parameters in the Sellmeier model

The IR pole was fixed at 1 x 10^{-8} eV. The thickness of the SiO_2 (native oxide) layer was fixed at 1.60 nm.

Table 2.9. Fit parameters for the Cauchy model

Parameter	Value	Error
A	1.682	0.001
C	0.000321	0.000004
Thickness 1 (nm)	0.49	0.003
Thickness 2 (nm)	0.97	0.004
Thickness 3 (nm)	1.57	0.004
Thickness 4 (nm)	3.34	0.006
Thickness 5 (nm)	4.16	0.007
Thickness 6 (nm)	6.47	0.010
Thickness 7 (nm)	8.66	0.013

المنارة للاستشارات
www.manaraa.com

Thickness 8 (nm)	18.64	0.016
Thickness 9 (nm)	24.74	0.019
Thickness 10 (nm)	33.29	0.026
Thickness 11 (nm)	41.28	0.029
Overall MSE	0.473	

المنارة للاستشارات
www.manaraa.com

Table 2.10. Spectral features for the Cauchy model

Identity	Composition	Feature or location in Range	Photon Energy (eV)	Wavelength (nm)	n	k	ε_1 (real)	ε_2 (imaginary)
Layer 2	Al_2O_3	Range Minimum	6.48	191.24	1.92	0.00	3.69	0.00
		Range Maximum	0.73	1688.17	1.68	0.00	2.68	0.00

المنارة للاستشارات
www.manaraa.com

Table 2.11. Fit parameters for the Sellmeier model

Parameter	Value	Error
A_{UV} (unitless)	0.675	0.014
E_{UV} (eV)	0.14539	0.0006
A_{IR} (unitless)	0.0147	0.0048
Thickness 1 (nm)	0.36	0.003
Thickness 2 (nm)	0.84	0.003
Thickness 3 (nm)	1.44	0.004
Thickness 4 (nm)	3.22	0.005
Thickness 5 (nm)	4.04	0.006
Thickness 6 (nm)	6.35	0.009
Thickness 7 (nm)	8.07	0.010
Thickness 8 (nm)	18.78	0.014
Thickness 9 (nm)	25.04	0.016
Thickness 10 (nm)	33.55	0.021
Thickness 11 (nm)	41.53	0.024
Overall MSE	0.394	

المنارة للاستشارات
www.manaraa.com

Table 2.12. Spectral features for the Sellmeier model

Photon Energy (eV)	Wavelength (nm)	n	k	ε_1 (real)	ε_2 (imaginary)
6.48	191.24	1.91	0.00	3.58	0.00
4.84	256.4	1.75	0.00	4.84	0.00
3.06	405.9	1.68	0.00	2.16	0.00
2.66	466.3	1.67	0.00	2.14	0.00
2.37	523.5	1.67	0.00	2.12	0.00
2.11	588.7	1.66	0.00	2.11	0.00
2.07	599.8	1.66	0.00	2.11	0.00
1.95	633.1	1.66	0.00	2.11	0.00
1.94	637.8	1.66	0.00	2.11	0.00
0.73	1688.17	1.64	0.00	2.66	0.00

المنارة للاستشارات
www.manaraa.com

2.12 Figures

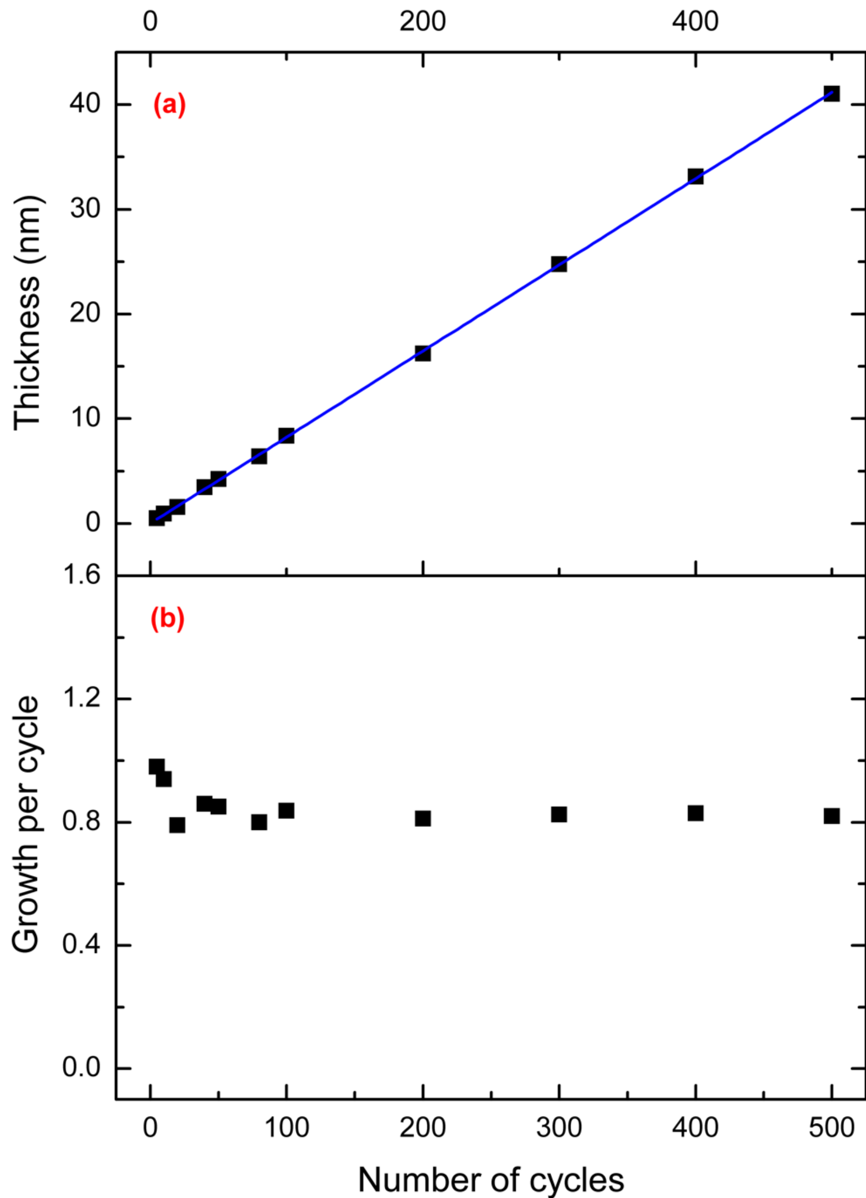

Figure 2.1. (a) Film thickness vs. cycle number for ALD of alumina from TMA and water at 332 ºC. The intercept of the fit line was zero, its slope was 0.082 nm/cycle, and its R-squared value was 0.99993. (b) GPC values (Å/Cycle) versus cycle number for the same alumina ALD depositions as in (a) demonstrating the near constant nature of these values, especially at higher numbers of cycles.

المنارة للاستشارات
www.manaraa.com

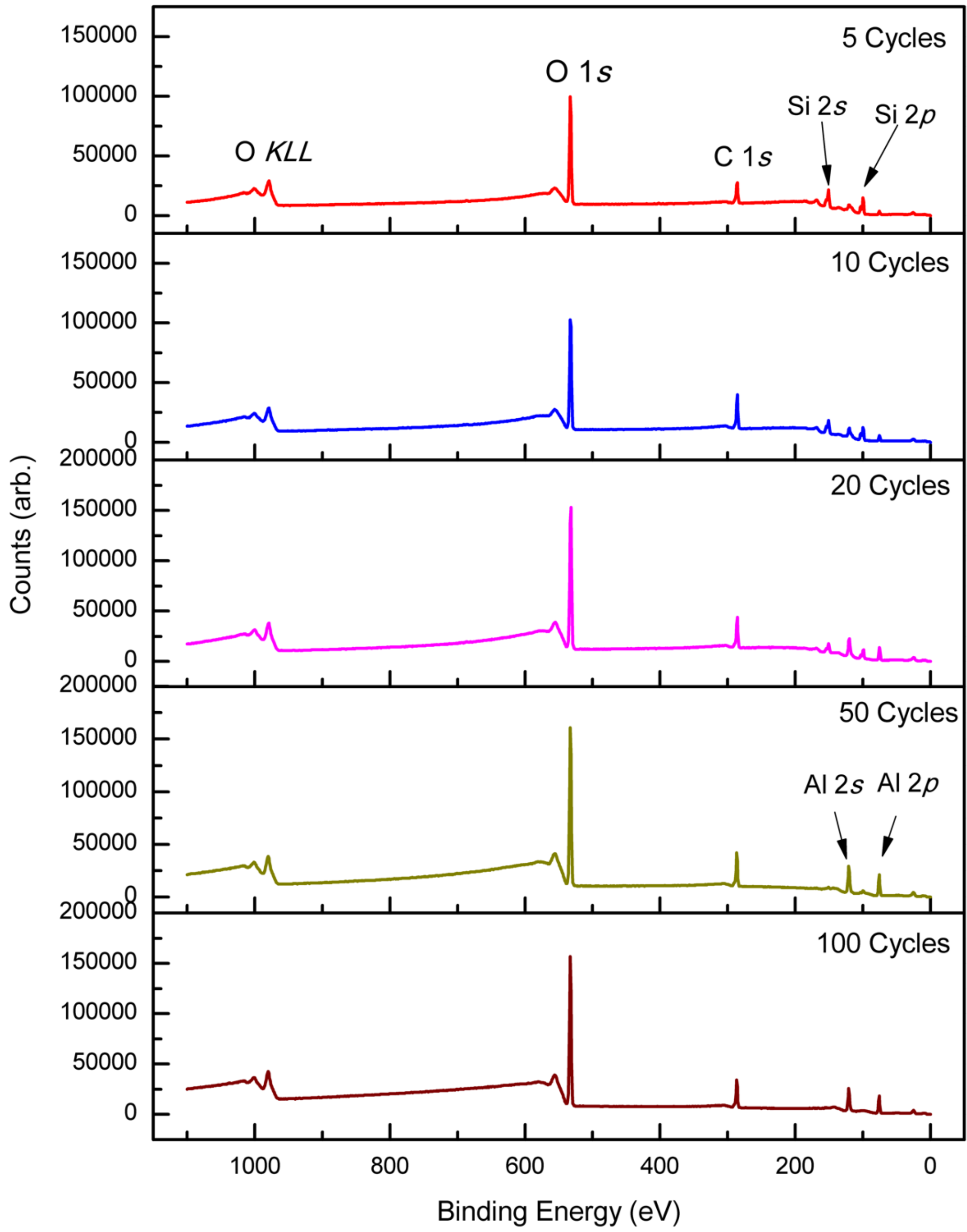

Figure 2.2. XPS survey spectra from 0 – 1100 eV of alumina films deposited by ALD onto silicon shards after 5, 10, 20, 50, and 100 cycles. Some of the data in this figure was previously published in a paper entitled "Tutorial on interpreting x-ray photoelectron spectroscopy survey spectra: Questions and answers on spectra from the atomic layer deposition of Al_2O_3 on silicon".[1] This information is reused here with permission from AIP Publishing.

المنارة للاستشارات
www.manaraa.com

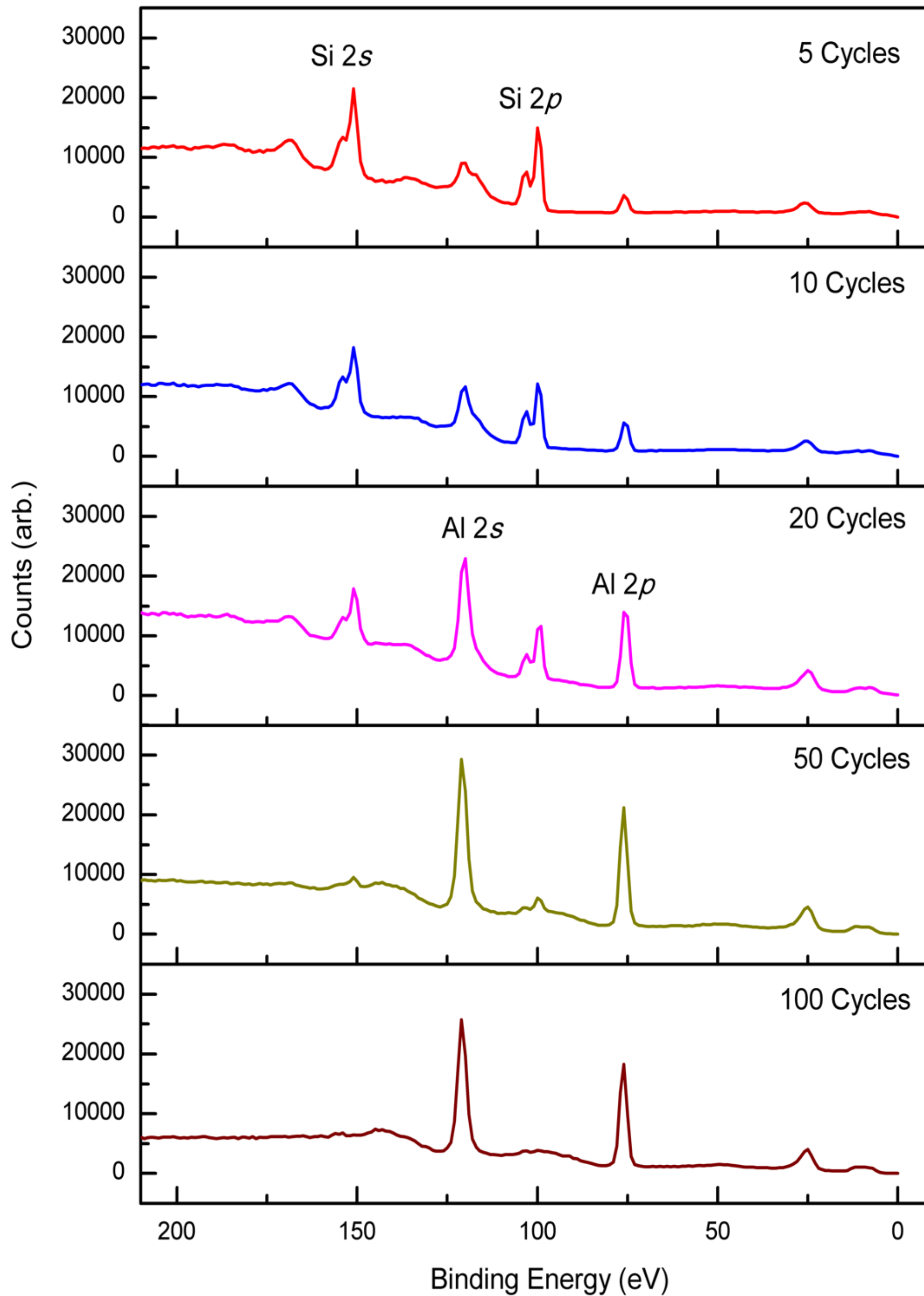

Figure 2.3. XPS survey spectra plotted from 0 – 210 eV of alumina films deposited by ALD onto silicon shards after 5, 10, 20, 50, and 100 cycles. Some of the data in this figure was previously published in a paper entitled “Tutorial on interpreting x-ray photoelectron spectroscopy survey spectra: Questions and answers on spectra from the atomic layer deposition of Al_2O_3 on silicon”.[1] This information is reused here with permission from AIP Publishing.

المنارة للاستشارات
www.manaraa.com

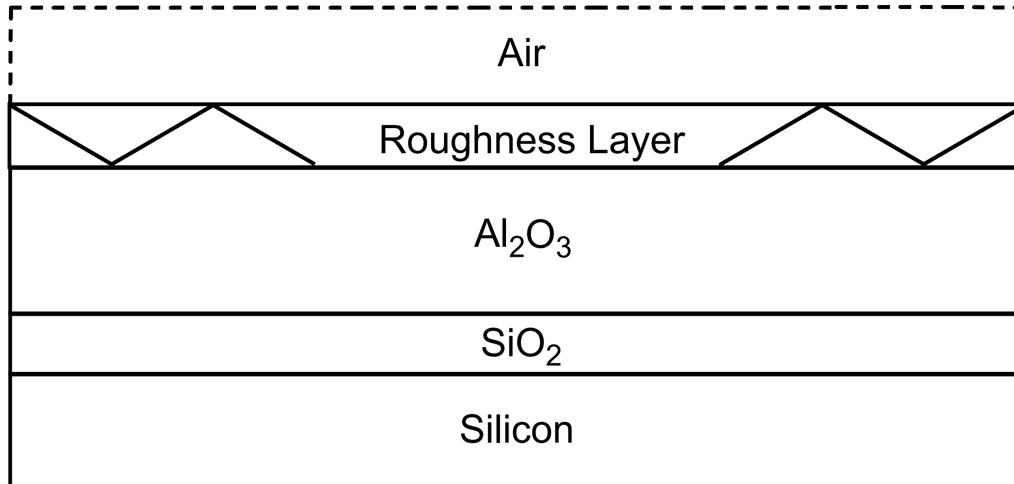

Figure 2.4. Representation of the materials/layers used to model the ALD alumina films on silicon created in this study. The optical functions for the substrate and the native oxide layer above it were obtained from the instrument software: Si_JAW and NTVE_JAW, respectively. Note that the SiO_2 film thickness in all the modeling was fixed at 1.6 nm, where the actual silica thicknesses measured prior to ALD varied between 1.57 nm and 1.62 nm.

المنارة للاستشارات
www.manaraa.com

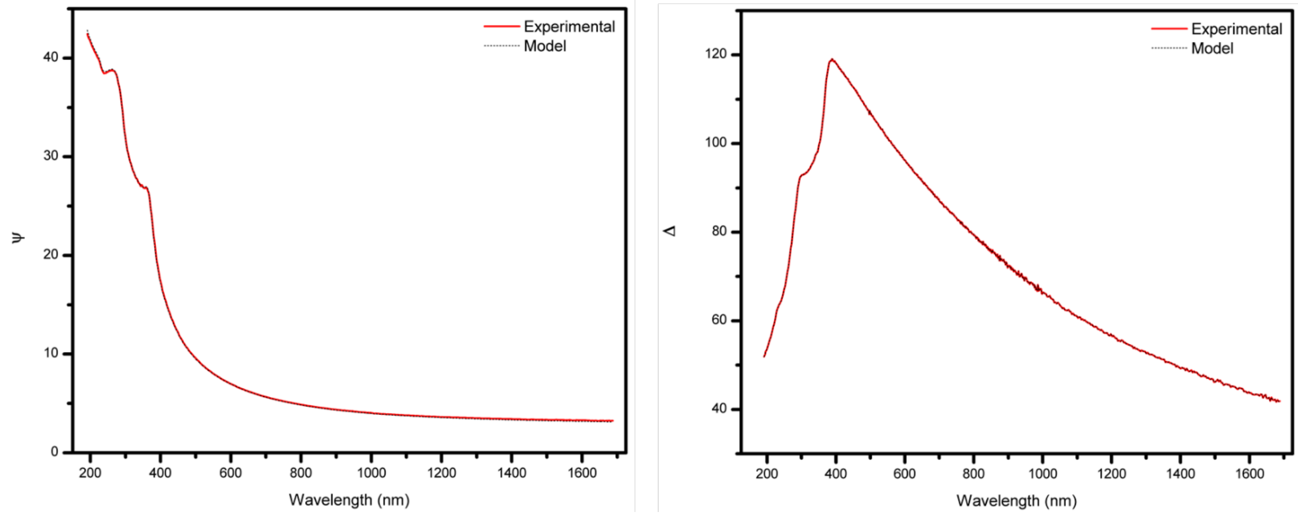

Figure 2.5. Experimental results (ψ and Δ) modeled using Cauchy's equation for an Al_2O_3 film prepared via 100 ALD cycles.

المنارة للاستشارات
www.manaraa.com

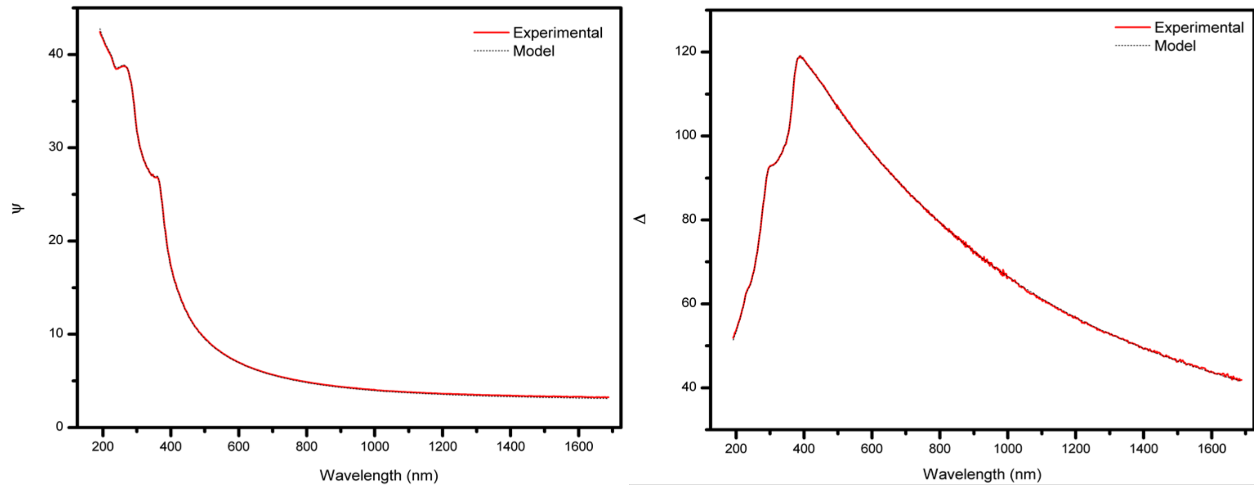

Figure 2.6. Experimental results (ψ and Δ) modeled using Sellmeier's equation for an Al_2O_3 film prepared via 100 ALD cycles.

المنارة للاستشارات
www.manaraa.com

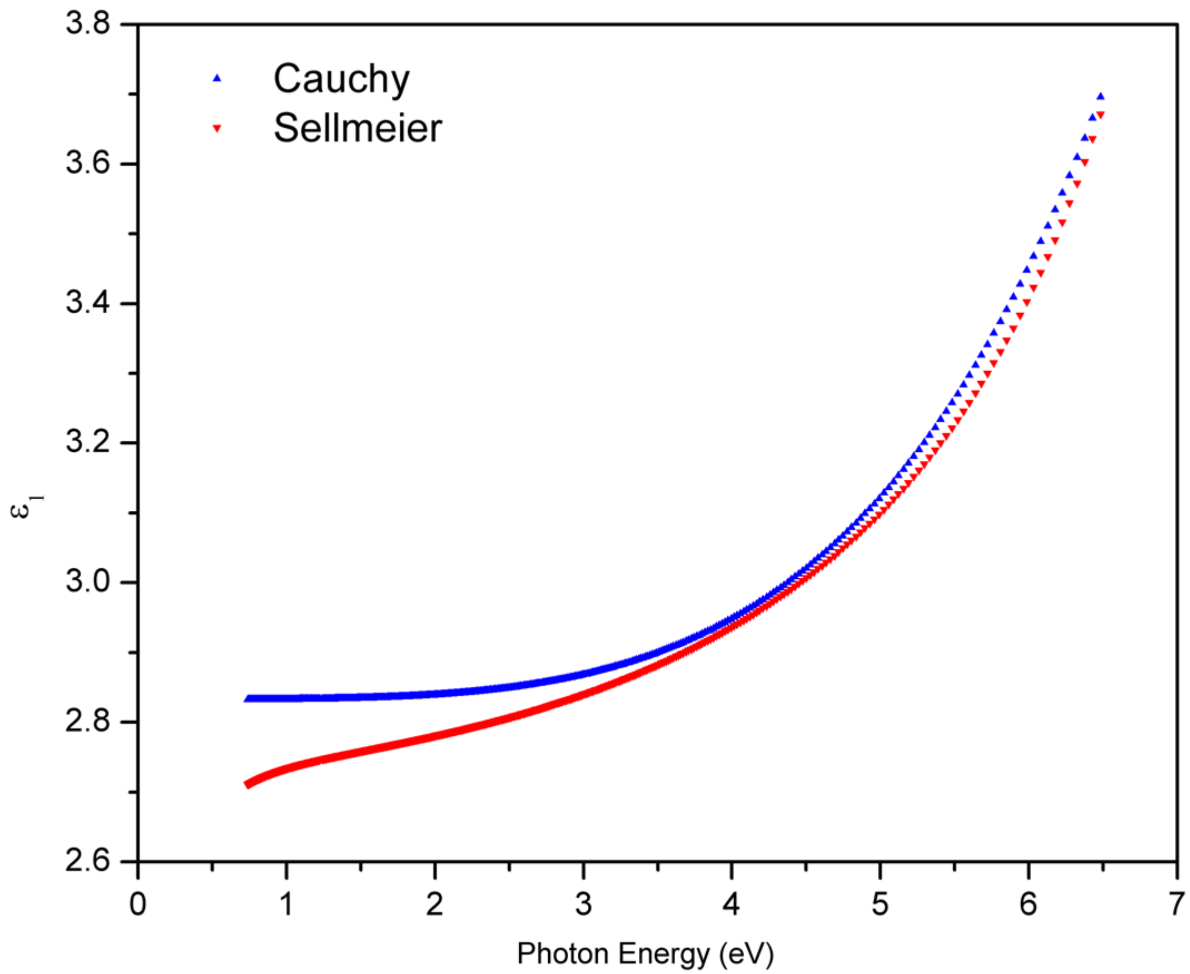

Figure 2.7. Real part (ε_1) of the complex dielectric function of alumina obtained from Cauchy and Sellmeier models as a function of photon energy.

المنارة للاستشارات
www.manaraa.com

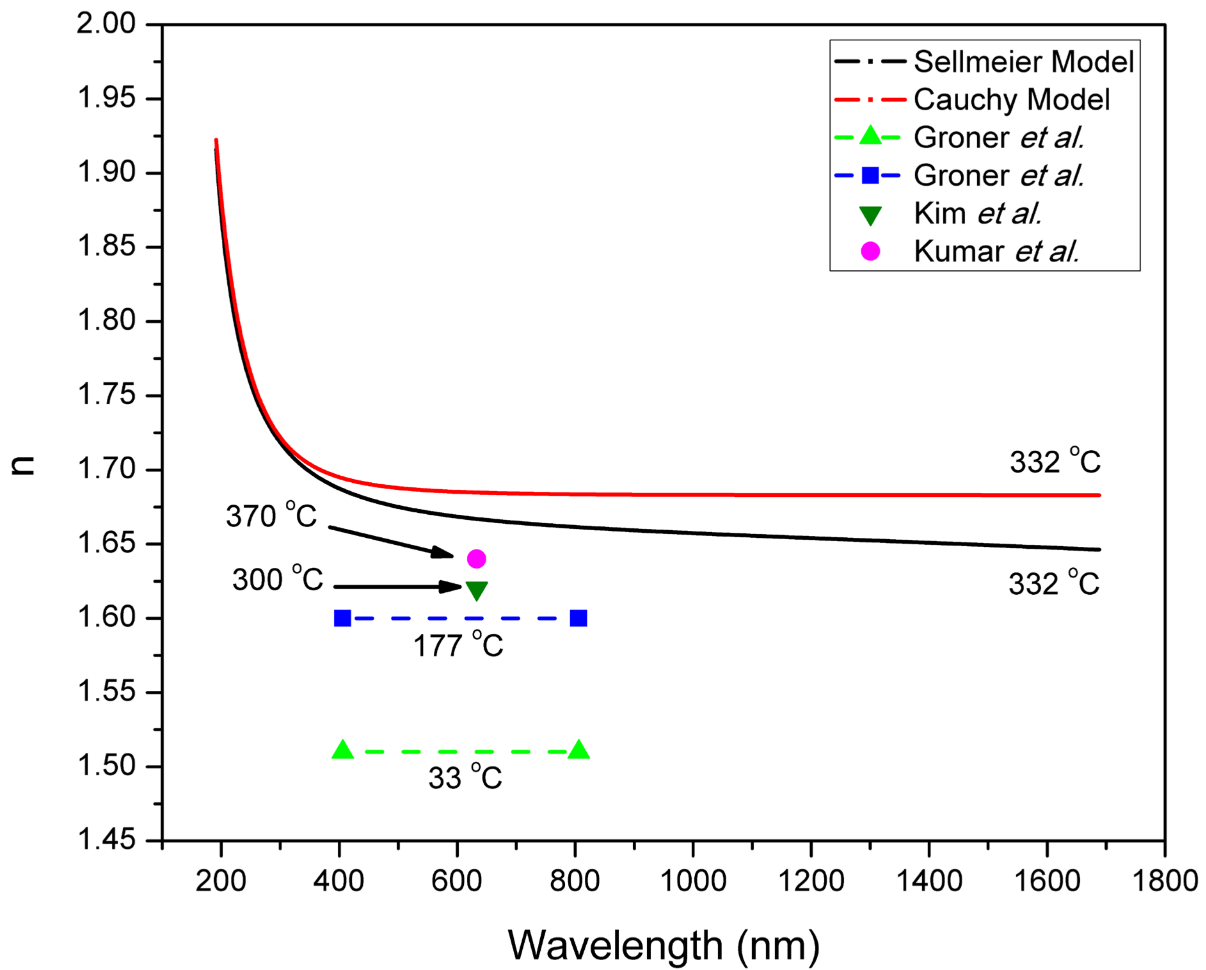

Figure 2.8. Comparison of optical functions determined for ALD alumina thin films obtained from the Cauchy and Sellmeier models in this study to literature results. The two single points are literature results at 633 nm. The other two results are represented as dashed lines because the authors of these studies specified a range of wavelengths, but not a particular wavelength.

المنارة للاستشارات
www.manaraa.com

2.13 References

1. D. Shah; D. I. Patel; T. Roychowdhury; G. B. Rayner; N. O'Toole; D. R. Baer; Linford, M. R., Tutorial on interpreting x-ray photoelectron spectroscopy survey spectra: Questions and answers on spectra from the atomic layer deposition of Al_2O_3 on silicon. *J. Vac. Sci. Technol. B* **2018,** *36*, 062902.
2. George, S. M., Atomic Layer Deposition: An Overview. *Chem. Rev.* **2010,** *110* (1), 111-131.
3. Leskelä, M.; Ritala, M., Atomic layer deposition (ALD): From precursors to thin film structures. *Thin Solid Films* **2002,** *409*, 138-146.
4. Sunotla, T., Atomic layer epitaxy. *Thin Solid Films* **1992,** *216*, 84-89.
5. Puurunen, R. L., Surface chemistry of atomic layer deposition: A case study for the trimethylaluminum/water process. *J. Appl. Phys.* **2005,** *97* (12), 121301-121311.
6. Suntola, T.; Anston, J. Chemistry. November 15 1977, 1977.
7. A. M. Shevjakov; G. N. Kuznetsova; Aleskovskii, V. B. In *Atomic layer deposition*, Proceddings of the second USSR conference on High-Temperature chemistry of Oxides, , Leningrad, USSR, 26-29 November 1965; Leningrad, USSR, 1965.
8. Kim, H.; Lee, H.-B.-R.; Maeng, W. J., Applications of atomic layer deposition to nanofabrication and emerging nanodevices. *Thin Solid Films* **2009,** *517*, 2563-2580.
9. Knisley, T. J.; Kalutarage, L. C.; Winter, C. H., Precursors and chemistry for the atomic layer deposition of metallic first row transition metal films. *Coord. Chem. Rev.* **2013,** *257* (23-24), 3222-3231.
10. Kanyal, S. S.; Jensen, D. S.; Miles, A. J.; Dadson, A. E.; Vail, M. A.; Olsen, R.; Scorza, F.; Nichols, J.; Vanfleet, R. R.; Davis, R. C.; Linford, M. R., Effects of catalyst thickness on the fabrication and performance of carbon nanotube-templated thin layer chromatography plates. *J. Vac. Sci. Technol. B* **2013,** *31* (3), 031203.
11. Kanyal, S.; Jensen, D.; Dadson, A.; Vanfleet, R.; Davis, R.; Linford, M. R., Atomic layer deposition of aluminum-free silica onto patterned carbon nanotube forests in the preparation of microfabricated thin-layer chromatography plates. *J. Planar Chromatogr.-Mod. TLC* **2014,** *27* (3), 151-156.
12. Johnson, R. W.; Hultqvist, A.; Bent, S. F., A brief review of atomic layer deposition: From fundamentals to applications. *Mater. Today* **2014,** *17* (5), 236-246.
13. H. Moshe; Y. Mastai, Atomic layer deposition on self-assembled-monolayers. In *Materials Science-Advanced Topics*, Mastai, Y., Ed. Intech: Isarel, 2013.
14. Broas, M.; Kanninen, O.; Vuorinen, V.; Tilli, M.; Paulasto-Kröckel, M., Chemically stable atomic-layer-deposited Al_2O_3 films for processability. *ACS Omega* **2017,** *2* (7), 3390-3398.
15. O. Sneh; R. B. Clark- Phelps; A. R. Londergan; J. Winkler; T. E. Seidel, Thin films atomic layer deposition equipment for semiconductor processing. *Thin Solid Films* **2002,** *402*, 248-261.
16. Ylivaara, O. M. E.; Liu, X.; Kilpi, L.; Lyytinen, J.; Schneider, D.; Laitinen, M.; Julin, J.; Ali, S.; Sintonen, S.; Berdova, M.; Haimi, E.; Sajavaara, T.; Ronkainen, H.; Lipsanen, H.; Koskinen, J.; Hannula, S.-P.; Puurunen, R. L., Aluminum oxide from trimethylaluminum and water by atomic layer deposition: The temperature dependence of residual stress, elastic modulus, hardness and adhesion. *Thin Solid Films* **2014,** *552*, 124-135.

المنارة للاستشارات
www.manaraa.com

17. Itano, M.; Kern, F. W.; Miyashita, M.; Ohmi, T., Particle removal from silicon wafer surface in wet cleaning process. *IEEE Transactions on Semiconductor Manufacturing* **1993,** *6* (3), 258-267.
18. Kern, W., The evolution of silicon wafer cleaning technology. *J. Electrochem. Soc.* **1990,** *137*, 1887-1892.
19. Seu, K. J.; Pandey, A. P.; Haque, F.; Proctor, E. A.; Ribbe, A. E.; Hovis, J. S., Effect of surface treatment on diffusion and domain formation in supported lipid bilayers. *Biophys. J.* **2007,** *92* (7), 2445-50.
20. Rammula, R.; Aarik, L.; Kasikov, A.; Kozlova, J.; Kahro, T.; Matisen, L.; Niilisk, A.; Alles, H.; Aarik, J., Atomic layer deposition of aluminum oxide films on graphene. *IOP Conference Series: Materials Science and Engineering* **2013,** *49*, 012014.
21. A. L. Brazeau; S. T. Barry, Atomic layer deposition of aluminum oxide thin films from a heteroleptic, amidinate-containing precursor. *Chem. Mater.* **2008,** *20*, 7287-7291.
22. Prokes, S. M.; Katz, M. B.; Twigg, M. E., Growth of crystalline Al_2O_3 via thermal atomic layer deposition: Nanomaterial phase stabilization. *APL Mater.* **2014,** *2* (3), 032105.
23. Manandhar, K.; Wollmershauser, J. A.; Boercker, J. E.; Feigelson, B. N., Growth per cycle of alumina atomic layer deposition on nano- and micro-powders. *J. Vac. Sci. Technol. A* **2016,** *34* (2), 021519.
24. Kukli, K.; Salmi, E.; Jõgiaas, T.; Zabels, R.; Schuisky, M.; Westlinder, J.; Mizohata, K.; Ritala, M.; Leskelä, M., Atomic layer deposition of aluminum oxide on modified steel substrates. *Surf. Coat. Technol.* **2016,** *304*, 1-8.
25. Aguilar-Gama, M. T.; Ramírez-Morales, E.; Montiel-González, Z.; Mendoza-Galván, A.; Sotelo-Lerma, M.; Nair, P. K.; Hu, H., Structure and refractive index of thin alumina films grown by atomic layer deposition. *J. Mater. Sci.* **2014,** *26* (8), 5546-5552.
26. N. Batra; J. Gope; J. Panigrahi; R. Singh; P. K. Singh, Influence of deposition temperature of thermal ALD deposited Al_2O_3 films on silicon surface passivation. *AIP Advances* **2015,** *5* (6), 067113.
27. Groner, M. D.; Fabreguette, F. H.; Elam, J. W.; George, S. M., Low-temperature Al_2O_3 atomic layer deposition. *Chem. Mater.* **2004,** *16*, 639-645.
28. Gharachorlou, A.; Detwiler, M. D.; Gu, X. K.; Mayr, L.; Klotzer, B.; Greeley, J.; Reifenberger, R. G.; Delgass, W. N.; Ribeiro, F. H.; Zemlyanov, D. Y., Trimethylaluminum and oxygen atomic layer deposition on hydroxyl-free Cu(111). *ACS Appl. Mater. Interfaces* **2015,** *7* (30), 16428-39.
29. Hilfiker, J. N.; Synowicki, R. A., Spectroscopic ellipsometry methods for thin absorbing coatings. *Soc. Vac. Coaters* **2008,** *505*, 511-516.
30. N. Madaan; S. S. Kanyal; D. Jensen; M. A. Vail; A. E. Dadson; M. H. Engelhard; H. Samha; M. R. Linford, Al_2O_3 *e*-Beam evaporated onto silicon (100)/SiO_2, by XPS. *Surf. Sci. Spectra* **2013,** *20* (43), 1-7.
31. Velez, K.; Quinson, J. F., Structural Characterization by SIMS of Alumina Coatings on Stainless Steel. *J. Sol-Gel Sci. Technol.* **2000,** *19* (1), 469-472.
32. S. Kanyal; D. Jensen; Z. Zhu; M. R. Linford, Al_2O_3 e-beam evaporated onto silicon (100)/SiO_2 by ToF-SIMS. *Surf. Sci. Spectra* **2015,** *22*.
33. Gupta, V.; Ganegoda, H.; Engelhard, M. H.; Terry, J.; Linford, M. R., Assigning oxidation states to organic compounds via predictions from X-ray photoelectron spectroscopy: A discussion of approaches and recommended improvements. *J. Chem. Educ.* **2014,** *91* (2), 232-238.

المنارة للاستشارات
www.manaraa.com

34. Jensen, D. S.; Kanyal, S. S.; Madaan, N.; Vail, M. A.; Dadson, A. E.; Engelhard, M. H.; Linford, M. R., Silicon (100)/SiO_2 by XPS. *Surf. Sci. Spectra* **2013,** *20* (36), 1-8.
35. Van der Heide, P., *Atoms, Ions, and their electronic structure*. John Wiley & Sons, Inc.: 2011; p 13-26.
36. Turner, N. H., Surface analysis: X-ray photoelectron spectroscopy and Auger electron spectroscopy. *Anal. Chem.* **1988,** *60* (12), 377-387.
37. Diwan, A.; Singh, B.; Roychowdhury, T.; Yan, D.; Tedone, L.; Nesterenko, P. N.; Paull, B.; Sevy, E. T.; Shellie, R. A.; Kaykhaii, M.; Linford, M. R., Porous, high capacity coatings for solid phase microextraction by sputtering. *Anal. Chem.* **2016,** *88* (3), 1593-600.
38. Eriksson, T. S.; Hjortsberg, A.; Niklasson, G. A.; Granqvist, C. G., Infrared optical properties of evaporated alumina films. *Appl. Opt.* **1981,** *20*, 2742-2746.
39. Kumar, P.; Wiedmann, M. K.; Winter, C. H.; Avrutsky, I., Optical properties of Al_2O_3 thin films grown by atomic layer deposition. *Appl. Opt.* **2009,** *48*, 5407-5412.
40. Huang, Y.; Tian, X.; Yang, S.; Fu, R. K. Y.; Chu, P. K., Optical and mechanical properties of alumina films fabricated on Kapton polymer by plasma immersion ion implantation and deposition using different biases. *Appl. Surf. Sci.* **2007,** *253* (24), 9483-9488.
41. Soserov, L.; Todorov, R., Optical properties of thin nanoporous aluminum oxide films formed by anodization. *Bulgarian Chem. Commun.* **2013,** *45*, 47-50.
42. Jung, J.-Y.; Brewster, M. Q., Optical properties of variable-composition aluminum/alumina thin films, Part 1. *J. Thermophys. Heat Transfer* **2015,** *29* (2), 376-389.
43. Jung, J.-Y.; Brewster, M. Q., Optical properties of variable-composition aluminum/alumina thin films, Part 2. *J. Thermophys. Heat Transfer* **2015,** *29* (2), 390-402.
44. Zhao, Z. W.; Tay, B. K.; Lau, S. P.; Xiao, C. Y., Microstructural and optical properties of aluminum oxide thin films prepared by off-plane filtered cathodic vacuum arc system. *J. Vac. Sci. Technol. A* **2003,** *21* (4), 906-910.
45. O'Leary, S. K.; Johnson, S. R.; Lim, P. K., The relationship between the distribution of electronic states and the optical absorption spectrum of an amorphous semiconductor: An empirical analysis. *J. Appl. Phys.* **1997,** *82* (7), 3334-3340.
46. He, L.-J.; Li, C.; Liu, X.-Z., The optical properties of alumina films prepared by electron beam evaporation at oblique incidence. *Mater. Lett.* **2013,** *101*, 1-4.
47. Koushki, E.; Mousavi, S. H.; Jafari Mohammadi, S. A.; Majles Ara, M. H.; de Oliveira, P. W., Optical properties of aluminum oxide thin films and colloidal nanostructures. *Thin Solid Films* **2015,** *592*, 81-87.
48. Patil, P.; Bendale, D. M.; Puri, R. K.; Puri, V., Refractive index and adhesion of Al_2O_3 thin films obtained from different processes - a compartive study. *Thin Solid Films* **1996,** *288*, 120-124.
49. Boidin, R.; Halenkovič, T.; Nazabal, V.; Beneš, L.; Němec, P., Pulsed laser deposited alumina thin films. *Ceram. Int.* **2016,** *42* (1), 1177-1182.
50. S. K. Kim; S. W. Lee; C. S. Hwang; Y. -S. Min; J. Y. Won; J. Jeong, Low Temperature (<100°C) Deposition of Aluminum Oxide Thin Films by ALD with O_3 as Oxidant. *J. Electrochem. Soc.* **2006,** *153* (5), F69 - F76.
51. Hilfiker, J. N.; Singh, N.; Tiwald, T.; Convey, D.; Smith, S. M.; Baker, J. H.; Tompkins, H. G., Survey of methods to characterize thin absorbing films with Spectroscopic Ellipsometry. *Thin Solid Films* **2008,** *516* (22), 7979-7989.
52. Tompkins, H. G., *A User's Guide to Ellipsometry*. 1st Edition ed.; Academic Press: 1992; p 1-260.

المنارة للاستشارات
www.manaraa.com

53. Kim, Y.; Lee, S. M.; Park, C. S.; Lee, S. I.; Lee, M. Y., Substrate dependence on the optical properties of Al2O3 films grown by atomic layer deposition. *Appl. Phys. Lett.* **1997,** *71* (25), 3604-3606.
54. Cushman, C. V.; Johnson, B. I.; Martin, A.; Lunt, B. M.; Smith, N. J.; Linford, M. R., Eagle XG® glass: Optical constants from 196 to 1688 nm (0.735–6.33 eV) by spectroscopic ellipsometry. *Surf. Sci. Spectra* **2017,** *24* (2), 026001.
55. Cushman, C. V.; Sturgell, B. A.; Martin, A. C.; Lunt, B. M.; Smith, N. J.; Linford, M. R., Eagle XG® glass, optical constants from 230 to 1690 nm (0.73 - 5.39 eV) by spectroscopic ellipsometry. *Surf. Sci. Spectra* **2016,** *23* (1), 55-60.
56. T. Roychowdhury; C. V. Cushman; R. A. Synowicki; Linford, M. R., Polydimethylsiloxane: Optical properties from 191-1688 nm (0.735-6.491 eV) of the Liquid material by spectroscopic ellipsometry. *Surf. Sci. Spectra* **2018,** *25*, 026001.
57. Khardani, M.; Bouaïcha, M.; Bessaïs, B., Bruggeman effective medium approach for modelling optical properties of porous silicon: comparison with experiment. *physica status solidi (c)* **2007,** *4* (6), 1986-1990.

المنارة للاستشارات
www.manaraa.com

CHAPTER 3: A New Holder/Container with a Porous Cover for Atomic Layer Deposition on Particles, with Detailed Characterization of the Resulting Materials

3.1 Statement of Attribution

This article was originally submitted as **Shah, D.**; Patel, D. I.; Major, G. H.; Linford, M. R. A New Holder/Container with a Porous Cover for Atomic Layer Deposition on Particles, with Detailed Characterization of the Resulting Materials *Surf. Interface Anal.* **2020**, *Submitted*. Some of the text and figures have been updated for clarity. The text and figures are reproduced with the permission from AIP publishing.

3.2 Abstract

Atomic layer deposition (ALD) is widely used in the semiconductor and materials industries for depositing thin films. Here we describe a holder/container for performing ALD on particles that does not require agitation. This device contains a broad, shallow, circular recess that holds the particles. Two different frits and combinations of stacked meshes were explored as a cover to this holder to restrict the movement of the particles while still allowing good conductance of the ALD reagent gases. As confirmed by spectroscopic ellipsometry (SE) on planar witness silicon shards, consistent, high quality film growth took place inside and outside the holder. The performance of the holder was demonstrated with ca. 5 µm zirconia particles that were coated with alumina from trimethylaluminum (TMA) and water, and with zinc oxide from diethylzinc (DEZ) and water. Deposition on different amounts of particles was investigated (50, 100, 200, and 500 mg). Parasitic chemical vapor deposition (CVD) appeared to be present when a greater number of particles or meshes was used. ALD coating on particles was also confirmed by X-ray photoelectron

www.manaraa.com

spectroscopy (XPS), transmission electron spectroscopy (TEM), and energy dispersive X-ray spectroscopy (EDS).

3.3 Introduction

Atomic layer deposition (ALD) is an increasingly important thin-film deposition technique that offers a high degree of control over film thickness and conformality, while enjoying important benefits over other vacuum techniques like physical vapor deposition (PVD) and chemical vapor deposition (CVD). ALD's advantages arise out of its use of distinct, alternating, self-limiting reactions of reactive, molecular, gas phase precursors with substrates.[1-4] That is, ALD does not require line-of-sight between the precursor source and the substrate.[5-7] ALD's unique capabilities have become increasingly valuable to the semiconductor industry as device feature sizes have shrunk.[8] Historically, especially in the laboratory, ALD has been widely performed on planar substrates such as silicon wafers and fused silica or glass slides.

Particles/powders are important in many areas of research and technology, e.g., in catalysis, pharmaceuticals, and batteries and energy.[9-11] Indeed, about three-quarters of the raw materials used in industrial processes come in the form of particles, granules, or powders.[12] Nevertheless, ALD on particulate substrates is more challenging than comparable depositions on planar substrates. A first reason for this difficulty is that particles have drastically larger surface areas compared to flat surfaces,[13] which, especially for large amounts of particles, often results in longer ALD dose and purge times. A second issue is particle agglomeration, which is a result of inter-particle forces and moisture present on them. Particle agglomeration can prevent conformal coating of powders and is difficult to eliminate,[14, 15] although particle drying/dehydration before thin film deposition often reduces agglomeration and allows powders to flow freely.[16] Third,

المنارة للاستشارات
www.manaraa.com

because of their very small masses, particles are easily dispersed by air currents. That is, they may be scattered during a pump down or venting procedure, which results in loss of the material and possible damage to the system. Fourth, diffusion is an inherently slow process so particles must often rotated or agitated in an ALD deposition, especially when large quantities of them are coated.

Particle coating by ALD has previously been reported in the literature[17-19] including in industrial fluidized bed reactors, rotary reactors, and centrifugally assisted reactors.[20-23] Suntola and co-workers were early pioneers in this area – they coated relatively large quantities, e.g., 10 g, of high-surface area silica and alumina particles by ALD in a flow-type reactor.[24-26] Their precursor and purge pulses lasted 4 and 6 h, respectively,[27] i.e., larger quantities of particles generally lead to longer purge and dose times, which can easily become impractical. An additional limitation of fluidized reactors is the reduced efficiency of the deposition process, as a constant flow of inert gas dilutes the concentration of the precursor, leading to longer precursor pulses and even longer purge times.[28] Of course the agitation employed in most ALD of particles requires additional equipment and therefore process optimization. Agitation may also damage particles.[29, 30] However, in spite of these challenges, and because of the importance of particles in science and technology, there are now multiple examples of particles or nanoparticles that have been coated by ALD for the pharmaceutical industry,[31, 32] catalysis,[33, 34] and energy/battery industries.[35-38]

In this report, we take a somewhat different approach to coating particles by ALD. We coat a single layer of ca. 5 μm zirconia particles in a relatively short amount of time in a holder that is covered by a frit or a series of stainless steel meshes. This device consists of a simple, circular, machined, recess that holds the particles (see **Figure 3.1 and 3.2**) that is covered by a porous barrier that prevents the particles from escaping while allowing the ALD reagent gases to move to them. Various iterations of this cover were considered, including two different porous

المنارة للاستشارات
www.manaraa.com

frits and different numbers of stacked meshes. There is no agitation in this system – beyond this holder, no special equipment is required. The quality of the ALD films was confirmed by spectroscopic ellipsometry (SE).

This holder and process are demonstrated on particles with ALD of alumina from trimethylaluminum (TMA) and water, and ALD of zinc oxide from diethylzinc (DEZ) and water (see **Figure 3.3**). An obvious limitation to this approach is that the part of the particle that is in direct contact with the holder may not be coated. Nevertheless, we have not been able to directly measure such defects, presumably because the particles used in this work are relatively large and their points of contact with the holder should be small. Additional particle characterization was by X-ray photoelectron spectroscopy (XPS), transmission electron microscopy (TEM), energy dispersive X-ray spectroscopy (EDX), and BET isotherms. In summary, we demonstrate a method for performing high-quality thermal ALD on modest quantities of particles using a relatively simple device.

Table 3.1. Descriptions of the deposition and analytical equipment employed in this work.

Technique	Equipment Vendor
Atomic layer deposition (ALD)	ALD150LX, Kurt J. Lesker Company, Jefferson Hills, PA, USA
Transmission electron microscopy (TEM)	FEI Tecnai F30 transmission electron microscope (TEM, Hillsboro, Oregon)

المنارة للاستشارات
www.manaraa.com

Scanning Electron Microscopy (SEM)	FEI Apreo C SEM, ThermoFisher Scientific, Waltham, MA, USA
X-ray Photoelectron Spectrometry (XPS)	SSX-100 (Serviced by Service Physics Inc., Bend, OR, USA)
Spectroscopic Ellipsometry (SE)	M-2000DI, J. A. Woollam Company, Lincoln, Nebraska, USA
Brunauer–Emmett–Teller (BET) isotherm measurements	Micromeritics Instrument Corp., Norcross, GA, USA

3.4 Experimental

3.4.1. Substrates

The small silicon witness shards used in this study (ca. 1 cm x 1 cm) were cut from 4” silicon wafers obtained from University Wafer (South Boston, MA).

3.4.2. Sample Cleaning

Prior to deposition, planar silicon substrates were cleaned for one minute in an air plasma using a Model No. PDC-32G plasma cleaner (Harrick Plasma, Ithaca, New York), or cleaned for 40 min in piranha solution (a ca. 7:3 mixture of H_2SO_4(conc.) and 30% H_2O_2) at 80 – 100 °C.[39, 40] *Note that piranha solution is dangerous and should be prepared and handled with*

المنارة للاستشارات
www.manaraa.com

great care, and only after appropriate training. After piranha cleaning, the substrates were washed extensively with high purity (18 MΩ) water.

3.4.3 ALD Deposition

Atomic layer deposition (ALD) was performed with an ALD150LX system (Kurt J. Lesker Co., Jefferson Hills, PA, USA). With this system, ultrathin films of alumina (Al_2O_3) and zinc oxide (ZnO) were deposited onto silicon shards and zirconia particles by thermal ALD from trimethylaluminum (TMA), diethylzinc (DEZ), and/or water precursors. The TMA and DEZ were purchased from STREM chemicals (Newburyport, MA). Silicon shards, which were terminated with ca. 1.5 nm of native oxide, were used as witness substrates.

These witness shards were plasma cleaned with an air plasma prior to ALD deposition. The zirconia particles (5 µm, Lot # BCBS1080V, Catalog # 230693-100G) were purchased from Sigma-Aldrich Corporation (St. Louis, MO) and used as received.[41] Unless otherwise stated, 100 mg of zirconia particles were coated in each run. The precursor sources were kept at room temperature during the depositions. The alumina depositions were performed at 332 ºC, which is the temperature recommended in the standard recipe from the manufacturer, and the ZnO depositions were performed at 200 °C, which is a commonly used temperature in the Literature.[42, 43] The time provided for the substrate and holder to reach the reactor temperature, also referred to as the equilibration time, was 5 min. Our ALD recipe consisted of four main steps: entry of the first precursor, purging of excess precursor and any byproduct, entry of the second precursor, and finally purging to remove any excess precursor or byproduct.

For these depositions (of both alumina and ZnO), the dose times were 105.0 ms for the metal precursor (TMA or DEZ) and 77.5 ms for water, and the purge time was 60 s in each

المنارة للاستشارات
www.manaraa.com

run. These dose and purge times are longer than would be used in a typical ALD deposition on a simple planar substrate. See Supporting Information for additional details. Ultra-pure nitrogen gas (99.999 %) was used as a carrier for the precursors through the ALD system and as the purge gas. Additional details about the ALD process are provided in a previously published study.[44]

Table 3.2. Process parameters for ALD on planar and powder substrates.

	Step 1 (lead)	**Step 2 (Isolate)**	**Step 3 (Dose)**	**Step 3 (Exposure)**
Reactant A (TMA)	2000 ms	500 ms	105 ms	5000 ms
Reactant A (TMA)	60000 ms	0	0	0
Reactant B (Water)	2000 ms	500 ms	77.5 ms	5000 ms
Reactant B (Water)	60000 ms	0	0	0

Table 3.3. Film thickness and GPC values for different numbers of ALD cycles for witness shards placed inside and outside the second frit (see Figure 4).

Cycles	**Outside Thickness** (nm)	**GPC (Outside) (Å/Cycle)**	**Inside Thickness** (nm)	**GPC (Inside) (Å/Cycle)**
5	0.60 nm	1.20	0.45 nm	0.9
10	1.45 nm	1.45	1.14 nm	1.14

المنارة للاستشارات
www.manaraa.com

25	2.36 nm	0.95	2.07 nm	0.83
50	4.73 nm	0.94	4.15 nm	0.83
75	7.44 nm	0.99	6.34 nm	0.84
100	9.88 nm	0.98	8.52 nm	0.85
125	12.47 nm	0.99	10.61 nm	0.85
250	25.46 nm	1.01	21.55 nm	0.86
375	38.38 nm	1.02	33.42 nm	0.89
500	49.62 nm	0.99	42.75 nm	0.85

3.4.4 XPS Data Collection

X-ray photoelectron spectroscopy (XPS) was performed with a Surface Science SSX-100 X-ray photoelectron spectrometer (serviced by Service Physics, Bend, OR) with a monochromatic Al K_α source, a hemispherical analyzer, and a take-off angle of 35°. Survey scans were recorded with a spot size of 800 µm x 800 µm and a nominal pass energy of 150 eV (instrument setting of 'resolution 4').[47] XPS was performed on coated and uncoated zirconia particles that had been pressed into conductive carbon tape to reduce sample charging. An electron flood gun was employed for charge compensation to powder substrates.[48] Peaks were shifted/referenced to the C 1*s* energy at 285.0 eV. While by no means a perfect solution, the C 1*s* peak position is a commonly used reference in XPS. For the samples in this study, this referencing

www.manaraa.com

produces consistent results.[49] XPS spectra from bare silicon wafers, alumina deposited on silicon, zinc oxide, and zirconia have previously been reported in the scientific literature.[50-53]

3.4.5 Brunauer–Emmett–Teller (BET) Studies

Brunauer–Emmett–Teller (BET) nitrogen adsorption data were obtained using a TriStar II surface area analyzer (Micromeritics Instrument Corp., Norcross, GA, USA) to measure the surface areas and pore sizes of the particles. Prior to data collection, samples were degassed at 200 °C for 12 h, and the surface areas were measured by N_2 adsorption at 77 K.

3.4.6 Spectroscopic Ellipsometry (SE)

SE data were acquired and analyzed from 191 – 1688 nm with an M-2000DI instrument (J. A. Woollam Co., Lincoln, Nebraska, USA) running under the instrument software (CompleteEase®). The models used to evaluate the thicknesses of the alumina or ZnO films on the witness silicon shards consisted of three layers: the silicon substrate, a thin layer of native oxide with a thickness set at 1.5 nm (the actual thickness of this layer, as measured by SE, generally varied between 1.50 and 1.55 nm), and a thin film of aluminum oxide or zinc oxide.

The optical functions for silicon, the native oxide of silicon, and ZnO were obtained from CompleteEase®. The optical function of the alumina layer was modeled with a Sellmeier dispersion relationship. Some of us recently published a more detailed description of this procedure.[42] The alumina and zinc oxide films were smooth, i.e., the roughness predicted by SE was less than 0.1 nm; addition of a roughness layer in our models did not substantially improve the mean squared error (MSE) of the fits, so it was omitted.[54] Indeed, the MSE values for this modeling of the alumina and zinc oxide films were less than 1.0, which suggests high quality fits.

3.4.7 Transmission Electron Microscopy (TEM) and Scanning Electron Microscopy (SEM)

المنارة للاستشارات
www.manaraa.com

Imaging and diffraction patterns were obtained using a Tecnai F30 TEM (FEI, Hillsboro, Oregon) operated at 300 keV. Coated and uncoated particles were mounted on copper grids for analysis using TEM and EDS. SEM and Energy Dispersive X-ray Spectroscopy (EDS) were performed with an FEI Apreo C SEM (Thermo Fisher Scientific, Waltham, MA, USA).

3.4.8 Particle Holder and Cover

The particle holder was made in the Precision Machine Lab (PML) at BYU out of stainless steel from a CAD design (see **Figure 3.1**). The frits employed were 10.4 cm in diameter. The first and second frits (no deposition inside the holder took place when the first frit was used, see below) were 0.23 and 0.30 cm thick, respectively. These frits were supplied by the Kurt J. Lesker Co. Layers of 635 mesh (Cat. No. P0058806, TWP Inc., Berkeley, CA) made of T316L stainless steel were also used as covers for the holder (see **Figure 3.4a and b**). They consist of woven, 0.0008" wires that yield a mesh fabric with a 20 µm pore size (635 square holes across one inch (see **Figure 3.4c**). The ring that held the layer of meshes (a torus ring) was purchased from the same vendor. The meshes were stacked on top of each other without any effort to orient them in any specific direction.

3.5 Results and Discussion

3.5.1. Development and Optimization of the Porous Cover for the Particle Holder

The goal of the initial part of this work was to find and optimize a porous cover for our particle holder. Ideally, this cover should (i) be inert, (ii) be porous enough to allow relatively free movement of the precursor and byproduct molecules, (iii) have small enough pores that the particles to be coated cannot escape, (iv) have large enough pores that it will not be easily clogged

المنارة للاستشارات
www.manaraa.com

by deposition that may take place on it, and (v) allow high quality ALD films to be produced through it. We investigated several different covers made from porous frits (two of them) and layers of meshes. To understand the effects of these covers on the thermal ALD of alumina, ‘witness’ shards of silicon were placed inside and outside the covered holder, which allowed the thicknesses and optical functions of the resulting films to be compared.

We began with an effort to find a frit that would act as a cover for our particle holder and allow ALD deposition through it while preventing particles from escaping. These studies were done with planar silicon – ALD on particles will be considered in the next section. Two different monolithic frits were investigated (see their SEM images in **Figures 3.4a** and **3.4b**). The first (see **Figure 3.4a**) appears to have been formed by sintering small metal particles, which yielded irregular, ca. 10 µm pores, while the second (see **Figure 3.4b**) appears to be made of metallic fibers in a closed weave with much larger (ca. 250 µm) pores. The EDX analysis of both frits showed Fe, Ni, and Cr, which suggests that they are made of stainless steel. The first frit with the smaller pore size showed very poor conductance. That is, no ALD deposition of alumina was observed on witness shards placed inside the holder covered with this frit. In contrast, **Figure 3.5** shows that good ALD of alumina (5 – 500 cycles) was possible through the second frit. That is, **Figure 3.5a** shows that there is only a modest difference between the thicknesses of the films produced inside and outside of the holder when this frit is used. However, an important question that remained here was whether the alumina films produced under these conditions inside and outside the holder were equivalent. Using a multi-sample SE analysis, the optical functions of alumina were calculated for the films produced inside and outside of the holder. **Figure 3.5b** shows that they are essentially identical, which suggests that the alumina deposited in both cases is essentially the same.

المنارة للاستشارات
www.manaraa.com

The previous set of experiments suggests that a frit with an appropriate pore size can act as an effective cover for particles during ALD. We next experimented with covers we created from stacks of meshes held together with a torus ring. Our purpose in these experiments was to discover a more versatile cover for our particle holder. The hypothesis was that the right number of stacked meshes might prevent the particles from escaping while also allowing good conductance of the reagent and product gases. This strategy might ultimately be more adaptable than the previous one – the number of meshes in a stack and their pore sizes can be quite easily altered to meet the demands of a particular deposition. We tested combinations of 2 – 7 stacked, 635 meshes (see **Figure 3.4c** for an SEM image of this mesh). As shown in **Figure 3.5a**, good ALD deposition, as defined by a constant, modest, relative difference between the film thicknesses obtained inside and outside the holder was possible with 2 – 4 stacked meshes.

A multi-sample SE analysis of the alumina films obtained inside and outside the holder prepared using 2 – 4 stacked meshes again showed that they had essentially the same optical properties (see **Figure 3.6a**). The optical functions obtained here (in **Figure 3.6b**) are also essentially identical to the optical functions obtained for alumina with the second frit (see **Figure 3.6b**). However, while the optical functions obtained in **Figures 3.5b** and **3.6b** are essentially identical, the growth-per cycle (GPC) values differ somewhat for these processes – the GPC values are lower for the films produced inside the holder. Also, when 5 – 7 stacked meshes were used, the throughput (conductance) of the covers decreases such that noticeably thinner films were obtained inside the holder. A subtlety in these results is that while the films produced inside the holder become noticeably thinner when more meshes are used, the film thicknesses *increase* somewhat on the witness samples outside the holder. This effect may be a result of parasitic CVD, i.e., the thicker layer of meshes may not allow the reagents to be fully removed with each purge.

المنارة للاستشارات
www.manaraa.com

In summary, we have confirmed that high quality ALD on planar substrates takes place through either frits or 2 – 4 layers of meshes with adequate conductance.

3.5.2. ALD of Alumina on Powders using the Holder

The work in the previous section suggests that high quality ALD depositions at reasonable rates take place through frits or meshes with adequate conductance. In order to test this recipe on particles, 100 mg of 5 μm ZrO_2 particles was placed inside the particle holder and covered with two '635' meshes. Alumina was then deposited by ALD on these particles. As before, witness silicon shards were placed inside and outside the holder. The thicknesses of the alumina films obtained in this manner are very similar to those obtained when no particles were present (see values listed in **Figure 3.7**). XPS of the particles (see also **Figure 3.8**) shows the expected Zr (3*d* and 3*p*) and Al (2*s* and 2*p*) peaks from the particles and alumina coating, where the Al peaks are only present after some ALD deposition of alumina (25, 50, 75, or 100 cycles) has taken place, and the Zr peaks gradually disappear as more and more layers of alumina are deposited.

Sven Tougaard has championed the idea that the nanostructures and layered arrangements of materials influence the baselines around their XPS signals.[55] Consistent with these observations, we note changes in the slopes of the baselines in the XPS spectra in **Figure 3.8** on the high binding energy side of the Zr 3*d* signal. In particular, the negative slopes of the baselines from 240 – 270 eV are -6.95, 8.85, 11.47, 12.47, and 7.83 counts/eV after 0, 25, 50, 75, and 100 ALD layers, respectively. These results are consistent with the deposition of an increasingly thick alumina layer on the zirconia particles. That is, as was observed in this study, slopes on the high binding energy sides of XPS peaks of pure materials are usually positive or around zero (note the positive slope in **Figure 3.8** after 0 ALD alumina cycles). However, as a substrate is coated with a film, an increasing degree of inelastic scattering of the photoelectrons from the substrate takes

المنارة للاستشارات
www.manaraa.com

place, which increases the slope of the baseline on the high binding energy (low kinetic energy) side of the peaks (note the increase in the baseline in **Figure 3.8** after 25, 50, and 75 ALD alumina cycles). However, as the over layer becomes thicker (see **Figure 3.8** for 100 ALD cycles), the slope of the baseline drops because the over layer, in effect, increasing becomes the substrate.

Charge compensation of insulating particles is often challenging in XPS.[56, 57] A consequence of coating zirconia particles (already an insulator) with another insulator (alumina) appears to be differential charging. That is, some distortion is present in the four main peaks (from Zr and Al) in the XPS survey spectra in **Figure 3.9** collected from the particles coated with 50, 75, and 100 ALD cycles of alumina. That this is most likely due to differential charging is confirmed by the fact that the distortion appears to be about the same in all the peaks of a given spectrum.

In all of the particle depositions studied to this point here, 100 mg of zirconia particles have been coated. In order to test the robustness of this process, 50, 100, 200, and 500 mg of particles were coated with 100 cycles of ALD alumina using the same recipe. As shown in **Figure 3.11**, the thicknesses of the alumina layers on silicon witness shards placed inside and outside the holder remain roughly constant in all of these depositions. However, slightly thicker alumina films were obtained when 200 and 500 mg of particles were coated – additional study might reveal whether these results are a statistical aberration, or whether the additional surface area of the particles makes it is harder to remove the ALD reagents, especially water, so that, as suggested above with a larger number of meshes, a small amount of parasitic CVD is taking place here. The XPS survey spectra for the 50, 100, and 200 mg particle depositions are nearly the same, e.g., the Zr 3*p* and 3*d* peaks have mostly disappeared from these spectra (see **Figure 3.12**). However, in the case of the 500 mg deposition, small, but distinct Zr 3*p* and 3*d* peaks are present in the spectra, which suggest that the same high quality, uniform ALD deposition is no longer

المنارة للاستشارات
www.manaraa.com

taking place. These results provide a range over which successful ALD depositions on these particles appear to be possible with this apparatus. Finally, we note that no loss of particles was observed in any of the ALD depositions on particles performed here.

TEM was used to directly characterize ALD alumina films on zirconia particles. The resulting images (see **Figures 3.12a** and **3.12b**), which are based on the Z-contrast between the substrate (higher electron density) and the film, suggest good film uniformity. A 35 nm long line spectrum (see **Figures 3.13a** and **3.13b**) using TEM/EDX showed both the expected elemental composition (Zr, Al, and O) and arrangement of materials in the coated particles. By TEM, the alumina film thickness was 9.78 nm after 100 ALD cycles (see **Figure 3.13a**), which is in quite good agreement with the value found by SE on the silicon witness shard inside the deposition chamber (8.50 nm, see **Figure 3.9**).

3.5.3 Zinc oxide deposition on zirconia particles

As an additional demonstration of the holder and cover for ALD of particles, we coated 100 mg of ZrO_2 particles with 0, 25, 50, 75, and 100 ALD cycles of DEZ and water to form ZnO using the same recipe employed above, with the exception that the deposition temperature was lowered to 200 ºC. SE of the silicon witness shards that were present during these depositions (see **Figure 3.14**) showed that (i) the ZnO film thickness increased steadily as the number of ALD cycles increased, and (ii) as before, films produced inside the holder were a little thinner than those produced outside of it. XPS of the coated particles (see **Figure 3.15**) showed that (i) the expected peaks from Zn appear after ZnO deposition (the Zn 3*p*, 3*s*, and 3*d* signals at ca. 140.0, 90.0, and 10.0 eV, respectively, see **Figure 3.16 – 3.18**),[58, 59] and (ii) the substrate signals from Zr decrease substantially in intensity after ZnO deposition.

المنارة للاستشارات
www.manaraa.com

Table 3.4. Representative process parameters for a Static dosing recipe for coating thin zinc oxide films on powder substrates. Note: the dose and purge times are 5 times the typical dose and purge times was 4 times the purge times used for deposition on silicon surfaces.

	Step 1 (lead)	Step 2 (Isolate)	Step 3 (Dose)	Step 3 (Exposure)
Reactant A (DEZ)	2000 ms	500 ms	105 ms	5000 ms
Reactant A (DEZ)	60000 ms	0	0	0
Reactant B (Water)	2000 ms	500 ms	77.5 ms	5000 ms
Reactant B (Water)	60000 ms	0	0	0

Table 3.5. Thickness and GPC data for zinc oxide data for different ALD cycles.

Number of cycles	Thickness nm	GPC (Å/cycle)
5	0.78	1.56
10	1.64	1.64
15	3.08	2.04
20	3.74	1.87
25	4.30	1.75

المنارة للاستشارات
www.manaraa.com

50	8.59	1.71
75	10.78	1.56
100	14.35	1.44
125	17.38	1.43
250	35.63	1.42

The loss of the substrate signals by XPS and the ability to fit the SE data from the planar films to simple models (see above), suggests reasonable, conformal coating of the ZrO_2 particles with ZnO. TEM was next performed on the ZnO-coated ZrO_2 particles. However, the Z-contrast between zirconia and zinc is less than that between zirconia and alumina, which made it difficult to acquire a line scan similar to the one shown in **Figure 3.19**. Nevertheless, TEM/EDS could be performed on specific spots on the particles. For example, **Figure 3.19** shows three spots that were probed on a ZnO-coated ZrO_2 particle. Stronger Zn EDS signals were obtained on the edges of the particle (at Points A and C) than in the middle (Point B) (see EDS results in the Supporting Information), which further confirms growth of ZnO by ALD (see EDS spectra from **Figures 3.20 to 3.22**).

3.6 Equilibration

A final series of experiments were done to evaluate the difference between the alumina thickness outside and inside placed witness shards. The most probable reason for the

المنارة للاستشارات
www.manaraa.com

difference in thickness between inside and outside placed witness shards could be the temperature difference. This difference in temperature occurs as the substrate heating takes places from the bottom (substrate heater is present below the reactor). We performed alumina depositions where the reaction chamber was heated like an oven, such that the temperature was constant throughout the chamber. The chamber was heated to 150 ºC, and the substrate was allowed 30 minutes to equilibrate, to make sure temperature was constant throughout the chamber.

Then, an ALD run of 100 cycles was performed using three different recipes (standard, VRM and static dosing recipes). These three recipes were used to eliminate any dependence of alumina deposition and mode of dosing. Alumina thickness and GPC were essentially similar on both the outside and inside placed silicon shards. This again strengthens our hypothesis that the quality of alumina films was similar, irrespective of the placement of silicon shards. This was essential to prove that the presence of the lid did not affect the process of alumina films deposition.

Table 3.6. A standard recipe for depositing zinc oxide showing the process parameters. They were used for the initial depositing experiments on silicon shards to obtain a wide range of zinc oxide films.

	Step 1 (Dose Time)	**Step 3 (Purge Time)**
Source 1 (Water)	15.5 ms	15000 ms
Source 3 (DEZ)	21.0 ms	15000 ms

www.manaraa.com

Table 3.7. Representative process parameters for powder deposition experiments for a variable residence mode (VRM) recipe. The precursors used for this deposition were TMA and water, with pressure ranging from 1.2 torr to 1.8 torr. RCN represents the number of ALD cycles in a recipe.

	Step 1 (Throttle lead)	**Step 2 (dose)**	**Step 3 (Exposure)**	**Step 3 (Purge Time)**
Src 1 (Water)	10	15.5 ms	2000	15000
Src 3 (TMA)	10	21.0 ms	3000	15000
RCN (cycles)	1	1	0	0
Throttle Pressure	8 torr	1.2 torr	8 torr	1.2 torr

Table 3.8. Film thickness and GPC for 100 cycle ALD run using different recipes. The chamber was heated at 150 ^{o}C as an oven, such that the temperature was essentially the same at all places inside the chamber.

	Outside Witness Shard	**Inside Witness Shard**	**Outside Witness Shard (Repeat)**	**Inside Witness Shard (Repeat)**
Static Dosing Recipe	10.72 nm	10.64 nm	11.05 nm	11.02 nm

المنارة للاستشارات
www.manaraa.com

Variable Residence Recipe	9.14 nm	8.96 nm	9.01 nm	8.92 nm
Standard Recipe	7.75 nm	7.74 nm	7.82 nm	7.81 nm

3.7. Conclusions

We have demonstrated thermal ALD of alumina and ZnO on zirconia particles using a specially designed holder that does not require particle agitation. Out of the two different frits and combinations of meshes were investigated, one of the frits and 2 – 4 meshes allowed good conductance of the reagents and growth of high-quality films at reasonable rates. By SE, XPS, and TEM/EDS, the ALD depositions appear to be regular, uniform, and conformal.

www.manaraa.com

3.8. Figures

BILL OF MATERIALS

NO.	PART NUMBER	DRAWING NUMBER	DESCRIPTION	QTY	U/M
01	D-P0055320	P0055320	POWDER CARRIER, ALD SS	1	EA
02	D-P0055344	P0055344	POWDER HOLDER TOP COVER (0.5 MEDIA GRADE)	1	EA
03	HBHU0440-01364P0		SCREW,BUTTON HEAD CAP,SS 4-40 X 1/8",AG PLATED	4	EA

SECTION A-A

NOTES:

1. ALL DIMENSIONS ARE IN INCHES, REFER TO TABLE 1 FOR STANDARD TOLERANCING INFORMATION.

POWDER HOLDER, ALD 150MM

A0055345

Figure 3.1. Engineering design of the particle holder obtained from Kurt J. Lesker.

www.manaraa.com

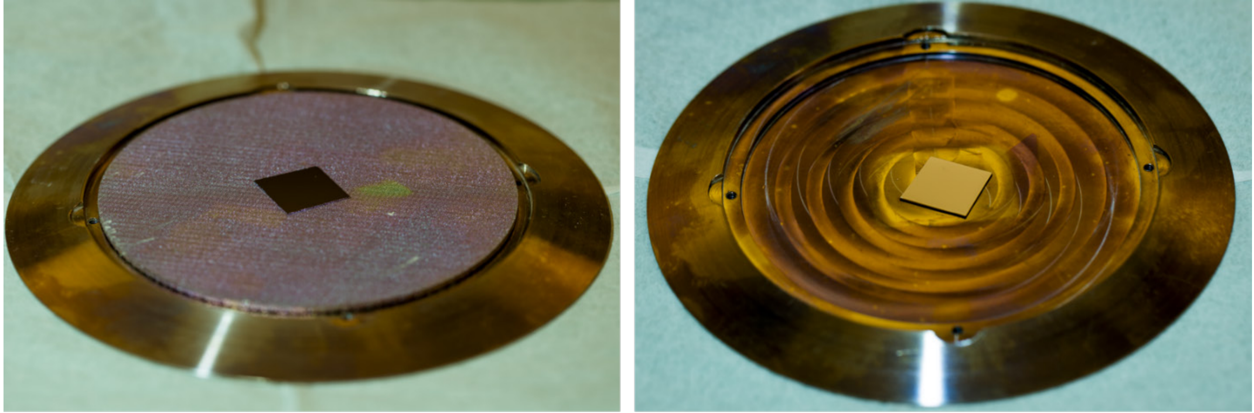

Figure 3.2. Left. Holder covered with a frit with a silicon witness shard on top of it. Right. Holder without cover with a witness shard in it.

المنارة للاستشارات
www.manaraa.com

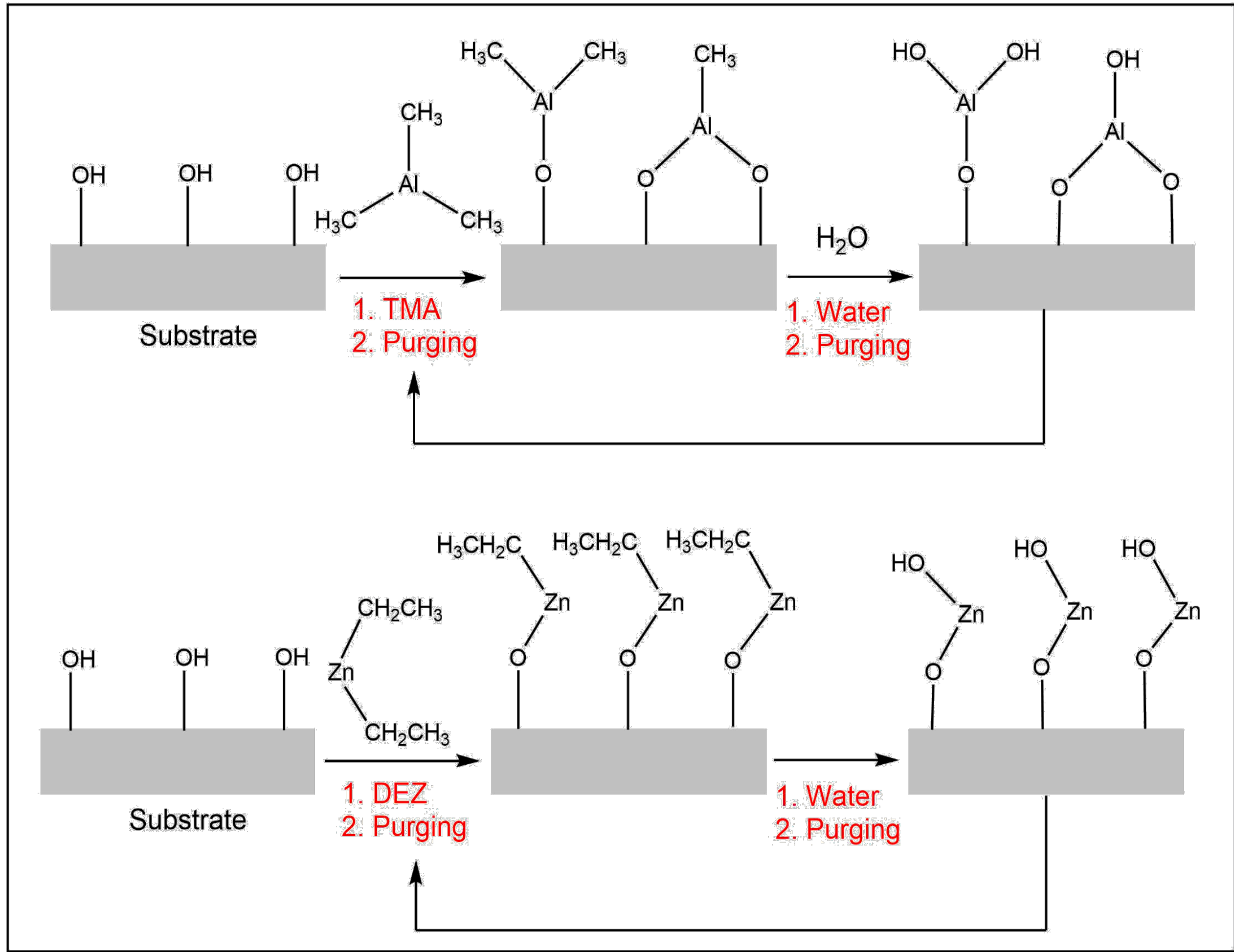

Figure 3.3. Representation of the chemistry in the deposition of alumina from trimethylaluminum (TMA) and water (top), and zinc oxide from diethylzinc (DEZ) and water (bottom).

المنارة للاستشارات
www.manaraa.com

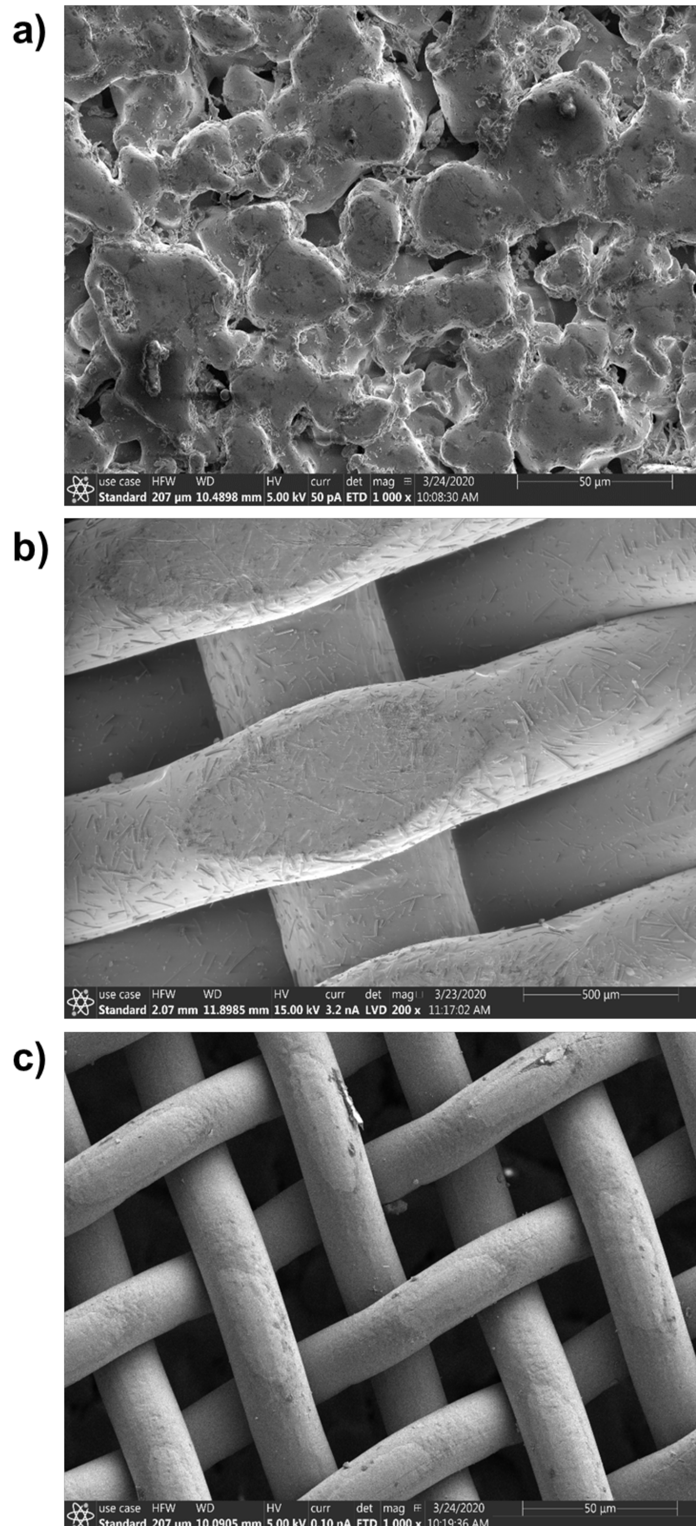

Figure 3.4. SEM images of the frits and mesh used as porous covers for the particle holder developed in this work. (a) First porous frit studied. (b) Second porous frit studied. (c) '635' mesh.

المنارة للاستشارات
www.manaraa.com

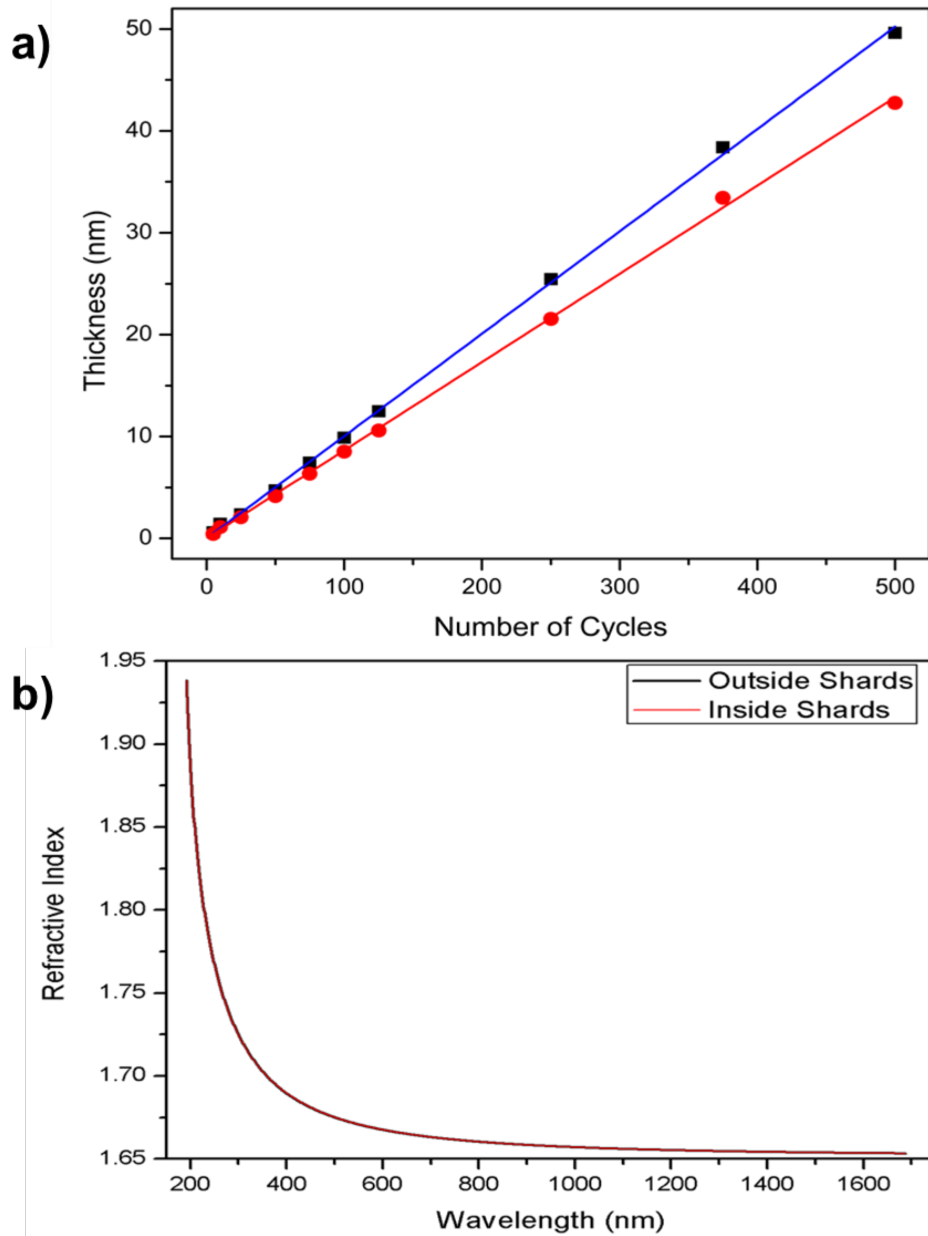

Figure 3.5. (a) Film thicknesses, t, for 5 - 500 cycles of ALD alumina on witness shards placed inside and outside the second frit (see **Figure 3.5b**). The linear fits (t = mx + b) to this data are $t_{outside} = 0.100x + 0.037$ with $R^2 = 0.99948$ (top line), and $t_{inside} = 0.087x - 0.033$ with $R^2 = 0.99928$ (bottom line). We do *not* claim that all of the digits in these numbers are significant. (**b)** Refractive indices obtained by SE from multi-sample analyses (MSA) of the data in **Figure 3.5a**, where each MSA used all the data in the corresponding data set.

المنارة للاستشارات
www.manaraa.com

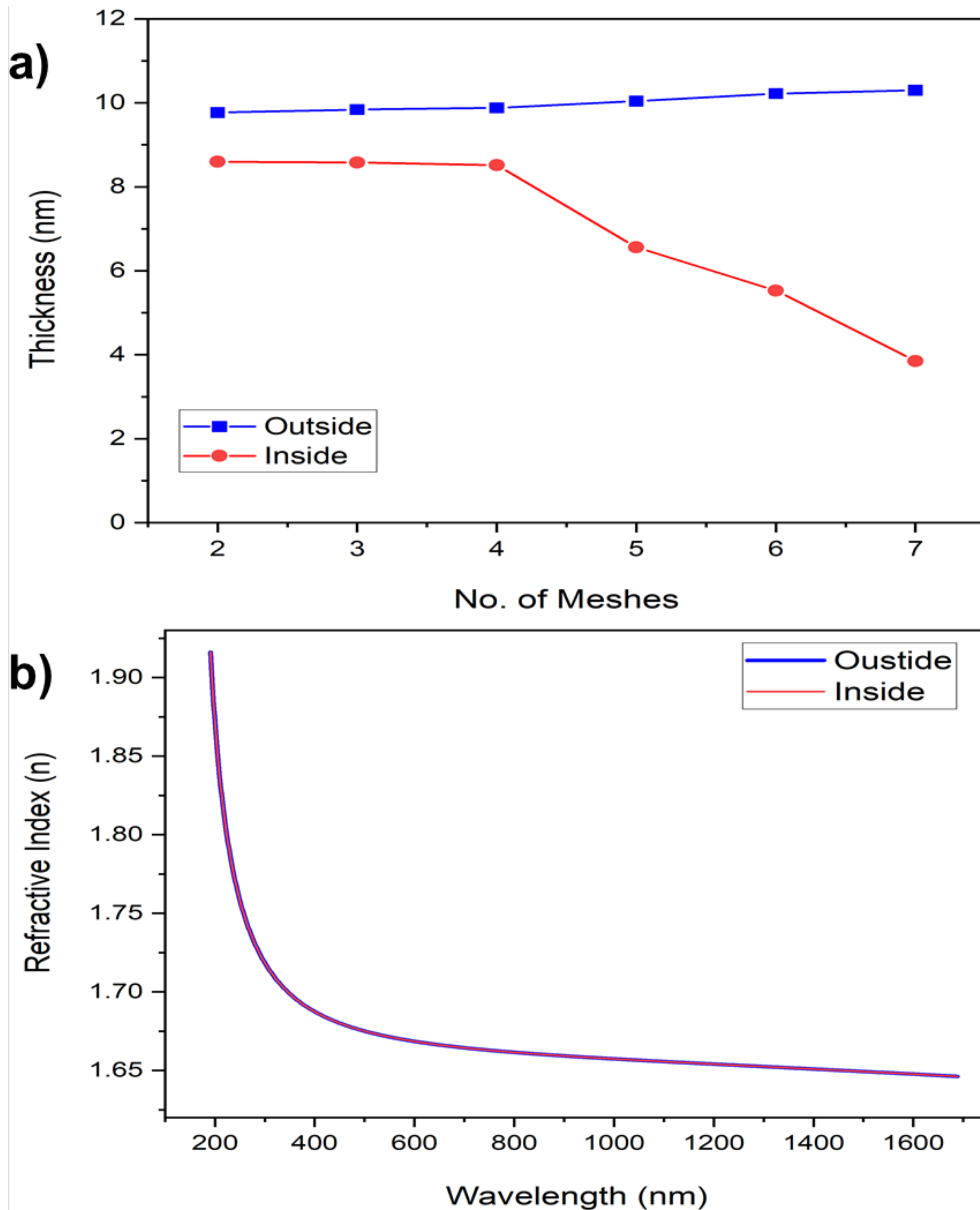

Figure 3.6. (a) Thicknesses of alumina films created via 100 ALD cycles as measured on silicon shards placed inside and outside the particle holder, where the holder was covered with 2 – 7 '635' meshes. (b) Refractive indices obtained by SE from MSAs of the alumina films deposited inside and outside the holder covered with 2 – 4 '635' meshes. That is, each MSA here used the SE data from 3 samples.

المنارة للاستشارات
www.manaraa.com

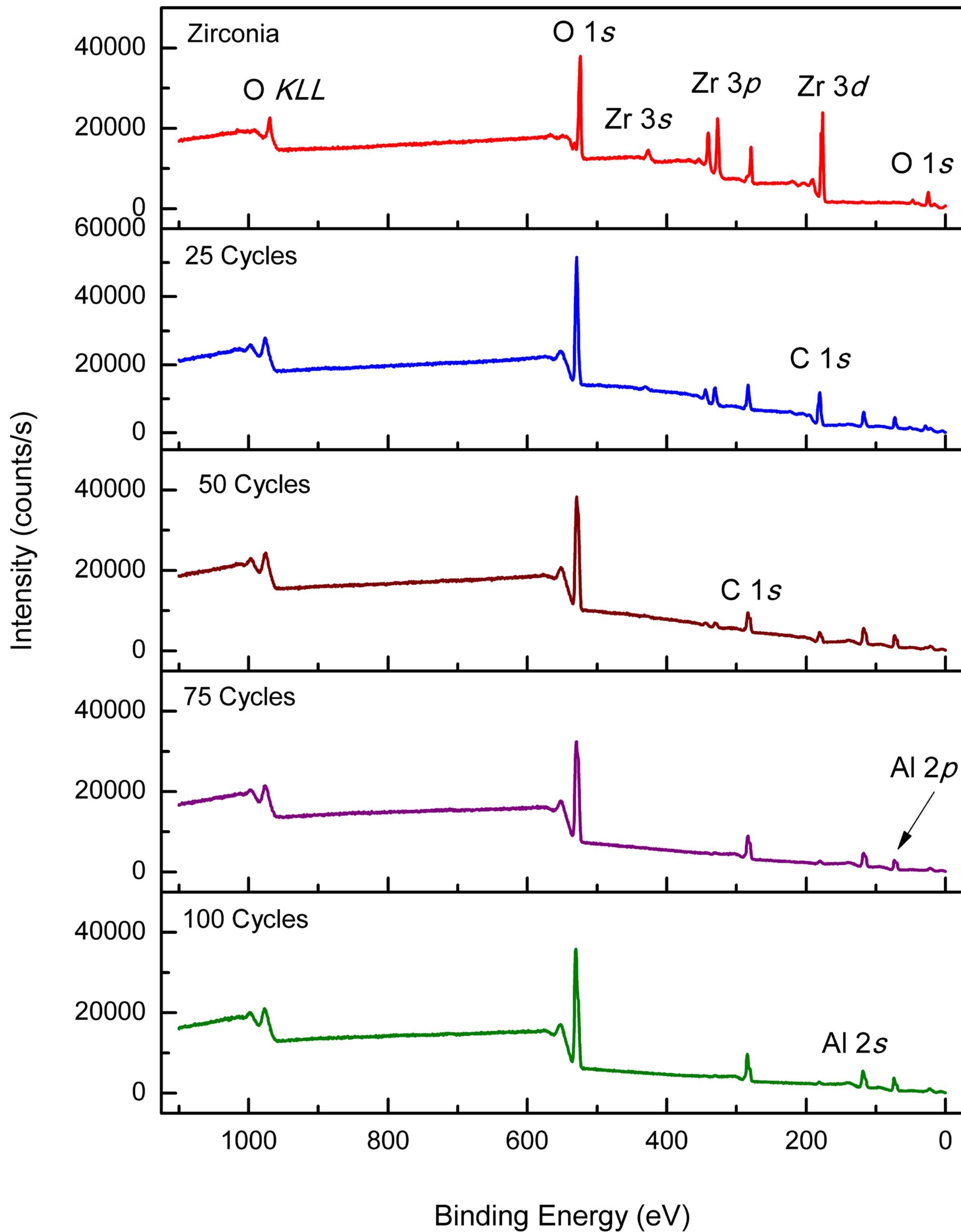

Figure 3.7. Entire XPS survey spectra for zirconia particles coated with 100 ALD cycles.

المنارة للاستشارات
www.manaraa.com

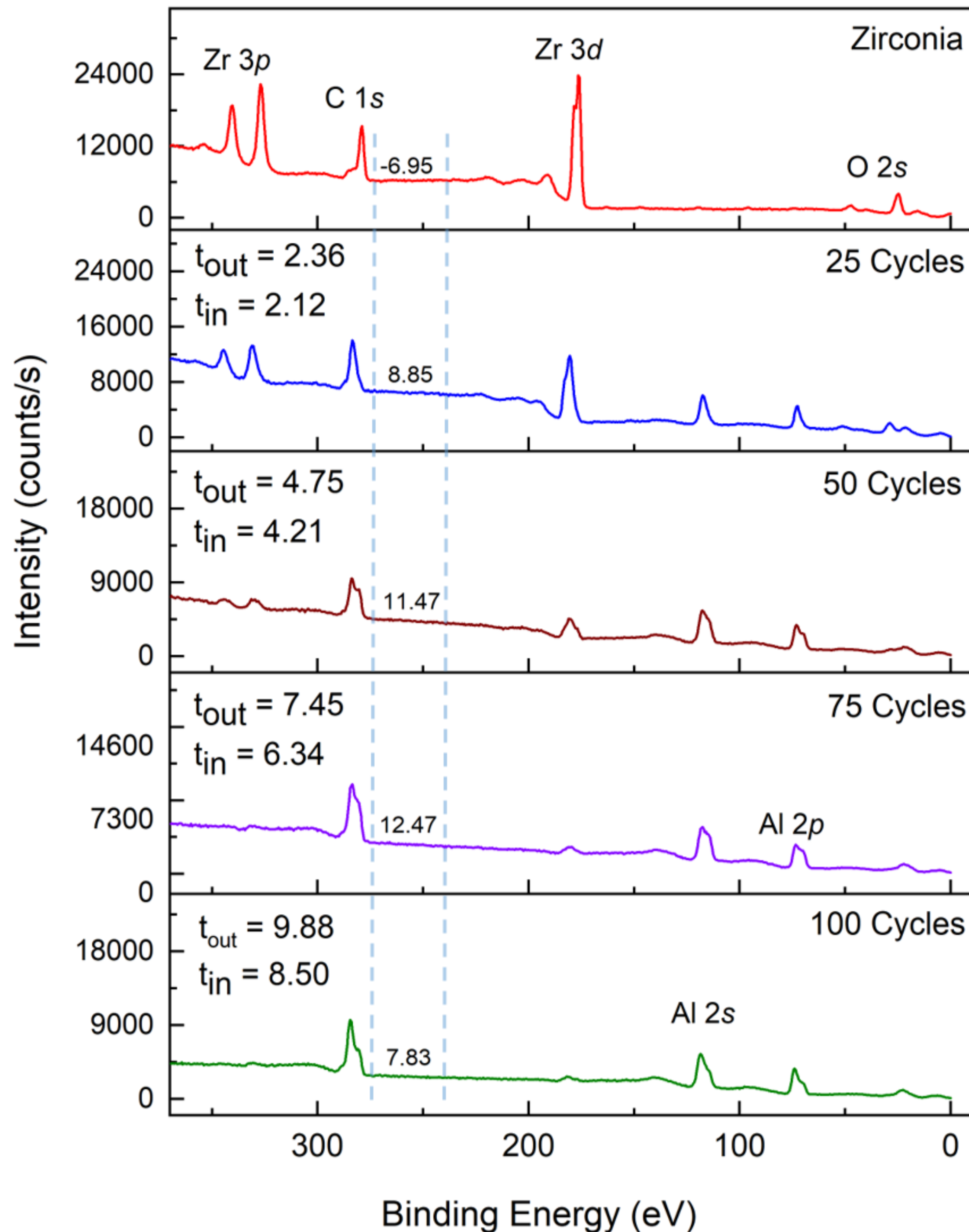

Figure 3.8. Abbreviated XPS survey spectra for alumina deposited on zirconia particles via 0, 25, 50, 75, and 100 ALD cycles. The Zr signals decrease as the number of ALD cycles increases. The negative slopes of the baselines from 240 – 270 eV in counts/eV are given between the dashed lines. The thicknesses of the alumina films measured by SE on silicon witness shards inside (t_{in}) and outside (t_{out}) the particle holder are also listed for each sample.

www.manaraa.com

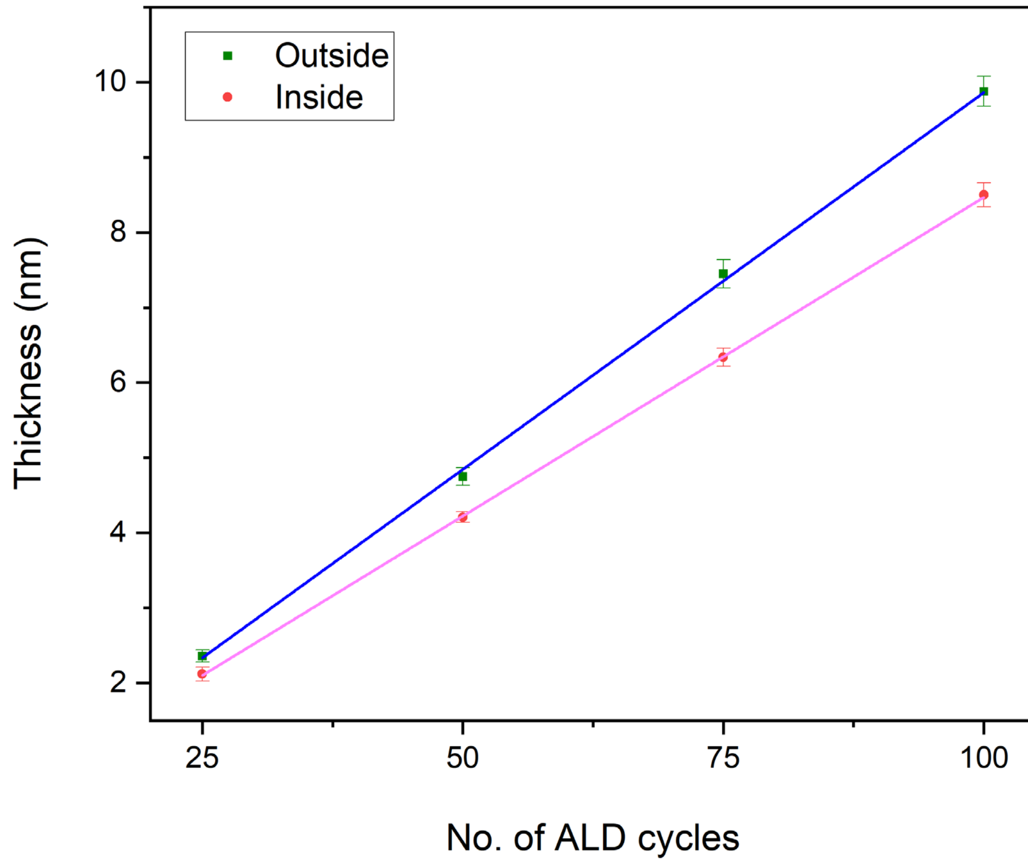

Figure 3.9. Same SE data as in Figure 6 in the main paper, except error bars are provided for the data points. The values of these data points and the error bars were obtained from the averages and standard deviations, respectively, of three measurements on each sample.

المنارة للاستشارات
www.manaraa.com

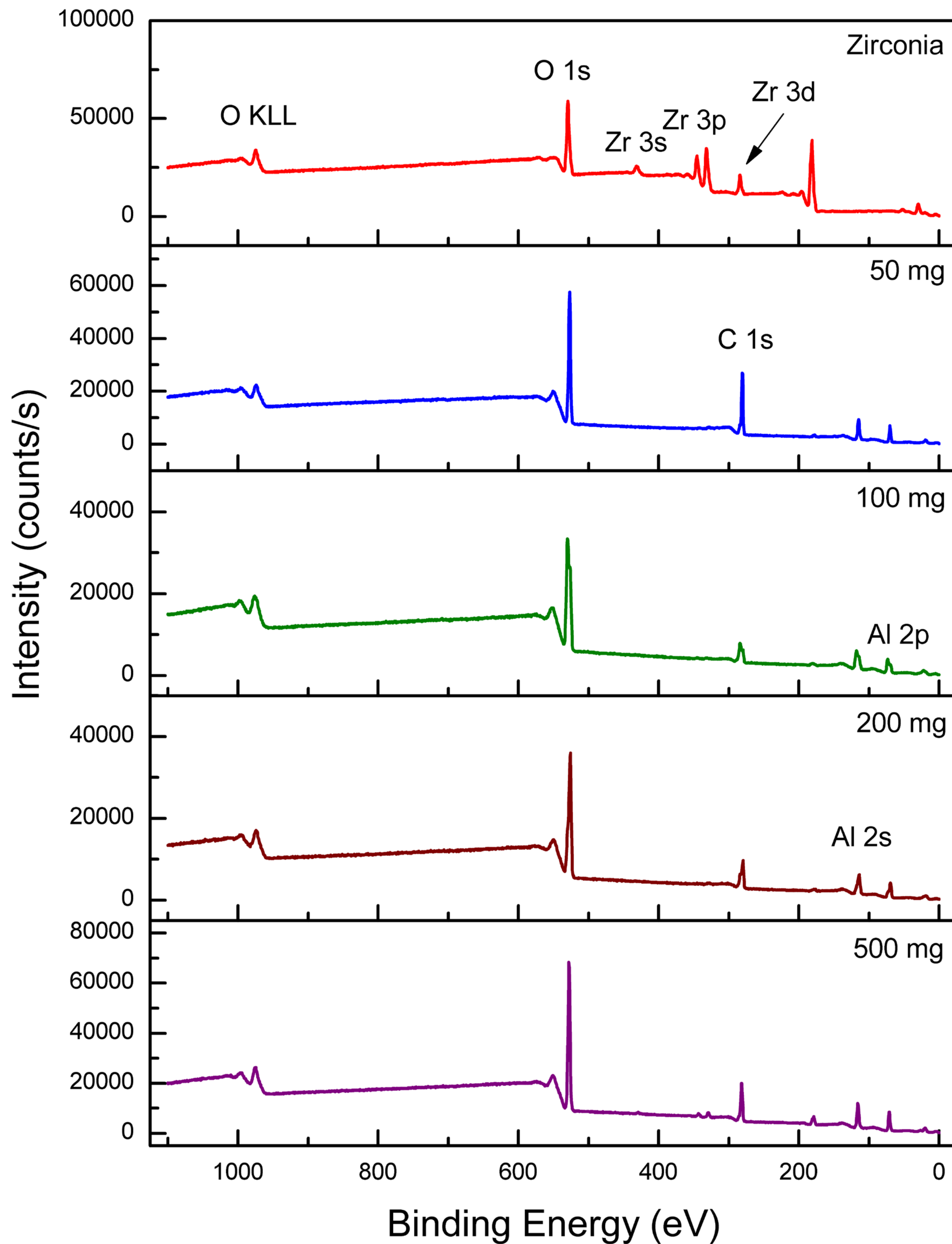

Figure 3.10. XPS survey spectra of alumina-coated zirconia particles, where 50 – 500 mg of particles were coated with 100 ALD cycles of TMA and water.

المنارة للاستشارات
www.manaraa.com

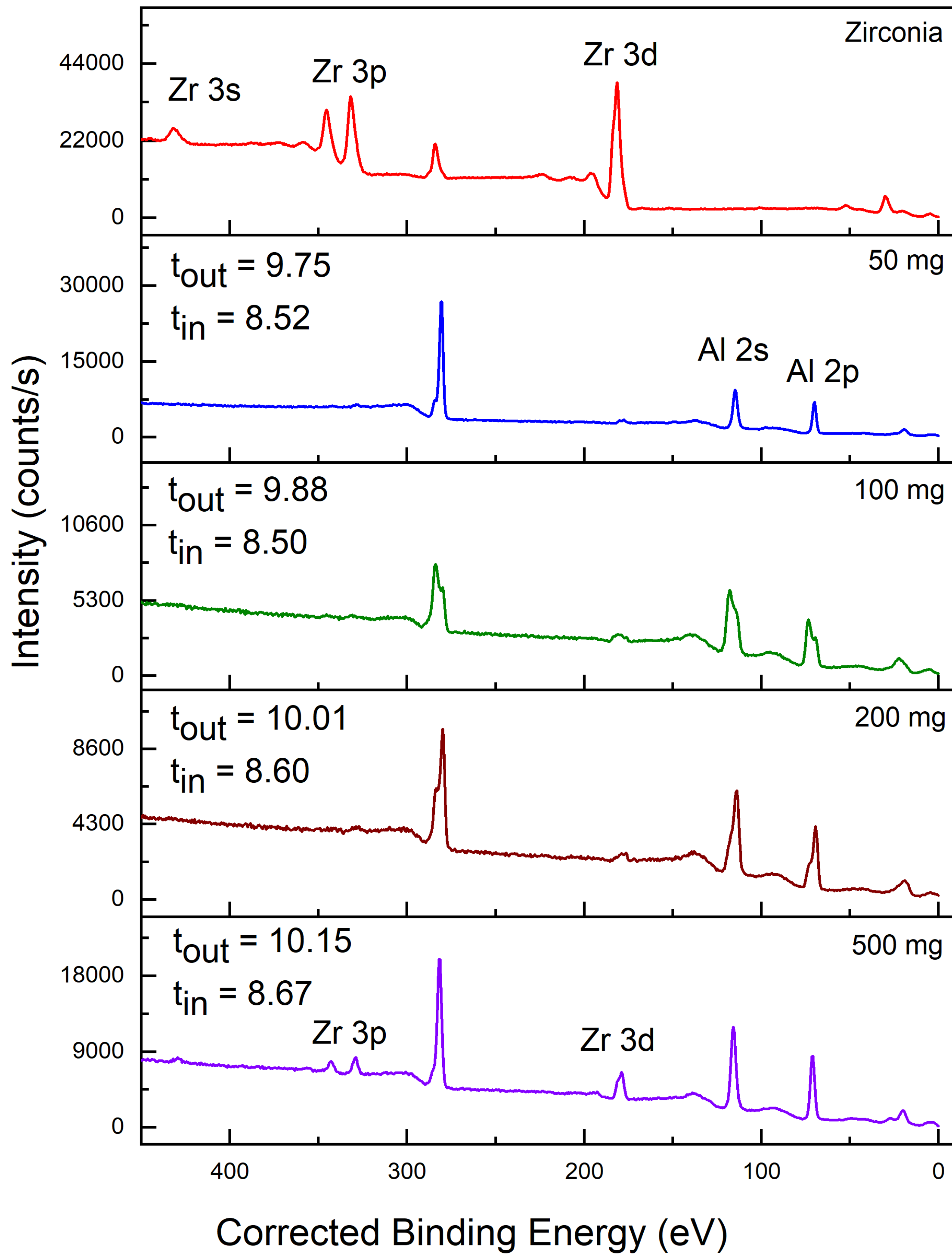

Figure 3.11. Same XPS spectra as in Supporting Information **Figure 3.11**, except over a shorter energy range, and the thicknesses of the witness samples inside and outside the chamber are given.

www.manaraa.com

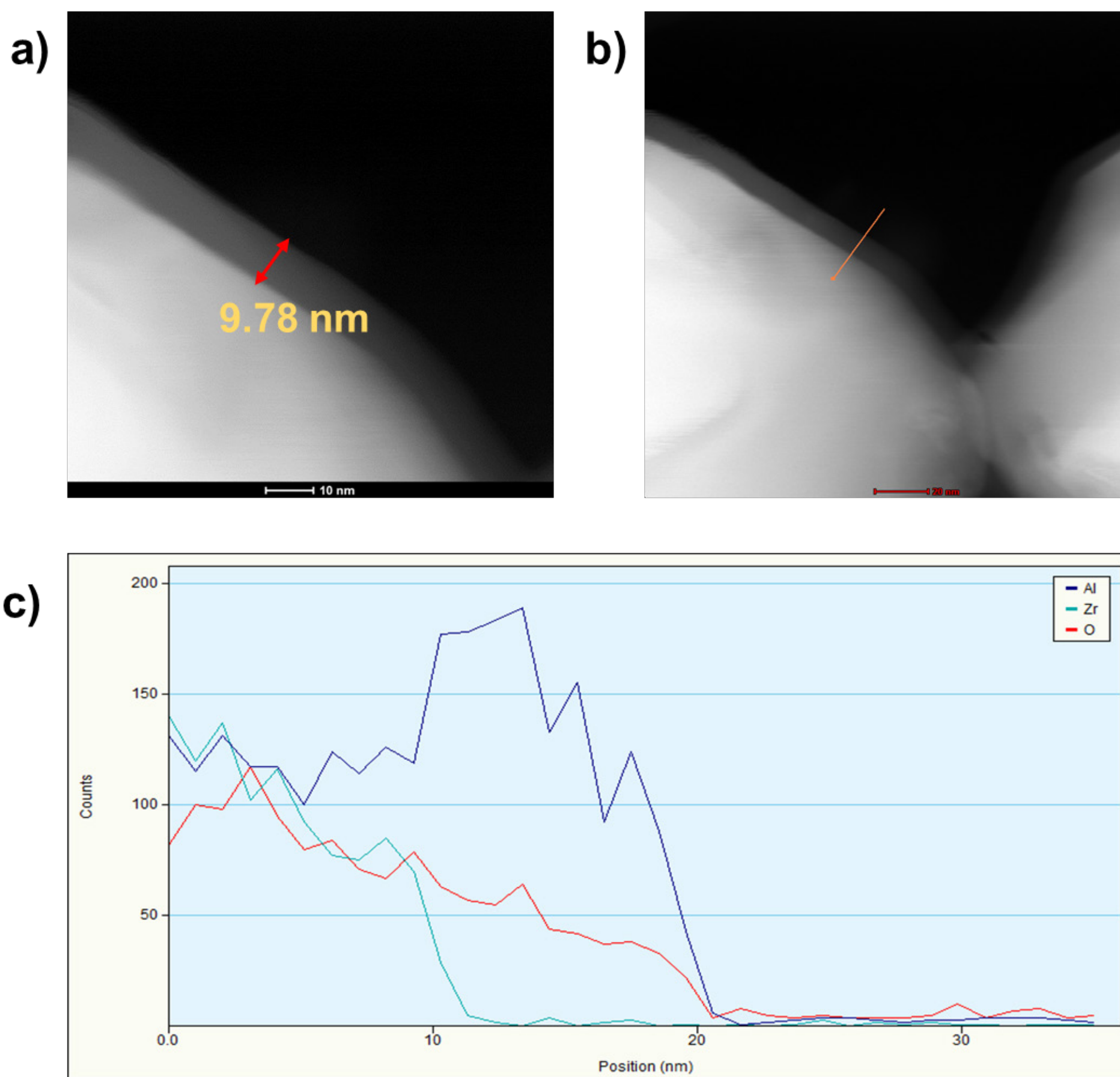

Figure 3.12. (a) and (b) TEM images of zirconia particles coated with 100 ALD cycles of alumina showing (a) a thickness measurement of the alumina film, and (b) the path of a line spectrum (35 data points with a dwell time of 3 s). (c) EDS spectra of Al, Zr, and O from the line spectrum in (b).

www.manaraa.com

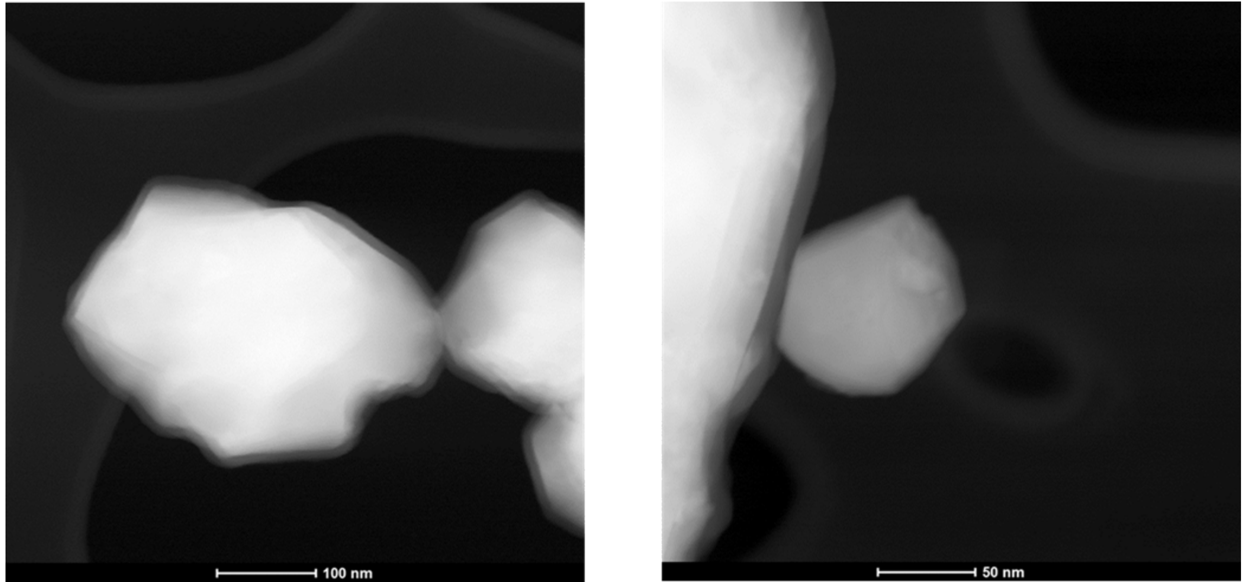

Figure 3.13. a) TEM images of the coated zirconia particles showing uniformity of thin alumina films surrounding the particles. These images show the thin film of alumina over the zirconia particles, which is possible because of the Z-contrast between zirconia (substrate) and alumina oxide (coating). Note that alumina is lighter than zirconia in these images.

المنارة للاستشارات
www.manaraa.com

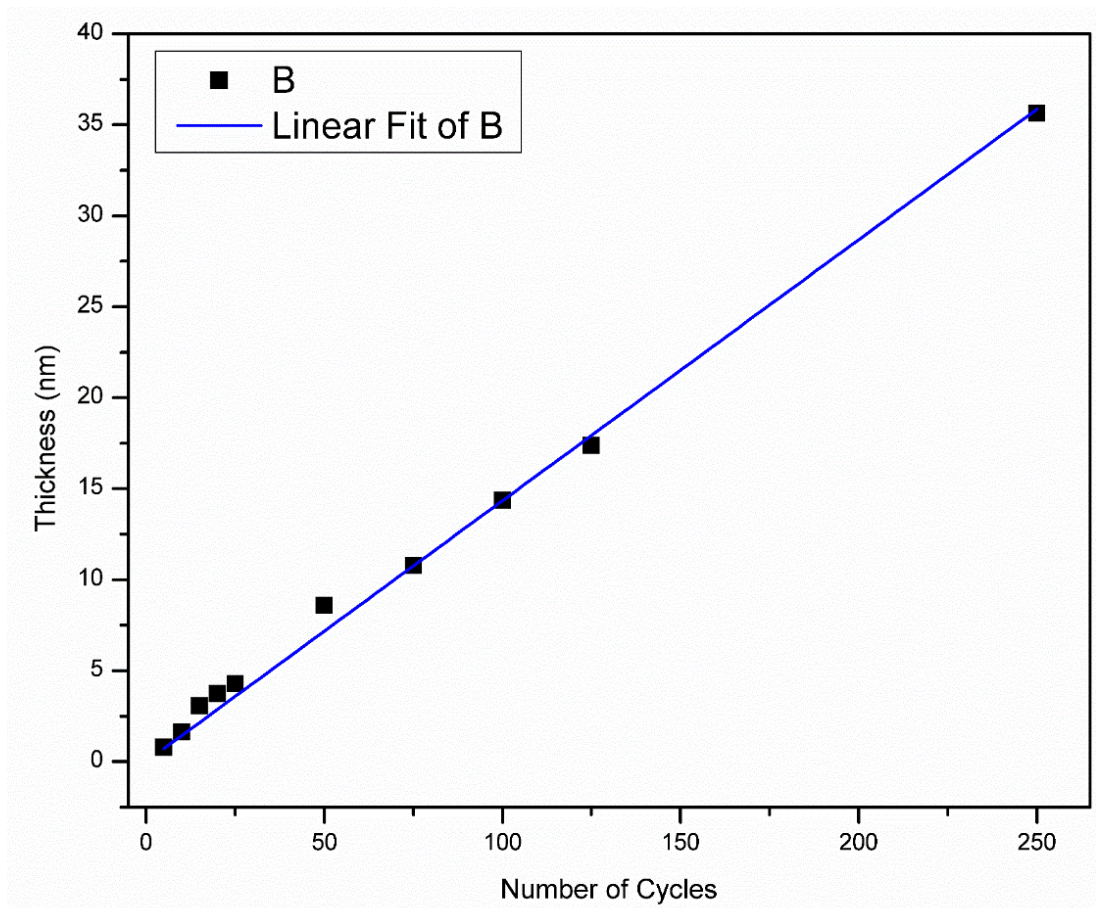

Figure 3.14. Thickness and GPC data for zinc oxide data for different ALD cycles. ALD cycles were increased from 5 to 250 sequentially, such that film thickness ranged from 1 nm to 35 nm.

المنارة للاستشارات
www.manaraa.com

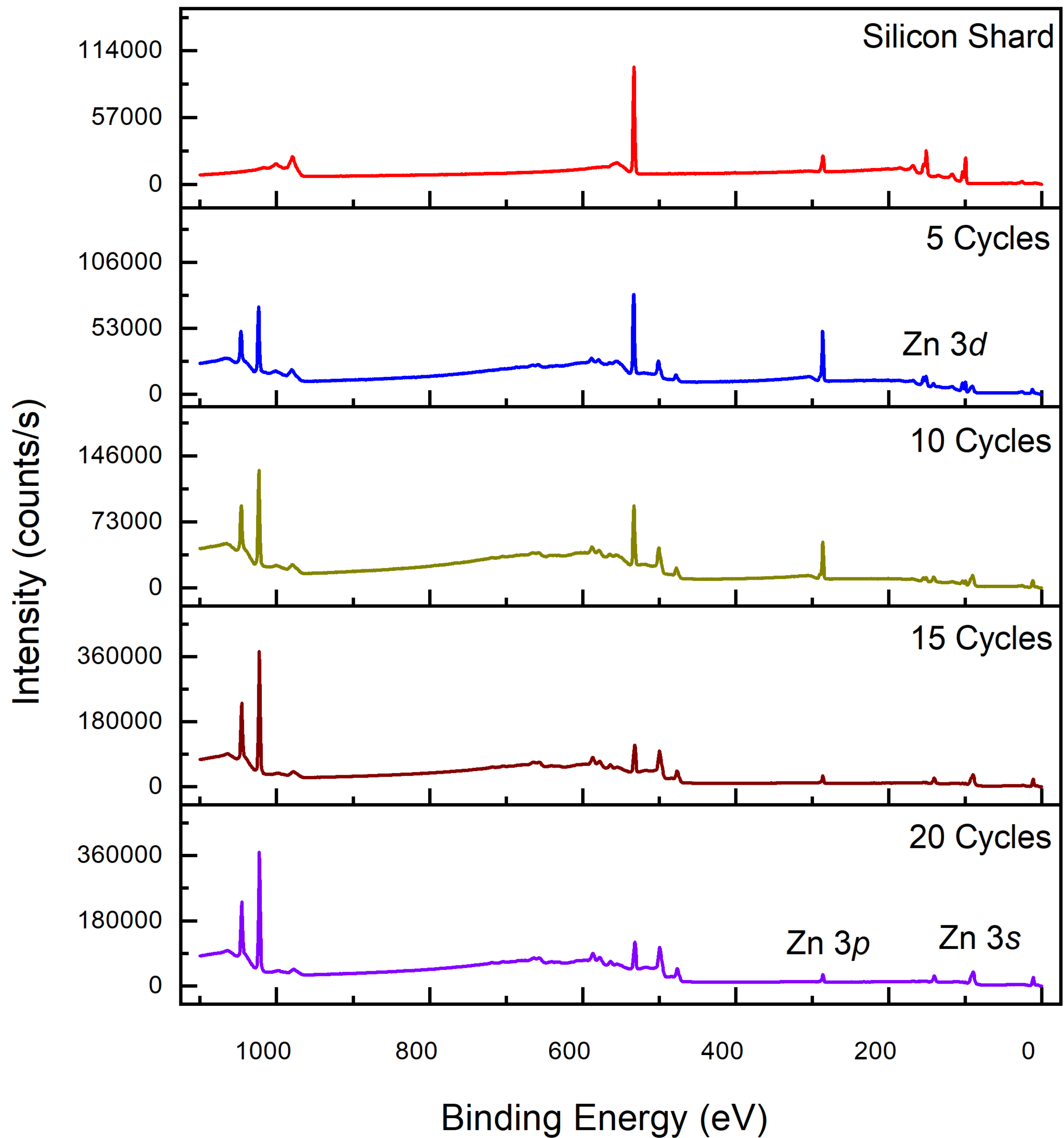

Figure 3.15. XPS results of zinc oxide deposition on flat surfaces using different number of ALD cycles. Dose time for DEZ and water was 21.0 ms and 15.5 ms, purge times for both precursors was 15 seconds. Deposition temperature was 200 ºC and equilibration time was 10 minutes.

www.manaraa.com

Figure 3.16. XPS results (210- 0 eV) of zinc oxide deposition on flat surfaces using different number of ALD cycles. Dose time for DEZ and water was 21.0 ms and 15.5 ms, purge times for both precursors was 15 seconds. Deposition temperature was 200 ^{o}C and equilibration time was 10 minutes.

المنارة للاستشارات
www.manaraa.com

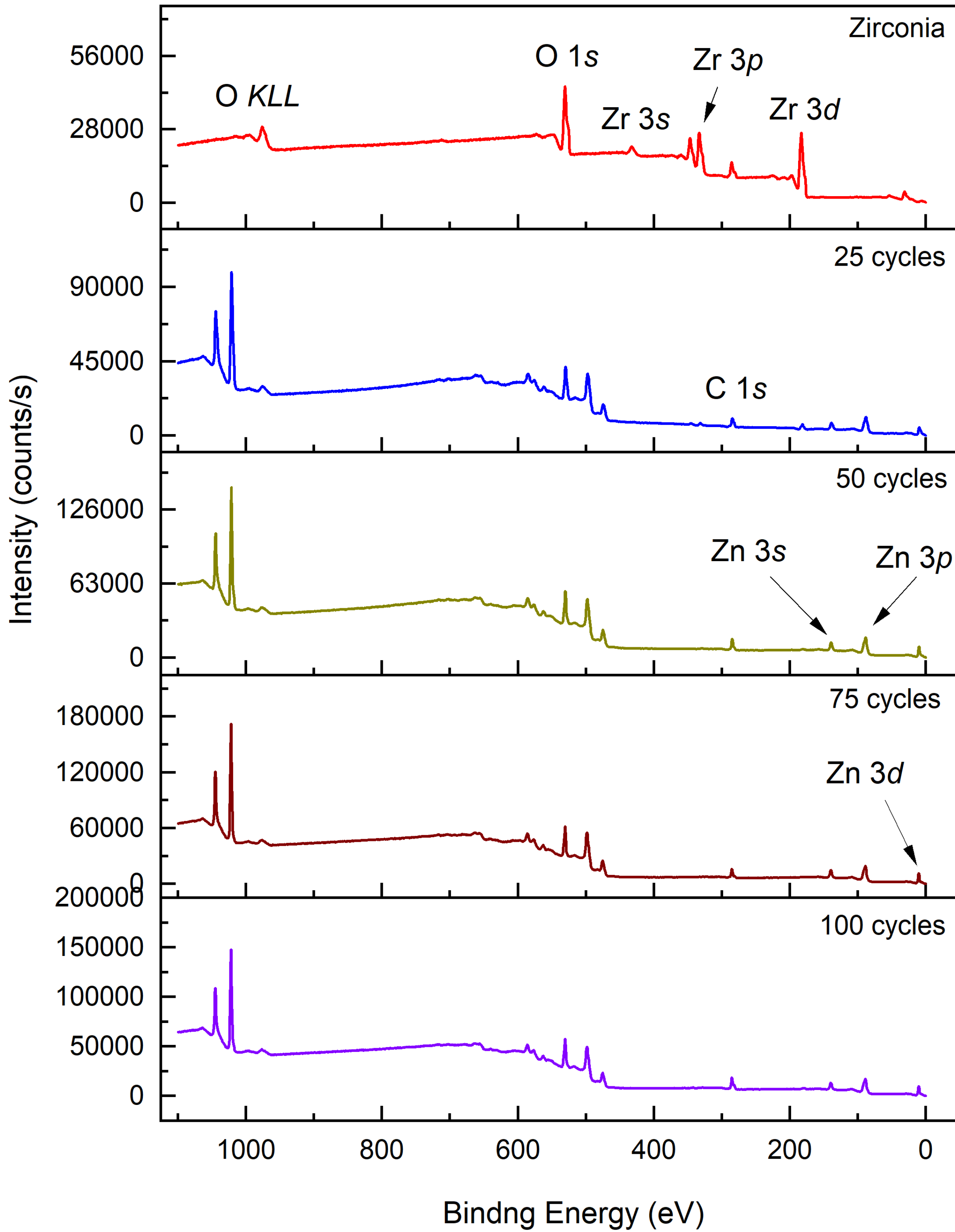

Figure 3.17. Entire XPS survey spectra for coated zirconia particles after 100 ALD cycles.

المنارة للاستشارات
www.manaraa.com

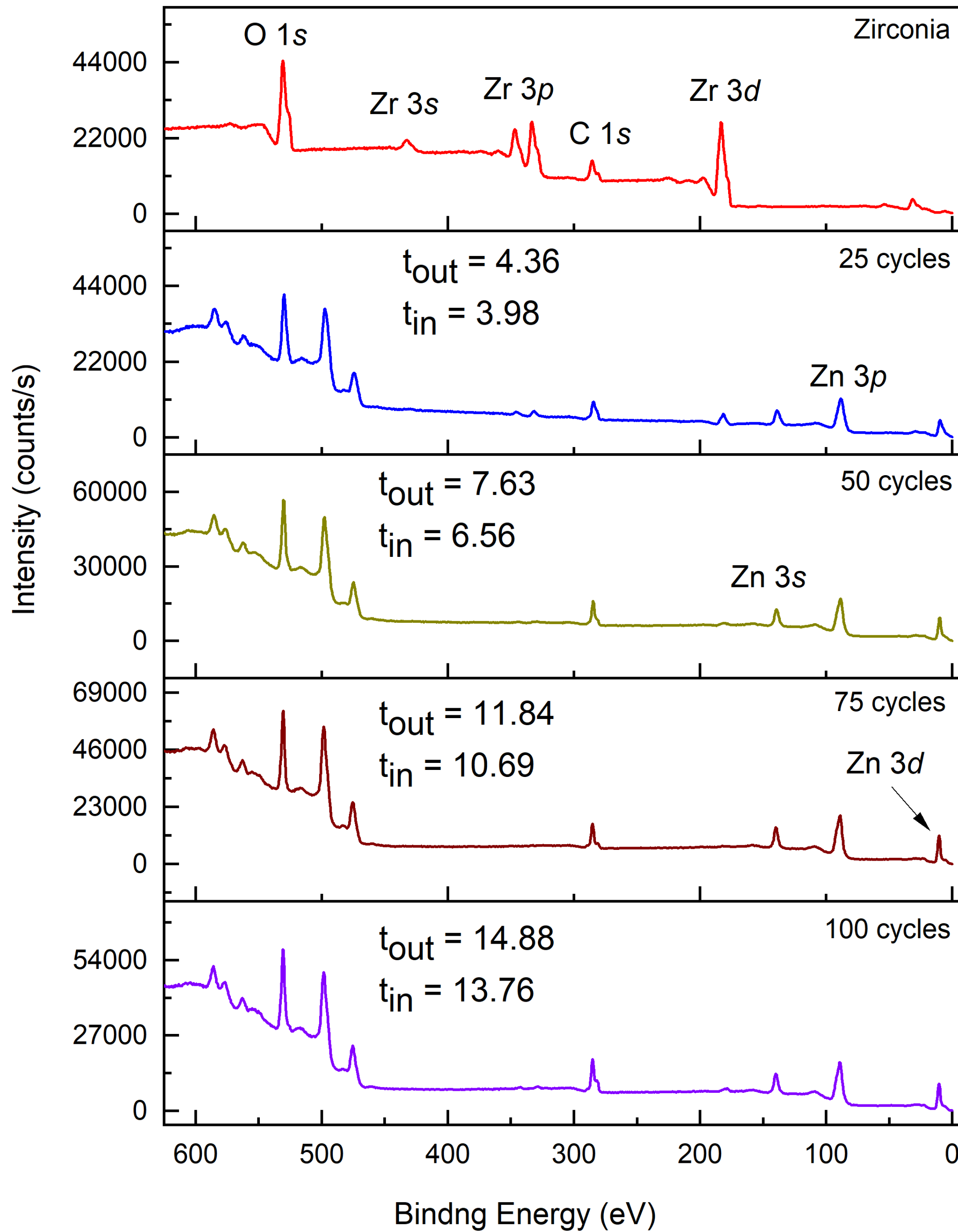

Figure 3.18. XPS survey spectra from 0 – 625 eV of ZrO_2 particles coated with ZnO by ALD as a function of the number of ALD cycles. The thicknesses of the zinc oxide films measured by SE on silicon witness shards inside (t_{in}) and outside (t_{out}) the particle holder are also listed for each run.

المنارة للاستشارات
www.manaraa.com

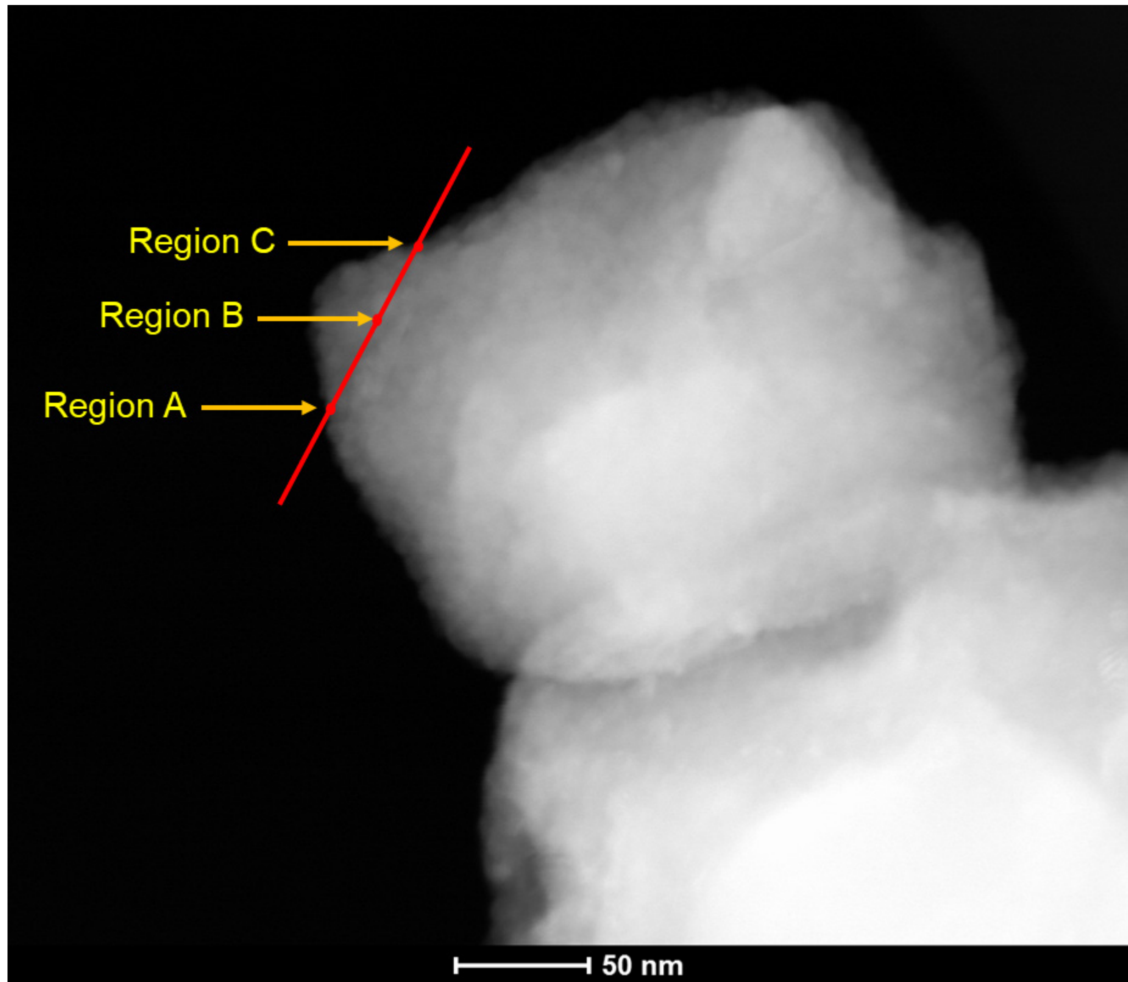

Figure 3.19. TEM image of zinc oxide coated particle showing the line spectra.

المنارة للاستشارات
www.manaraa.com

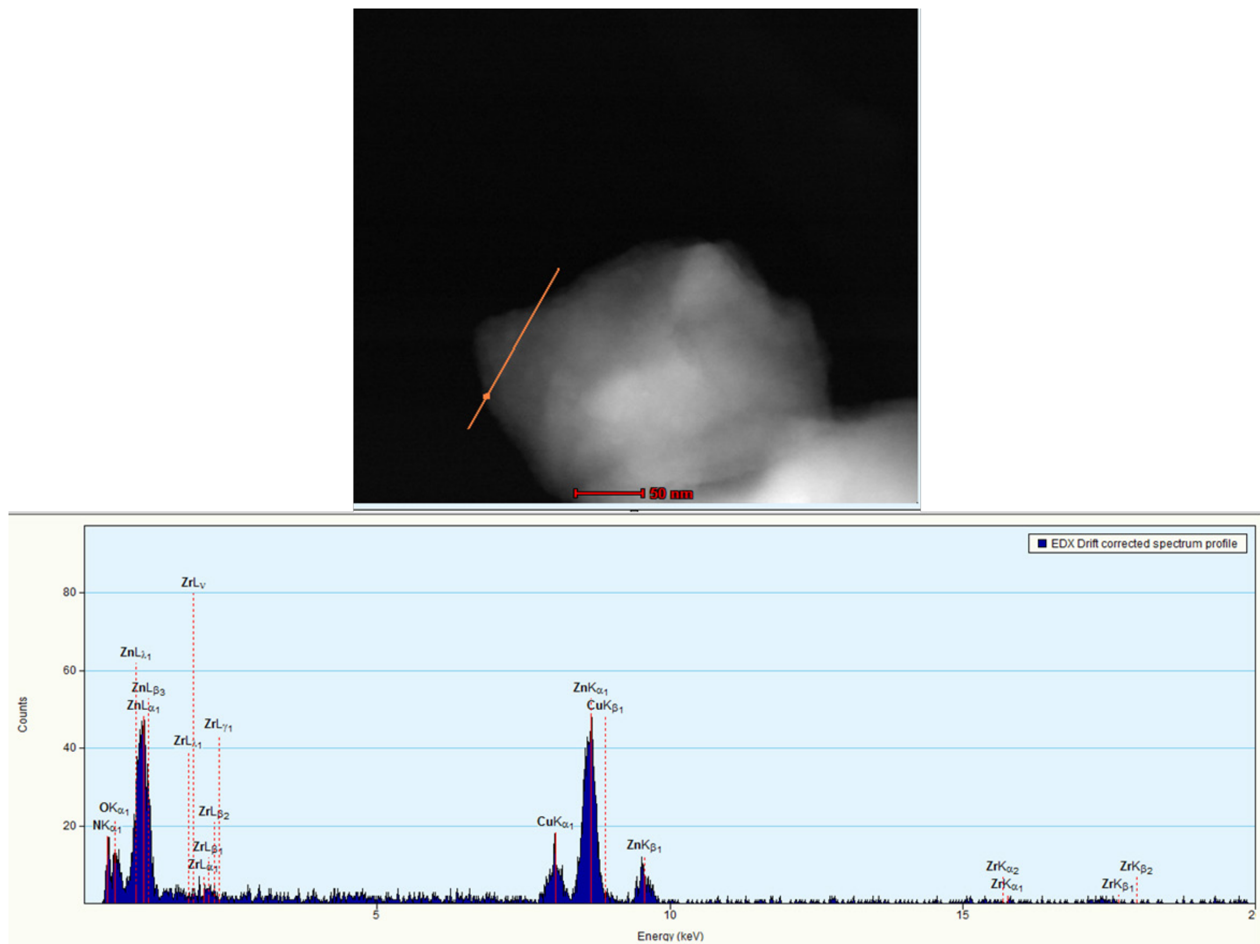

Figure 3.20. EDS spectrum (bottom) for the data point indicted as an orange dot in the image (top) of a zirconia particle coated by ALD with 100 cycles of DEZ and water to form ZnO. Copper peaks are present due to the copper grid on which the particles were mounted. Minor oxygen and nitrogen peaks are present due to small amounts of air in the chamber.

www.manaraa.com

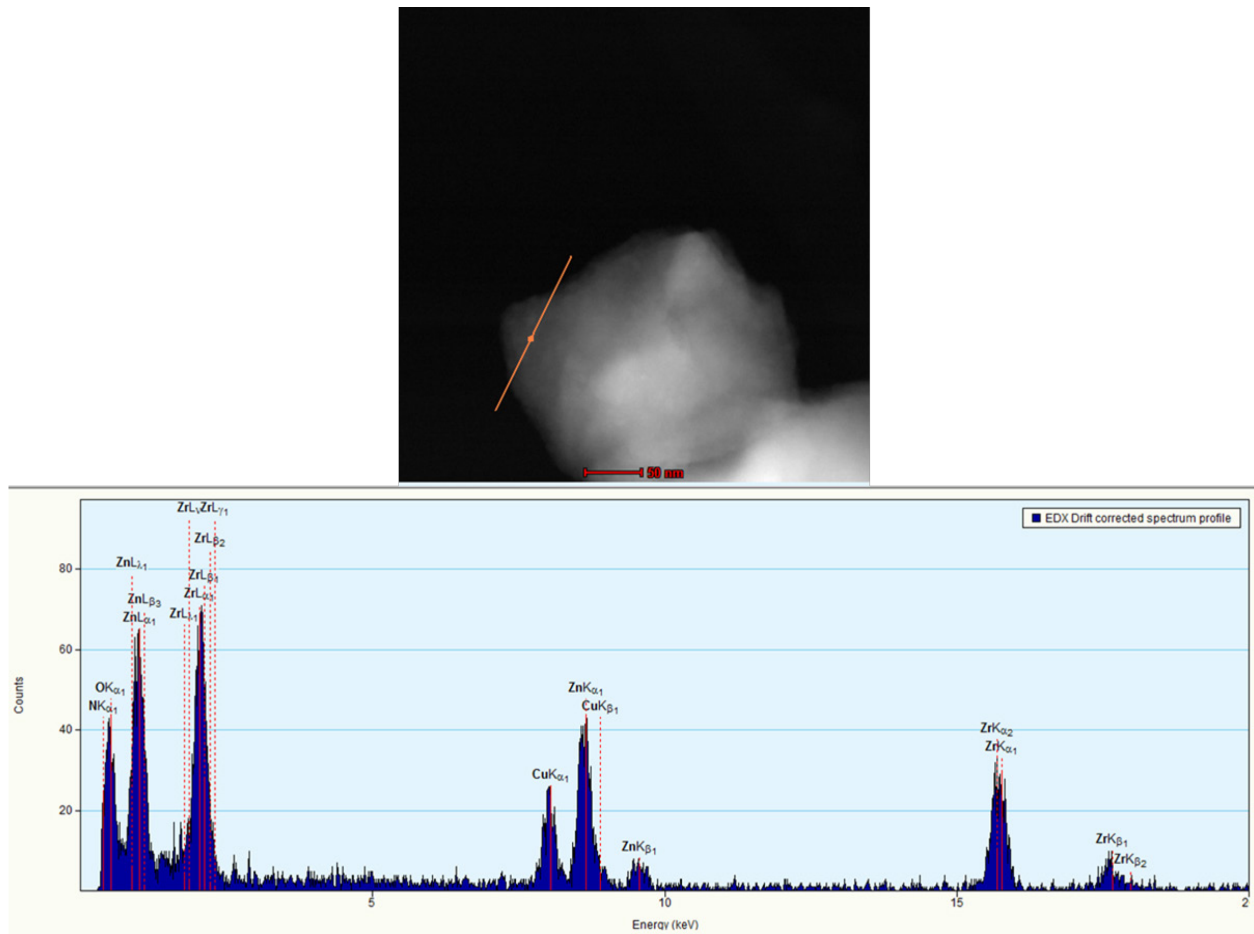

Figure 3.21. EDS spectrum (bottom) for the data point indicted as an orange dot in the image (top) of a zirconia particle coated by ALD with 100 cycles of DEZ and water to form ZnO. Copper peaks are present due to the copper grid on which the particles were mounted. Minor oxygen and nitrogen peaks are present due to small amounts of air in the chamber.

المنارة للاستشارات
www.manaraa.com

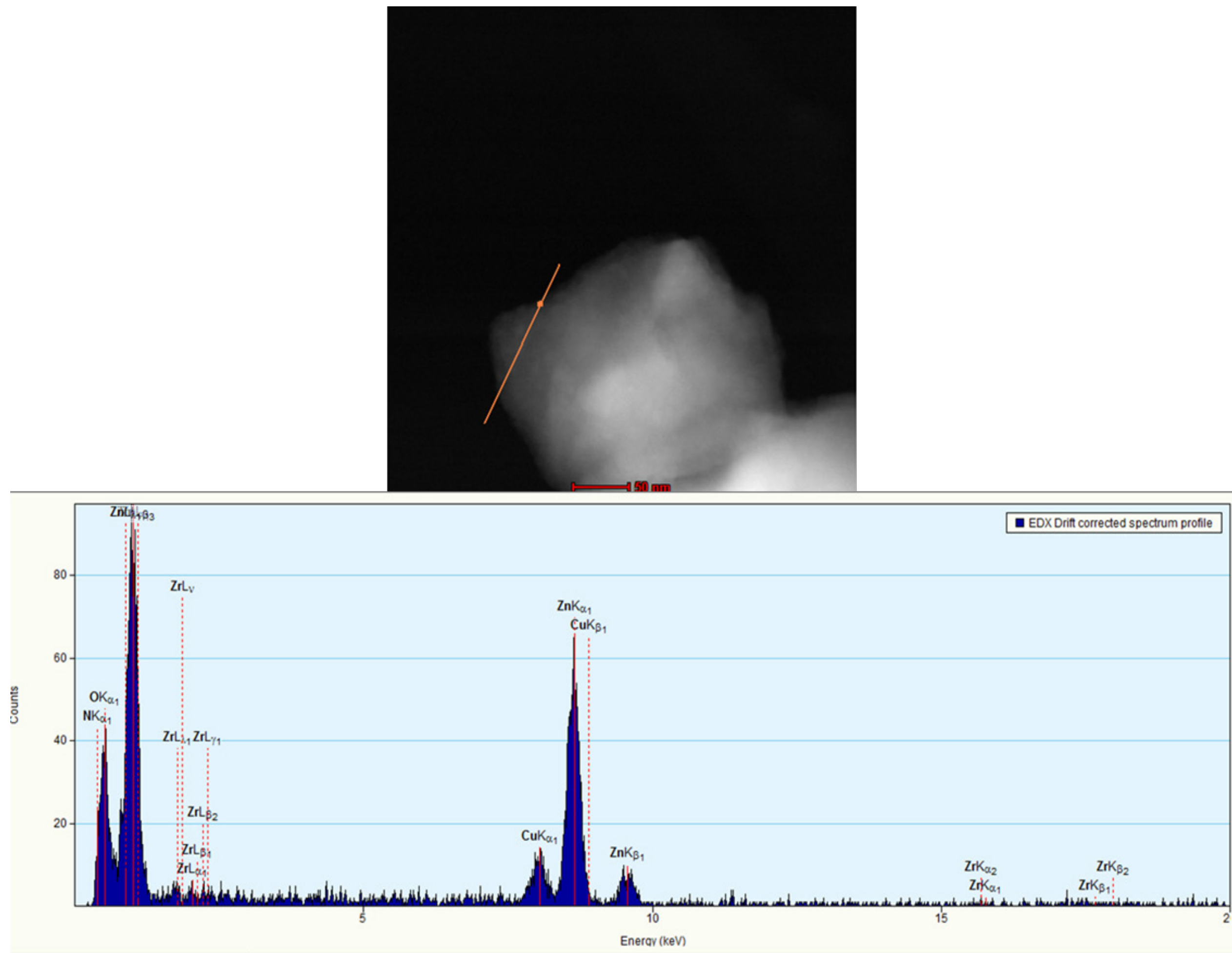

Figure 3.22. EDS spectrum (bottom) for the data point indicted as an orange dot in the image (top) of a zirconia particle coated by ALD with 100 cycles of DEZ and water to form ZnO. Copper peaks are present due to the copper grid on which the particles were mounted. Minor oxygen and nitrogen peaks are present due to small amounts of air in the chamber.

www.manaraa.com

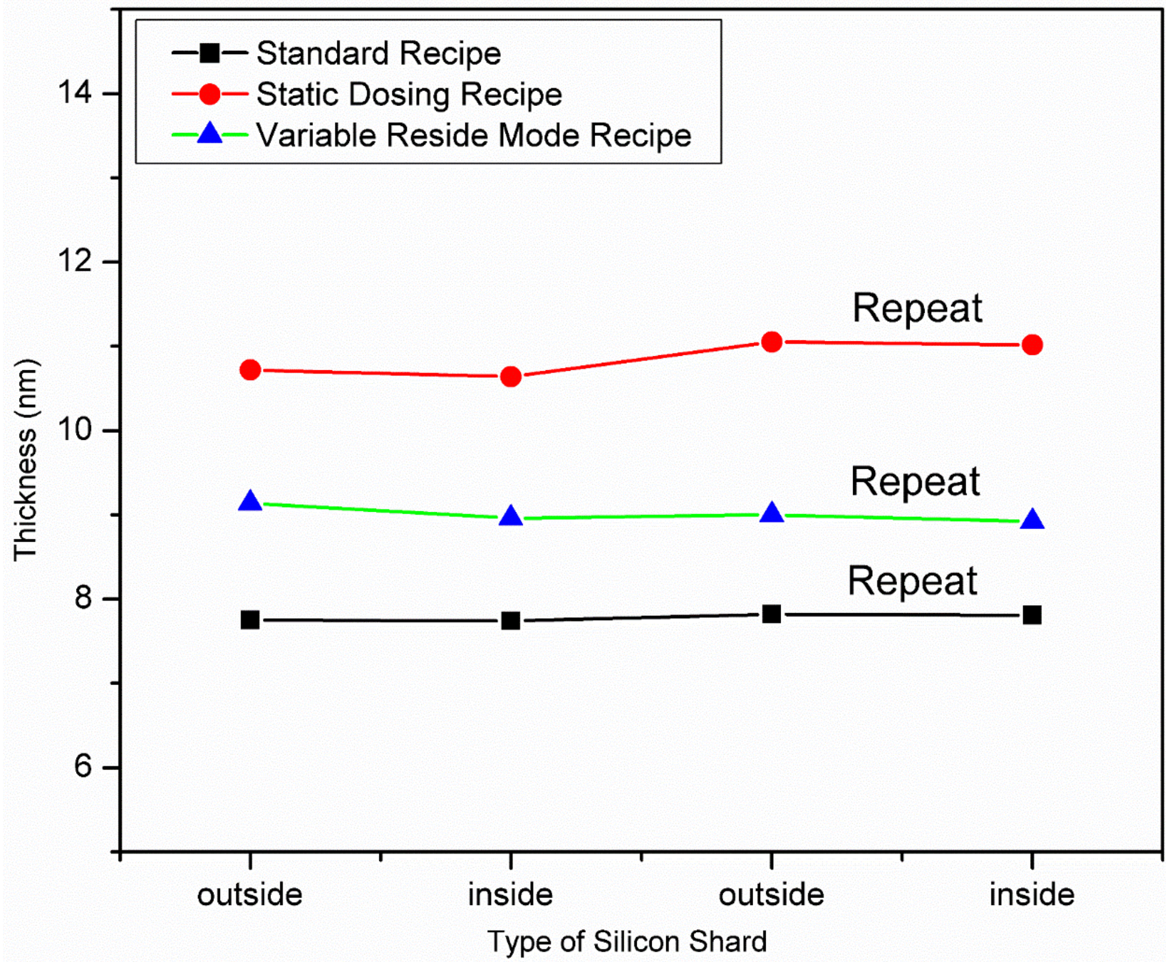

Figure 3.23. Film thickness and GPC for a 100-cycle ALD run using different recipes. The chamber was heated at 150 °C as an oven, such that the temperature was essentially the same at all places inside the chamber. The substrate was allowed to equilibrate at 150 °C for 30 min prior to deposition.

المنارة للاستشارات
www.manaraa.com

3.8 References

1. S. M. George, Atomic layer deposition: An overview. *Chem. Rev.* **2010,** *110*, 111-131.
2. R. W. Johnson; A. Hultqvist; S. F. Bent, A brief review of atomic layer deposition: From fundamentals to applications. *Mater. Today* **2014,** *17* (5), 236-246.
3. G. P. Gakis; C. Vahlas; H. Vergnes; S. Dourdain; Y. Tison; H. Martinez; J. Bour; D. Ruch; A. G. Boudouvis; B. Caussat; E. Scheid, Investigation of the initial deposition steps and the interfacial layer of Atomic Layer Deposited (ALD) Al2O3 on Si. *Appl. Surf. Sci.* **2019,** *492*, 245-254.
4. M. Leskelä; M. Ritala, Atomic Layer Deposition Chemistry: Recent Developments and Future Challenges. *Angew. Chem. Int. Edit.* **2003,** *42* (45), 5548-5554.
5. A. Gharachorlou; M. D. Detwiler; X. K. Gu; L. Mayr; B. Klotzer; J. Greeley; R. G. Reifenberger; W. N. Delgass; F. H. Ribeiro; D. Y. Zemlyanov, Trimethylaluminum and oxygen atomic layer deposition on hydroxyl-free Cu(111). *ACS Appl. Mater. Interfaces* **2015,** *7* (30), 16428-39.
6. H. Moshe; Y. Mastai, *Atomic layer deposition on self-assembled-monolayers*. Intech: Isarel, 2013.
7. G. Rampelberg; D. Longrie; C. Deduytsche; C. Detavernier, Plasma Enhanced Atomic Layer Deposition on Powders. *ECS Transactions* **2014,** *64* (9), 51-62.
8. H. Kim; H. Lee; H. -B. -R. Lee; W. J. Maeng, Applications of atomic layer deposition to nanofabrication and emerging nanodevices. *Thin Solid Films* **2009,** *517*, 2563-2580.
9. S. Adhikari; S. Selvaraj; D. -H. Kim, Progress in Powder Coating Technology Using Atomic Layer Deposition. *Adv. Mater. Interfaces* **2018,** *5* (16), 1800581.
10. K. -C. Kim; S. -S. Lim; S. H. Lee; J. Hong; D. -Y. Cho; A. Y. Mohamed; C. M. Koo; S. -H. Baek; J. -S. Kim; S. K. Kim, Precision Interface Engineering of an Atomic Layer in Bulk Bi_2Te_3 Alloys for High Thermoelectric Performance. *ACS Nano* **2019,** *13* (6), 7146-7154.
11. C. Detavernier; J. Dendooven; S. P. Sree; K. F. Ludwig; J. A. Martens, Tailoring nanoporous materials by atomic layer deposition. *Chem. Soc. Rev.* **2011,** *40* (11), 5242-5253.
12. B. Caussat; C. Vahlas, CVD and Powders: A Great Potential to Create New Materials. *Chemical Vapor Deposition* **2007,** *13* (9), 443-445.
13. K. Kikuchi; M. Miura; K. Kanomata; B. Ahmmad; S. Kubota; F. Hirose, Room temperature atomic layer deposition of TiO_2 on gold nanoparticles. *J. Vac. Sci. Technol., A* **2017,** *35* (1).
14. W. Yao; G. Guangsheng; W. Fei; W. Jun, Fluidization and agglomerate structure of SiO_2 nanoparticles. *Powder Technol.* **2002,** *124* (1), 152-159.
15. J. P. K. Seville; C. D. Willett; P. C. Knight, Interparticle forces in fluidisation: a review. *Powder Technol.* **2000,** *113* (3), 261-268.
16. L. F. Hakim; J. L. Portman; M. D. Casper; A. W. Weimer, Aggregation behavior of nanoparticles in fluidized beds. *Powder Technol.* **2005,** *160* (3), 149-160.
17. Strempel, V. E.; Knemeyer, K.; Naumann d'Alnoncourt, R.; Driess, M.; Rosowski, F., Investigating the Trimethylaluminium/Water ALD Process on Mesoporous Silica by In Situ Gravimetric Monitoring. *Nanomaterials* **2018,** *8* (6), 365.
18. Fryauf, D. M.; Phillips, A. C.; Bolte, M. J.; Feldman, A.; Tompa, G. S.; Kobayashi, N. P., Scaling Atomic Layer Deposition to Astronomical Optic Sizes: Low-Temperature Aluminum Oxide in a Meter-Sized Chamber. *ACS Applied Materials & Interfaces* **2018,** *10* (48), 41678-41689.

المنارة للاستشارات
www.manaraa.com

19. Hakim, L. F.; George, S. M.; Weimer, A. W., Conformal nanocoating of zirconia nanoparticles by atomic layer deposition in a fluidized bed reactor. *Nanotechnology* **2005,** *16* (7), S375-S381.
20. L. F. Hakim; J. A. McCormick; G. -D. Zhan; A. W. Weimer; P. Li; S. M. George, Surface Modification of Titania Nanoparticles Using Ultrathin Ceramic Films. *J. Am. Ceram. Soc.* **2006,** *89* (10), 3070-3075.
21. J. A. McCormick; B. L. Cloutier; A. W. Weimer; S. M. George, Rotary reactor for atomic layer deposition on large quantities of nanoparticles. *J. Vac. Sci. Technol., A* **2007,** *25* (1), 67-74.
22. C. A. Wilson; J. A. McCormick; A. S. Cavanagh; D. N. Goldstein; A. W. Weimer; S. M. George, Tungsten atomic layer deposition on polymers. *Thin Solid Films* **2008,** *516* (18), 6175-6185.
23. A. P. Didden; J. Middelkoop; W. F. A. Besling; D. E. Nanu; R. van de Krol, Fluidized-bed atomic layer deposition reactor for the synthesis of core-shell nanoparticles. *Rev. Sci. Instrum.* **2014,** *85* (1), 013905.
24. E. L. Lakomaa; S.Haukka; T. Suntola, Atomic layer growth of TiO_2 on silica. *Appl. Surf. Sci.* **1992,** *60-61*, 742-748.
25. E. L. Lakomaa; S.Haukka; T. Suntola, Analytical and chemical techniques in the study of surface species in atomic layer epitaxy. *Thin Solid Films* **1993,** *225* (1), 280-283.
26. M. Lindblad; L. P. Lindfors; T. Suntola, Preparation of Ni/Al_2O_3 catalysts from vapor phase by atomic layer epitaxy. *Catal. Lett.* **1994,** *27* (3), 323-336.
27. D. Longrie; D. Deduytsche; C. Detavernier, Reactor concepts for atomic layer deposition on agitated particles: A review. *J. Vac. Sci. Technol., A* **2013,** *32* (1), 010802.
28. J. D. Ferguson; K. J. Buechler; A. W. Weimer; S. M. George, SnO2 atomic layer deposition on ZrO_2 and Al nanoparticles: Pathway to enhanced thermite materials. *Powder Technol.* **2005,** *156* (2), 154-163.
29. G. P. Gakis; H. Vergnes; E. Scheid; C. Vahlas; A. G. Boudouvis; B. Caussat, Detailed investigation of the surface mechanisms and their interplay with transport phenomena in alumina atomic layer deposition from TMA and water. *Chem. Eng. Sci.* **2019,** *195*, 399-412.
30. R. L. Puurunen, Correlation between the growth-per-cycle and the surface hydroxyl group concentration in the atomic layer deposition of aluminum oxide from trimethylaluminum and water. *Appl. Surf. Sci.* **2005,** *245* (1), 6-10.
31. J. A. McCormick; B. L. Cloutier; A. W. Weiner; S. M. George, Rotary reactor for atomic layer deposition on large quantities of nanoparticles. *J. Vac. Sci. Technol., A* **2007,** *25* (1), 67-74.
32. T. O. Kääriäinen; M. Kemell; M. Vehkamäki; M. -L. Kääriäinen; A. Correia; H. A. Santos; L. M. Bimbo; J. Hirvonen; P. Hoppu; S. M. George; D. C. Cameron; M. Ritala; M. Leskelä, Surface modification of acetaminophen particles by atomic layer deposition. *Int. J. Pharm.* **2017,** *525* (1), 160-174.
33. Ma, Z.; Brown, S.; Howe, J. Y.; Overbury, S. H.; Dai, S., Surface Modification of Au/TiO_2 Catalysts by SiO_2 via Atomic Layer Deposition. *J. Phys. Chem. C* **2008,** *112* (25), 9448-9457.
34. Azizpour, H.; Talebi, M.; Tichelaar, F. D.; Sotudeh-Gharebagh, R.; Guo, J.; van Ommen, J. R.; Mostoufi, N., Effective coating of titania nanoparticles with alumina via atomic layer deposition. *Appl. Surf. Sci.* **2017,** *426*, 480-496.
35. X. Liang; K. S. Barrett; Y. -B. Jiang; A. W. Weimer, Rapid Silica Atomic Layer Deposition on Large Quantities of Cohesive Nanoparticles. *ACS Appl. Mater. Interfaces* **2010,** *2* (8), 2248-2253.

المنارة للاستشارات
www.manaraa.com

36. Yan, B.; Li, X.; Bai, Z.; Song, X.; Xiong, D.; Zhao, M.; Li, D.; Lu, S., A review of atomic layer deposition providing high performance lithium sulfur batteries. *J. Power Sources* **2017,** *338*, 34-48.
37. Ritala, M.; Leskelä, M., Atomic layer epitaxy - a valuable tool for nanotechnology? *Nanotechnology* **1999,** *10* (1), 19-24.
38. Wang, X.; Yushin, G., Chemical vapor deposition and atomic layer deposition for advanced lithium ion batteries and supercapacitors. *Energy Environ. Sci.* **2015,** *8* (7), 1889-1904.
39. Kern, W., The evolution of silicon wafer cleaning technology. *J. Electrochem. Soc.* **1990,** *137*, 1887-1892.
40. Diwan, A.; Singh, B.; Roychowdhury, T.; Yan, D.; Tedone, L.; Nesterenko, P. N.; Paull, B.; Sevy, E. T.; Shellie, R. A.; Kaykhaii, M.; Linford, M. R., Porous, high capacity coatings for solid phase microextraction by sputtering. *Anal. Chem.* **2016,** *88* (3), 1593-600.
41. R. J. O'Toole; C. J. Bartel; M. U. Kodas; A. J. Horrell; S. Ricote; N. P. Sullivan; C. J. Gump; C. B. Musgrave; A. W. Weimer, Particle atomic layer deposition of alumina for sintering yttria-stabilized cubic zirconia. *J. Am. Ceram. Soc.* **2019,** *102* (5), 2283-2293.
42. Guziewicz, E.; Godlewski, M.; Krajewski, T.; Wachnicki, Ł.; Szczepanik, A.; Kopalko, K.; Wójcik-Głodowska, A.; Przeździecka, E.; Paszkowicz, W.; Łusakowska, E.; Kruszewski, P.; Huby, N.; Tallarida, G.; Ferrari, S., ZnO grown by atomic layer deposition: A material for transparent electronics and organic heterojunctions. *Journal of Applied Physics* **2009,** *105* (12), 122413.
43. Illiberi, A.; Roozeboom, F.; Poodt, P., Spatial Atomic Layer Deposition of Zinc Oxide Thin Films. *ACS Applied Materials & Interfaces* **2012,** *4* (1), 268-272.
44. D. Shah; D. I. Patel; T. Roychowdhury; G. B. Rayner; N. O'Toole; D. R. Baer; M. R. Linford, Tutorial on interpreting x-ray photoelectron spectroscopy survey spectra: Questions and answers on spectra from the atomic layer deposition of Al_2O_3 on silicon. *J. Vac. Sci. Technol., B* **2018,** *36* (6), 062902.
45. C. Guerra-Nuñez; M. Döbeli; J. Michler; I. Utke, Reaction and Growth Mechanisms in Al_2O_3 deposited via Atomic Layer Deposition: Elucidating the Hydrogen Source. *Chem. Mater.* **2017,** *29* (20), 8690-8703.
46. T. Weckman, K. L., Atomic Layer Deposition of Zinc Oxide: Diethyl Zinc Reactions and Surface Saturation from First-Principles. *J. Phys. Chem., C* **2016,** *120* (38), 21460-21471.
47. A. Diwan; B. Singh; T. Roychowdhury; D. Yan; L. Tedone; P. N. Nesterenko; B. Paull; E. T. Sevy; R. A. Shellie; M. Kaykhaii; M. R. Linford, Porous, High Capacity Coatings for Solid Phase Microextraction by Sputtering. *Anal. Chem.* **2016,** *88* (3), 1593-1600.
48. J. Cazaux, About the charge compensation of insulating samples in XPS. *J. Electron Spectrosc. Relat. Phenom.* **2000,** *113* (1), 15-33.
49. J. M. Gorham; W. A. Osborn; J. W. Woodcock; K. C. Scott; J. M. Heddleston; A. R. Walker; J. W. Gilman, Detecting Carbon in Carbon: Exploiting Differential Charging to Obtain Information on the Chemical Identity and Spatial Location of Carbon Nanotube Aggregates in Composites by Imaging X-ray Photoelectron Spectroscopy. *Carbon* **2016,** *96*, 1208-1216.
50. D. S. Jensen; S. S. Kanyal; N. Madaan; M. A. Vail; A. E. Dadson; M. E. Engelhard; M. R. Linford, Silicon (100)/SiO_2 by XPS. *Surf. Sci. Spectra* **2013,** *20* (36), 1-8.
51. D. Barreca; G. A. Battiston; R. Gerbasi; E. Tondello; P. Zanella, Zirconium Dioxide Thin Films Characterized by XPS. *Surf. Sci. Spectra* **2000,** *7* (4), 303-309.

المنارة للاستشارات
www.manaraa.com

52. R. Al-Gaashani; S. Radiman; A. R. Daud; N. Tabet; Y. Al-Douri, XPS and optical studies of different morphologies of ZnO nanostructures prepared by microwave methods. *Ceramics Int.* **2013,** *39* (3), 2283-2292.
53. Madaan, N.; Kanyal, S.; Jensen, D.; Vail, M.; Dadson, A.; Engelhard, M.; Samha, H.; Linford, M., Al_2O_3 e-beam evaporated onto silicon (100)/SiO_2, by XPS. *Surf. Sci. Spectra* **2013,** *20*, 43-48.
54. D. Shah; D. I. Patel; T. Roychowdhury; D. Jacobsen; J. Erikson; M. R. Linford, Optical Function of Atomic Layer Deposited Alumina (0.5-41.0 nm) from 191 – 1688 nm by Spectroscopic Ellipsometry *Surf. Sci. Spectra* **2019,** *Accepted*.
55. Tougaard, S., Improved XPS analysis by visual inspection of the survey spectrum. *Surf. Interface Anal.* **2018,** *50* (6), 657-666.
56. Suzer, S., Differential Charging in X-ray Photoelectron Spectroscopy: A Nuisance or a Useful Tool? *Anal. Chem.* **2003,** *75* (24), 7026-7029.
57. Cros, A., Charging effects in X-ray photoelectron spectroscopy. *J. Electron Spectroscopy and Related Phenomena* **1992,** *59* (1), 1-14.
58. Al-Gaashani, R.; Radiman, S.; Daud, A. R.; Tabet, N.; Al-Douri, Y., XPS and optical studies of different morphologies of ZnO nanostructures prepared by microwave methods. *Ceramics International* **2013,** *39* (3), 2283-2292.
59. Hammer, G. E.; Shemenski, R. M., The oxidation of zinc in air studied by XPS and AES. *Journal of Vacuum Science & Technology A* **1983,** *1* (2), 1026-1028.

المنارة للاستشارات
www.manaraa.com

CHAPTER 4: Substrate Protection and Deprotection with Salt Films to Prevent Surface Contamination and Enable Selective Atomic Layer Deposition

4.1 Statement of Attribution

This article was originally submitted as **Shah, D.**; Patel, D. I.; Roychowdhury, T.; Johnson, B., I.; Linford, M. R. Substrate Protection and Deprotection with Salt Films to Prevent Surface Contamination and Enable Selective Atomic Layer Deposition *Appl. Surf. Sci.,* **2020**, Submitted. Here, the texts and figures are reproduced with the permission from AIP publishing.

4.2 Abstract

Surface contamination can decrease surface reactivity, and removal of surface contaminants adds additional steps to a process. Here we demonstrate surface protection from contamination and one-sided atomic layer deposition (ALD) by means of protective, sacrificial, thermally evaporated NaCl layers. This approach allows clean silicon surfaces to be stored under ambient conditions for extended periods of time in a pristine state, and ALD to be performed selectively on one side of a surface. For the ALD depositions, planar substrates are (i) selectively coated on one side with ca. 100 nm of NaCl by thermal evaporation, (ii) non-selectively coated using traditional ALD, and (c) rinsed with water to remove the NaCl layer. Water treatment removes the salt film and any ALD deposition on top of it. Salt film deposition, surface protection, and selective ALD are confirmed by X-ray photoelectron spectroscopy (XPS) and spectroscopic ellipsometry (SE). Selective, thermal ALD of alumina and ZnO are demonstrated, and protective salt films of different thicknesses (10, 50, and 100 nm) are investigated.

المنارة للاستشارات
www.manaraa.com

Keywords: Substrate protection, salt film deposition, area selective deposition, atomic layer deposition, thermal evaporation, XPS, sodium chloride, spectroscopic ellipsometry, X-ray photoelectron spectroscopy

4.3 Introduction

Surface contamination decreases surface reactivity, and the additional steps required to clean substrates increase the time and expense of a process. Hence, the prevention or mitigation of surface contamination is an important task. A common surface contaminant is adventitious carbon, which is present on almost all surfaces stored under ambient conditions.[1] Preferred methods for removing adventitious carbon from inorganic substrates include plasma-cleaning and piranha solution.[2] Here we show that thin, thermally-evaporated sodium chloride films can be used to protect silicon substrates from ambient/adventitious carbon contamination. In addition, we use this method to protect surfaces from unwanted atomic layer deposition (ALD) so that they can be selectively coated on one side.

ALD is an increasingly important method that provides a high degree of control over thin film growth, and many materials, including metal oxides, nitrides, and sulfides, can be deposited by ALD.[3-5] Accordingly, ALD is now well accepted in semiconductor manufacturing and nanotechnology.[6, 7] One of the most significant advantages of ALD is that it is a bottom-up approach for adding atoms to a material in a layer-by-layer fashion.[8] ALD uses gas phase precursors, which are often generated from liquids or solids with sufficiently high vapor pressures. The molecular precursor gases used in many ALD experiments are highly reactive and have relatively long mean free paths.[9] Thus, it can be challenging to limit where they might travel and

المنارة للاستشارات
www.manaraa.com

react, i.e., like chemical vapor deposition, ALD is not a line-of-sight technique.[10] Of course, these conditions are advantageous for depositions on irregular substrates, e.g., high aspect ratio structures, powders, and porous materials.[11-13] However, ALD is limited when selective or spatial deposition is required. That is, there are times when one would wish to perform ALD without coating an entire substrate. For example, we desired to create high quality, thin film optical standards by ALD on only one side of fused silica substrates for spectroscopic ellipsometry and transmission UV-VIS studies.

We could not prevent easily measured, irregular ALD deposition of Al_2O_3 from trimethylaluminum (TMA) and water precursors on the backsides of substrates even when they were placed face-to-face with other highly polished surfaces.[14] The problem of directing ALD deposition has led to a new sub-discipline within the field known as area-selective ALD (AS-ALD).[15, 16] AS-ALD is often achieved by exploiting the differences in surface chemistry of substrates, which may result in nucleation delay. AS-ALD[17-21] offers advantages over traditional ALD in catalysis,[22] nanoelectronics,[23] synthesis of core-shell nanoparticles,[24] and nanopatterned devices.[25] AS-ALD combines the benefits of conventional ALD with directional thin film deposition processes like thermal deposition.[16, 21, 26]

Sodium chloride is an extremely common and inexpensive material.[27] It has low toxicity, and it is soluble in water. Evaporation, i.e., sublimation of NaCl, is advantageous because it is a line-of-sight deposition technique. An additional advantage of NaCl is that it is stable under most ALD deposition conditions. Here we present a straightforward approach for depositing and removing a barrier layer of ca. 100 nm of NaCl that allows for substrate protection, including the long-term storage of pristine silicon surfaces, and that can additionally be used to achieve selective ALD deposition on only one side of a substrate (see **Figure 4.1**).[28] There are several examples in

المنارة للاستشارات
www.manaraa.com

the patent literature of the use of thin salt films for substrate protection.[29-31] The advantages of using salt films as protective layers include ease of deposition, ease of removal, and lack of cross-contamination/migration of the protective layer. Other line-of-sight deposition techniques, e.g., pulsed laser deposition, could similarly be useful for depositing protective salt films.[32, 33] After coating with a salt layer, ALD may be performed on the substrate with the salt-protected side facing down (see **Figure 4.2**). After ALD, the surface is rinsed with water, which removes the salt coating and any unwanted ALD deposition on it. NaCl deposition and removal are confirmed by X-ray photoelectron spectroscopy (XPS) and/or spectroscopic ellipsometry (SE). We investigate here NaCl films of three thicknesses (10, 50, and 100 nm) as barrier layers, and show that this approach works effectively for the selective thermal ALD deposition of both alumina and ZnO.

4.4. Experimental

4.4.1. Substrates

The small silicon shards used in this study (ca. 1 cm x 1 cm) were cut from 4" wafers (University Wafer, South Boston, MA). The fused silica slides (1" x 2" x 1 mm) were purchased from Ted Pella (Redding, CA). These silicon and fused silica substrates were stored at room temperature and atmospheric pressure, and were cleaned before ALD and thermal evaporation.

4.4.2. Sample cleaning

Prior to deposition, substrates were cleaned for one minute in an air plasma in a Model No. PDC-32G plasma cleaner (Harrick Plasma, Ithaca, New York), or cleaned for 40 min in piranha solution (a ca. 7:3 mixture of H_2SO_4(conc.) and 30% H_2O_2) at 80 – 100 °C.[34, 35] *Note that piranha solution*

www.manaraa.com

is extremely dangerous and should be handled with great care. After piranha cleaning, the substrates were washed extensively with high purity (18 MΩ) water.

4.4.3. Thermal deposition

Sodium chloride was evaporated using a DV-502A deposition system from Denton Vacuum (Moorestown, NJ). Depositions of ca. 100 nm took about 10 min.[36] The system had a rotating sample stage to improve film uniformity, an Inficon quartz-crystal thickness monitor (QCM), and a shutter activated by the QCM to precisely control the film thickness. Depositions ceased when the QCM thickness reached the desired value set at 10, 50, or 100 nm, where the QCM had previously been calibrated and the density of NaCl inputted into it. Fused silica slides and/or silicon wafers were mounted on the rotating platform of the system with vacuum tape. A small amount of sodium chloride (approx. 100 mg) was place in an aluminum boat connected to two electrodes. The system was then pumped to high vacuum (10^{-5} – 10^{-7} torr). During the deposition, the platform was rotated at 100 rpm to ensure uniform salt deposition on the substrate.

4.4.4. Atomic layer deposition[37, 38]

ALD of alumina was performed with a Kurt J. Lesker (Jefferson Hills, PA) ALD-150LX™ system.[37, 38] The precursors used for alumina deposition were trimethylaluminum (TMA) and water. Our ALD instrument is equipped with an *in-situ* FS-1® ellipsometer (FilmSense, Lincoln, Nebraska) that measures the thickness of ALD alumina films during a deposition. Our deposition of Al_2O_3 followed the manufacturer's recommended recipe as follows. The ALD chamber was heated to 332 ºC prior to initiation of the deposition, and this temperature was maintained during the deposition. The dose times for TMA and water were 21.0 ms and 15.5 ms, respectively, with 15,000 ms purge times for both precursors. Additional details about the ALD process and its

المنارة للاستشارات
www.manaraa.com

optimization can be found in our previous studies.[37, 38] The precursors used for zinc oxide deposition were diethylzinc (DEZ) and water. Dose times for DEZ and water were 21.0 ms and 15.5 ms, respectively, with 15,000 ms purge times for both precursors. For deposition of zinc oxide, 100 ALD cycles were used and the deposition temperature was 200 ºC.

4.4.5. Spectroscopic ellipsometry (SE)[39, 40]

Spectroscopic ellipsometry was performed using a J.A. Woollam (Lincoln, NE) M-2000DI ellipsometer over a wavelength range of 191-1688 nm.[41, 42] This ellipsometer can collect data at different angles and is equipped with a CCD array detector, a rotating compensator, and a near IR extension (out to 1688 nm).[42] Additional details about the use of spectroscopic ellipsometry can be found in our previously published articles.[38]

4.4.6. X-ray photoelectron spectroscopy (XPS)[35]

X-ray photoelectron spectroscopy (XPS) was performed with a Surface Science SSX-100 X-ray photoelectron spectrometer (serviced by Service Physics, Bend, OR) with a monochromatic Al K_α source, a hemispherical analyzer, and a take-off angle of 35°. Survey scans were recorded with a spot size of 800 μm x 800 μm and a resolution of 4 (nominal pass energy of 150.0 eV). An electron flood gun for charge compensation was employed for XPS measurements. XPS peaks were referenced to the C 1*s* hydrocarbon signal (taken at 285.0 eV) when sample charging was observed. While this method is less than ideal, it is adequate to allow peak identification. Additional details about the use of X-ray photoelectron spectroscopy for elemental analysis can be found in our previous published articles.[43, 44]

4.4.7. Removal of sodium chloride

المنارة للاستشارات
www.manaraa.com

Sodium chloride barrier layers were removed by sonicating three times in high purity water for 5 min, where the water was replaced after each sonication. Care was taken in cleaning the glassware for this work and also the tweezers that held the substrates.

4.5. Results and Discussion

4.5.1. Sodium chloride deposition for surface protection

To determine the most effective barrier layer for protecting silicon wafers from contamination and preventing ALD, three different thicknesses of sodium chloride (nominal/QCM thicknesses of 10, 50, and 100 nm) were evaporated onto silicon and/or fused silica substrates. NaCl on the silicon wafers changed their apparent color from grey to a blueish-purple hue. By eye, these depositions (the color across the silicon surface) were uniform. There was no change in the appearance of the transparent fused silica slides after NaCl deposition. The presence of these NaCl films was confirmed by X-ray photoelectron spectroscopy (XPS) and spectroscopic ellipsometry (SE). For example, **Figure 4.3** shows XPS of a fused silica surface that was coated on one side with ca. 100 nm of NaCl. As expected, the NaCl-coated side shows only peaks attributable to Na and Cl (Na 2*s* and Na 2*p* signals at 64.0 eV and 31.0 eV, respectively,[45-47] and Cl 2*s* and Cl 2*p* signals 271.0 eV and 200.0 eV, respectively),[48] and adventitious carbon (see **Figure 4.3a**). In contrast, the uncoated side of the substrate shows no Na or Cl – only Si, O, and C (see **Figure 4.3b**). The absence of substrate signals from the NaCl-coated side of the substrate is consistent with a NaCl film that is without pinholes and at least 10 nm thick (XPS probes 5 – 10 nm into materials).

www.manaraa.com

As a second example, a NaCl film (QCM thickness of 100 nm) was evaporated onto a piece of a silicon wafer. It was then analyzed by SE, where the film and substrate were modeled as the silicon substrate, a layer of native oxide (1.6 nm, as measured before the NaCl deposition), an NaCl film, and a roughness layer (a Bruggeman effective medium approximation layer based on a 50:50 mixture of void (air) and NaCl). The optical constants from the instrument software were used for all the layers (Si, native oxide, and NaCl), where the NaCl optical constants were based on a Sellmeier dispersion model. This model produced a fit with a NaCl film thickness of 106.9 nm, a roughness of 4.7 nm, and a reasonable mean squared error (MSE) value of 5.7.

Uniqueness plots for the fit, based on the film thickness and roughness, were generated.[49] The resulting 'V' or 'U' shapes suggested that the fit parameters were not correlated. Allowing the parameters in the NaCl Sellmeier model to vary or introducing thickness non-uniformity into the model did not significantly improve the quality of the fit or change the resulting thickness (these fits were also unique).[49] Thermal salt deposition in our system was moderately uniform. In the case of a different ca. 100 nm salt film deposited over a 4" silicon wafer, the thickness was 98.5 ± 4.3 nm (average and standard deviation of 10 measurements), where the maximum and minimum thicknesses measured by SE over the wafer were 104.7 nm and 91.8 nm. In contrast, our ALD film deposition was much more uniform.[50, 51] For example, after 100 cycles of TMA and water, the thickness of an Al_2O_3 film over a 4" silicon wafer was 8.4 ± 0.1 nm (average and standard deviation of 10 measurements), where the maximum and minimum thicknesses measured here were 8.3 nm and 8.5 nm.

4.5.2 Substrate protection with evaporated NaCl

To test the ability of a salt layer to protect a silicon wafer from contamination, plasma cleaned silicon surfaces were coated with ca. 100 nm of NaCl, where the thicknesses and

المنارة للاستشارات
www.manaraa.com

chemistries of these films were confirmed by SE and/or XPS (see above). The NaCl-coated surfaces were then exposed to the laboratory environment for 1, 3, and 7 months. They were then rinsed with water to remove the NaCl barrier layer, their advancing water contact angles were measured, and 100 cycles of ALD alumina from TMA and water were deposited on them. This deposition of alumina was used to test the availability/accessibility of the surface silanols, i.e., it was expected that a contaminated surface would show less reactivity than a clean one. Table 1 shows the results from these experiments. The first four rows of the table demonstrate that there is no statistical difference between the surface that was cleaned and immediately coated with ALD alumina and those that were coated with NaCl, exposed to the laboratory environment for extended periods of time, rinsed (deprotected), and coated with ALD alumina. As a control experiment, a silicon wafer was plasma cleaned, *not* coated with NaCl or anything else, and exposed to the laboratory environment for 67 days. After rinsing with water, its contact angle was noticeably higher than those of the pristine or NaCl-protected and deprotected silicon surfaces. The ALD film of alumina on this surface is also noticeably thinner and less uniform (the standard deviation is higher). These results suggest that salt barrier layers keep cleaned silicon wafers in their pristine state for extended periods of time.

Table 4.1. Experimental data for NaCl-coated and uncoated silicon shards after exposure to the laboratory environment and ALD of alumina.

Sample (Coated or Uncoated with ca. 100 nm NaCl after plasma cleaning)	Time surface exposed to the laboratory environment	Increase in apparent SiO_2 thickness*	Advancing water contact angle*	Thickness of alumina after 100 ALD cycles*,†

المنارة للاستشارات
www.manaraa.com

Uncoated	0 days	0.08 ± 0.03 nm	<10°	8.4 ± 0.1 nm
Coated	1 mo.	0.07 ± 0.02 nm	<10°	8.4 ± 0.1 nm
Coated	3 mo.	0.10 ± 0.03 nm	<10°	8.3 ± 0.1 nm
Coated	7 mo.	0.07 ± 0.03 nm	<10°	8.5 ± 0.1 nm
Uncoated	67 days	0.15 ± 0.03 nm	35° (After water treatment)	7.5 ± 0.3 nm

***After exposure to the lab and water wash.**

†Averages and standard deviations of three measurements on one sample.

4.5.3. ALD on salt-protected substrates and deprotection of these surfaces

To test the ability of salt-coated surfaces to prevent/direct ALD deposition, NaCl-coated fused silica substrates were placed in our ALD tool, with the uncoated surface face up, and alumina was deposited via 100 cycles of TMA and water. **Figure 4.5** shows the resulting XPS spectra. Rather strong Al 2*s* and 2*p* signals are clearly visible on both the 'NaCl-coated' and 'uncoated' surfaces, although the spectrum from the 'NaCl-coated' surface also contains signals

المنارة للاستشارات
www.manaraa.com

from Na and Cl. Clearly, the alumina film on the 'NaCl-coated' surface of the substrate was not thick enough to obscure the signals from the salt and/or it is patchy/incomplete. Obviously, these results are a manifestation of ALD's lack of directionality. TMA may react with the NaCl film via water that may have been present in it before the deposition, or that is introduced during ALD. Removal of the NaCl barrier layer on the alumina-coated fused silica slide was accomplished by sonicating/rinsing with water. This process removed unwanted alumina deposition on the backside of the surface. For example, **Figure 4.5** shows Al 2s and 2p XPS signals from the front side of the substrate, which was not coated with NaCl, while only the substrate signals (Si 2*s* and 2*p*), and no peaks from Na, Cl, or Al are observed on the backside of the slide. SE similarly confirmed the complete removal of salt films after sonication/rinsing.

4.5.4. Effect of salt thickness on deprotection

Different thicknesses of NaCl (10, 50 and 100 nm) were evaporated onto one side of fused silica substrates to test their ability to direct/limit ALD deposition. After ALD of Al_2O_3 on the surfaces and sonication/rinsing, these substrates were analyzed by XPS. As shown in **Figure 4.7**, small aluminum signals were present on the fused silica slides that had previously been coated with 10 and 50 nm of NaCl (see **Figure 4.6**). However, no aluminum signals were observed on the surface that was coated with 100 nm of NaCl. That is, 100 nm of NaCl appears to be an adequate barrier layer to prevent Al_2O_3 ALD deposition.

4.5.5. ALD of zinc oxide on NaCl-protected fused silica

To test the generality of our approach, fused silica was coated on one side with ca. 100 nm of NaCl, after which the material was coated with ZnO by ALD via 100 cycles of diethylzinc and

المنارة للاستشارات
www.manaraa.com

water, and then sonicated/rinsed with water. After this deprotection, Zn is only present on the side of the substrate that was originally unprotected (see **Figure 4.8** and **4.9**).

4.6 Conclusions

We have demonstrated a method for protecting surfaces from unwanted contamination and ALD deposition using thin sodium chloride films. This process employs thermal evaporation as a directional coating method and ALD as a non-directional one. This approach consists of coating a surface with an evaporated salt film to prevent environmental contamination or coating one side of a substrate with a salt film to prevent unwanted ALD deposition. The salt film can be easily removed by sonication/rinsing in water. Moderately thick NaCl films (100 nm) effectively direct ALD deposition of Al_2O_3 and ZnO and prevent surface contamination. Results of area-selective depositions and surface protection are confirmed by XPS and SE.

المنارة للاستشارات
www.manaraa.com

4.7 Figures

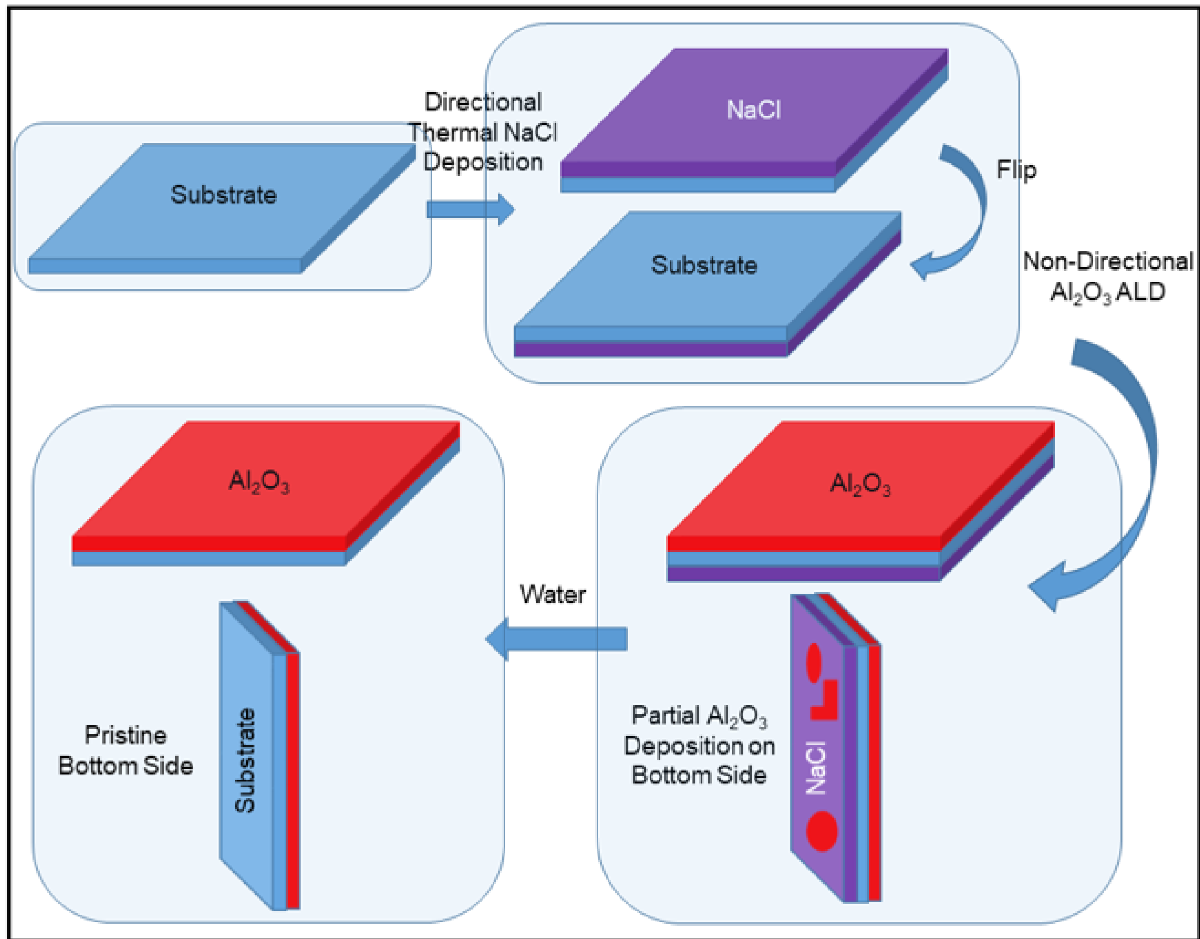

Figure 4.1. Protection of a substrate with a thin salt film, conventional ALD on the unprotected side of the substrate, and removal of the salt film, which removes unwanted ALD deposition on the backside of the substrate.

المنارة للاستشارات
www.manaraa.com

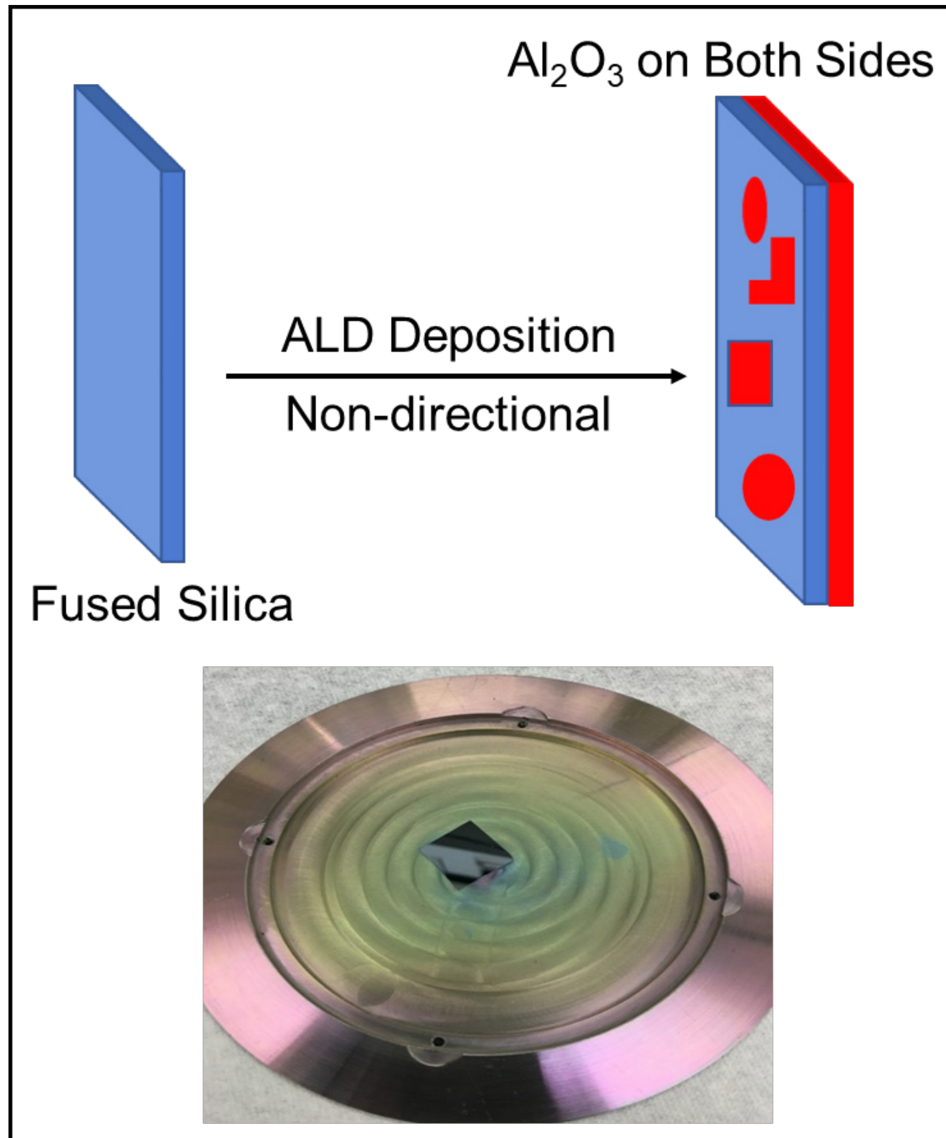

Figure 4.2. Schematic illustrating non-directional deposition of alumina in the ALD. The side, which shows non-uniform deposition of alumina, was in contact with loading tool. The exposed side of fused silica shows uniform alumina deposition.

المنارة للاستشارات
www.manaraa.com

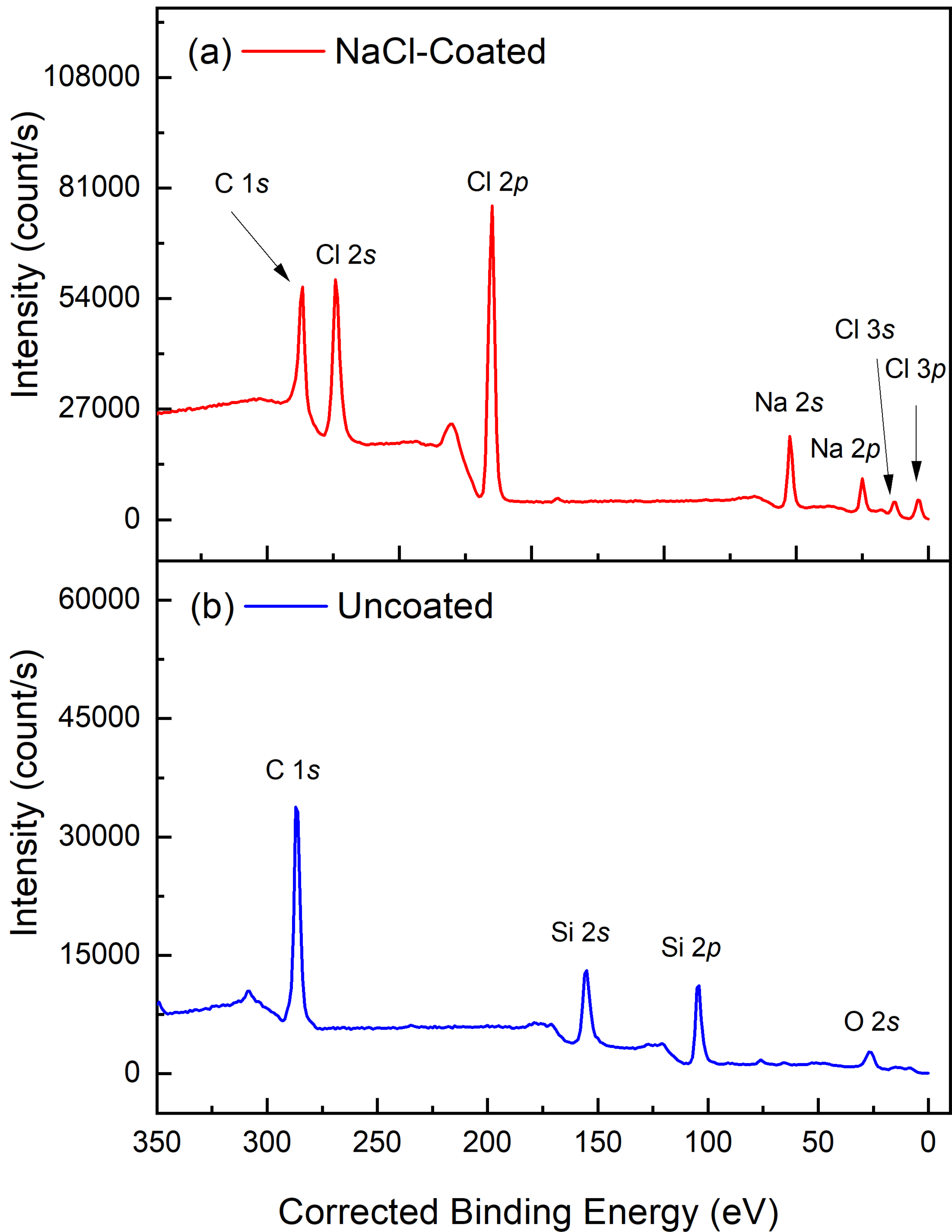

Figure 4.3. XPS spectra from 0 – 350 eV of (a) a ca. 100 nm film of NaCl evaporated onto a fused silica slide, and (b) an uncoated fused silica slide.

المنارة للاستشارات
www.manaraa.com

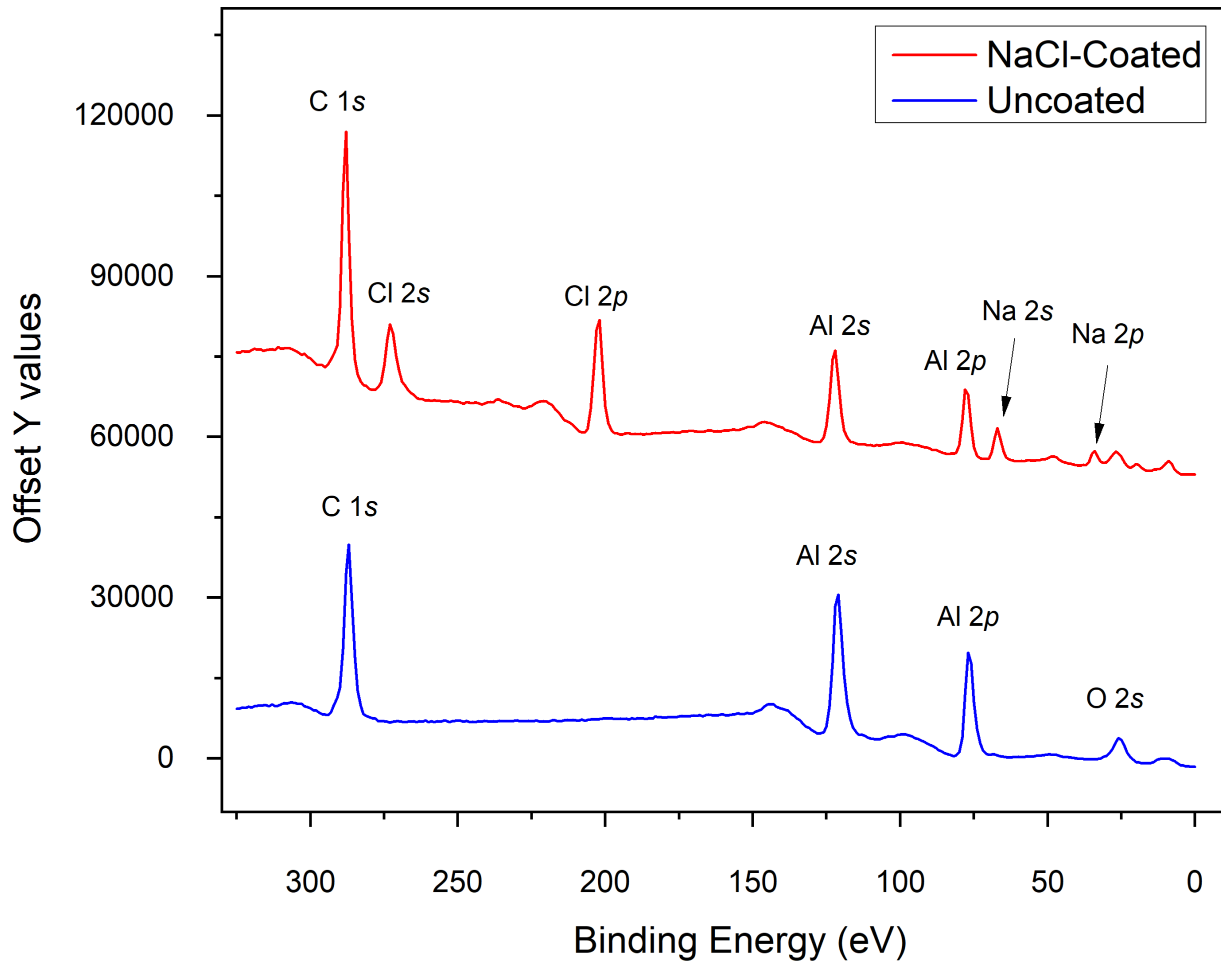

Figure 4.4. XPS spectra from 0 – 350 eV. (Top) NaCl – coated fused silica after ALD deposition of Al_2O_3 via 100 cycles of TMA and water. (Bottom) - Fused silica after the same ALD deposition. Note that the uncoated surface was facing up during the deposition.

المنارة للاستشارات
www.manaraa.com

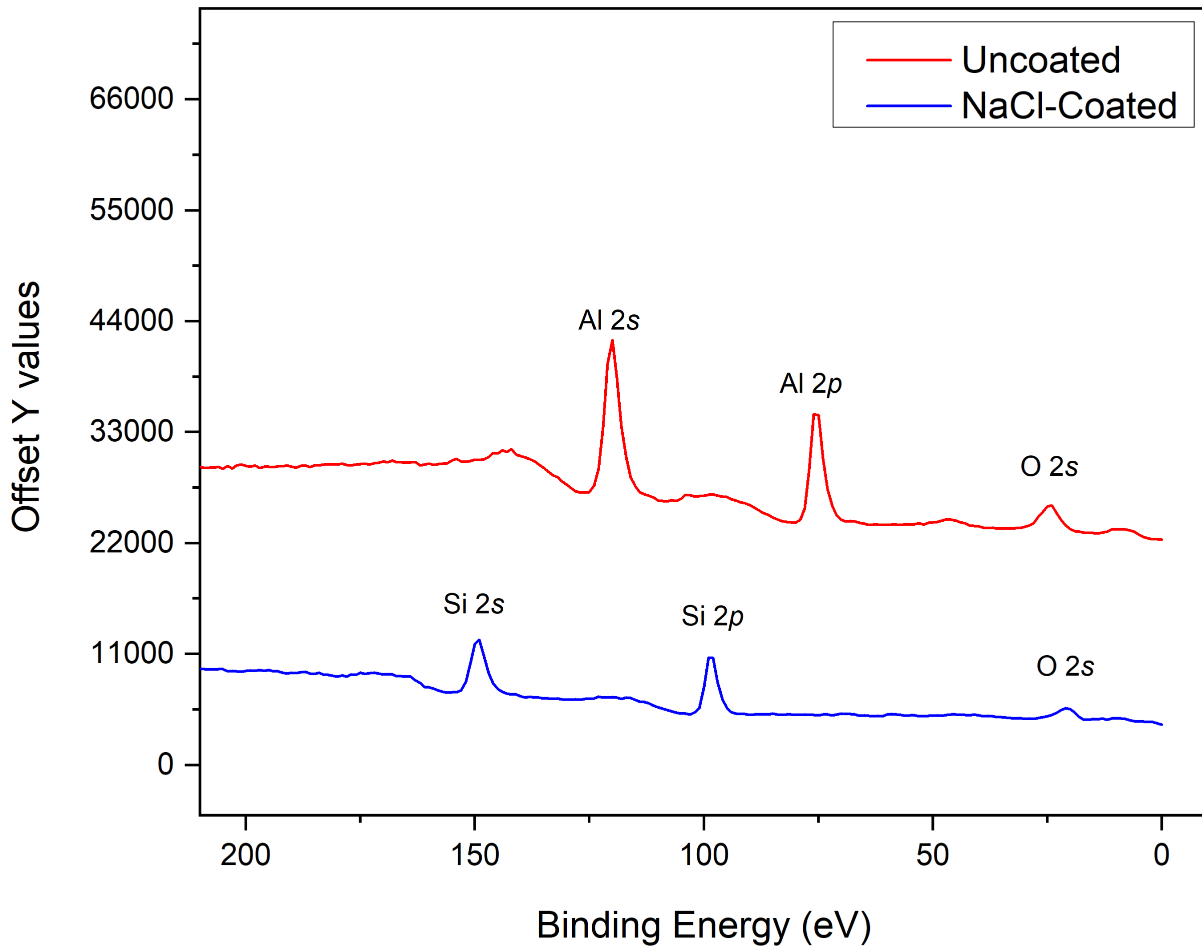

Figure 4.5. XPS spectra from 0 – 325 eV obtained from a fused silica substrate after three stepwise processes (i) protection with NaCl on one side, (ii) ALD of Al_2O_3, and (iii) sonication/rinsing with water.

المنارة للاستشارات
www.manaraa.com

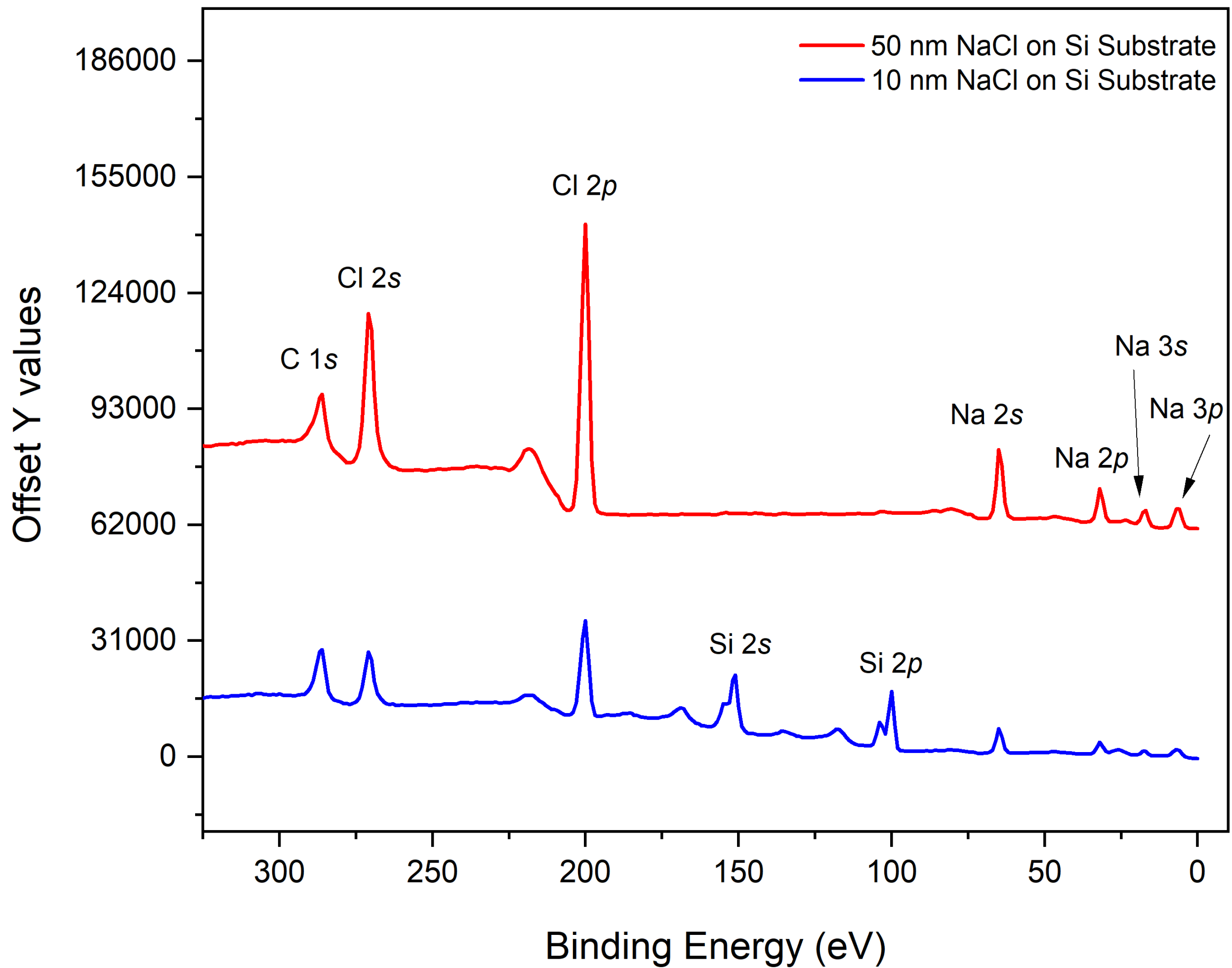

Figure 4.6. XPS spectra from 0 – 325 eV of two different thicknesses of NaCl coated on fused silica slides. (Top) NaCl (50 nm) on the surface of the fused silica slide, note that film thickness completely mask over the silanol groups eliminating any probability of silanol groups reacting with ALD precursors. (Bottom) NaCl (10 nm) film thickness showing the Na and Cl peaks along with Si peaks. This suggests lack of complete coverage of the surface by NaCl film. The small peak in the 50 nm NaCl coating is a loss peak associated with Cl 2*p*.

المنارة للاستشارات
www.manaraa.com

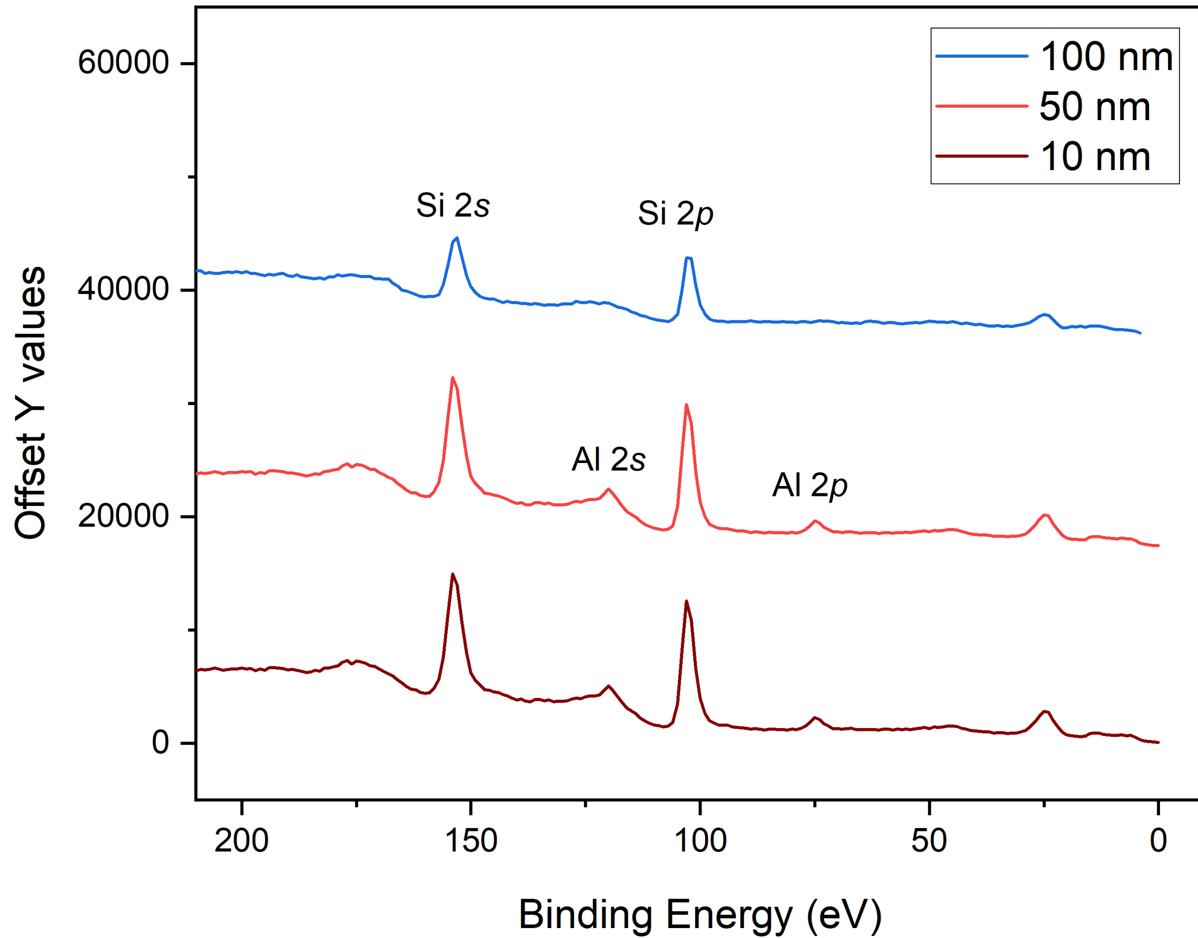

Figure 4.7. XPS spectra from 0 – 210 eV of the salt-protected sides of three different fused silica substrates previously coated on one side with 10 (top), 50 (middle), and 100 (bottom) nm of NaCl after ALD of Al_2O_3 and sonication/rinsing with water. Note the small peaks corresponding to Al 2*s* and Al 2*p* at 118.0 eV and 74.0 eV, which suggest small amount of alumina was deposited on quart slide.

المنارة للاستشارات
www.manaraa.com

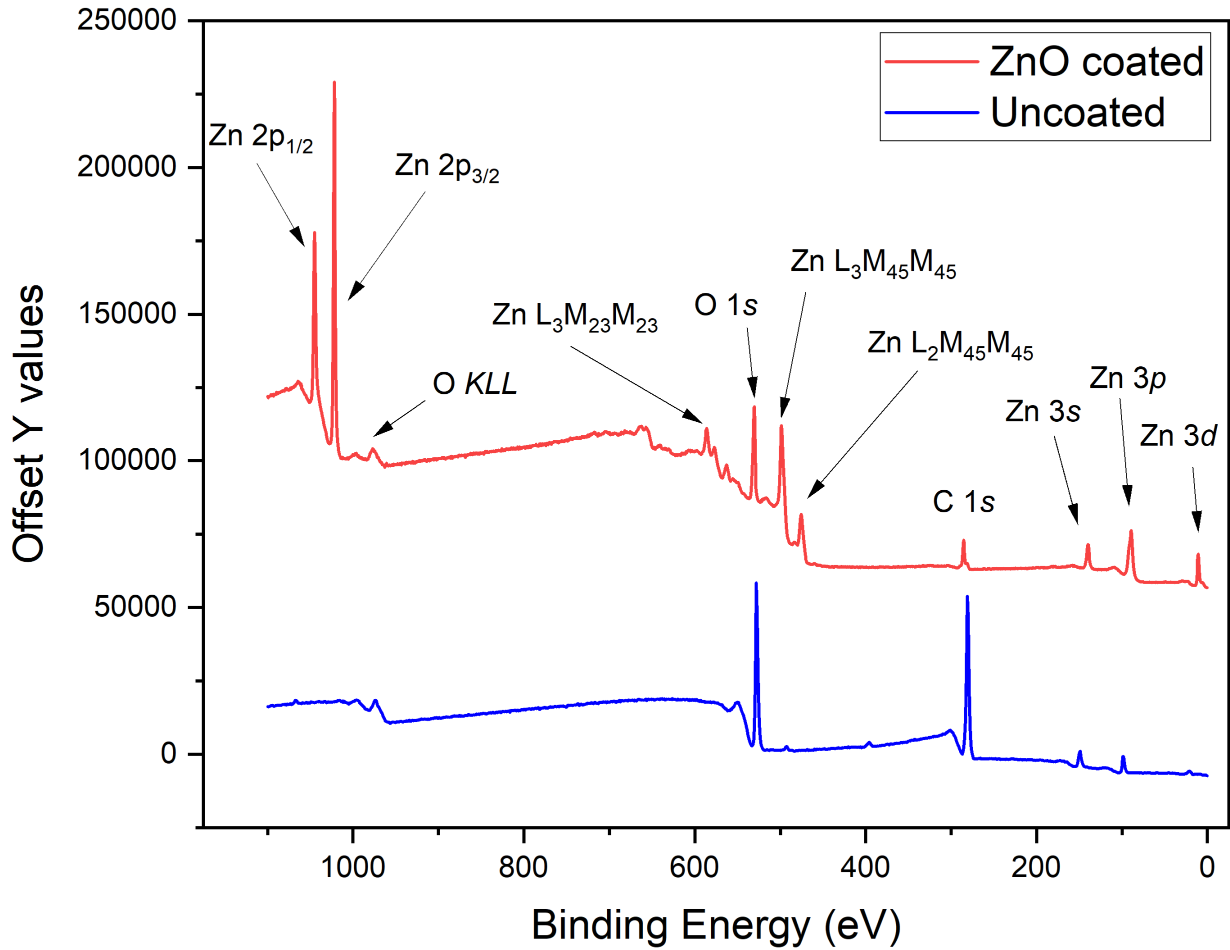

Figure 4.8. XPS spectra from 0 – 1100 eV of a fused silica substrate after (i) one side was coated with NaCl, (ii) ALD of ZnO, and (iii) deprotection of the substrate by sonication/rinsing with water. Zn is only present on the side of the surface that was not protected with NaCl.

المنارة للاستشارات
www.manaraa.com

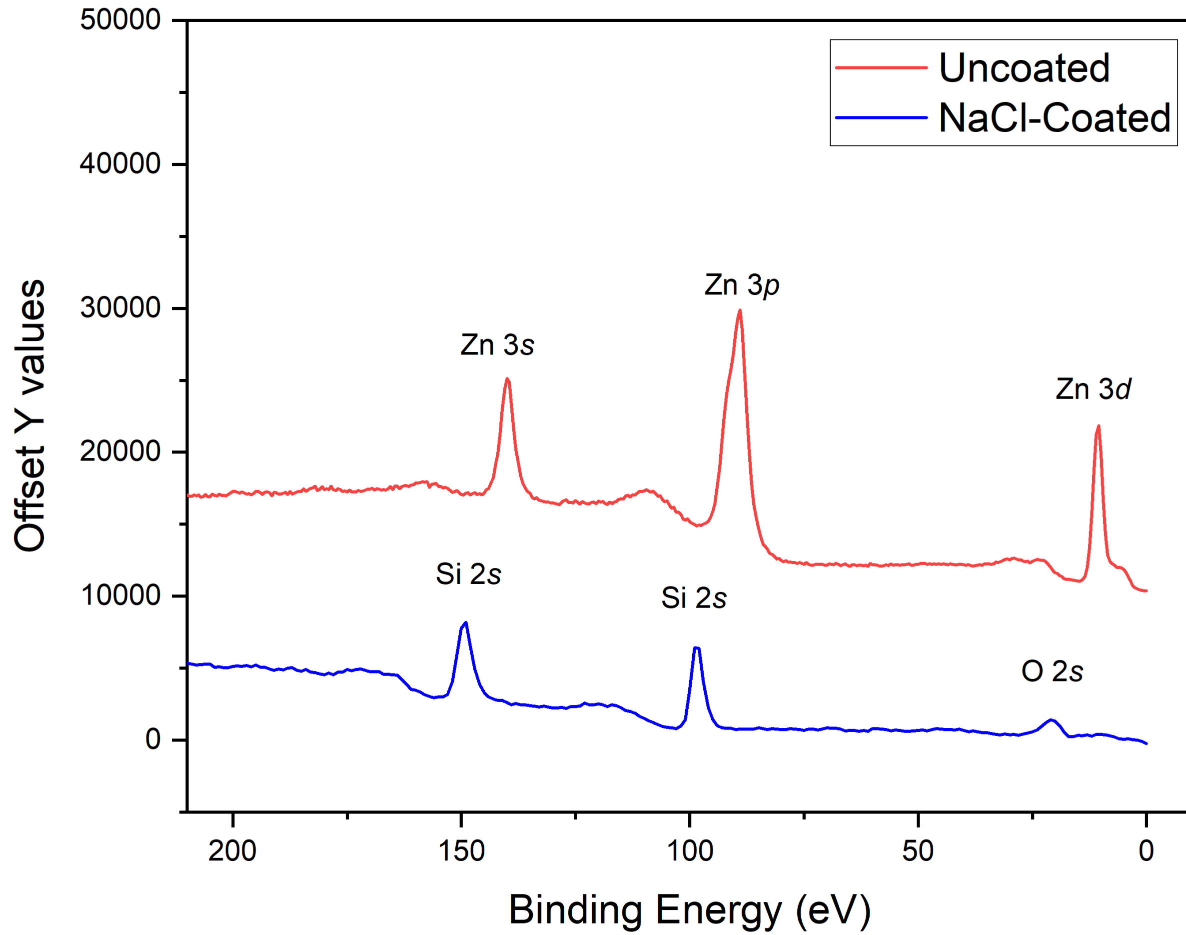

Figure 4.9. XPS spectra from 0 – 200 eV of a fused silica substrate after (i) one side was coated with NaCl, (ii) ALD of ZnO, and (iii) deprotection of the substrate by sonication/rinsing with water. Zn is only present on the side of the surface that was not protected with NaCl.

المنارة للاستشارات
www.manaraa.com

4.8 References

1. Radamson, H. H.; He, X.; Zhang, Q.; Liu, J.; Cui, H.; Xiang, J.; Kong, Z.; Xiong, W.; Li, J.; Gao, J.; Yang, H.; Gu, S.; Zhao, X.; Du, Y.; Yu, J.; Wang, G., Miniaturization of CMOS. *Micromachines (Basel)* **2019,** *10* (5), 293.
2. Ritala, M.; Leskela, M., Atomic layer deposition. In *Handbook of thin-film materials*, Nalwa, N. S., Ed. Academic Publisher: 2002; Vol. 1, pp 103-160.
3. Leskelä, M.; Ritala, M., Atomic layer deposition (ALD): From precursors to thin film structures. *Thin Solid Films* **2002,** *409*, 138-146.
4. George, S. M., Atomic layer deposition: An overview. *Chem. Rev.* **2010,** *110*, 111-131.
5. Puurunen, R. L., A Short History of Atomic Layer Deposition: Tuomo Suntola's Atomic Layer Epitaxy. *Chem. Vap. Deposition* **2014,** *20* (10-11-12), 332-344.
6. Alvaro, E.; Yanguas-Gil, A., Characterizing the field of Atomic Layer Deposition: Authors, topics, and collaborations. *PLOS ONE* **2018,** *13* (1), e0189137.
7. Knaut, M.; Junige, M.; Neumann, V.; Wojcik, H.; Henke, T.; Hossbach, C.; Hiess, A.; Albert, M.; Bartha, J. W., Atomic layer deposition for high aspect ratio through silicon vias. *Microelectron. Eng.* **2013,** *107*, 80-83.
8. Oviroh, P. O.; Akbarzadeh, R.; Pan, D.; Coetzee, R. A. M.; Jen, T.-C., New development of atomic layer deposition: processes, methods and applications. *Sci Technol Adv Mater* **2019,** *20* (1), 465-496.
9. Hagen, D. J.; Pemble, M. E.; Karppinen, M., Atomic layer deposition of metals: Precursors and film growth. *Appl. Phys. Rev.* **2019,** *6* (4), 041309.
10. Cremers, V.; Puurunen, R. L.; Dendooven, J., Conformality in atomic layer deposition: Current status overview of analysis and modelling. *Appl. Phys. Rev.* **2019,** *6* (2), 021302.
11. Puurunen, R. L.; Gao, F. In *Influence of ALD temperature on thin film conformality: Investigation with microscopic lateral high-aspect-ratio structures*, 2016 14th International Baltic Conference on Atomic Layer Deposition (BALD), 2-4 Oct. 2016; 2016; pp 20-24.
12. Adhikari, S.; Selvaraj, S.; Kim, D.-H., Progress in Powder Coating Technology Using Atomic Layer Deposition. *Adv. Mater. Interfaces* **2018,** *5* (16), 1800581.
13. Fang, M.; Ho, J. C., Area-Selective Atomic Layer Deposition: Conformal Coating, Subnanometer Thickness Control, and Smart Positioning. *ACS Nano* **2015,** *9* (9), 8651-8654.
14. Mameli, A.; Merkx, M. J. M.; Karasulu, B.; Roozeboom, F.; Kessels, W. M. M.; Mackus, A. J. M., Area-Selective Atomic Layer Deposition of SiO_2 Using Acetylacetone as a Chemoselective Inhibitor in an ABC-Type Cycle. *ACS Nano* **2017,** *11*, 9303-9311.
15. Mameli, A.; Karasulu, B.; Verheijen, M. A.; Barcones, B.; Macco, B.; Mackus, A. J. M.; Kessels, W. M. M. E.; Roozeboom, F., Area-Selective Atomic Layer Deposition of ZnO by Area Activation Using Electron Beam-Induced Deposition. *Chem. Mater.* **2019,** *31* (4), 1250-1257.
16. Jiang, X. H., H.; Prinz, F. B.; Bent, S. F. , Application of atomic layer deposition of platinum to solid oxide fuel cells *Chem. Mater.* **2008,** *20*, 3897-3905.
17. Pickrahn, K. L.; Gorlin, Y.; Seitz, L. C.; Garg, A.; Nordlund, D.; Jaramillo, T. F.; Bent, S. F., Applications of ALD MnO to electrochemical water splitting. *Phys. Chem. Chem. Phys.* **2015,** *17* (21), 14003-11.
18. Niu, W.; Li, X.; Karuturi, S. K.; Fam, D. W.; Fan, H.; Shrestha, S.; Wong, L. H.; Tok, A. I., Applications of atomic layer deposition in solar cells. *Nanotechnology* **2015,** *26* (6), 064001.

المنارة للاستشارات
www.manaraa.com

19. Cheng, N.; Banis, M. N.; Liu, J.; Riese, A.; Li, X.; Li, R.; Ye, S.; Knights, S.; Sun, X., Extremely stable platinum nanoparticles encapsulated in a zirconia nanocage by area-selective atomic layer deposition for the oxygen reduction reaction. *Adv Mater* **2015,** *27* (2), 277-81.
20. Mackus, A. J. M.; Merkx, M. J. M.; Kessels, W. M. M., From the Bottom-Up: Toward Area-Selective Atomic Layer Deposition with High Selectivity. *Chem. Mater.* **2019,** *31* (1), 2-12.
21. Yan, H.; Lin, Y.; Wu, H.; Zhang, W.; Sun, Z.; Cheng, H.; Liu, W.; Wang, C.; Li, J.; Huang, X.; Yao, T.; Yang, J.; Wei, S.; Lu, J., Bottom-up precise synthesis of stable platinum dimers on graphene. *Nat. Commun.* **2017,** *8* (1), 1070.
22. Mackus, A. J. M.; Bol, A. A.; Kessels, W. M. M., The use of atomic layer deposition in advanced nanopatterning. *Nanoscale* **2014,** *6* (19), 10941-10960.
23. Weber, M. J.; Mackus, A. J. M.; Verheijen, M. A.; van der Marel, C.; Kessels, W. M. M., Supported Core/Shell Bimetallic Nanoparticles Synthesis by Atomic Layer Deposition. *Chem. Mater.* **2012,** *24* (15), 2973-2977.
24. Haider, A.; Yilmaz, M.; Deminskyi, P.; Eren, H.; Biyikli, N., Nanoscale selective area atomic layer deposition of TiO_2 using e-beam patterned polymers. *RSC Advances* **2016,** *6* (108), 106109-106119.
25. Vos, M. F. J.; Chopra, S. N.; Verheijen, M. A.; Ekerdt, J. G.; Agarwal, S.; Kessels, W. M. M.; Mackus, A. J. M., Area-Selective Deposition of Ruthenium by Combining Atomic Layer Deposition and Selective Etching. *Chem. Mater.* **2019,** *31* (11), 3878-3882.
26. Bobb-Semple, D.; Nardi, K. L.; Draeger, N.; Hausmann, D. M.; Bent, S. F., Area-Selective Atomic Layer Deposition Assisted by Self-Assembled Monolayers: A Comparison of Cu, Co, W, and Ru. *Chem. Mater.* **2019,** *31* (5), 1635-1645.
27. Tekiel, A.; Topple, J.; Miyahara, Y.; Grütter, P., Layer-by-layer growth of sodium chloride overlayers on an Fe(001)-p(1 × 1)O surface. *Nanotechnology* **2012,** *23* (50), 505602.
28. Arrieta, A.; Mera, S.; Diamant, R.; Fernández-Guasti, M.; Sosa, R.; Escobar-Alarcón, L.; Muñoz, A. F.; Haro-Poniatowski, E., Synthesis and characterization of sodium chloride thin films obtained by pulsed laser deposition. *Appl. Phys. A* **1999,** *69*, S491-S493.
29. Shinar, J.; Shinar, R., An Overview of Organic Light-Emitting Diodes and their Applications. In *Comprehensive Nanoscience and Technology*, Andrews, D. L.; Scholes, G. D.; Wiederrecht, G. P., Eds. Academic Press: Amsterdam, 2011; pp 73-107.
30. Ghareh Bagh, F. S.; Mjalli, F. S.; Hashim, M. A.; Hadj-Kali, M. K. O.; AlNashef, I. M., Solubility of Sodium Chloride in Ionic Liquids. *Ind. Eng. Chem. Res.* **2013,** *52* (33), 11488-11493.
31. Arrieta, A.; Mera, S.; Diamant, R.; Fernández-Guasti, M.; Sosa, R.; Escobar-Alarcón, L.; Muñoz, A. F.; Haro-Poniatowski, E., *Synthesis and characterization of sodium chloride thin films obtained by pulsed laser deposition*. 1999; Vol. 69, p S491-S493.
32. Kern, W., The evolution of silicon wafer cleaning technology. *J. Electrochem. Soc.* **1990,** *137*, 1887-1892.
33. Diwan, A.; Singh, B.; Roychowdhury, T.; Yan, D.; Tedone, L.; Nesterenko, P. N.; Paull, B.; Sevy, E. T.; Shellie, R. A.; Kaykhaii, M.; Linford, M. R., Porous, high capacity coatings for solid phase microextraction by sputtering. *Anal. Chem.* **2016,** *88* (3), 1593-600.
34. Shah, D.; Patel, D. I.; Roychowdhury, T.; Jacobsen, D.; Erickson, J.; Linford, M. R., Optical function of atomic layer deposited alumina (0.5–41.0 nm) from 191 to 1688 nm by spectroscopic ellipsometry with brief literature review. *Surf. Sci. Spectra* **2019,** *26* (2), 026001.
35. Shah, D.; Roychowdhury, T.; Hilfiker, J. N.; Linford, M. R., Polyethylene glycol: Optical constants from 191 to 1688 nm (0.735–6.491 eV) by spectroscopic ellipsometry. *Surf. Sci. Spectra* **2020,** *27* (1), 016001.

المنارة للاستشارات
www.manaraa.com

36. Roychowdhury, T.; Shah, D.; Hilfiker, J. N.; Linford, M. R., Polymethyl methacrylate: Optical properties from 191 to 1688 nm (0.735–6.491 eV) by spectroscopic ellipsometry. *Surf. Sci. Spectra* **2020,** *27* (1), 016002.
37. Singh, B. H., R.; Linford, M. R., Good practices for XPS (and other types of) peak fitting: Use Chi squared, use the abbe criterion, show the sum of fit components, Show the (normalized) residuals, Choose an appropriate background, estimate fit parameter uncertainities, Limit the number of fit parameters, use information from other techniques, and use common sense. *Vacu. Techno. Coat,* **2015,** *December*.
38. Singh, B. H.-G., A.; Terry, J.; Linford, M. R., Good practices for XPS peak fitting, II. *Vacu. Techno. Coat.* **2016,** *August*.
39. Precht, R.; Stolz, S.; Mankel, E.; Mayer, T.; Jaegermann, W.; Hausbrand, R., Investigation of sodium insertion into tetracyanoquinodimethane (TCNQ): results for a TCNQ thin film obtained by a surface science approach. *Phys. Chem. Chem. Phys.* **2016,** *18* (4), 3056-3064.
40. Oswald, S.; Thoss, F.; Zier, M.; Hoffmann, M.; Jaumann, T.; Herklotz, M.; Nikolowski, K.; Scheiba, F.; Kohl, M.; Giebeler, L.; Mikhailova, D.; Ehrenberg, H., Binding Energy Referencing for XPS in Alkali Metal-Based Battery Materials Research (II): Application to Complex Composite Electrodes. *Batteries* **2018,** *4* (3).
41. Savintsev, A.; Gavasheli, Y.; Kalazhokov, Z.; Kalazhokov, K., X-ray photoelectron spectroscopy studies of the sodium chloride surface after laser exposure. *J. Phys.: Conf. Ser.* **2016,** *774*, 012118.
42. Zhang, X.; Schiros, T.; Nordlund, D.; Shin, Y. C.; Kong, J.; Dresselhaus, M.; Palacios, T., X-Ray Spectroscopic Investigation of Chlorinated Graphene: Surface Structure and Electronic Effects. *Adv. Func. Mater.* **2015,** *25* (26), 4163-4169.
43. Hilfiker, J. N.; Singh, N.; Tiwald, T.; Convey, D.; Smith, S. M.; Baker, J. H.; Tompkins, H. G., Survey of methods to characterize thin absorbing films with Spectroscopic Ellipsometry. *Thin Solid Films* **2008,** *516* (22), 7979-7989.
44. Elers, K. E.; Blomberg, T.; Peussa, M.; Aitchison, B.; Haukka, S.; Marcus, S., Film Uniformity in Atomic Layer Deposition. *Chem. Vap. Deposition* **2006,** *12*, 13-24.
45. Jia, E.; Zhou, C.; Wang, W., Uniformity and passivation research of Al_2O_3 film on silicon substrate prepared by plasma-enhanced atom layer deposition. *Nanoscale Res Lett* **2015,** *10*, 129-129.

المنارة للاستشارات
www.manaraa.com

CHAPTER 5: Analysis of Non-conventional samples by Near-Ambient Pressure XPS (NAP-XPS) and examples of XPS Peak Fitting in Material Characterization

5.1 Introduction

X-ray photoelectron Spectroscopy is a surface analytical technique that can measure the elemental composition, chemical states, and electronic states of a material.[1, 2] It is used to probe the topmost 5-15 nm of the surface or substrate. Conventional XPS is performed under ultra-high vacuum (UHV) to allow photoelectrons to travel to the the detector and to limit surface contamination, which cause photoemission attenuation and may decrease detection accuracy.[3] XPS detects and analyzes core electrons from a substrate or thin film deposited on the substrate.

High vacuum is needed to prolong the travel distance of ejected core electrons. This leads to long pumping times and it restricts the number of samples which can be analyzed by XPS.[4] However, there are numerous samples like liquid samples, gases, biological tissues, and cellular substrates etc. that can only be analyzed at higher pressures (2500 Pa or higher in some cases). These samples are incompatible with very low vacuum and will be affected to different extents by degassing or charging due to their vacuum incompatibility and/or insulating nature. A few examples of such samples include polymers, gases at moderate to higher pressures, most biological specimens, most liquid samples, most consumer goods, e.g., Foods, cosmetics, etc., and materials that outgas significantly.

Near-ambient pressure X-ray photoelectron spectroscopy (NAP-XPS) was developed to analyze non-traditional materials that are unable to be analyzed at lower pressures.[5] One of the key differences between NAP-XPS and conventional XPS is that the sample is held at

www.manaraa.com

a much higher pressure in NAP-XPS, for example, ca. 2500 Pa, or even higher in some cases. This is in contrast to conventional XPS, where the main chamber (or analysis chamber) in some cases will be held at significantly lower pressure, ca. 10^{-6} Pa. Some of the advantages of NAP-XPS include reduced sample preparation (often none is needed) and lower pump down times.[6] In NAP-XPS, sample loading and analysis in NAP-XPS can be achieved in a few minutes.

NAP-XPS has a unique way of dealing with charge compensation, where the instrument does not require an electron flood or other similar device. This has been referred to as environmental charge compensation.[7] NAP-XPS compensates for development of positive charge (charging) on the surface of sample in a convenient manner by taking advantage of the residual inert gas (such as nitrogen, argon) that surrounds the sample. That is, X-rays ionize atoms in the gas around the sample and bathe the sample in electrons. The resulting free electrons and cations provide charge compensation for the sample. Of course, the degree of charge compensation here depends on the pressure of the gas around the sample – in the limit of extremely low background pressure little if any charge compensation takes place.

The first, stand-alone, dedicated benchtop NAP-XPS instrument (the EnviroESCA instrument) was very recently introduced by SPECS Surface Nano Analysis GmbH, Berlin, Germany.[4] Chapter 5 focuses on the characterization and analysis of several unconventional materials using this new SPECS instrument, which would be challenging to achieve via conventional XPS. These materials demonstrate the wide range of samples that can now be analyzed with the instrument, and include liquid water,[8] Coca-Cola,[9] a coffee bean,[10] nitrogen gas,[11] zirconia particles,[12] a human tooth,[13] and printed and unprinted office paper.[14] We deposited these data sets in Surf. Sci. Spectra as separate publications.

www.manaraa.com

Section 5.1.1 Liquid water, by near-ambient pressure XPS

5.1.1.1 Statement of Attribution

This document was originally published as Shah, D.; Patel, D. I.; Bahr, S.; Dietrich, P.; Meyer, M.; Thißen, A.; Linford, M. R., Liquid Water, by near-ambient pressure XPS. *Surf. Sci. Spectra* **2019,** *26* (2), 024003.[8] Here, the texts and figures are reproduced with the permission from AIP publishing.

Some information fields are omitted from this document to improve its readability in this format. We refer readers to the original document for complete sample, instrument information, and spectral features.

5.1.1.2 Abstract

Near ambient pressure X-ray photoelectron spectroscopy (NAP-XPS) is a less traditional form of XPS that allows samples to be analyzed at relatively high pressures, i.e., at ca. 2500 Pa, or higher in some cases. With NAP-XPS, XPS can be used to analyze moderately volatile liquids, biological samples, porous materials, and/or polymeric materials that outgas significantly. In this submission, we show survey, O 1*s*, O *KLL*, and valence band NAP-XPS spectra from liquid water, a material that could not be analyzed at moderate pressures by conventional XPS. The O 1*s* signal was fit to two components attributed to liquid and vapor phase water. The carbon in the survey spectrum is attributed to contaminants in the water and/or adventitious carbon.

Keywords: Near-ambient pressure X-ray photoelectron spectroscopy, XPS, water

5.1.1.3 Introduction

المنارة للاستشارات
www.manaraa.com

The analysis of aqueous solutions is of great importance in many areas of science, including analytical chemistry and the biological sciences. Near ambient pressure – X-ray photoelectron spectroscopy (NAP-XPS) is an important technique that allows XPS to be performed on unconventional samples, including moderately volatile liquids, biological samples, porous materials, and/or polymeric materials that outgas significantly.[15-18] Because many of these unconventional materials contain some water, the NAP-XPS spectra of liquid water should be important references for future researchers. This set of articles and the NAP-XPS technique have previously been introduced in Surface science spectra.[19] Data were collected with the SPECS EnviroESCA instrument,[6, 7, 20] and the material was analyzed directly without any sample preparation.

At the moderately low pressures of the NAP-XPS analytical chamber, aqueous solutions show signals from both liquid and vapor phase water. The most characteristic NAP-XPS peak associated with water vapor is the O 1*s* signal at or above 535 eV.[21] NAP-XPS spectra showing this signal have previously been reported in the literature.[22-24] In this contribution, we also show a C 1*s* peak from the sample. Sources of this carbon may include contaminants in the water, which will segregate to the water surface if they are hydrophobic, and/or adventitious carbon.

The O 1*s* spectrum shown here contains two peaks: a gas phase signal at 535.8 eV and a second signal from liquid water at 533.6 eV.[25, 26] These two O 1*s* peaks have different widths, i.e., as expected, the gas phase peak is noticeably narrower.[27] The liquid phase peak was fitted with a Gaussian-Lorentzian sum function (GLS) with 20% Lorentzian character.[28] The gas phase peak was fitted with a Gaussian-Lorentzian product (GLP) function with 80 % Lorentzian character. The Lorentzian fraction in these synthetic peaks was varied to obtain the best fit, as

المنارة للاستشارات
www.manaraa.com

determined by the residual standard deviation of the fit. A Tougaard background was used for this fit.[29] The presence of gas phase signals is a unique feature of NAP-XPS.[6] The O *KLL* Auger signal around 980.0 eV is also shown here.[5] The reference level used for this study is the Fermi level of the instrument.

Table 5.1.1.1. Spectral features of interest

Figure number	Element/ Transition	Peak Energy (eV)	Peak Width FWHM (eV)	Peak Area (eV x cts/s)	Peak Assignment
5.1.1.1	C 1*s*	285.0	4.40	20985.0	Adventitious Carbon
5.1.1.1	O 1*s*	535.0	2.69	2791.5	Oxygen
5.1.1.1	O 2*s*	27.0	4.20	1284.9	Oxygen
5.1.1.1	O KLL	498.1	--	--	Oxygen
5.1.1.1	C 1*s*	510.2*	---	32308.3	---
5.1.1.2	O 1s	533.6	1.56	1665.6	H_2O (l)
5.1.1.2	O 1s	535.6	0.63	813.0	H_2O (g)

* Peak energy value indicated as kinetic energy. Work function of the spectrometer used for this study was 4.4463 eV.

المنارة للاستشارات
www.manaraa.com

5.1.1.4 Specimen Description

a. **Host Material:** H_2O (l)
b. **CAS Registry #:** 7732-18-5
c. **Host Material Characteristics:** homogeneous; powder; amorphous; inorganic compound;
d. **Chemical Name:** Water
e. **Source:** A water bottle purchased from a grocery store in Berlin.
f. **Host Composition:** H_2O
g. **Form:** liquid
h. **Structure:** H_2O (l)
i. **History & Significance:** Water is ubiquitous. It is released by many materials that can be analyzed by NAP-XPS.
j. **As Received Condition:** Liquid water.
k. **Analyzed Region:** Liquid and vapor phase water encountered by the X-ray beam.
l. **Ex Situ Preparation/Mounting:** N/A
m. **In Situ Preparation:** N/A
n. **Charge Control:** Residual gas (Argon, 300 Pa)
o. **Temp. During Analysis:** 300 K
p. **Pressure During Analysis:** 300 Pa
q. **Pre-analysis Beam Exposure:** 30s.

5.1.1.5 Instrument Description

a. **Manufacturer and Model:** SPECS EnviroESCA
b. **Analyzer Type:** spherical sector

المنارة للاستشارات
www.manaraa.com

c. **Detector:** other 1D Delay line detector (1D-DLD)

d. **Number of Detector Elements:** 25

e. **Analyzer Mode:** constant pass energy

f. **Analyzer Pass Energy**: 100 eV (survey spectrum) and 20 eV (narrow spectra)

g. **Throughput ($T=E^N$):** N=0

h. **Excitation Source Window:** silicon nitride

i. **Excitation Source:** Al Ka monochromatic

j. **Source Energy:** 1486.6 eV

k. **Source Strength:** 42 W

l. **Source Beam Size:** 250 μm x 250 μm

m. **Signal Mode:** multichannel direct

n. **Incident Angle:** 55 °

o. **Source-to-Analyzer Angle:** 55 °

p. **Emission Angle:** 0 °

q. **Specimen Azimuthal Angle:** 0 °

r. **Acceptance Angle from Analyzer Axis:** 22 °

s. **Analyzer Angular Acceptance Width:** 44 °

5.1.1.6 Data Analysis Method

a. **Energy Scale Correction:** There was no energy correction required for spectra in this study.

b. **Recommended Energy Scale Shift:** 0 eV

c. **Peak Shape and Background Method:** The liquid phase peak (O-1) was fitted with a Gaussian-Lorentzian sum function (GLS) with 20% Lorentzian character. The gas phase

المنارة للاستشارات
www.manaraa.com

peak (O-2) was fitted with a Gaussian-Lorentzian product (GLP) function with 80 % Lorentzian character. The Lorentzian fraction in these synthetic peaks was varied to obtain the best fit, as determined by the residual standard deviation of this fit. A Tougaard background was used for this fit.

d. **Quantitation Method:** N/A

المنارة للاستشارات
www.manaraa.com

Section 5.1.2 Coca-cola, by near-ambient pressure XPS

5.1.2.1 Statement of Attribution

This document was originally published as Shah, D.; Cushman, C. V.; Bahr, S.; Dietrich, P.; Meyer, M.; Thißen, A.; Linford, M. R., Coca-cola, by near-ambient pressure XPS. *Surf. Sci. Spectra* **2019,** *26* (2), 024005.[9] The O 1*s* spectrum in this document was previously published in Vacuum Technology & Coating (VT&C) magazine (Matthew R. Linford, Tuhin Roychowdhury, Dhruv Shah 'Near Ambient Pressure XPS (NAP-XPS). A New Paradigm for the Technique.' *Vacuum Technology & Coating, August 2018.*) It is gratefully used here with VT&C's permission (see https://www.vtcmag.com).[4]

Some information fields are omitted from this document to improve its readability in this format. We refer readers to the original document for complete sample, instrument information, and spectral features.

5.1.2.2 Abstract

Near ambient pressure-X-ray Photoelectron Spectroscopy (NAP-XPS) is a less traditional form of XPS that allows samples to be analyzed at relatively high pressures, i.e., at ca. 2500 Pa, or higher in some cases. With NAP-XPS, XPS can probe moderately volatile liquids, biological samples, porous materials, and/or polymeric materials that outgas significantly. We present survey spectrum, O 1*s* and C 1*s* narrow scans, of a commercial soft drink, Coca-Cola. Clearly this is a material that could not be analyzed at moderate pressures by conventional XPS. The C 1*s* narrow scan was fit to five synthetic components. The O 1*s* narrow scan shows strong contributions from both liquid and gas phase water. A small N 1*s* signal in the survey spectrum

المنارة للاستشارات
www.manaraa.com

was attributed to background nitrogen. The shape of the uniqueness plot corresponding to the C 1*s* fit suggests that the fit parameters are statistically significant.

5.1.2.3 Introduction

The analysis of food and beverages to assure their quality and safety is of great importance to consumers, companies, and governmental regulators.[30, 31] Accordingly, we present here the near ambient pressure – X-ray photoelectron spectroscopy (NAP-XPS) characterization of Coca-Cola as an example of a surface analysis of a beverage.[19] Data were collected with the SPECS EnviroESCA instrument,[7, 20, 32] and the material was analyzed directly without any sample preparation.

To the best of our knowledge, this is the first paper reporting XPS analysis of a soft drink or energy drink. As expected, however, the literature contains multiple analyses of soft drinks using other techniques such as high performance liquid chromatography (HPLC) and X-ray fluorescence.[33-35] Coca-Cola represents a non-traditional material for XPS analysis; its analysis in the liquid form would not be possible under the normal experimental conditions of a conventional XPS instrument. Some of the main constituents of Coca-Cola, as analyzed by other techniques, are water, a carbohydrate sweetener (corn syrup and cane sugar appear to be used for this beverage in the United States and in other countries, respectively), and caffeine.[33-36]

The NAP-XPS survey spectrum of Coca-Cola is dominated by photoemission from oxygen and carbon. Small N 1*s*, O 2*s*, and valence band signals are also observed. The N 1*s* signal is at 405.0 eV and attributed to residual nitrogen gas in the analysis chamber.

When organic molecules have carbon atoms in different oxidation states, they give rise to different, chemically shifted signals in the C 1*s* envelope.[37, 38] The peak-fitted C 1*s* spectrum

المنارة للاستشارات
www.manaraa.com

presented here shows a strong signal from carbon bonded to carbon and hydrogen (-*C*-C/*C*-H) at 285.2 eV (C-1). Another large signal appears at 286.7 eV (C-3). Based on its position, this signal was attributed primarily to carbon in the sugar in the drink (-*C*-O, C-3).

The C 1*s* spectrum then shows a peak of reasonable intensity at 288.2 eV assigned to carbonyl/acetal carbon (-*C*=O, O-*C*-O, C-4). This type of carbon is also expected from the sugar. Finally, there appears to be a small carbon component at 289.4 eV, arising from carboxyl carbon (O-*C*=O, C-5). The rather high oxidation state of this carboxyl group should result in a secondary shift of any carbon atom next to it. Accordingly, a peak of equal area to the C-5 carboxyl group at 285.9 eV (C-2) is included in the fit. This general approach to peak fitting C 1*s* narrow scans is well documented in the scientific literature.[37, 38]

Carbonated beverages contain dissolved carbon dioxide. Accordingly, there is the possibility that a small quantity of carbon dioxide or carbonic acid may be present in the sample at the point of analysis even after degassing. However, the fitted C 1*s* narrow scan presented here shows no evidence for carbon in this oxidation state.

A uniqueness plot for the C 1*s* fit[39] was generated by setting one parameter in the fit to a series of specific values (the C-3 peak width was sequentially changed), while allowing all of the other parameters in the fit to vary, as they did in the original fit to the C 1*s* spectrum. That is, in the uniqueness analysis, all of the peak heights varied, the C-1 peak position was allowed to vary, all of the peaks positions were constrained relative to the C-1 peak (the C-2, C-3, C-4, and C-5 peaks were constrained to be +0.7, +1.5, +3.0, and +4.2 eV from the C-1 signal), the C-3 peak width was successively constrained to have different values while all the other remaining parameters were allowed to vary as they had in the original fit. Otherwise, in the uniqueness

المنارة للاستشارات
www.manaraa.com

analysis all the peaks were constrained to have the same width. The U-shaped uniqueness plot that was obtained indicates that the fit parameters have statistical significance.

The O 1*s* narrow scan shows two major components that are attributed to oxygen from liquid water at 533.3 eV and oxygen from gas phase water at ca. 535.6 eV.[5, 6, 21] The NAP-XPS O 1*s* spectrum from gas phase water has previously been presented in the literature.[22, 40-43] As expected, the peak from the gas phase water is narrower than the one from the liquid.[6] The small N 1*s* peak in the survey spectrum is presumably due to residual nitrogen gas from the air and/or from the nitrogen that is used to vent the analytical chamber.

All of the synthetic peaks used in this work were Gaussian-Lorentzian product (GLP30) functions with 30 % Lorentzian character.[44] The fraction of Lorentzian character was varied from 10 – 70 % to obtain the best fits, as determined by the minimum value of the residual standard deviation of the fits. All fits were performed with universal polymer (U-Poly) Tougaard[45, 46] backgrounds, which were not subtracted from the data in the results shown here, i.e., the original data are presented. Finally, all peak fitting was with CasaXPS (Casa Software Ltd., Version 2.3.18PR1.0).

Table 5.1.2.1. Spectral features of interest

Figure number	**Element/ Transition**	**Peak Energy (eV)**	**Peak Width FWHM (eV)**	**Peak Area (eV x cts/s)**	**Sensitivity Factor**	**Concentration (at. %)**	**Peak Assignment**
5.1.2.1	O 1*s*	534.0	4.49	17295.2	…	…	Oxygen

المنارة للاستشارات
www.manaraa.com

5.1.2.1	C 1*s*	286.0	4.36	2872.6	…	…	Carbon
5.1.2.1	N 1*s*	402.0	4.71	560.6	…	…	Nitrogen
5.1.2.1	Valence Band	8.0	3.98	297.5	…	…	Valence Band
5.1.2.2	C 1*s*	285.2	1.09	107.9	1.0	42.5	-C-C/C-H
5.1.2.2	C 1*s*	285.9	1.09	5.4	1.0	2.1	-C-C(=O)O
5.1.2.2	C 1*s*	285.2	1.09	104.5	1.0	41.1	-C-O
5.1.2.2	C 1*s*	285.2	1.09	30.7	1.0	12.1	(-C=O, O-C-O, and/or -C(=O)-N)
5.1.2.2	C 1*s*	285.2	1.09	5.4	1.0	4.1	(O-C=O)
5.1.2.3	O 1*s*	533.6	1.63	1116.3	2.47	75.0	H_2O(l)
5.1.2.3	O 1*s*	535.6	0.53	371.4	2.47	25.0	H_2O(g)

5.1.2.4 Specimen Description

a. **Host Material:** Coca-Cola

b. **CAS Registry #:** N/A

للاستشارات المنارة
www.manaraa.com

c. **Host Material Characteristics:** homogeneous; liquid; amorphous; organic compound; Other

d. **Chemical Name:** Coca-Cola

e. **Source:** A bottle of Coca-Cola purchased from a fast food restaurant in Berlin, Germany.

f. **Host Composition:** Coca-Cola

g. **Form:** Liquid

h. **Structure:** N/A

i. **History & Significance:** Coco-Cola is an extremely common soft drink that is available in many countries. Its formulation varies somewhat from country to country. For example, corn syrup is used as the sweetener in the beverage in the United States, while sugar is employed for this purpose in some other countries, including Germany. Coca-Cola is available in related forms, including diet Coca-Cola, sugar-free Coca-Cola, reduced-calorie Coca-Cola, etc.

j. **As Received Condition:** As purchased, commercial soft drink. The sample was outgassed using sonication to remove carbon dioxide from it to avoid ‘fizzing over’ in the chamber.

k. **Analyzed Region:** The surface of the soft drink.

l. **Ex Situ Preparation/Mounting:** Sample was poured into a Petri dish and analyzed.

m. **In Situ Preparation:** N/A

n. **Charge Control:** Residual gas (Water vapor and Nitrogen gas, 500 Pa)

o. **Temp. During Analysis:** 300 K

p. **Pressure During Analysis:** 500 Pa

q. **Pre-analysis Beam Exposure:** 30 s.

www.manaraa.com

5.1.2.5 Instrument Description

a. **Manufacturer and Model:** SPECS EnviroESCA
b. **Analyzer Type:** spherical sector
c. **Detector:** other 1D Delay line detector (1D-DLD)
d. **Number of Detector Elements:** 25
e. **Analyzer Mode:** constant pass energy
f. **Throughput ($T=E^N$):** N=0
g. **Excitation Source Window:** Silicon nitride
h. **Excitation Source:** Al Ka monochromatic
i. **Source Energy:** 1486.6 eV
j. **Source Strength:** 42 W
k. **Source Beam Size:** 250 µm x 250 µm
l. **Signal Mode:** multichannel direct
m. **Incident Angle:** 55 °
n. **Source-to-Analyzer Angle:** 55 °
o. **Emission Angle:** 0 °
p. **Specimen Azimuthal Angle:** 0 °
q. **Acceptance Angle from Analyzer Axis:** 22 °
r. **Analyzer Angular Acceptance Width:** 44 °

5.1.2.6 Data Analysis Method

a. **Energy Scale Correction:** No correction was needed for this study.
b. **Recommended Energy Scale Shift:** 0

المنارة للاستشارات
www.manaraa.com

c. **Peak Shape and Background Method:** All peak fitting was with Gaussian-Lorentzian product functions with 30% Lorentzian character (GLP30). The degree of Lorentzian character in the synthetic GLP peaks were adjusted from 10 – 70% to optimize the fits. The C 1*s* peak fit was performed with a universal polymer (U-Poly) Tougaard background. All peak fitting was performed with CasaXPS (Casa Software Ltd., Version 2.3.18PR1.0).

d. **Quantitation Method:** N/A.

5.1.2.7 Acknowledgments

The O 1*s* spectrum in this document was previously published in Vacuum Technology & Coating (VT&C) magazine (Matthew R. Linford, Tuhin Roychowdhury, Dhruv Shah 'Near Ambient Pressure XPS (NAP-XPS). A New Paradigm for the Technique.' *Vacuum Technology & Coating, August 2018.*) It is gratefully used here with VT&C's permission (see https://www.vtcmag.com).

www.manaraa.com

Section 5.1.3 Coffee bean, by near-ambient pressure XPS

5.1.3.1 Statement of Attribution

This document was originally published as Shah, D.; Bahr, S.; Dietrich, P.; Meyer, M.; Thißen, A.; Linford, M. R. Coffee bean, by near-ambient pressure XPS. *Surf. Sci. Spectra* **2019,** *26* (2), 024006.[9] Here, the texts and figures are reproduced with the permission from AIP publishing. The survey and C 1*s* narrow scans were published previously in an application note (#000388) by SPECS, GmbH, (Berlin, Germany) entitled "XPS surface analysis of a coffee bean with EnviroESCA".

Some information fields are omitted from this document to improve its readability in this format. We refer readers to the original document for complete sample, instrument information, and spectral features.

5.1.3.2 Abstract

Near ambient pressure x-ray photoelectron spectroscopy (NAP-XPS) is a less traditional form of XPS that allows samples to be analyzed at relatively high pressures, i.e., up to 2500 Pa, or higher in some cases. NAP-XPS can probe moderately volatile liquids, biological samples, porous materials, and/or polymeric materials that outgas significantly. We present NAP-XPS C 1*s* and O 1*s* narrow scans and a survey spectrum of a coffee bean, a material that would be difficult to be analyze by conventional XPS. The survey spectrum shows small amounts of sulfur and calcium.

5.1.3.3 Introduction

المنارة للاستشارات
www.manaraa.com

The analysis of food and beverages to assure their quality and safety is of great importance to consumers and governmental regulators.[30, 31] Accordingly, we demonstrate here the analysis of a foodstuff by near ambient pressure – x-ray photoelectron spectroscopy (NAP-XPS), i.e., a coffee bean.[19] Data were collected with the SPECS EnviroESCA instrument,[7] and the material (a coffee bean) was analyzed directly without any sample preparation.

Non-conducting and outgassing samples like coffee beans are a challenge for classical XPS. Accordingly, NAP-XPS analysis of foodstuffs represents a new opportunity to quickly study their compositions, purity, provenance, etc.[31] Near-ambient XPS, is a less conventional form of XPS, which works at higher working pressure.[7, 32] The working pressure during the analysis was 100 Pa and the background gas was argon. The survey spectrum of the coffee bean analyzed herein is dominated by a large C 1*s* peak.

The uncorrected position of this peak indicates that the sample charged during data collection. The narrow spectra were energy corrected to position C 1*s* at 285.0 eV.[47] The energy correction positioned C 1*s* at 285.9 eV for the survey spectrum. The tail to lower binding energy in the C 1*s* narrow scan is probably due to incomplete charge neutralization of the surface. A moderately large O 1*s* peak is also present in the survey spectrum, along with smaller N 1*s*, Ca 2*p*, S 2*s*, and S 2*p* signals. The most probable source for nitrogen in the survey spectrum is residual gas used to vent the system. Coffee beans contain small amounts of calcium and sulfur.[48, 49]

The sulfur observed in the survey spectrum was attributed, at least in part, to 2-furfurythiol, which contributes strongly to coffee's flavor and characteristic smell.[50, 51] The literature contains reports of the analysis of coffee by other techniques, which include high performance liquid chromatography and ultra-high performance liquid chromatography.[52, 53] A Universal Polymer (U Poly) Tougaard background was used for calculation of peak widths and

المنارة للاستشارات
www.manaraa.com

peak areas.[45, 54] C 1*s* narrow scan shows a broad peak at 285.0 eV. O 1*s* narrow scan contains a peak at 530.9 eV.[21]

Table 5.1.3.1. Spectral features of interest

Figure number	Element/ Transition	Peak Energy (eV)	Peak Width FWHM (eV)	Peak Area (eV x cts/s)	Sensitivity Factor	Concentration (at. %)	Peak Assignment
5.1.3.1	O 1*s*	533.0	3.87	6370.5	…	…	Oxygen
5.1.3.1	O *KLL**	495.5	4.18	976.3	…	…	O KLL
5.1.3.1	N 1*s*	402.1	5.08	1662.4	…	…	Nitrogen
5.1.3.1	O 2*s*	26.1	2.97	292.1	…	…	Oxygen
5.1.3.1	S 2*p*	169.1	2.44	320.7			Sulfur
5.1.3.1	S 2*p*	233.1	5.04	402.4	…	…	Sulfur
5.1.3.1	C 1*s*	285.9	3.00	17261.8	…	…	Carbon
5.1.3.1	Ca 2*p*	348.1	6.04	1536.1	…	…	Calcium
5.1.3.1	C *KLL**	259.2	1.64	340.1	…	…	Carbon
5.1.2.3	C 1*s*	285.0	1.86	3211.7	1.00	86.3	C-C/C-H

المنارة للاستشارات
www.manaraa.com

5.1.2.3	O 1*s*	530.9	2.89	1225.0	2.47	13.7	C-O

*Peak energy value indicated as kinetic energy. Work function of the spectrometer used for this study was 4.4463 eV.

5.1.3.4 Specimen Description (ACCESSION #01541)

a. **Host Material:** Coffee bean
b. **CAS Registry #:** unknown
c. **Host Material Characteristics:** inhomogeneous; solid; amorphous; organic compound; Other
d. **Chemical Name:** Coffee bean
e. **Source:** Grocery store in Berlin, Germany
f. **Host Composition:** Coffee bean
g. **Form:** Solid
h. **Structure:** Unknown
i. **History & Significance:** Coffee beans are ground to obtain coffee, a caffeinated beverage consumed widely all over of the world.
j. **As Received Condition:** A single roasted coffee bean was selected, put in a Petri dish, and placed on the sample plate of the instrument. No other sample preparation was performed.
k. **Analyzed Region:** Region of the coffee bean encountered by the X-ray beam.
l. **Ex Situ Preparation/Mounting:** Sample was placed on the instrument stage.
m. **In Situ Preparation:** N/A
n. **Charge Control:** Residual gas (Argon, 100 Pa)
o. **Temp. During Analysis:** 300 K

المنارة للاستشارات
www.manaraa.com

p. **Pressure During Analysis:** 100 Pa

q. **Pre-analysis Beam Exposure:** 30 s.

5.1.3.5 Instrument Description

a. **Manufacturer and Model:** SPECS EnviroESCA

b. **Analyzer Type:** spherical sector

c. **Detector:** other 1D Delay line detector (1D-DLD)

d. **Number of Detector Elements:** 25

e. **Analyzer Mode:** constant pass energy

f. **Throughput ($T=E^N$):** N=0

g. **Excitation Source Window:** silicon nitride

h. **Excitation Source:** Al Ka monochromatic

i. **Source Energy:** 1486.6 eV

j. **Source Strength:** 42 W

k. **Source Beam Size:** 250 µm x 250 µm

l. **Signal Mode:** multichannel direct

m. **Incident Angle:** 55 °

n. **Source-to-Analyzer Angle:** 55 °

o. **Emission Angle:** 0 °

p. **Specimen Azimuthal Angle:** 0 °

q. **Acceptance Angle from Analyzer Axis:** 22 °

r. **Analyzer Angular Acceptance Width:** 44 °

المنارة للاستشارات
www.manaraa.com

5.1.3.6 Data Analysis Method

a. **Energy Scale Correction:** The survey scan and C 1*s* and O 1*s* narrow scans were shifted by -8.1 eV, which positioned the hydrocarbon (C-C/C-H, C-1) signal in the C 1*s* narrow scan at 285.0 eV.[47]

b. **Recommended Energy Scale Shift:** -8.1 eV.

c. **Peak Shape and Background Method:** A Universal Polymer Tougaard background (U Poly Tougaard) was used for calculation of peak areas and peak widths.[54] All the analysis performed in this work was with CasaXPS (Casa Software Ltd., Version 2.3.18PR1.0).

d. **Quantitation Method:** Data was analyzed using CasaXPS.

5.1.3.7 Acknowledgements

The survey and C 1*s* narrow scans in this submission were published previously in an application note (#000388) by SPECS, GmbH, (Berlin, Germany) entitled “XPS surface analysis of a coffee bean with EnviroESCA”. Content from this application note is reused here with their permission.

المنارة للاستشارات
www.manaraa.com

Section 5.1.4 Nitrogen gas (N_2), by near-ambient pressure XPS

5.1.4.1 Statement of Attribution

This document was originally published as Shah, D.; Bahr, S.; Dietrich, P.; Meyer, M.; Thißen, A.; Linford, M. R. Nitrogen gas (N_2), by near-ambient pressure XPS. *Surf. Sci. Spectra* **2019,** *26* (1), 014023.[10] Here, the texts and figures are reproduced with the permission from AIP publishing. The survey and N 1*s* spectra in this document were previously published in Vacuum Technology & Coating (VT&C) magazine (Matthew R. Linford, Tuhin Roychowdhury, Dhruv Shah 'Near Ambient Pressure XPS (NAP-XPS). A New Paradigm for the Technique.' *Vacuum Technology & Coating, August 2018.*) This content is gratefully used here with VT&C's permission (see https://www.vtcmag.com).

Some information fields are omitted from this document to improve its readability in this format. We refer readers to the original document for complete sample, instrument information, and spectral features.

5.1.4.2 Abstract

Near ambient pressure-x-ray photoelectron spectroscopy (NAP-XPS) is a less traditional form of XPS that allows samples to be analyzed at relatively high pressures, i.e., at ca. 2500 Pa, or even higher in some cases. With NAP-XPS, XPS can probe moderately volatile liquids, biological samples, porous materials, and/or polymeric materials that outgas significantly. In this submission, we show NAP-XPS survey and narrow scans from nitrogen gas (N_2), a material that could not be analyzed at moderate pressures by conventional approaches. Nitrogen gas is an important reference material for NAP-XPS because residual N_2 from the air and/or venting produces an N 1*s* signal in many NAP-XPS spectra. Nitrogen gas may also be deliberately

المنارة للاستشارات
www.manaraa.com

employed as the gaseous background for NAP-XPS experiments. The survey spectrum of N_2 gas contains N 1*s*, N 2*s*, and N *KLL* (Auger), and valence band signals.

5.1.4.3 Introduction

We present here the near ambient pressure – X-ray photoelectron spectroscopy (NAP-XPS) characterization of nitrogen gas, N_2. Data were collected with the SPECS EnviroESCA instrument,[7] and the N_2(g) was analyzed directly without any sample preparation. Conventional XPS instruments operate under high vacuum (ca. $1.34e^{-6}$ Pa or lower), while NAP-XPS data are collected at pressures close to 2500 Pa, or even higher in some cases.[15-18] N_2 gas is a common constituent of many of the gas phases that surround samples in NAP-XPS.

The NAP-XPS survey spectrum of N_2(g) shows N 1*s*, N 2*s*, N *KLL* (Auger) and valence band signals. NAP-XPS spectra showing these signals have previously been presented in the literature. For example, Siegbahn *et al.* previously reported the XPS spectra of various gaseous molecules, including N_2, O_2, and NO_2.[55] The N 1*s* signal they reported for N_2 appeared at 410.0 eV with a FWHM of 0.9 eV. In this study, the N 1*s* peak appears at 406.0 eV because it was referenced to the Fermi level of the instrument.

This value is similar to that reported by Honda and Hirokawa.[56] If we referenced our peak signals to the vacuum level, our N 1s signal would appear at 410.4 eV.[47] Also present in the survey spectrum is a small O 1*s* peak at 540.0 eV, which is attributed to O_2 gas.[21] The small amount of oxygen present in our spectrum was from opening/closing the instrument door during sample transfer. Compared to the XPS spectra of solids, the NAP-XPS spectra of N_2 gas appear unusual because of their flat backgrounds. The absence of a background that rises towards higher

المنارة للاستشارات
www.manaraa.com

binding energies indicates that photoelectrons from gas phase N_2 do not undergo inelastic collisions.

Table 5.1.4.1. Spectral features of interest

Figure number	Element/ Transition	Peak Energy (eV)	Peak Width FWHM (eV)	Peak Area (eV x cts/s)	Peak Assignment
5.1.4.1	N 1*s*	406.0	1.92	23132.9	$N_2(g)$
5.1.4.1	O 1*s*	540.0	2.80	818.1	$O_2(g)$
5.1.4.1	N *KLL**	363.2*	5.50	3804.1	Nitrogen Auger
5.1.4.2	N 1*s*	405.9	0.52	2906.9	$N_2(g)$
5.1.4.3	N *KLL**	362.9*	3.32	639.2	Nitrogen Auger

*Peak energy value indicated as kinetic energy. Work function of the spectrometer used for this study was 4.4463 eV.

5.1.4.4 Specimen Description

a. **Host Material:** Nitrogen gas, N_2
b. **CAS Registry #:** 7727-37-9
c. **Host Material Characteristics:** homogeneous; gas; amorphous; inorganic material
d. **Chemical Name:** Nitrogen

المنارة للاستشارات
www.manaraa.com

e. **Source:** Nitrogen was obtained from a pressurized canister from a commercial source: Air Liquide, Düsseldorf, Germany.
f. **Host Composition:** Nitrogen
g. **Form:** Gas
h. **Structure:** N_2
i. **History & Significance:** Nitrogen is the chief component of air; hence it is an important reference material for NAP-XPS.
j. **As Received Condition:** A canister under pressure.
k. **Analyzed Region:** Nitrogen gas as encountered by the X-ray beam.
l. **Ex Situ Preparation/Mounting:** N/A.
m. **In Situ Preparation:** N/A
n. **Charge Control:** Using the sample gas (N_2, 200 Pa)
o. **Temp. During Analysis:** 300 K
p. **Pressure During Analysis:** 200 Pa
q. **Pre-analysis Beam Exposure:** 30 s.

5.1.4.5 Instrument Description

a. **Manufacturer and Model:** SPECS EnviroESCA
b. **Analyzer Type:** spherical sector
c. **Detector:** other 1D delay line detector (1D-DLD)
d. **Number of Detector Elements:** 25
e. **Analyzer Mode:** constant pass energy
f. **Throughput ($T=E^N$):** N=0
g. **Excitation Source Window:** silicon nitride

للاستشارات المنارة
www.manaraa.com

h. **Excitation Source:** Al Kα monochromatic
i. **Source Energy:** 1486.6 eV
j. **Source Strength:** 42 W
k. **Source Beam Size:** 250 μm x 250 μm
l. **Signal Mode:** multichannel direct
m. **Incident Angle:** 55 ˚
n. **Source-to-Analyzer Angle:** 55 ˚
o. **Emission Angle:** 0 ˚
p. **Specimen Azimuthal Angle:** 0 ˚

5.1.4.6 Data Analysis Method

a. **Energy Scale Correction:** There were no energy corrections to the spectra in this study.
b. **Recommended Energy Scale Shift:** 0
c. **Peak Shape and Background Method:** There was no peak fitting performed for this study. A linear background was used for calculation of the area under peak.
d. **Quantitation Method:** N/A.

5.1.4.7 Acknowledgments

The survey and N 1*s* spectra in this document were previously published in Vacuum Technology & Coating (VT&C) magazine (Matthew R. Linford, Tuhin Roychowdhury, Dhruv Shah 'Near Ambient Pressure XPS (NAP-XPS). A New Paradigm for the Technique.' *Vacuum Technology & Coating, August 2018.*) This content is gratefully used here with VT&C's permission (see https://www.vtcmag.com).

المنارة للاستشارات
www.manaraa.com

Section 5.1.5 Zirconia particles, by near-ambient pressure XPS

5.1.5.1 Statement of Attribution

This document was originally published as Shah, D.; Bahr, S.; Dietrich, P.; Meyer, M.; Thißen, A.; Linford, M. R. Nitrogen (N_2), by near-ambient pressure XPS. *Surf. Sci. Spectra* **2019,** *26* (2), 024001.[10] Here, the texts and figures are reproduced with the permission from AIP publishing. Some information fields are omitted from this document to improve its readability in this format. We refer readers to the original document for complete sample, instrument information, and spectral features.

5.1.5.2 Abstract

Near ambient pressure-X-ray photoelectron spectroscopy (NAP-XPS) is a less traditional form of XPS that allows samples to be analyzed at relatively high pressures, i.e., at ca. 2500 Pa, or even higher in some cases. With NAP-XPS, XPS can probe particles, moderately volatile liquids, biological samples, porous materials, and/or polymeric materials that outgas significantly. In this submission we show survey, narrow (Zr 3*p*, Zr 3*d*, and O 1*s*), and Auger (O *KLL*) NAP-XPS scans of ZrO_2 particles. Charge compensation for this insulating sample took place via the residual gas in the chamber. Zirconia is an important ceramic material. Accordingly, the NAP-XPS spectra of zirconia should be useful references.

5.1.4.3 Introduction

Zirconia is an important material. It finds numerous applications as a coating, and also as a substrate for various deposition techniques.[57, 58] For example, zirconia is used as a

المنارة للاستشارات
www.manaraa.com

protective coating on titania particles, and it is a commonly used ceramic material in dentistry.[59] Here we present the near ambient pressure – X-ray photoelectron spectroscopy (NAP-XPS) characterization of zirconium oxide (ZrO_2) particles. The zirconia particles analyzed in this work are insulating, which means that surface analysis by XPS may be challenging because of sample charging and/or differential charging.

NAP-XPS works at higher pressures than conventional XPS (up to 2500 Pa, or higher in some cases), hence eliminating the need for charge compensation – charge compensation takes place through the residual gas in the chamber.[15, 22] The ability to analyze samples at higher pressures makes NAP-XPS an ideal surface analytical technique for many non-conventional materials.[60]

Historically, XPS has been performed under ultrahigh vacuum (UHV). These conditions allow photoelectrons to travel to the detector, however, many important samples are not UHV compatible. The need for XPS analysis of materials with little vacuum compatibility has led to the development of near-ambient pressure XPS (NAP-XPS).[15] Higher operating pressure inside the sample chamber leads to lower signal strength at higher binding energy (lower kinetic energy).[40] Data were collected with the SPECS EnviroESCA instrument,[7] and the zirconia particles were analyzed directly without any sample preparation.

The survey spectrum of the zirconia particles shows zirconium and oxygen as major components, and carbon as a minor one. In this spectrum, the Zr 3*s*, Zr $3p_{1/2}$, Zr $3p_{3/2}$, Zr 3*d*, Zr 4*s*, Zr 4*p*, O 2*s* peaks appear at 433.0 eV, 347.0 eV, 333.0 eV, 183.0 eV, 53.1 eV, 30.9 eV, and 23.0 eV respectively.[61] The Zr 3d peak consists of overlapping Zr $3d_{3/2}$ and Zr $3d_{5/2}$ signals. The O 1*s* and O *KLL* peaks occur at 527.1 eV and 976.0 eV, respectively.[21, 62, 63] The C 1*s* peak was used as a reference to energy correct the survey and narrow scans.[47] A expanded survey spectrum of the

المنارة للاستشارات
www.manaraa.com

zirconia particles shows all the signals from 0 – 600 eV; this survey spectrum helps to identify the zirconium peaks.

The narrow scan of the Zr 3*d* region appears to show two overlapping peaks attributable to the Zr $3d_{3/2}$ and Zr $3d_{5/2}$ signals. The Zr 3*p* narrow scan clearly shows two peaks attributable to the Zr $3p_{1/2}$ and Zr $3p_{3/2}$ signals. Oxygen, which is a major constituent of zirconium oxide, appears as a single broad peak at 527.1 eV.

Table 5.1.5.1. Spectral features of interest

Figure number	Element/ Transition	Peak Energy (eV)	Peak Width FWHM (eV)	Peak Area (eV x cts/s)	Sensitivity Factor	Concentration (at. %)	Peak Assignment
5.1.5.1	O 1*s*	530.0	4.87	43579.4	2.48	63.31	ZrO_2
5.1.5.1	O *KLL*[*]	510.0	6.86	8074.1	…	…	ZrO_2
5.1.5.1	O 2*s*	23.0	3.80	429.5	…	…	ZrO_2
5.1.5.1	Zr 3*s*	433.0	5.10	6300.3	7.55	32.17	ZrO_2
5.1.5.1	Zr $3p_{1/2}$	347.0	5.21	23385.0	…	…	ZrO_2
5.1.5.1	Zr $3p_{3/2}$	333.0	5.38	39825.7	…	…	ZrO_2
5.1.5.1	C 1*s*	285.0	4.65	1372.3	…	…	ZrO_2

المنارة للاستشارات
www.manaraa.com

5.1.5.1	Zr 3*d*	183.0	5.26	67045.1	…	…	ZrO_2
5.1.5.1	Zr 3*d*	53.1	5.26	67046.1	…	…	ZrO_2
5.1.5.1	Zr 4*p*	30.9	4.40	8682.1	…	…	ZrO_2
5.1.5.3	Zr 3*d*	181.3	4.39	11515.6	…	…	ZrO_2
5.1.5.4	Zr $3p_{3/2}$	329.4	3.72	6631.7	…	…	ZrO_2
5.1.5.4	Zr $3p_{1/2}$	343.8	3.51	3517.7	…	…	ZrO_2
5.1.5.1	O 1*s*	527.1	3.38	9139.9	…	…	ZrO_2

*Peak energy value indicated as kinetic energy. Work function of the spectrometer used for this study was 4.4463 eV.

5.1.5.4 Specimen Description

a. Host Material: Zirconium Oxide

b. CAS Registry #: 1314-23-4

c. Host Material Characteristics: Homogeneous; solid; unknown crystallinity; inorganic compound; Other

d. Chemical Name: Zirconium oxide, Zirconia

e. Source: A 50 g sample of zirconium (IV) oxide, 99 % trace metal analysis, 5 µm diameter, was purchased from Sigma-Aldrich. A small amount of these particles were used in this analysis.

f. Host Composition: Zirconium oxide

المنارة للاستشارات
www.manaraa.com

g. Form: Solid

h. Structure: ZrO_2

i. History & Significance: Zirconium oxide is one of the most studied ceramic materials. It is commonly used as a hard ceramic in fields like dentistry. Zirconium oxide is a common substrate for thin-film deposition processes.

j. As Received Condition: The material was used as received without any sample preparation.

k. Analyzed Region: Zirconium oxide particles were gently pressed as pellets and mounted on carbon tape. The surface of the zirconium oxide particles was analyzed using x-rays.

l. Ex Situ Preparation/Mounting: N/A

m. In Situ Preparation: N/A

n. Charge Control: Residual gas (Nitrogen gas, 200 Pa)

o. Temp. During Analysis: 300 K

p. Pressure During Analysis: 200 Pa

q. Pre-analysis Beam Exposure: 30 s.

5.1.5.5 Specimen Description

a. Manufacturer and Model: SPECS EnviroESCA

b. Analyzer Type: spherical sector

c. Detector: other 1D Delay line detector (1D-DLD)

d. Number of Detector Elements: 25

e. Analyzer Mode: constant pass energy

f. Throughput ($T=E^N$): N=0

g. Excitation Source Window: silicon nitride

h. Excitation Source: Al Ka monochromatic

المنارة للاستشارات
www.manaraa.com

i. Source Energy: 1486.6 eV

j. Source Strength: 42 W

k. Source Beam Size: 250 m x 250 m

l. Signal Mode: multichannel direct

m. Incident Angle: 55°

n. Source-to-Analyzer Angle: 55°

o. Emission Angle: 0°

p. Specimen Azimuthal Angle: 0°

q. Acceptance Angle from Analyzer Axis: 22°

r. Analyzer Angular Acceptance Width: 44°

5.1.5.6 Data Analysis Method

a. Energy Scale Correction: The spectra were shifted to position the C 1*s* peak at 285.0 eV.[47]

b. Recommended Energy Scale Shift: An energy correction of -18.1 eV should be applied to survey and Zr 3*d*, Zr 3*p*, O 1*s* narrow spectra. An energy correction of -15.1 eV was applied to the shortened survey spectrum.

c. Peak Shape and Background Method: A Shirley background was used to calculate peak area for different regions in the survey and narrow spectra.[29]

d. Quantitation Method: The elemental composition was calculated using standard SPECS software.

المنارة للاستشارات
www.manaraa.com

Section 5.1.6 Human tooth, by near-ambient pressure XPS

5.1.6.1 Statement of Attribution

This document was originally published as Shah, D.; Roychowdhury, T.; Bahr, S.; Dietrich, P.; Meyer, M.; Thißen, A.; Linford, M. R. Human Tooth, by near-ambient pressure x-ray photoelectron spectroscopy. *Surf. Sci. Spectra* **2019,** *26* (1), 014016.[10] Here, the texts and figures are reproduced with the permission from AIP publishing. Some information fields are omitted from this document to improve its readability in this format. We refer readers to the original document for complete sample, instrument information, and spectral features.

5.1.6.2 Abstract

Near ambient pressure X-ray photoelectron spectroscopy (NAP-XPS) is a less traditional form of XPS that allows samples to be analyzed at relatively high pressures, i.e., at ca. 2500 Pa. NAP-XPS can be used to analyze moderately volatile liquids, biological samples, porous materials, and/or polymeric materials that outgas significantly. We present the NAP-XPS survey, C 1*s*, O 1*s*, Ca 2*p*, and P 2*p* narrow scans from an adult molar tooth, a biological material that would be challenging to analyze by conventional XPS.

No pretreatment or cleaning of this dental specimen was performed prior to analysis. Three different regions (top, middle, and root) of the tooth were analyzed. The survey spectra, which differed considerably from each other, show the presence of carbon, oxygen, nitrogen, calcium, and phosphorous. Tin and sulfur are also present in small amounts on the top part of the tooth. C 1*s* narrow spectra are well fitted with four synthetic peaks.

5.1.6.3 Introduction

المنارة للاستشارات
www.manaraa.com

Human tooth are common body parts used for mechanically breaking down food by cutting and crushing it. They also contribute to the general, facial appearance of an individual; consumers spend large amounts of money annually to straighten and whiten their tooth. Human teeth generally consist of four major parts: tooth enamel, dentin, cementum, and dental pulp.[64] Tooth enamel represents the upper, white visible protective covering of the tooth. It is mostly minerals (96%), with hydroxyapatite [$Ca_{10}(PO_4)(OH)_2$] being one of its primary components.[65, 66] Fluoride treatment has a protective effect on teeth as it substitutes into hydroxyapatite, which increases the material's resistance to acids.[67] We did not see any evidence of fluorine in the survey scans of our samples of teeth.

There have been several reports of XPS analyses of teeth using conventional instrumentation.[65, 67-71] However, conventional XPS is a less than ideal technique for analyzing human teeth because of their insulating nature and their ability to outgas significantly. Accordingly, in this analysis of a human tooth, we employ NAP-XPS, which should be better suited for this type of sample.[18, 22, 60, 72] The pre-molar adult human tooth analyzed in this study was donated by a volunteer. Three of its regions were sampled: top, middle, and root. This study confirms that human tooth can be analyzed directly by XPS without any special pretreatment.

The C 1*s* narrow scans obtained in this work were fit with four synthetic components, which represent different oxidation states for carbon.[37, 65, 68] Aliphatic carbon, carbon bonded to carbon and hydrogen (*C*-C/*C*-H, C(0), C-1) at ca. 285.0 eV, is the major synthetic carbon component in all the C 1*s* envelopes. The second carbon component (*C*-O, C(I), C-2), i.e., carbon bonded through a single bond to oxygen, appears at ca. 286.4 eV. A third form of carbon (*C*=O and/or O-*C*-O, C(II), C-3) appears at ca. 287.9 eV. It is attributed to carbonyl carbon and/or carbon bonded to oxygen via two different single bonds. The last carbon component appears at ca. 289.3

www.manaraa.com

eV. It is attributed to carboxyl carbon (O-*C*=O, C(III), C-4). We recognize that the carbon observed on these uncleaned samples may or may not represent the true chemistry of the tooth. Nevertheless, the methodology outlined here for fitting C 1*s* narrow scans should be useful in the analysis of other similar materials.

All of the synthetic peaks used for fitting a given C 1*s* envelope were constrained to have the same width. This general approach for peak fitting (keeping all of the peak widths roughly constant in a fit) is employed by Beamson and Briggs in their analysis of organic polymers.[38] The synthetic peaks used to fit the C 1*s* envelopes here were Gaussian-Lorentzian product (GLP30) functions,[28] with 30% Lorentzian character, where the Lorentzian character was first varied from 10 – 90% to obtain the best fits, as determined by the lowest values of the residual standard deviations of the fits. All of the fits employed Tougaard backgrounds.[45] The C 1*s* spectra were shifted in energy so that the aliphatic component of the fits was at 285.0 eV.

Uniqueness plots[73] were generated to test for fit parameter correlation in the C 1*s* fits. This was done by constraining the peak width of the C-1 fit component to different designated values (0.24 to 3.94 eV), while allowing the remaining parameters to vary as they had in the original fit. For example, in the uniqueness plot of the C 1*s* envelope from the top part of the adult tooth (see **Figure 5.1.6.5.**), all of the peak heights varied, the C-1 peak position varied, all of the other peak positions were constrained relative to the C-1 peak (the C-2, C-3, and C-4 peaks were constrained to be +1.4, +2.9, and +4.3 eV from the C-1 signal), and the peak widths were constrained to be same (although this parameter varied as it had in the original fit), except for the width of the C-1 peak, which was forced to take on a range of specific values. Similar approaches were used to obtain uniqueness plots for the other C 1s spectra. 'U-shaped' uniqueness plots were

المنارة للاستشارات
www.manaraa.com

obtained for all the fits (see example in **Figure 5.1.6.5.)**, which show that the fit parameters in these fits have statistical significance.

The insulating nature of the samples required charge correction for all of the survey and narrow scans. The narrow scans were shifted such that the hydrocarbon part (reference peak) for each part of adult tooth was at 285.0 eV. This mandated a different energy correction for each part of the analyzed tooth. The energy correction used for the top, middle, and root of the tooth were -3.3 eV, -8.7 eV, and -6.2 eV. The pressure in the analytical chamber and charging state of the sample were constant over the entire set of measurements for each individual sample region. Thus, the different degrees of charging for the three analyzed regions reflects inhomogeneities in the surface/material chemistry of the sample at the three spots that were probed. Data were collected with the Specs EnviroESCA instrument, and tooth samples were analyzed directly without any sample preparation.[7] The EnviroESCA works at much higher pressures than conventional XPS (up to 2500 Pa).[74]

Table 5.1.6.1. Spectral features of interest

Figure number	**Element/ Transition**	**Peak Energy (eV)**	**Peak Width FWHM (eV)**	**Peak Area (eV x cts/s)**	**Peak Assignment**
5.1.6.1	O 2s	26.7	4.03	2495.6	Oxygen
5.1.6.1	P 2*p*	133.7	2.96	955.6	Phosphorous
5.1.6.1	S 2*p*	165.7	3.72	654.3	Sulfur

المنارة للاستشارات
www.manaraa.com

5.1.6.1	P 2*s*	190.7	4.34	1125.3	Phosphorous
5.1.6.1	C 1*s*	285.7	4.15	13051.6	Carbon
5.1.6.1	Ca 2*p*	347.7	3.50	2756.8	Calcium
5.1.6.1	N 1*s*	399.7	2.90	4612.8	Nitrogen
5.1.6.1	Sn 3*d*	486.7	2.72	6027.6	Tin
5.1.6.1	O *KLL*[#]	509.4[#]	4.99	26503.1*	Oxygen Auger
5.1.6.2	O 2*s*	24.3	3.95	3672.8	Oxygen
5.1.6.2	P 2*p*	132.3	3.10	3122.1	Phosphorous
5.1.6.2	P 2*s*	190.3	4.10	2716.2	Phosphorous
5.1.6.2	C 1*s*	285.3	3.56	5198.4	Carbon
5.1.6.2	Ca 2*p*	346.4	3.39	15139.4	Calcium
5.1.6.2	N 1*s*	399.3	5.95	2586.7	Nitrogen
5.1.6.2	Ca 2*s*	439.3	4.19	4744.9	Calcium
5.1.6.2	Sn 3*d*	487.4	2.91	713.9	Tin
5.1.6.2	O 1*s*	531.3	3.23	25250.9	Oxygen
5.1.6.2	O *KLL*[#]	509.2[#]	…	19062.9*	Oxygen Auger

المنارة للاستشارات
www.manaraa.com

5.1.6.2	C *KLL*[#]	289.1[#]	…	959.0*	Carbon Auger
5.1.6.3	O 2s	25.5	3.82	2136.9	Oxygen
5.1.6.3	P 2*p*	133.5	3.17	1887.8	Phosphorous
5.1.6.3	P 2*s*	190.5	4.23	1653.2	Phosphorous
5.1.6.3	C 1*s*	285.5	4.26	8289.5	Carbon
5.1.6.3	Ca 2*p*	347.5	3.57	8225.8	Calcium
5.1.6.3	N 1*s*	399.5	5.13	3713.6	Nitrogen
5.1.6.3	Ca 2*s*	438.5	4.57	2788.9	Calcium
5.1.6.3	Sn 3*d*	486.5	2.37	1049.7	Tin
5.1.6.3	O 1*s*	531.5	3.34	17706.9	Oxygen
5.1.6.3	O *KLL*[#]	510.1	5.33	16086.3*	Oxygen Auger
5.1.6.1.1	C 1*s*	285.0	1.94	587.7	*C*-C/*C*-H
5.1.6.1.1	C 1*s*	286.4	1.94	400.5	*C*-O
5.1.6.1.1	C 1*s*	288.9	1.94	269.3	*C*=O, O-*C*-O, and/or *C*(=O)-N)
5.1.6.1.1	C 1*s*	289.3	1.94	58.77	O-*C*=O

المنارة للاستشارات
www.manaraa.com

5.1.6.2.1	C 1*s*	285.0	2.22	311.8	C-C/C-H
5.1.6.2.1	C 1*s*	286.5	2.22	48.86	C-O
5.1.6.2.1	C 1*s*	287.9	2.22	101.4	C=O, O-C-O, and/or C(=O)-N)
5.1.6.2.1	C 1*s*	289.3	2.22	43.05	O-C=O
5.1.6.3.1	C 1*s*	285.0	2.10	802.3	C-C/C-H
5.1.6.3.1	C 1*s*	286.3	2.10	227.4	C-O
5.1.6.3.1	C 1*s*	288.8	2.10	258.4	C=O, O-C-O, and/or C(=O)-N)
5.1.6.3.1	C 1*s*	289.3	2.10	55.30	O-C=O
5.1.6.1.2	O 1*s*	531.9	2.61	2373.1	Oxygen
5.1.6.2.2	O 1*s*	527.9	3.08	1438.5	Oxygen
5.1.6.3.2	O 1*s*	531.8	2.47	1719.3	Oxygen
5.1.6.1.3	Ca $2p_{3/2}$	348.1	1.93	595.1	Calcium
5.1.6.1.3	Ca $2p_{1/2}$	351.7	1.72	197.2	Calcium
5.1.6.2.3	Ca $2p_{3/2}$	347.1	1.83	3520.8	Calcium

المنارة للاستشارات
www.manaraa.com

5.1.6.2.3	Ca $2p_{1/2}$	350.9	1.67	1353.9	Calcium
5.1.6.3.3	Ca $2p_{3/2}$	347.6	1.87	1096.4	Calcium
5.1.6.3.3	Ca $2p_{1/2}$	351.0	1.63	400.4	Calcium
5.1.6.1.4	P $2p$	133.9	2.29	392.6	Phosphorous
5.1.6.2.4	P $2p$	133.1	2.20	1177.3	Phosphorous
5.1.6.3.4	P $2p$	133.4	1.99	369.8	Phosphorous

#Peak energy value indicated as kinetic energy. Work function of the spectrometer used for this study was 4.4463 eV.

5.1.6.4 Specimen Description

a. Host Material: Human tooth was analyzed at three different spots, Top of Tooth (01527); Middle of Tooth (01528); Root of Tooth (01529).
b. CAS Registry #: N/A
c. Host Material Characteristics: inhomogeneous; solid; amorphous; dielectric; biological material; Other
d. Chemical Name: Human tooth
e. Source: A volunteer donated a tooth, and this study was performed according to the common ethical rules fixed by the European Commission.
f. Host Composition: Human tooth
g. Form: Solid
h. Structure: Unknown

المنارة للاستشارات
www.manaraa.com

i. History & Significance: Human teeth are amongst the hardest known biological materials.[75] Their compositions vary from point to point.[64, 67] The chemical composition of tooth also changes significantly with age.[76]

j. As Received Condition: A human molar was investigated as received at 100 Pa. Different regions of the tooth were analyzed.

k. Analyzed Region: As indicated in **Figure 5.1.6.6.**

l. Ex Situ Preparation/Mounting: No treatment was performed before analysis.

m. In Situ Preparation: N/A

n. Charge Control: Charge compensation for the sample was done using the residual gas in the analytical chamber. The residual gas mostly consisted of nitrogen (N_2) from venting along with minor amounts of ambient air from opening/closing of the sample chamber while introducing/removing the sample, along with any other species that may have outgassed from the sample.

o. Temp. During Analysis: 300 K

p. Pressure During Analysis: 100 Pa

q. Pre-analysis Beam Exposure: 30 s.

5.1.6.5 Specimen Description

a. Manufacturer and Model: Specs EnviroESCA

b. Analyzer Type: spherical sector

c. Detector: other

d. Number of Detector Elements: 25

e. Analyzer Mode: constant pass energy

f. Throughput ($T=E^N$): N=0

المنارة للاستشارات
www.manaraa.com

g. Excitation Source Window: silicon nitride
h. Excitation Source: Al Ka monochromatic
i. Source Energy: 1486.6 eV
j. Source Strength: 42 W
k. Source Beam Size: 250 μm x 250 μm
l. Signal Mode: multichannel direct
m. Incident Angle: 55 $^\circ$
n. Source-to-Analyzer Angle: 55 $^\circ$
o. Emission Angle: 0 $^\circ$
p. Specimen Azimuthal Angle: 0 $^\circ$
q. Acceptance Angle from Analyzer Axis: 0 $^\circ$
r. Analyzer Angular Acceptance Width: 44 $^\circ$

5.1.6.6 Data Analysis Method

a. Energy Scale Correction: The three survey spectra were shifted by -3.3 eV (top), -8.7 eV (middle), and -6.2 eV (root). All of the narrow scans for the top part of tooth were shifted by -3.4 eV which positioned the hydrocarbon (C-C/C-H, C-1) signal at 285.0 eV. Similarly, all the narrow scans for the middle and root of the tooth were shifted by -8.7 eV and -6.2 eV, respectively.
b. Recommended Energy Scale Shift: The three survey spectra were shifted by -3.3 eV (top), -8.7 eV (middle), and -6.2 eV (root). All of the narrow scans for the top part of tooth were shifted by -3.3 eV which positioned the hydrocarbon (C-C/C-H, C-1) signal at 285.0 eV. Similarly, all the narrow scans for the middle and root of the tooth were shifted by -8.7 eV and -6.2 eV, respectively.

المنارة للاستشارات
www.manaraa.com

c. Peak Shape and Background Method: All peak fitting was with Gaussian-Lorentzian product functions with 30% Lorentzian character (GLP30). The degree of Lorentzian character in the synthetic GLP peaks was adjusted from 10 – 90% to optimize the fits. All peak fitting was performed with CasaXPS (Casa Software Ltd., Version 2.3.18PR1.0).

d. Quantitation Method: N/A

المنارة للاستشارات
www.manaraa.com

Section 5.1.7 Printed and unprinted office paper, by near-ambient pressure XPS

5.1.7.1 Statement of Attribution

This document was originally published as Shah, D.; Bahr, S.; Dietrich, P.; Meyer, M.; Thißen, A.; Linford, M. R. Printed and Unprinted Office paper, by near-ambient pressure XPS. *Surf. Sci. Spectra* **2019,** *26* (1), 024009.[10] Here, the texts and figures are reproduced with the permission from AIP publishing. Some information fields are omitted from this document to improve its readability in this format. We refer readers to the original document for complete sample, instrument information, and spectral features.

5.1.7.2 Abstract

Near ambient pressure-X-ray photoelectron spectroscopy (NAP-XPS) is a less traditional form of XPS that allows samples to be analyzed at relatively high pressures, i.e., at ca. 2500 Pa, or even higher in some cases. With NAP-XPS, XPS can probe moderately volatile liquids, biological samples, porous materials, and/or polymeric materials that outgas significantly. Here, we show NAP-XPS survey spectra, C 1*s* and O 1*s* narrow scans of two samples of paper (a white office paper and the non-sticky side of a yellow post-it note). The white office paper was analyzed at three specific positions, while unprinted portion, light blue and a dark blue letter printed on 'SPECS' logo. Survey spectra show the presence of carbon, oxygen, nitrogen, and calcium in all the samples. The yellow paper shows a small amount of silicon. Fits to the C 1*s* and O 1*s* regions are shown.

5.1.7.3 Introduction

المنارة للاستشارات
www.manaraa.com

Paper and paper products are among most commonly used materials in our daily life.[77] Paper is used in books, magazines, documents, packaging, newspapers, money, labels, and paper towels. It is widely used in many research laboratories, e.g., in filter paper.[77] Paper is an insulator, consisting of biopolymers derived from wood, which include cellulose and lignin. Other fillers may also be present. The chemical composition control the final quality of the product and the adhesion and durability of ink on it. [78, 79]

Printed paper has been analyzed by conventional XPS.[78] Since paper is an insulating sample that requires external charge compensation, it will outgas significantly, hence, conventional XPS is not the ideal technique for analysis of paper.[80] Accordingly, we present here XPS analyses of printed and unprinted paper obtained via near ambient pressure – x-ray photoelectron spectroscopy (NAP-XPS), a technique that is much better suited for insulating samples.[32] [19] Data were collected with the SPECS EnviroESCA instrument, and paper samples were analyzed directly without any sample preparation.[7] The EnviroESCA works at much higher pressures than conventional XPS (greater than 2500 Pa).[7]

The paper samples analyzed in this study were taken from a notepad with a printed 'SPECS' logo on it and a yellow post-it note. The white, unprinted part of the sample was analyzed directly. In addition, the light blue ink used to print the "S", "P", "C", and "S" was analyzed, as was the dark blue ink in the letter "ϵ" of the logo. The non-sticky side of a yellow post-it note was also analyzed.

The main elements present in samples of the printed and unprinted paper were carbon and oxygen. Peaks with lesser intensity due to nitrogen and calcium were present in survey spectra,[21] and the yellow post-it note showed a significant amount of silicon. [21] The printed and unprinted papers differ, presumably because of the ink, which was expected to completely obscure

المنارة للاستشارات
www.manaraa.com

any XPS signal from the paper substrate. The unprinted white paper shows a noticeably higher oxygen-to-carbon ratio than the yellow paper and printed letters.

The C 1*s* envelopes from the four samples were fit to four synthetic components, which represent different oxidation states for carbon.[81] Carbon bonded to carbon and hydrogen (-*C*-C/*C*-H, C(0), C-1) at ca. 285.1 eV is an important fit component of all the C 1*s* envelopes, and is the largest component in all the C 1*s* envelopes, except that from the white paper.[47] The second carbon signal in the fits appears at ca. 286.6 eV. It is attributed primarily to carbon attached to oxygen via a single bond. i.e., cellulosic carbon (-*C*-O, C(I), C-2). The carbonyl/acetal carbon represents the third major component(s) of the C 1s spectrum.

It appears at ca. 288.2 eV (-*C*=O, C(II); O-*C*-O, C-3). All of the peak envelopes also show a fourth component at 289.8 eV that is attributed to carboxyl carbon (O-*C*=O, C(III), C-4). The synthetic peaks used to fit the C 1*s* envelopes were Gaussian-Lorentzian product (GLP30) functions,[28] where the Lorentzian character of the peaks was varied from 10 – 70% to obtain the best fits, as determined by the lowest values of the residual standard deviation. All of the peaks had universal polymer (U-Poly) Tougaard backgrounds.[45]

Uniqueness plots were generated to test for fit parameter correlation.[73] This was done by setting and then resetting one parameter in the fit (the C-2 width here) to a series of specific values, while allowing all of the other parameters in the fit to vary as they did in the original fit. For example, in the uniqueness analysis of the C 1*s* envelope from the white paper, all of the peak heights varied, the C-1 peak position varied, all of the other peak positions were constrained relative to the C-1 peak (the C-2, C-3, and C-4 peaks were constrained to be +1.5, +2.7, and +4.3 eV from the C-1 signal), and the peak widths were constrained to be same, except for the width of the C-2 peak, which was forced to take on a range of specific values. Universal polymer (U Poly)

المنارة للاستشارات
www.manaraa.com

Tougaard backgrounds were used in these fits.[54] The peak widths were constrained to be equal for all the synthetic C 1*s* components. The peak positions of different C 1*s* components were constrained to be same for the other samples, as noted in the "Spectral Features Table" below. 'U-shaped' uniqueness plots were obtained for all the fits which suggests that the fit parameters in our fits have statistical significance.

In general, oxygen peak shifts in XPS are smaller than C 1*s* chemical shifts, which makes peak assignments in O 1*s* peak fitting more challenging.[78, 82] However, paper and wood samples have been shown to have at least two major O 1*s* components that have been identified as oxygen in lignin (E_b = 532.4 ± 0.2 eV) and oxygen in carbohydrates (E_b = 533.7 ± 0.2 eV).[83, 84] It has been suggested that contact with air and humidity leads to adsorbed water in the material that (i) leads to O 1*s* signals at 533.0 – 533.5 eV, and (ii) perturbs the other oxygen signals, which necessitates the addition of other fit components at lower and higher binding energy.[78, 85, 86] The presence of ink and other additives in the paper further complicates the O 1*s* peak envelope and necessitates the use of four oxygen components.[79, 80]

Ultimately, our O 1*s* spectra were fit with four synthetic components following the approach that Lützenkirchen-Hecht *et al.* used on printed paper.[78] Their protocol was an amalgamation of several previous approaches on similar materials.[82, 85, 87, 88] For our O 1*s* peak fitting, the synthetic peaks were Gaussian-Lorentzian product (GLP30) functions with 30% Lorentzian character that were constrained to have equal widths.[28] The fraction of Lorentzian character in these peaks had been originally varied from 10 – 70 % to obtain the best fits, as determined by the minimum value of the residual standard deviation of the fits. The peak positions of the four different oxygen components in these fits were fixed to their literature values of 531.6

المنارة للاستشارات
www.manaraa.com

eV, 532.8 eV, 533.4 eV, and 534.2 eV respectively.[78, 89, 90] This was possible because the C(0) reduced carbon signal was at 285.0 eV in each C 1*s* narrow scan.

As shown below, the Lützenkirchen-Hecht *et al.* approach yielded a reasonably good fit to the O 1*s* narrow scan of the white, unprinted paper sample. However, the fits were not as good for the other O 1*s* spectra shown in this work. Accordingly, a second approach was considered. It simply consisted of fitting with three synthetic peaks of equal widths and arbitrary positions. This approach has literature precedent.[78, 82] The synthetic components used here were Gaussian-Lorentzian product functions with 30% Lorentzian character (GLP30). The fraction of Lorentzian character in these peaks had originally been varied from 10 – 70 % to obtain the best fits, as determined by the minimum value of the residual standard deviation of the fits. The widths of the peaks were constrained to be same in each fit.

As noted, no constraints were placed on the peak positions or areas of the three synthetic components. Universal polymer (U-Poly) Tougaard backgrounds were used in these fits.[45, 54] As suggested by the residual standard deviations of the fits, the three-peak approach yielded better results in all cases. As indicated in the '**GUIDE TO FIGURES**' below, there was a fair amount of variation in the positions of the fit components in this approach, which suggests that the fit components may not correspond to the same chemical species in the different fits. This is not unexpected because of the significant physical differences between the samples, e.g., printed vs. unprinted.

While the more constrained four-peak approach gave less than ideal results, it suggested a mechanism by which the results could be compared. That is, the percentages of the total fitted area of each of the four synthetic peaks were plotted. Here, the fit of the unprinted white paper is dominated by the O-2 and O-3 components, which account for 62% and 29% of the total

المنارة للاستشارات
www.manaraa.com

area, respectively. The contribution of the O-2 peak in the other samples (blue printed, dark blue printed, and the yellow Post-it note) is also significant, but not to quite the same degree as in the white paper. The O-3 peak is not as important in these other samples as in the unprinted, white paper. In general, the O-1 and O-2 peaks are most important in the blue printed, dark blue printed, and the yellow Post-it note materials. Overall, **Figure 5.1.7.5.** suggests that the different O 1*s* narrow scans have different profiles/fingerprints, where the two printed materials are most similar, and they, in turn, are similar to the yellow Post-it note than to the unprinted paper. This literature reported methodology can be used for analysis of similar samples.

Uniqueness plots for the O 1*s* peak fits obtained by the four-peak approach were obtained by varying the O-2 peak width in a manner similar to that used to create the C 1*s* uniqueness plots.[73] All of the resulting uniqueness plots were 'U-shaped', which suggests that the fit parameters in these fits also have statistical significance. All peak fitting performed in this work was with CasaXPS (Casa Software Ltd., Version 2.3.18PR1.0).

Table 5.1.7.1. Spectral features of interest

Figure number	Element/ Transition	Peak Energy (eV)	Peak Width FWHM (eV)	Peak Area (eV x cts/s)	Sensitivity Factor	Concentration (at. %)	Peak Assignment
5.1.7.1	O 1*s*	531.8	3.29	18324.8			Oxygen
5.1.7.1	C 1*s*	285.0	3.66	13068.7			Carbon

المنارة للاستشارات
www.manaraa.com

5.1.7.1	N 1*s*	401.8	4.81	1915.4			Nitrogen
5.1.7.1	O *KLL*	507.4*	8.12	3833.2			Oxygen Auger
5.1.7.1	O 2*s*	24.8	3.93	780.8			Oxygen
5.1.7.1	Ca 2*p*	345.8	3.21	726.1			Calcium
5.1.7.1	C *KLL*	262.8*	2.97	238.3			Carbon Auger
5.1.7.2	C 1*s*	285.0	3.10	14595.0			Carbon
5.1.7.2	C *KLL*	259.2*	2.16	100.6			Carbon Auger signal
5.1.7.2	O 1*s*	533.0	3.38	9447.3			Oxygen
5.1.7.2	O 2*s*	26.0	5.55	280.1			Oxygen
5.1.7.2	O *KLL*	506.2*	5.44	967.0			Oxygen Auger signal
5.1.7.2	N 1*s*	403.0	4.68	2137.9			Nitrogen
5.1.7.3	C 1*s*	285.0	4.10	19626.6			Carbon

المنارة للاستشارات
www.manaraa.com

5.1.7.3	C KLL	256.2*	2.84	366.0			Carbon Auger signal
5.1.7.3	O 1*s*	532.9	4.64	10930.3			Oxygen 1*s*
5.1.7.3	O 2*s*	26.9	4.72	319.9			Oxygen 2*s*
5.1.7.3	O *KLL**	506.2 *	5.44	967.0			Oxygen Auger signal
5.1.7.3	N 1*s*	402.0	5.16	1481.3			Nitrogen
5.1.7.4	C 1*s*	285.0	2.82	13343.2			Carbon 1s
5.1.7.4	Si 2*p*	153.0	3.15	1820.9			Silicon
5.1.7.4	Si 2*s*	102.0	2.76	1624.5			Silicon
5.1.7.4	O 1*s*	532.0	3.01	8300.9			Oxygen
5.1.7.4	O 2*s*	25.0	3.86	582.5			Oxygen
5.1.7.4	O *KLL*	503.2*	7.73	728.3			Oxygen Auger signal
5.1.7.4	Ca 2*p*	347.0	3.07	1327.9			Calcium

المنارة للاستشارات
www.manaraa.com

5.1.7.4	N 1*s*	403.0	3.71	1633.9			Nitrogen
5.1.7.1.1	C 1*s*	285.1	1.43	395.2	1	27.9%	_C_-C/_C_-H
5.1.7.1.1	C 1*s*	286.6	1.43	821.1	1	58.0%	_C_-O
5.1.7.1.1	C 1*s*	288.2	1.43	163.1	1	11.6%	_C_=O, O-_C_-O, and/or _C_(=O)-N)
5.1.7.1.1	C 1*s*	288.8	1.43	35.24	1	2.5%	O-_C_=O
5.1.7.2.1	C 1*s*	285.0	1.50	1141.7	1	70.5%	_C_-C/_C_-H
5.1.7.2.1	C 1*s*	286.5	1.50	234.0	1	14.5%	_C_-O
5.1.7.2.1	C 1*s*	287.7	1.50	103.0	1	6.4%	_C_=O, O-_C_-O, and/or _C_(=O)-N)
5.1.7.2.1	C 1*s*	289.2	1.50	140.4	1	8.7%	O-_C_=O
5.1.7.3.1	C 1*s*	285.0	1.52	1501.7	1	74.2%	_C_-C/_C_-H
5.1.7.3.1	C 1*s*	286.5	1.52	270.1	1	13.4%	_C_-O
5.1.7.3.1	C 1*s*	287.9	1.52	87.89	1	4.3%	_C_=O, O-_C_-O, and/or _C_(=O)-N)

المنارة للاستشارات
www.manaraa.com

5.1.7.3.1	C 1*s*	289.1	1.52	164.5	1	8.1%	O-*C*=O
5.1.7.4.1	C 1*s*	285.0	1.52	1267.1	1	81.9%	*C*-C/*C*-H
5.1.7.4.1	C 1*s*	286.5	1.52	76.8	1	8.4%	*C*-O
5.1.7.4.1	C 1*s*	287.9	1.52	73.6	1	5.0%	*C*=O, O-*C*-O, and/or *C*(=O)-N)
5.1.7.4.1	C 1*s*	289.2	1.52	35.15	1	4.8%	O-*C*=O
5.1.7.1.2a	O 1*s*	531.6	1.50	143.5	2.93	6.87%	-C=*O*
5.1.7.1.2a	O 1*s*	532.8	1.50	1278.3	2.93	61.16%	C-*O*-C
5.1.7.1.2a	O 1*s*	533.4	1.50	575.6	2.93	27.5%	O-C-*O*
5.1.7.1.2a	O 1*s*	534.2	1.50	92.9	2.93	4.44%	Oxygen component associated with additives, and/or wood extractives[78]
5.1.7.1.2b	O 1*s*	531.3	1.62	121.3	2.93	5.7%	-C=*O*

المنارة للاستشارات
www.manaraa.com

5.1.7.1.2b	O 1*s*	532.9	1.62	1918.2	2.93	90.7%	C-<u>*O*</u>-C
5.1.7.1.2b	O 1*s*	534.3	1.62	85.2	2.93	4.0%	O-C-<u>*O*</u>
5.1.7.2.2a	O 1*s*	531.6	1.50	192.3	2.93	18.5%	-C=<u>*O*</u>
5.1.7.2.2a	O 1*s*	532.8	1.50	542.4	2.93	52.22%	C-<u>*O*</u>-C
5.1.7.2.2a	O 1*s*	533.4	1.50	66.8	2.93	6.5%	O-C-<u>*O*</u>
5.1.7.2.2a	O 1*s*	534.2	1.50	237.2	2.93	22.83%	Oxygen component associated with additives, and/or wood extractives[78]
5.1.7.2.2b	O 1*s*	532.3	1.71	596.5	2.93	57.23%	-C=<u>*O*</u>
5.1.7.2.2b	O 1*s*	533.8	1.71	426.4	2.93	40.9%	C-<u>*O*</u>-C
5.1.7.2.2b	O 1*s*	536.0	1.71	19.5	2.93	1.87%	O-C-<u>*O*</u>
5.1.7.3.2a	O 1*s*	531.6	1.50	377.6	2.93	30.9%	-C=<u>*O*</u>
5.1.7.3.2a	O 1*s*	532.8	1.50	590.5	2.93	48.32%	C-<u>*O*</u>-C
5.1.7.3.2a	O 1*s*	533.4	1.50	76.4	2.93	6.3%	O-C-<u>*O*</u>

المنارة للاستشارات
www.manaraa.com

5.1.7.3.2a	O 1*s*	534.2	1.50	177.5	2.93	14.5%	Oxygen component associated with additives, and/or wood extractives[78]
5.1.7.3.2b	O 1*s*	531.2	1.65	71.4	2.93	5.8%	-C=*O*
5.1.7.3.2b	O 1*s*	532.2	1.67	713.1	2.93	58.2%	C-*O*-C
5.1.7.3.2b	O 1*s*	533.6	1.67	443.8	2.93	36.2%	O-C-*O*
5.1.7.4.2a	O 1*s*	531.6	1.50	469.6	2.93	43.33%	-C=*O*
5.1.7.4.2a	O 1*s*	532.8	1.50	551.8	2.93	50.91%	C-*O*-C
5.1.7.4.2a	O 1*s*	533.4	1.50	0	2.93	0.0%	O-C-*O*
5.1.7.4.2a	O 1*s*	534.2	1.50	5.77	2.93	5.8%	Oxygen component associated with additives,

المنارة للاستشارات
www.manaraa.com

							and/or wood extractives[78]
5.1.7.4.2b	O 1*s*	531.8	1.63	295.0	2.93	28.3%	-C=<u>*O*</u>
5.1.7.4.2b	O 1*s*	532.4	1.63	590.0	2.93	56.4%	C-<u>*O*</u>-C
5.1.7.4.2b	O 1*s*	533.6	1.63	161.3	2.93	15.4%	O-C-<u>*O*</u>

#Peak energy value indicated as kinetic energy. Work function of the spectrometer used for this study was 4.4463 eV.

5.1.7.4 Specimen Description

a. Host Material: Printed paper was analyzed at three different spots, White, Unprinted Part (1533-01); Light Blue Printed Part (1534-01); Dark Blue Printed Part (1535-01) along with non-sticky side of yellow post-it note (1536-01).
b. CAS Registry #: N/A
c. Host Material Characteristics: Inhomogeneous; solid; amorphous; dielectric; organic compound; Other
d. Chemical Name: N/A
e. Source: Printed and unprinted office paper was used in this work. In particular, white, unprinted office paper, and the SPECS logo with blue and dark blue printed parts were analyzed. The non-sticky side of a yellow post-it note was also analyzed. These four specimens were analyzed and compared.
f. Host Composition: Cellulose and lignin, which are principal components of paper, as well as ink.

المنارة للاستشارات
www.manaraa.com

g. Form: Solid
h. Structure: N/A
i. History & Significance: Paper is one of the oldest and most often used materials in our daily lives. It appears in books, magazines, newspaper, paper towels, wallpaper, etc. The chemical composition and surface properties of paper are important as they significantly alter the quality of a final print. The quality of a final print is also affected by the ink.
j. As Received Condition: The paper samples under investigation were placed on a sample plate, fixed with carbon tape, and analyzed without any additional treatment.
k. Analyzed Region: Random regions of the printed and unprinted paper samples.
l. Ex Situ Preparation/Mounting: The paper samples were placed on the sample plate, fixed with carbon tape, and analyzed without any additional sample preparation.
m. In Situ Preparation: N/A
n. Charge Control: Residual gas (Argon, 100 Pa)
o. Temp. During Analysis: 300 K
p. Pressure During Analysis: 100 Pa
q. Pre-analysis Beam Exposure: 30 s.

5.1.7.5 Instrument Description

a. Manufacturer and Model: SPECS EnviroESCA
b. Analyzer Type: spherical sector
c. Detector: other
d. Number of Detector Elements: 25
e. Analyzer Mode: constant pass energy
f. Throughput ($T=E^N$): N=0

المنارة للاستشارات
www.manaraa.com

g. Excitation Source Window: silicon nitride

h. Excitation Source: Al Ka monochromatic

i. Source Energy: 1486.6 eV

j. Source Strength: 42 W

k. Source Beam Size: 250 μm x 250 μm

l. Signal Mode: multichannel direct

m. Incident Angle: 55˚

n. Source-to-Analyzer Angle: 55˚

o. Emission Angle: 0˚

p. Specimen Azimuthal Angle: 0˚

q. Acceptance Angle from Analyzer Axis: 22˚

r. Analyzer Angular Acceptance Width: 44˚

5.1.7.6 Data Analysis Method

a. **Energy Scale Correction:** The survey spectra were shifted by -10.1 eV, which positioned the C 1s signals at 285.0 eV. The C 1*s* narrow scans were shifted by -9.0 eV, which positioned the hydrocarbon (*C*-C/*C*-H, C-1) signal at 285.0 eV.[47] The three O 1*s* narrow spectra were also shifted by -9.0 eV.[21]

b. **Recommended Energy Scale Shift:** -10.1 eV for survey scan and -9.0 eV for narrow spectra.

c. **Peak Shape and Background Method:** All peak fitting was with Gaussian-Lorentzian product (GLP) functions. The degree of Lorentzian character in the synthetic Gaussian Lorentzian (GLP30) peaks was adjusted from 10 – 70% to optimize the fits.[28] Universal

المنارة للاستشارات
www.manaraa.com

polymer (U Poly) Tougaard backgrounds were used in these fits.[54] All peak fitting performed in this work was with CasaXPS (Casa Software Ltd., Version 2.3.18PR1.0).

d. **Quantitation Method:** Elemental compositions were calculated using CasaXPS.

المنارة للاستشارات
www.manaraa.com

5.2 Figures

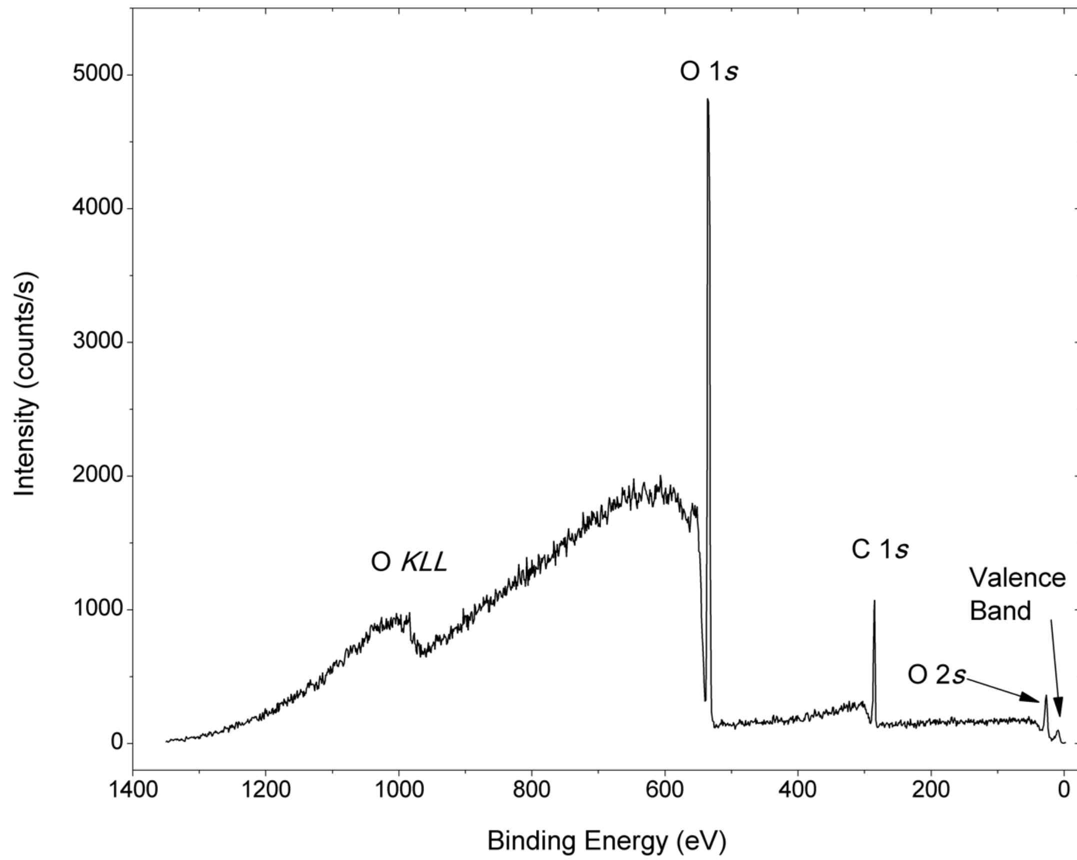

Figure 5.1.1.1. NAP-XPS survey spectrum of liquid water.

المنارة للاستشارات
www.manaraa.com

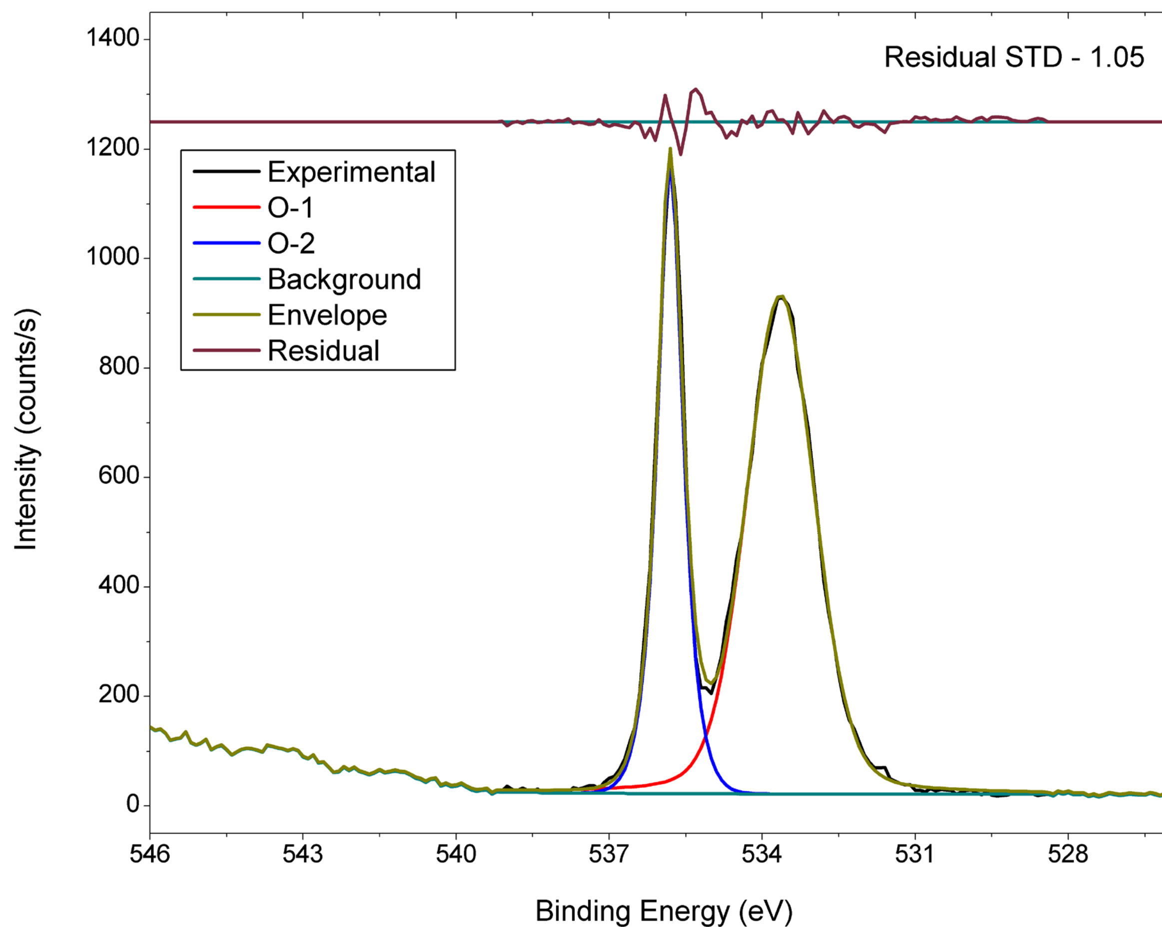

Figure 5.1.1.2. NAP-XPS O 1*s* spectrum stack of liquid water collected at different nozzle length.

المنارة للاستشارات
www.manaraa.com

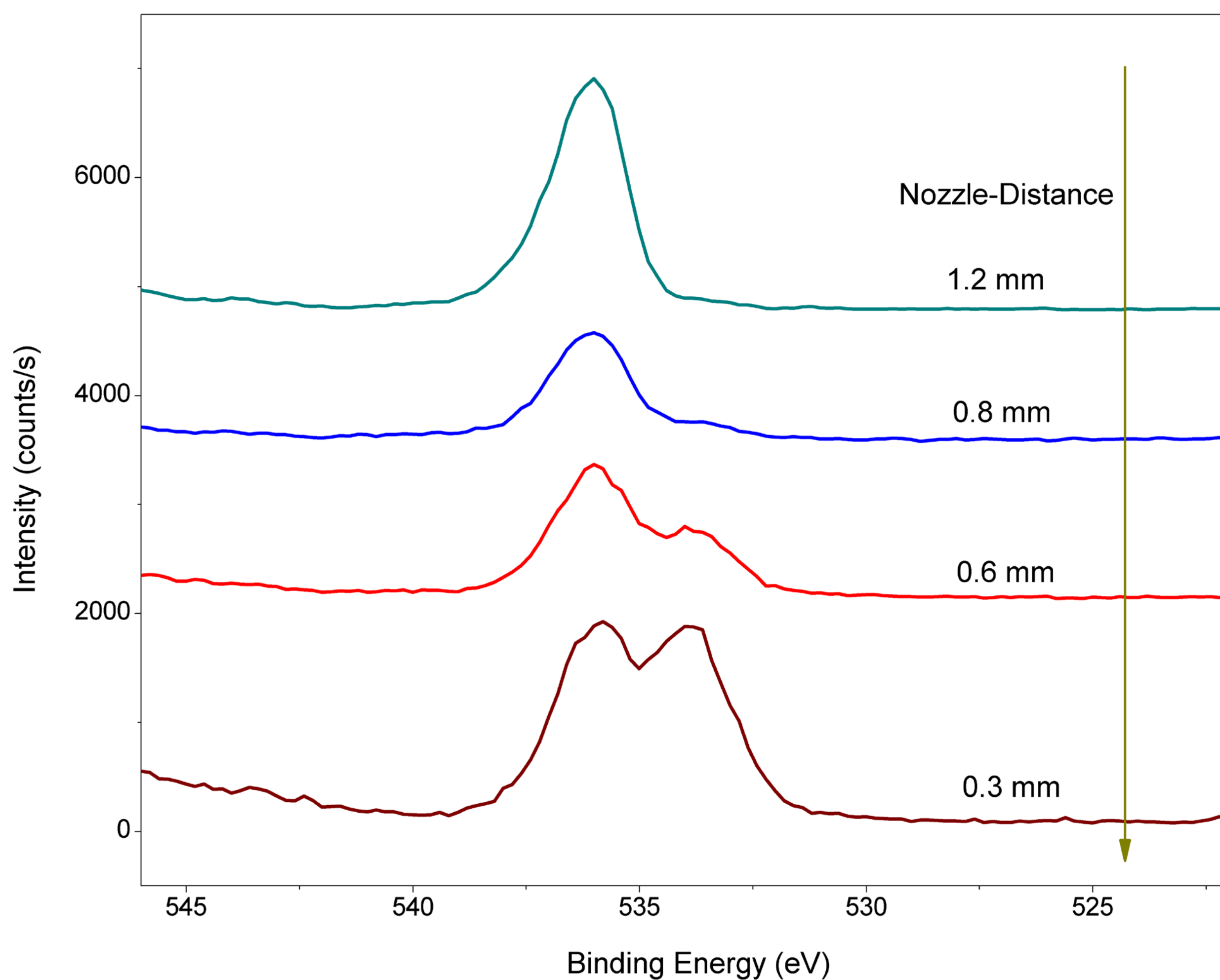

Figure 5.1.1.3. NAP-XPS O 1*s* spectrum stack of liquid water collected at different nozzle length.

المنارة للاستشارات
www.manaraa.com

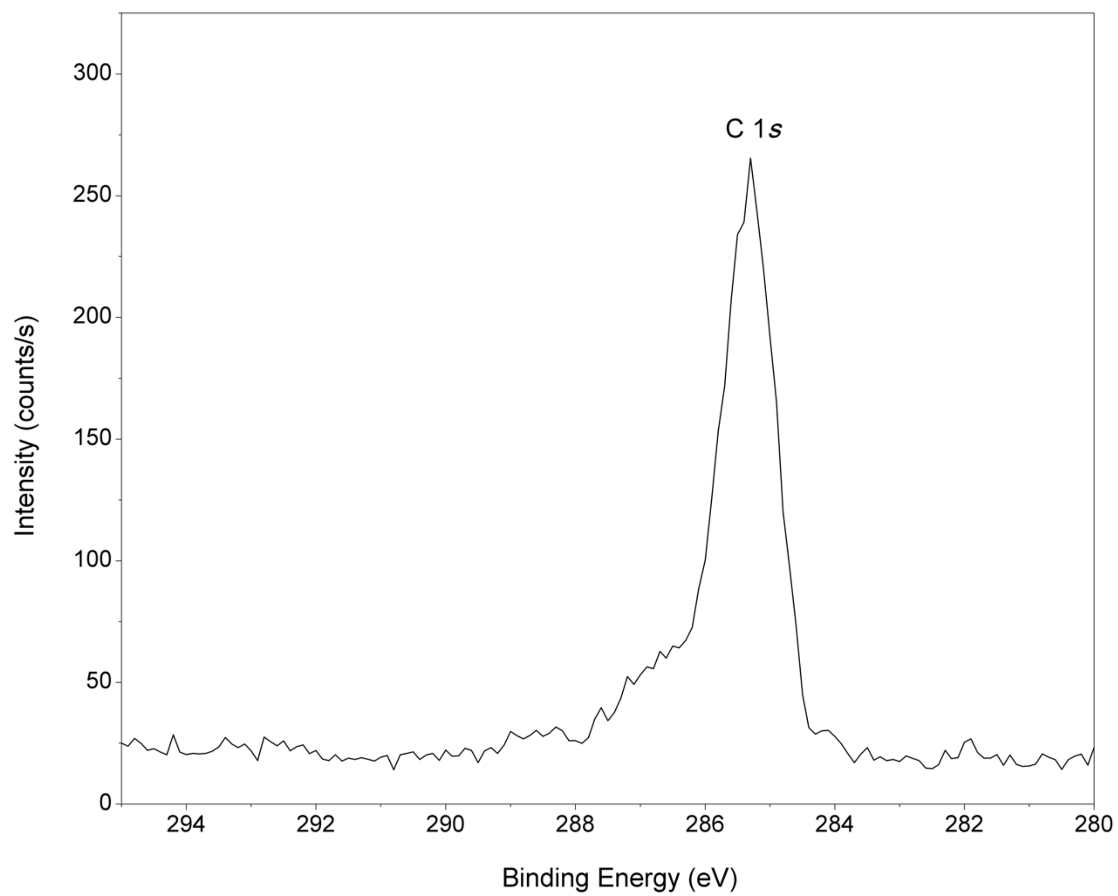

Figure 5.1.1.4. NAP-XPS O 1*s* spectrum of liquid water.

المنارة للاستشارات
www.manaraa.com

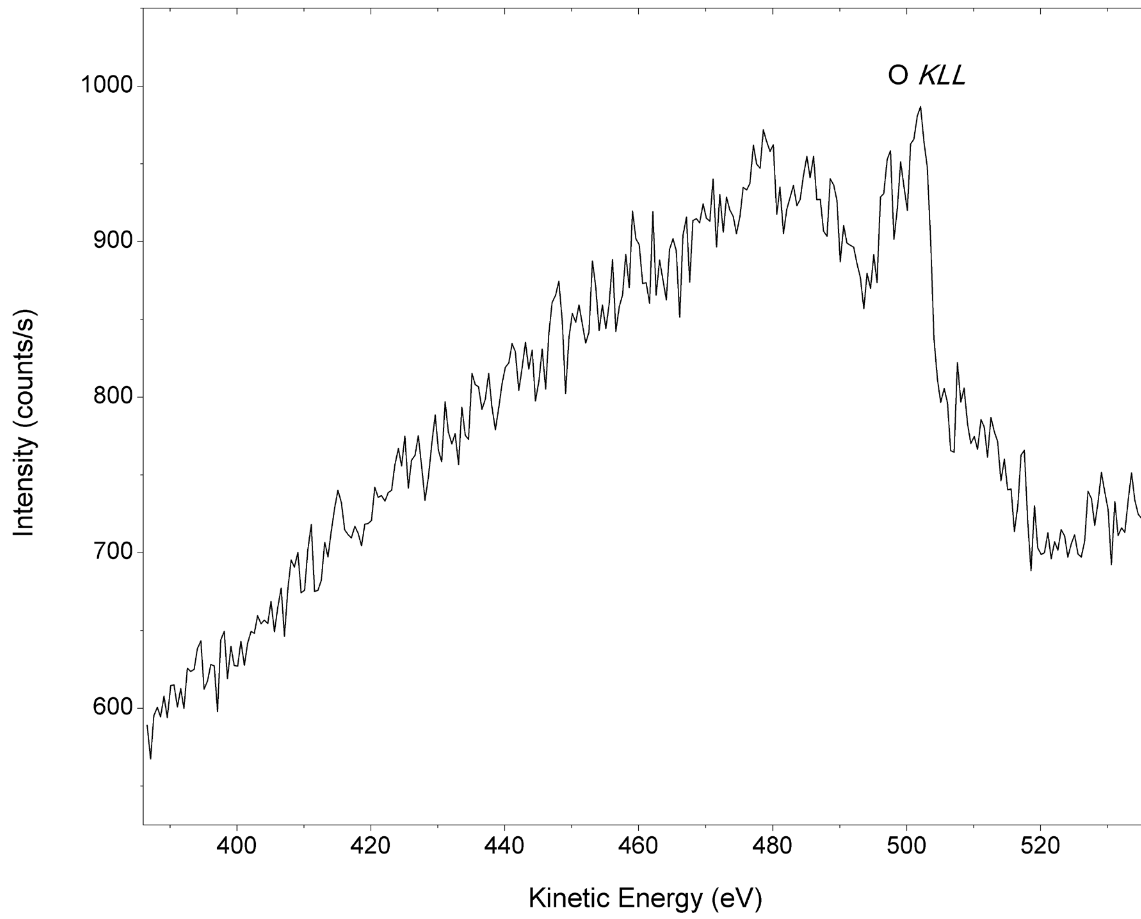

Figure 5.1.1.5. NAP-XPS O *KLL* spectrum of liquid water.

المنارة للاستشارات
www.manaraa.com

Figure 5.1.2.1. NAP-XPS Survey spectrum of Coca-Cola.

المنارة للاستشارات
www.manaraa.com

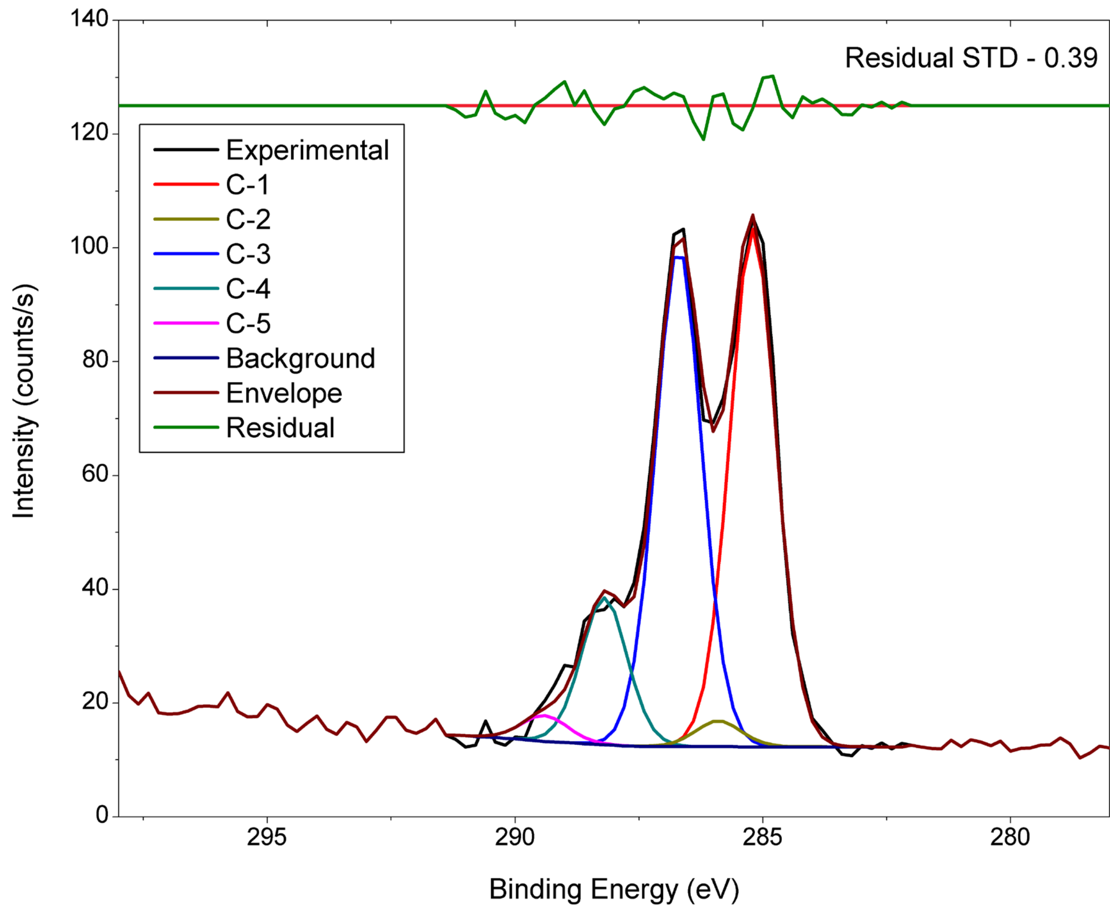

Figure 5.1.2.2. NAP-XPS C 1*s* spectrum of Coca-Cola.

المنارة للاستشارات
www.manaraa.com

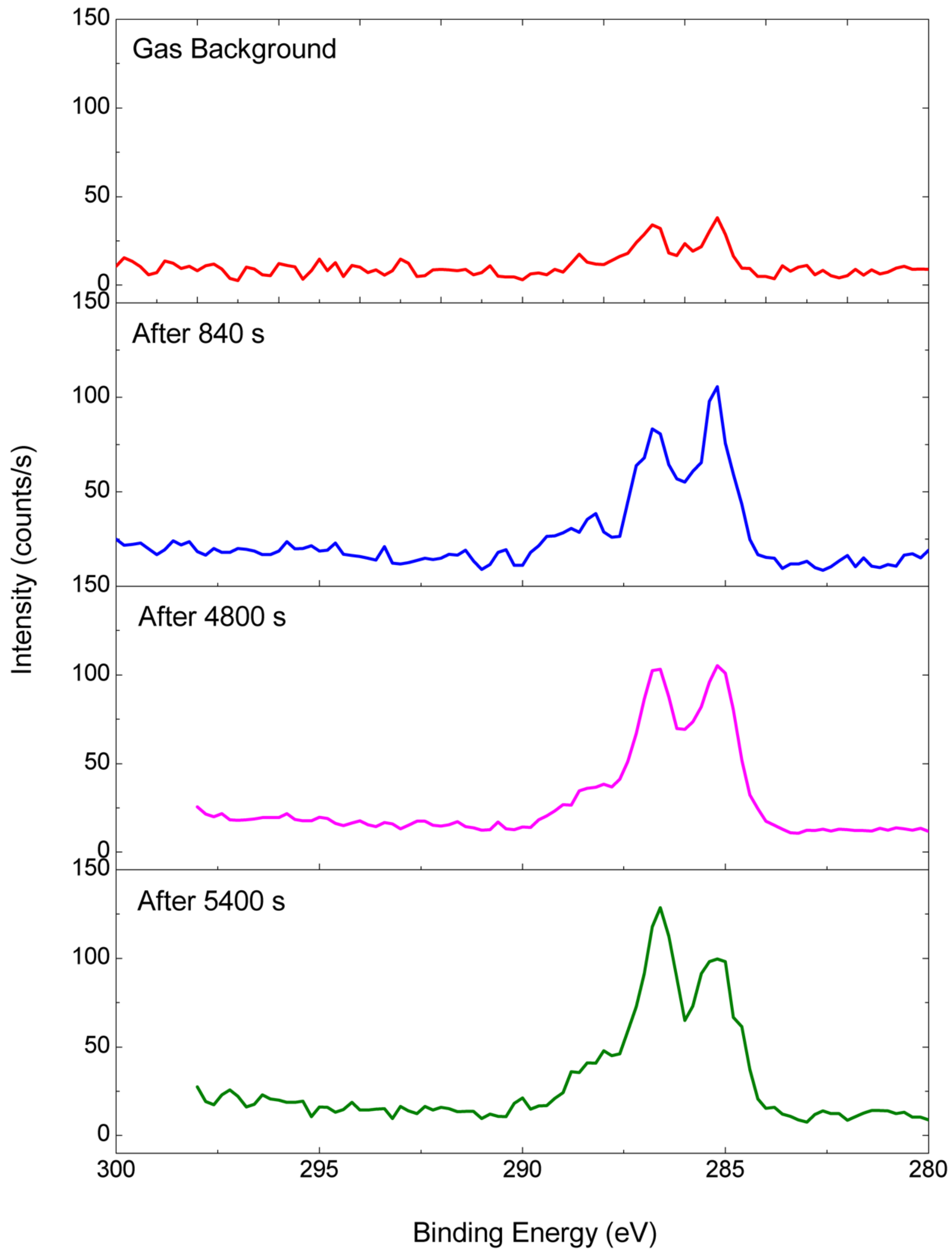

Figure 5.1.2.3. Stack of NAP-XPS C 1*s* spectrum of Coca-Cola.

المنارة للاستشارات
www.manaraa.com

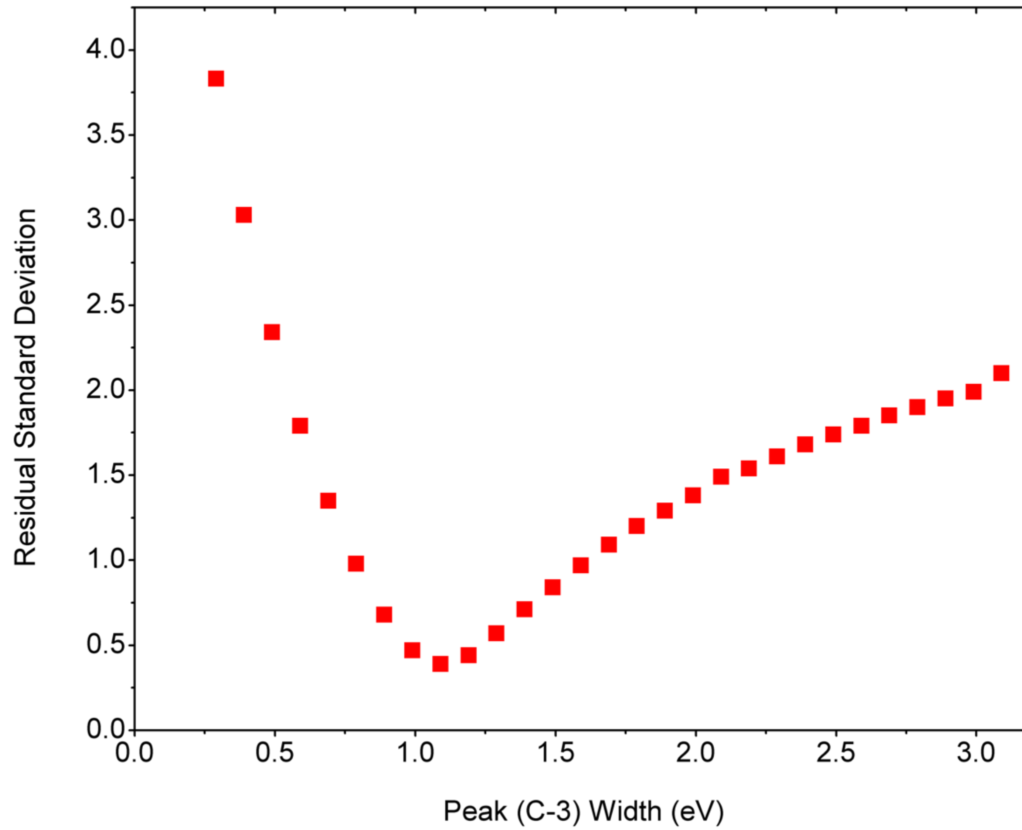

Figure 5.1.2.4. Uniqueness plot of the C 1*s* fit (varying C-3) of Coca-Cola.

المنارة للاستشارات
www.manaraa.com

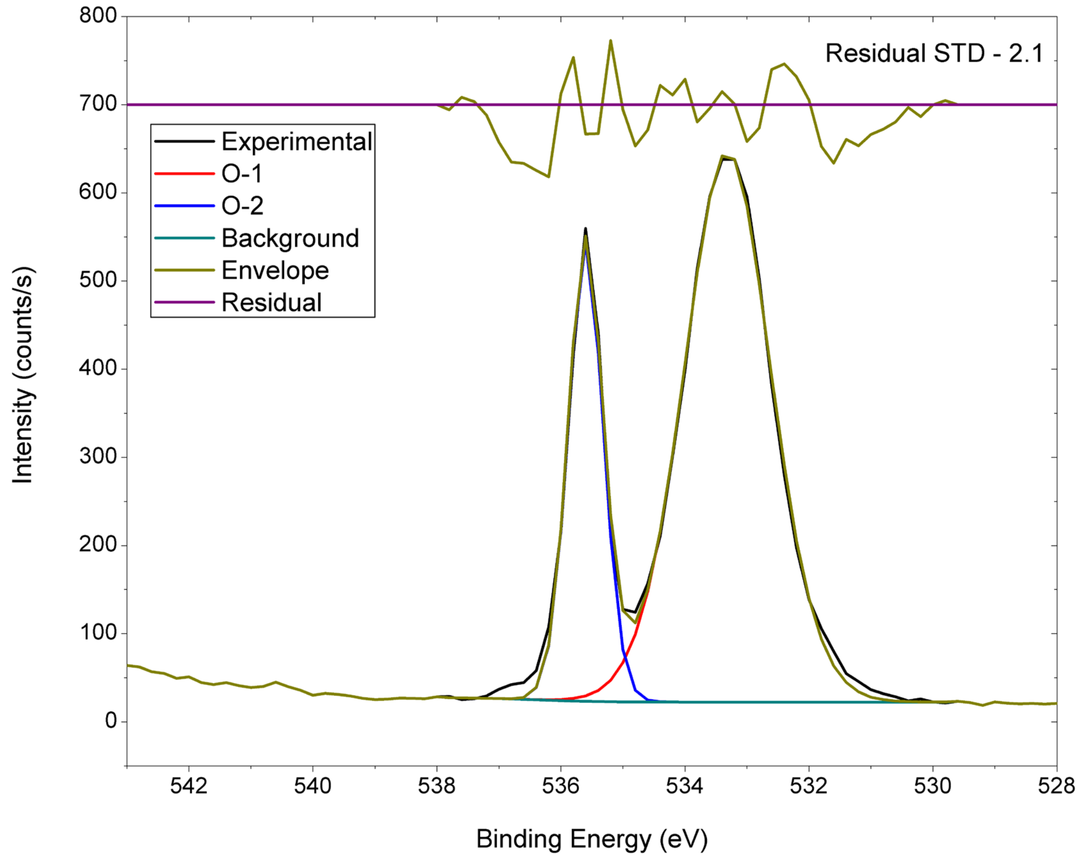

Figure 5.1.2.5. NAP-XPS O 1*s* spectrum of Coca-Cola.

المنارة للاستشارات
www.manaraa.com

Figure 5.1.3.1. NAP-XPS Survey spectrum of Coffee bean.

المنارة للاستشارات
www.manaraa.com

Figure 5.1.3.2. Expanded NAP-XPS Survey spectrum of Coffee bean.

المنارة للاستشارات
www.manaraa.com

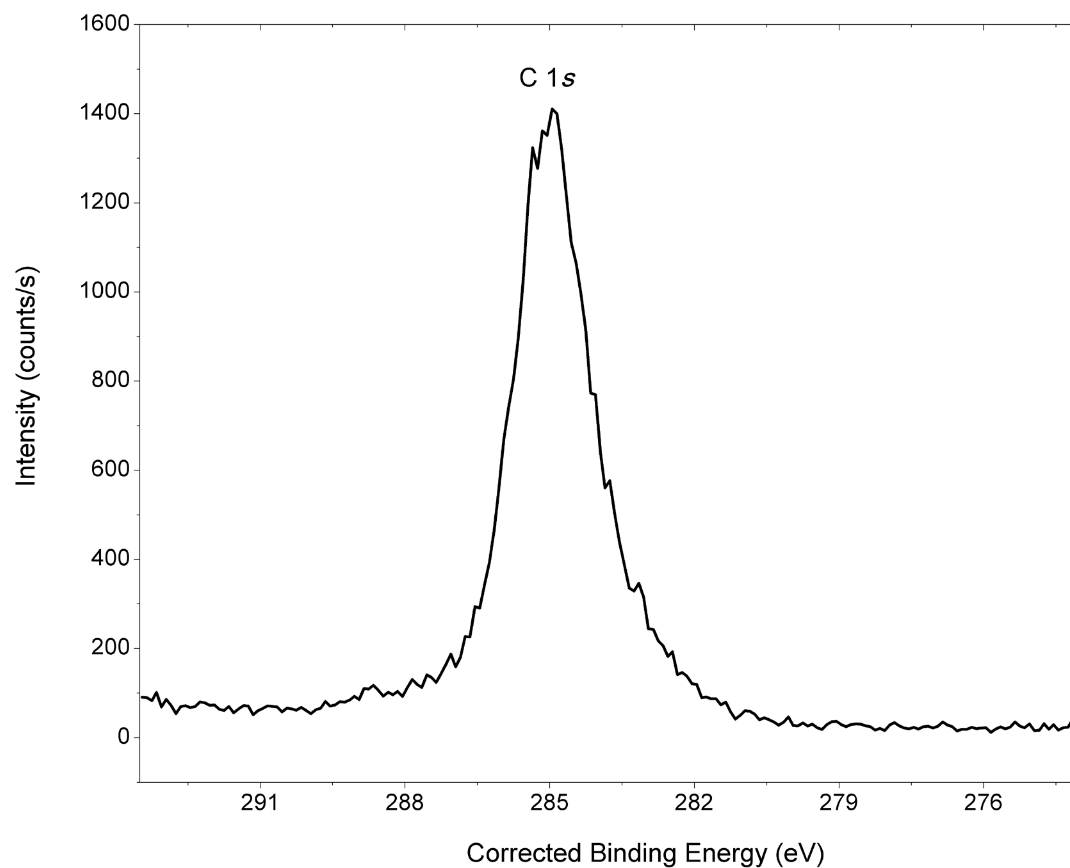

Figure 5.1.3.3. NAP-XPS C 1*s* spectrum of Coffee bean.

المنارة للاستشارات
www.manaraa.com

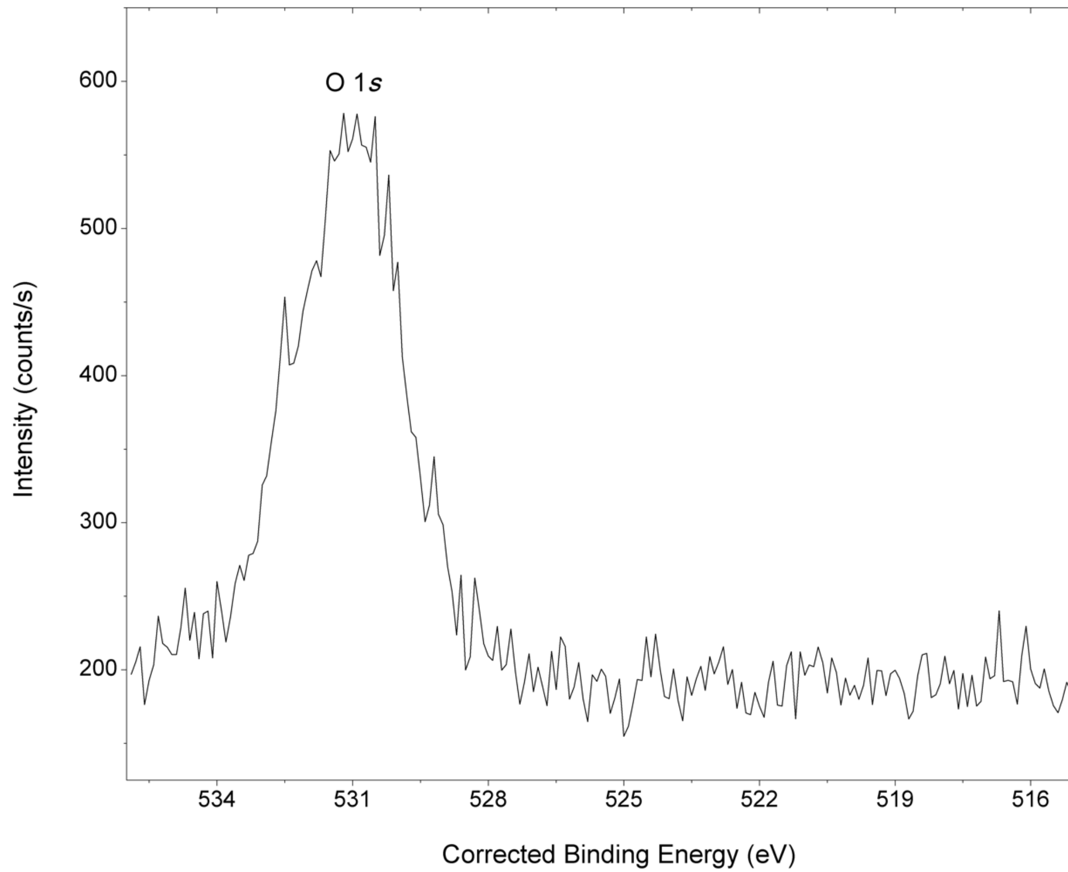

Figure 5.1.3.4. NAP-XPS O 1*s* spectrum of Coffee bean.

المنارة للاستشارات
www.manaraa.com

Figure 5.1.4.1. NAP-XPS Survey spectrum of Nitrogen (N_2) gas.

المنارة للاستشارات

www.manaraa.com

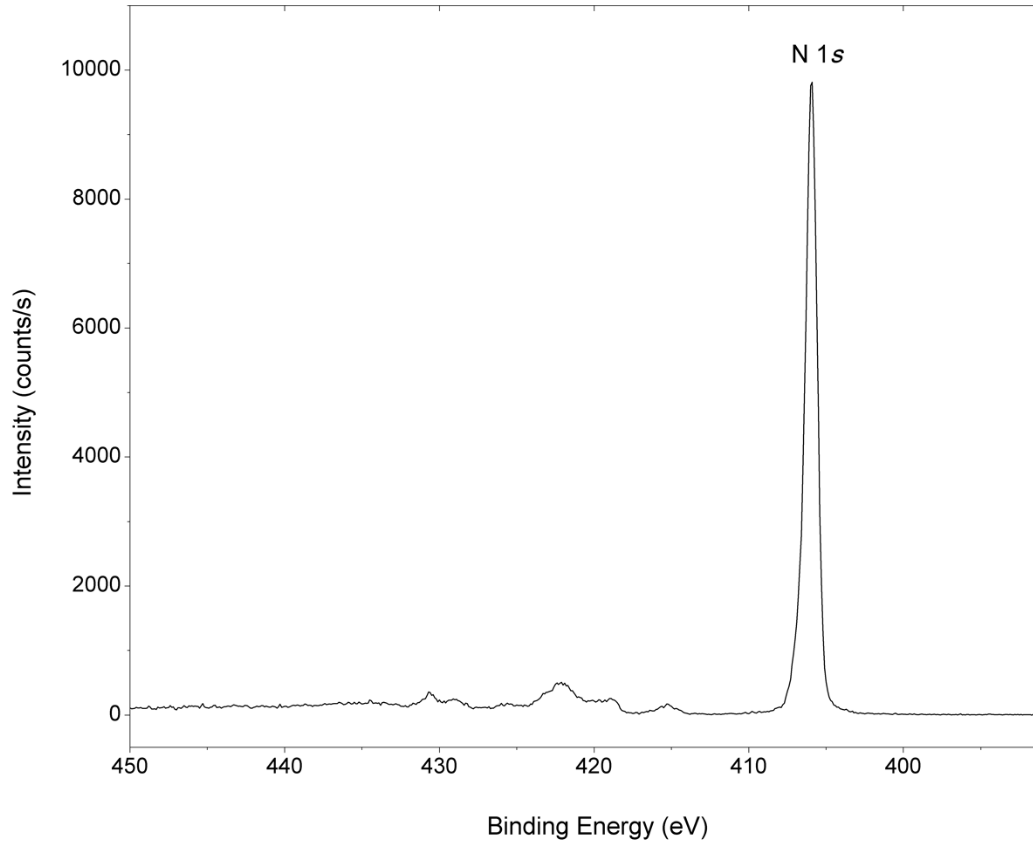

Figure 5.1.4.2. NAP-XPS N 1*s* spectrum of Nitrogen (N_2) gas.

المنارة للاستشارات
www.manaraa.com

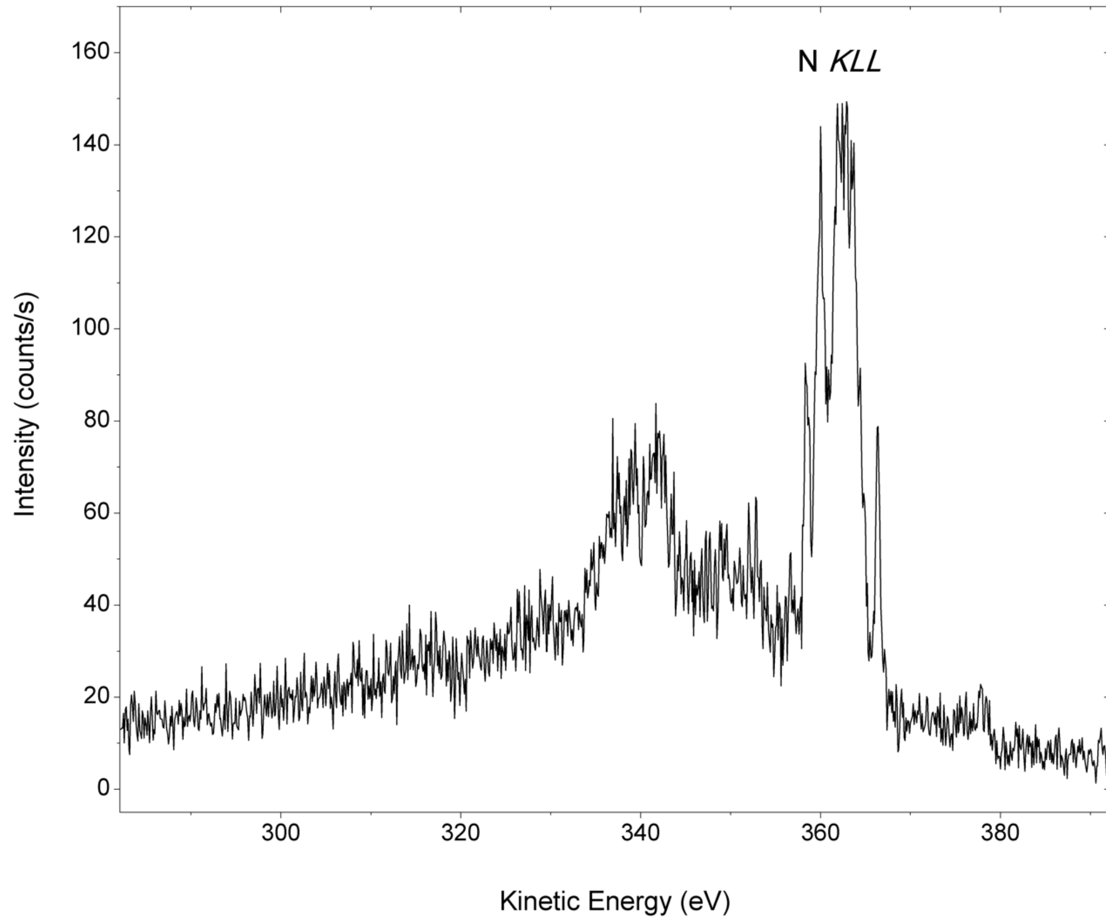

Figure 5.1.4.3. NAP-XPS N *KLL* spectrum of Nitrogen (N_2) gas.

المنارة للاستشارات
www.manaraa.com

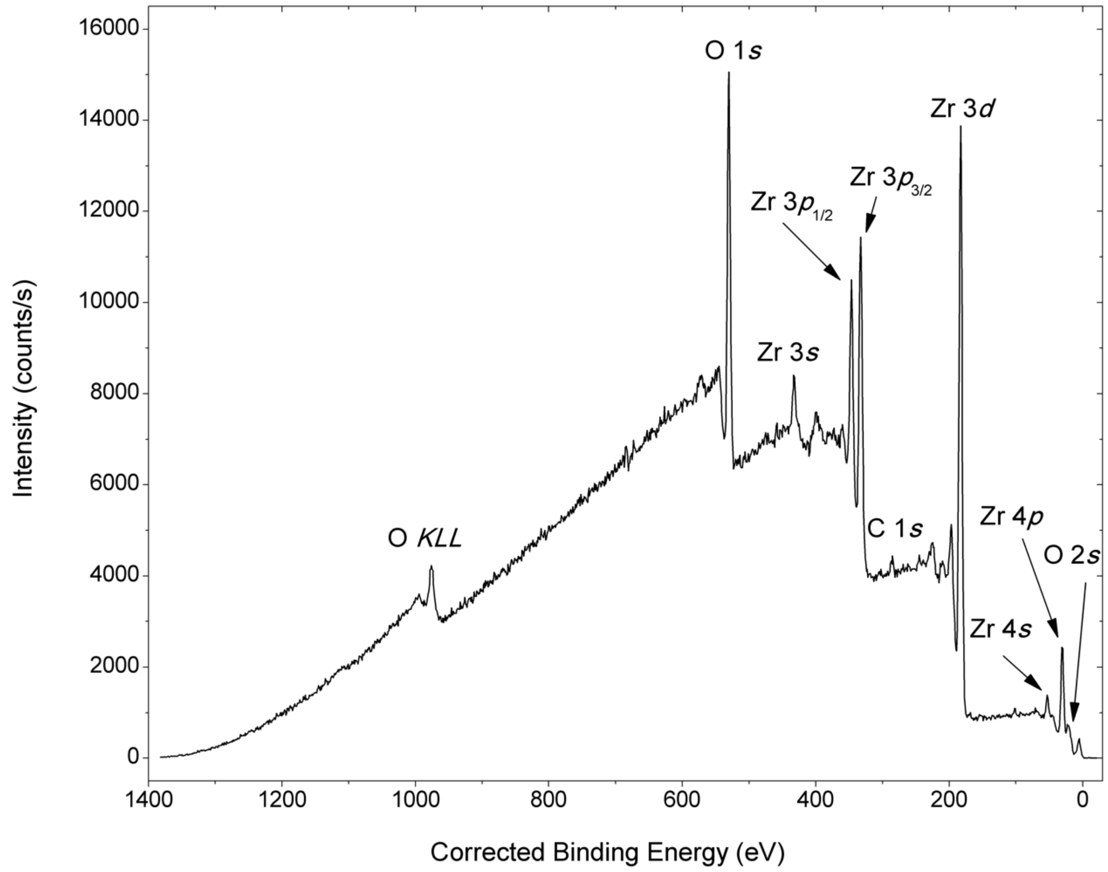

Figure 5.1.5.1. NAP-XPS Survey spectrum of Zirconia (ZrO_2) particles.

المنارة للاستشارات
www.manaraa.com

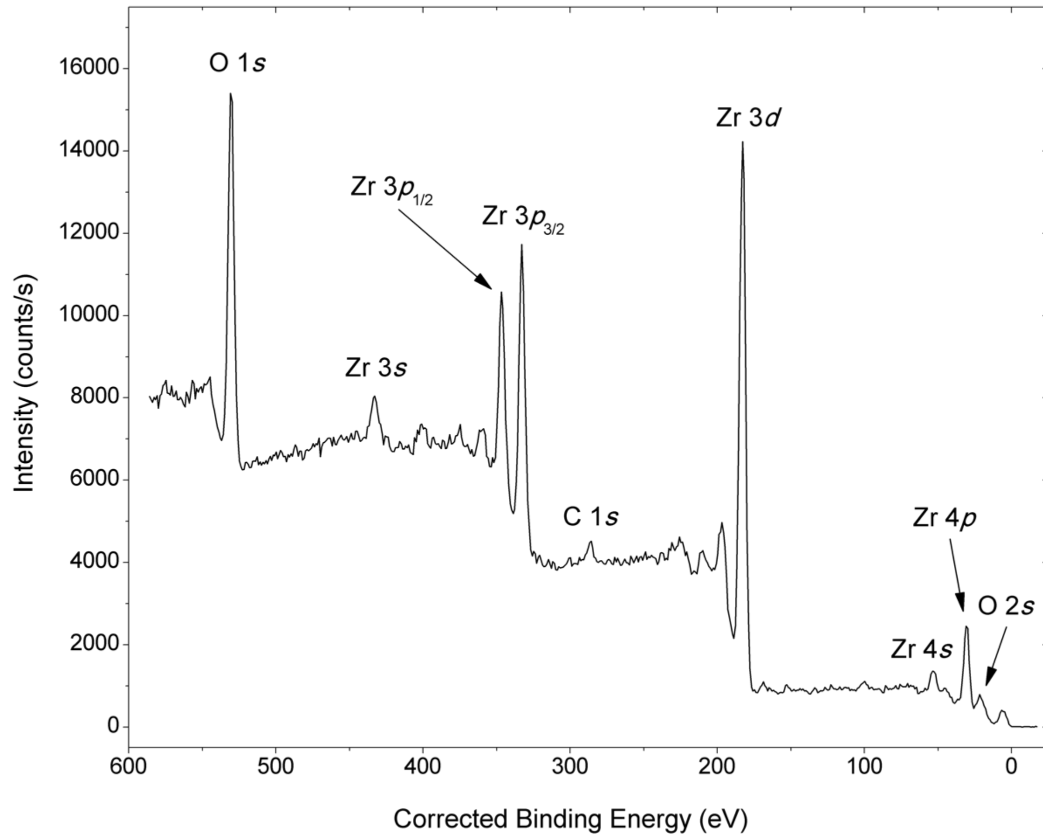

Figure 5.1.5.2. Expanded NAP-XPS Survey spectrum of Zirconia (ZrO_2) particles.

المنارة للاستشارات
www.manaraa.com

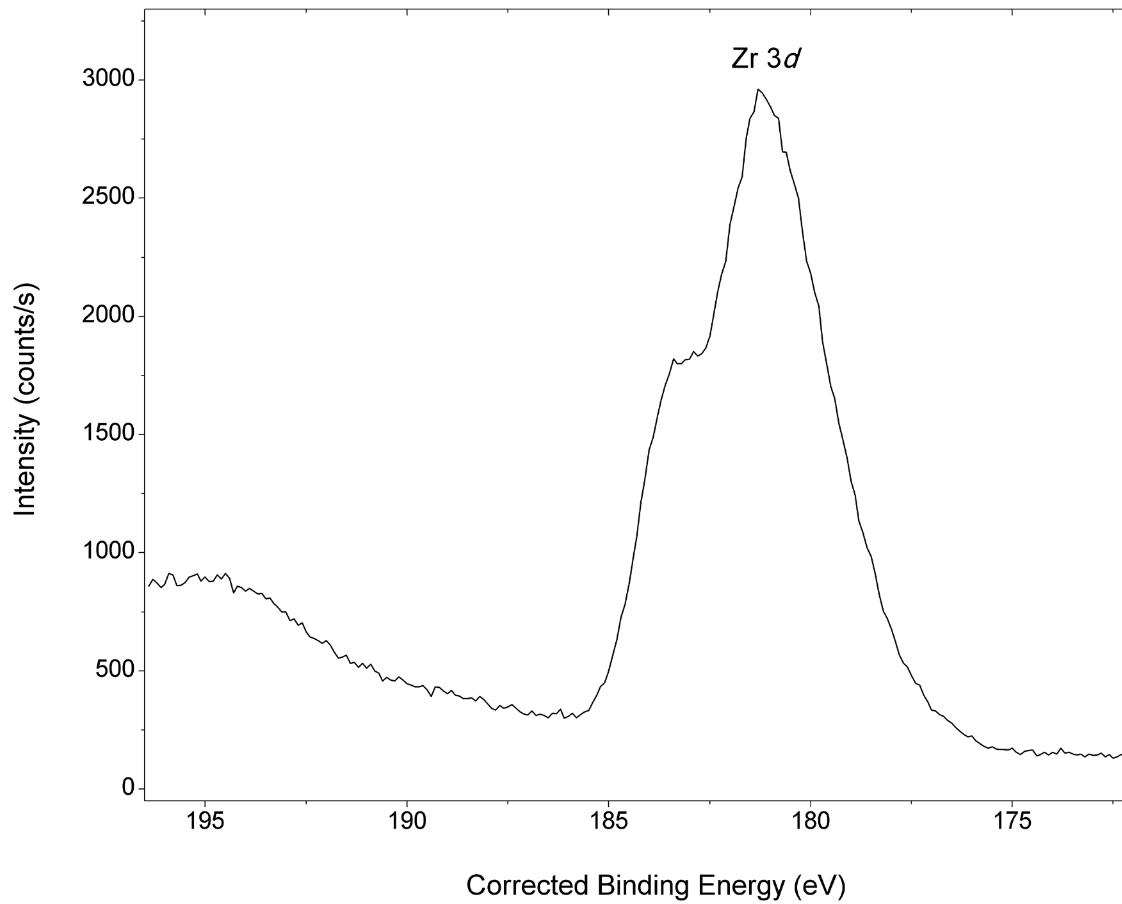

Figure 5.1.5.3. NAP-XPS 3*d* spectrum of Zirconia (ZrO_2) particles.

المنارة للاستشارات
www.manaraa.com

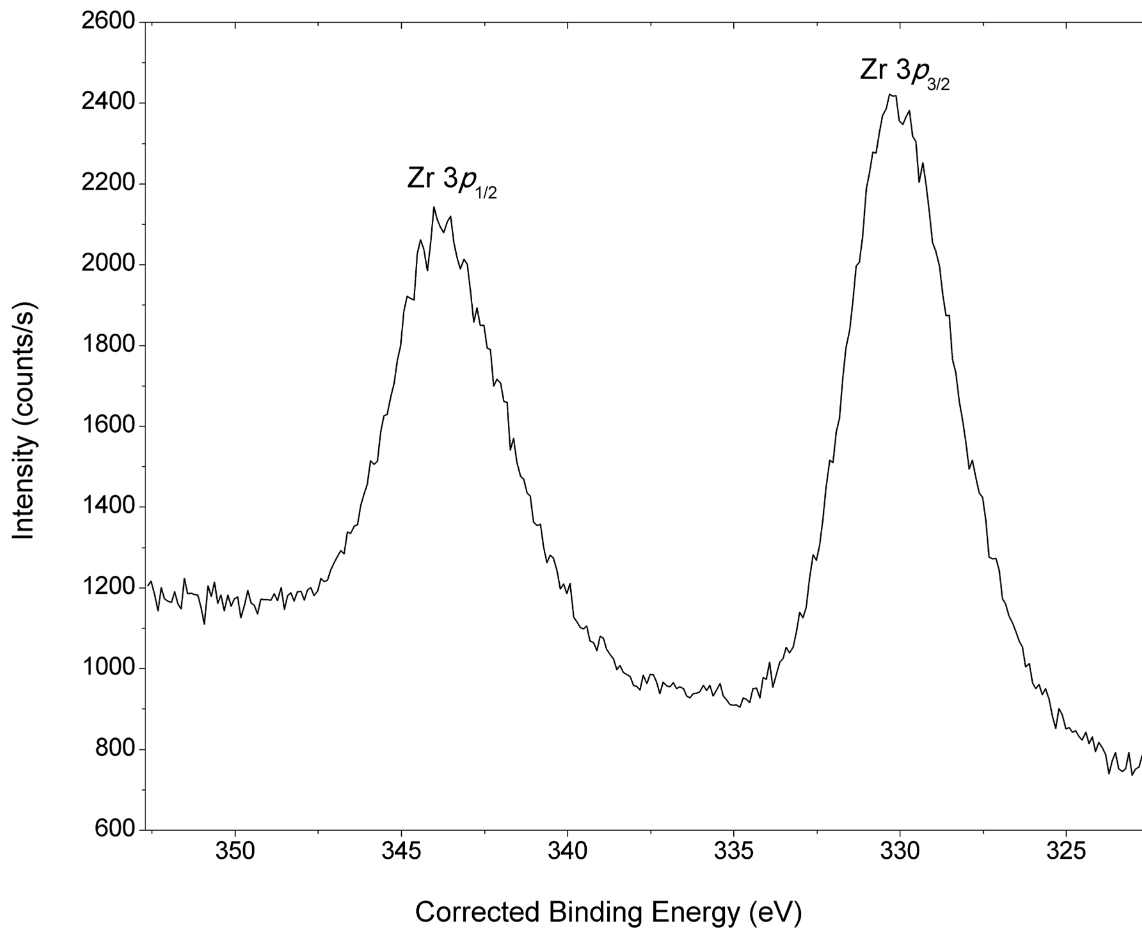

Figure 5.1.5.4. NAP-XPS Zr 3*p* spectrum of Zirconia (ZrO_2) particles.

المنارة للاستشارات
www.manaraa.com

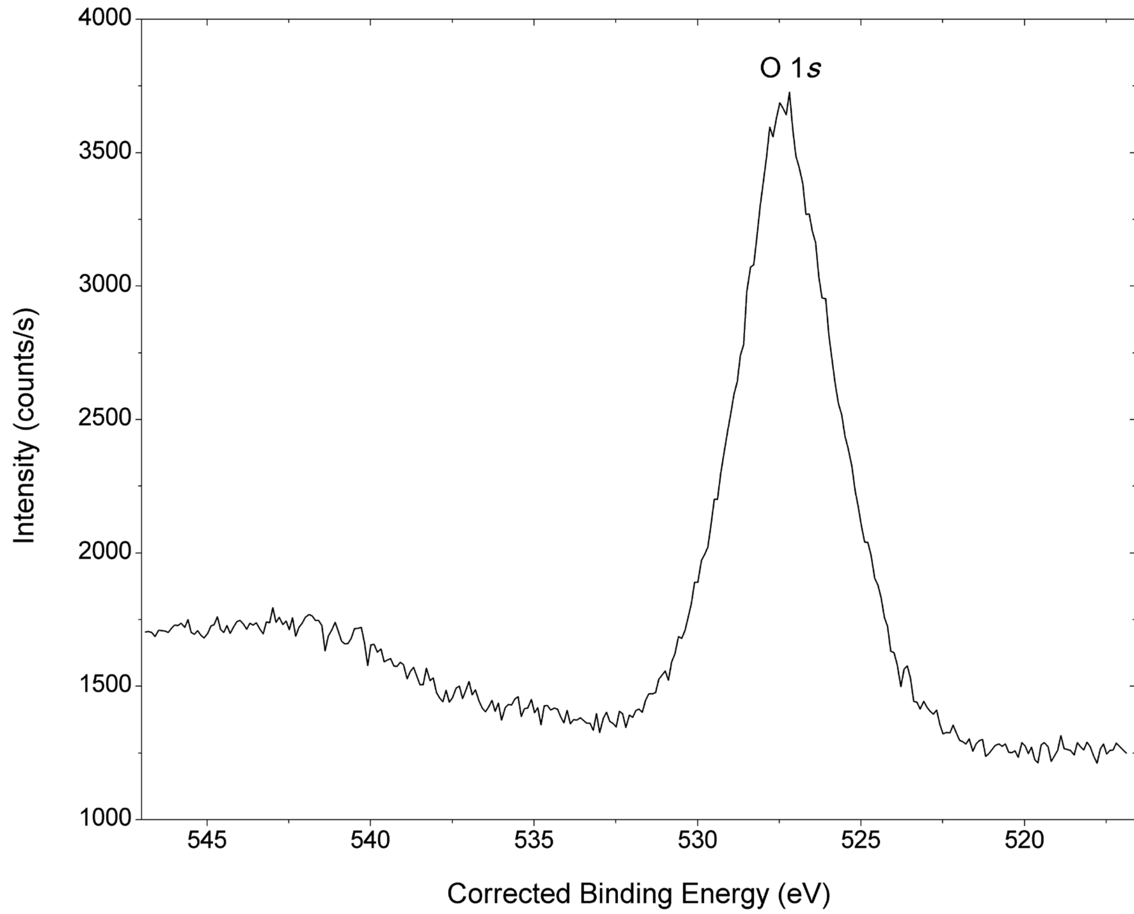

Figure 5.1.5.5. NAP-XPS O 1*s* spectrum of Zirconia (ZrO_2) particles.

المنارة للاستشارات
www.manaraa.com

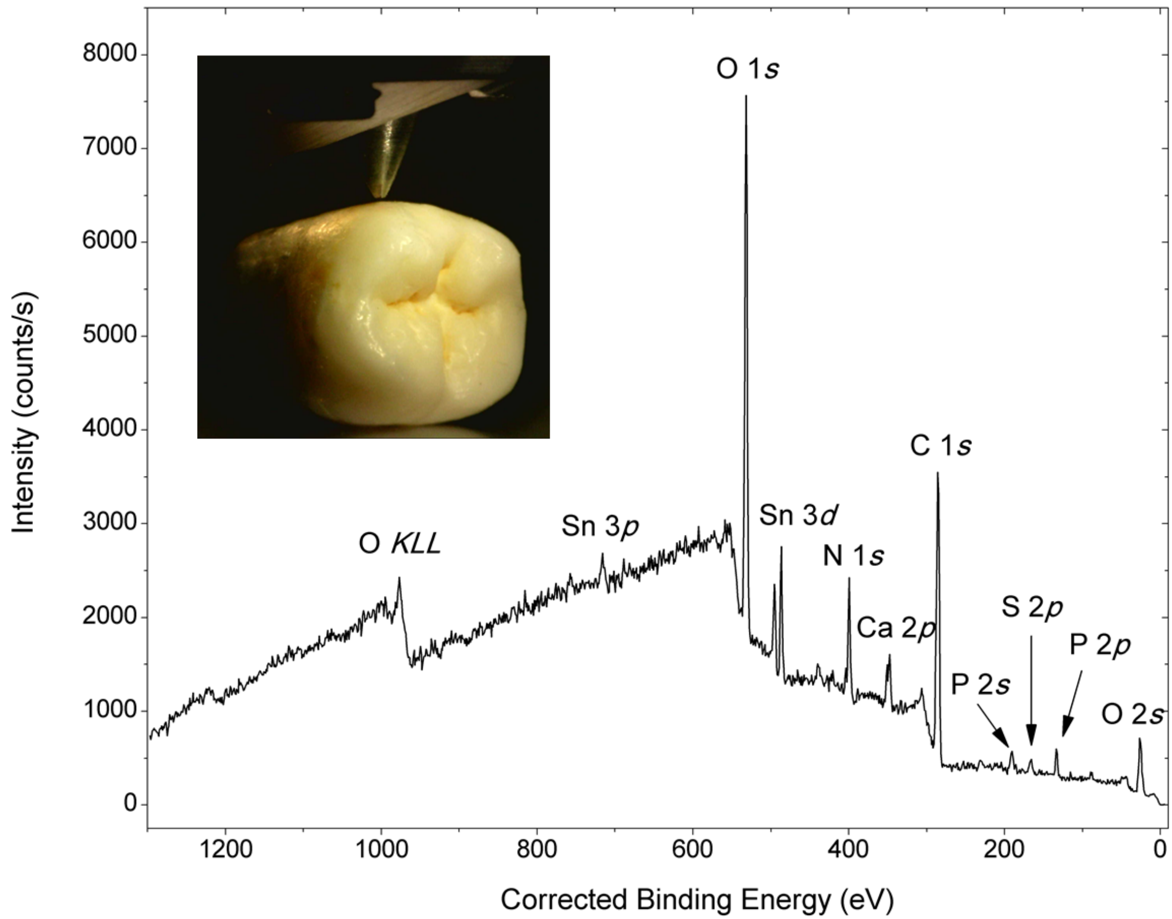

Figure 5.1.6.1. NAP-XPS survey spectrum of Top Part of a Molar human tooth.

المنارة للاستشارات
www.manaraa.com

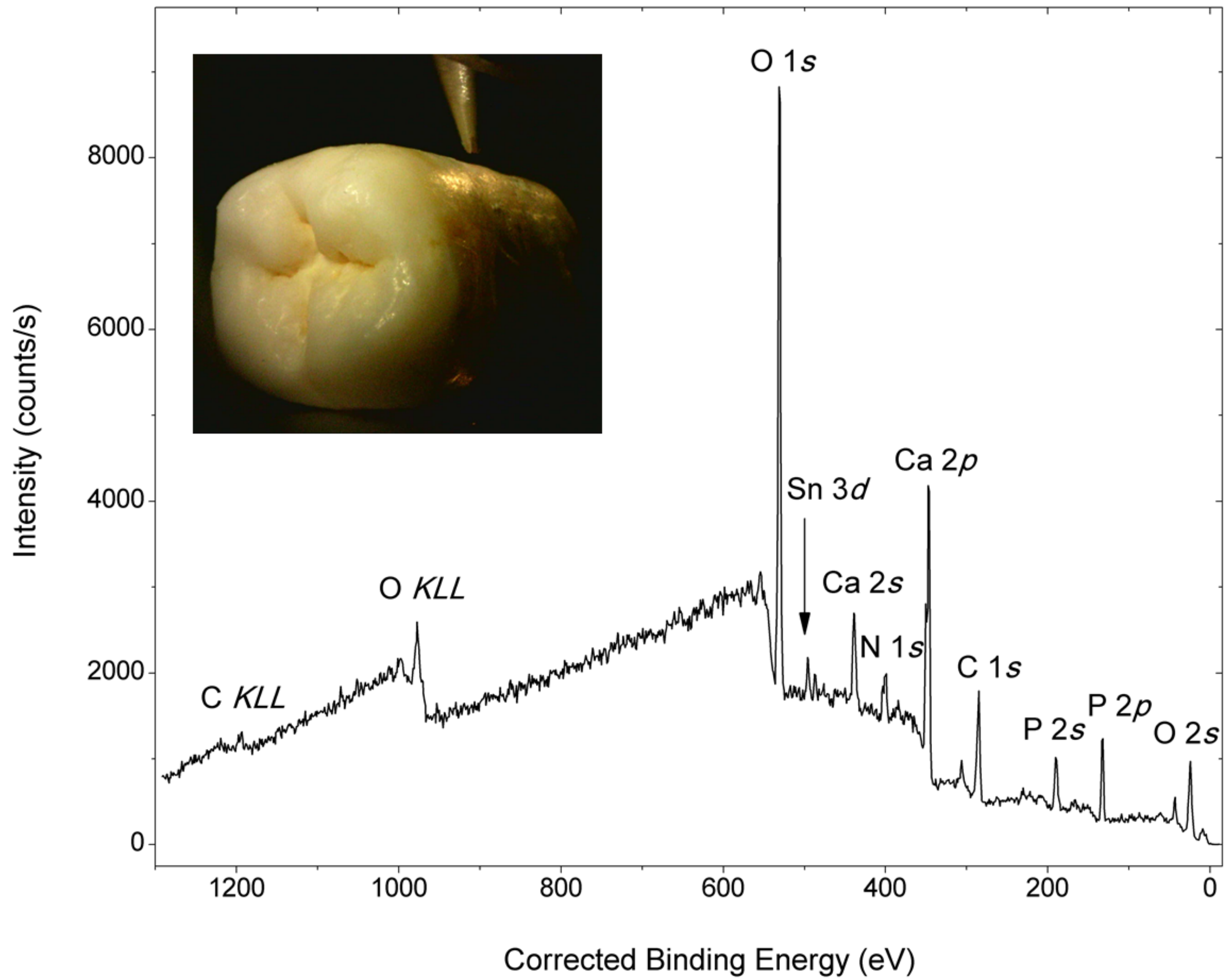

Figure 5.1.6.2. NAP-XPS survey spectrum of Middle Part of a Molar human tooth.

المنارة للاستشارات
www.manaraa.com

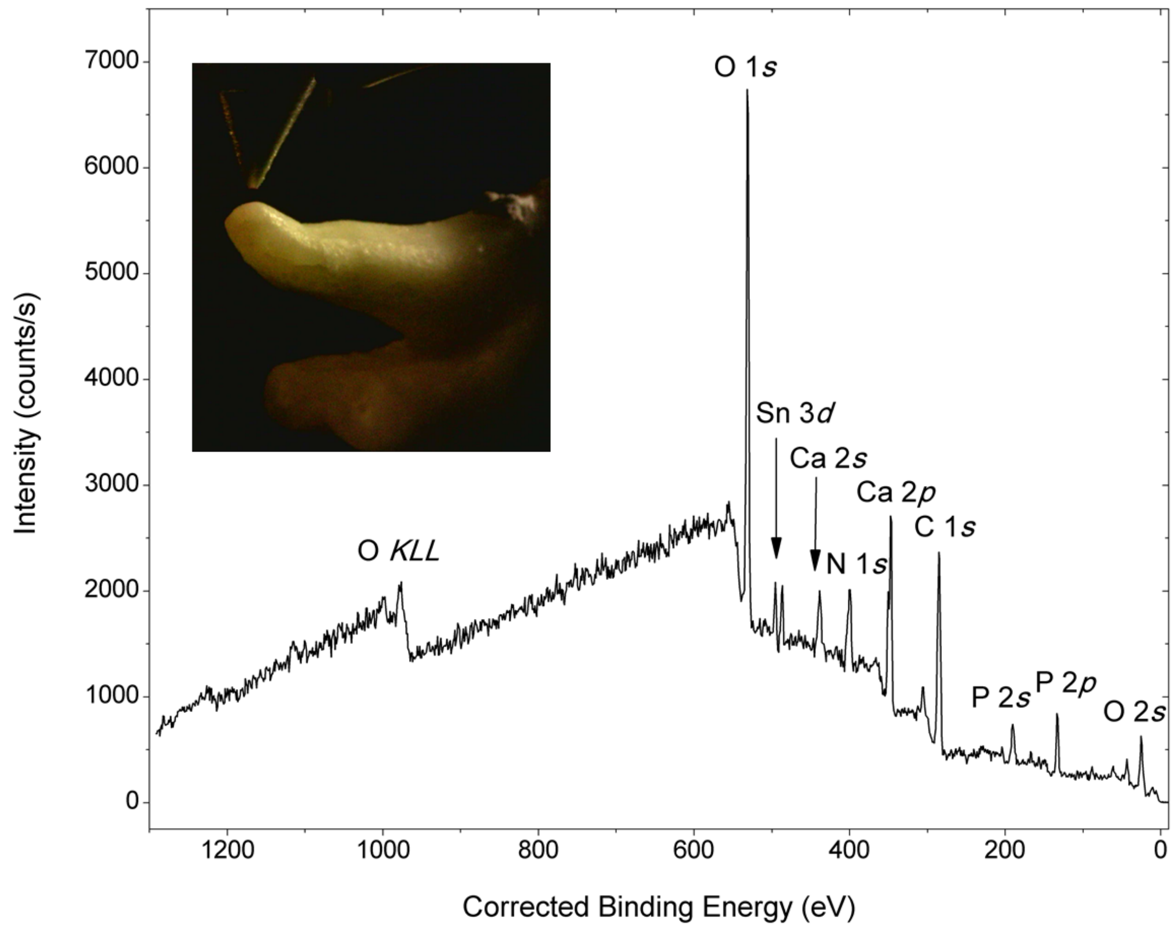

Figure 5.1.6.3. NAP-XPS survey spectrum of Root Part of a Molar human tooth.

المنارة للاستشارات
www.manaraa.com

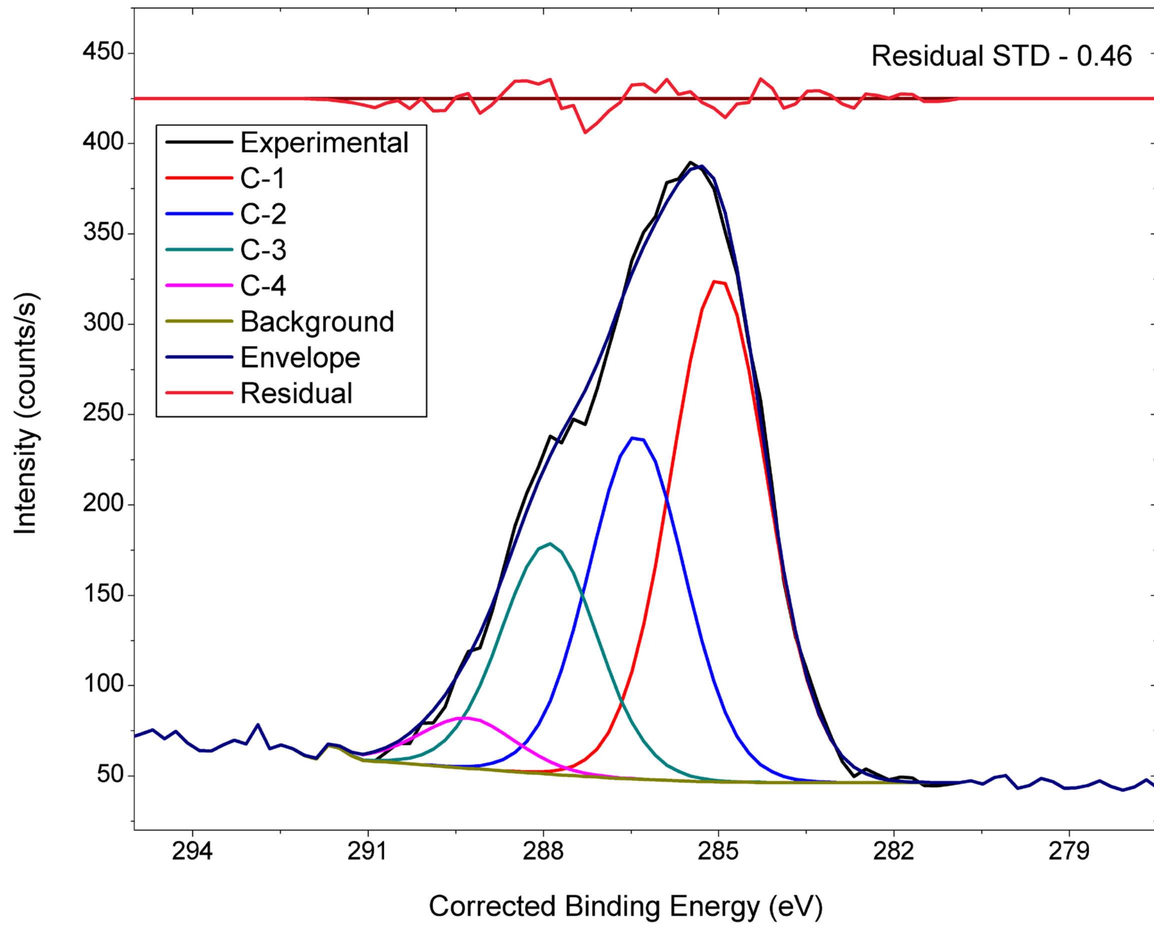

Figure 5.1.6.1.1. NAP-XPS C 1*s* spectrum of Top Part of a Molar human tooth.

www.manaraa.com

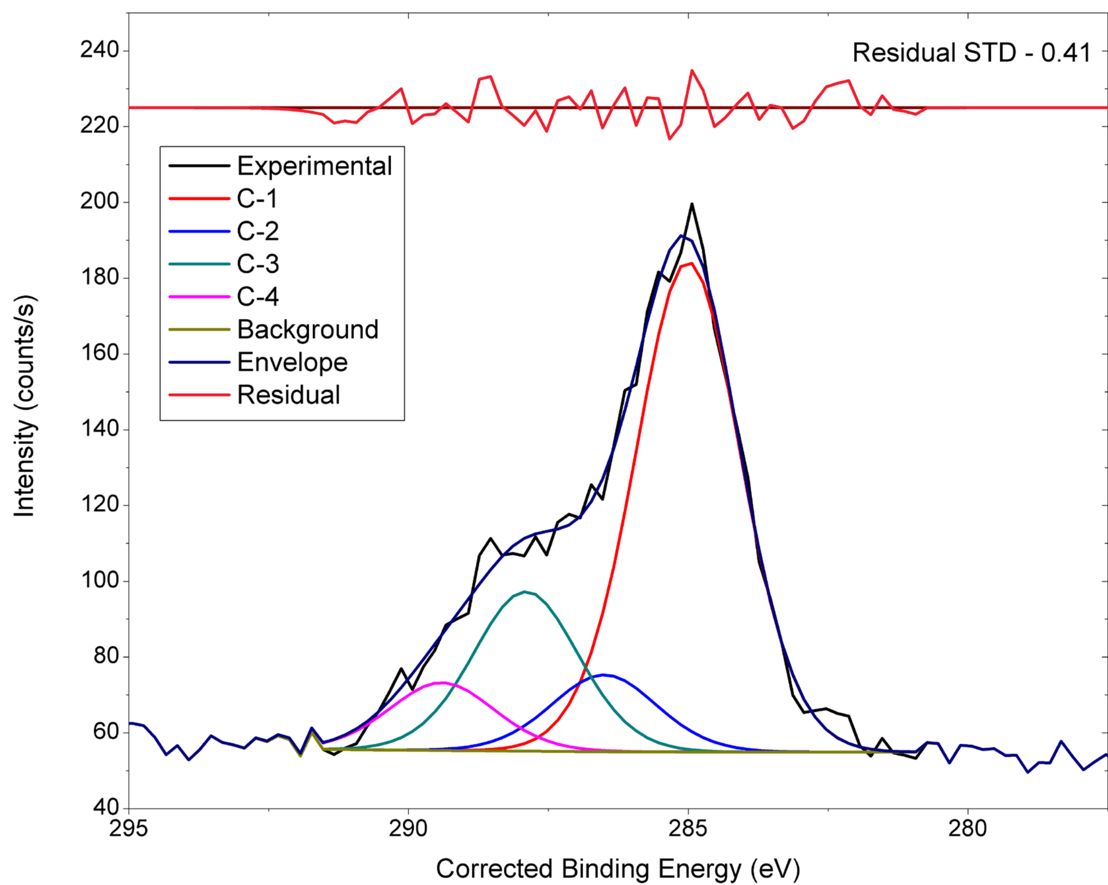

Figure 5.1.6.2.1. NAP-XPS C 1*s* spectrum of Middle Part of a Molar human tooth.

المنارة للاستشارات
www.manaraa.com

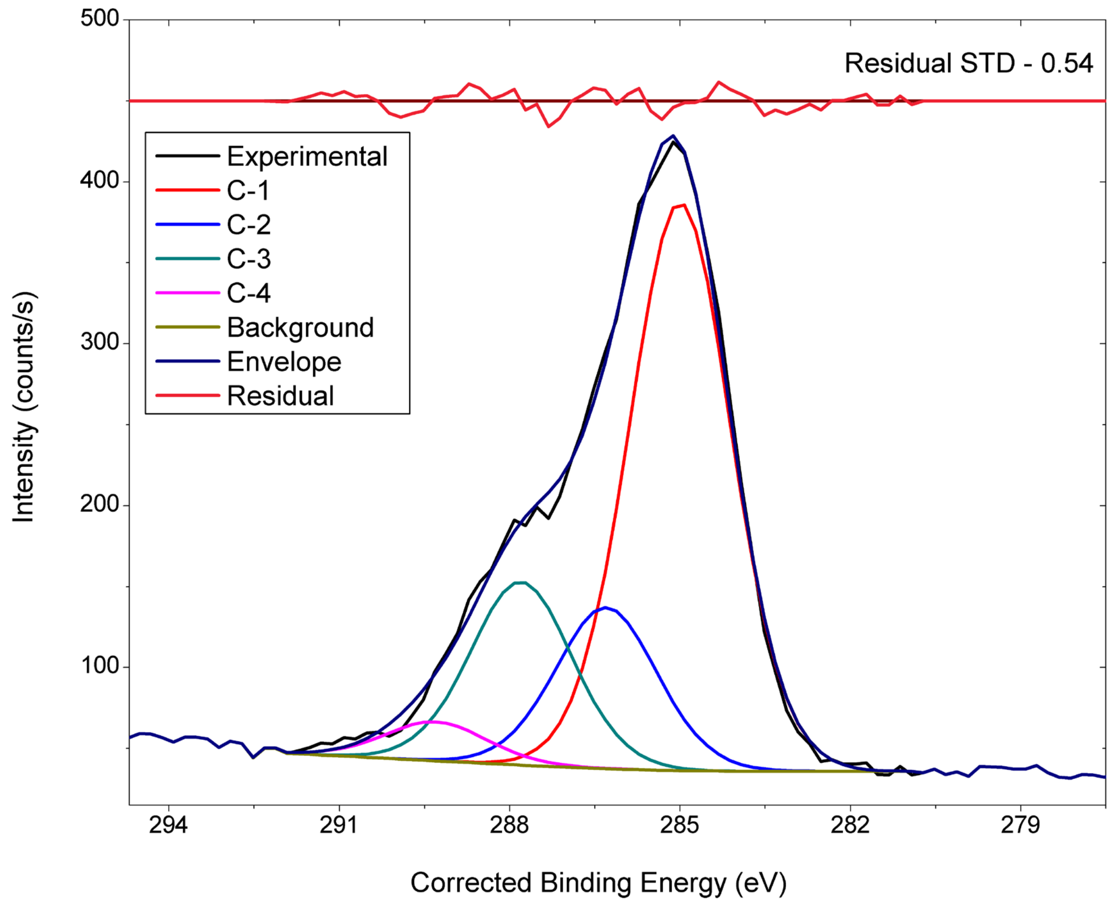

Figure 5.1.6.3.1. NAP-XPS C 1*s* spectrum of Root Part of a Molar human tooth.

www.manaraa.com

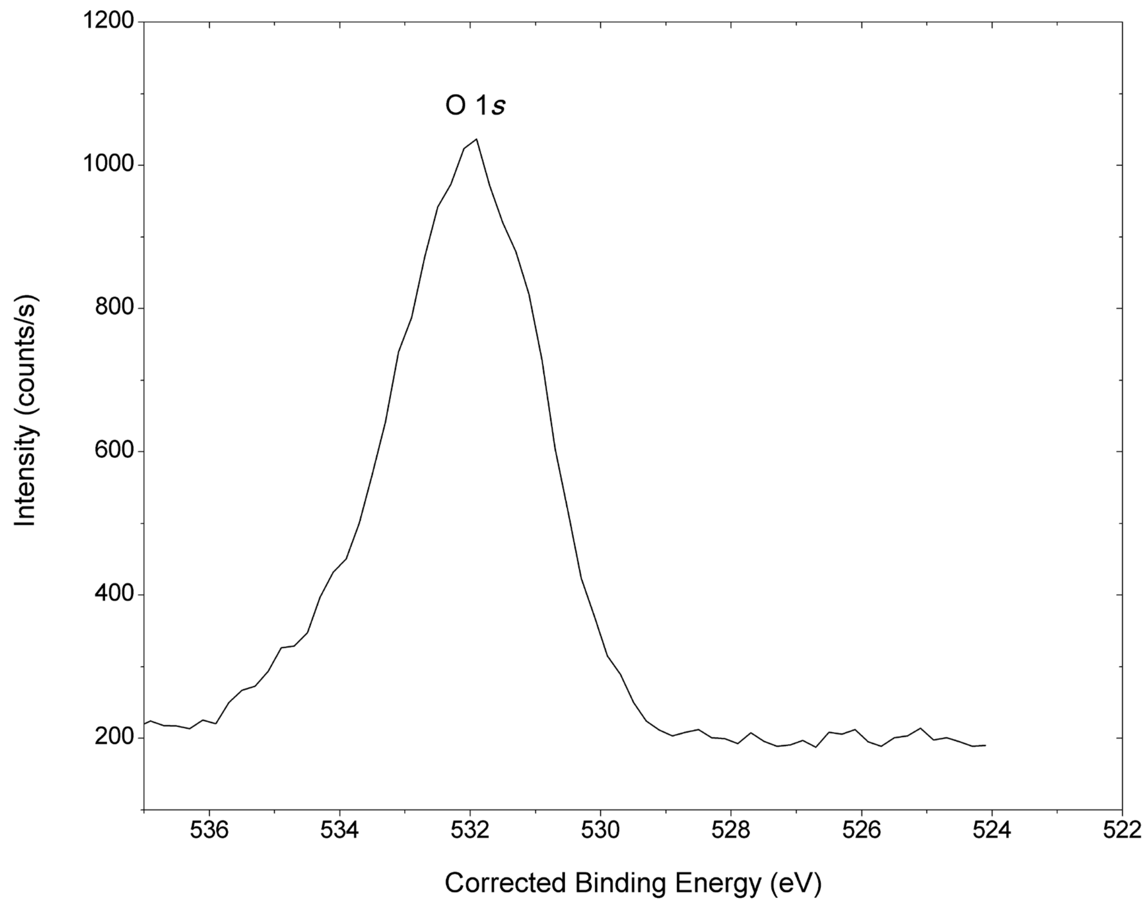

Figure 5.1.6.1.2. NAP-XPS O 1*s* spectrum of Top Part of a Molar human tooth.

المنارة للاستشارات
www.manaraa.com

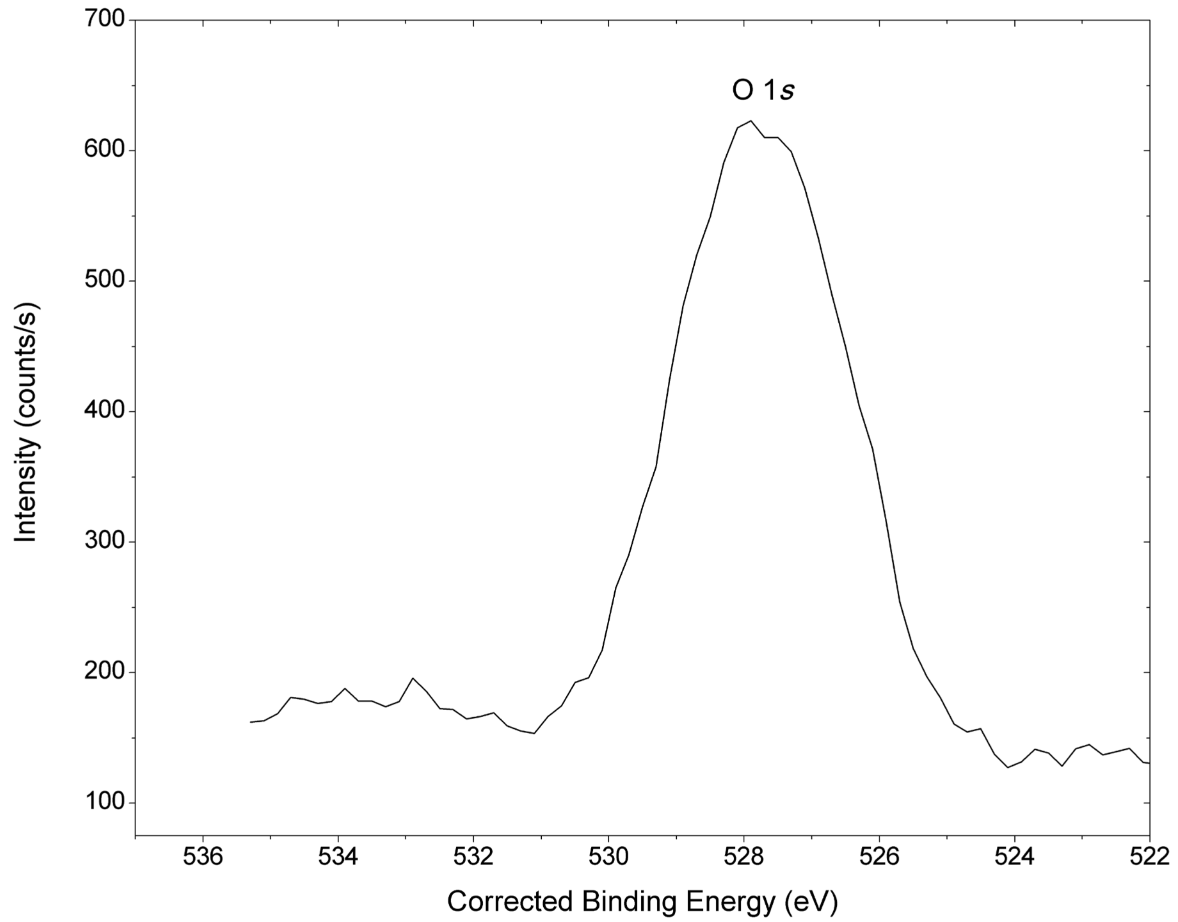

Figure 5.1.6.2.2. NAP-XPS O 1*s* spectrum of Middle Part of a Molar human tooth.

المنارة للاستشارات
www.manaraa.com

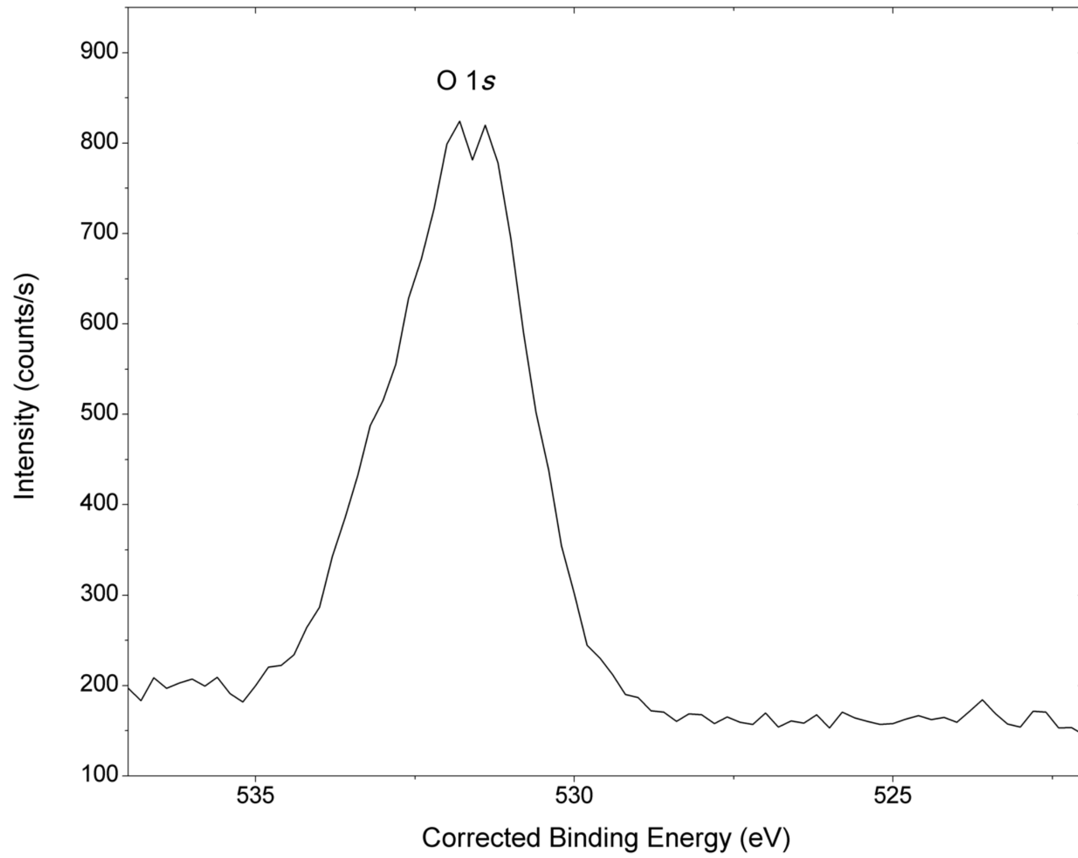

Figure 5.1.6.3.2. NAP-XPS O 1*s* spectrum of Root Part of a Molar human tooth.

المنارة للاستشارات
www.manaraa.com

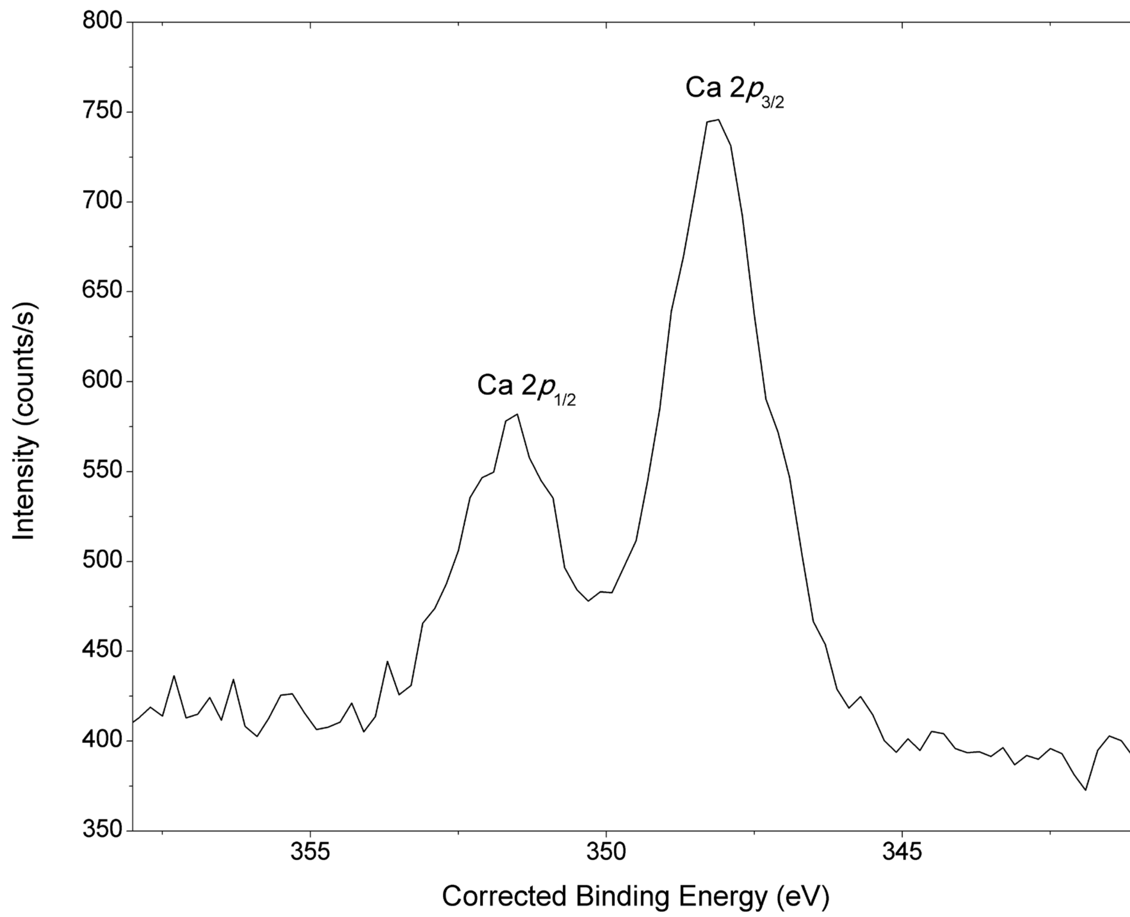

Figure 5.1.6.1.3. NAP-XPS Ca 2*p* spectrum of Top Part of a Molar human tooth.

المنارة للاستشارات
www.manaraa.com

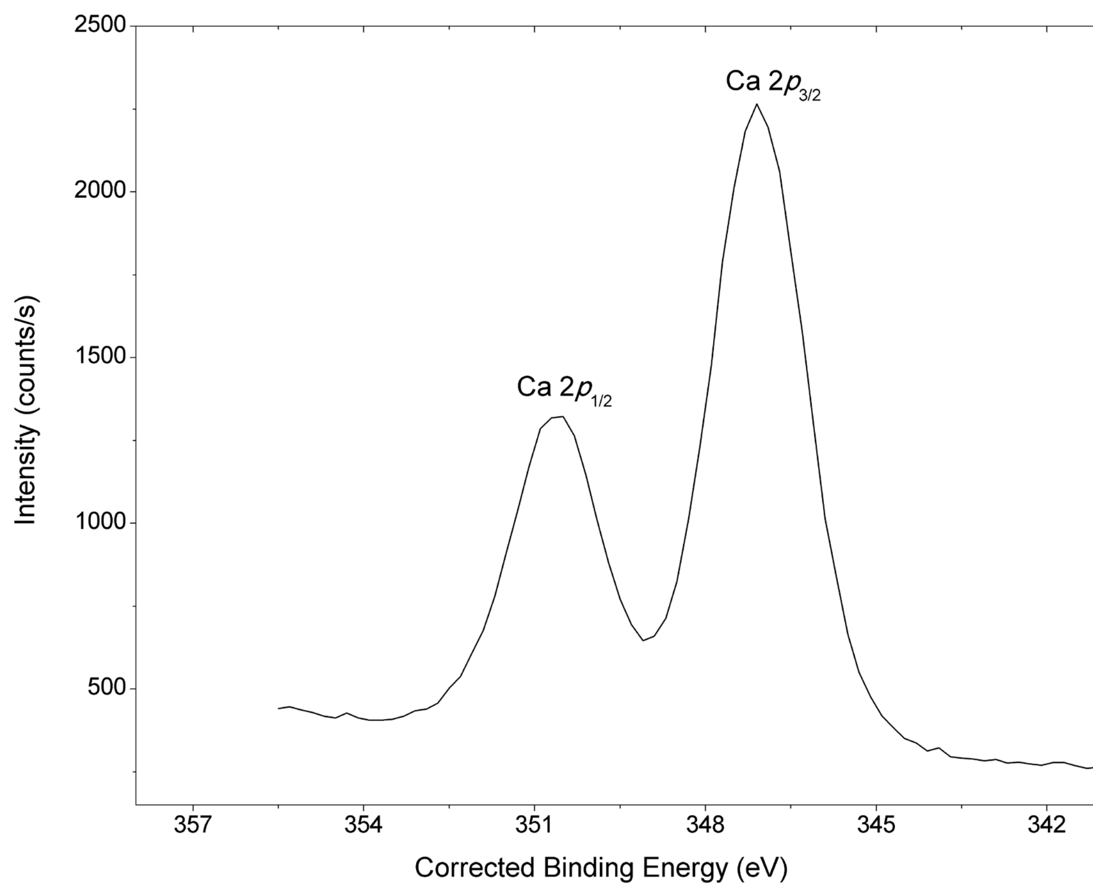

Figure 5.1.6.2.3. NAP-XPS Ca 2*p* spectrum of Middle Part of a Molar human tooth.

المنارة للاستشارات
www.manaraa.com

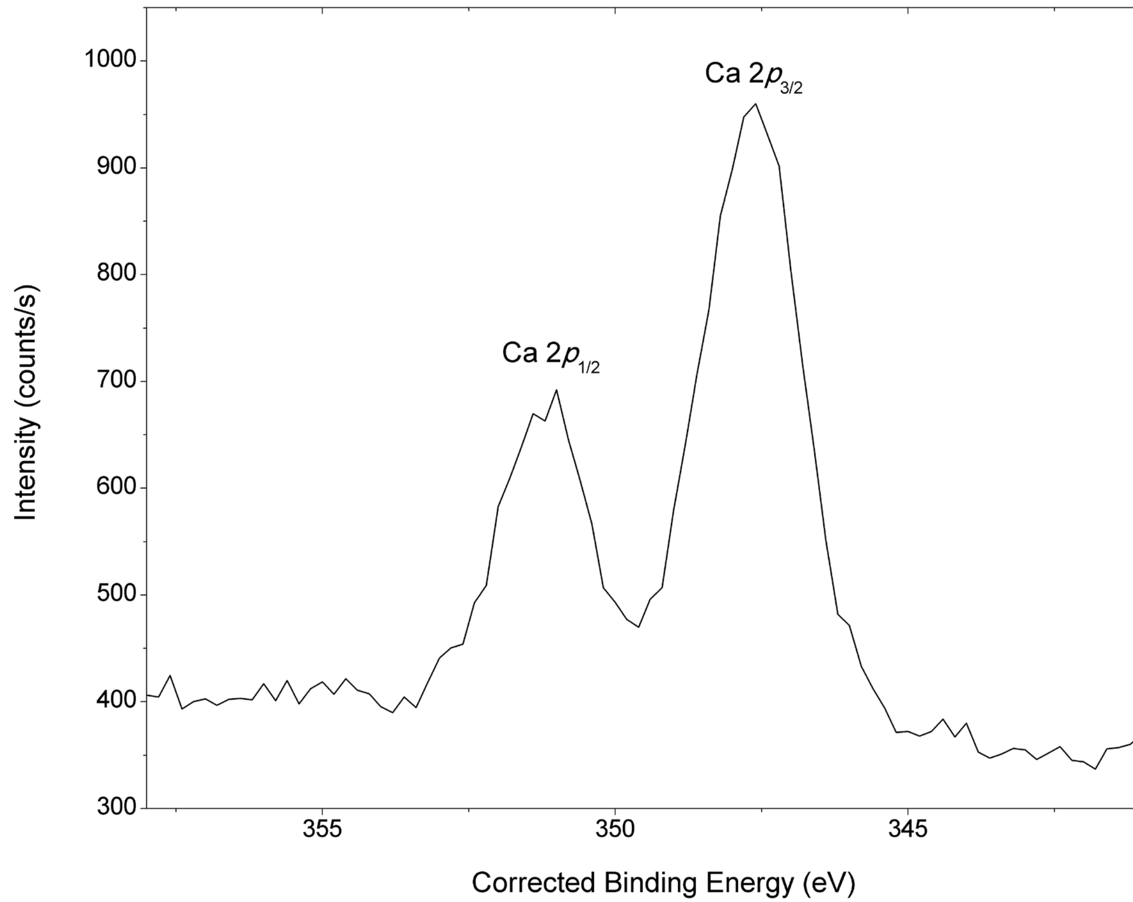

Figure 5.1.6.3.3. NAP-XPS Ca 2*p* spectrum of Root Part of a Molar human tooth.

المنارة للاستشارات
www.manaraa.com

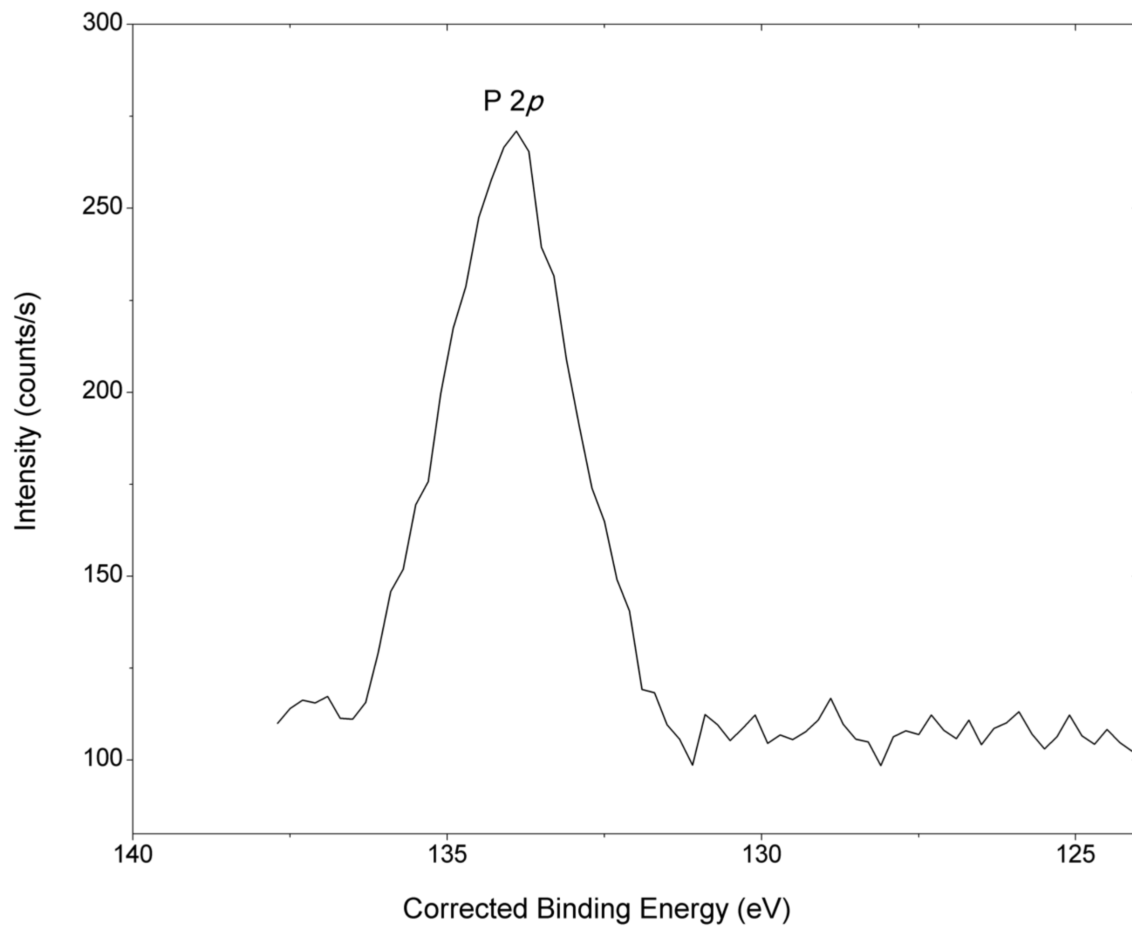

Figure 5.1.6.1.4. NAP-XPS P 2*p* spectrum of Top Part of a Molar human tooth.

المنارة للاستشارات
www.manaraa.com

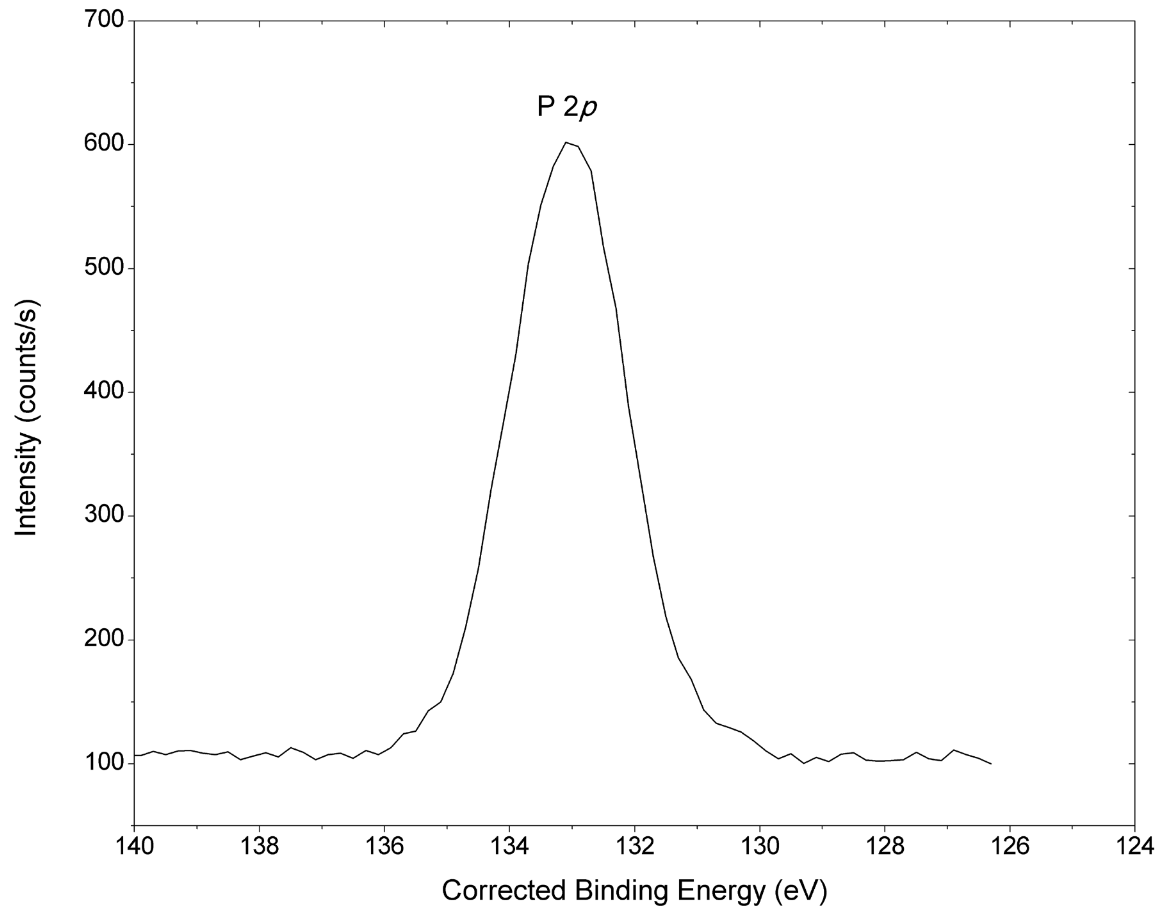

Figure 5.1.6.2.4. NAP-XPS P 2*p* spectrum of Middle Part of a Molar human tooth.

المنارة للاستشارات
www.manaraa.com

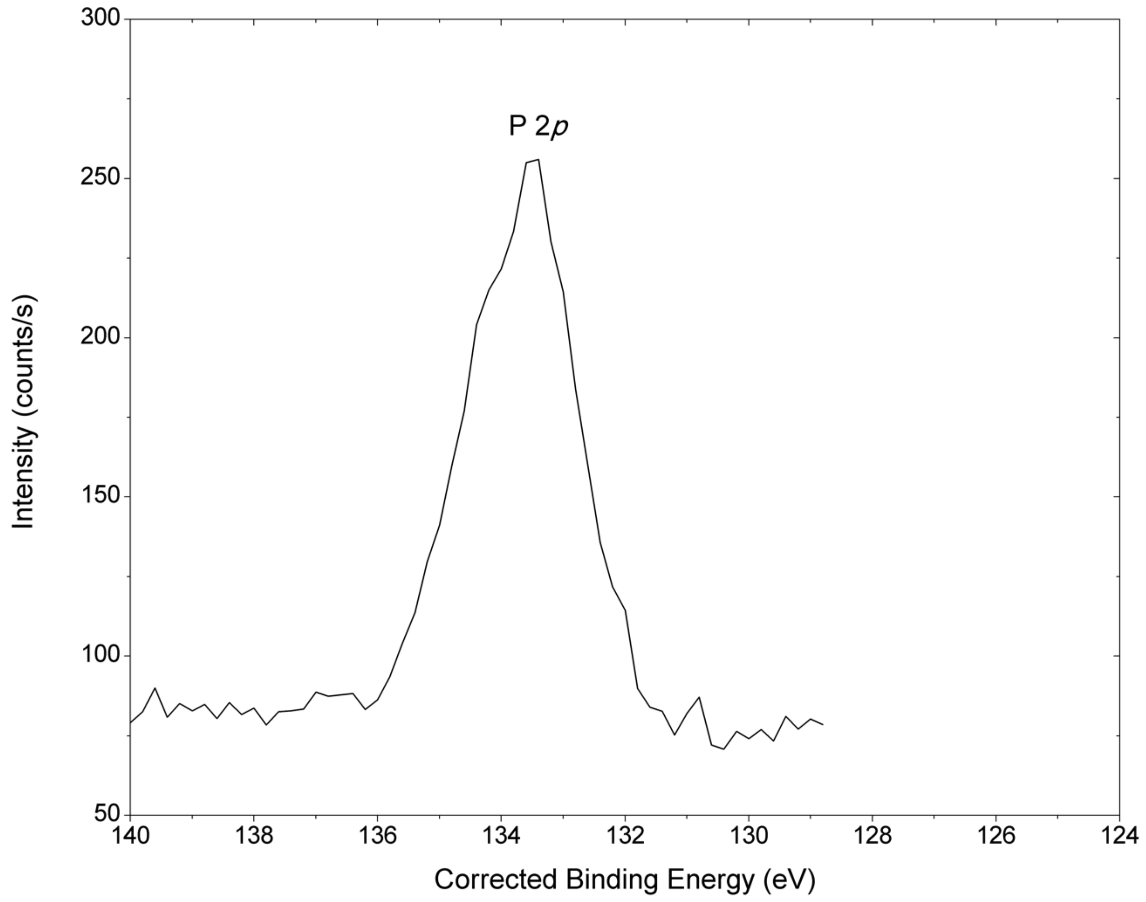

Figure 5.1.6.3.4. NAP-XPS P 2*p* spectrum of Root Part of a Molar human tooth.

المنارة للاستشارات
www.manaraa.com

Top Part

Middle Part

Root Part

Figure 5.1.6.4. Different parts of human tooth analyzed by NAP-XPS in this study.

المنارة للاستشارات
www.manaraa.com

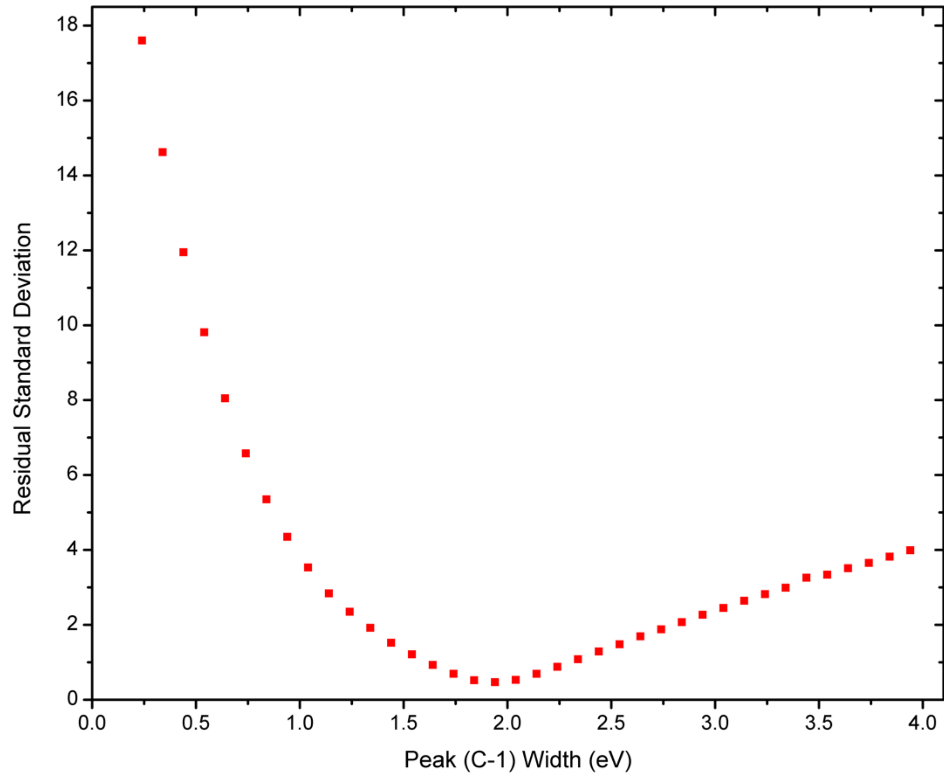

Figure 5.1.6.5. Uniqueness plot of the C 1s fit for top part of the Adult tooth.

المنارة للاستشارات

www.manaraa.com

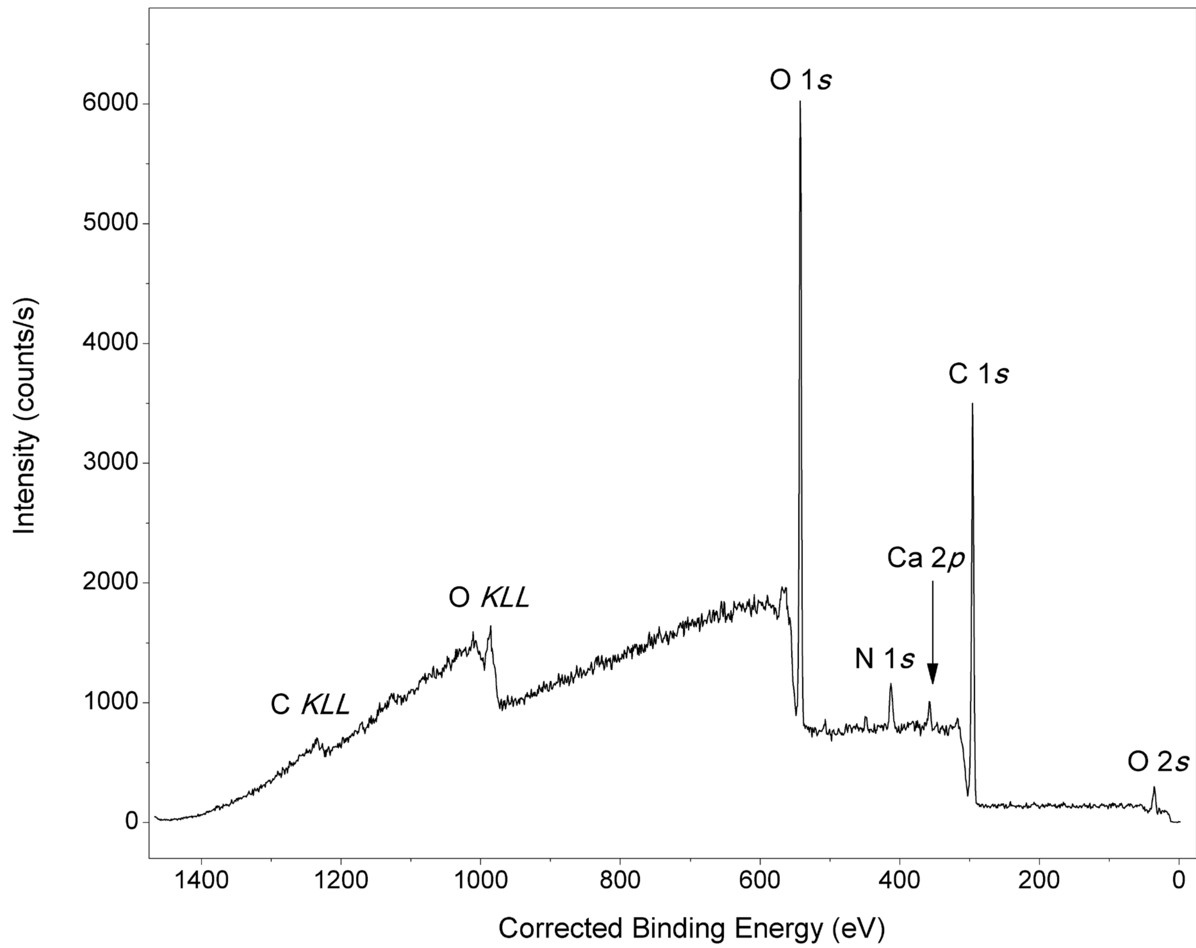

Figure 5.1.7.1. NAP-XPS survey spectrum of white unprinted paper.

المنارة للاستشارات
www.manaraa.com

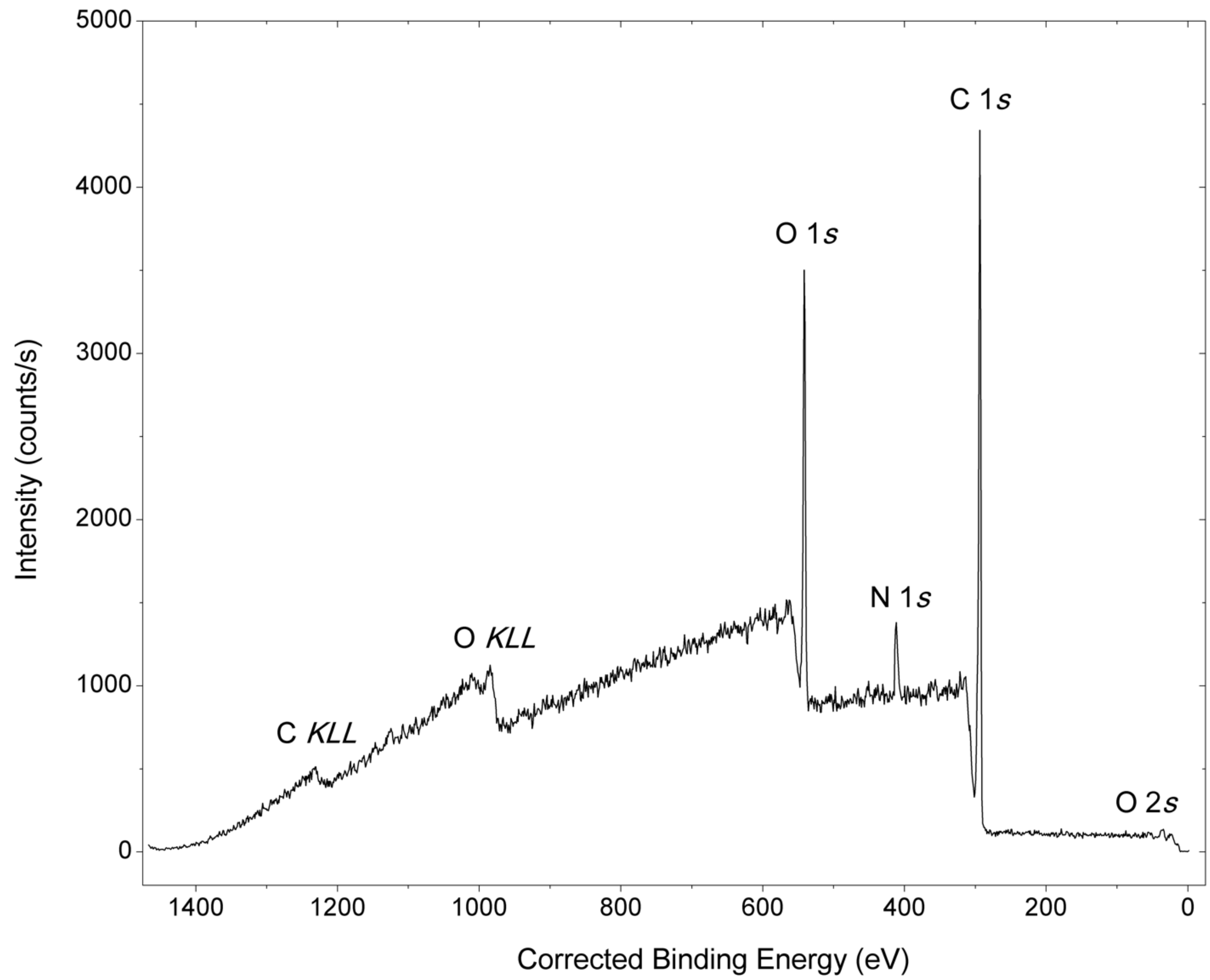

Figure 5.1.7.2. NAP-XPS survey spectrum of blue printed-paper.

المنارة للاستشارات
www.manaraa.com

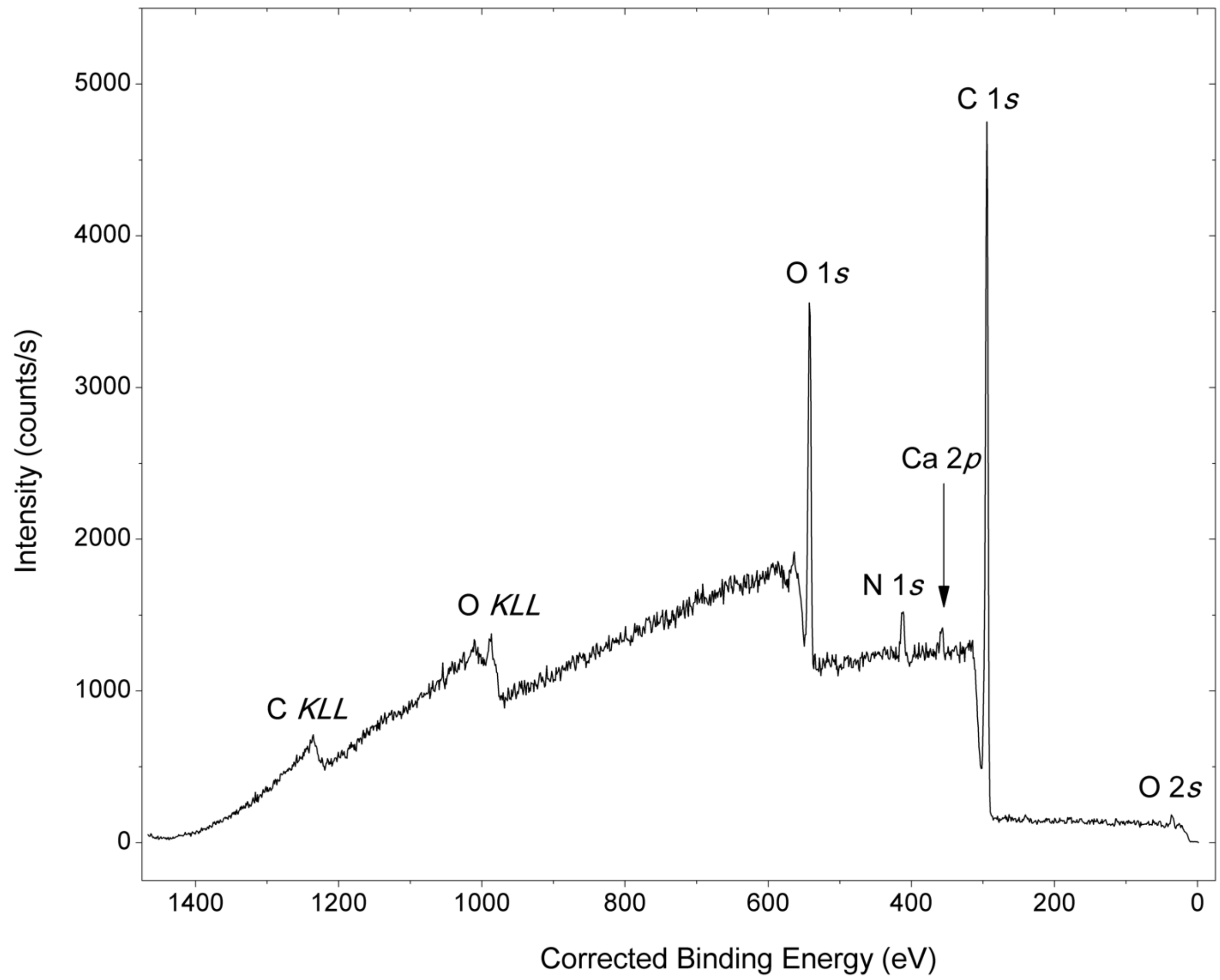

Figure 5.1.7.3. NAP-XPS survey spectrum of dark blue printed-paper.

المنارة للاستشارات
www.manaraa.com

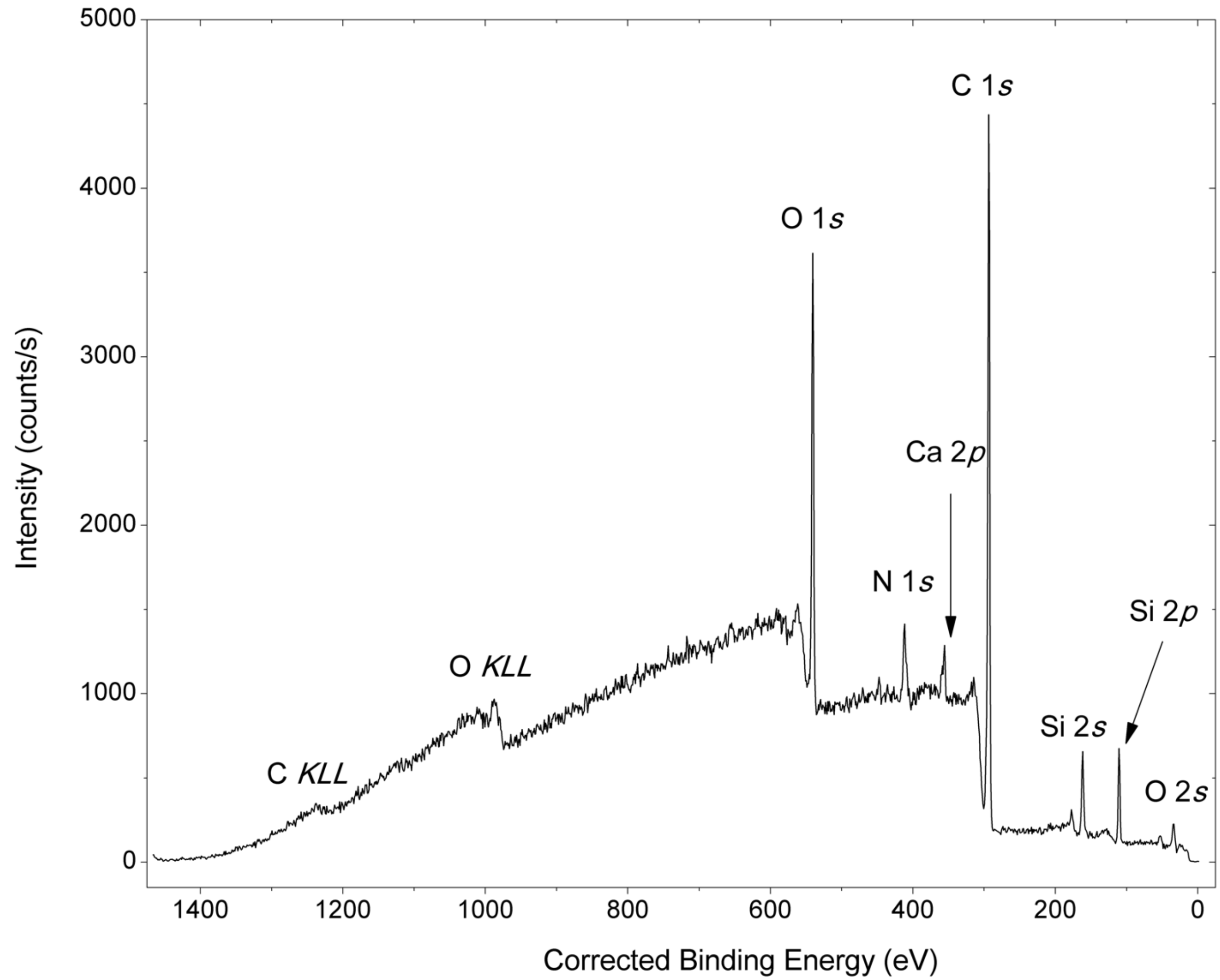

Figure 5.1.7.4. NAP-XPS survey spectrum of yellow post-it note.

المنارة للاستشارات
www.manaraa.com

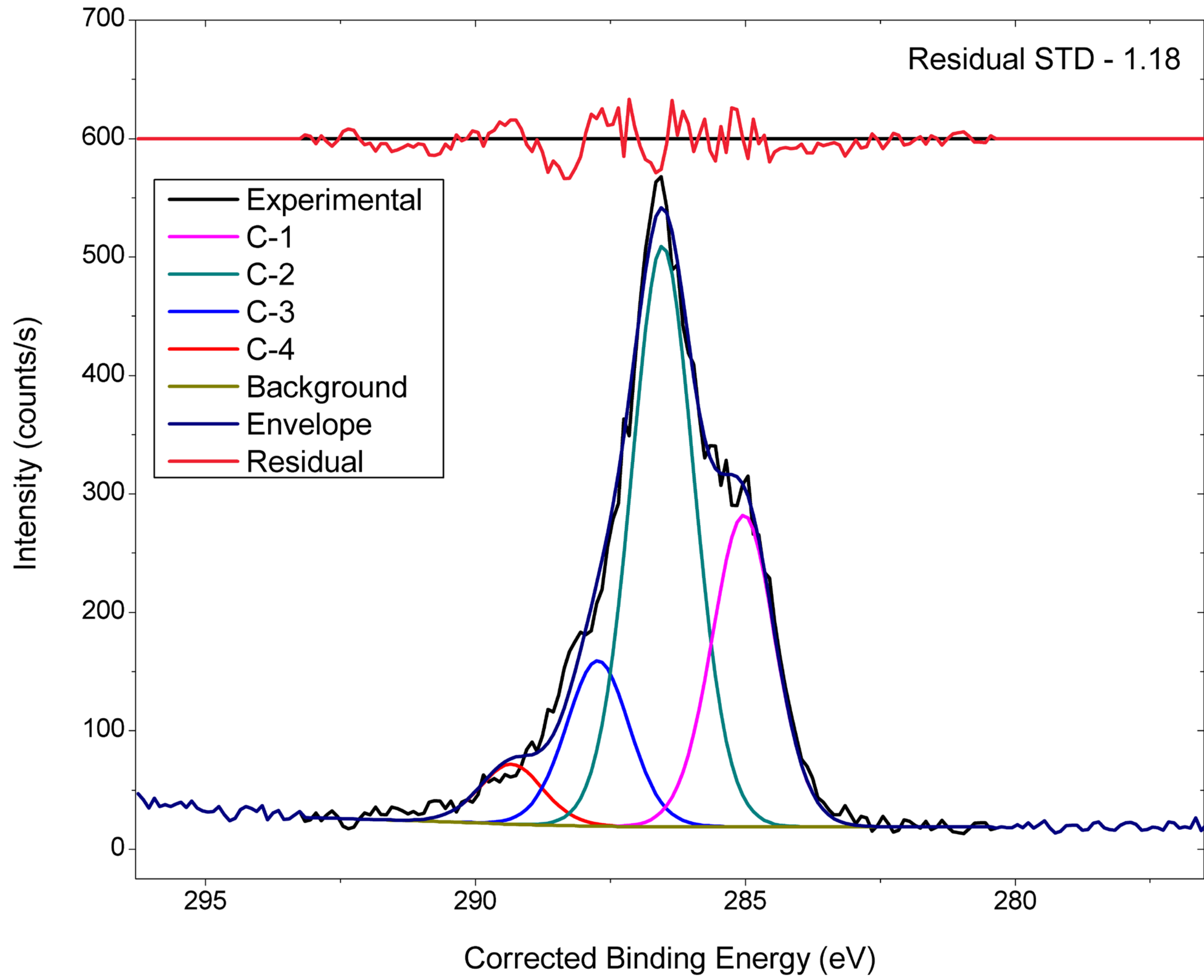

Figure 5.1.7.1.1. NAP-XPS C 1*s* spectrum of white unprinted paper.

المنارة للاستشارات
www.manaraa.com

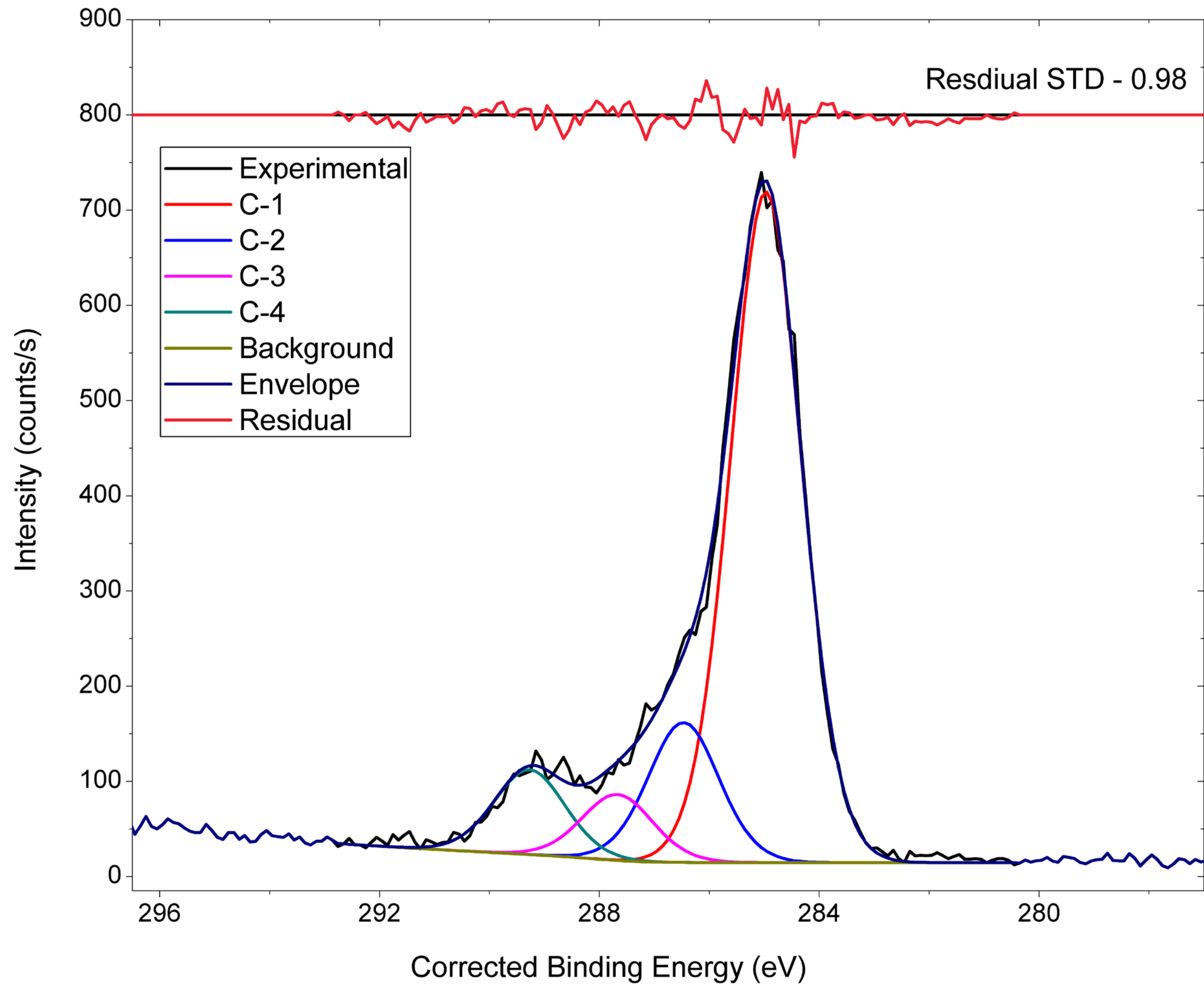

Figure 5.1.7.2.1. NAP-XPS C 1*s* spectrum of blue printed paper.

المنارة للاستشارات
www.manaraa.com

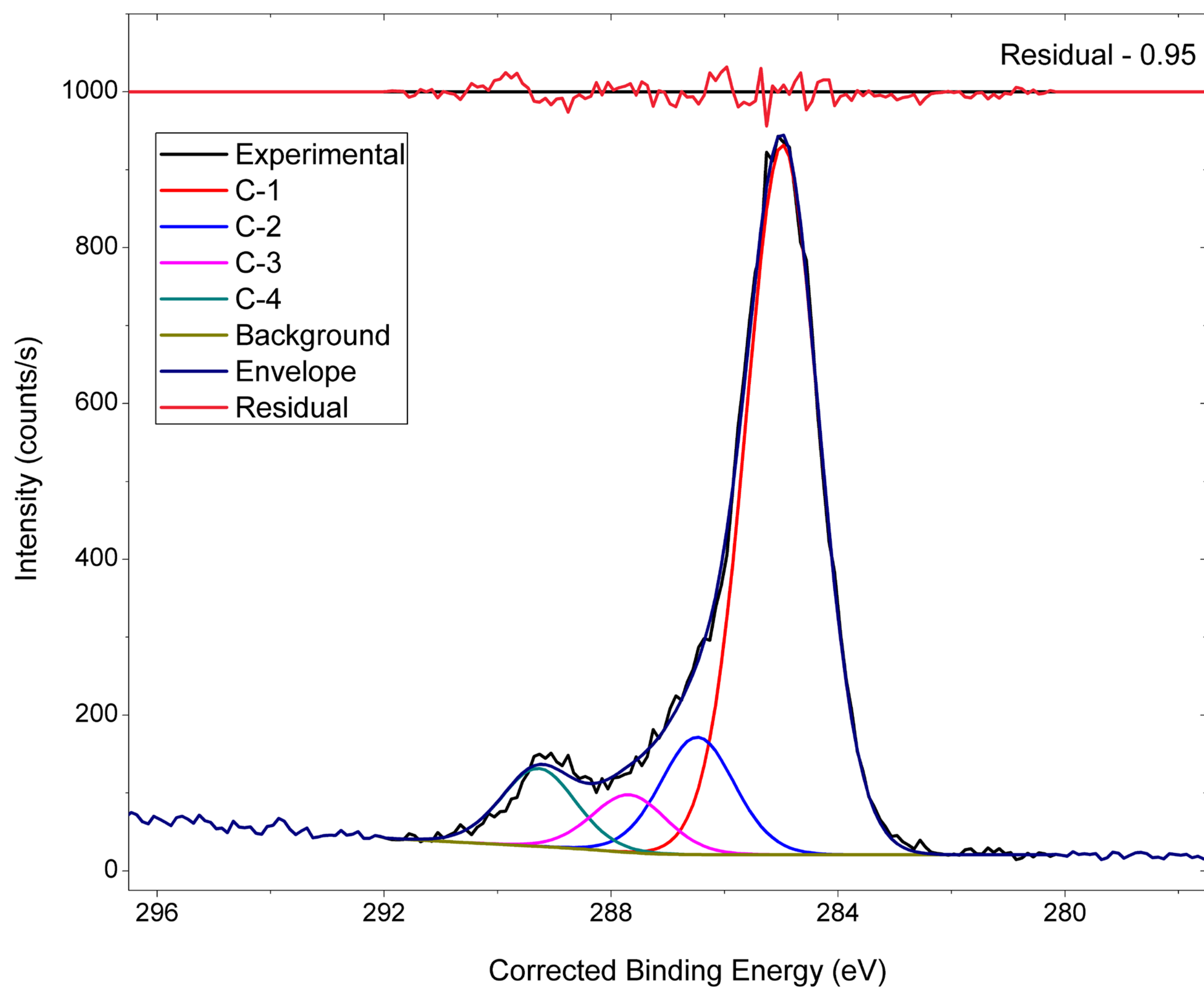

Figure 5.1.7.3.1. NAP-XPS C 1*s* spectrum of dark blue printed paper.

المنارة للاستشارات
www.manaraa.com

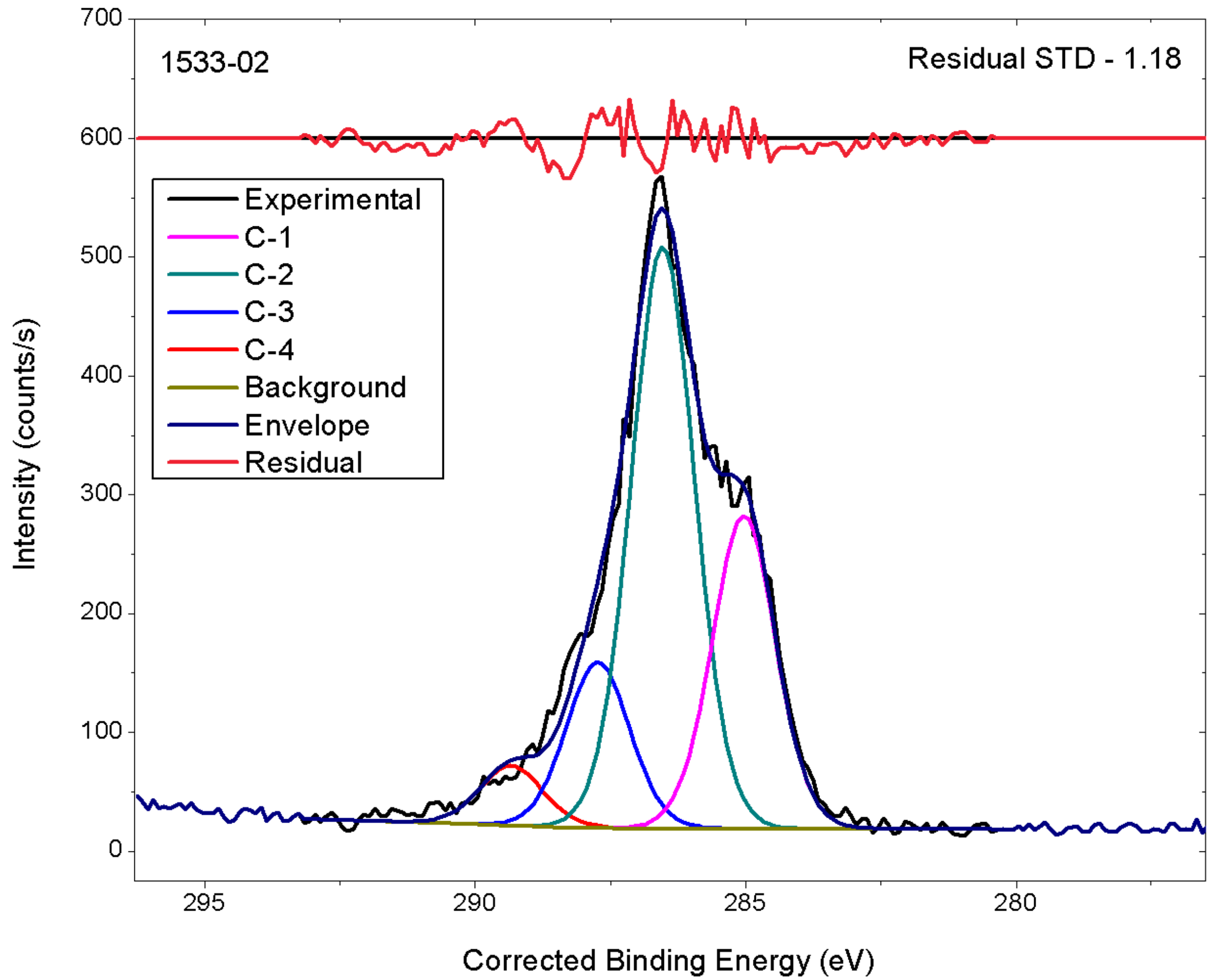

Figure 5.1.7.4.1. NAP-XPS C 1*s* spectrum of yellow post-it note.

www.manaraa.com

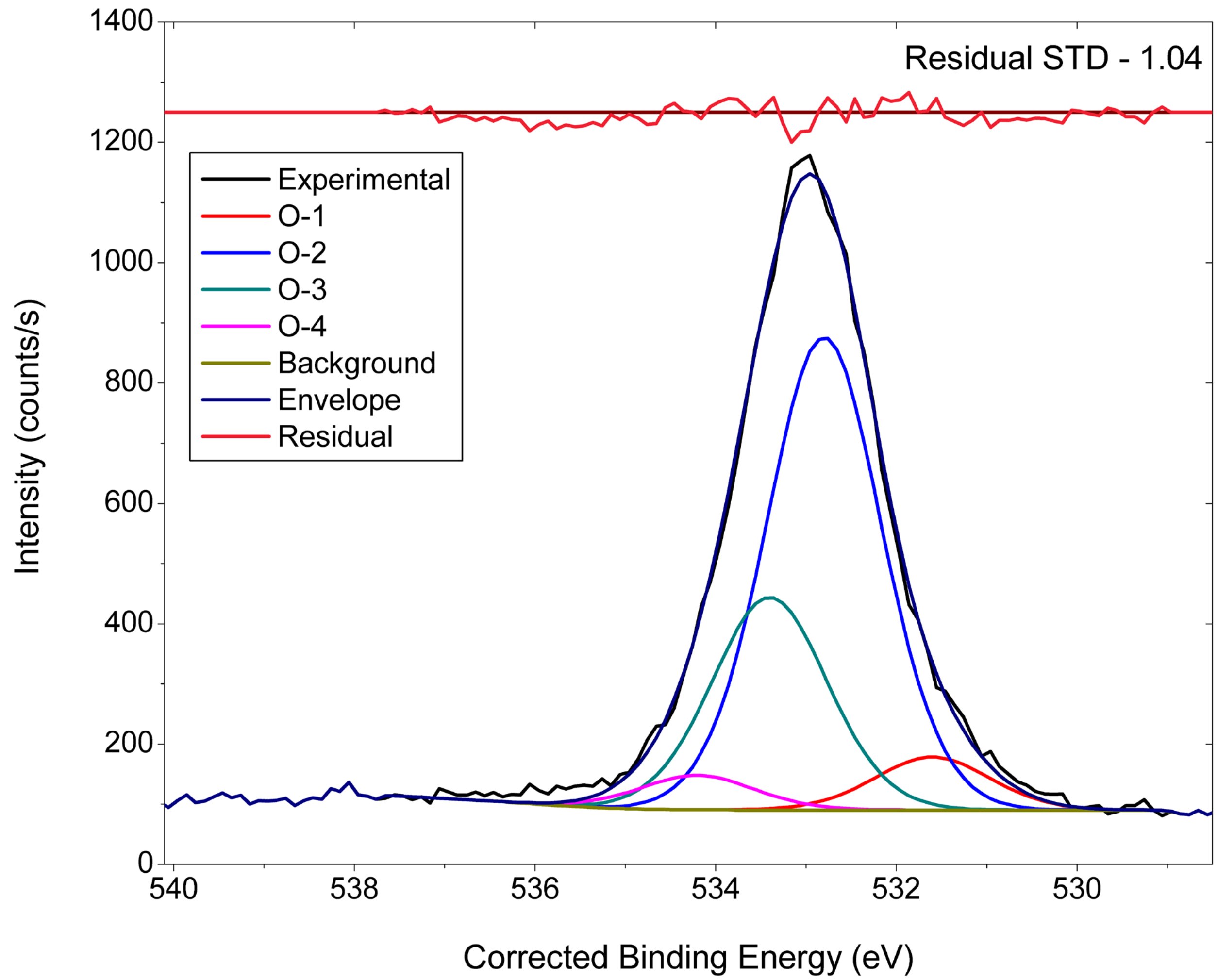

Figure 5.1.7.1.2a NAP-XPS O 1*s* spectrum of white unprinted paper.

المنارة للاستشارات
www.manaraa.com

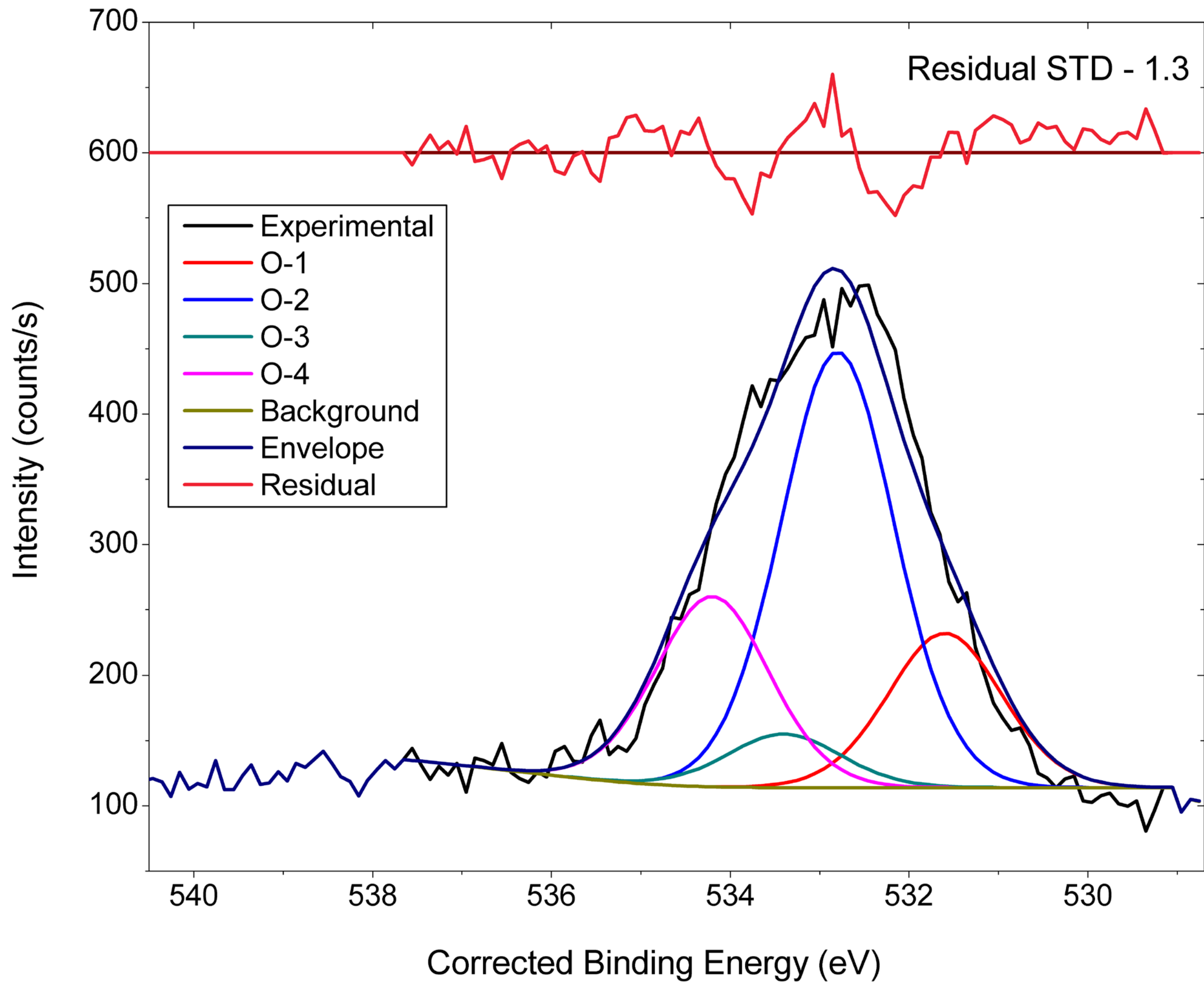

Figure 5.1.7.2.2a NAP-XPS O 1*s* spectrum of blue printed paper.

www.manaraa.com

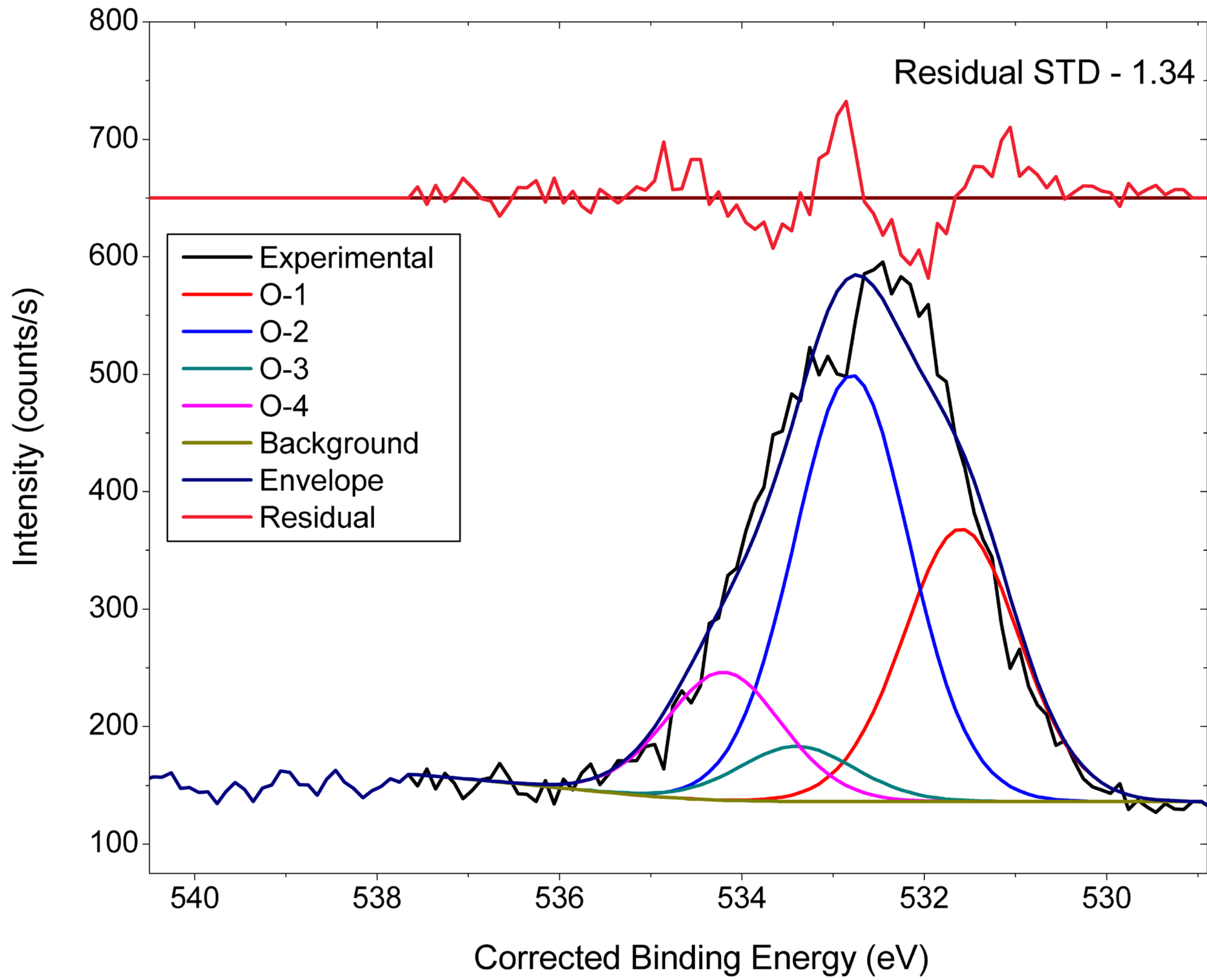

Figure 5.1.7.3.2a NAP-XPS O 1*s* spectrum of dark blue printed paper.

المنارة للاستشارات
www.manaraa.com

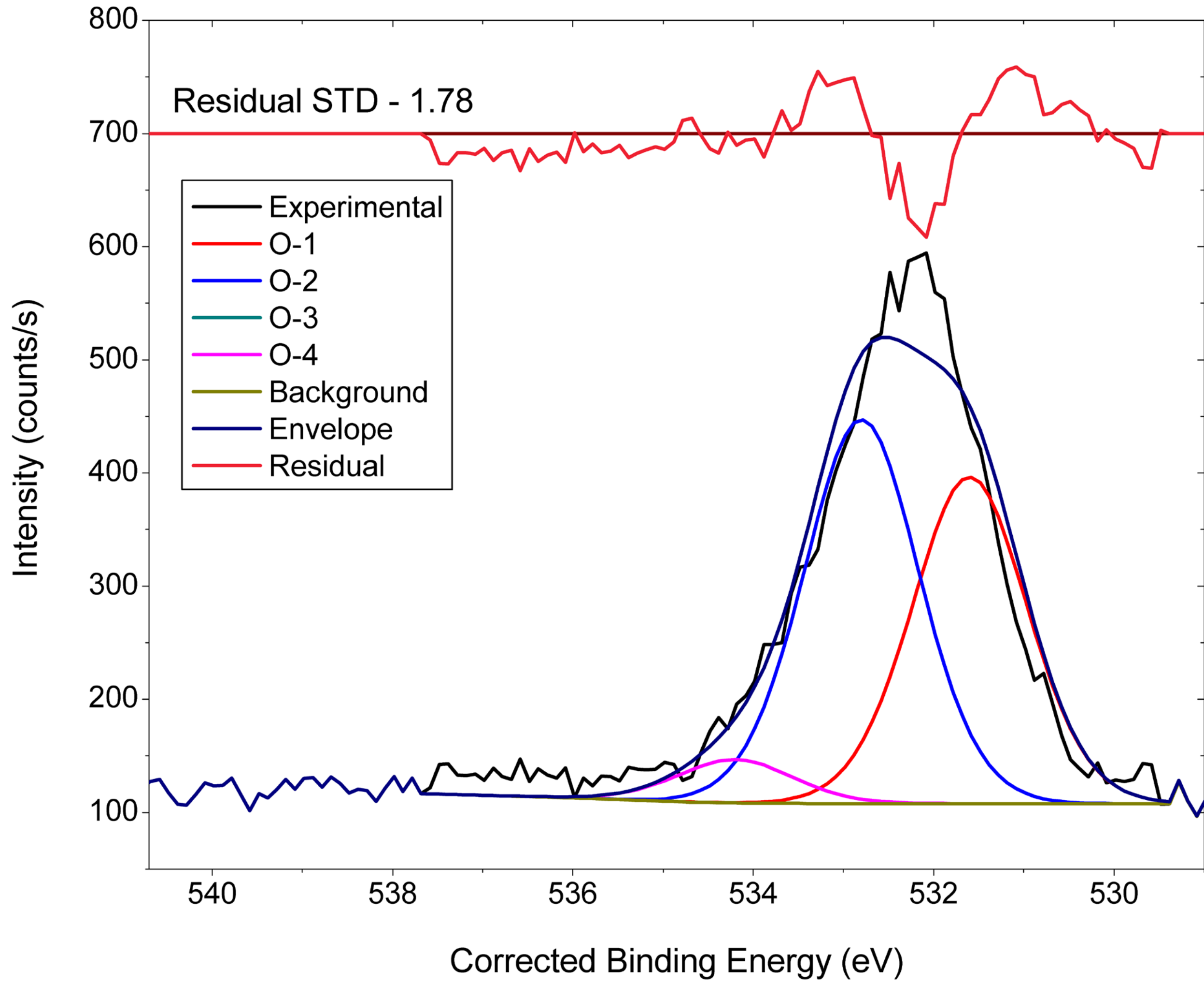

Figure 5.1.7.4.2a NAP-XPS O 1*s* spectrum of yellow post it note.

المنارة للاستشارات
www.manaraa.com

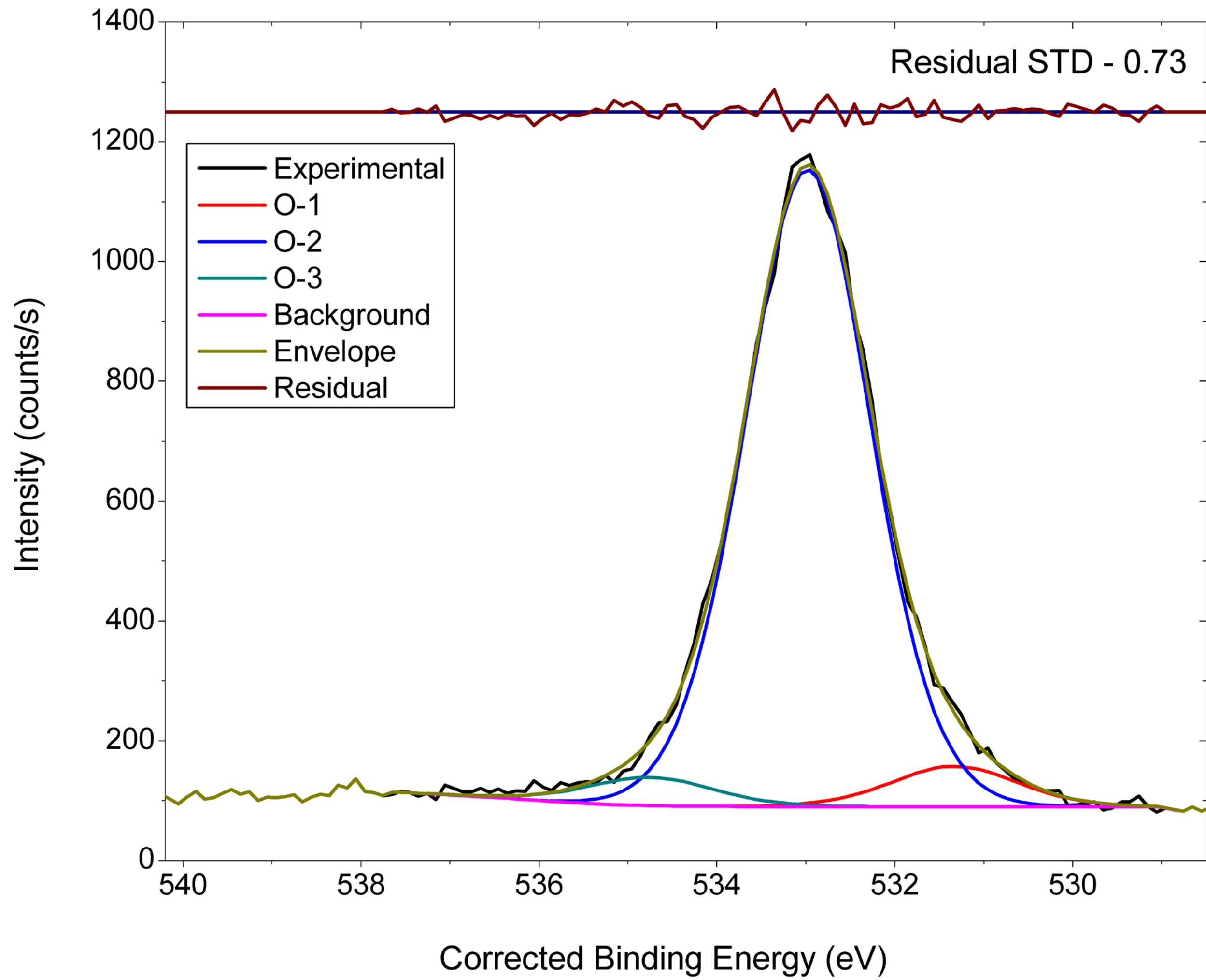

Figure 5.1.7.1.2b NAP-XPS O 1*s* spectrum of white unprinted paper (alternate fit).

المنارة للاستشارات
www.manaraa.com

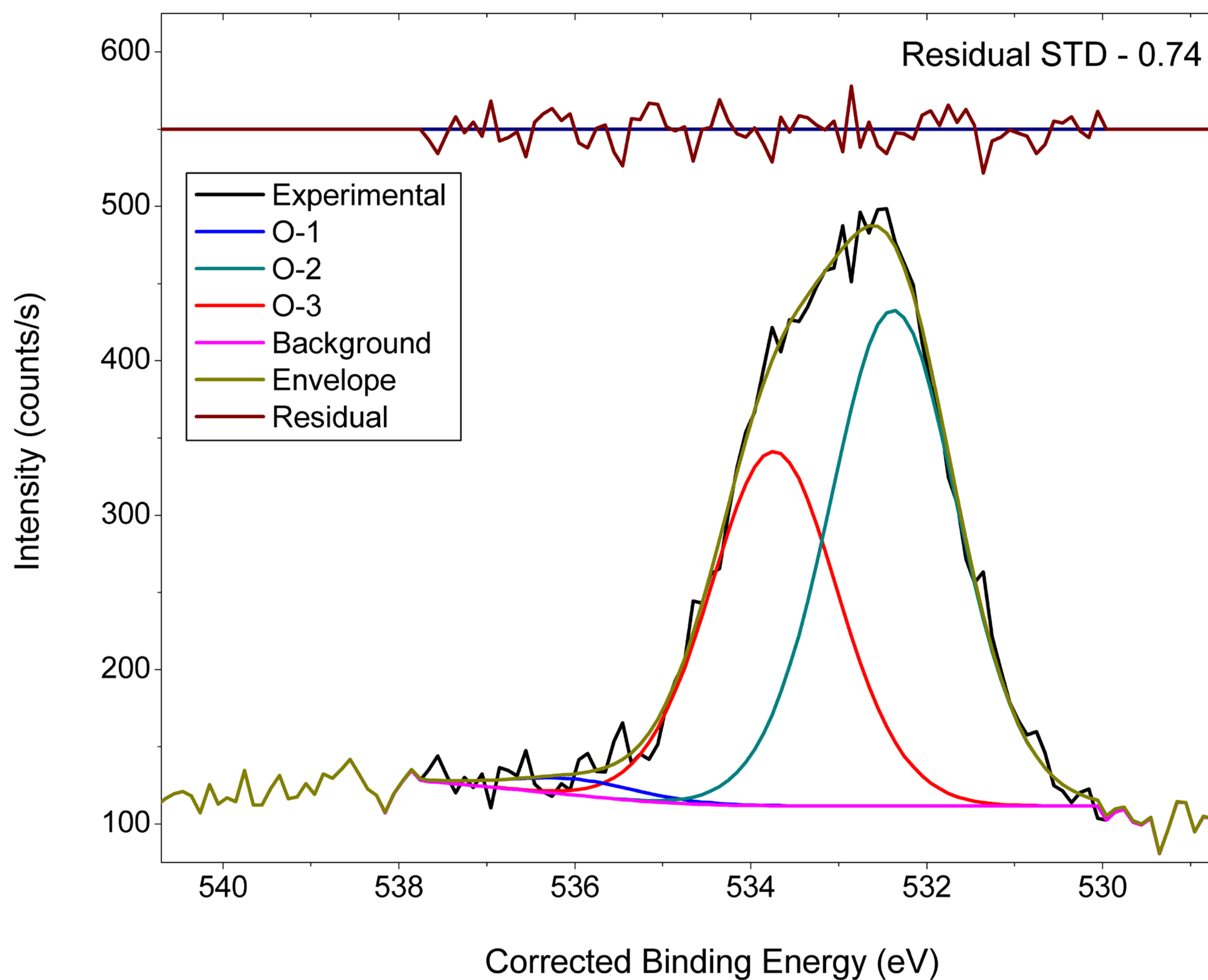

Figure 5.1.7.2.2b NAP-XPS O 1*s* spectrum of blue printed paper (alternate fit).

المنارة للاستشارات
www.manaraa.com

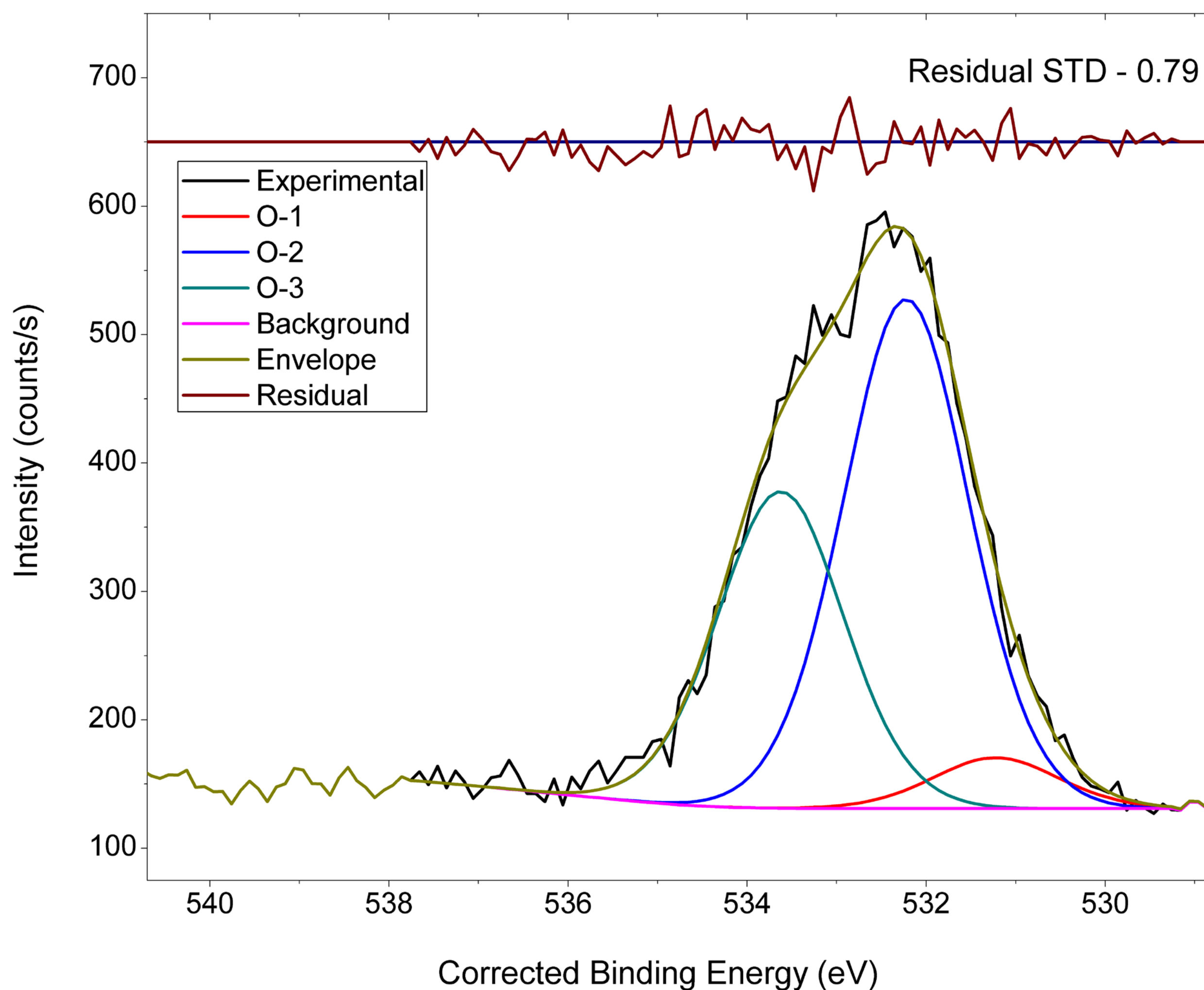

Figure 5.1.7.3.2b NAP-XPS O 1*s* spectrum of dark blue paper (alternate fit).

المنارة للاستشارات
www.manaraa.com

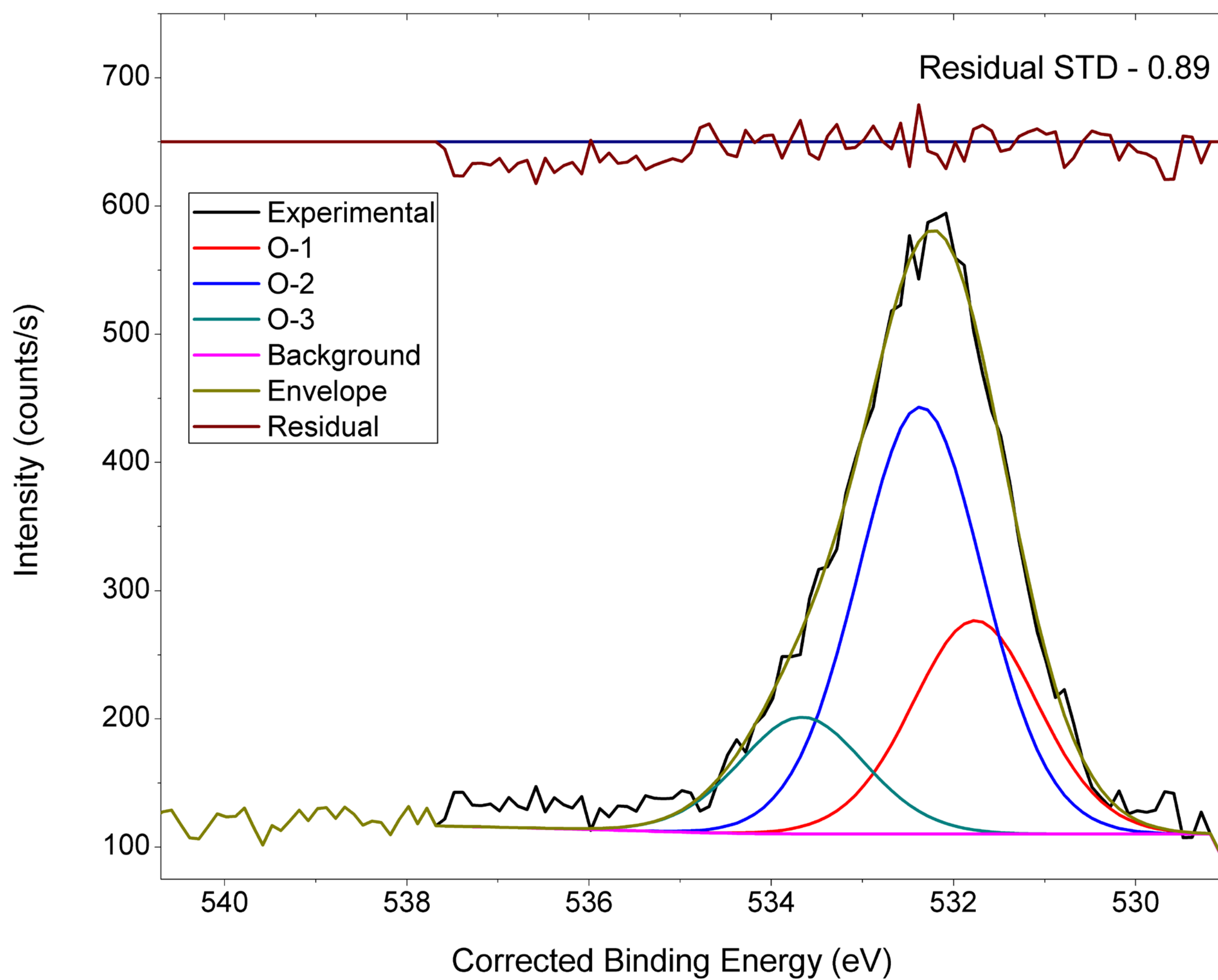

Figure 5.1.7.4.2b NAP-XPS O 1*s* spectrum of yellow post-it note (alternate fit).

المنارة للاستشارات
www.manaraa.com

Figure 5.1.7.5 White paper notepad containing the SPECS logo analyzed by NAP-XPS.

المنارة للاستشارات
www.manaraa.com

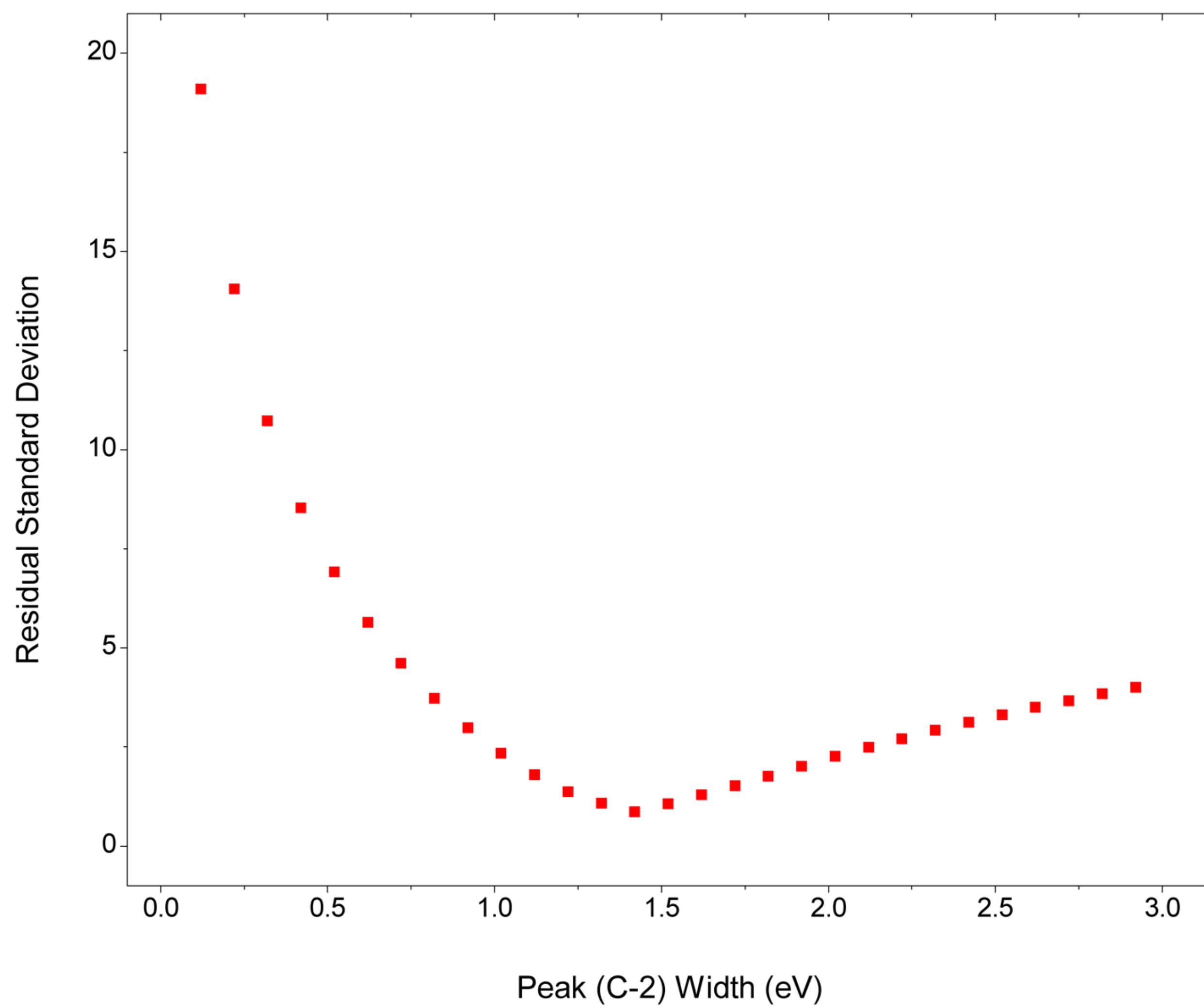

Figure 5.1.7.6 Uniqueness plot of the C 1*s* fit for the white unprinted paper.

المنارة للاستشارات
www.manaraa.com

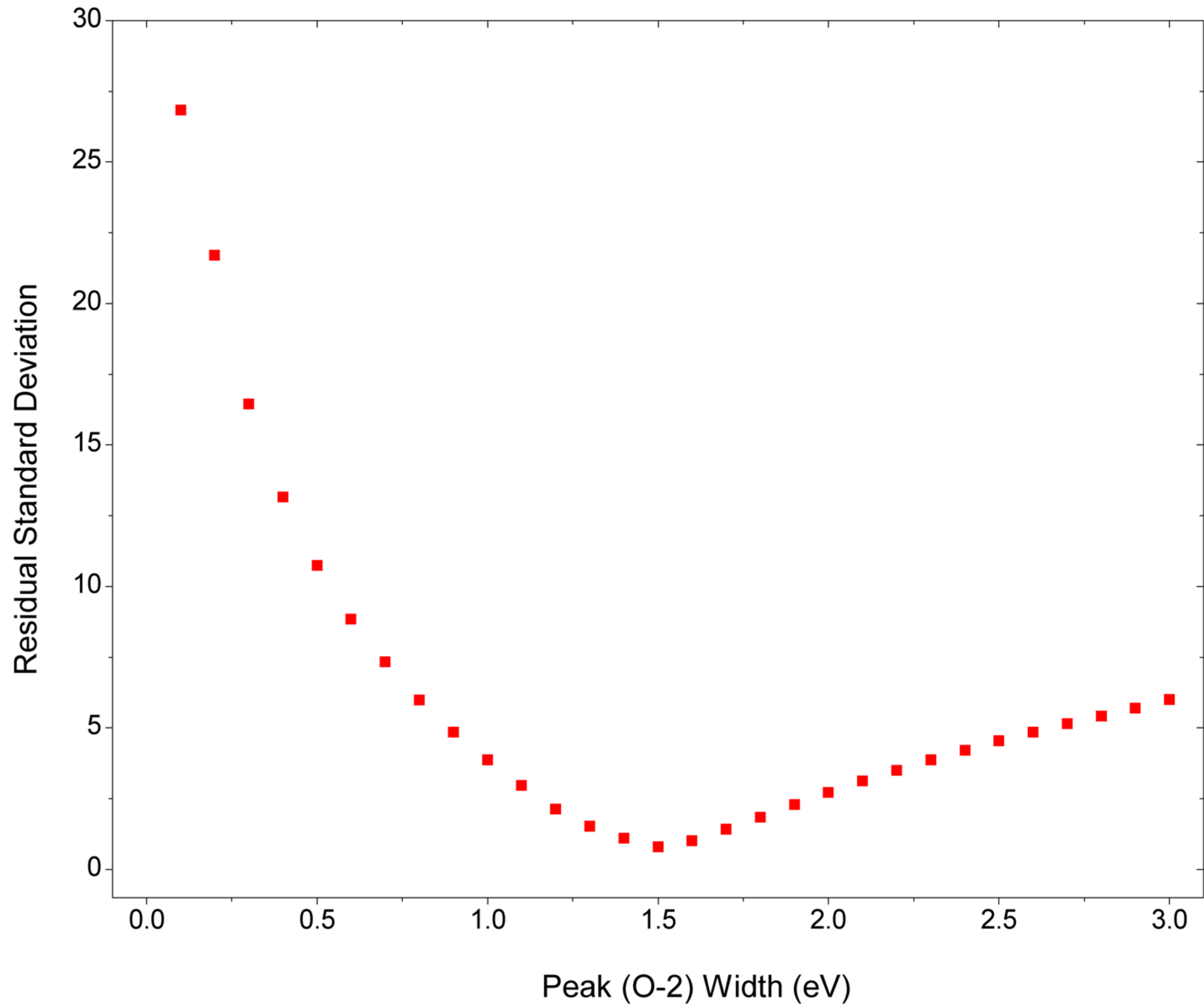

Figure 5.1.7.7 Uniqueness plot of the O 1s fit performed with four fit components for white, unprinted paper.

المنارة للاستشارات
www.manaraa.com

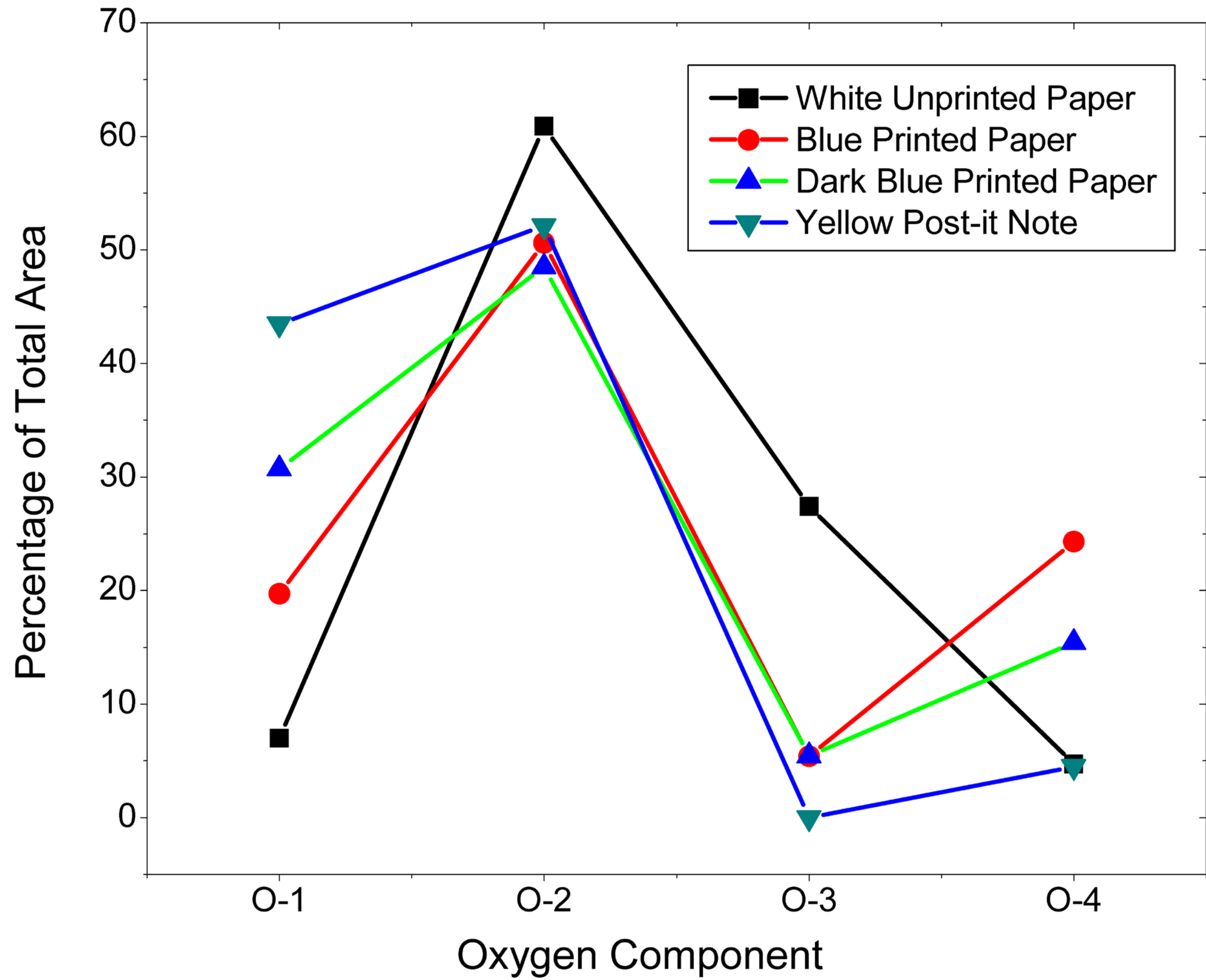

Figure 5.1.7.8 Percentages of the total fitted area of each of the synthetic peaks in the four-component O 1s fits performed in this study.

المنارة للاستشارات
www.manaraa.com

5.3 References

1. Turner, N. H., Surface analysis: x-ray photoelectron spectroscopy and Auger electron spectroscopy. *Anal. Chem.* **1988,** *60* (12), 377-387.
2. Oswald, S., X-Ray Photoelectron Spectroscopy in Analysis of Surfaces Update based on the original article by Steffen Oswald, Encyclopedia of Analytical Chemistry, © 2000, John Wiley & Sons, Ltd. *Encyclopedia of Analytical Chemistry* **2013**.
3. Briggs, D., *Handbook of X-ray and ultraviolet photoelectron spectroscopy*.
4. Linford, M. R.; Roychowdhury, T.; Shah, D., Near Ambient Pressure XPS (NAP-XPS). A New Paradigm for the Technique. *Vacuum Technology & Coating* August 2018, pp 26-28.
5. Linford, M. R.; Roychowdhury, T.; Shah, D., Near Ambient Pressure XPS (NAP-XPS). A New Paradigm for the Technique. *Vac. Technol. Coat.* **2018,** *August* (8), 26-28.
6. C. V. Cushman; C. T. Dahlquist; P. M. Dietrich; S. Bahr; A. Thissen; O. Schaff; J. Banerjee; N. J. Smith; M. R. Linford, Trends in Advanced XPS Instrumentation. 5. Near-Ambient Pressure XPS. *Vac. Technol. Coat.* **2017,** *August* (8), 23-31.
7. Dietrich, P. M.; Bahr, S.; Yamamoto, T.; Meyer, M.; Thissen, A., Chemical surface analysis on materials and devices under functional conditions – Environmental photoelectron spectroscopy as non-destructive tool for routine characterization. *J. Electron Spectros. Relat. Phenomena* **2019,** *231*, 118.
8. Shah, D.; Patel, D. I.; Bahr, S.; Dietrich, P.; Meyer, M.; Thißen, A.; Linford, M. R., Liquid Water, by near-ambient pressure XPS. *Surf. Sci. Spectra* **2019,** *26* (1), 024003.
9. Shah, D.; Cushman, C. V.; Bahr, S.; Dietrich, P.; Meyer, M.; Thißen, A.; Linford, M. R., Coca-Cola, by near-ambient pressure XPS. *Surf. Sci. Spectra* **2019,** *26* (2), 024005-01 to 06.
10. Shah, D.; Bahr, S.; Dietrich, P.; Meyer, M.; Thißen, A.; Linford, M. R., Coffee bean, by near-ambient pressure XPS. *Surf. Sci. Spectra* **2019,** *26* (1), Accepted.
11. Shah, D.; Bahr, S.; Dietrich, P.; Meyer, M.; Thißen, A.; Linford, M. R., Nitrogen gas (N_2), by near-ambient XPS. *Surf. Sci. Spectra* **2019,** *26* (1), 014023-01 to 05.
12. Shah, D.; Bahr, S.; Dietrich, P.; Meyer, M.; Thißen, A.; Linford, M. R., Zirconium oxide particles, by near-ambient XPS. *Surf. Sci. Spectra* **2019,** *26* (2), 024001-01 to 07.
13. Shah, D.; Roychowdhury, T.; Bahr, S.; Dietrich, P.; Meyer, M.; Thißen, A.; Linford, M. R., Human tooth, by near-ambient pressure x-ray photoelectron spectroscopy. *Surf. Sci. Spectra* **2019,** *26* (1), 014016-01 to 014016-33.
14. Shah, D.; Bahr, S.; Dietrich, P.; Meyer, M.; Thißen, A.; Linford, M. R., Printed and unprinted office paper, by near-ambient XPS. *Surf. Sci. Spectra* **2019,** *26* (2), Accepted.
15. A. Jürgensen; N. Esser; R. Hergenröder, Near ambient pressure XPS with a conventional X-ray source. *Surf. Interface Anal.* **2012,** *44* (8), 1100-1103.
16. C. Jeong; H. Yun; H. Lee; S. Muller; J. Lee; B. S. Mun, Performance test of new near-ambient-pressure XPS at Korean Basic Science Institute and its application to CO oxidation study on Pt_3Ti polycrystalline surface. *Curr. Appl. Phys.* **2016,** *16* (1), 73-78.
17. S. K. Erikson; K. Edstrom; A. Hagfeldt; M. Hahlin; H. Rensmo; H. Siegbahn; J. M. Kahk; I. J. Villar-Garcia; D. J. Payne; M. J. Webb; H. Grennberg; R. Yakimova; M. O. M. Edwards; P. G. Karlsson; K. Backlund; J. Ahlund, A versatile photoelectron spectrometer for pressures up to 30 mbar. *Rev. Sci. Instrum.* **2014,** *46* (6).
18. F. D. Ogletree; H. Bluhm; E. D. Hebenstreit; M. Salmeron, Photoelectron spectroscopy under ambient pressure and temperature conditions. *Nucl. Instrum. Methods Phys. Res., Sect. A* **2009,** *601* (1), 151-160.

المنارة للاستشارات

www.manaraa.com

19. Patel, D. I.; Roychowdhury, T.; Jain, V.; Shah, D.; Johnson, B. I.; Avval, T. G.; Chatterjee, S.; Bahr, S.; Dietrich, P.; Meyer, M.; Thißen, A.; Linford, M. R., Introduction to Near Ambient pressure-X-ray Photoelectron Spectroscopy (NAP-XPS) Characterization of Various Materials. *Surf. Sci. Spectra* **2019,** *26* (1), 016801.
20. Rodriguez, C.; Dietrich, P.; Torres-Costa, V.; Cebrián, V.; Gómez-Abad, C.; Díaz, A.; Ahumada, O.; Manso Silván, M., Near ambient pressure X-ray photoelectron spectroscopy monitoring of the surface immobilization cascade on a porous silicon-gold nanoparticle FET biosensor. *Appl. Sci. Spectra* **2019,** *492*, 362-368.
21. D. Shah; D. I. Patel; T. Roychowdhury; G. B. Rayner; N. O'Toole; D. R. Baer; M. R. Linford, A Tutorial on Interpreting X-ray Photoelectron Spectroscopy (XPS) Survey Spectra: Questions on Spectra from the Atomic Layer Deposition (ALD) of Al_2O_3 on Silicon. *J. Vac. Sci. Technol. B* **2018,** *36*, 062902.
22. M. Salmeron; R. Schlögl, Ambient pressure photoelectron spectroscopy: A new tool for surface science and nanotechnology. *Surf. Sci. Rep.* **2008,** *63* (4), 169-199.
23. Axnanda, S.; Crumlin, E. J.; Mao, B.; Rani, S.; Chang, R.; Karlsson, P. G.; Edwards, M. O. M.; Lundqvist, M.; Moberg, R.; Ross, P.; Hussain, Z.; Liu, Z., Using "Tender" X-ray Ambient Pressure X-Ray Photoelectron Spectroscopy as A Direct Probe of Solid-Liquid Interface. *Sci. Rep.* **2015,** *5*, 9788.
24. L. Trotochaud; A. R. Head; S. Pletincx; O. Karslıoğlu; Y. Yu; A. Waldner; L. Kyhl; T. Hauffman; H. Terryn; B. Eichhorn; H. Bluhm, Water Adsorption and Dissociation on Polycrystalline Copper Oxides: Effects of Environmental Contamination and Experimental Protocol. *J. Phys. Chem. B* **2018,** *122* (2), 1000-1008.
25. Bluhm, H., Photoelectron spectroscopy of surfaces under humid conditions. *J. Electron Spectros. Relat. Phenomena* **2010,** *177* (2-3), 71-84.
26. Crumlin, E. J.; Bluhm, H.; Liu, Z., In situ investigation of electrochemical devices using ambient pressure photoelectron spectroscopy. *J. Electron Spectros. Relat. Phenomena* **2013,** *190*, 84-92.
27. Dhananjay I. Patel; Shah, D.; Bahr, S.; Dietrich, P.; Meyer, M.; Thißen, A.; Linford, M. R., Water vapor, by near-ambient pressure XPS. *Surf. Sci. Spectra* **2019,** *26* (1), 014026.
28. V. Jain; M. C. Biesinger; M. R. Linford, The Gaussian-Lorentzian Sum, Product, and Convolution (Voigt) functions in the context of peak fitting X-ray photoelectron spectroscopy (XPS) narrow scans. *Appl. Surf. Sci.* **2018,** *447*, 548-553.
29. Végh, J., The Shirley background revised. *J. Electron. Spectrosc. Relat. Phenom.* **2006,** *151* (3), 159-164.
30. Rouxhet, P. G.; Misselyn-Bauduin, A. M.; Ahimou, F.; Genet, M. J.; Adriaensen, Y.; Desille, T.; Bodson, P.; Deroanne, C., XPS analysis of food products: toward chemical functions and molecular compounds. *Surf. Interface Anal.* **2008,** *40* (3-4), 718-724.
31. Nikolova, Y.; Petit, J.; Sanders, C.; Gianfrancesco, A.; Scher, J.; Gaiani, C., Toward a better determination of dairy powders surface composition through XPS matrices development. *Colloids and Surfaces B: Biointerfaces* **2015,** *125*, 12-20.
32. Kjærvik, M.; Hermanns, A.; Dietrich, P.; Thissen, A.; Bahr, S.; Ritter, B.; Kemnitz, E.; Unger, W. E. S., Detection of suspended nanoparticles with near-ambient pressure x-ray photoelectron spectroscopy. *J. Phys.: Condensed Matter* **2017,** *29* (47), 474002.
33. B. Srdjenovic; V. Djordjevic-Milic; N. Grujic; R. Injac; Lepojevic, Z., Simultaneous HPLC Determination of Caffeine, Theobromine, and Theophylline in Food, Drinks, and Herbal Products. *J. Chrom. Sci.* **2008,** *46*, 144-150.

المنارة للاستشارات
www.manaraa.com

34. H. J. Issaq; D. Weiss; C. Ridlon; S. D. Fox; G. M. Muschik, The Determination of Aspartame in Diet Soft Drinks by High Performance Liquid Chromatography. *J. Liq. Chrom.* **1986,** *9* (8), 1791-1801.
35. I. Gerald; D. E. Arthur; Adedayo, A., Determination of Caffeine in Beverages: A review. *Am. J. Engineer. Res.* **2014,** *3*, 124-137.
36. Strohl, A. N., A study of colas: An HPLC experiment. *J. Chem. Edu.* **1985,** *62* (5), 447.
37. Gupta, V.; Ganegoda, H.; Engelhard, M. H.; Terry, J.; Linford, M. R., Assigning oxidation states to organic compounds via predictions from X-ray photoelectron spectroscopy: A discussion of approaches and recommended improvements. *J. Chem. Educ.* **2014,** *91* (2), 232-238.
38. Beamson, G.; Briggs, D., *High resolution XPS of organic polymers : The Scienta ESCA300 database*. Wiley: Chichester [England]; New York, 1992.
39. Singh, B.; Diwan, A.; Jain, V.; Herrera-Gomez, A.; Terry, J.; Linford, M. R., Uniqueness plots: A simple graphical tool for identifying poor peak fits in X-ray photoelectron spectroscopy. *Appl. Surf. Sci.* **2016,** *387*, 155-162.
40. Axanda, S.; Crumlin, E. J.; Mao, B.; Rani, S.; Chang, R.; Karlsson, P. G.; Edwards, M. O. M.; Lundqvist, M.; Moberg, R.; Ross, P.; Hussain, Z.; Liu, Z., Using "Tender" X-ray Ambient Pressure X-Ray Photoelectron Spectroscopy as A Direct Probe of Solid-Liquid Interface. *Sci. Rep.* **2015,** *5*, 9788.
41. Toyoda, N.; Yamada, I., XPS study of effects of water vapor during Ar-GCIB irradiations on PMMA. *Appl. Surf. Sci.* **2014,** *310*, 112-114.
42. Trotochaud, L.; Head, A. R.; Pletincx, S.; Karsliuglu, O.; Yu, Y.; Waldner, A.; Kyhl, L.; Hauffman, T.; Terryn, H.; Eichhorn, B.; Bluhm, H., Water Adsorption and Dissociation on Polycrystalline Copper Oxides: Effects Environmental Contamination and Experimental Protocol. *J. Phys. Chem. B* **2018,** *122*, 1000-1008.
43. Yu, L.; Takagi, Y.; Nakamura, T.; Sekizawa, O.; Sakata, T.; Uruga, T.; Tada, M.; Iwasawa, Y.; Samjeske, G.; Yokoyama, T., Non-contact electric potential measurements of electrode components in an operating polymer electrolyte fuel cell by near ambient pressure XPS. *Phys. Chem. Chem. Phys.* **2017,** *19*, 30798-30803.
44. Jain, V.; Biesinger, M. C.; Linford, M. R., The Gaussian-Lorentzian Sum, Product, and Convolution (Voigt) functions in the context of peak fitting X-ray photoelectron spectroscopy (XPS) narrow scans. *Appl. Surf. Sci.* **2018,** *447*, 548-553.
45. Seah, M. P., Background subtraction: I. General behaviour of Tougaard-style backgrounds in AES and XPS. *Surf. Sci.* **1999,** *420* (2), 285-294.
46. Tougaard, S.; Jørgensen, B., Inelastic background intensities in XPS spectra. *Surface Science* **1984,** *143* (2), 482-494.
47. Swift, P., Adventitious carbon—the panacea for energy referencing? *Surf. Interface Anal.* **1982,** *4* (2), 47-51.
48. Stelmach, E.; Pohl, P.; Szymczycha-Madeja, A., The content of Ca, Cu, Fe, Mg and Mn and antioxidant activity of green coffee brews. *Food Chemistry* **2015,** *182*, 302-308.
49. Rizzi, G. P., Formation of Sulfur-Containing Volatiles under Coffee Roasting Conditions. In *Caffeinated Beverages*, American Chemical Society: 2000; Vol. 754, pp 210-215.
50. Yang, N.; Liu, C.; Liu, X.; Degn, T. K.; Munchow, M.; Fisk, I., Determination of volatile marker compounds of common coffee roast defects. *Food Chem* **2016,** *211*, 206-214.
51. Nurok, D.; Anderson, J. W.; Zlatkis, A., Profiles of sulfur containing compounds obtained from Arabica and Robusta coffees by capillary column gas chromatography. *Chromatographia* **1978,** *11* (4), 188-192.

المنارة للاستشارات
www.manaraa.com

52. Andrzejewski, D.; Roach, J. A. G.; Gay, M. L.; Musser, S. M., Analysis of Coffee for the Presence of Acrylamide by LC-MS/MS. *Journal of Agricultural and Food Chemistry* **2004,** *52* (7), 1996-2002.
53. O'Driscoll, D. J., Analysis of coffee bean extracts by use of ultra-performance liquid chromatography coupled to quadrupole time-of-flight mass spectrometry. *MethodsX* **2014,** *1*, 264-268.
54. Tougaard, S., Quantitative analysis of the inelastic background in surface electron spectroscopy. *Surf. Interface Anal.* **1988,** *11* (9), 453-472.
55. J. Hedmen; P. -F. Heden; C. Nordling; Siegbahn, K., Energy slitting of core electron levels in paramagnetic molecules *Phys. Lett.* **1969,** *26*, 178-179.
56. Honda, F.; Hirokawa, K., X-ray photoelectron spectroscopic observation of nitrogen-containing gases adsorbed at high pressures on some transition metals. *J. Electron. Spectrosc. Relat. Phenom.* **1977,** *10* (2), 125-136.
57. Manicone, P. F.; Rossi Iommetti, P.; Raffaelli, L., An overview of zirconia ceramics: Basic properties and clinical applications. *J. Dent.* **2007,** *35* (11), 819-826.
58. Zhang, Y.; Malzbender, J.; Mack, D. E.; Jarligo, M. O.; Cao, X.; Li, Q.; Vaßen, R.; Stöver, D., Mechanical properties of zirconia composite ceramics. *Ceram. Int.* **2013,** *39* (7), 7595-7603.
59. Scheffe, J. R.; Francés, A.; King, D. M.; Liang, X.; Branch, B. A.; Cavanagh, A. S.; George, S. M.; Weimer, A. W., Atomic layer deposition of iron(III) oxide on zirconia nanoparticles in a fluidized bed reactor using ferrocene and oxygen. *Thin Solid Films* **2009,** *517* (6), 1874-1879.
60. G. Olivieri; G. Giorgi; J. B. Green; R. G. Brown; A. Matthew, 5 years of ambient pressure photoelectron spectroscopy (APPES) at the Swiss Light Source (SLS). *J. Electron Spectrosc. Relat. Phenom.* **2017,** *216*, 1-16.
61. Moulder, J. F., *Handbook of X-ray Photoelectron Spectroscopy: A Reference Book of Standard Spectra for Identification and Interpretation of XPS Data*. Physical Electronics Division, Perkin-Elmer Corporation: 1992.
62. Barreca, D.; Battiston, G. A.; Gerbasi, R.; Tondello, E.; Zanella, P., Zirconium Dioxide Thin Films Characterized by XPS. *Surf. Sci. Spectra* **2000,** *7* (4), 303-309.
63. Bespalov, I.; Datler, M.; Buhr, S.; Drachsel, W.; Rupprechter, G.; Suchorski, Y., Initial stages of oxide formation on the Zr surface at low oxygen pressure: An in situ FIM and XPS study. *Ultramicroscopy* **2015,** *159 Pt 2*, 147-151.
64. Suddick, R. P.; Harris, N. O., Historical Perspectives of Oral Biology: A Series. *Crt. Rev. Oral Biol. Med.* **1990,** *1* (2), 135-151.
65. Nelson, A. E.; Hildebrand, N. K. S.; Major, P. W., Mature Dental Enamel [Calcium Hydroxyapatite, $Ca_{10}(PO_4)_6(OH)_2$] by XPS. *Surf. Sci. Spec.* **2002,** *9* (1), 250-259.
66. Taube, F.; Ylmén, R.; Shchukarev, A.; Nietzsche, S.; Norén, J., Morphological and chemical characterization of tooth enamel exposed to alkaline agents. *J. Dent.* **2009,** *38*, 72-81.
67. Muller, F.; Zeitz, C.; Mantz, H.; Ehses, K. H.; Soldera, F.; Schmauch, J.; Hannig, M.; Hufner, S.; Jacobs, K., Elemental depth profiling of fluoridated hydroxyapatite: saving your dentition by the skin of your teeth? *Langmuir* **2010,** *26* (24), 18750-9.
68. Kang, B.-S.; Sul, Y.-T.; Oh, S.-J.; Lee, H.-J.; Albrektsson, T., XPS, AES and SEM analysis of recent dental implants. *Acta Biomaterialia* **2009,** *5* (6), 2222-2229.
69. Lou, L.; Nelson, A. E.; Heo, G.; Major, P. W., Surface chemical composition of human maxillary first premolar as assessed by X-ray photoelectron spectroscopy (XPS). *Appl. Sci. Spectra* **2008,** *254* (21), 6706-6709.

المنارة للاستشارات
www.manaraa.com

70. Hercules, D. M.; Craig, N. L., Fluorine and Tin Uptake by Enamel Studied by X-Ray Photoelectron Spectroscopy (ESCA). *J. Dent. Res.* **1978,** *57* (2), 296-305.
71. Zamudio-Ortega, C. M.; Contreras-Bulnes, R.; Scougall-Vilchis, R. J.; Morales-Luckie, R. A.; Olea-Mejía, O. F.; Rodríguez-Vilchis, L. E., Morphological, chemical and structural characterisation of deciduous enamel: SEM, EDS, XRD, FTIR and XPS analysis. *Eur J Paediatr Dent* **2014,** *15* (3), 275-280.
72. Erikson, S. K.; Edstrom, K.; Hagfeldt, A.; Hahlin, M.; Rensmo, H.; Siegbahn, H.; Kahk, J. M.; Villar-Garcia, I. J.; Payne, D. J.; Webb, M. J.; Grennberg, H.; Yakimova, R.; Edwards, M. O. M.; Karlsson, P. G.; Backlund, K.; Ahlund, J., A versatile photoelectron spectrometer for pressures up to 30 mbar. *Rev. Sci. Instrum.* **2014,** *46* (6).
73. B. Singh; A. Diwan; V. Jain; A. Herrera-Gomez; J. Terry; M. R. Linford, Uniqueness plots: A simple graphical tool for identifying poor peak fits in X-ray photoelectron spectroscopy. *Appl. Surf. Sci.* **2016,** *387*, 155-162.
74. Jürgensen, A.; Esser, N.; Hergenröder, R., Near ambient pressure XPS with a conventional X-ray source. *Surf. Interface Anal.* **2012,** *44* (8), 1100-1103.
75. Barber Asa, H.; Lu, D.; Pugno Nicola, M., Extreme strength observed in limpet teeth. *Journal of The Royal Society Interface* **2015,** *12* (105), 20141326.
76. Gutiérrez-Salazar, M. d. P.; Reyes-Gasga, J., Microhardness and chemical composition of human tooth *Mater. Res.* **2003,** *6*, 367-373.
77. Nichols, D. M.; Cunningham, S. J., The use of paper in everyday student life. In *Proceedings of the 10th International Conference NZ Chapter of the ACM's Special Interest Group on Human-Computer Interaction*, ACM: Auckland, New Zealand, 2009; pp 65-68.
78. Lützenkirchen-Hecht, D.; Rohrmann, K.; Stöcker, T.; Thiel, W., XPS investigations of ink-jet printed paper. *Surf. Interface Anal.* **2007,** *39* (11), 845-851.
79. Sahin, H. T.; Arslan, M. B., A study on physical and chemical properties of cellulose paper immersed in various solvent mixtures. *Int. J. Mol. Sci.* **2008,** *9* (1), 78-88.
80. Bañuls-Ciscar, J.; Abel, M.-L.; Watts, J. F., Characterisation of cellulose and hardwood organosolv lignin reference materials by XPS. *Surf. Sci. Spectra* **2016,** *23* (1), 1-8.
81. V. Gupta; H. Ganegoda; M. H. Engelhard; J. Terry; M. R. Linford, Assigning Oxidation States to Organic Compounds via Predictions from X-ray Photoelectron Spectroscopy: A Discussion of Approaches and Recommended Improvements. *J. Chem. Edu.* **2014,** *91* (2), 232-238.
82. Chen, S.; Tanaka, H., Surface analysis of paper containing polymer additives by X-ray photoelectron spectroscopy I: Application to paper containing dry strength additives. *J. Wood Sci.* **1998,** *44* (4), 303-309.
83. Kamdem, D. P.; Riedl, B.; Adnot, A.; Kaliaguine, S., ESCA spectroscopy of poly(methyl methacrylate) grafted onto wood fibers. *J. Appl. Polymer Sci.* **1991,** *43* (10), 1901-1912.
84. Johansson, L.-S.; Campbell, J. M.; Koljonen, K.; Stenius, P., Evaluation of surface lignin on cellulose fibers with XPS. *Appl. Surf. Sci.* **1999,** *144-145*, 92-95.
85. Clark, D. T.; Cromarty, B. J.; Dilks, A., A theoretical investigation of molecular core binding and relaxation energies in a series of oxygen-containing organic molecules of interest in the study of surface oxidation of polymers. *J. Polymer Sci.* **1978,** *16* (12), 3173-3184.
86. Inari, G. N.; Petrissans, M.; Lambert, J.; Ehrhardt, J. J.; Gérardin, P., XPS characterization of wood chemical composition after heat-treatment. *Surf. Interface Anal.* **2006,** *38* (10), 1336-1342.

المنارة للاستشارات
www.manaraa.com

87. Ahmed, A.; Adnot, A.; Kaliaguine, S., ESCA study of the solid residues of supercritical extraction of Populus tremuloïdes in methanol. *J. Appl. Polymer Sci.* **1987,** *34* (1), 359-375.
88. Hua, X.; Kaliaguine, S.; Kokta, B. V.; Adnot, A., Surface analysis of explosion pulps by ESCA. *Wood Sci. Technol.* **1993,** *28* (1), 1-8.
89. Briggs, D.; Beamson, G., XPS studies of the oxygen 1s and 2s levels in a wide range of functional polymers. *Anal. Chem.* **1993,** *65* (11), 1517-1523.
90. Watts, J. F., High resolution XPS of organic polymers: The Scienta ESCA 300 database. G. Beamson and D. Briggs. 280pp., £65. John Wiley & Sons, Chichester, ISBN 0471 935921, (1992). *Surf. Interface Anal.* **1993,** *20* (3), 267-267.

المنارة للاستشارات
www.manaraa.com

CHAPTER 6: Conclusions and Future Work

During my graduate work, I have been involved with four main projects including (i) deposition of thin films on flat surfaces using atomic layer deposition, (ii) deposition of thin films on powder substrates and its characterization, (iii) Unilateral ALD selectively on a side of quartz substrate, and (iv) characterization of unconventional materials by NAP-XPS. The common theme in all the projects involves thin film deposition using atomic layer deposition, accompanied by its characterization using surface analytical tools. The key findings from each chapter are discussed in the following section.

6.1 Key Findings from Each Chapter

Chapter 2 details the experimental conditions used for thin film deposition on flat surfaces. These conditions gave highly reproducible results with a near-constant growth per cycle of 0.83 Å/nm. These results were used to design experiments for deposition of thin films on powder substrates. The thin films produced on flat surfaces were combined to perform a multiple sample analysis to obtain optical constants of alumina.

Chapter 3 introduces thin film deposition on powder substrates with the help of a unique cover which is used to prevent escape of powder substrates into the instrument. The biggest challenge associated with thin film deposition on powder substrates is the drastic increase in surface area, for example, a 100 mg sample of zirconia has ca. 4200 times (calculated by BET) the surface area of a 1cm x 1 cm silicon shard. I worked with ALD engineers at Lesker to design novel recipes for powder deposition. I relied on increasing the efficiency of thin film deposition process

المنارة للاستشارات
www.manaraa.com

and increase in dose time for precursors to compensate for the drastic increase in surface area. The thin films were characterized by spectroscopic ellipsometry, X-ray photoelectron spectroscopy, and transmission electron microscopy (TEM). This represents one of the first studies to show thin film deposition on powder substrates in a non-agitated manner, i.e., without any external movement. I believe this an important contribution to the field, as most of the initial experiments are performed on a small sample (less than 1 g). The other advantage of these experiments is the lack of any special equipment for coating thin films on powder substrates.

Chapter 4 details the experiments for selective deposition on a single side of glass, quartz, silicon shard using a combination of techniques like thermal evaporation and atomic layer deposition. Thermal deposition (Denton system) has the advantages of high growth rate, highly directional while ALD has advantages of producing highly conformal, hence, non-directional deposition. The approach was to combine the limitations of thermal deposition with advantages of atomic layer deposition to produce selective deposition on a single side of substrates, unilateral ALD. Application of such deposition would be to achieve selective deposition of thin film on a substrate for obtaining transmission data.

Chapter 5 includes detailed analysis of unconventional materials via NAP-XPS, which would be a challenge for conventional XPS as these materials outgas significantly. NAP-XPS offers the advantage of environmental charge compensation, which is useful for insulating samples. These materials represent the wide range of samples that can now be analyzed with the first, standalone SPECS instrument, and include liquid water, beverage like Coca-Cola, a coffee bean, nitrogen gas, zirconia particles, a human tooth, printed and unprinted office paper. All these samples are unconventional and difficult to be analyzed by conventional XPS.

المنارة للاستشارات
www.manaraa.com

6.2 Future Work

In the realm of thin film deposition by atomic layer deposition, we will continue to work on optimization of thin film deposition on powder substrates. The next steps include extending the substrates and materials, which are deposited by ALD. We are working on extending the scope of thin film deposition on powder substrates. We are working on using Unilateral ALD for maintaining the integrity of thin film samples on different substrates.

Additionally, I characterized thin films deposited on several substrates using various material characterization techniques, with a focus on SE, XPS, TEM, SEM and SE modelling/XPS peak fitting. I reported the determination of optical functions of liquid samples like polyethylene glycol (PEG) by SE, which required various experimental adaptations to the ellipsometer. Analysis of liquid samples by spectroscopic ellipsometer are uncommon. Accordingly, more liquids need to be analyzed by SE to make this technique more available to the scientific community, which would be beneficial to future readers. We will continue to deposit optical constants of more samples in the online database like Surface Science Spectra.

We are in the process of publishing and depositing some more important reference materials to Surface Science Spectra.

المنارة للاستشارات
www.manaraa.com

Appendix 1: Good Surface Characterization Starts with Good Sample Preparation - Poor Equipment Maintenance Leads to Poor Sample Quality

A1.1 Statement of Attribution

This document was originally published as Shah, D.; Roychowdhury, T.; Jain, V.; Sudy, J. E.; Bingaman, D.; Linford, M. R., Good Surface Characterization Starts with Good Sample Preparation - Poor Equipment Maintenance Leads to Poor Sample Quality. *Vacuum Coating & Technology* July **2017**, pp 24-28.[1] Some information fields are modified to improve its readability in this format. We refer readers to the original document for complete sample, instrument information, and spectral features.

A1.2 Introduction

The Linford lab at BYU focuses on surface modification and characterization. I deposit films of Ångstrom, nanometer and micron dimensions,[2] where surface and material characterization is critical to understand what we have made. These films are prepared using physical vapor deposition (PVD), e.g., sputtering or e-beam evaporation,[3] chemical vapor deposition (CVD), e.g., gas phase silane deposition,[4] and atomic layer deposition (ALD).[5,6]

I routinely use analytical tools like X-ray photoelectron spectroscopy (XPS), low energy ion scattering (LEIS),[7] time-of-flight secondary ion mass spectrometry (ToF-SIMS), and spectroscopic ellipsometry to characterize our materials.[7, 8] In this article, we continue our discussion of the influence of sample preparation on surface characterization.[9] In many cases, good sample preparation/synthesis hinges on a series of relatively small actions and precautions.[10] In

www.manaraa.com

particular, we provide six suggestions for improving sample preparation so that the subsequent sample analysis will be more meaningful.[11] These include:

1. Do some research/reading on the material you will be making
2. Use high quality reagents, at least at first, and understand the chemistry of your reagents
3. Maintain the base pressure in your deposition chamber
4. Maintain the O-rings in your deposition system
5. Monitor the performance of vacuum systems with pump down and rate-of-rise curves
6. Carefully transport samples to their place of analysis

Suggestion #1. Do some research/reading on the material you will be making

In most cases, user will save time and make a better thin film or material if you first read the literature to see what has worked and not worked for other people. Remember here the old joke that: 'Two weeks in the laboratory can save you an afternoon in the library'. Another suggestion would be to interact with your peers or colleagues, who can make suggestions about the issue at hand.

Suggestion #2. Use high quality reagents, at least at first, and understand the chemistry of your reagents

At least during the initial stages of thin film and material development it is often better to work with higher quality reagents. This is for two reasons. First, if something goes wrong in a preparation/deposition or if a material does not perform or work out the way you had hoped, you probably won't need to worry about whether it was because your starting material was impure – you will probably get to the root cause of your problem faster if you have fewer things to worry about. Second, those of us interested in publishing our results know that if we use poor quality

المنارة للاستشارات
www.manaraa.com

materials in our studies, we will probably be dinged by future reviewers of the work. Reviewers are concerned by presence of impurities in lower quality reagents because they introduce uncertainty into reactions. However, not every synthesis needs the highest quality reagents, and high purity reagents can be quite expensive.

A possible strategy here might be to initially prepare one's materials with highest quality starting materials and to then try to lower quality reagents to see if the change makes any difference. Also, look for chemical incompatibilities between reagents, between your reagents and the materials in your deposition system, and understand the thermal stabilities of these materials. For example, we often think of nitrogen, N_2, as an inert gas, and because of the triple bond between the nitrogen atoms in it, it does lack reactivity under many circumstances. However, nitrogen becomes increasingly reactive at higher temperatures (> 250 °C),[12] where it can combine with active metals like lithium and titanium to form nitrides.[13] Accordingly, nitrogen will probably make a poor inert 'blanket' for an elevated temperature reaction or deposition. Argon is a better choice as inert gas when working at higher temperature.

Suggestion #3. Maintain the base pressure in your deposition chamber

Higher pressures in vacuum deposition systems are bad because they indicate higher concentrations of unwanted gases. We see this from the ideal gas law: $PV = nRT$, where P, V, n, R, and T refer to the pressure, volume, number of moles of gas, the gas constant, and the temperature, respectively. This law provides an increasingly good approximation for the properties of a gas as its pressure drops. In particular, we can rewrite the ideal gas law as $P_i = (n_i/V)RT = c_iRT$, which shows that the partial pressure of each component in a gas mixture is directly proportional to the concentration ($C_i = n_i/V$) of gas. The basic laws of chemical kinetics indicate

المنارة للاستشارات
www.manaraa.com

that many chemical reactions, e.g., many first and second order reactions, depend on the concentrations of the corresponding reactants. Thus, higher pressures in deposition systems often provide higher concentrations of impurities that can more readily react with our growing films and thus decrease their quality.

There are a number of factors that can increase the pressure in a vacuum system. Here are a few:

i. Well-maintained pumps usually last a long time. Poorly maintained vacuum pumps may not achieve their expected base pressures.[14]

ii. The seals, including O-ring seals on doors, should be well maintained. This point will be discussed in greater detail below.

iii. We mentioned in our previous article[15] that unwanted buildup of deposited films on chamber walls and surfaces can trap water and other molecules and gases, which makes it harder to reach a base pressure. This latter problem is an example of a virtual leak.

iv. In general, the longer the exposure of the interior of a chamber to ambient air the slower the rate of pump down. Higher humidity is a particularly bad actor here.[16, 17]

Finally, note that (i) the degree to which a higher pressure affects a deposition depends on the type of deposition, and (ii) the presence of contamination can also lead to incorrect results during surface analysis, e.g., XPS and ToF-SIMS.

Suggestion #4. Maintain the O-rings in your deposition system

Most vacuum systems use seals of various kinds, including gaskets and O-rings, to achieve and maintain their low pressures. Gaskets can be made of metals or elastomers. Metal gaskets, typically made of copper, can achieve excellent, clean, relatively inexpensive, and reliable seals. Copper gaskets do, however, require a little time and effort to install so they are best used in

المنارة للاستشارات
www.manaraa.com

places on systems that are to remain connected and sealed. O-rings (elastomeric gaskets) are a cost effective solution for doors of systems and gate valves that need to be repeatedly opened and closed.

A new-unbaked O-ring contains contaminants trapped inside it.[18] Accordingly, when an O-ring is used as a seal in a system, contaminants can slowly diffuse out of it. The pumping time required to remove these contaminants can be weeks or even months. Baking and/or heating accelerates this release process, but at the price of introducing the contaminants into a chamber. The consequences of these contaminants are described above. A way to limit/prevent this contamination is to pre-bake O-rings under vacuum before installation.

Of course, one should never wash an O-ring with any solvent as it will lead to absorption of the organic material (swelling of the elastomer). The best way to clean an O-ring is to wipe it with a lint-free tissue and dry it under vacuum. All vacuum components, including O-rings, should only be touched or handled with tweezers and/or gloves and never with bare hands. Tweezers should be cleaned with isopropanol (IPA) prior to use. Acetone should be avoided as it leaves a residue on various substrates. Sputter targets should be wiped with an appropriate solvent, e.g., IPA, prior to use to remove unwanted carryover/particles from previous runs.[19]

Suggestion #5. Monitor the performance of vacuum systems with pump down and rate-of-rise curves

Vacuum systems require regular maintenance and evaluation. In addition to a system log, which should be kept as a record of the various users, materials deposited, run times, date the system was used, problems encountered, and maintenance of a system, a simple tool that can help in maintaining a system is the pump down curve. Pump down curves are plots of the pressure in the system vs. pumping time. **Figure A1.1** shows a pump down curve for our turbo

المنارة للاستشارات
www.manaraa.com

pumped PVD 75 sputter system (Kurt J. Lesker Co., Jefferson Hills, PA). If such curves are taken regularly and archived, they can be compared to a ‘standard’ pump down curve that should be generated when the system is functioning well. Note that, as implied above, a change in a pump down curve does not necessarily mean that there is something wrong with the pumps. Also, in many cases, a drop-in system performance will be gradual so the shapes of pump down curves may not change abruptly with time.

However, these shapes can point directly to problems with a deposition system. For example, if the pressure in a pump down curve bottoms out at a higher level than in the standard curve you probably have a leak. On the other hand, if you reach the same base pressure as in your standard curve but more slowly, you probably have outgassing/desorption in your system. Rate-of-rise curves can also be very helpful in equipment maintenance.

To generate these curves, you isolate the system by closing the valve to the main pump. The rise in pressure with time in the system is then monitored. In general, if the pressure in your system keeps rising linearly with time you have a leak. If it asymptotically approaches a constant value, you are probably dealing with outgassing. As with pump down curves, a rate-of-rise curve should be created when the system is performing well so that one has a standard to compare to. Rate-of-rise curves usually only take ca. 10 minutes to run, and since they do not involve venting the system it is usually pretty easy to reach your base pressure again. Remember, that, in general, it is easier to clean and maintain an instrument than to fix it.

Suggestion #6. Carefully transport samples to their place of analysis

It is often the case that samples are prepared and then analyzed in different locations. In some cases, these different locations can be on opposite sides of the world! Here are

المنارة للاستشارات
www.manaraa.com

a few suggestions for sample transport. First, only handle your samples with clean tweezers, and make sure they are stored in clean containers. Of course you should avoid any rough handling of your samples, which would include dropping them. Try to analyze your samples as soon as possible after preparing them. Also, look for opportunities to analyze samples in situ while they are prepared, e.g., performing *in situ* ellipsometry of growing atomic layer deposition (ALD) films. If samples must be stored, apply what you know about their chemistry to determine the best way to keep them – whether they should be held under ultrahigh vacuum, in a dessicator, under nitrogen, or just in a clean container filled with air.

A1.3 Conclusion

We have presented six suggestions for improved instrument maintenance, sample preparation, and sample handling that should lead to better surface and material analysis. They include doing research on the material you will make, using high quality reagents, maintaining the pressure in your system, maintaining the O-ring seals in your deposition system, using pump down curves to keep your finger on the pulse of your system, and carefully transporting your samples to their place of analysis. Following these tips should lead to improved sample preparation and material characterization.

المنارة للاستشارات
www.manaraa.com

A1.4 Figures

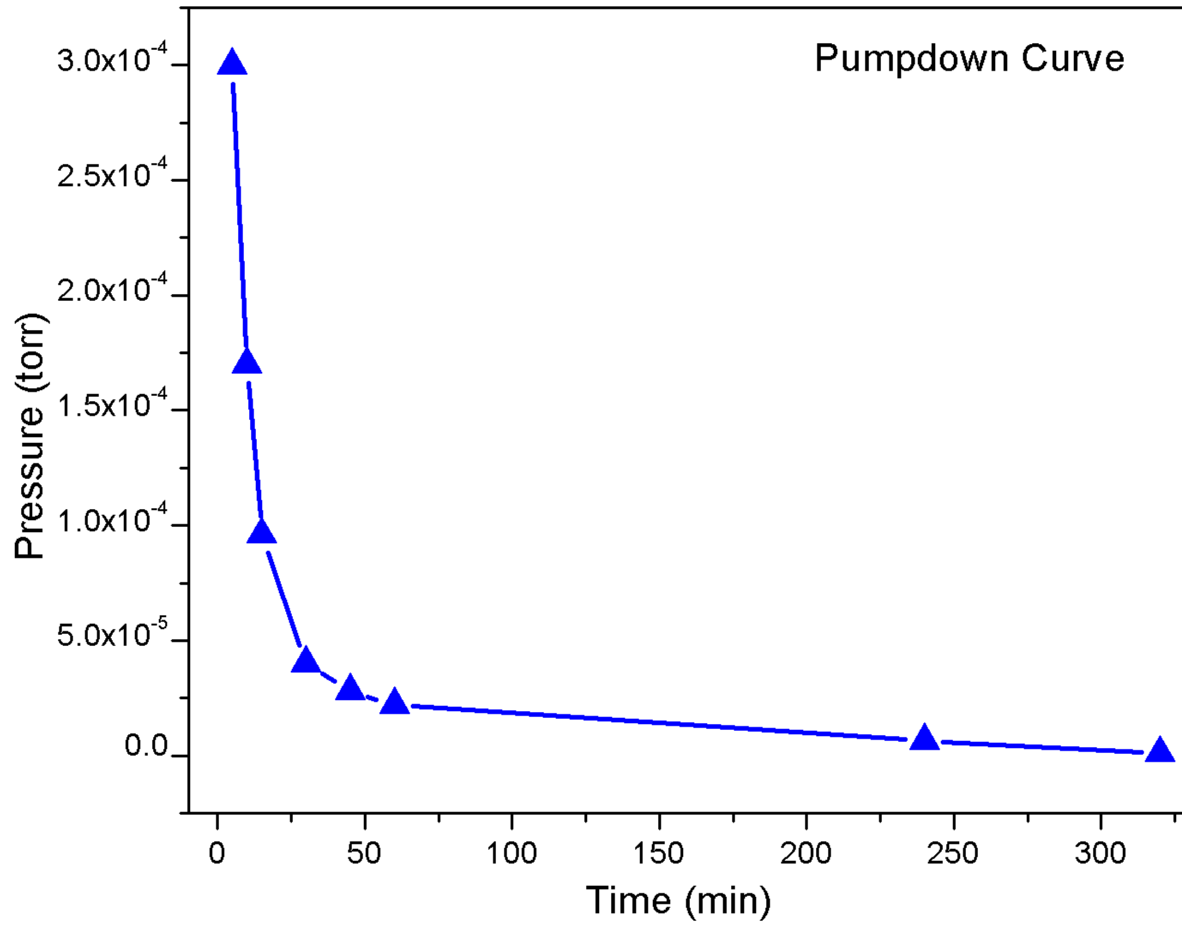

Figure A1.1. Pump down curve (pressure vs. time) obtained for the turbo-pumped PVD 75 sputter system in our lab at BYU (curve generated April 2017).[20]

المنارة للاستشارات
www.manaraa.com

A1.5 References

1. Roychowdhury, T.; Jain, V.; Shah, D.; Sudy, J. E.; Bingaman, D.; Linford, M. R., Good Surface Characterization Starts with Good Sample Preparation - Poor Equipment Maintenance Leads to Poor Sample Quality. *Vac. Coat. Technol.* July **2017**, pp 24-28.
2. Feldman, L. C. M., J. W., *Fundamentals of Surface and Thin Film Analysis*. Elsevier Science Publishing Co., Inc: New York, **1986**; Vol. 22.
3. Wang, H.; Madaan, N.; Bagley, J.; Diwan, A.; Liu, Y.; Davis, R. C.; Lunt, B. M.; Smith, S. J.; Linford, M. R., Spectroscopic ellipsometric modeling of a Bi–Te–Se write layer of an optical data storage device as guided by atomic force microscopy, scanning electron microscopy, and X-ray diffraction. *Thin Solid Films* **2014,** *569*, 124-130.
4. Zhang, F.; Sautter, K.; Larsen, A. M.; Findley, D. A.; Davis, R. C.; Samha, H.; Linford, M. R., Chemical vapor deposition of three aminosilanes on silicon dioxide: surface characterization, stability, effects of silane concentration, and cyanine dye adsorption. *Langmuir* **2010,** *26* (18), 14648-54.
5. Jensen, D. S.; Kanyal, S. S.; Madaan, N.; Miles, A. J.; Davis, R. C.; Vanfleet, R.; Vail, M. A.; Dadson, A. E.; Linford, M. R., Ozone priming of patterned carbon nanotube forests for subsequent atomic layer deposition-like deposition of SiO2 for the preparation of microfabricated thin layer chromatography plates. *J. Vac. Sci. Technol. B* **2013,** *31* (3), 031803.
6. Jilani, A.; Abdel-wahab, M. S.; Hammad, A. H., Advance Deposition Techniques for Thin Film and Coating. In *Modern Technologies for Creating the Thin-film Systems and Coatings*, Nikitenkov, N. N., Ed. InTech: Rijeka, 2017; p Ch. 08.
7. Cushman, C. V.; Brüner, P.; Zakel, J.; Major, G. H.; Lunt, B. M.; Smith, N. J.; Grehl, T.; Linford, M. R., Low energy ion scattering (LEIS). A practical introduction to its theory, instrumentation, and applications. *Anal. Methods* **2016,** *8* (17), 3419-3439.
8. Gupta, V.; Ganegoda, H.; Engelhard, M. H.; Terry, J.; Linford, M. R., Assigning Oxidation States to Organic Compounds via Predictions from X-ray Photoelectron Spectroscopy: A Discussion of Approaches and Recommended Improvements. *J. Chem. Edu.* **2014,** *91* (2), 232-238.
9. Roychowdhury, T. J., V.; Shah, D.; Sudy, J. E.; Bingaman, D.; Linford, M. R, Good surface characterization starts with good sample preparation poor equipment maintenance leads to poor sample quality. *Vac. Coat. Technol.* 2017.
10. Mukhopadhyay, S. M., Sample Preparation for Microscopic and Spectroscopic Characterization of Solid Surfaces and Films. In *Introduction*, Mitra, S., Ed. John Wiley & Sons, Inc.: 2003; p 377.
11. Dun, J. G. P., D. N.; van Bronswijk, W. , An excerise to illustrate the importance of sample preparation in chemical analysis. *J. Chem. Ed.* **1997,** *74* (10), 1188-1190.
12. Mosen, A. W. K., R. E.; Mitchell, H. P., , A high temperature inert gas fusion apparatus. *Talanta* **1966,** *13*, 371-379.
13. Gas, U. Nitrogen Properties, uses and Applications. http://www.uigi.com/nitrogen.html.
14. College, N. C. Nitpicking your vacuum systems. http://www.normandale.edu/departments/stem-and-education/vacuum-and-thin-film-technology/vacuum-lab/articles/nitpicking-your-vacuum-system.
15. Roychowdhury, T. J., V.; Shah, D.; Sudy, J. E.; Bingaman, D.; Linford, M. R., Good surface characterization starts with good sample preparation-Poor equipment maintenance leads to poor sample quality. *Vac. Coat. Technol.* **2017**.

المنارة للاستشارات
www.manaraa.com

16. College, N. C. Anatomy of pumpdowns. http://www.normandale.edu/departments/stem-and-education/vacuum-and-thin-film-technology/vacuum-lab/articles/anatomy-of-a-pumpdown.
17. Danielson, P. Pumpdown effects of water vapor buildup. http://www.normandale.edu/departments/stem-and-education/vacuum-and-thin-film-technology/vacuum-lab/articles/pumpdown-effects-of-water-vapor-buildup.
18. College, N. C. Use and misuse of O-rings. http://www.normandale.edu/departments/stem-and-education/vacuum-and-thin-film-technology/vacuum-lab/articles/use-and-misuse-of-o-rings.
19. Sciencing, How to remove acetone residue. Walker, T., Ed. **2017**.
20. College, N. C. Conditioning vaccum chambers. http://www.normandale.edu/departments/stem-and-education/vacuum-and-thin-film-technology/vacuum-lab/articles/conditioning-vacuum-chambers.

المنارة للاستشارات
www.manaraa.com

Appendix 2: Material characterization using X-ray photoelectron spectroscopy (XPS) and tutorial on principles of XPS

A2.1 Statement of Attribution

This document was originally published as Shah, D.; Roychowdhury, T.; Rayner, G. B.; O' Toole, N.; Baer, D. R.; Linford, M. R., A Tutorial on interpreting X-ray photoelectron spectroscopy (XPS) survey spectra: questions on spectra from the atomic layer deposition (ALD) of Al_2O_3 on silicon *J. Vac. Sci. Technol. B,* **2018**, *36*(6), 062902-1 to 062902-10. Here, the texts and figures are reproduced with the permission from AIP publishing. Some information fields are modified to improve its readability in this format. We refer readers to the original document for complete sample, instrument information, and spectral features.

A2.2 Abstract

X-ray photoelectron spectroscopy (XPS) has become the most widely used method for chemically analyzing surfaces. In XPS, photoelectrons are generated by irradiating a surface with X-rays. As the importance and popularity of XPS have grown, it has drawn users without significant XPS experience, and incorrect and incomplete interpretations of XPS spectra regularly appear in the literature. This tutorial is designed as a tool to guide less experienced users in analyzing XPS survey spectra. Here, we analyze a series of XPS survey spectra collected during the atomic layer deposition of Al_2O_3 from trimethylaluminum and water precursors. Prior to this, brief explanations of XPS and atomic layer deposition (ALD) are presented. This tutorial is structured as a series of questions and answers that the interested reader may choose to engage in. The XPS spectra are examined to extract information about the elements present in the film,

www.manaraa.com

presence of contamination, and the nature of the film growth process. The questions and answers in this tutorial address important fundamental issues common to the interpretation of many XPS survey spectra in the specific context of the ALD growth process.

A2.3 Introduction

A2.3.1 X-ray Photoelectron Spectroscopy

Over the past few decades, X-ray photoelectron spectroscopy (XPS) has become the most widely employed method for the chemical analysis of surfaces. During this time, XPS has gone from a tool that is mostly used by experienced specialists to one that is widely used and requested by both seasoned XPS analysts and novice users alike. Accordingly, the number of papers published on the technique has increased significantly,[1] and the number of available instruments continues to increase markedly – it appears that more than 140 new instruments are sold each year worldwide.[2] And while the proliferation of the technique has some very positive aspects, it has also created some challenges for the surface analysis community by bringing inexperienced users into the field that sometimes collect and/or analyze their data in an inappropriate fashion and then report their efforts in the literature. For example, it is not uncommon for users of XPS at the Environmental Molecular Sciences Laboratory (EMSL), a user facility, to ask that analyses similar to those appearing in the literature be reproduced at EMSL. Unfortunately, it is often found that the data or approach that is referenced is incomplete, misinterpreted, or flawed in some significant way.

The growth in the use of XPS coincides with a maturity of the method and advances in the instrumentation. As early as 1990,[3, 4] it was anticipated that as XPS matured, useful

المنارة للاستشارات
www.manaraa.com

applications would be constrained by a lack of available experts. As part of the effort to address this challenge, protocols and standard practices for XPS have been developed by ASTM Committee E42 on Surface Analysis[5] and ISO Technical Committee 201 on Surface Chemical Analysis.[6]

As many XPS practices became increasingly common, the community met to discuss protocols, practices, and approaches that would enable the development of XPS expert systems.[4] Each of these approaches involved participation and input from the community of users to identify best practices. The developed standards and guidance provide important information and direction to new users. Another effort within the community to improve the accessibility of XPS is Surface Science Spectra (SSS). SSS publishes carefully vetted, peer-reviewed XPS spectra. It has now published thousands of spectra from many different and diverse samples. Part of submission to SSS includes describing the instrumentation and recording the parameters under which the data are collected. Some of us have also written instructional articles on XPS in Vacuum Technology & Coating and the peer-reviewed literature.[7-11]

This tutorial is intended to be one of a series of articles providing information to assist newer users of XPS in performing analyses that are correct, and of appropriate quality, so that they can reasonably and accurately answer the questions they are asking.[12] This article focuses on information that can be obtained from survey spectra, which are often the first spectra collected on a new sample. In particular, this article focuses on understanding the information available from real survey spectra obtained from alumina films grown by atomic layer deposition (ALD). It is written in the form of questions and answers with the hope that readers will test and expand their understanding of the basic principles of XPS as they work through this paper. XPS survey scans should be routinely collected as part of most XPS measurements, and it is often the case that such

www.manaraa.com

spectra must be interpreted before any additional data collection can take place. As observed by Jim Castle, a great deal of information, beyond that often extracted by most users, can be obtained from survey spectra.[13, 14] Future tutorials will address other types of spectra such as narrow scans and angle resolved data collection and analysis. Of course, in additional to the fundamentals of the technique that are described here, a deep knowledge of XPS requires that a user have an understanding of its underlying physics. Unfortunately, some of this knowledge is being lost because today's XPS systems can be run by non-expert users.

The topics covered in this appendix requires a superficial understanding of XPS, some of which can be extracted from the brief XPS primer included in this paper, while other questions require a deeper understanding of its physics that can be obtained from the references noted in this paper and materials provided in the introductory tutorial of this series.

While addressing questions regarding the presence of contaminants or process consistency, sample handling, instrument setup and calibration, and the strategy of data collection is important, they are not the subject of this tutorial. In addition, the questions in this tutorial focus on the significant information that can be extracted from qualitative analysis of the spectra and do not include efforts or approaches that would relate to obtaining the quantitative information that might be extracted from survey spectra. The questions and answers that follow focus on information that can be extracted from survey spectra. A typical spectral analysis starts by identifying the major peak(s) present, then examining the nature of minor peaks, which are sometimes related to the major peaks. One then extracts the information available about chemical states and what can be learned from relative peak intensities. The questions and answers that follow is consistent with this useful approach.

المنارة للاستشارات
www.manaraa.com

Analysis of any sample starts from what is already known about it. Therefore, in this case the elements expected will be those associated with the substrate and deposition process plus likely sources of contamination. Although some XPS practitioners will be able to answer most, if not all of the questions below without assistance, many users will require additional or reference information. In addition to the brief explanation of some of the key principles of XPS provided here in the Introduction, information can be obtained from a variety of sources including books,[15, 16] data in the journal Surface Science Spectra, which can be accessed online, and handbooks, e.g., Physical Electronics (PHI) has produced a very useful one.[17]

These resources are available in most XPS laboratories or possibly on the Internet. There is also a wealth of information about the technique in the technical literature. This includes very short introductions to surface methods,[18, 19] introductory monographs,[20, 21] and extended volumes covering many aspects of the method.[22, 23] Books and journal articles also focus on more specific applications of XPS including: materials science,[24] nanoparticles,[25, 26] corrosion,[27] biological[26, 28] and environmental surfaces.[29] A variety of Guides and Standards have been developed for XPS by Standards Committees ASTM E42 Surface Analysis[30] and ISO TC201Surface Chemical Analysis.[4, 6] Crist[31] provides a list of the significant number of XPS handbooks and data bases, noting as well some of their challenges and inconsistencies. NIST provides several types of XPS related data[32] including a useful program for simulation of XPS spectra (Simulation of Electron Spectra for Surface Analysis (SESSA)).[33, 34] A great deal of information about XPS can also be found on the WWW including webinar-tutorials,[35-37] and other collections of useful information.[38, 39]

A2.4 Experimental

المنارة للاستشارات
www.manaraa.com

A2.4.1 XPS data collection

X-ray photoelectron spectroscopy (XPS) was performed with a Surface Science SSX-100 X-ray photoelectron spectrometer (serviced by Service Physics, Bend, OR) with a monochromatic Al K_α source, a hemispherical analyzer, and a take-off angle of 35°.[40] Survey scans were recorded with a spot size of 800 μm x 800 μm and a nominal pass energy of 150 eV (instrument setting of 'resolution 4'). Peaks were referenced to the C 1s hydrocarbon signal taken at 285.0 eV. The C 1*s* peak is commonly used as a reference peak in XPS spectra due to its nearly universal presence.[41, 42] For the current samples such referencing has been demonstrated to produce consistent results. However, even though referencing to C 1*s* is very common, it can give unreliable results.[41, 42]

The principal reason for this is variation in the position of the C 1*s* signal from 284.07 – 285.2 eV. While this ca. 1.2 eV range may not seem large, a peak shift of even 0.5 eV is often substantial in the XPS world. Hence, such referencing should be used with caution and additional referencing is recommended. No electron flood gun (charge compensation) was employed for these measurements. XPS was performed on a bare silicon substrate and after 10, 50, and 100 TMA-H_2O ALD cycles. XPS spectra from bare silicon wafers and alumina deposited on silicon have previously been reported in the literature.[43, 44] Reproducibility of sample preparation and analysis is always an important issue to carefully consider and address.

A2.5 Results and Discussion

XPS survey spectra were collected from a bare silicon wafer terminated with ca. 1.5 nm of native oxide (**Figures A2.1a and A2.1a**), and after deposition on this substrate of 10

المنارة للاستشارات
www.manaraa.com

(**Figures A2.1b and A2.2b**), 50 (**Figures A2.1c and A2.2c**), and 100 (**Figures A2.1d and A2.2d**) ALD cycles of TMA and water. Figure A2.1 shows full survey spectra from 0 – 1100 eV, and Figure A2.2 shows the same spectra plotted over a reduced energy range (from 0 – 210 eV). We have identified a series of peaks/spectral features using lower case Roman numerals in these spectra.

In **Figure A2.1a**, signal (i) is the C 1*s* signal due to presence of adventitious carbon. It is seen in almost all XPS spectra of air-exposed samples – almost all surfaces, organic and inorganic, are contaminated with some adventitious carbon, i.e., carbon from the environment. Exceptions include surfaces with very low surface energies such as polytetrafluoroethylene (PTFE) and polydimethylsiloxane (PDMS). An example of a surface with little or no carbon (of any type) is freshly etched hydrogen-terminated silicon.

In **Figure A2.1a**, signal (ii) is the O 1***s*** signal. It is very commonly found in XPS spectra because so many materials are oxides or have a layer of oxidized material on them. XPS is more sensitive to oxygen than to carbon so if you had equal amounts of oxygen and carbon at a surface, your O 1s signal would be more intense.[44] Of course this is assuming that the atoms are not arranged in some unusual way such that the oxygen is covered by (attenuated by) the carbon. Atomic sensitivity factors (ASFs) account for the differences in intensity (photoemission probabilities) between the elements in XPS. Signals are divided by ASFs to allow them to be directly compared. The ASF for oxygen is 0.66, and the ASF for carbon is 0.25, i.e., XPS is more than twice as sensitive to oxygen as to carbon. Signal (iii) corresponds to the O Auger signal. It accompanies the O 1*s* signal (you do not get one without the other) so it is very commonly found in XPS spectra. Note that the Auger signal here is the group of peaks labeled as '(iii)'.

المنارة للاستشارات
www.manaraa.com

In **Figure A2.2a**, Notice that peaks (v), (vi), (viii), and (ix) decrease in relative intensity and peaks (xiii) and (xiv) increase as we proceed from Figure A2.2a to A2.2d. Accordingly, we assign peaks (v), (vi), (viii), and (ix) to the substrate (silicon) and peaks (xiii) and (xiv) to the film (aluminum). As the substrate is covered, its corresponding signals should decrease in intensity – a thicker and thicker alumina layer will attenuate the photoelectrons from the substrate and the aluminum signals should increase in intensity as more alumina was deposited on the surface.

In the survey spectra in **Figure A2.2a**, peaks (v) and (vi) come at lower binding energy and peaks (viii) and (ix) come at higher binding energy. In an atom, the 2*s* electrons are more tightly held than the 2p electrons, i.e., the 2s electrons are closer to the nucleus so they experience a higher effective nuclear charge and have higher binding energies. Accordingly, peaks (v) and (vi) come from the 2p electrons and peaks (viii) and (ix) come from the 2s electrons. XPS is quite remarkable because it allows one to 'see' the quantum/shell structure of atoms.

In the survey spectra in **Figure A2.2c**, peak (xiv) comes at lower binding energy and peak (xiii) comes at higher binding energy. In an atom, the 2*s* electrons are more tightly held than the 2*p* electrons (see previous answer). Accordingly, peak (xiv) comes from the 2*p* electrons and peak (xiii) comes from the 2*s* electrons. The atomic numbers (numbers of protons) of aluminum and silicon are 13 and 14, respectively. Since silicon has more protons than aluminum, electrons around a silicon atom will be more tightly held and have higher binding energies.

The silicon wafers used as substrates in the ALD deposition are made of bulk, i.e., pure/reduced silicon that is covered with a thin (ca. 1.5 nm) layer of oxide, which is more or less SiO_2. We could refer to the silicon in the bulk and the native oxide layer as Si(0) and Si(IV),

المنارة للاستشارات
www.manaraa.com

respectively.[7] Oxygen is extremely electronegative, and silicon is moderately electropositive. Thus, when silicon and oxygen bind, they form a polar, covalent bond with the electron density skewed/pulled towards oxygen. As a result, the remaining electrons in the silicon atoms 'feel' the nuclear charge more keenly and it requires more energy to remove them, i.e., they come at higher binding energy.

Thus we see that peak (v) is the Si 2*p* peak that comes from the reduced bulk (at 99 eV), and peak (vi) is the Si 2*p* peak that comes from the native oxide above it (at 103 eV).[44] Similarly, peaks (viii) and (ix) correspond to the Si 2*s* bulk and native oxide signals, respectively. However, this explanation is an oversimplification – these effects are not always followed. Binding energy represents the energy configuration of atoms in their final states. That is, ejection of a core electron represents a substantial perturbation for an atom. It obviously becomes an ion in the process, and the electrons that remain in the atom must readjust to a greater effective nuclear charge. The ALD deposition of Al_2O_3 only produces one form of aluminum, which is the oxidized form. There is no reduced/bulk/metallic aluminum present here. Thus, we see single peaks for aluminum, where peaks (xiii) and (xiv) correspond to the Al 2*s* and 2*p* signals of alumina (not aluminum) at 118 and 74 eV, respectively.

In **Figure A2.3a**, Signal (iv) is the F 1*s* peak and fluorine is a common surfactant contaminant that is readily detected by XPS. Fluorine is regularly seen in XPS spectra, but not as common as carbon and oxygen. Since the substrate here is supposed to be a clean silicon wafer, fluorine and carbon are contaminants.[45] XPS is about four times more sensitive to fluorine (peak (iv)) than to carbon (peak (i)). That is, if you multiplied the C 1s signal by four you would be able to directly compare its area to the F 1s signal.

المنارة للاستشارات
www.manaraa.com

In **Figure A2.1a**, Peak (iii) is the O Auger signal. Auger signals are regularly seen in XPS spectra – see the brief tutorial on XPS in the Introduction for a discussion of Auger electrons. Although Auger peak positions (plotted on a binding energy scale) can be found in a number of references and handbooks, it can be useful to understand how to approximate their energies based on energy levels. We can estimate the energy of the oxygen Auger electrons as follows. We started with the ejection of an O 1*s* photoelectron that had a binding energy of ca. 525 eV. When a valence electron with a binding energy of ca. 25 eV falls into the hole in the 1*s* orbital, 500 eV of energy is released. This energy is then used to eject an electron at the valence band, which 'costs' ca. 25 eV. Thus, the Auger electron has ca. 475 eV of kinetic energy, i.e., 525 eV – 25 eV – 25 eV = 475 eV.

In addition to using approximate values for all the key numbers in this calculation, this approximation ignores the perturbation to the atom caused by the loss of a core electron, etc. Because the K shell and valence (V) shells are involved in this process, we can refer to these signals as oxygen KVV Auger electrons. This is mostly done in elements like boron and carbon, where the valence electrons reside in the L-shell. We previously noted the fundamental equation in XPS, i.e., the photoelectric equation, which is $h\nu \approx BE + KE$.[46] Obviously this equation can be rewritten as $BE \approx h\nu - KE$. This means that the apparent binding energy of the O Auger electrons will be 1025 eV = 1500 eV – 475 eV, which is pretty close to where we find the broad O Auger signal. The O Auger KVV signal is also referred to as the KLL signal in the literature because the valence electrons of oxygen (its 2s and 2p electrons) are at the n = 2 level (the L level) of the atom. More precisely, the use of KVV vs. KLL should be applied when the L-shell electrons reside in the valence band (as is the case with B and C) instead of being upper core-level electrons (as is the case with O and above).

المنارة للاستشارات
www.manaraa.com

Carbon has a relatively strong KVV Auger signal. The position of the C 1s signal is ca. 285 eV. Hence the kinetic energy of the carbon Auger electron will be 285 eV – 25 eV – 25 eV = 235 eV. The apparent binding energy of these electrons will then be approximately 1500 eV – 235 eV = 1265 eV. Since the survey scans shown here only go to 1100 eV, we don't see this signal.

In **Figure A2.1a**, Peaks (i), (ii), and (iv) are photoelectron signals. Their binding energies are fixed; they will be the same whether generated with Al K alpha or Mg K alpha X-rays. However, Auger signals change positions in XPS binding energy plots when the excitation source changes. The important point here is that no matter how you generate the core hole in Auger (it could be by ions, electrons, or photons), you get the same Auger emission. That is, while the kinetic energy of a photoelectron depends directly on the energy of the photon used to eject it, the kinetic energy of an Auger electron it fixed – it does not depend on the energy of the X-ray (or other particle) used to initiate the process. Now, since in XPS we convert measured kinetic energies into reported binding energies via the photoelectric equation, the apparent binding energies of Auger electrons shift depending on the source used to excite them because the energy of the photon changes in the photoelectric equation.

In **Figure A2.2a**, Peaks (vii) are plasmon loss signals. A plasmon is a quantized oscillation of the electrons and nuclei in a material.[47] For example, the peak labeled (viia) correspond to Si 2*p* electrons that excited one plasmon as they exited the material, and the peak labeled (viib) corresponds to Si 2*p* electrons that excited two plasmons as they exited the material, etc. Peaks (viia) and (viib) come at higher binding energy than peaks (v) and (vi) because the corresponding electrons left the material with less kinetic energy (they lost energy when they excited one or more plasmons). Thus, by $h\nu \approx BE + KE$ they appear to have higher binding

المنارة للاستشارات
www.manaraa.com

energies. From the perspective of obtaining oxidation state information about silicon, the plasmons (the '(vii)' peaks) are undesirable because they overlap with the Si 2s signal, i.e., note that peaks (ix) and (viii) overlap with the third Si 2p plasmon loss peak.

Certainly, the presence of the plasmon signal will complicate analysis of this peak area. Notice also the overlap between peak (viia) and the Al 2s peak in Figures 3b and 3c. This analysis provides at least some of the justification for material scientists' focus on the Si 2p signal over the Si 2s signal in the literature. However, these plasmons can also be rich in information. An experienced XPS analyst would notice the difference between the plasmon loss features on the oxygen and silicon peaks in our spectra. Their difference suggests that the silicon and oxygen signals do not, for the most part, come from the same part of the sample – most of the silicon signal comes from the bulk of the material, while the oxygen is localized in the native oxide layer.

In **Figure A2.2a**, Peak (xi) appears in all the survey spectra. It comes at low binding energy and is from the valence band of the material. In general, it is a result of multiple overlapping orbitals in a material – it is not a single, defined peak like the core-level signals. The valence band signal can be useful for identifying some materials – it can act as a fingerprint. It can also identify changes in materials. With first principles modeling, it can sometimes yield useful information, but it is otherwise often difficult to interpret. The X-rays that eject core electrons from atoms travel much further in materials than the photoelectrons they generate. In other words, in XPS, the incident X-rays eject many electrons that cannot escape from the solid and/or that lose some energy before they escape. Thus, the rising backgrounds on the high-energy sides of the peaks in XPS spectra (and they will always be on the higher BE side of peaks) correspond to electrons that have lost variable amounts of energy (undergone inelastic collisions/losses) before escaping from the

المنارة للاستشارات
www.manaraa.com

material. For the same reasons, this loss of kinetic energy makes them, appear as if they have higher binding energy.

In **Figure A2.1c**, peak (xii) is the oxygen 2s signal. If you see a prominent O 1s signal in a spectrum, you should look for the corresponding O 2s signal at 25 eV and for the O KVV Auger signal, which we have discussed. All three should appear together. The step size in energy in XPS survey scans can be large enough that the energies at which the data are acquired do not correspond to the maxima of the signals coming from a sample. Thus, peak heights in XPS survey scans are not always a fully reliable reflection of surface concentrations. The under sampling that results in this artifact causes aliasing in Fourier theory, i.e., if a Fourier transform were taken of the data, higher frequency components would effectively appears as lower frequency ones.[64] Thus, the changes in the ratios of peaks (v) and (vi) in Figure 3 will be better understood through narrow scans of these peak envelopes taken with smaller energy step sizes and higher energy resolution; peak areas of narrow scans usually provide a more accurate indication of signal intensity and sample composition than those obtained from survey spectra.

In **Figure A2.3a**, the surface was contaminated with fluorine. Peak (xv) at 690 eV is the F 1s signal. The group of signals around peak (xvi) is the F KVV Auger signal. We can estimate the position of the F Auger signal as we did for carbon and oxygen above.

In **Figure A2.2c**, we previously identified the peaks at 25 eV as the O 2*s* signal. The shoulder on this peak in Figure 6 at higher binding energy (33 eV) is the F 2s signal. It is additional evidence for fluorine. It is much less intense than the F 1s peak so it will only be apparent in a spectrum if the F 1s signal is moderately large. Neal Fairley, the developer of CasaXPS,

المنارة للاستشارات
www.manaraa.com

recently produced a video on the F 1s and 2s signals.[29] In a well calibrated/functioning system the corrected F 1s and 2s signals should correspond to the same amount of fluorine.

An arbitrary scale is used when the y-axis is represented without numerical values. This can be done when either an absolute scale is not necessary to describe the spectrum or spectra, or when the y-axes of several spectra have been adjusted for comparison (normalized), or both. (As an aside, assuming no sample damage, the acquisition time in XPS becomes increasingly irrelevant as the signal-to-noise of a spectrum increases. Once the signal-to-noise ratio is sufficiently high, collecting more data will not change the spectrum in any substantial way – it usually becomes a waste of time and resources.)

You will see XPS spectra plotted both ways in the literature – with binding energy increasing to the right or to the left. Accordingly, it is important to be able to interpret them regardless of how they are graphed. Nevertheless, the most common current convention, which is followed by most databases, handbooks, and the data journal Surface Science Spectra, is to plot XPS data on a decreasing binding energy scale (increasing kinetic energy scale). This allows for uniformity in the comparison of XPS data and facilitates the straightforward comparison of X-ray-induced Auger spectra with those generated by an Auger spectrometer (electron source). The XPS community should adhere to this convention.

The baseline around C 1*s* peak (ca. 285.1 eV) is almost flat and does not show any signs of rise. This is an indication of the fact that carbon is present adventitiously on the surface. Since all the carbon signal is coming from the surface without any impedance, there is no rise in the baseline. This is different to the silicon and oxygen signal (see **Figure A2.4**) which predominantly come from underneath the surface, leading to significant increase in the baseline.

المنارة للاستشارات
www.manaraa.com

A2.6 Conclusions

This tutorial explores information that can be extracted from XPS survey spectra during ALD film growth. It was based on XPS survey spectra taken from a bare silicon wafer, and pieces of silicon after deposition of 10, 50, and 100 TMA/water ALD cycles. A series of questions have been presented on these spectra, which were designed to test one's basic understanding of XPS spectral interpretation. This quiz shows that a wide range of information is available from survey spectra. For example, contamination can be readily detected, and aspects of the ALD film growth process can be examined/verified at critical times. The questions are similar to the process an experienced analyst might follow in interpreting the features present in survey spectra and understanding relationships among them, including secondary features of the primary peaks. We hope that the content and format of this article will be useful to the reader and help him or her better understand the basic principles of X-ray photoelectron spectroscopy.

A2.7 Acknowledgments

The XPS spectra and corresponding samples in this work were previously described in a journal article that has been submitted for publication.

المنارة للاستشارات
www.manaraa.com

A2.8 Figures

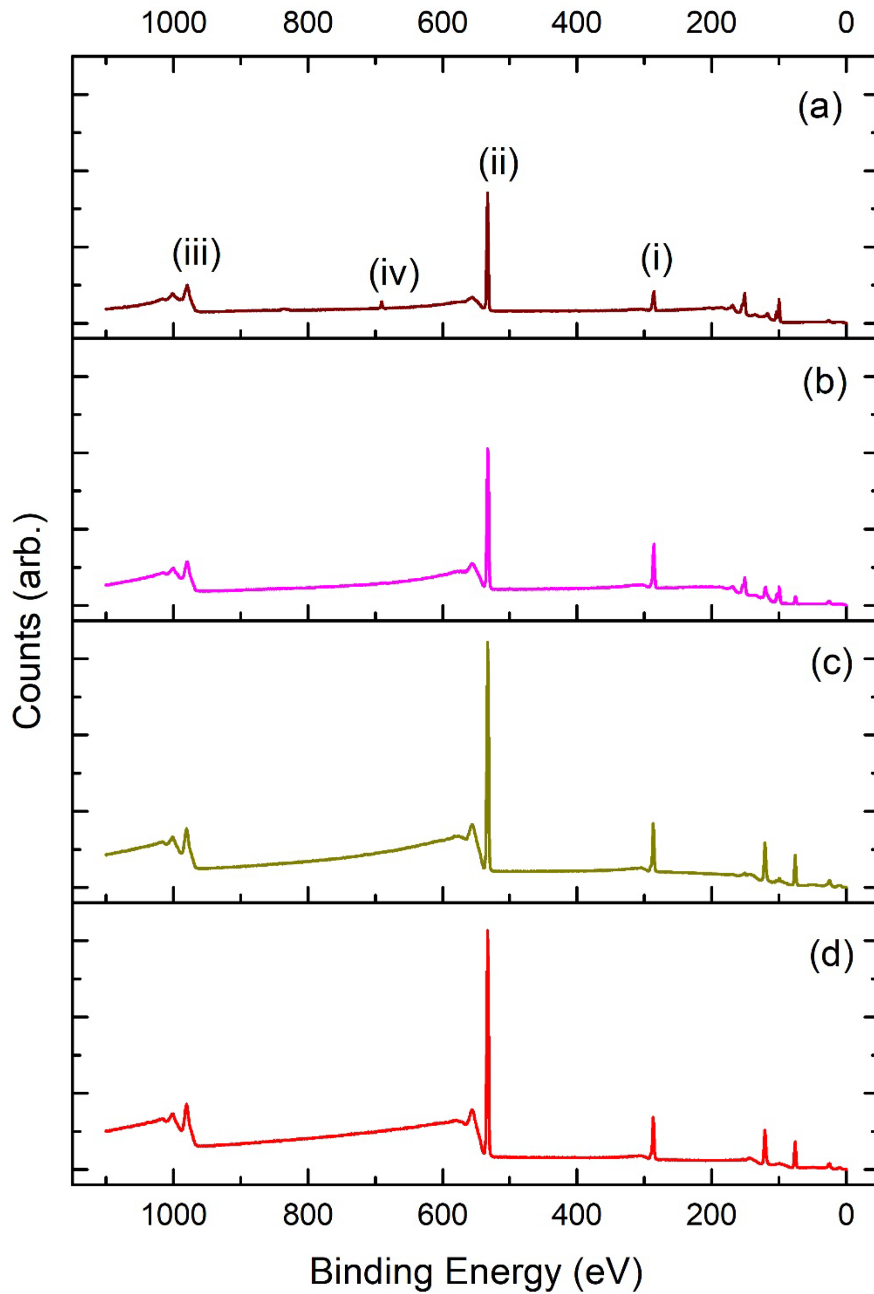

Figure A2.1 (Color online). XPS survey spectra shown from 0 – 1100 eV of ALD alumina films on silicon substrates. (a) The bare silicon substrate, and the silicon surface after (b) 10, (c) 50, and (d) 100 TMA/water ALD cycles. The lower case Roman numerals are used to indicate peaks in the spectra.

المنارة للاستشارات
www.manaraa.com

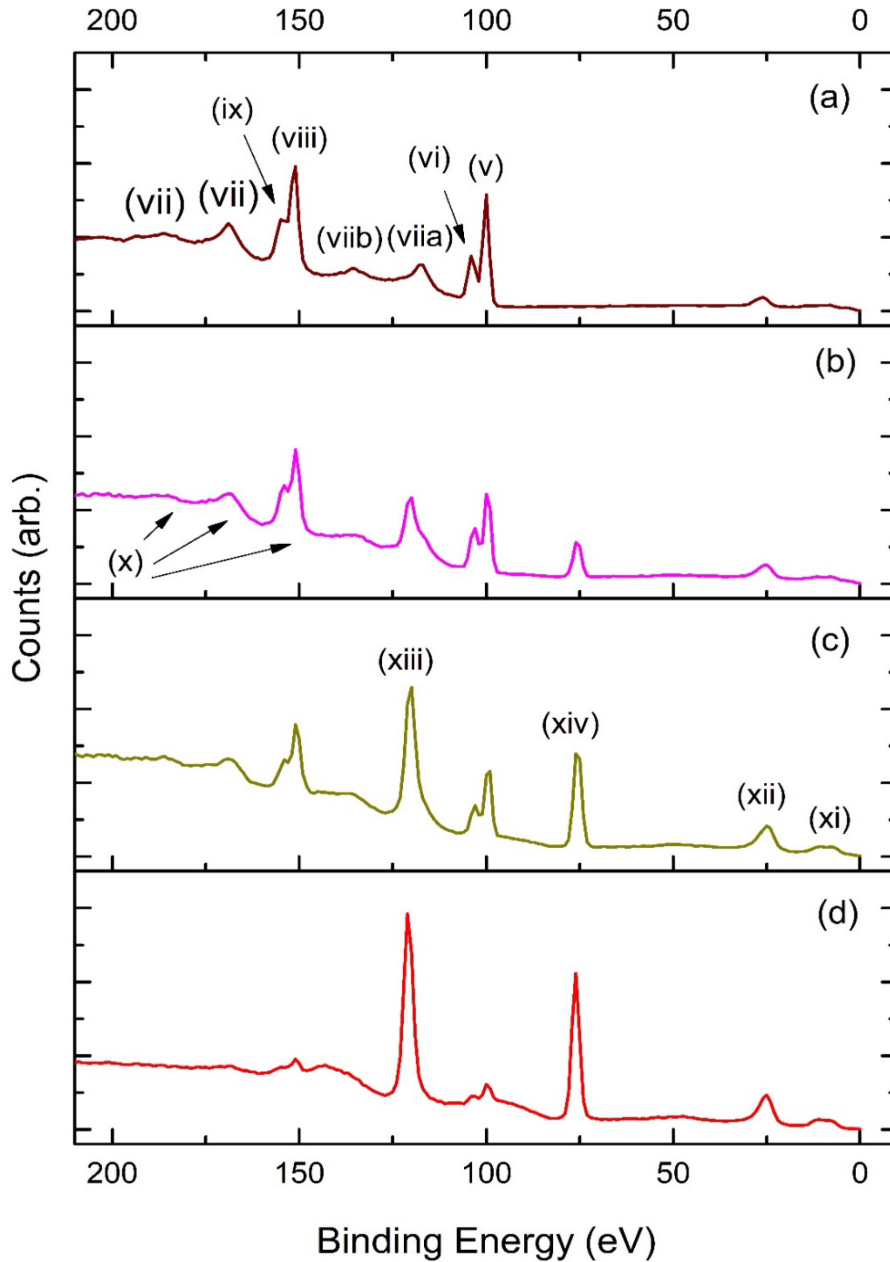

Figure A2.2. (Color online). XPS survey spectra shown from 0 – 210 eV of ALD alumina films on silicon substrates. (a) The bare silicon substrate, and the silicon surface after (b) 10, (c) 50, and (d) 100 TMA/water ALD cycles. The lower case Roman numerals are used to indicate peaks/features in the spectra.

المنارة للاستشارات
www.manaraa.com

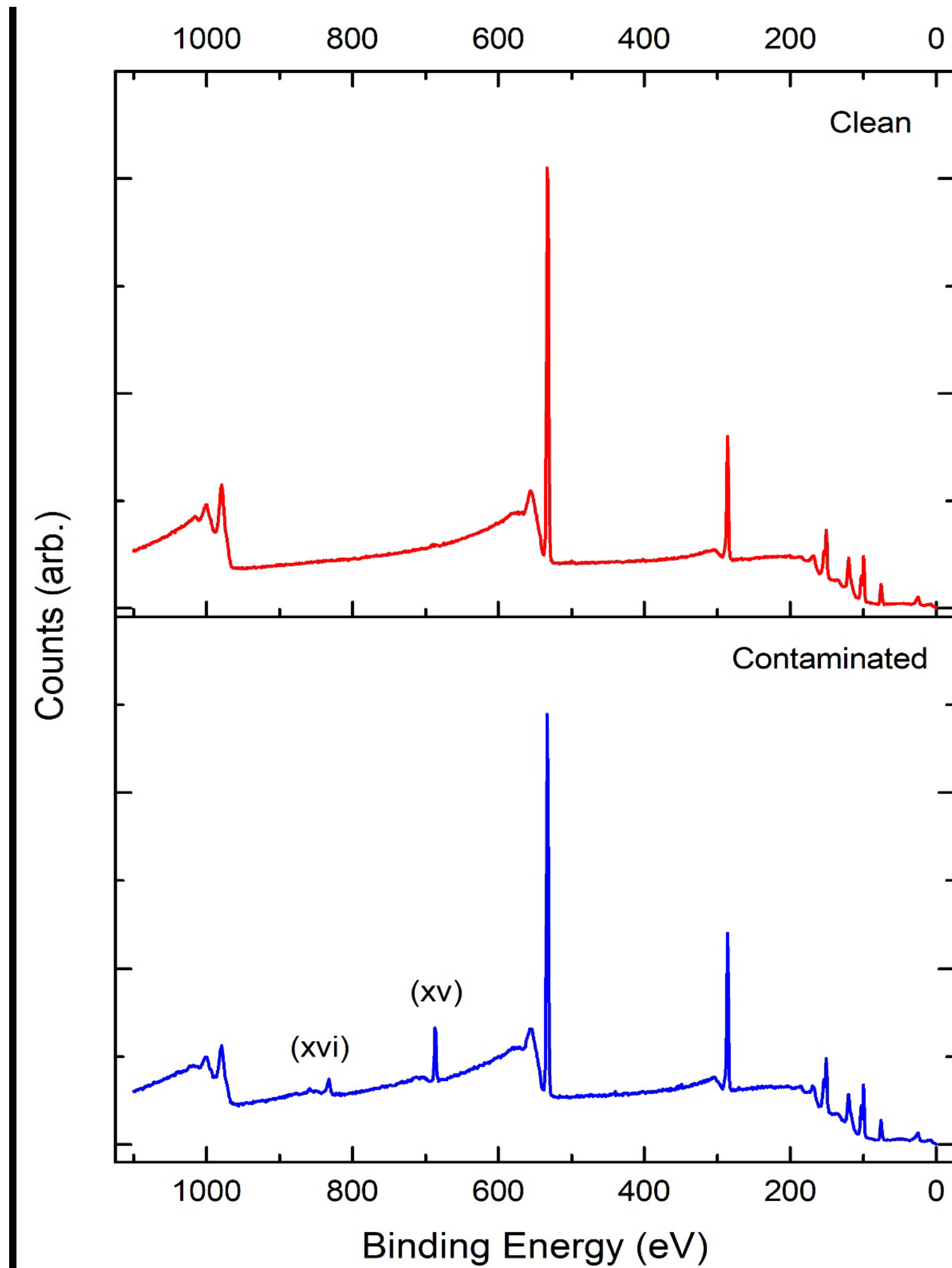

Figure A2.3. (Color online). XPS survey spectra from 0 – 1100 eV of two ALD alumina films prepared on silicon substrates with 10 TMA/water cycles. One surface had been treated in a dirty plasma chamber and had thus become 'Contaminated'. The lower case Roman numerals are used to indicate peaks/features in the spectra.

المنارة للاستشارات
www.manaraa.com

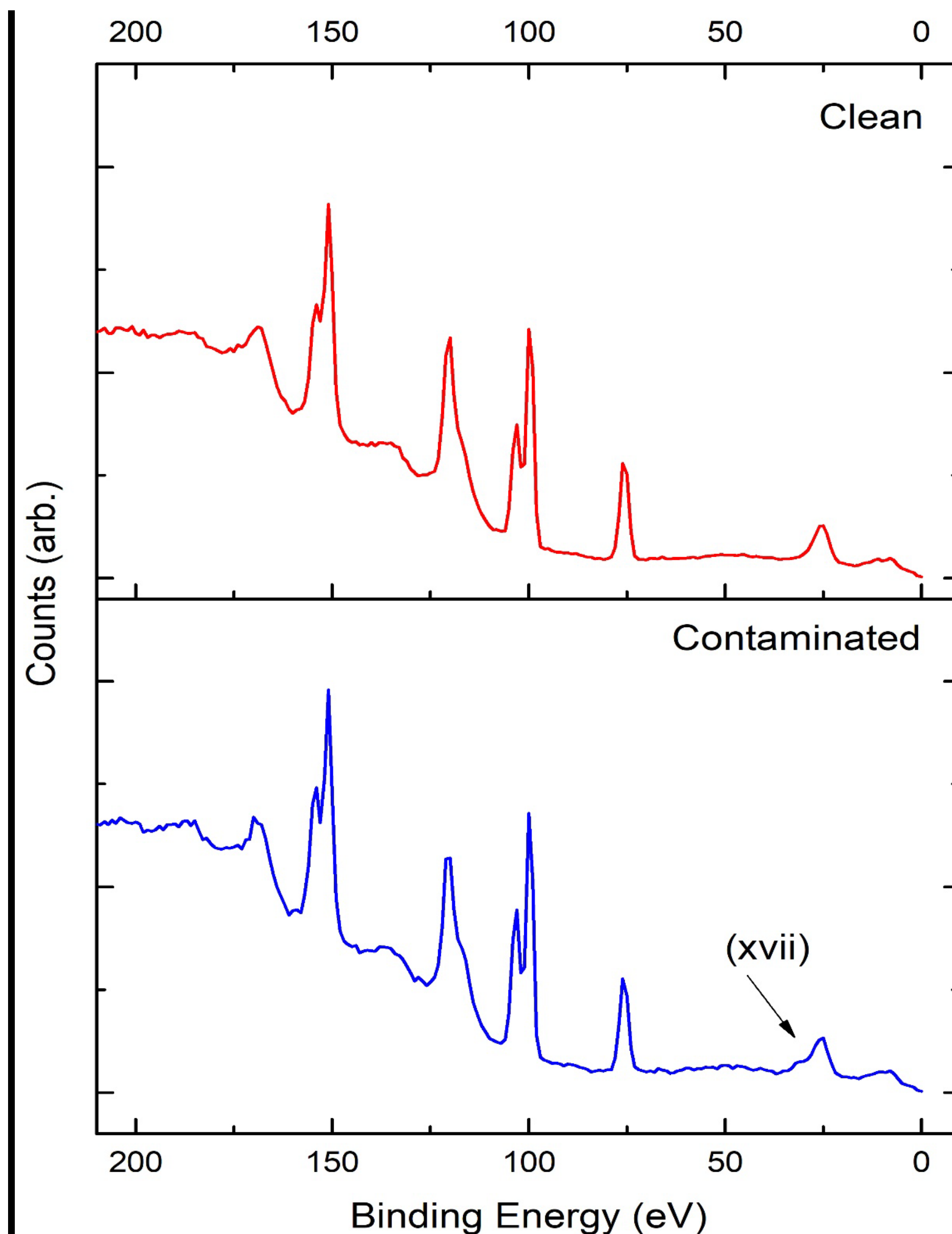

Figure A2.4. (Color online). XPS survey spectra from 0 – 210 eV of two ALD alumina films prepared on silicon substrates with 10 TMA/water cycles. One surface had been treated in a dirty plasma chamber and had thus become ‘Contaminated’. The lower-case Roman numerals are used to indicate peaks/features in the spectra.

www.manaraa.com

A2.9 References

1. C. J. Powell, Growth of Surface Analysis and the Development of Databases and Modeling Software for Auger-Electron Spectroscopy and X-ray Photoelectron Spectroscopy. *Microscopy Today* 2016, pp 16-23.
2. https://www.grandviewresearch.com/industry-analysis/xps-market.
3. J. E. Castle, M. A. B., *J. Electron Spectrosc. Relat. Phenom.* **1999,** *105*, 245.
4. J. E. Castle, C. J. P., Report on the 34th IUVSTA Workshop 'XPS: from spectra to results – towards an expert system'. *Surf. Interface Anal.* **2004,** *36*, 225-237.
5. C. J. Powell, Growth and trends in Auger-electron spectroscopy and x-ray photoelectron spectroscopy for surface analysis. *J. Vac. Sci. Technol., A* **2003,** *21* (5), S42-S53.
6. C. J. Powell, R. S., K. Yoshihara, S. Ichimura,, Development of standards for reliable surface analyses by ISO technical committee 201 on surface chemical analysis. *Surf. Interface Anal.* **2015,** *47*, 127–134.
7. V. Gupta, H. G., M. H. Engelhard, J. Terry, M. R. Linford, , Assigning oxidation states to organic compounds via predictions from X-ray photoelectron spectroscopy: A discussion of approaches and recommended improvements. *J. Chem. Educ.* **2013,** *91* (2), 232-238.
8. B. Singh, A. D., V. Jain, A. Herrera-Gomez, J. Terry, M. R. Linford, , Uniqueness plots: A simple graphical tool for identifying poor peak fits in X-ray photoelectron spectroscopy. *Appl. Surf. Sci.* **2016,** *387*, 155-162.
9. V. Jain, M. C. B., M. R. Linford, , The Gaussian-Lorentzian Sum, Product, and Convolution (Voigt) functions in the context of peak fitting X-ray photoelectron spectroscopy (XPS) narrow scans. *Appl. Surf. Sci.* **2018,** *447*, 548-553.
10. B. Singh, R. H., M. R. Linford, , Good practices for XPS (and other types of) peak fitting: Use Chi squared, use the abbe criterion, show the sum of fit components, Show the (normalized) residuals, Choose an appropriate background, estimate fit parameter uncertainities, Limit the number of fit parameters, use information from other techniques, and use common sense. *Vac. Techno. Coat,* **2015,** *December*.
11. B. Singh, A. H.-G., J. Terry, M. R. Linford, , Good practices for XPS peak fitting, II. *Vac. Techno. Coat.* **2016,** *August*.
12. D. R. Baer, K. A., C. R. Brundle, J. E. Castle, M. H. Engelhard, K. J. Gaskell, J. T. Grant, M. R. Linford, C. J. Powell, P. M. A. Sherwood, V. S. Smentkowski, Practical guides for X-Ray Photoelectron Spectroscopy: Initial Questions. *J. Vac. Sci. Technol., B* **2018,** *To Be Submitted*.
13. J. E. Castle, Module to guide the expert use of x-ray photoelectron spectroscopy by corrosion scientists. *J. Vac. Sci. Technol., A* **2007,** *25* (1), 1-27.
14. Castle, J. E.; Powell, C. J., Report on the 34th IUVSTA workshop'XPS: From Spectra to Results—Towards an Expert System'. *Surf. Interface Anal.* **2004,** *36* (3), 225-237.
15. P. van der Heide, *X-ray Photoelectron Spectroscppy: An introduction to principles and practices*. John Wiley & Sons: 2011.
16. J. F. Watts, J. W., *An Introduction to Surface Analysis by XPS and AES*. John Wiley & Sons: 2003.
17. J. F. Moulder, W. F. S., P. E. Sobol, K. D. Bomben, K. D., 1992.
18. Baer, D. R., Introduction to Special Issue on Advances and Applications of Surface Analysis Methods. *Microscopy Today* 2016, pp 12-15.

المنارة للاستشارات
www.manaraa.com

19. Introduction to XPS: X-ray Photoelectron Spectroscopy. http://www.npl.co.uk/science-technology/surface-and-nanoanalysis/surface-and-nanoanalysis-basics/introduction-to-xps-x-ray-photoelectron-spectroscopy (accessed June 11, 2018).
20. Watts, J. F.; Wolstenholme, J., *An Introduction to Surface Analysis by XPS and AES*. John Wiley and Sons: Chichester, UK, 2003.
21. van der Heide, P., *X-Ray Photoelectron Spectroscopy: An Introduction to Principles and Practices*. John Wiley & Sons, Inc.: Chichester, 2011.
22. Briggs, D.; Grant, J. T., *Surface Analysis by Auger and X-ray Photoelectron Spectroscopy,* . IM Publications, : Chichester, 2003.
23. Briggs, D.; Seah, M. P., *Practical Surface Analysis by Auger and X-ray Photoelectron Spectroscopy,*
. John Wiley and Sons, : Chichester, UK, 1983.
24. Hofmann, S., *Auger- and X-ray Photoelectron Spectroscopy in Materials Science.* . Springer: Heidelberg, 2013.
25. Baer, D. R.; Engelhard, M. H.; Johnson, G. E.; Laskin, J.; Mueller, K.; Munusamy, P.; Thevuthasan, S.; Wang, H.; Washton, N.; Elder, A.; Baisch, B. L.; Karakoti, A.; Kuchibhatla, S. V. N. T.; Moon, D. W., Surface Characterization of Nanomaterials and Nanoparticles: important needs and challenging opportunities. *J. Vac. Sci. Technol. A* **2013,** *31*, 050820
26. Baer, D. R.; Engelhard, M. H., XPS Analysis of Nanostructured Materials and Biological Surfaces. *J. Electron Spectrosc. Relat. Phenom.* **2010,** *178-179*, 415-432.
27. Castle, J. E., Module to guide the expert use of x-ray photoelectron spectroscopy by corrosion scientists. *J. Vac. Sci. Technol. A* **2007,** *25* (1), 1-27.
28. McArthur, S. L.; Mishra, G.; Easton, C. D., Applications of XPS in Biology and Biointerface Analysis. In *Surf. Anal. Tech. Biol.*, Smentkowski, V. S., Ed. Springer International Publishing: Cham, 2014; pp 9-36.
29. Shchukarev, A.; Ramstedt, M., Cryo-XPS: probing intact interfaces in nature and life. *Surf. Interface Anal.* **2016,** *49*, 349-356.
30. International, A., ASTM E2735-13 Standard Guide for Selection of Calibrations Needed for X-ray Photoelectron Spectroscopy (XPS) Experiments, , , . ASTM International: West Conshohocken, PA, , 2013.
31. Crist, B. V., XPS in industry—Problems with binding energies in journals and binding energy databases. *J. Electron Spectrosc. Relat. Phenom.* **2018**.
32. NIST Data Gateway. https://srdata.nist.gov/gateway/gateway?keyword=surface+analysis+technique (accessed June 11, 2018).
33. S. M. W. Werner, W. S., and J. C. Powell, NIST Database for the Simulation of Electron Spectra for Surface Analysis (SESSA): Version 2.0. *National Institute of Standards and Technology. Gaithersburg, MD* **2015**.
34. Smekal, W., Werner, Wolfgang S. M., Powell, Cedric J., Simulation of electron spectra for surface analysis (SESSA): A novel software tool for quantitative Auger-electron spectroscopy and X-ray photoelectron spectroscopy. *Surf. Interface Anal.* **2005,** *37* (11), 1059-1067.
35. XPS Simplified: XPS data interpretation. https://www.thermofisher.com/us/en/home/industrial/spectroscopy-elemental-isotope-analysis/spectroscopy-elemental-isotope-analysis-learning-center/spectroscopy-elemental-isotope-analysis-resource-library/xps-data-interpretation-webinar.html (accessed June 11, 2018).

المنارة للاستشارات
www.manaraa.com

36. Fairley, N. CasaXPS: Processing Software for XPS, AES, SIMS and More. http://www.casaxps.com/ (accessed June 1, 2018).
37. Surface Science Tutorials. http://mmrc.caltech.edu/SS_XPS/XpS%20Tutorials.html (accessed June 11, 2018).
38. M.C., B. X-ray Photoelectron Spectroscopy (XPS) Reference Pages. http://www.xpsfitting.com/ (accessed June 11, 2018).
39. Surface Science Resources. http://mmrc.caltech.edu/SS_XPS/SS_resources.html (accessed June 11, 2018).
40. P. Van der Heide, Atoms, Ions, and their electronic structure. In *X-Ray Photoelectron Spectroscopy*, John Wiley & Sons, Inc.: 2011; pp 13-26.
41. G. Greczynski, L. H., C 1s Peak of Adventitious Carbon Aligns to the Vacuum Level: Dire Consequences for Material's Bonding Assignment by Photoelectron Spectroscopy. *ChemPhysChem* **2017,** *18* (12), 1507-1512.
42. G. Greczynski, L. H., Reliable determination of chemical state in x-ray photoelectron spectroscopy based on sample-work-function referencing to adventitious carbon: Resolving the myth of apparent constant binding energy of the C 1s peak. *Appl. Surf. Sci.* **2018,** *451*, 99-103.
43. Madaan, N. K., S. S.; Jensen, D. S.; Vail, M. A.; Dadson, A. E.; Engelhard, M. H.; Samha, H.; Linford, M. R., Al_2O_3 *e*-Beam evaporated onto silicon (100)/SiO_2, by XPS. *Surf. Sci. Spectra* **2013,** *20* (43), 1-7.
44. Jensen, D. S. K., S. S.; Madaan, N.; Vail, M. A.; Dadson, A. E.; Engelhard, M. H.; Linford, M. R., Silicon (100)/SiO_2 by XPS. *Surf. Sci. Spectra* **2013,** *20* (36), 1-8.
45. A. M. Ferraria, J. D. L. d. S., A. M. Botelho do Rego,, XPS studies of directly fluorinated HDPE: problems and solutions. *Polymer* **2003,** *44* (23), 7241-7249.
46. N. H. Turner, J. A. S., Surface analysis: X-ray photoelectron spectroscopy and Auger electron spectroscopy. *Anal. Chem.* **2000,** *72*, 99-110.
47. M. Kurth, P. C. J. G., E. J. Mittemeijer,, Determination of the intrinsic bulk and surface plasmon intensity of XPS spectra of magnesium. *Appl. Surf. Sci.* **2003,** *220* (1-4), 60-78.

المنارة للاستشارات
www.manaraa.com

Appendix 3: Polyethylene glycol: Optical constants from 191 to 1688 nm (0.735–6.491 eV) by spectroscopic ellipsometry

A3.1 Statement of Attribution

This document was originally published as Shah, D.; Roychowdhury, T.; Hilfiker, J. N.; Linford, M. R., Polyethylene Glycol: Optical constants from 191 – 1688 nm (0.735 – 6.491 eV) by spectroscopic ellipsometry *Surf. Sci. Spectra,* **2020**, *27*(1), 016001-1 to 016001-07. Some information fields are modified to improve its readability in this format. We refer readers to the original document for complete sample, instrument information, and spectral features.

A3.2 Abstract

Polyethylene glycol (PEG) is an important polymer with numerous industrial and therapeutic applications. Accordingly, the optical constants of PEG should be a useful resource to other scientists and engineers. Herein, we report the optical functions of PEG as determined from reflection spectroscopic ellipsometry (SE) and transmission ultraviolet-visible spectroscopy. These functions were obtained from a commercial liquid sample of PEG that had a molecular weight of 285–315 g/mol. Since this sample is a liquid, the reflection and transmission measurements required special experimental considerations.

The reflection SE measurements necessitated roughening (frosting) the inside of the vessel (Petri dish) that contained PEG and leveling the instrument instead of the liquid sample. The transmission measurements were obtained via a dual-cuvette approach that removed the effects of the cuvettes and their interfaces. From these measurements, the extinction coefficient of

المنارة للاستشارات
www.manaraa.com

the PEG was determined between 205 and 1700 nm. Since PEG has very low absorption over the measured wavelength range, and because of the relatively wide wavelength range considered here, the refractive index was fit with a Sellmeier model for wavelengths from 191 to 1688 nm. The interface at the liquid surface was modeled with a Bruggeman effective medium approximation. The optical functions obtained in this work agree well with previously reported values. For example, we obtained the following nx values for the material, where x is the wavelength in nanometers: n300 = 1.493, n500 = 1.459, and n1000 = 1.443.

Keywords: spectroscopic ellipsometry, optical model, Sellmeier, surface interface, polyethylene glycol, PEG300

A3.3 Technical Information

Accession #: 01612

Technique: SE

Host Material: PEG/air ambient

Instrument: J. A. Woollam Company, M-2000DI

Published Spectra: 5

Spectra in Electronic Record: 5

Spectral Category: Reference

A3.4 Introduction

Polyethylene glycol (PEG) is an organic polymer comprised of carbon, oxygen, and hydrogen. It consists of pairs of methylene (CH_2) units separated by ether linkages (O-C-O).[1] Its degree of crosslinking and molecular weight dictates whether it will have the form of a hard solid,

المنارة للاستشارات
www.manaraa.com

elastomer, or liquid.[2, 3] Polyethylene glycol is usually a low molecular weight polymer (<1000 g/mol) while polyethylene oxide is a higher molecular weight polymer (>10,000 g/mol).[4] PEG is soluble in water, methanol, ethanol, acetonitrile, and dichloromethane. It is an important component of many nonionic surfactants.[5, 6] PEG has a low glass transition temperature,[7] low toxicity, and tunable viscosity,[8] all of which make it a good candidate as a lubricant in aqueous and non-aqueous environments.[9] The uses and applications of PEG are extremely widespread;[10] a keyword search under "polyethylene glycol" in Google Scholar produced nearly 406,000 hits. A similar search on Scifinder® gave us 559,369 references. Some of PEG's specific applications are in semiconductor manufacturing,[11] biologics,[12, 13] therapeutics,[14, 15] and as a plasticizer.[16]

Spectroscopic ellipsometry (SE) is one of the most important tools for characterizing surfaces and materials.[17, 18] It is fast and convenient. In most cases it does not require any special pre-treatment of samples, and it is generally performed in the open laboratory environment. Under appropriate conditions, SE can measure thin film thicknesses and the optical properties of substrates, films, and interfaces. It is also sensitive to the presence of interfaces, film roughness, gradients in films, and material anisotropies.[19]

The vast majority of materials analyzed by SE are planar solids with surfaces that are smooth compared to the wavelengths of light that probe them. A classic example here is a coated silicon wafer. In contrast, in this work we probed a liquid sample, which required various experimental adaptations.[20] First, the liquid polymer was poured into a sand-blasted glass Petri dish, which was frosted on its inside surface to eliminate reflections from the container.[21] Hence, the ellipsometric information was obtained from the reflection at the air-polymer interface so the liquid could be modeled as having infinite depth. The second experimental challenge was the alignment of the sample such that the light reflected from the sample surface reached the detector.

المنارة للاستشارات
www.manaraa.com

A solid sample can be aligned with respect to a light beam and/or instrument by adjusting the stage it is on. However, the alignment of a stage beneath a liquid sample does not change its level, which is dictated by gravity. Hence, for liquid samples, the instrument must be aligned and not the sample. A third technical challenge associated with this work concerned the transmission measurements. It is not fully correct to use an empty cuvette as the reference for a liquid-filled cuvette because the interfaces between glass-liquid are different from between glass-air.

Accordingly, transmission data were collected through multiple cuvettes filled with PEG, each with a different path length (2mm, 5mm, and 10mm).[22] This allows the extinction coefficient of the PEG to be calculated using a dual-cuvette method, which eliminates the effects of window losses.[22, 23] Measuring the transmission through three different cuvettes allows three different ratios for calculating the extinction coefficient per the following equation:

$$k = \frac{\lambda}{4\pi} \frac{\ln\left(T_1/T_2\right)}{z_2 - z_1}$$

Additional details related to the data collection in this study have been previously published.[20, 21, 24, 25] The figure below show three transmitted intensity spectra originating from cuvettes with different path lengths, which were then used with the equation above to determine the extinction coefficient. We graphed the average extinction coefficients from these three calculations between 205 nm and 1700 nm with the maximum and minimum values shown as our error bars. As expected, our calculation error is larger at shortest and longest wavelengths where we have both very low transmitted intensities and much lower signal-to-noise.

www.manaraa.com

A3.5 Specimen Description

Sample Description:	PEG sample obtained from a commercial supplier (Merck kGaA, (Darmstadt, Germany)
History & Significance	PEG is an extremely important polymer with a wide range of applications
Analyzed Region:	Reflection ellipsometry and transmission data were collected with an ellipsometer on the liquid from 191 to 1688 nm
Specimen Temperature During Analysis:	~300 K
Maximum Chamber Pressure During Analysis, Pa:	Ambient
Sample Conditions During Measurement:	The liquid sample was exposed to air during the analysis.
***Ex Situ* Preparation and Mounting:**	To achieve accurate reflection ellipsometric measurements of transparent samples, it is helpful to suppress unwanted reflections from container surfaces. This was done here by sand blasting the

المنارة للاستشارات
www.manaraa.com

	inner surface of the glass petri dish that held the liquid sample. Before using the dish, the particle contamination that was created during sand blasting was removed with a jet of dry nitrogen. The blasted Petri dish was then washed with soap and water, rinsed with isopropyl alcohol, and dried with nitrogen. Liquid PEG was poured into the Petri dish, which was mounted on the ellipsometer stage.
In Situ Preparation:	None

المنارة للاستشارات
www.manaraa.com

A3.6 Specimen Component Layers

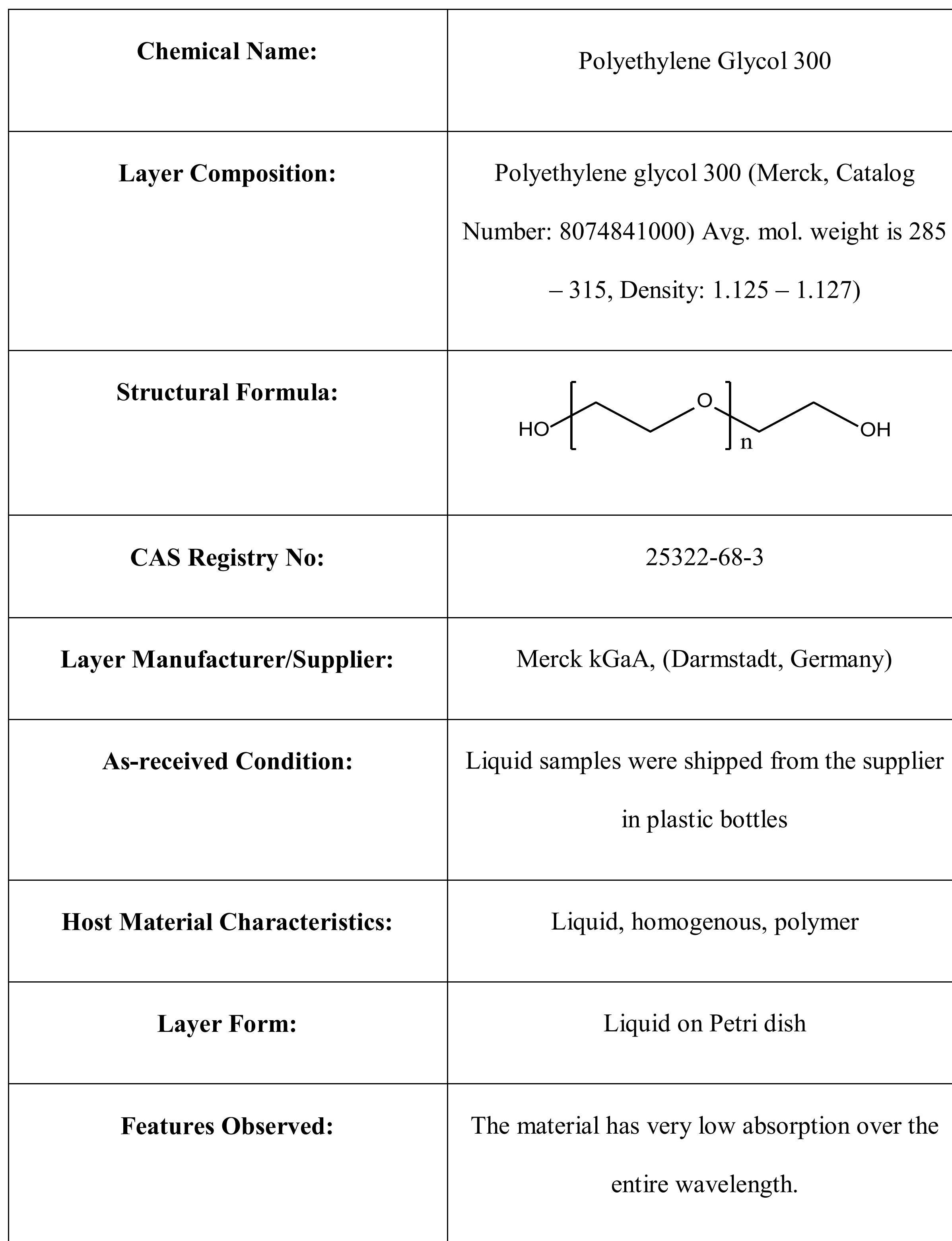

Chemical Name:	Polyethylene Glycol 300
Layer Composition:	Polyethylene glycol 300 (Merck, Catalog Number: 8074841000) Avg. mol. weight is 285 – 315, Density: 1.125 – 1.127)
Structural Formula:	HO O n OH
CAS Registry No:	25322-68-3
Layer Manufacturer/Supplier:	Merck kGaA, (Darmstadt, Germany)
As-received Condition:	Liquid samples were shipped from the supplier in plastic bottles
Host Material Characteristics:	Liquid, homogenous, polymer
Layer Form:	Liquid on Petri dish
Features Observed:	The material has very low absorption over the entire wavelength.

المنارة للاستشارات
www.manaraa.com

A3.7 Instrument Configuration

Instrument Details	Ellipsometer
Instrument Manufacturer:	J. A. Woollam Company
Manufacturer Model No:	M - 2000DI
Instrument Configuration:	Variable angle spectroscopic ellipsometer equipped with a CCD array detector, a rotating analyzer, and a near IR extension to allow data collection out to 1688 nm
Spectral Range:	191 - 1688 nm
Measurement Angle(s) of Incidence:	53°, 54°, 55°, 56°, 57°
Acquired Data Type:	Ψ, Δ, and transmittance

المنارة للاستشارات
www.manaraa.com

A3.8 Data Analysis

The methodology used in this study to acquire and work up the data was presented in a paper that was previously published by our group on polydimethylsiloxane (PDMS).[24] This reference describes (i) how the instrument was leveled with respect to the sample, and not the other way around, (ii) how two cuvettes with different internal path lengths were used to obtain the transmission spectra, and (iii) the mathematical equations and approach used to analyze the data. Data analysis was performed with the CompleteEase® software package from the J.A. Woollam Company.

In this work, reflection measurements from the liquid were taken at various angles of incidence, i.e., from 53° to 57°, to bracket the Brewster angle of PEG.[8, 26] The theory of ellipsometry is based on the Fresnel equations for polarized light interacting with multi-layered planar substrates. The fundamental equation of ellipsometry is expressed in terms of two parameters, psi (ψ) and delta (Δ), as follows:[17, 18]

$$\frac{\tilde{r}_p}{\tilde{r}_s} = \tan \psi e^{i\Delta}$$

where $\tilde{r}_p$ and $\tilde{r}_s$ are the complex Fresnel reflection coefficients of the sample for p- (in the plane of incidence) and s- (perpendicular to the plane of incidence) polarized light. The angle ψ provides information about the ratio of two amplitudes, and Δ is the phase shift between the two components. Spectroscopic ellipsometry measures the ratio of the two light components as a function of wavelength. The so-called variable angle spectroscopic ellipsometry (VASE) method increases the sensitivity of the measurements due to the different optical path lengths traversed. The reflection measurements were plotted as a function of wavelength and angle of incidence (see

المنارة للاستشارات
www.manaraa.com

Figure A3.4). As expected, ψ is at or close to zero near the Brewster angle for the sample, i.e., $\frac{r_p}{r_s}$ = 0 at these points.

The Δ values obtained in this study are either 0˚ or 180˚ over most of the wavelength range, which is consistent with the assignment of PEG as a transparent dielectric. The low absorption of the material was confirmed in the transmission measurements (see Figure 2). Accordingly, it seems appropriate to model this material with a Sellmeier function, which yielded a reasonable fit to the data.[27] In particular, a weighted mean squared error (MSE) of 1.239 was obtained. In our model, the substrate (PEG) is fitted with a Sellmeier function, along with a Bruggeman effective median approximation (BEMA) layer that accounted for the surface (liquid-air) interface.[28] This surface interface is an important part of many ellipsometric models, and a roughness layer modeled with the BEMA decreases the MSE value of the fit from 1.640 to 1.239.

A3.9 Oscillator or effective medium approximation equations

The pole-pole model (Sellmeier) can be described by the following equation:[29]

$$\epsilon_1(\lambda) = \varepsilon_\infty + \frac{A_{UV}\lambda^2}{\lambda^2 - \lambda_{UV}^2} + \frac{A_{IR}\lambda^2}{\lambda^2 - \lambda_{IR}^2},$$

where *n* is the refractive index, A_{UV} is the UV amplitude, A_{IR} is the IR amplitude, λ_{UV} is the position of the UV pole, λ_{IR} is the position of the IR pole, and the λ(nm) is the wavelength for which the refractive index is being calculated. However, in this work λ(nm) is expressed as energy (E_{UV} and E_{IR} - see **Table A3.1** for details). ε_∞ is the low-frequency offset. The values for λ_{UV} and λ_{IR} are provided in terms of energy (eV) instead of wavelength. ε_∞, and A_{UV} and A_{IR} are unitless. (This

المنارة للاستشارات
www.manaraa.com

portion of this text on the pole-pole model was taken from our recently published paper on the optical properties of silicon dioxide).

The Bruggeman effective medium approximation (BEMA) is given by the following equation.

$$f_a \frac{\varepsilon_a - \varepsilon}{\varepsilon_a + 2\varepsilon} + f_b \frac{\varepsilon_b - \varepsilon}{\varepsilon_b + 2\varepsilon} = 0$$

where f_a is the volume fraction of material a, f_b is the volume fraction of material b, and ε is the dielectric constant of the composite material derived from the dielectric constants of the component materials ε_a and ε_b.[28] The surface interface layer was modeled using a BEMA layer consisting of 50% void and 50% PEG. (This portion of the text on the BEMA was taken from our recently published papers on the optical properties of EagleXG®).[29, 30]

The MSE for the fits was calculated using:

$$MSE = \sqrt{\frac{1}{3n - m} \sum_{i=1}^{n} \left[\left(\frac{N_{Ei} - N_{Gi}}{0.001} \right)^2 + \left(\frac{C_{Ei} - C_{Gi}}{0.001} \right)^2 + \left(\frac{S_{Ei} - S_{Gi}}{0.001} \right)^2 \right]}$$

where n is the number of wavelengths, i.e., (ψ, Δ) pairs, m is the number of variable parameters in the model and σ represents a standard deviation. Terms superscripted with an exp denote the experimentally measured values at a given data point i, and terms superscripted with a mod indicate the data generated by the model at the data point i.[24, 29]

Free Parameters in the Model: Explained above

Fixed Parameters in the Model The energy of the IR pole (E_{IR}) was fixed at 1×10^{-8} eV.

المنارة للاستشارات
www.manaraa.com

Table A3.1. Fit parameters for PEG300 (Sellmeier with BEMA roughness layer)

Parameter	**Value**	**Error**
Roughness (nm)	0.42	0.008
A_{UV} (unitless)	39.80	0.599
E_{UV} (eV)	8.94	0.024
ε_{∞} (unitless)	1.592	0.005
A_{IR} (eV)	0.006	0.0003
MSE	1.239	0.00

المنارة للاستشارات
www.manaraa.com

A3.10 Figures

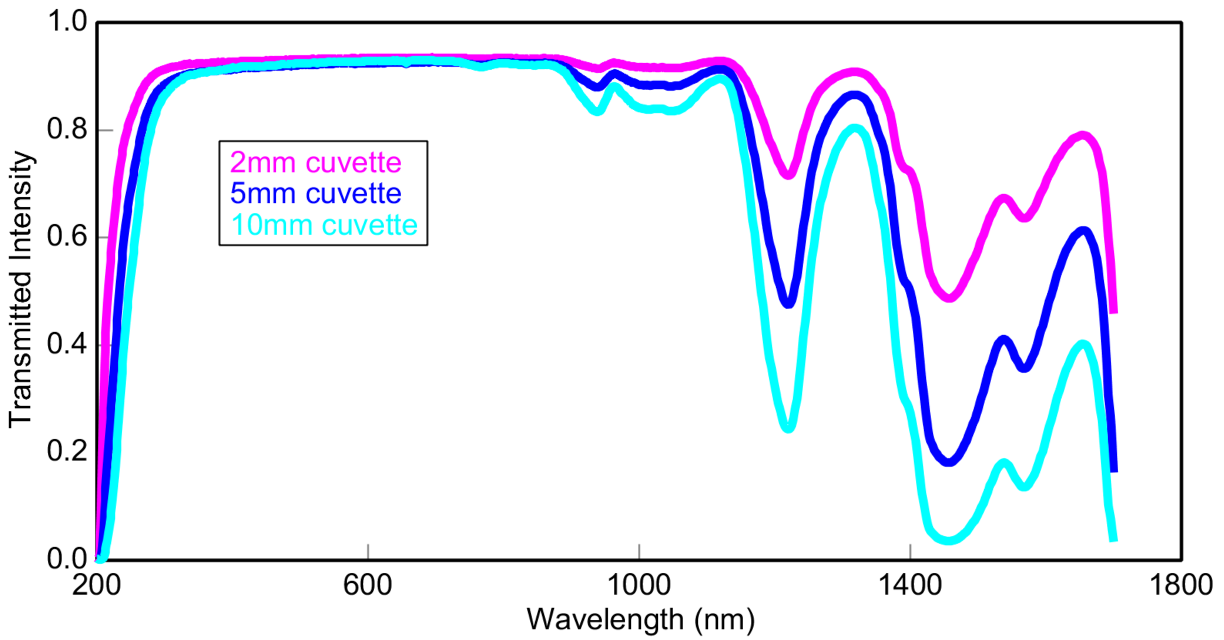

Figure A3.1. Transmission intensities for PEG calculated using cuvettes with three different path lengths (2 mm, 5 mm, and 10 mm).

المنارة للاستشارات
www.manaraa.com

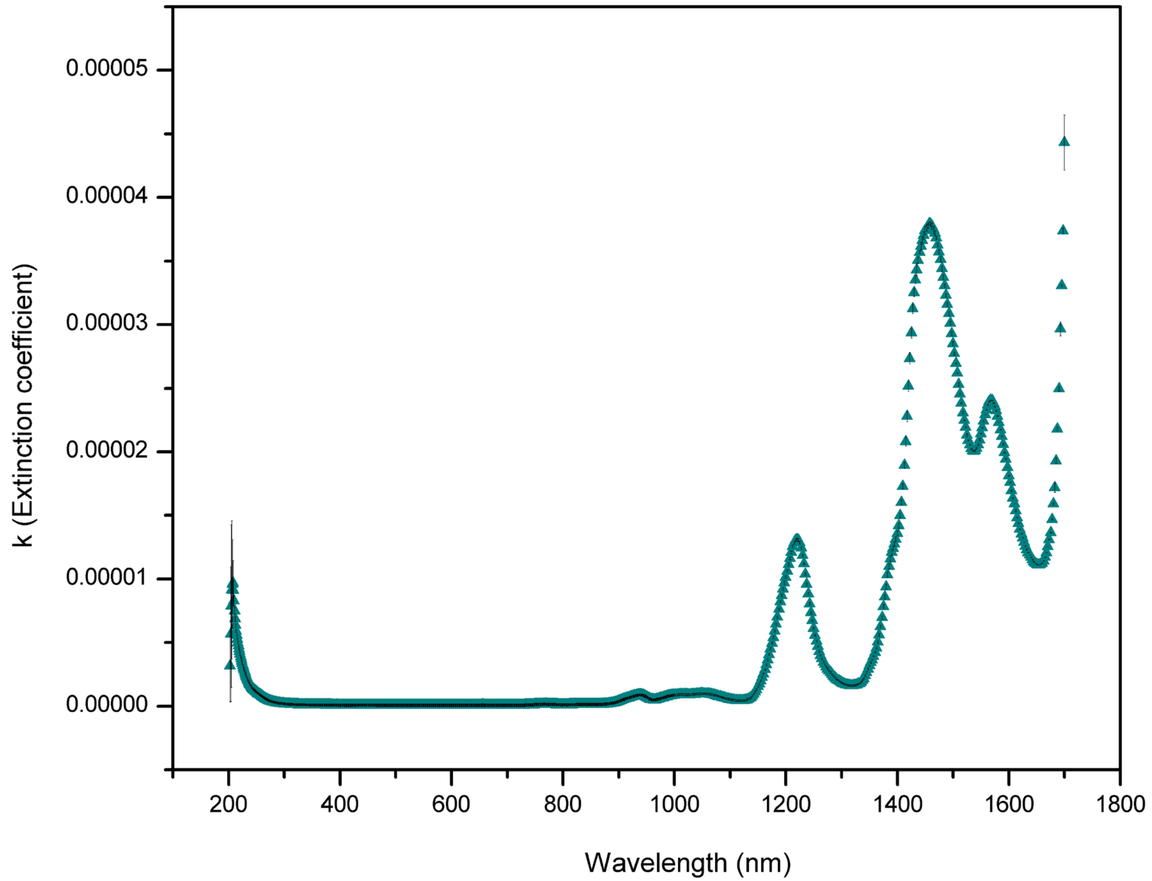

Figure A3.2. Extinction coefficient of PEG measured from three different dual-cuvette ratios where the range of results was used to show error-bars at each wavelength. In general, the error bars are about the same size as the symbols in this plot. However, they are rather large at the largest and shortest wavelengths considered here.

المنارة للاستشارات
www.manaraa.com

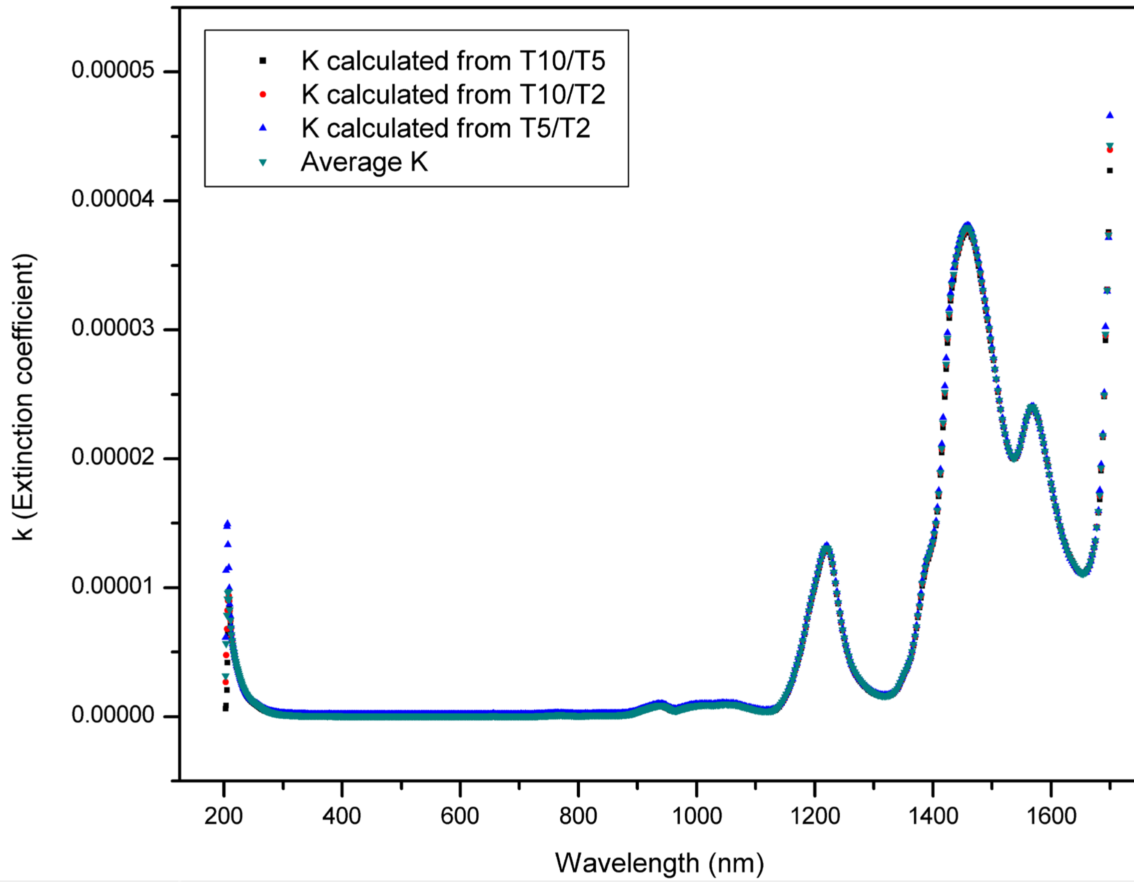

Figure A3.3. Extinction coefficient, k(λ), for PEG.

المنارة للاستشارات
www.manaraa.com

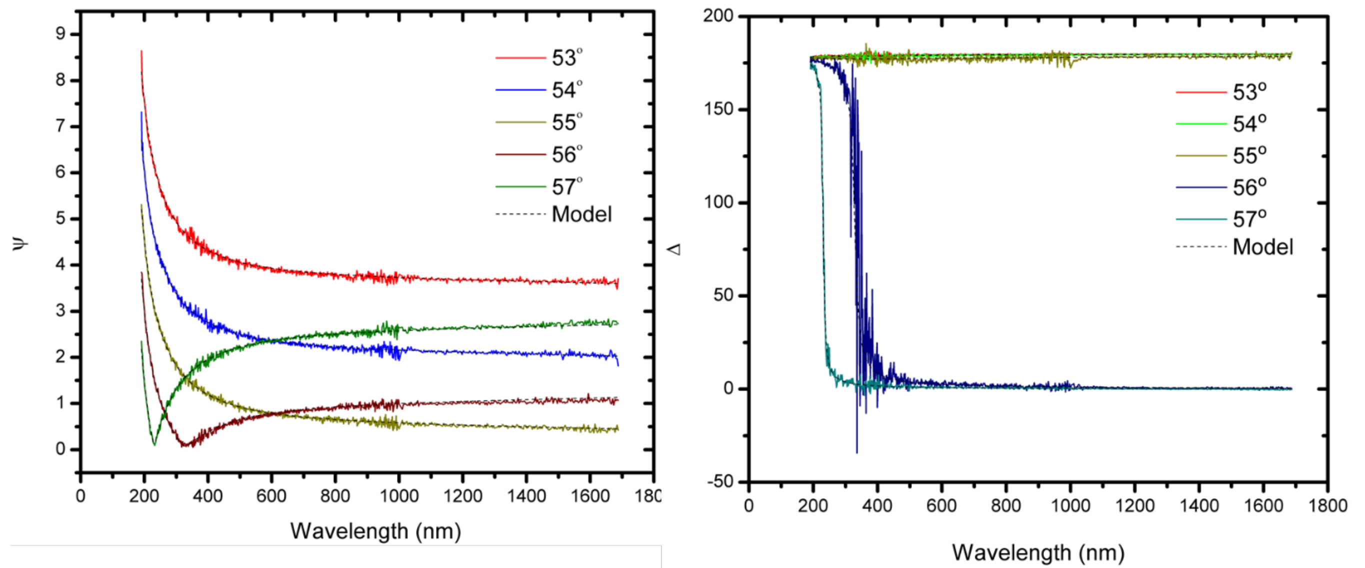

Figure A3.4. Experimental results (ψ and Δ) for PEG300 modeled using a Sellmeier function and a BEMA surface interface layer.

المنارة للاستشارات
www.manaraa.com

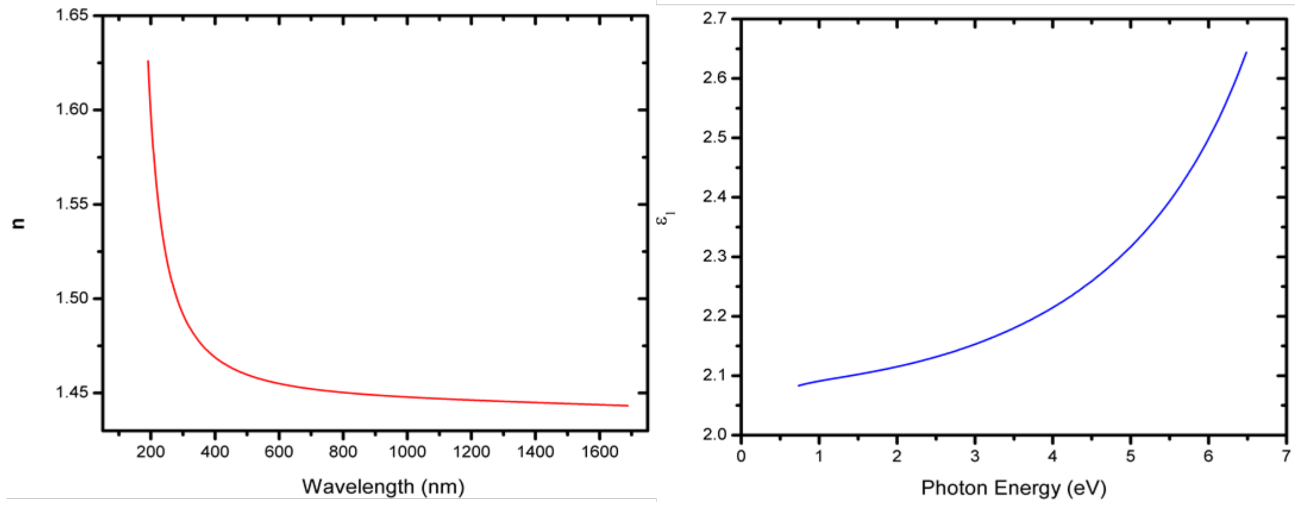

Figure A3.5. Optical constants (n and ϵ_1) obtained for PEG.

المنارة للاستشارات
www.manaraa.com

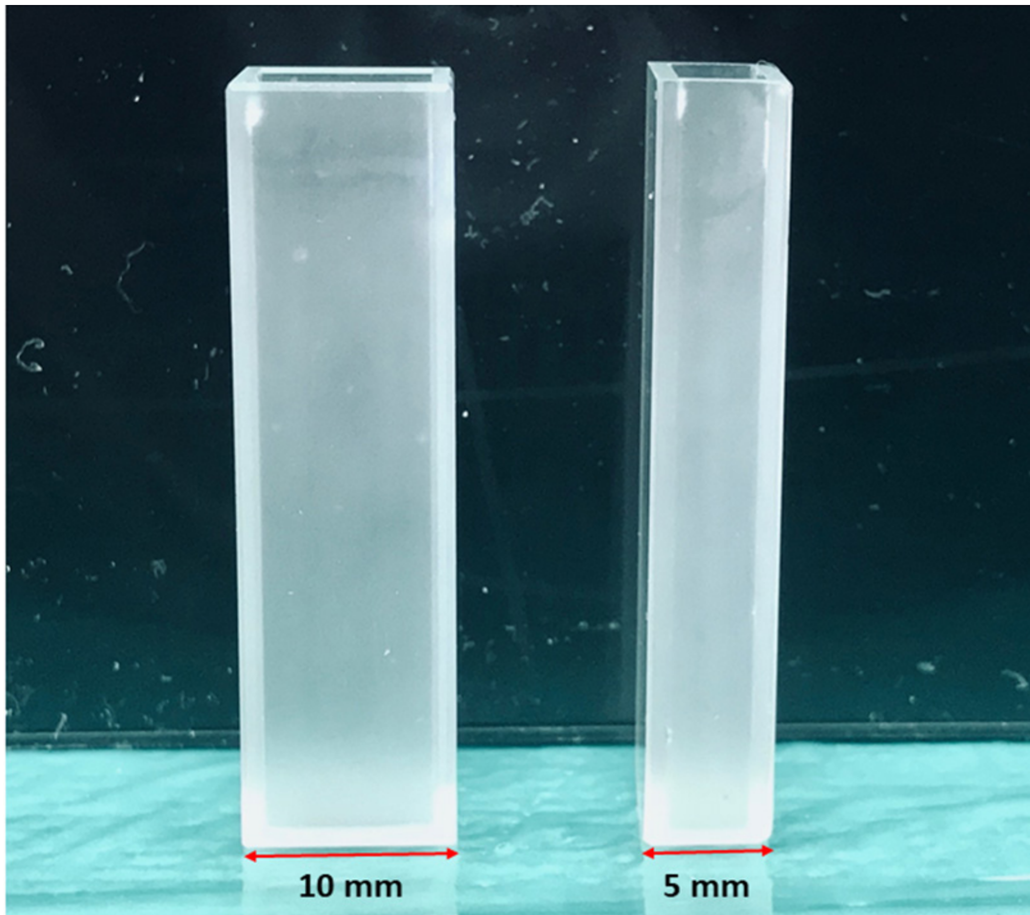

Figure A3.6. Pictures of two fused silica cuvettes used in this study.

المنارة للاستشارات
www.manaraa.com

A3.11 References

1. Allen, C.; Dos Santos, N.; Gallagher, R.; Chiu, G. N.; Shu, Y.; Li, W. M.; Johnstone, S. A.; Janoff, A. S.; Mayer, L. D.; Webb, M. S.; Bally, M. B., Controlling the physical behavior and biological performance of liposome formulations through use of surface grafted poly(ethylene glycol). *Biosci Rep* **2002,** *22* (2), 225-250.
2. del Pino, P.; Yang, F.; Pelaz, B.; Zhang, Q.; Kantner, K.; Hartmann, R.; Martinez de Baroja, N.; Gallego, M.; Möller, M.; Manshian, B. B.; Soenen, S. J.; Riedel, R.; Hampp, N.; Parak, W. J., Basic Physicochemical Properties of Polyethylene Glycol Coated Gold Nanoparticles that Determine Their Interaction with Cells. *Angew. Chem. Int. Ed.* **2016,** *55* (18), 5483-5487.
3. Harris, J. M.; Sedaghat-Herati, M. R.; Sather, P. J.; Brooks, D. E.; Fyles, T. M., Synthesis of New Poly(Ethylene Glycol) Derivatives. In *Poly(Ethylene Glycol) Chemistry: Biotechnical and Biomedical Applications*, Harris, J. M., Ed. Springer US: Boston, MA, 1992; pp 371-381.
4. French, A. C.; Thompson, A. L.; Davis, B. G., High-Purity Discrete PEG-Oligomer Crystals Allow Structural Insight. *Angew. Chem. Int. Ed.* **2009,** *48* (7), 1248-1252.
5. Winger, M.; de Vries, A. H.; van Gunsteren, W. F., Force-field dependence of the conformational properties of α,ω-dimethoxypolyethylene glycol. *Mol. Phys.* **2009,** *107* (13), 1313-1321.
6. Ottani, S.; Vitalini, D.; Comelli, F.; Castellari, C., Densities, Viscosities, and Refractive Indices of Poly(ethylene glycol) 200 and 400 + Cyclic Ethers at 303.15 K. *J. Chem. Eng. Data* **2002,** *47* (5), 1197-1204.
7. Grøtli, M.; Gotfredsen, C. H.; Rademann, J.; Buchardt, J.; Clark, A. J.; Duus, J. Ø.; Meldal, M., Physical Properties of Poly(ethylene glycol) (PEG)-Based Resins for Combinatorial Solid Phase Organic Chemistry: A Comparison of PEG-Cross-Linked and PEG-Grafted Resins. *J. Comb. Chem.* **2000,** *2* (2), 108-119.
8. Yasmin, M.; Gupta, M., Density, Viscosity, Velocity and Refractive Index of Binary Mixtures of Poly(Ethylene Glycol) 200 with Ethanolamine, m-Cresol and Aniline at 298.15 K. *J. Solution Chem.* **2011,** *40* (8), 1458.
9. Harris, J. M., Introduction to Biotechnical and Biomedical Applications of Poly(Ethylene Glycol). In *Poly(Ethylene Glycol) Chemistry: Biotechnical and Biomedical Applications*, Harris, J. M., Ed. Springer US: Boston, MA, 1992; pp 1-14.
10. Zalipsky, S.; Lee, C., Use of Functionalized Poly(Ethylene Glycol)s for Modification of Polypeptides. In *Poly(Ethylene Glycol) Chemistry: Biotechnical and Biomedical Applications*, Harris, J. M., Ed. Springer US: Boston, MA, 1992; pp 347-370.
11. Liang, J.; Li, L.; Chen, D.; Hajagos, T.; Ren, Z.; Chou, S. Y.; Hu, W.; Pei, Q., Intrinsically stretchable and transparent thin-film transistors based on printable silver nanowires, carbon nanotubes and an elastomeric dielectric. *Nat. Commun.* **2015,** *6*, 7647.
12. Pashankar, D. S.; Loening-Baucke, V.; Bishop, W. P., Safety of Polyethylene Glycol 3350 for the Treatment of Chronic Constipation in Children. *Arch. Pediatr. Adolesc. Med.* **2003,** *157* (7), 661-664.
13. Inada, Y.; Takahashi, K.; Yoshimoto, T.; Ajima, A.; Matsushima, A.; Saito, Y., Application of polyethylene glycol-modified enzymes in biotechnological processes: organic solvent-soluble enzymes. *Trends Biotechnol.* **1986,** *4* (7), 190-194.
14. Haag, R.; Kratz, F., Polymer Therapeutics: Concepts and Applications. *Angew. Chem. Int. Ed.* **2006,** *45* (8), 1198-1215.

المنارة للاستشارات
www.manaraa.com

15. Nucci, M. L.; Shorr, R.; Abuchowski, A., The therapeutic value of poly(ethylene glycol)-modified proteins. *Adv. Drug Deliv. Rev.* **1991,** *6* (2), 133-151.
16. Wolosewick, J. J., The application of polyethylene glycol (PEG) to electron microscopy. *J. Cell Biol.* **1980,** *86* (2), 675.
17. Johs, B.; Woollam, J. A.; Herzinger, C. M.; Hilfiker, J. N.; Synowicki, R. A.; Bungay, C. L. In *Overview of variable-angle spectroscopic ellipsometry (VASE): II. Advanced applications*, SPIE's International Symposium on Optical Science, Engineering, and Instrumentation, SPIE: 1999; p 30.
18. Woollam, J. A.; Johs, B. D.; Herzinger, C. M.; Hilfiker, J. N.; Synowicki, R. A.; Bungay, C. L. In *Overview of variable-angle spectroscopic ellipsometry (VASE): I. Basic theory and typical applications*, SPIE's International Symposium on Optical Science, Engineering, and Instrumentation, SPIE: 1999; p 26.
19. Hilfiker, J. N.; Pribil, G. K.; Synowicki, R.; Martin, A. C.; Hale, J. S., Spectroscopic ellipsometry characterization of multilayer optical coatings. *Surf. Coat. Technol.* **2019,** *357*, 114-121.
20. Synowicki, R. A.; Pribil, G. K.; Cooney, G.; Herzinger, C. M.; Green, S. E.; French, R. H.; Yang, M. K.; Burnett, J. H.; Kaplan, S., Fluid refractive index measurements using rough surface and prism minimum deviation techniques. *J. Vac. Sci. Technol, B* **2004,** *22* (6), 3450-3453.
21. Synowicki, R. A., Suppression of backside reflections from transparent substrates. *Phys. Status Solidi C* **2008,** *5* (5), 1085-1088.
22. Otanicar, T. P.; Phelan, P. E.; Golden, J. S., Optical properties of liquids for direct absorption solar thermal energy systems. *Solar Energy* **2009,** *83* (7), 969-977.
23. Li, X. C.; Zhao, J. M.; Liu, L. H.; Tan, J. Y., Optical properties of edible oils within spectral range from 300 to 2500 nm determined by double optical pathlength transmission method. *Appl. Opt.* **2015,** *54* (13), 3886-3893.
24. Roychowdhury, T.; Cushman, C. V.; Synowicki, R. A.; Linford, M. R., Polydimethylsiloxane: Optical properties from 191 to 1688 nm (0.735–6.491 eV) of the liquid material by spectroscopic ellipsometry. *Surf. Sci. Spectra* **2018,** *25* (2), 026001.
25. Roychowdhury, T.; Jain, V.; Synowicki, R. A.; Linford, M. R., Special considerations for analyzing liquids by spectroscopic ellipsometry. *Vac. Technol. Coat.* **2018,** *December*, 30-34.
26. Binboga, N.; Kisakürek, D.; Baysal, B. M., Effect of molecular weight on the refractive index increments of polystyrene, poly(ethylene glycol), poly(propylene glycol), and poly(dichlorophenylene oxide) in solution. *J. Poly. Sci.* **1985,** *23* (5), 925-931.
27. Herzinger, C. M.; Johs, B.; McGahan, W. A.; Woollam, J. A.; Paulson, W., Ellipsometric determination of optical constants for silicon and thermally grown silicon dioxide via a multi-sample, multi-wavelength, multi-angle investigation. *J. Appl. Phys.* **1998,** *83* (6), 3323-3336.
28. Khardani, M.; Bouaïcha, M.; Bessaïs, B., Bruggeman effective medium approach for modelling optical properties of porous silicon: comparison with experiment. *Phys. Status Solidi C* **2007,** *4* (6), 1986-1990.
29. Cushman, C. V.; Sturgell, B. A.; Martin, A. C.; Lunt, B. M.; Smith, N. J.; Linford, M. R., Eagle XG® glass, optical constants from 230 to 1690 nm (0.73 - 5.39 eV) by spectroscopic ellipsometry. *Surf. Sci. Spectra* **2016,** *23* (1), 55-60.
30. Cushman, C. V.; Johnson, B. I.; Martin, A.; Lunt, B. M.; Smith, N. J.; Linford, M. R., Eagle XG® glass: Optical constants from 196 to 1688 nm (0.735–6.33 eV) by spectroscopic ellipsometry. *Surf. Sci. Spectra* **2017,** *24* (2), 026001.

المنارة للاستشارات
www.manaraa.com

Appendix 4: A Tutorial on Spectroscopic Ellipsometry (SE), 2. The Cauchy Model

A4.1 Statement of Attribution

This document was originally published as two separate articles. The details of these two articles are as follows: Shah, D.; Patel, D. I.; Hilfiker, J. N.; Linford, M. R., A tutorial on spectroscopic ellipsometry (SE), 2. the Cauchy model. *Vacuum Coating & Technology* May **2019**, *20*(5), 29-33. Some information fields are modified to improve its readability in this format. We refer readers to the original document for complete sample, instrument information, and spectral features.

A4.2 Introduction

Ellipsometry is an important tool for analyzing surfaces.[1-3] It involves measuring the change in polarization of polarized light when it reflects from and possibly passes through a surface. Spectroscopic ellipsometry (SE) involves making ellipsometric measurements at multiple wavelengths of light. In some cases, especially when films are thicker, additional, useful, information is obtained by performing ellipsometry at multiple angles. At each wavelength, SE measures the parameters psi (Ψ), which is the ratio of the amplitudes of the p- and s-polarized light, and delta (Δ), which is the phase difference between them.

Most ellipsometric analysis involves the creation of models and a subsequent optimization of the model parameters to obtain agreement between the experimental and theoretical data. SE is very often used to determine film thicknesses and the optical constants of substrates and films. In addition, SE can yield surface roughness values, concentrations of dopants, material conductivity, the thicknesses of interfacial layers, and information about material

المنارة للاستشارات
www.manaraa.com

anisotropy and grading. Most surface labs have at least one ellipsometer (in the Linford lab at BYU we regularly use two different instruments), and ellipsometry is often used in conjunction with other surface analytical techniques, such as X-ray photoelectron spectroscopy (XPS), time-of-flight secondary ion mass spectrometry (ToF-SIMS), low energy ion scattering (LEIS), and atomic force microscopy (AFM), etc.

A4.3 Instrumentation

Because of its speed and convenience (it is fast, almost always non-destructive, almost always performed in the air, and often requires no sample preparation), it is often the first technique used to analyze a thin film. Since SE is a ratiometric technique, (i) it is insensitive to fluctuations in light intensity from the source, (ii) it doesn't require calibration of light sources, and (iii) for in situ measurements, it is insensitive to a little contamination on instrument windows. While SE data can usually be collected very quickly – often within a few seconds, the data analysis that follows can be fairly involved. In this article we discuss one of the classic problems that most people doing ellipsometry will encounter many times – the analysis of a transparent film on a well-defined substrate like a silicon wafer.

In particular, we focus on a well-known and simple model for determining the optical constants of transparent films: The Cauchy model. The Cauchy relationship (Equation 1) is one of the most common dispersion models used in ellipsometry.[2] In general, it has good validity if λ is not too large. In the case that λ does become quite large, the values of n will dip down and a Sellmeier model will be more appropriate for modeling $n(\lambda)$. This is the third article in a series we are writing on spectroscopic ellipsometry. The first consisted of a tutorial on spectroscopic

www.manaraa.com

ellipsometry,[4] and the second described a method for determining the thicknesses of thin oxide layers on semiconductor substrates.[5]

A4.4 Principles of Ellipsometry

We begin with a simple observation, which is that the optical constants of transparent materials are often shaped like a ski. For example, **Figure 1** shows the optical constants of SiO_2, Al_2O_3, and ZrO_2. In each case, we see a rise in n, the index of refraction, towards shorter wavelengths (higher energies) and a leveling out of the optical constants towards longer wavelengths. Figure 1 also helps us understand that the optical constants of different materials can differ in magnitude and shape. The general 'ski' shape we see in Figure 1 is often well matched by the Cauchy dispersion model, which can be expressed as follows:

$$(1) \qquad n(\lambda) = A + \frac{B}{\lambda^2} + \frac{C}{\lambda^4}.$$

Here, A, B, and C are fit parameters that control the shape of $n(\lambda)$. In particular, A is the index of refraction of the material at long wavelengths, i.e., as λ becomes large, λ^2 and λ^4 become very large and cause $n(\lambda)$ to approach A. The parameters B and C then control the curvature of the function at shorter wavelengths. Clearly, if $B = C = 0$, n has a constant value at all wavelengths. We would say here that there is no dispersion.

Mathematically, one can see that as λ becomes smaller, C will play a more and more dominant role in determining the shape of $n(\lambda)$. That is, A controls $n(\lambda)$ at longer wavelengths, B controls the curvature of $n(\lambda)$ at moderately long wavelengths, and C more strongly affects it at short wavelengths. However, in many cases C is unnecessary – $n(\lambda)$ is often well fit with only A and B. This is somewhat remarkable.

المنارة للاستشارات
www.manaraa.com

Spectroscopic ellipsometry generally probes a material at hundreds of wavelengths, and a material will have a different value of n at each value of λ. The fact that we can describe the n values at all of these wavelengths with two or three parameters in a simple equation like Equation 1 is quite amazing. The Cauchy relationship produces a smooth line (not one with noise) that fits the values of n. This is appropriate because the real optical constants of a material cannot change abruptly, i.e., while they may have noise on them from the measurement that generated them, this noise is unphysical.

A4.5 Data Analysis in Spectroscopic Ellipsometry

Now let's suppose that we have what we believe is a transparent thin film on a substrate and that we have performed spectroscopic ellipsometry on it. How do we analyze the data? The first step is probably to take a look at it. A telltale sign of a transparent thin film is a series of peaks/oscillations in Ψ (see **Figure A4.3** – note that there are oscillations in Δ too).

The implication here is that you are getting constructive and destructive interference from light reflecting off of the top of the film and from the film-substrate interface, where the closer the spacings between the oscillations, the thicker is the film. Interference fringes occur in transparent regions of materials, but they disappear when a material becomes absorbing, i.e., when the light is no longer able to penetrate the film, reflect from the film-substrate interface, and pass through the film again so that it can interfere with the light reflected from the top of the film. Figure 3 shows an example of this phenomenon.

We will now consider the data set in **Figure A4.2**, which came from a PECVD film of SiO_2 on silicon. We will build a model for this thin film system, but we will not use a Cauchy

المنارة للاستشارات
www.manaraa.com

dispersion relationship in our first attempt. Rather, we will base our model on what we know about our material. Accordingly, we assign our substrate to be silicon, where we use here the optical constants of silicon in our instrument software (see **Figure A4.2**). The optical constants of crystalline silicon are very well known so the values in the software should be a good representation of our substrate's optical constants.

Next, we look for the optical constants of PECVD SiO_2 in our instrument software, but the best we can find are some generic optical constants for SiO_2. However, believing that these should be moderately close to those of PECVD SiO_2, we start with them. Our next step is to manually increase the thickness of the SiO_2 layer in our model to generate a series of interference fringes that match those in the data we are trying to fit (see **Figure A4.4**).

We do this so that our fit algorithm will not fall into a local minimum that will be far from the global minimum we desire. Now that we appear to be fairly close to the true thickness of the film (the modeled, dotted lines in **Figure A4.4** were generated with a 530.0 nm SiO_2 film), we fit the experimental data using the instrument software using this starting point, where we allow the thickness of the SiO_2 film to vary in the model. The result of this fit is shown in **Figure A4.5**. The SiO_2 film thickness predicted by this model is 528.36 nm with a mean squared error (MSE) of 86.787. (We recognize that we are probably keeping too many significant figures in many of the numbers in this article. We do this to report exactly the results from the instrument software, not to claim that all the digits in these numbers have physical meaning.)

It seems like we've made some progress. We have a model that probably matches the physical nature of our film fairly well. After optimizing it, we get experimental and theoretical values of Ψ that match moderately well. At this point, we would probably be pretty confident that our SiO_2 film is somewhere around 530 nm thick. However, most people that do spectroscopic

المنارة للاستشارات
www.manaraa.com

ellipsometry would probably consider these results to be mediocre at best. That is, there is noticeable disagreement between the theoretical and experimental data, and the mean squared error (MSE) for the fit is pretty high: 86.787. Could we improve these results? We recall that we used the optical constants of SiO_2 that we found in the instrument software to model those of our film and that the optical constants of thin films depend on how they are deposited. Based on the interference fringes we are seeing, and what we know about SiO_2, we guess that our film is probably transparent over the entire wavelength region of this measurement, so we apply the Cauchy equation as a model for its optical constants.

We begin by allowing A and B in the Cauchy equation (**Equation 1**) and also the film thickness to vary. We use A = 1.45 as a starting point for this parameter because this is close to the expected index of refraction of SiO_2. When we allow the instrument software to fit the experimental data using this starting point, we get a significantly improved result. Our experimental and theoretical values for Ψ match each other more closely than before, and the MSE for the fit has dropped to 33.300 (see Figure 7). The film thickness predicted by this modeling is 506.14 nm. An implication of these results is that the previous model that used the optical constants of SiO_2 from the instrument software gave only a moderately reasonable estimate for the thickness of the SiO_2 film.

As a final step in our modeling, we 'turn on' the C parameter to see if it improves our results. In this case, allowing this parameter to vary in the model improves our fit significantly (see **Figure A4.7**). While the SiO_2 film thickness hardly changed (it is now 506.11 nm), the MSE for the fit has dropped to 19.749, which points to a much better fit and further implies that the C parameter in the Cauchy model should be used in this modeling. **Figure A4.8** shows the optical constants of this Cauchy model, which we propose are a good estimate for those of the thin film

المنارة للاستشارات
www.manaraa.com

we have been examining. They predict a value for n of just under 1.5 in the visible region of the spectrum, which is not unreasonable. Note again their ski-like shape. We can improve this model a little more by adding a roughness layer to the film. However, this will be the topic of a different article. For now, we hope that this article has helped clarify some of the reasons for using a dispersion relationship to model the optical constants of a thin film.

Here are two notes on subtleties associated with this modeling. First, we deliberately started our modeling with a two-parameter (A and B) Cauchy before considering the three-parameter (A, B, and C) model. In general, it is better to gradually introduce free parameters into a model rather than let a large number of them vary right from the start. Second, you will notice that we focused on Ψ in our fitting, ignoring Δ. This was for convenience. Plots of all the Ψ and Δ data obtained at multiple angles of incidence in an ellipsometric analysis can be very busy (see **Figure A4.2**), so it is often easier to work with a subset of the data.

www.manaraa.com

A4.6 Figures

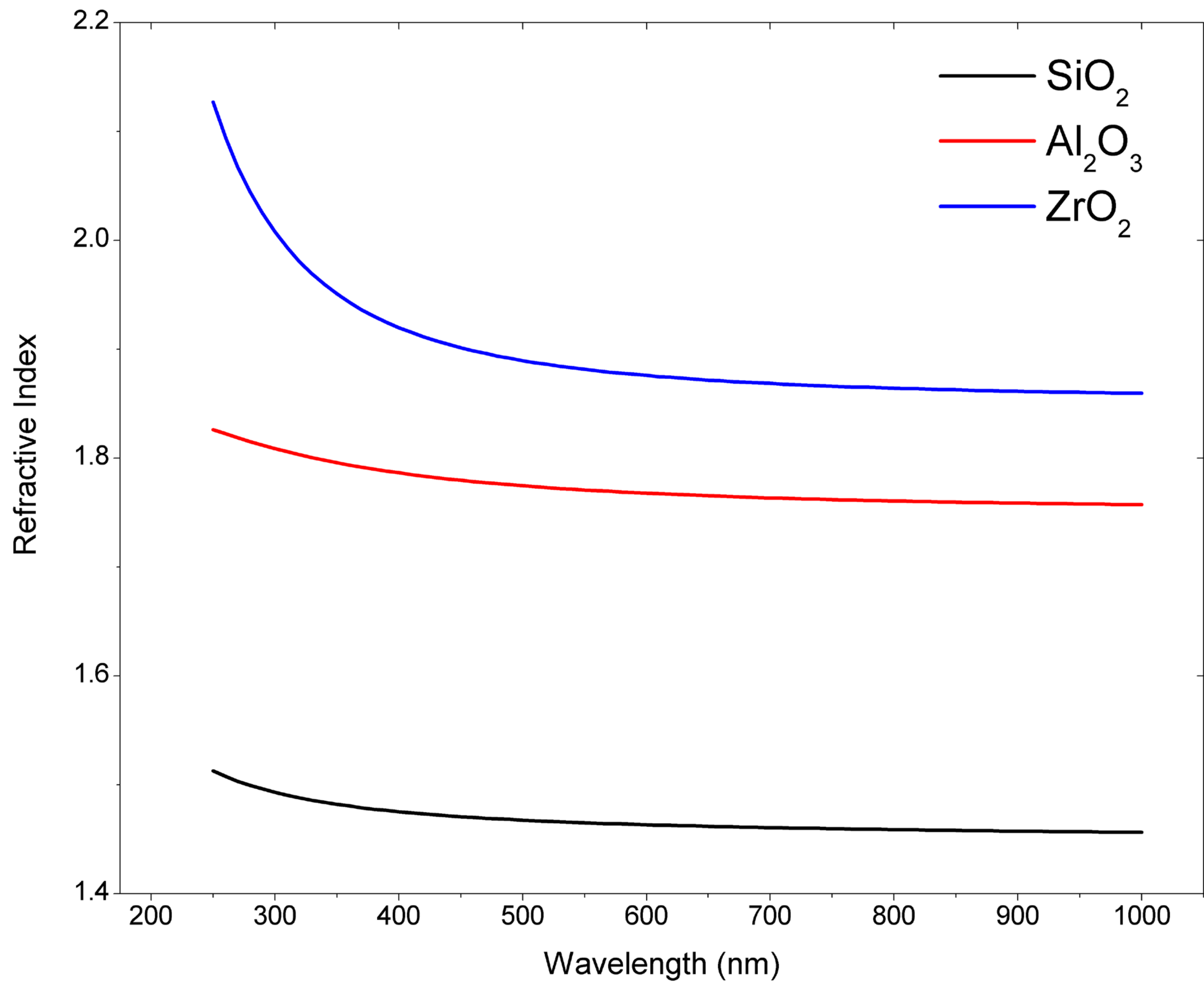

Figure A4.1. Optical constants of three dielectrics: SiO_2, Al_2O_3, and ZrO_2, modeled using the Cauchy model.

www.manaraa.com

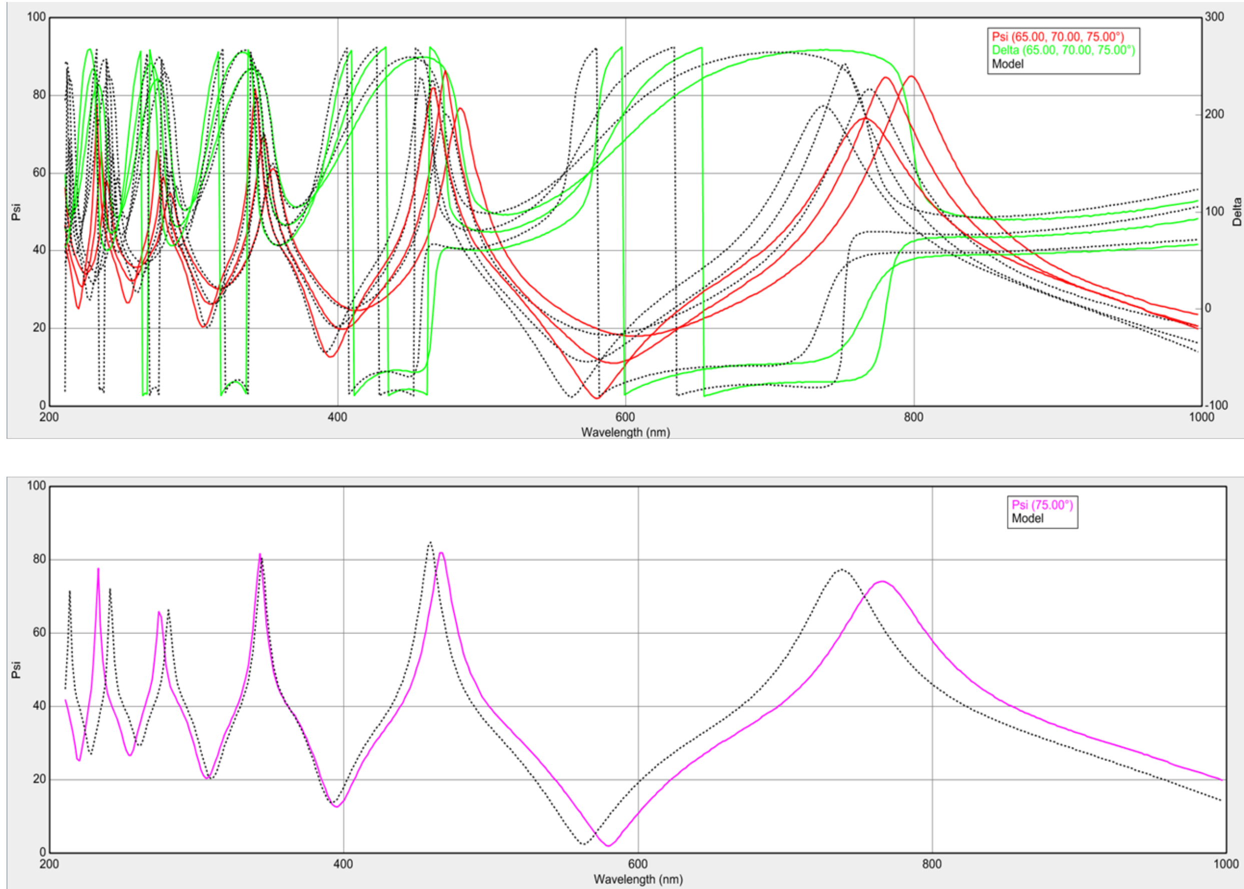

Figure A4.2. Ψ and Δ values (colored lines) and an initial attempt to fit them (grey lines) from a film of PECVD SiO_2 on silicon. The data were collected at three different angles (65°, 70°, and 75°), and over a moderately wide wavelength range (210.7 - 997.5 nm). (Top) All the Ψ and Δ data. (Bottom) The Ψ data collected at 75° (purple line) and an initial attempt to fit it (grey line).

المنارة للاستشارات
www.manaraa.com

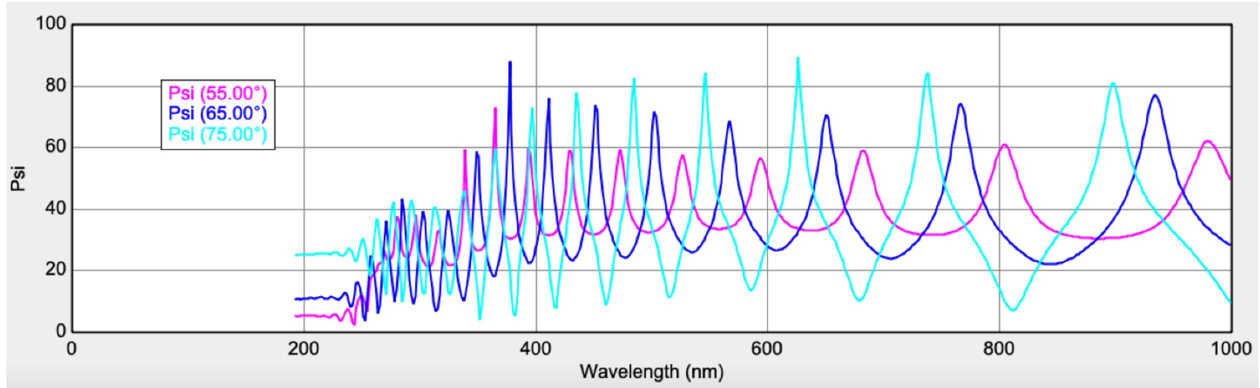

Figure A4.3. Ellipsometric (Ψ) data from a film of YbF_3 on Ge. The decrease in oscillations (interference fringes) at shorter wavelengths suggests this film is absorbing light here.

المنارة للاستشارات
www.manaraa.com

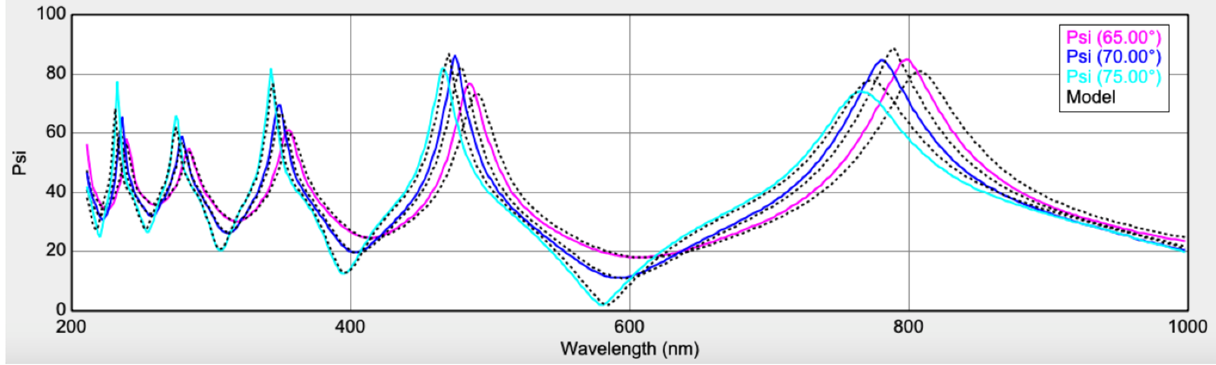

Figure A4.4. Experimental values of Ψ (colored lines) and an initial attempt at fitting them (dotted lines), which consisted of manually increasing the thickness of the SiO_2 film in the model in Figure 4 until the experimental data and theoretical curves matched reasonably well. The thickness of the SiO_2 film in the model here was 530.0 nm.

المنارة للاستشارات
www.manaraa.com

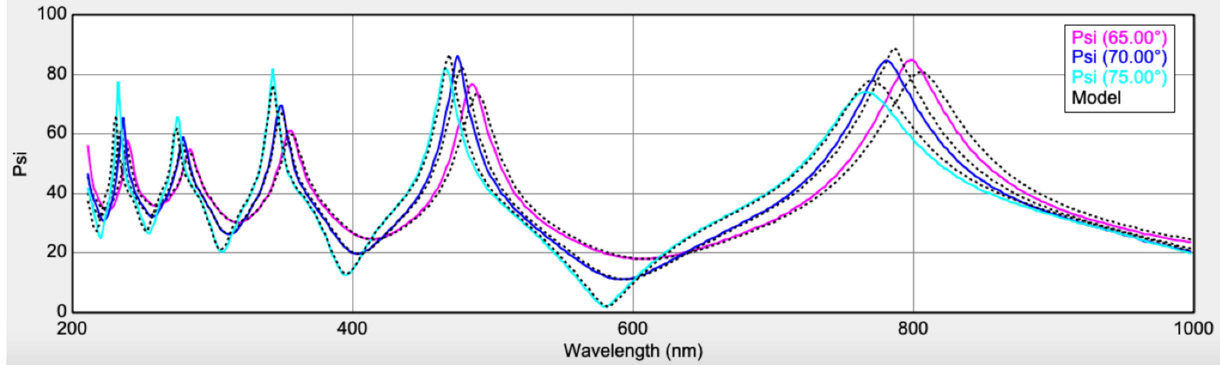

Figure A4.5. Experimental values of Ψ (colored lines) and an attempt at fitting them (dotted lines) using the model in Figure 4. This modeling was performed with the instrument software, where the thickness of the SiO_2 layer was allowed to vary and the starting point for this fit was the conditions outlined in the caption to Figure 5. The thickness predicted by this modeling was 528.36 nm with a mean squared error (MSE) of 86.787.

المنارة للاستشارات
www.manaraa.com

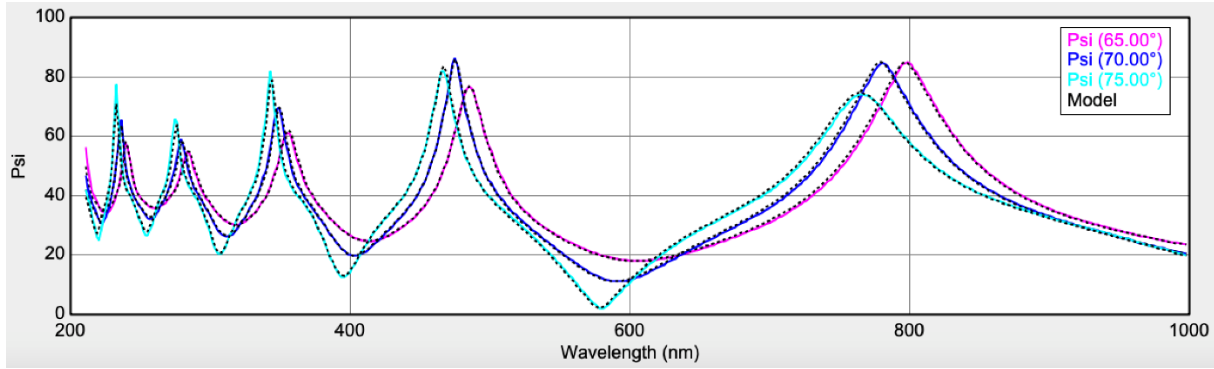

Figure A4.6. Experimental values of Ψ (colored lines) and an attempt at fitting them (dotted lines) based on a two-parameter (A and B) Cauchy model. The SiO_2 film thickness predicted by this modeling was 506.14 nm with a mean squared error (MSE) of 33.300.

www.manaraa.com

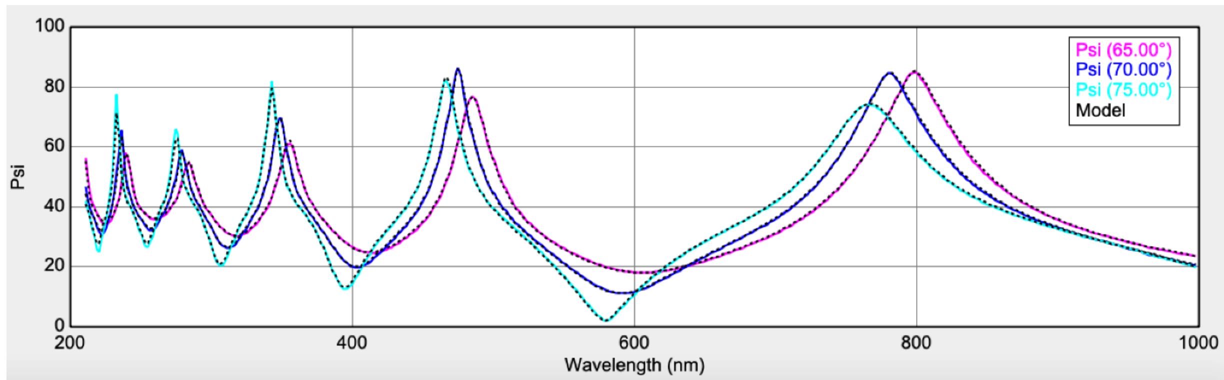

Figure A4.7. Experimental values of Ψ (colored lines) and an attempt at fitting them (dotted lines) based on a three-parameter (A, B, and C) Cauchy model. The SiO_2 film thickness predicted by this modeling was 506.11 nm with a mean squared error (MSE) of 19.749.

المنارة للاستشارات
www.manaraa.com

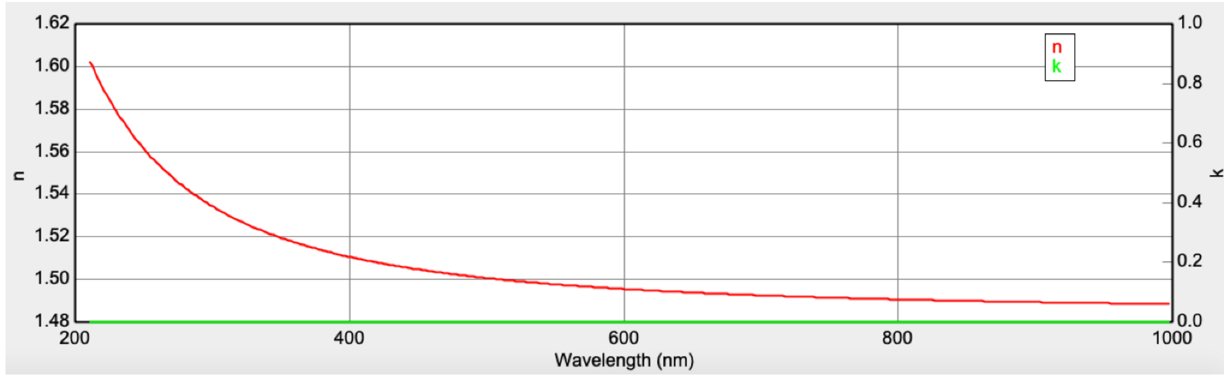

Figure A4.8. Optical constants predicted by the three-parameter Cauchy model for the SiO_2 film on Si considered in this article.

المنارة للاستشارات
www.manaraa.com

A4.7 References

1. J. A. Woollam; B. Johs; C. M. Herzinger; J. N. Hilfiker; R. Synowicki; Bungay, C. L., Overview of Variable Angle Spectroscopic Ellispsometryn (VASE), Part 1: Basic Theory and Typical Applications. *Crt. Rev. Opt. Sci. Technol.* **2000,** *72*, 1-24.
2. Tompkins, H. G.; Hilfiker, J. N., *Spectroscopic Ellipsometry: Practical Application to Thin Film Characterization.* Momentum Press: New York, 2016.
3. Fujiwara, H., *Spectroscopic Ellipsometry: Principles and Applications*. John Wiley & Sons: New York, 2008; Vol. 1.
4. B. I. Johnson; J. N. Hilfiker; M. R. Linford, Some Fundamentals of Spectroscopic Ellipsometry. *Vacu. Technol. Coatings* **2019,** *March*, 31-36.
5. T. G. Avval; B. I. Johnson; J. N. Hilfiker; Linford, M. R., A Tutorial on Spectroscopic Ellipsometry (SE), 1. Determination of the Thicknesses of Thin Oxide Layers on Semiconductor Substrates. *Vacu. Technol. Coatings* **2019,** *April 29-33.*

المنارة للاستشارات

www.manaraa.com

Appendix 5: A Tutorial on Spectroscopic Ellipsometry (SE), 4. Using the 'Angle Offset' when fitting Ellipsometric Data

A5.1 Statement of Attribution

This document was originally published as Shah, D.; Patel, D. I.; Hilfiker, J. N.; Johs, B. D.; Linford, M. R., A tutorial on spectroscopic ellipsometry (SE), 4. Using the 'angle offset' when fitting ellipsometric data. *Vacuum Coating & Technology* July **2019**, *20*(7), 33-36. Some information fields are modified to improve its readability in this format. We refer readers to the original document for complete sample, instrument information, and spectral features.

A5.2 Introduction

Ellipsometry measures the change in polarization state of light when it is reflected from or transmitted through a sample surface.[1-7] For most samples, i.e., samples that are optically isotropic, this change in polarization state requires measurements at an oblique angle of incidence. At normal (or near-normal) angles, the p- and s- polarization modes become degenerate, i.e., they are the same, and the polarization state of the reflected beam is essentially unaltered. At oblique angles, p- and s- polarized light reflect differently from samples, which causes a change in polarization upon reflection.

Therefore, an oblique angle of incidence is required for ellipsometric measurements (see **Figure A5.1**), and accurately knowing the angle of incidence is important for ellipsometric data analysis. To provide additional characterization of a sample, the angle of incidence of the light beam in an ellipsometric measurement can be changed. This technique is referred to as Variable Angle Spectroscopic Ellipsometry (VASE).[5, 8]

المنارة للاستشارات
www.manaraa.com

Since ellipsometric measurements are very sensitive to the angle of incidence, the "Angle" can also be used as a fit parameter in data analysis. For some samples, a small change in the angle can lead to significant changes in the overall fit and thickness of a film. We will demonstrate this phenomenon using the data in **Figure A5.5**, which was measured from a native oxide coated silicon wafer in a sputter deposition chamber with windows pointed nominally at 70° relative to the sample surface. We can fit this data with a standard model incorporating known optical constants for both the silicon substrate and the native oxide in much the manner described in our second article.[5] While the nominal angle is defined, the window alignment is not perfect and the actual measurement beam deviates from this angle.

When we model the data using our nominal angle of 70°, we get a decent fit with an MSE of 7.78 and the thickness of the native oxide film is determined to be 1.38 nm (see **Figure A5.2**). However, when we fit the angle of incidence using the 'angle offset' feature in the software, we get a better match to the data with an MSE of 2.30 and a native oxide thickness of 1.49 nm (see Figure 3). Even though the angle offset is a few tenths of a degree, it has a significant impact on the MSE and the overall fit quality. Once the angle of incidence has been resolved for the chamber, it can be fixed for future measurements of samples where the optical constants are unknown. This is a common "calibration" procedure to determine an accurate angle of incidence when it is not well known.

We have access to an FS-1 in situ ellipsometer, which can collect data while a thin film is being deposited in our atomic layer deposition (ALD) system.[10, 11] In the FS-1 software, we can fit the angle of incidence at which the data is collected. This is a very important feature for in situ measurements, since it is not possible to directly measure the angle of the ellipsometer beam with respect to the sample when the optics are mounted on the chamber. Ellipsometer viewports

المنارة للاستشارات
www.manaraa.com

are mounted on the chamber at a nominal angle, but the *actual* angle of incidence depends on the height and tilt of the internally mounted sample. The in situ alignment procedure accommodates the position of the sample by tilting the source and detector optics such that the beam reflected from the sample is centered on the detector aperture, and the detector optics are aligned to the beam.

The actual angle of incidence is then determined by acquiring the ellipsometric data on a known sample (typically a native oxide terminated silicon wafer), and fitting for the "Angle" parameter using an analysis model with known optical constants (this is shown in **Figure A5.3**). Note that in the optical model, temperature-dependent optical constants are required for the Si substrate,[12] as the ALD process occurs at higher temperatures. To minimize correlation between the substrate temperature and the angle of incidence fit parameters, the temperature was fixed at the nominal value of 300 °C (as reported by the thermocouple in the substrate heater block). In this case, the angle of incidence was determined to be 70.394°, which is near the nominal design angle (70°) for the ellipsometer viewports.

Once the in situ Angle of incidence is determined, it should be *fixed* at this value for subsequent data analysis. **Figure A5.4** demonstrates the analysis of the thickness and index of refraction of the alumina film after the deposition (the data for this analysis is selected near t = 55 min). To simplify the optical model, a "Pseudo" layer was used for the substrate. The FS-1 Pseudo layer directly inverts the ellipsometry Psi and Delta values (at the specified time) into "n&k" values, using the formula shown below. Note that this formula *requires* the angle of incidence, **θ**, which should be fixed in the model to avoid parameter correlation.

المنارة للاستشارات
www.manaraa.com

$$\langle\epsilon\rangle=\langle\epsilon_1\rangle+i\langle\epsilon_2\rangle=\langle\tilde{n}\rangle^2=(\langle n\rangle+i\langle k\rangle)^2=\sin(\theta)^2\left[1+\tan(\theta)^2\left(\frac{1-\tan(\Psi)e^{i\Delta}}{1+\tan(\Psi)e^{i\Delta}}\right)^2\right]$$

The Pseudo layer combines the substrate and native oxide layer into a single "effective" substrate. This is an approximation, but it is valid for many applications, and provides multiple advantages: 1) the optical model is simplified, 2) temperature dependent optical constants are not required for the substrate, and 3) small residual errors in the ellipsometric parameters are cancelled. However, it is important to emphasize that the angle of incidence must be determined and fixed before using the Pseudo layer to determine the effective optical constants for the substrate. Using the Pseudo layer in the example of **Figure A5.5** resulted in an excellent data fit, as quantified by the low Fit Diff value of 0.0005, with alumina film thickness and index values of 8.59 nm and 1.62, respectively.

A5.3 Conclusions

Angle offset can be a useful and important fit parameter when analyzing ellipsometric data. In fact, it is required when determining the actual angle of incidence for in situ ellipsometry measurements. However, unless the optical constants of the substrate are known, it is often best to leave the angle fixed at its nominal value.

المنارة للاستشارات
www.manaraa.com

A5.4 Figures

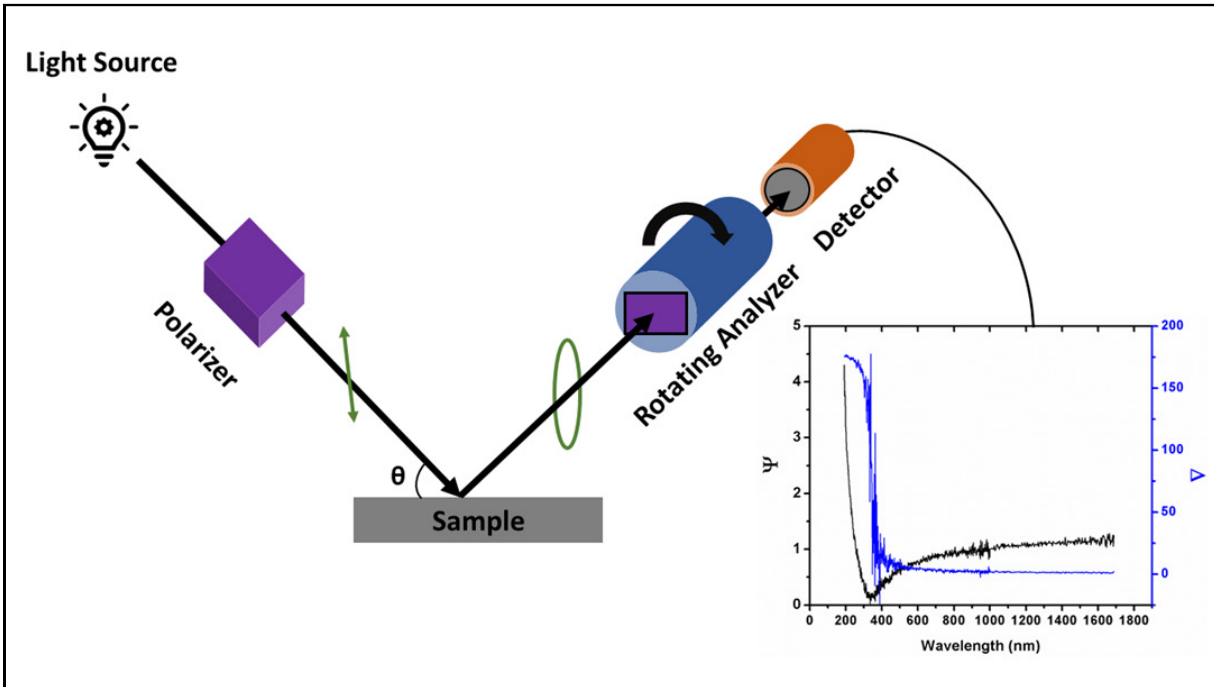

Figure A5.1. Simplified model of an ellipsometer.

www.manaraa.com

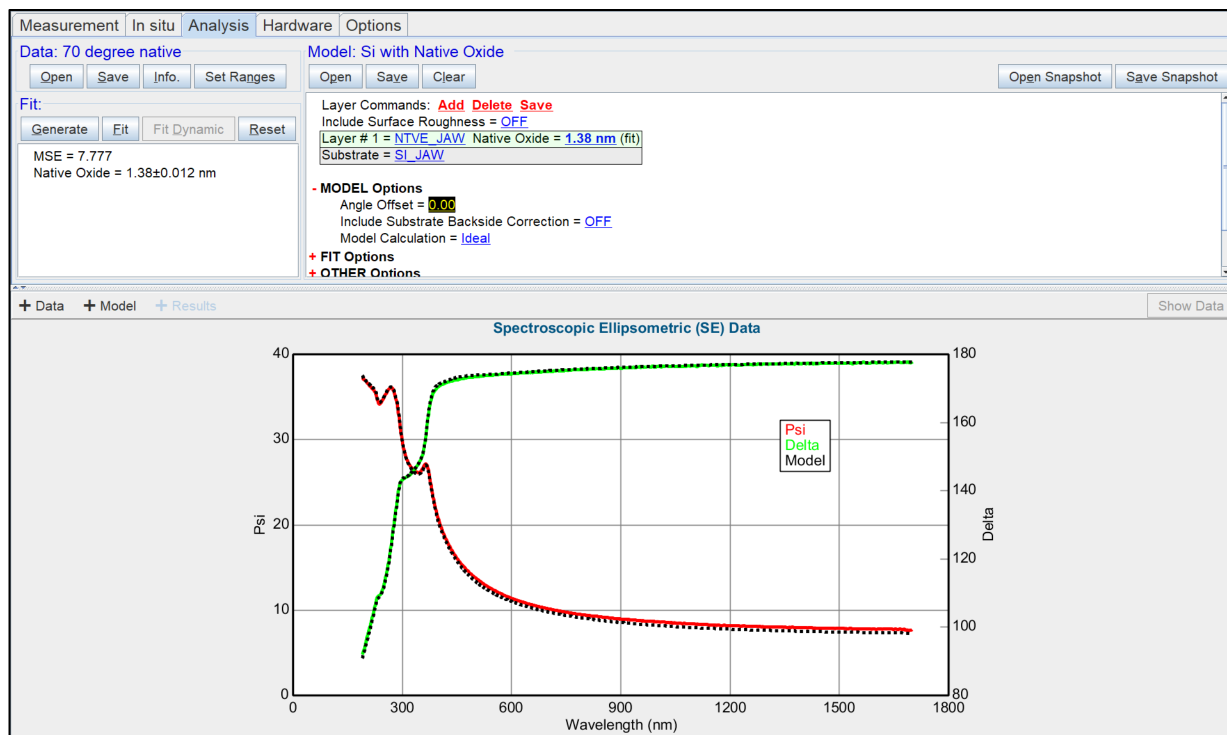

Figure A5.2. Analysis of a 'native oxide' film on a silicon shard using the 'NTVE_JAW' model. Note that the angle offset was fixed at 0.00°. The thickness of the film was 1.38 nm and the MSE for the fit was 7.78.

المنارة للاستشارات
www.manaraa.com

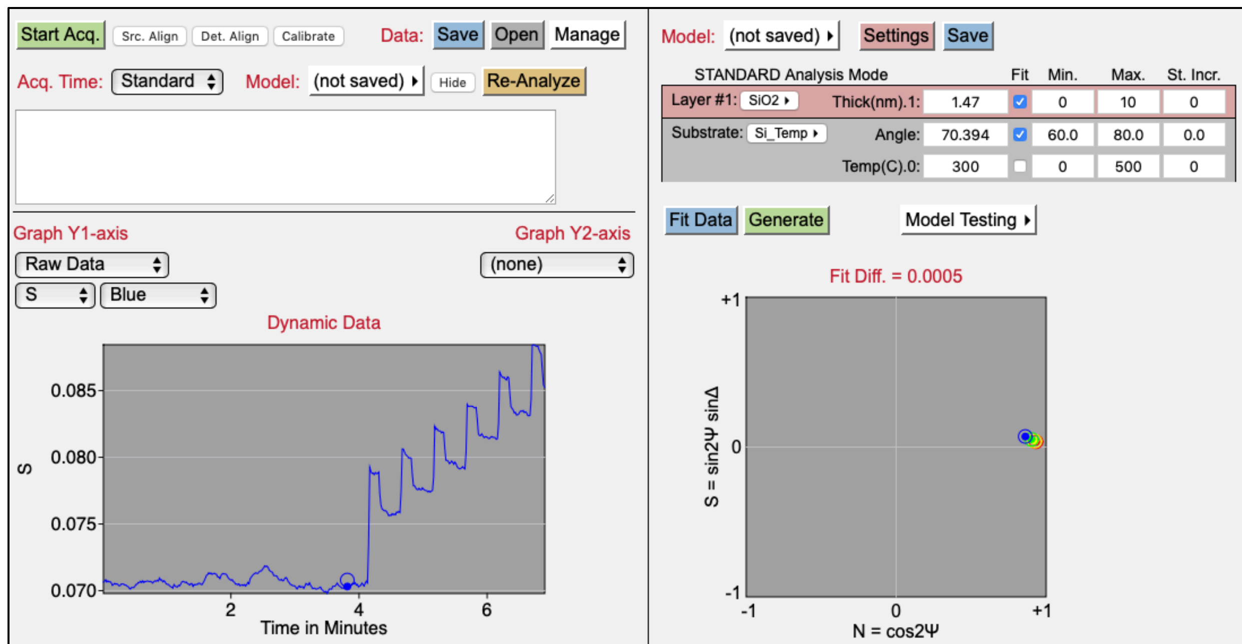

Figure A5.3. Determination of the in situ angle of incidence. We are fitting a data point just before the alumina deposition starts by ALD (near t = 4 min). Here, the angle and native oxide layer are fit parameters, and the Si substrate temperature is fixed at the nominal value of 300 °C.

المنارة للاستشارات
www.manaraa.com

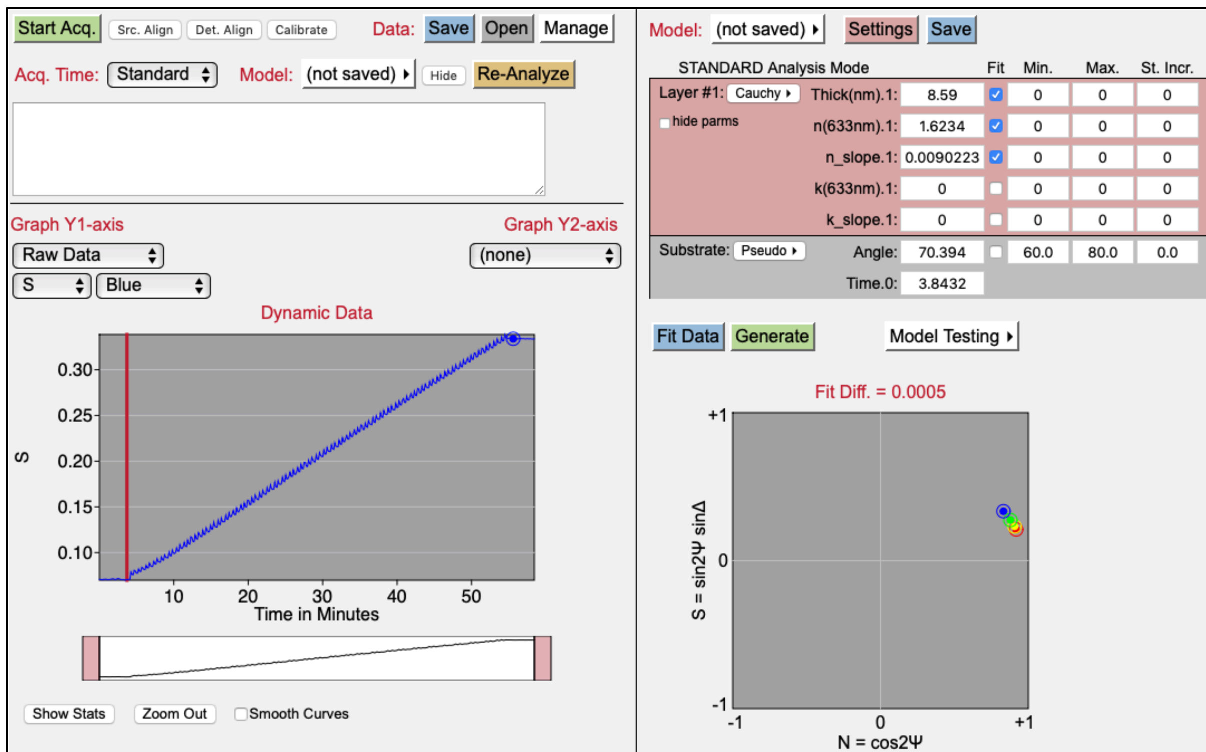

Figure A5.4. Analysis of an ALD alumina film using the FS-1 software. The Angle is *fixed* at the value determined from the model in **Figure A5.3**. The substrate "Pseudo" optical constants are determined from the data acquired immediately before the deposition is started (near t = 4 min). The alumina film thickness and Cauchy parameters for the index of refraction are selected as fitting parameters.

www.manaraa.com

A5.5 References

1. Johnson, B. I.; Hilfiker, J. N.; Linford, M. R., Some Fundamentals of Spectroscopic Ellipsometry. *Vacu. Technol. Coatings* **2019,** *March*, 31-36.
2. Avval, T. G.; Johnson, B. I.; Hilfiker, J. N.; Linford, M. R., A Tutorial on Spectroscopic Ellipsometry (SE), 1. Determination of the Thicknesses of Thin Oxide Layers on Semiconductor Substrates. *Vacu. Technol. Coatings* **2019,** *April* 29-33.
3. Shah, D.; Patel, D. I.; James N. Hilfiker; Linford, M. R., A Tutorial on Spectroscopic Ellipsometry (SE), 2. The Cauchy Model. *Vacu. Technol. Coatings* **2019,** *May*, 29-33.
4. Patel, D. I.; Shah, D.; James N. Hilfiker; Johs, B.; Linford, M. R., A Tutorial on Spectroscopic Ellipsometry (SE), 4. Surface Roughness. *Vacu. Technol. Coatings* **2019,** *June*, 32-35.
5. Woollam, J. A.; Johs, B.; Herzinger, C. M.; Hilfiker, J. N.; Synowicki, R.; Bungay, C. L., Overview of Variable Angle Spectroscopic Ellispsometryn (VASE), Part 1: Basic Theory and Typical Applications. *Crt. Rev. Opt. Sci. Technol.* **2000,** *72*, 1-24.
6. Tompkins, H. G.; Hilfiker, J. N., *Spectroscopic Ellipsometry: Practical Application to Thin Film Characterization.* Momentum Press: New York, 2016.
7. Fujiwara, H., *Spectroscopic Ellipsometry: Principles and Applications*. John Wiley & Sons: New York, 2008; Vol. 1.
8. Johs, B.; Woollam, J. A.; Herzinger, C. M.; Hilfiker, J. N.; Synowicki, R. A.; Bungay, C. L., *Overview of variable-angle spectroscopic ellipsometry (VASE): II. Advanced applications*. SPIE: 1999; Vol. 10294.
9. Zalczer, G.; Gurfein, V., Spectroscopic ellipsometry near the Brewster angle on transparent substrates. *Review of Scientific Instruments* **1992,** *63* (4), 2132-2134.
10. Shah, D.; Patel, D. I.; Avval, T. G.; Allen, N.; Johs, B. D.; Linford, M. R., Installation of an FS-1 ellipsometer on ana Atomic Layer Deposition (ALD) system. Part 1. Hardware Considerations. *Vacu. Technol. Coatings* **2019,** *Jan 2019*, 32-34.
11. Shah, D.; Patel, D. I.; Avval, T. G.; Allen, N.; Johs, B. D.; Linford, M. R., Installation of an FS-1 in situ ellipsometer on an Atomic Layer Deposition (ALD) system. Part 2. Software Considerations. *Vacu. Technol. Coatings* **2019,** *Feb 2019*, 33-36.

www.manaraa.com